National Library of Canada

Acquisitions and Bibliographic Services Branch

395 Wellington Street
Ottawa, Ontario
K1A 0N4

Bibliothèque nationale du Canada

Direction des acquisitions et des services bibliographiques

395, rue Wellington
Ottawa (Ontario)
K1A 0N4

NOTICE

The quality of this microform is heavily dependent upon the quality of the original thesis submitted for microfilming. Every effort has been made to ensure the highest quality of reproduction possible.

If pages are missing, contact the university which granted the degree.

Some pages may have indistinct print especially if the original pages were typed with a poor typewriter ribbon or if the university sent us an inferior photocopy.

Reproduction in full or in part of this microform is governed by the Canadian Copyright Act, R.S.C. 1970, c. C-30, and subsequent amendments.

AVIS

La qualité de cette microforme dépend grandement de la qualité de la thèse soumise au microfilmage. Nous avons tout fait pour assurer une qualité supérieure de reproduction.

S'il manque des pages, veuillez communiquer avec l'université qui a conféré le grade.

La qualité d'impression de certaines pages peut laisser à désirer, surtout si les pages originales ont été dactylographiées à l'aide d'un ruban usé ou si l'université nous a fait parvenir une photocopie de qualité inférieure.

La reproduction, même partielle, de cette microforme est soumise à la Loi canadienne sur le droit d'auteur, SRC 1970, c. C-30, et ses amendements subséquents.

Canada

UNIVERSITY OF ALBERTA

LAURENTIDE MELTWATER SYSTEMS: GEOMORPHIC AND SEDIMENTARY EVIDENCE

by

TRACY ANNE BRENNAND

A thesis submitted to the Faculty of Graduate Studies and Research in partial fulfilment of the requirements for the degree of Doctor of Philosophy

DEPARTMENT OF GEOGRAPHY

Edmonton, Alberta

Fall 1993

National Library of Canada
Bibliothèque nationale du Canada

Acquisitions and Bibliographic Services Branch
Direction des acquisitions et des services bibliographiques

395 Wellington Street
Ottawa, Ontario
K1A 0N4

395, rue Wellington
Ottawa (Ontario)
K1A 0N4

Your file Votre référence

Our file Notre référence

The author has granted an irrevocable non-exclusive licence allowing the National Library of Canada to reproduce, loan, distribute or sell copies of his/her thesis by any means and in any form or format, making this thesis available to interested persons.

L'auteur a accordé une licence irrévocable et non exclusive permettant à la Bibliothèque nationale du Canada de reproduire, prêter, distribuer ou vendre des copies de sa thèse de quelque manière et sous quelque forme que ce soit pour mettre des exemplaires de cette thèse à la disposition des personnes intéressées.

The author retains ownership of the copyright in his/her thesis. Neither the thesis nor substantial extracts from it may be printed or otherwise reproduced without his/her permission.

L'auteur conserve la propriété du droit d'auteur qui protège sa thèse. Ni la thèse ni des extraits substantiels de celle-ci ne doivent être imprimés ou autrement reproduits sans son autorisation.

ISBN 0-315-88439-8

Canada

Energy, Mines and Resources Canada

Énergie, Mines et Ressources Canada

Geological Survey of Canada
601 Booth Street
Ottawa, Canada
K1A 0E8

Commission géologique du Canada
601, rue Booth
Ottawa, Canada
K1A 0E8

(DRS) TEL: (613) 992-3059
FAX: (613) 992-2468

Your file Votre référence

Our file Notre référence

Sept, 9 1993

Graduate studies
University of Alberta
Edmonton Alberta

Re: Brennand/Sharpe paper

To whom it may concern:

The paper: **Ice sheet dynamics and subglacial meltwater regime inferred from form and sedimentology of glaciofluvial systems: Victoria Island, District of Franklin, NWT** was a combined effort by Tracy Brennand and David Sharpe, largely resulting from Brennands efforts. I have no problems with this paper comprising part of Ms Brennand thesis requirements. It has been accepted for publication by the Canadian Journal of Earth Sciences.

Sincerely
Dave Sharpe

Dr. D. R. Sharpe

University of Alberta Inter-departmental Correspondence

Graduate Studies
2-8 University Hall

9 September 1993

Dr. John Shaw
Department of Geography

Dear Sir/Madam,

The papers:

1. Tunnel Channels and Associated Landforms, South-Central Ontario: their implications for ice-sheet hydrology.

2. Geomorphology, sedimentology, stratigraphic context, and landform associations of the Harricana glaciofluvial complex, Abitibi region, Quebec: implications for genesis, meltwater regime and ice-sheet dynamics.

were co-authored by Tracy Brennand and myself. I give her permission for the use of this material in her thesis.

Yours sincerely,

John Shaw
Professor and Chair

JS/fm

Ministry of Natural Resources
Ministère des Richesses naturelles
Ontario

Provincial Remote Sensing Office, 90 Sheppard Ave. East, 4th Floor
North York, Ontario M2N 3A1. Tel:(416)314-1300 Fax: (416)314-1337

October 13, 1992

Ms. Tracey A. Brennand
Department of Geography
University of Alberta
Edmonton, Alberta
T6G 2H4

Dear Tracey:

I am writing in response to your request to Frank Kenny who is currently on leave for one year.

You had an inquiry regarding obtaining permission for reproducing a digital TM scene for publication and how to go about this.

You may certainly reproduce the image. I would suggest that you provide proper credit in the publication (i.e. to PRSO). The easiest and cheapest way to reproduce this image is to photograph the screen although this may not give satisfying results. Alternately, I would recommend transferring your enhanced image to tape and sending it to RADARSAT International in Vancouver for tape-to-film transcription. See enclosed price list for more information.

Sincerely,

R. Mussakowski

Richard Mussakowski
Geoscience Applications Specialist

Enc.

RM/sf

Energy, Mines and Resources Canada
Énergie, Mines et Ressources Canada

Surveys, Mapping and Remote Sensing
Levés, Cartographie et Télédétection

May 3, 1993

6040

Tracy A. Brennand
Department of Geography
University of Alberta
Edmonton, Alberta
T6G 2H4

Dear Tracy A. Brennand,

Thank you for your letter of April 25, 1993 in which you requested authorization to reproduce and publish the following photographs from the National Air Photo Library in the Canadian Journal of Earth Sciences.

Photograph numbers: A27083-123,124
A27083-189,190
A27083-104,105

The Product and Services Division authorizes the use as requested subject to the conditions listed below:

a) that the authorization is for non-exclusive use,

b) that it applies only to the photographs and publications named above,

c) that the photograph numbers (roll and frame number) appear with each photograph or part thereof each time it is used in the publication,

d) that the following copyright notice be included in the publication, either in an acknowledgements section of the publication or adjacent to each photograph. "This aerial photograph (or: "The aerial photograph on pages xx, xx and xx) c (copyright year as shown in the attached listing) Her Majesty the Queen in Right of Canada, reproduced from the collection of the National Air Photo Library with permission of Energy Mines and Resources Canada.",

e) that we be supplied, free of charge, with one copy of the publication for our library.

Canada

Products and Services Division
615 Booth Street
Ottawa, Ontario
K1A 0E9

Produits et services
615, rue Booth
Ottawa (Ontario)
K1A 0E9

This authorizaton will come into effect upon receipt of a copy of this letter signed with an acceptance by Tracy A. Brennand.

Yours truly

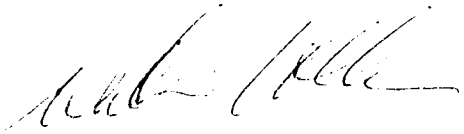

William Voller
Chief
National Air Photo Library

WV/jc

TELEPHONE (613) 995-4560
FAX (613) 995-4568

Signature	Title	Date

NATIONAL AIR PHOTO LIBRARY
PHOTOTHÈQUE NATIONALE DE L'AIR

Roll Number Numéro du rouleau	Copyright Year Année de copyright
A27083-123,124	April 25, 1987
A27083-189,190	April 25, 1987
A27083-104,105	April 25, 1987

Verified by/Vérifié par _____ Date _____

Ministry of Natural Resources
Ministère des Richesses naturelles
Ontario

INFORMATION MANAGEMENT SERVICES BRANCH, P. O. Box 7000, Peterborough, Ontario Canada K9J 8M5 Telephone: (705) 740-1600 Facsimile: (705) 740-1666
DIRECTION DE LA GESTION ET DES SERVICES INFORMATIONNELS, C. P. 7000, Peterborough, Ontario Canada K9J 8M5 Telephone: (705) 740-1600 Fac-similé: (705) 740-1666

May 11, 1993

Ms. Tracy A. Brennand
Department of Geography
University of Alberta
Edmonton, Alberta
T6G 2H4

Dear Tracy:

Re: Ontario Minisry of Natural Resources - Aerial Photo Copyright

As per our telephone conversation of today, I am giving you authorization to use the two Ontario Ministry of Natural Resources aerial photo's: 71-4406-6-151 & 152 to be published in the Canadian Journal of Earth Sciences. Each reprint/copy of the photo(s) shall clearly show the following information in the bottom left corner: **Aerial Photo's Supplied Courtesy of the Ontario Ministry of Natural Resources.**

Thank you for your letter and good luck on your thesis.

Yours truly,

D Yorke

Derick Yorke
Resource Specialist

Energy, Mines and Resources Canada
Énergie, Mines et Ressources Canada

Surveys, Mapping and Remote Sensing
Levés, Cartographie et Télédétection

October 30, 1992

3029

Tracy A. Brennand
Department of Geography
University of Alberta
Edmonton, Alberta
T6G 2H4

Dear Ms. Brennand

Thank you for your letter of September 21,1992 in which you requested authorization to reproduce and publish the following photographs from the National Air Photo Library in 'The Canadian Journal of Earth Sciences'.

Photograph numbers: T324R - 63, A16170 - 49, 109, 110, 155, 156, 186, 187, 188

The Product and Services Division authorizes the use as requested subject to the conditions listed below:

a) that the authorization is for non-exclusive use,

b) that it applies only to the photographs and publications named above,

c) that the photograph numbers (roll and frame number) appear with each photograph or part thereof each time it is used in the publication,

d) that the following copyright notice be included in the publication, either in an acknowledgements section of the publication or adjacent to each photograph. "This aerial photograph (or: "The aerial photograph on pages xx, xx and xx) © (copyright year as shown in the attached listing) Her Majesty the Queen in Right of Canada, reproduced from the collection of the National Air Photo Library with permission of Energy, Mines and Resources Canada.",

e) that we be supplied, free of charge, with one copy of the publicatioon for our library.

This authorization will come into effect upon receipt of a copy of this letter signed with an acceptance by Tracy Brennand.

Yours truly

William Voller
Chief
National Air Photo Library

WV/hw

TELEPHONE (613) 995-4560
FAX (613) 995-4568

SIGNATURE	TITLE	DATE
[signature]	Ms.	8/01/93

NATIONAL AIR PHOTO LIBRARY
PHOTOTHÈQUE NATIONALE DE L'AIR

Roll Number Numéro du rouleau	Copyright Year Année de copyright
T324 R-63	5/1/49
A16170 - 49, 109, 110, 155, 156 - 156, 157, 158	11/2/48

Verified by/Vérifié par A. Lobb Date

UNIVERSITY OF ALBERTA
RELEASE FORM

NAME OF AUTHOR: **Tracy Anne Brennand**

TITLE OF THESIS: **Laurentide meltwater systems: geomorphic and sedimentary evidence**

DEGREE: **Doctor of Philosophy**

YEAR THIS DEGREE GRANTED: **Fall 1993**

Permission is hereby granted to the University of Alberta to reproduce single copies of this thesis and to lend or sell such copies for private, scholarly or scientific purposes only.

The author reserves all other publication and other rights in association with the copyright in the thesis, and except as hereinbefore provided neither the thesis nor any substantial portion thereof may be printed or otherwise reproduced in any material form whatever without the author's prior written permission.

TAB

Geological Survey of Canada
Terrain Science Division
601 Booth Street
Ottawa, Ontario
K1E 0E8, Canada

DATE: September 8, 1993

UNIVERSITY OF ALBERTA

FACULTY OF GRADUATE STUDIES AND RESEARCH

The undersigned certify that they have read, and recommend to Faculty of Graduate Studies and Research for acceptance, a thesis entitled **Laurentide meltwater systems: geomorphic and sedimentary evidence** submitted by **Tracy Anne Brennand** in partial fulfilment of the requirements of the degree of **Doctor of Philosophy.**

J. Shaw

J. Shaw (supervisor)

R. B. Rains

J. H. England

G. P. Kershaw

T. F. Moslow

R. D. Powell (external examiner)

DATE: September 9, 1993

Abstract

By understanding the genesis of individual glacial landforms informed reconstructions of ice-sheet dynamics can be made; models must be constrained by geomorphic and sedimentary evidence. This thesis investigates Laurentide tunnel channel and esker genesis on Victoria Island, Northwest Territories, in south-central Ontario, and in Québec by combined consideration of landform associations, morphology, sedimentology and glacial hydrologic theory.

Associated streamlined fields have been interpreted as the products of erosion by turbulent separated flows within catastrophically released subglacial meltwater sheets. Recent theoretical modelling of ice-sheet hydrology suggests progressive channelization of meltwater during the collapse of such a sheet. A geometric model is presented of the interaction of rough ice base and bed surfaces with inferred meltwater flow paths. Late-stage sheet flow scours, megachannels and tunnel channels are identified, described and interpreted as evidence of such progressive channelization and flow diversion processes, governed by the geometric interactions between the recoupling ice base and bed and the thermodynamic feedbacks within an increasingly discontinuous meltwater sheet.

Subglacial or grounding-line sedimentary environments are inferred for all of the Laurentide eskers investigated, based on their association with tunnel channels, upslope flow paths, minimal postformational disturbance of their sediments, down-esker trends in clast roundness, and low variability in paleoflow direction estimates. Sand-gravel couplets and fine-grained rhythmites record pulsed flows which may have been seasonal. Results from an architectural approach to esker sedimentology suggest unsteady flows down nonuniform conduits, with the style of sedimentation controlled by conduit geometry. Fans, beads, and extended, hummocky zones associated with subglacial eskers record high discharge events which caused localized floatation to capture adjacent cavities or allow localized sheet-flow events. Traditionally interpreted as an interlobate moraine, the Harricana glaciofluvial complex is inferred to be a large subglacial esker.

Probable changes from cold-based to warm-based or polythermal ice conditions, and from catastrophic to seasonally-controlled meltwater systems are inferred for the Laurentide Ice Sheet from landform associations, geomorphic and sedimentary evidence. Regional ice stagnation or stagnation zone retreat is inferred during esker sedimentation. The conventionally interpreted genesis of so-called interlobate moraines is questioned. Geographic differences and temporal changes in the Laurentide meltwater system, and its implications for ice-sheet behaviour, must be accounted for in future ice-sheet models.

Acknowledgements

This journey began in high school, and I thank my Geography teachers, Verity Frampton and David Marshall, for their enthusiasm, patience and encouragement - I was not an easy student. As an Undergraduate in Britain I came under the guidance of Jean Grove, Martin Sharp, Keith Richards, and David Stoddart. I appreciate their perseverance, scholarly attitudes, and good humour in the field. I thank my tutor John Marks for his wisdom and his encouragement to do graduate work. In Canada, I thank, first, my student colleagues at Queen's University, including Drew, Ruth, Dave, Lyn and Tim - you helped make my Transatlantic move easy and fun. I thank the physical geography faculty for their knowledge, their teaching, and their humour.

I thank my colleague Dave Sharpe for allowing me to join his Victoria Island project in 1988, and for hours of stimulating discussion. This fieldwork was funded under project 830018 Geological Survey of Canada, with additional funding from John Shaw (NSERC Operating Grant). I thank Mike Byerley and Tim Warman for their willing assistance in the field, and for making my arctic adventure a smooth one. I also thank my assistants, Lyn Murray and Colin Booth, who made the months of hot, humid field work in Ontario and Québec enjoyable. This fieldwork was funded by my Canadian Commonwealth Scholarship and an NSERC Operating Grant to John Shaw.

Most of the ideas presented in this thesis blossomed in the nurturing atmosphere at the University of Alberta. I thank all members of the Geography Department for their warmth, joy, interest, friendship and great conversation. I thank Bonny, Gesche, Trevor, Lee, Rob, Darren, James, Dave and Kevin for encouraging and listening to my stream of consciousness. I thank Ron Eyton for patiently introducing me to the exciting world of satellite image and digital elevation model manipulation. Bruce Rains has often been the bright light on dark days, a man always willing to entertain the improbable, get through the bullshit, and with a warm heart reminding me that life is what you make it. Thank you Bruce.

At a technical level this thesis would not have been as well illustrated if it had not been for the computer drafting skills of F. Sequin (GSC), M. Wecke (GSC), and Dan Hemmenway (U of A), the manual drafting of Mike Fisher (U of A), the photographic work of Randy Pakan (U of A) and David Epp (U of A), and the satellite image and digital terrain model manipulation of Lee Weissling (U of A). I thank Frank Kenny (Ontario Centre for Remote Sensing) for providing the LANDSAT data for southern Ontario.

To John Shaw, who was/is my supervisor, colleague and friend, we have been through may storms but are finally finding rainbows. I thank you John, you were there when hunters tried to shoot down this fledgling, you kept faith in me when I lacked faith in myself, you patiently discussed even my most ridiculous ideas in a constructive manner, and most of all you have been a great friend. I have learnt from you the art of observation, good science, and courage. I hope that I can make you proud.

A thesis can never be done without strong emotional support from outside the academic sphere. I thank my parents for believing in my capabilities, for always bringing me back to the real world when I got unhealthily wrapped up in my academic life, and for giving me unconditional love. This thesis would never have been completed without the support, encouragement, patience, compassion, love and friendship of my partner Laurie, who's belief in me surpassed my own on numerous occasions. We have been through sunshine and shadows and move together into a new day.

Table of Contents

Chapter		Page
1.	**Introduction**	1
	Tunnel channel genesis debate	1
	Esker genesis debate	3
	Thesis organization	5
	References	6
2.	**Ice-sheet dynamics and subglacial meltwater regime inferred from form and sedimentology of glaciofluvial systems: Victoria Island, District of Franklin, Northwest Territories.**	8
	Introduction	8
	Ferguson Lake glaciofluvial complex	8
	Environment/landform associations	8
	Streamlined forms: observations	12
	Streamlined forms: interpretation	12
	Tunnel channels: observations	16
	Tunnel channels: interpretation	17
	Tunnel channels: form, sedimentology, and context	17
	Depositional ridges: observations	18
	Depositional ridges: interpretation	19
	Inferred sequence of events	20
	Augustus Hills glaciofluvial system	22
	Landform associations	22
	Sedimentary package	24
	Interpretation/discussion	27
	Depositional environment	27
	Meltwater regime	28
	Namaycush Lake glaciofluvial complex	29
	Landform associations/ridge morphology	29
	Sedimentary sequences in fans: observations	32
	Fans and extended deposits: interpretation	32
	Discussion: depositional environment and meltwater regime	34
	Implications for ice-sheet dynamics	34
	References	36
3.	**Tunnel channels and associated landforms, south-central Ontario: their implications for ice-sheet hydrology**	39
	Introduction	39
	Background	40
	Modelling of geometric interactions	43
	Late-stage sheet flow scours between drumlins	43

Chapter Page

Description 43
Interpretation 48
Bedrock geology and megachannels 49
Description 49
Interpretation 52
Tunnel channel system 53
Description 53
Eastern channels: description 58
Western channels: description 58
Interpretation 60
Transverse ridges within tunnel channels 64
Description 64
Interpretation 67
Eskers 68
Description 68
Interpretation 68
Discussion 70
The Dummer Moraine 70
The Oak Ridges glaciofluvial complex 72
Implications for ice-sheet hydrology 73
References 75

4. **Macroforms, large bedforms and rhythmic sedimentary sequences in subglacial eskers, south-central Ontario: implications for esker genesis and meltwater regime** 83
Introduction 83
Theories of esker genesis 86
Geologic setting 87
Bedrock geology 87
Quaternary geology/landform associations 87
Gross morphology 88
Main esker ridges 88
Fans 90
Beads with minor ridges 90
Extended, hummocky zones 90
Down-esker trends 90
Clast lithology, sphericity and roundness 90
Observations 91
Interpretations 91
Paleoflow direction estimates 97
General depositional environment 100
Sedimentology of the main esker ridges 101
Composite macroforms 103

Chapter Page

Heterogeneous, unstratified gravel 103
Massive, imbricate, clast-supported gravel 109
Imbricate, polymodal gravel 110
Plane-bedded gravel 110
Cross-bedded gravel 112
Pseudoanticlinal macroforms 115
Oblique accretion avalanche bed macroforms 117
Vertically alternating sand and gravel units 120
Discussion: esker ridge macroforms 124
Sedimentology of major and minor fans, beads with minor ridges, and laterally-fining deposits 125
Observations 125
Hummocky or in-phase wave structures 127
Interpretations/discussion 131
Sedimentology of anabranched reaches of the main esker ridges and hummocky, extended zones 132
Observations 132
Interpretations 133
Discussion: implications for esker genesis and meltwater regime 134
Subglacial, closed-conduit flow and macroforms 134
The sliding-bed facies 135
Conduit maintenance between seasons/events 136
References 138

5. **Geomorphology, sedimentology, stratigraphic context, and landform associations of the Harricana glaciofluvial complex, Abitibi region, Québec: implications for genesis, meltwater regime, and ice-sheet dynamics** 150
Introduction 150
Interlobate moraines 153
Background research on the Harricana glaciofluvial complex 154
Morphology, clast characteristics and paleoflow direction estimates 157
Morphology 157
Down-complex trends in in situ *clast characteristics* 161
Bedrock geology of the study area 161
Clast lithology 170
Clast roundness 171
Clast sphericity and shape 172
Paleoflow direction estimates 173
Gravel fabrics 173
Cross-bedded and cross-laminated sand 179
Environmental constraints inferred from down-complex trends 179
Sedimentology of the Harricana glaciofluvial complex 180

Chapter Page

Heterogeneous, unstratified gravel 180
Plane-bedded gravel 185
Imbricate, polymodal gravel and sandy in-phase wave structures 187
Cross-bedded gravel 191
Composite macroforms 192
Oblique accretion avalanche bed (OAAB) macroforms 195
Pseudoanticlinal macroforms 200
Vertically alternating sand and gravel facies 200
Sedimentary macroforms and environments: discussion 202
Subaqueous fan and grounding-line sedimentary assemblages 203
Discussion: stratigraphic context, landform associations and implications for ice-sheet hydrology and dynamics 204
Stratigraphic context 205
Landform associations 208
Implications for ice-sheet hydrology and dynamics 210
References 213

6. **Summary, discussion and future research considerations** 222
Tunnel channel genesis 222
Tunnel channels: future research avenues 223
Esker genesis 223
Eskers: future research avenues 225
Laurentide meltwater systems: implications for ice-sheet models 225
Laurentide meltwater systems: future research avenues 226
References 228

APPENDIX 1 229

APPENDIX 2 230

APPENDIX 3 235

APPENDIX 4 241

APPENDIX 5 245

APPENDIX 6 247

APPENDIX 7 248

APPENDIX 8 287

APPENDIX 9 292

List of Tables

Table		Page
3.1	Traditional and proposed glacial landform sequences, south-central Ontario	73
4.1	Literature on site of esker deposition	86
4.2	Evidence used to determine the site of esker deposition (from Charlesworth (1957), Flint (1957), and Banerjee and McDonald (1975))	87
4.3	Lithologic frequency and mean roundness and mean sphericity by lithology for clast samples from the Tweed esker	92
4.4	Gravel fabric statistics	99
4.5	Paleoflow direction statistics from cross-bed and cross-lamination measurements	99
4.6	Grain-size statistics from heterogeneous, unstratified gravel	103
4.7	Summary fabric and transport orientation data for individual gravel facies	107
4.8	Estimates of flow depth and velocity for in-phase wave structures	131
5.1	Morpho-genetic classification of the Harricana glaciofluvial complex between latitudes 50°N and 48°N, after Allard (1974)	155
5.2	Expected characteristics of linear synchronous and time-transgressive glaciofluvial deposits	158
5.3	Morphology of the Harricana glaciofluvial complex	160
5.4	Clast lithology in percent for *in situ* samples from the Harricana glaciofluvial complex	162
5.5	Mean Roundness by lithology for *in situ* clasts from the Harricana glaciofluvial complex	163
5.6	Percent frequency of visual roundness classes by pit for *in situ* clasts from the Harricana glaciofluvial complex	164
5.7	Mean Sphericity by lithology for *in situ* clasts from the Harricana glaciofluvial complex	165
5.8	Gravel fabric statistics	176
5.9	Paleoflow direction statistics derived from cross-bed and cross-lamination measurements	178
5.10	Gravel facies deposited under closed-conduit and open-channel conditions	181
5.11	Fabric and transport orientation data for gravel facies and structures	182 -183

Table		Page
5.12	Estimates of flow depth and velocity for sandy in-phase wave structures	189
5.13	Stratigraphic correlation for Abitibi-Timiskaming and surrounding areas as proposed in the literature	206

List of Figures

Figure		Page
1.1	Location of study sites with respect to proposed limits of the late Wisconsinan Laurentide Ice Sheet (Prest 1984). Southern and eastern Victoria Island, Northwest Territories: FL, Ferguson Lake; AH, Augustus Hills; NL, Namaycush Lake. SCO, south-central Ontario. HGC, Harricana glaciofluvial complex; boxed area investigated.	2
2.1	Location map showing generalized patterns of streamlined forms, tunnel channels, and eskers on southern and eastern Victoria Island, Northwest Territories. Boxes show location of Augustus Hills glaciofluvial system (Fig. 2.7), Ferguson Lake glaciofluvial complex (Fig. 2.2), and Namaycush Lake glaciofluvial system (Fig. 2.10). FL, Ferguson Lake; LP, Lady Pelly; MP, Mount Pelly; NL, Namaycush Lake; WB, Wellington Bay. Modified from Fyles (1963) and Sharpe (1992*c*).	9
2.2	Map of Ferguson Lake glaciofluvial complex showing landform associations, study sites, and location of Figure 2.3. See Figure 2.1 for location.	10
2.3	Air photograph mosaic of Ferguson Lake glaciofluvial complex with section locations (V018-V023). Flow from the north-northeast. CL, crescentic lakes within tunnel channel; D, drumlinoid ridges; DCR, double-crested ridges; F, flutes; L, lobe adjacent to tunnel channel; ME, major esker; R, residual hills within tunnel channel; S, subdued streamlined forms; SE, smaller eskers within tunnel channel; TC, tunnel channel with scalloped margins. Air photographs A16170-186, A16170-187 and A16170-188 copyright 16 July 1958 Her Majesty the Queen in Right of Canada, reproduced from the collection of the National Air Photo Library with permission of Energy, Mines and Resources Canada.	11
2.4	Legend for sedimentary logs.	13
2.5	Sedimentary logs from the Ferguson Lake site, with paleocurrent estimates, event-sequence symbols, and elevation above sea level. See Figure 2.4 for legend. *a*. Landforms adjacent to and associated with the tunnel channel: fluted ridges (482, 483); residual hill in tunnel channel (355); and lobe adjacent to tunnel channel (301). *b*. Esker ridge (V019-V023) and double-crested ridge (V018).	14-15
2.6	Schematic illustration of the temporal (*a-e*) sequence of events at the Ferguson Lake site (note scale changes). *a*. Tunnel channel cut into preexisting glacial sediments by earlier catastrophic subglacial meltwater flow in R/N-channel. Overbank deposition of splay lobe. *b*. Formation of streamlined terrain, and scalloped margins, crescentic scours and return-eddy deposits of tunnel channel, by catastrophic subglacial meltwater sheet flow.	21

Figure		Page
	c. Further erosion of tunnel channel and formation of shallower scour channels and residual hills by catastrophic subglacial meltwater flow in R/N-channel. *d*. Ice stagnation and formation of major esker by seasonally controlled, subglacial meltwater flow in R-channel. *e*. Formation of double-crested ridges and minor eskers in open conduits (presence of ice roof unknown).	
2.7	Map of section locations and morphology at the Augustus Hills site. See Figure 2.1 for location.	23
2.8	Sedimentary logs from the Augustus Hills site, with paleocurrent estimates, event-sequence symbols, and elevation above sea level. See Figure 2.4 for legend.	25
2.9	Augustus Hills. *a*. Grain-size frequency by section. *b*. Structural frequency by section (flat beds include primarily proximal plane beds and primarily distal draped lamination). *c*. Mean event-sequence thickness by section. Sections arranged in order, from proximal (right) to distal. Note sections represent point data, but connecting lines are drawn to aid visual clarity. See text for sections omitted.	26
2.10	Map of landform associations at the Namaycush Lake site, and location of Figure 2.11. See Figure 2.1 for location.	30
2.11	Air photograph mosaic showing esker (E), fans (1-3), extended deposits (4), and section locations (V033, V034) at the Namaycush Lake site. See Figure 2.10 for location. Air photographs A16170-49, A16170-109, and A16170-110 copyright 16 July 1958 Her Majesty the Queen in Right of Canada, reproduced from the collection of the National Air Photo Library with permission of Energy, Mines and Resources Canada.	31
2.12	Sedimentary logs from the Namaycush Lake site with paleocurrent estimates, event-sequence symbols, and elevation above sea level. See Figure 2.4 for legend.	33
3.1	Study area showing drumlin fields, eskers, Dummer Moraine, Oak Ridges glaciofluvial complex and locations of figures 3.4, 3.6, 3.7 and 3.10. Modified from Barnett *et al.* (1991).	41
3.2	Geometric model of the interaction between two mismatched surfaces (ICE base and BED) at 30 m gap width (*a*). Note: gap width between the two surfaces is greatly exaggerated here, to aid visual clarity; *b*. Gap width between the two surfaces in *a*. once they are interlocked (RESIDUAL = ICE - BED); *c*. More visual rendition of residual volume (RESIDUAL × -1); low points are zones of high potential meltwater discharge.	44

Figure		Page
3.3	Classed contour map of potential water depths on the inverted surface (Fig. 3.2*c*). Grey scale class interval 10 m (white, 0 m to -10 m). Potential channelized flow within declining sheet flow (black arrows); potential channelized flow connecting cavities to other cavities or channels (dashed arrows).	45
3.4	Distribution of elongate scours (west), scour zones (east), tunnel channels, transverse ridges in tunnel channels, eskers, and the Oak Ridges glaciofluvial complex in south-central Ontario. See Figure 3.1 for location.	46
3.5	Air photograph stereopair showing tunnel channels (TC), and esker (E) in a tunnel channel, drumlinized residuals (DR) between tunnel channels and sinuous late-stage sheet flow scours (thin arrows) on drumlinized residuals. Air photographs A27083-123 and A27083-124 copyright 25 April 1987 Her Majesty the Queen in Right of Canada, reproduced from the collection of the National Air Photo Library with Permission of Energy, Mines and Resources Canada.	47
3.6	Bedrock geology of south-central Ontario with Formation boundaries. Modified from Carson (1980*a*, 1980*b*, 1980*c*, 1981*a*, 1981*b*, 1981*c*). See Figure 3.1 for location.	50
3.7	Contrast-stretched, edge-enhanced LANDSAT 4 image of part of the tunnel channel system around Tweed (TM 16-29, band 5, 24-Oct-82), Ontario Ministry of Natural Resources, Provincial Remote Sensing Office). Scale bar is 10 km. See Figure 3.1 for location. Note: serrated Shield margin with numerous Precambrian reentrants (top); drumlin field (lower left); multiple escarpment levels (upper right); and Marlbank esker passing through Beaver Lake channel (right).	51
3.8	View across fault-guided tunnel channel incised into Paleozoic limestone at Kingsford; now occupied by Salmon River. (Photographer: Brennand 1989).	54
3.9	Air photograph stereopair showing drumlins truncated (TR) by tunnel channel (TC) containing Tweed esker (TE), ~12 km north of Trenton. Air photographs A27083-189 and A27083-190 copyright 25 April 1987 Her Majesty the Queen in Right of Canada, reproduced from the collection of the National Air Photo Library with permission of Energy, Mines and Resources Canada.	55
3.10	Location of the high-stand shoreline of Glacial Lake Iroquois (after Mirynech 1962) in relation to tunnel channel paths. See Figure 3.1 for location.	57
3.11	Air photograph stereopair showing a potential zone of localized sheet flow (SF) and flow interference (FI) between two tunnel channels (TC), one of	59

Figure		Page
	which is blind-ended (TCB), ~12 km west-southwest of Marlbank. Streamlined bedrock residual (R) within tunnel channel. Air photographs A27083-104 and A27083-105 copyright 25 April 1987 Her Majesty the Queen in Right of Canada, reproduced from the collection of the National Air Photo Library with permission of Energy, Mines and Resources Canada.	
3.12	Transverse ridges adjacent to the southern end of Tweed esker, and within a tunnel channel. (Photographer: Brennand 1989).	65
3.13	Air photograph stereopair of part of a field of transverse ridges (TR) within a tunnel channel, adjacent to Tweed esker (TE), ~10 km north-northwest of Brighton. TCM is northern margin of tunnel channel. Air photographs 71-4406-6-151 and 71-4406-6-152 supplied courtesy of the Ontario Ministry of Natural Resources.	66
4.1	Bedrock geology (modified from Ontario Geological Survey 1991) and esker distribution (modified from Barnett *et al.* 1991) in the study area. A, Actinolite.	84
4.2	Morphologic elements of the main eskers studied. Tributary ridges are not shown. The only obvious bead is mapped at pit N35.	85
4.3	Crest long profiles rotated to bring the high-stand shoreline (750' or 228.6 m) of Glacial Lake Iroquois back to a horizontal plane. *a*. Tweed esker. b. Campbellford esker. *c*. Norwood esker.	89
4.4	Clast lithology for the Tweed esker unit (*a*) and oversize (*b*) samples. Lines connecting points are not meant to imply continuous variation, but merely to aid in graphical interpretation. The vertical line is the location of the Shield margin. Actinolite is located on Figure 4.1.	93
4.5	Mean and grand mean maximum projection sphericity (Ψ_p, Sneed and Folk 1958) for the Tweed unit (*a, c*) and oversize (*b, d*) clasts. Lines connecting points are not meant to imply continuous variation, but merely to aid in graphical interpretation. The vertical line is the location of the Shield margin. For lithologic abbreviations see Table 4.3. Actinolite is located on Figure 4.1.	94
4.6	Mean and grand mean roundness for the Tweed esker unit (*a, c*) and oversize (*b, d*) clasts. Lines connecting points are not meant to imply continuous variation, but merely to aid in graphical interpretation. The vertical line is the location of the Shield margin. Roundness classes after Powers (1953): WR, well rounded,; R, rounded; SR, subrounded; SA, subangular; A, angular. For lithologic abbreviations see Table 4.3. Actinolite is located on Figure 4.1.	95
4.7	Paleoflow direction measurements for the Tweed (T), Campbellford (C) and	98

Figure		Page
	Norwood (N) eskers. TJS1, C43, etc. are pit locations. Gravel fabrics presented as lower-hemisphere projections (contour interval is 2 standard deviations), and cross-lamination and cross-bed measurements as rose diagrams. Rose diagrams are plots of actual number of observations. Longest segment at pit C31 represents 37 observations; the same scale is used for all rose diagrams except at pit N36 (displayed at 50%; longest segment represents 71 observations).	
4.8	*a*. Normal faults lateral to an undisturbed ridge core, Campbellford esker (pit C32; Fig. 4.2). Note alternating sand and gravel units. *b*. Diapiric fold at the core of Tweed esker (pit T14; Fig. 4.2). Metre rods for scale.	102
4.9	Part of a composite macroform, Norwood esker (pit N36; Fig. 4.2). Note climbing gravel dunes (right). Flow to the left. Metre rods for scale.	104
4.10	Heterogeneous, unstratified gravel facies: *a*. Poorly delineated lenses of bimodal clast-supported, polymodal and openwork gravel. Visually chaotic fabric, Campbellford esker (pit C30; Fig. 4.2). *b*. Vaguely delineated lenticular organization and cluster imbrication of larger clasts, Norwood esker (pit N36; Fig. 4.2). Metre grid for scale.	105
4.11	Heterogeneous, unstratified gravel facies: *a*. Grain-size distributions. *b*. Partitioning of facies. Grain-size data for sample T23/1-1' is an amalgamation of samples T23/1-1a and T23/1-1b. *c*. Grain-size histogram demonstrating polymodal texture (unit C43/1-1; Table 4.6; Appendix 6).	106
4.12	*a*. Massive, imbricate, clast-supported gravel alternating with sand (truncated at arrow), Tweed esker (pit T12; Fig. 4.2). Metre rod for scale. *b*. Imbricate, polymodal gravel within an in-phase wave structure, Norwood esker (unit N36/7-6 (1989); Table 4.7). Metre grid for scale. *c*. Plane-bedded gravel, Campbellford esker (pit C31; Fig. 4.2). Tape extended to 0.5 m.	111
4.13	*a*. Trough cross-bedded gravel, Campbellford esker (pit C43; Fig. 4.2). Flow out of face. *b*. Rhythmically-graded foresets of tabular cross-bedded gravel, Tweed esker (pit T16; Fig. 4.2). Flow to the right. Metre grid for scale. *c*. Rhythmically-graded gravel triplet, Campbellford esker (pit C30; Fig. 4.2). Note convoluted laminations in sand, part A (bottom). Scale in cm. *d*. Rhythmically-graded gravel in tabular beds on the scale of the esker ridge, Tweed esker (pit T26; Fig. 4.2). Tape extended to 0.5 m.	113
4.14	Grain-size histograms for rhythmically-graded gravel, Campbellford esker (pit C30; Fig. 4.2). Parts A and B show fining-upward sequence and a reduction in the percentage of matrix. Raw data in Appendix 6.	114
4.15	Pseudoanticlinal macroform composed of heterogeneous, unstratified gravel with a crest-convergent fabric, Tweed esker (pit TJS1; Fig. 4.2). Fabric data	116

Figure		Page
	in Appendix 4, statistics in Table 4.7. Metre rods (arrows) for scale. Primary flow was into the photograph (southward).	
4.16	Oblique accretion avalanche bed macroform, Marlbank esker (pit M42; Fig. 4.2): *a*. High-angled inclined avalanche beds truncated by lateral scour-and-fill structures. Primary flow was into the photograph. Metre rods for scale. *b*. Graded gravel within inclined avalanche beds. Metre grid for scale.	118
4.17	Grain-size histogram for polymodal, gravelly sand within an oblique accretion avalanche bed macroform, Marlbank esker (pit M6*; Fig. 4.2), unit M6*/1-A. Raw data in Appendix 6.	119
4.18	Vertically alternating sand and gravel units with sharp contacts (couplets), Norwood esker (pit N36; Fig. 4.2). Metre rod for scale.	121
4.19	*a*. Schematic jökulhlaup hydrographs. 1. Sudden meltwater release associated with the drainage of a large water body. 2. Progressive enlargement of the catchment area of a main conduit associated with capture of minor conduits and cavities. Both show a rapid reduction in meltwater discharge on the falling limb (modified from Haeberli 1983). *b*. Critical shear velocities (U_*) for traction and suspension transport. Data for critical suspension criterion ($U_*/w > 1.0$, where w = settling velocity) and flow regime from Mamak (1964, cited in Graf and Acaroglu 1966). Data for critical traction criterion (Shields' criterion) from Blatt *et al.* (1980) and Walker (1975), and diameter (d) > 100 mm U_* calculated from $U = 0.46d^{0.50}$ (cf. Williams 1983) and $15U_* \approx \bar{U}$ (Walker 1975), assuming $U \approx \bar{U}$.	123
4.20	*a*. Ball-and-pillow structures in the upper part of a minor fan along the Tweed esker (pit T17; Fig. 4.2). Scraper is 20 cm long. *b*. Tabular, gently inclined architecture of a minor fan along the Tweed esker (pit T17; Fig. 4.2). Arrow marks the location of Figure 4.20*a*. Shovel handle is ~ 1 m long.	126
4.21	In-phase wave structures in a major fan or fan complex at pit N36 (Fig. 4.2). *a*. Diffusely-graded sandy in-phase wave structures draped by fine sand and silt, with a scour-and-fill structure (arrow) and dispersed clasts within hummocks. *b*. Gravel in-phase wave structures draped by fine sand and silt. Note water-escape/load structure (arrow), and drag and load structures at base of gravel hummocks. Metre rods for scale.	128
5.1	Pattern of eskers and moraines adjacent to the Harricana glaciofluvial complex mapped within boxed area with the exception of the Sakami Moraine. Data sources: (1) relief simplified from Yelle (1976); (2) eskers mapped from G. Tremblay (1974), Chauvin (1977), Veillette (1986, 1990), Sado and Carswell (1987); (3) moraines mapped from Hardy (1976), Veillette (1986), Sado and Carswell (1987) and Vincent (1989). Dots are	151

Figure		Page
	proposed northern (Hardy 1976) and southern (Veillette 1986) extensions of the Harricana complex. The proposed northern island chain part of the Harricana complex (Wilson 1938) extends beyond the mapped area.	
5.2	Cross-striated sites mapped in dissected zone of Abitibi Uplands, and adjacent to the Harricana glaciofluvial complex (boxed area). Data sources: (1) relief simplified from Yelle (1976); (2) striae mapped from Veillette (1986); (3) proposed grounded Cochrane limit mapped from Veillette *et al.* (1991).	152
5.3	Harricana complex divided into depositional segments separated by "gaps". Location of pits, tributary eskers, and Lake Obalski.	156
5.4	Crest long profile along the axis of the Harricana glaciofluvial complex from Point de la Fougère Rouge on the coast of James Bay (51°48'54"N 79°21"18"W) to just south of Val d'Or (48°00'00"N 77°56'30"W), constructed from contours and spot heights on 1:250 000 scale NTS sheets. High-water levels of Angliers and Early Kinojévis phases of Glacial Lake Ojibway approximated from Vincent and Hardy (1979).	159
5.5	Proportion of clast lithologies from *in situ* samples recorded in the Harricana glaciofluvial complex presented as pie graphs (see Table 5.4 for percentage values and 95% confidence limit sampling errors) and superimposed over adjacent Abitibi sub-province (Superior province) bedrock geology (modified from MERQ-OGS 1983). Stars are location of gabbroic bedrock discussed in the text.	166
5.6	*a*. Percent frequency of granitoid and metabasaltic clasts in *in situ* samples superimposed over bedrock geology along the axis of the Harricana glaciofluvial complex. Geologic transect starts at 51°15'N 79°00'W and ends at 48°01'N 77°06'W. *b*. Cumulative frequency of lithologies recorded in each pit (prefixed with "Q" in text) presented in downflow order. See Table 5.4 for numeric data and confidence intervals. Lines connecting points are not meant to imply continuous variation, but merely to aid visual interpretation.	167
5.7	*a*. Downflow trend in the mean roundness (Powers 1953) of granitoid and metabasaltic clasts in *in situ* samples; geologic transect same as Figure 5.5. *b*. Grand mean roundness for each lithologic class recorded. *c*. Frequency of occurrence of each visual roundness class by pit. Pits (prefixed with "Q" in text) arranged in downflow order. See Tables 5.5 and 5.6 for numeric data and confidence intervals. Lines connecting points are not meant to imply continuous variation, but merely to aid visual interpretation.	168
5.8	*a*. Downflow trends in the mean sphericity (Ψ_p, Sneed and Folk 1958) of	169

Figure		Page
	granitoid and metabasaltic clasts in *in situ* samples; geologic transect same asFigure 5.5. Lines connecting points are not meant to imply continuous variation, but merely to aid visual interpretation. *b*. Grand mean sphericity for each lithologic class recorded. See Table 5.7 for numeric data and confidence intervals, and Figure 5.7 for legend. *c*. Zingg (1935) shape classification for all clasts measured. a, clast long axis; b, clast intermediate axis; c, clast short axis.	
5.9	Paleoflow direction estimates from gravel fabric measurements. Fabrics displayed as equal area lower hemisphere plots. Statistics presented in Table 5.8.	174
5.10	Paleoflow direction estimates from cross-bed and cross-lamination measurements in sand. Statistics presented in Table 5.9.	175
5.11	Examples of gravel fabric plots for southeast dipping cross-bedded gravel (*a*. Q23/1-1) and a large downflow dipping avalanche bed macroform (*b*. Q12/1-1aLHS) with 'parallel' and 'flipped' clasts. All plots are equal area lower hemisphere projections. Statistics presented in Table 5.11.	177
5.12	Individual facies within the Harricana complex. *a*. Heterogeneous, unstratified gravel exhibiting vaguely lenticular, textural organization (unit Q21/1-1aRHS). Grid is 1 m^2. *b*. Heterogeneous, unstratified gravel with imbricate clast clusters (unit Q23/1-3). *c*. Imbricate, polymodal, matrix-rich coarse gravel with clasts occurring preferentially along poorly defined convex-up bedding surfaces (unit Q26/1-1LHS; Table 5.11). *d*. Imbricate, polymodal fine gravel with diffusely-graded laminae (unit Q2B/2-1; Table 5.11). *e*. Grading in cross-bedded gravel (unit Q23/1-1; Table 5.11). *f*. Bimodal, clast-supported gravel with contorted laminae in sand (unit Q5/3-1) at the base of large-scale, downflow-inclined, tabular beds. Ten centimetre intervals on scale.	184
5.13	Sediments exposed in long axis of part of a composite macroform at pit Q23 (Fig. 5.3). FO, approximate pit face orientation.	186
5.14	Large antidune backset beds with tabular rafts of unconsolidated sediment below tabular cross-bedded medium-coarse sand at pit Q20 (Fig. 5.3). FO, approximate pit face orientation.	188
5.15	Sandy in-phase wave structures at pit Q2B (Fig. 5.3). Note: the metre scale is in different locations in the sketch and the photographic panorama. FO, approximate pit face orientation.	190
5.16	Shear planes and folds within debris-flow diamicton along the flank of the Harricana complex at pit Q23 (Fig. 5.3). Ten centimetre intervals on scale.	193

Figure		Page
5.17	Composite macroform at pit Q18 (Fig. 5.3). Person for scale. FO, approximate pit face orientation.	194
5.18	*a*. Downflow accreting avalanche bed macroform at pit Q12 (Fig. 5.3). Section is ~10 m high. Flow out of face. *b*. Close-up of avalanche beds at pit Q12 showing 'parallel' and 'flipped' clasts.	196
5.19	Alternating oblique accretion avalanche bed macroform at pit Q3 (Fig. 5.3). Flow into face. FO, approximate pit face orientation.	198
5.20	Close-ups of sedimentary style within alternating oblique accretion avalanche bed macroform at pit Q3 (Fig. 5.3). *a*. Clast clusters along beds. *b*. Rhythmic grading of finer gravel. Grid is 1 m^2.	199
5.21	Low-angled pseudoanticlinal structure at pit Q8 (Fig. 5.3). Arrow is location of fabric from unit Q8/1-1LHS (Table 5.11). Flow into face. Section is 5.5 m high.	201
5.22	Vertically alternating sand and gravel facies at pit Q21 (Fig. 5.3). Scale is 1 m.	202

List of Appendices

Appendix		Page
1	Paleoflow direction estimates from cross-bedded and cross-laminated sand within esker fans, Victoria Island, Northwest Territories	229
2	Clast size, lithology, sphericity, roundness and a-axis orientation data for unit clasts within the Tweed esker	230
3	Clast size, lithology, sphericity and roundness data for oversize clasts from the Tweed esker	235
4	Fabric data from gravel facies and structures within south-central Ontario eskers	241
5	Paleoflow direction measurements from cross-bedded and cross-laminated sand and gravel within south-central Ontario eskers	245
6	Grain-size data for gravel facies and structures within south-central Ontario eskers	247
7	Clast size, sphericity, roundness and a-axis orientation data for *in situ* clasts within the Harricana glaciofluvial complex, Québec	248
8	Fabric data from gravel facies and structures within the Harricana glaciofluvial complex, Québec	287
9	Paleoflow measurements on cross-bedded and cross-laminated sand within the Harricana glaciofluvial complex, Québec	292

CHAPTER 1

Introduction

At its maximum (~18 ka BP), the late Wisconsinan Laurentide Ice Sheet covered most of interior Canada, extending north to Victoria Island and Baffin Island, west to coalesce with the Cordilleran Ice Sheet in the Alberta foothills, east to the Labrador Sea, and south into the northern United States: Montana, South Dakota, Iowa, Illinois, Indiana, Ohio, New York, Connecticut and Maine (Dyke and Prest 1987) - an area of between 10.2 and 11.3 $\times$ 10^6 km^2 (Fulton and Prest 1987). During deglaciation, a considerable volume of meltwater was generated, contributing to a global sea level rise of 121 $\pm$ 5 m (Fairbanks 1989). Consequently, the Canadian landscape today bears witness to meltwater activity in a variety of glaciofluvial landforms and deposits (*cf.* Prest *et al.* 1968). Although some landforms and deposits may be attributed to other glacial processes, this thesis focuses on glaciofluvial landforms. The primary objective is to broaden our understanding of two of these landforms: tunnel channels and eskers. Two basic questions are posed. 1. How did tunnel channels and eskers form? 2. Are the processes responsible for their formation related and do they record an evolution in the ice sheet drainage system? Both questions are approached through combined consideration of landform associations, morphology, sedimentology and glacial hydrologic theory.

It would take a lifetime to draw informed generalizations (taking into account the high variability of landform associations, morphology and sedimentology) about tunnel channel and esker genesis and their hydrologic implications within the limits of the Laurentide Ice Sheet. However, I wanted to base my thesis on as broad a range of observations as possible. Consequently, I chose three different regions (Fig. 1.1) for the following reasons: their distribution towards the geographic centre, southern and northern margins of the Laurentide Ice Sheet (Fig. 1.1); differences in the scales, morphology and sedimentology of their tunnel channels and eskers; and their accessibility. What follows is a brief overview of current debate on tunnel channel and esker genesis, and a rationalization for the choice of my study sites in light of these debates.

Tunnel channel genesis debate

Tunnel channels are subglacial meltwater channels cut into glacigenic sediment or bedrock. However, there is much debate about their genesis. The debate centres around whether meltwater discharge was catastrophic (e.g., Wright 1973) or more steady state (e.g., Boulton and Hindmarsh 1987) during tunnel channel formation; whether the channels were formed synchronously (e.g., Wright 1973) or time-transgressively (e.g., Mooers 1989); and whether the basal substrate had any bearing on their genesis or form (cf. Boulton and Hindmarsh 1987). I chose south-central Ontario (Fig. 1.1) to investigate these contrasting theories. This is an ideal region as tunnel channels were known to cross-cut

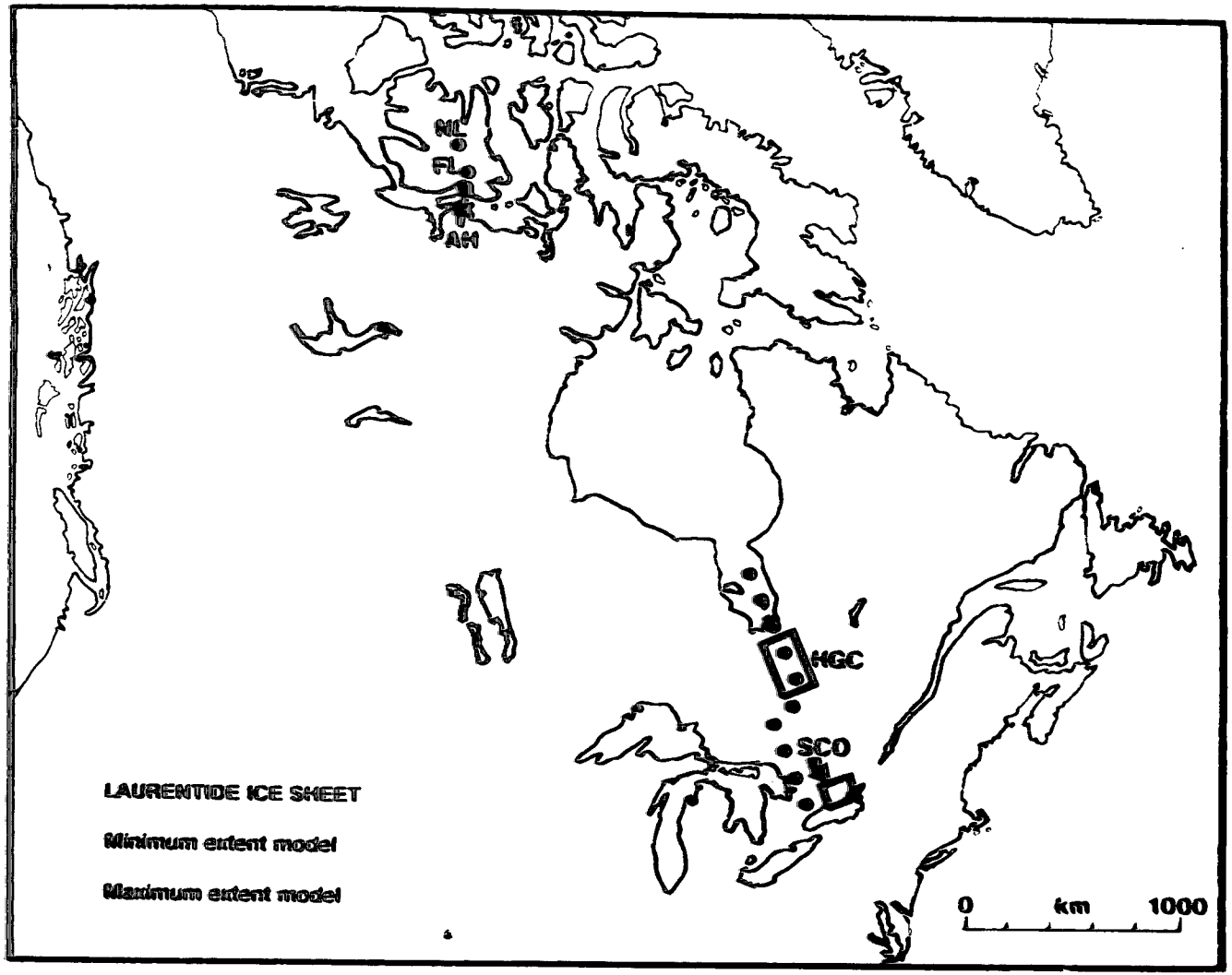

Figure 1.1. Location of study sites with respect to proposed limits of the late Wisconsinan Laurentide Ice Sheet (Prest 1984). Southern and eastern Victoria Island, Northwest Territories: FL, Ferguson Lake; AH, Augustus Hills; NL, Namaycush Lake. SCO, south-central Ontario. HGC, Harricana glaciofluvial complex; boxed area investigated.

the Peterborough-Trenton drumlin field, contain eskers, and extend across the region in both bedrock and glacigenic sediments (cf. Shaw and Gorrell 1991). The tunnel channels and their relationships to other subglacial landforms can be mapped in detail using the excellent air photograph coverage at both 1:15 000 and 1:50 000 scales. Cross-cutting and superimposition relationships can be assessed in terms of their implications for ice-sheet hydrology. A complementary investigation was undertaken at Ferguson Lake on southern Victoria Island (Fig. 1.1). Detailed observations of geomorphology and landform associations are facilitated by excellent air photograph coverage and geomorphic expression in this natural, poorly-vegetated landscape.

Esker genesis debate

"An esker is a linear accumulation of gravelly and/or sandy stratified sediment that was deposited by a stream confined on both sides by glacial ice. In some cases, though not necessarily, the stream was also confined on the top and/or bottom by glacial ice." (Banerjee and McDonald 1975, p. 132). Eskers, then, may be deposited in supraglacial, englacial, subglacial or ice-marginal environments, although there is general agreement that large Pleistocene eskers were formed subglacially or ice marginally in deltaic, fan or reentrant environments (cf. Banerjee and McDonald 1975). There are, however, disagreements as to whether subglacial conduits were flowing full (closed) or partly full (open, at atmospheric or triple-point pressure) at the time of esker sedimentation (cf. Shreve 1972 versus Hooke 1984), and as to whether eskers were deposited in time-transgressive segments (e.g., Hebrand and Åmark 1989) or synchronously (e.g., Shreve 1985). Previous research into esker genesis has been conducted at one of two scales: (*i*) external morphology (e.g., St-Onge 1984); or (*ii*) detailed site observation (e.g., Aario 1971). The latter have mostly concentrated on the finer-grained deposits (e.g., Gorrell and Shaw 1991), and coarser-grained esker ridges have received little attention. The exception has been descriptions of rhythmicity or sand-gravel couplets within esker ridges (e.g., Shaw 1972; Banerjee and McDonald 1975). Pulsed meltwater discharges, possibly as annual events, have been invoked (cf. Banerjee and McDonald 1975). Research on the hydrologic system of contemporary glaciers also suggests seasonally (e.g., Willis *et al.* 1990) and episodically (e.g., Nye 1976; Kamb 1987) changing meltwater systems. In addition, the architectural approach to fluvial sedimentology (Miall 1985) may be applied to eskers to define or isolate their building blocks. Consequently, I proposed to take a fresh look at esker sediments, particularly at the ridges themselves, using an architectural approach to their sedimentology, and keeping in mind the probability that seasonally or episodically changing meltwater systems may have governed Laurentide esker formation.

At the outset of this project I placed an unreasonable expectation on the sedimentological data to provide all the answers to the question of esker genesis; a traditional approach is to describe and interpret the sediments in order to infer the depositional environment. As the project progressed I

became increasingly perplexed that the sediments could be interpreted in a number of ways (e.g., open channel or closed conduit) - a problem of equifinality. Finally, I came to the conclusion that it is necessary to consider 'context information', that is landform associations, esker morphology and path, and down-esker trends in paleoflow-direction estimates and clast characteristics, in order to define the general environmental conditions for esker deposition. Having inferred these conditions, esker sedimentology is interpreted within that framework. The architectural elements identified within the esker ridges and the sediments in associated deposits then provide a key to the detailed mechanics of esker formation and the meltwater regime under which they evolved.

An architectural approach to esker sedimentology requires extensive vertical exposures. South-central Ontario (Fig. 1.1) is a densely populated region, with a high demand for aggregate for the construction and building industry; gravel quarries are common. Consequently, this region was chosen to investigate the architecture of esker sediments. This approach requires traditional sedimentology whereby each facies at each site is identified, described and interpreted. This is particularly critical because the flow-dynamic conditions responsible for esker gravel deposition are not well understood and must be carefully inferred from comparison with gravels in a variety of environments including pipes, open channels, turbidity currents and volcaniclastic deposits.

A companion investigation is made of the Harricana glaciofluvial complex (Fig. 1.1) in the Abitibi-Timiskaming region of Québec. This is a relatively continuous, linear accumulation of stratified sand and gravel closely associated with an extensive, integrated, esker system and streamlined forms. Although time-transgressive formation in an interlobate position had been inferred for the complex from the arrangement of adjacent landforms and sediments (e.g., Veillette 1986), no detailed or integrated investigation of the morphology and sedimentology of the complex itself had been undertaken. Gravel facies observations and interpretations, the architectural approach to sedimentology and the use of 'context information', developed during the investigation of the south-central Ontario eskers, are applied to the Harricana complex. They provide a powerful approach, giving new insight into the general environmental conditions and the detailed genesis of this complex.

A contrasting investigation is made of three esker systems on southern and eastern Victoria Island, Northwest Territories (Fig. 1.1) These systems have relatively small isolated eskers, extending from or lying in tunnel channels, and cross-cutting fields of streamlined forms. Fieldwork was carried out in 1988 as a member of a Geological Survey of Canada expedition, under the co-ordination of Dr. David Sharpe. Similar landform association, morphologic and sedimentologic reasoning to that used in south-central Ontario is invoked for the Victoria Island eskers. The main differences in the Victoria Island eskers to those in south-central Ontario were their small size, isolation, and sandy texture. As sedimentary exposures are poor and limited more traditional, vertical sedimentary logs are used.

Thesis Organization

This thesis is presented as four papers. The first (Chapter 2) investigates three glaciofluvial systems on Victoria Island (Fig. 1.1). Because exposures are limited, the architectural method is precluded and the approach taken is the most traditional. Implications for ice-sheet hydrology are proposed. The second and third papers (Chapters 3 and 4) present detailed observations and interpretations of the genesis of tunnel channels and associated landforms, and eskers, respectively, in south-central Ontario (Fig. 1.1). Although the papers were written in the reverse order, the sequence used here is preferred because the tunnel channels were incised before the eskers were deposited within them. In addition, a regional overview of the deglacial hydrologic system is inferred from more regional observations of landform associations in the tunnel channel paper. The fourth paper (Chapter 5) investigates the genesis of the Harricana glaciofluvial system (Fig. 1.1) and its implications for ice-sheet hydrology and dynamics. The regional conclusions are highly relevant to stratigraphic, glacial and chronologic studies of the area. The final chapter (Chapter 6) discusses the major findings of the thesis and suggests future research avenues in light of these findings.

References

Aario, R. 1971. Associations of bedforms and paleocurrent patterns in an esker delta, Haapajärvi, Finland. Annales Academiae Scientiarum Fennicae, Series A, III. Geologica-Geographica.

Banerjee, I., and McDonald, B.C. 1975. Nature of esker sedimentation. *In* Glaciofluvial and glaciolacustrine sedimentation. *Edited by* A.V. Jopling and B.C. McDonald. Society of Economic Paleontologists and Mineralogists, Special Publication 23, pp. 304-320.

Boulton, G.S., and Hindmarsh, R.C.A. 1987. Sediment deformation beneath glaciers: rheology and geological consequences. Journal of Geophysical Research, 92: 9059-9082.

Dyke, A.S., and Prest, V.K. 1987. Late Wisconsinan and Holocene history of the Laurentide Ice Sheet during the Late Wisconsin maximum. Géographie physique et Quaternaire, 41: 237-263.

Fairbanks, R.G. 1989. A 17,000-year glacio-eustatic sea level record: influence of glacial melting rates on the Younger Dryas event and deep-ocean circulation. Nature, 342: 637-642.

Fulton, R.J., and Prest, V.K. 1987. The Laurentide Ice Sheet and its significance. Géographie physique et Quaternaire, 41: 181-186.

Gorrell, G., and Shaw, J. 1991. Deposition in an esker, bead and fan complex, Lanark, Ontario, Canada. Sedimentary Geology, 72: 285-314.

Hebrand, M., and Åmark, M. 1989. Esker formation and glacier dynamics in eastern Skåne and adjacent areas, southern Sweden. Boreas, 18: 67-81.

Hooke, R. LeB. 1984. On the role of mechanical energy in maintaining subglacial water conduits at atmospheric pressure. Journal of Glaciology, 30: 180-187.

Kamb, B. 1987. Glacier surge mechanisms based on linked cavity configuration of the basal water conduit system. Journal of Geophysical Research, 92: 9083-9100.

Mooers, H.D. 1989. On the formation of tunnel valleys of the Superior Lobe, central Minnesota. Quaternary Research, 32: 24-35.

Nye, J.F. 1976. Water flow in glaciers: jökulhlaups, tunnels and veins. Journal of Glaciology, 17: 179-207.

Prest, V.K. 1984. The late Wisconsinan glacier complex. *In* Quaternary Stratigraphy of Canada - A Canadian Contribution to IGCP Project 24. *Edited by* R.J. Fulton. Geological Survey of Canada, Paper 84-10, pp. 21-36.

Prest, V.K., Grant, D.R., and Rampton, N. 1968. Glacial map of Canada. Geological Survey of Canada Map 1253A, scale 1:5 000 000.

Shaw, J. 1972. Sedimentation in the ice-contact environment, with examples from Shropshire (England). Sedimentology, 18: 23-62.

Shaw, J., and Gorrell, G. 1991. Subglacially formed dunes with bimodal and graded gravel in the Trenton drumlin field, Ontario. Géographie physique et Quaternaire, 45: 21-34.

Shreve, R.L. 1972. Movement of water in glaciers. Journal of Glaciology, 11: 205-214.

Shreve, R.L. 1985. Esker characteristics in terms of glacial physics, Katahdin esker system, Maine. Geological Society of America Bulletin, 96: 639-646.

St-Onge, D.A. 1984. Surficial deposits of the Redrock Lake area, District of Mackenzie. Geological Survey of Canada, Paper 84-1A, pp. 271-278.

Veillette, J.J. 1986. Former ice flows in the Abitibi-Timiskaming region: implications for the configuration of the late Wisconsinan ice sheet. Canadian Journal of Earth Sciences, 23: 1724-1741.

Willis, I.C., Sharp, M.J., and Richards, K.S. 1990. Configuration of the drainage system of Midtalsbreen, Norway, as indicated by dye-tracing experiments. Journal of Glaciology, 36: 89-101.

Wright, H.E., Jr. 1973. Tunnel valleys, glacial surges, and subglacial hydrology of the Superior Lobe, Minnesota. *In* The Wisconsinan Stage. *Edited by* R.F. Black, R.P. Goldthwaite, and H.B. Willman. Geological Society of America, Memoir 136, pp. 251-276.

CHAPTER 2

Ice-sheet dynamics and subglacial meltwater regime inferred from form and sedimentology of glaciofluvial systems: Victoria Island, District of Franklin, Northwest Territories[1]

Introduction

Glacial hydrology and hydraulics have an important impact on ice-sheet behaviour (Paterson 1981). The nature of this impact on Pleistocene ice sheets is being assessed by the study of a variety of landforms such as eskers (e.g., Hebrand and Åmark 1989; Gorrell and Shaw 1991), tunnel channels (e.g., Wright 1973; Barnett 1990) and drumlins (e.g., Shaw *et al.* 1989). Direct modelling (e.g., Shoemaker 1992*a*; Arnold and Sharp 1992) is also helping to reveal the role of meltwater storage and release. With this increasing emphasis on meltwater action, it is pertinent to search for a more detailed understanding of glacial hydrologic systems.

Glaciofluvial landforms and sediments can be used to infer process. Consequently, it is the aim of this paper to describe and interpret glaciofluvial complexes at three sites on Victoria Island (Fig. 2.1) and to use these to assess the formative meltwater conditions. Differences in esker morphology, sedimentology, and landform associations are used to infer the necessary ice-sheet dynamics associated with their formation. Channelized glaciofluvial complexes are the focus of this paper, but streamlined forms are discussed where appropriate. It is demonstrated that these complexes were formed by meltwater in subglacial, grounding-line, or reentrant environments, under both active (early) and stagnant (late) ice conditions. Meltwater processes modified the landscape and the behaviour of the ice sheet across eastern and southern Victoria Island (Sharpe 1992*a*). In turn, ice-sheet dynamics influenced glaciofluvial landform styles.

Ferguson Lake glaciofluvial complex

Environment/landform associations

Ferguson Lake glaciofluvial complex extends about 55 km in a north-south arc, north of Ferguson Lake (Figs. 2.1 and 2.2). It may be associated with a glaciofluvial system extending northwest through Mount Pelly and Lady Pelly, south of Ferguson Lake (Fig. 2.1). The northern part of this system trends parallel and then obliquely to a diverging field of streamlined forms with a northeast-southwest orientation (Figs. 2.1-2.3). Approximately 15 km north of Ferguson Lake a smaller eske.

---

[1] A version of this paper has been accepted for publication as:
Brenannd, T.A., and Sharpe, D.R. in press. Ice-sheet dynamics and meltwater regime inferred from form and sedimentology of glaciofluvial systems: Victoria Island, District of Franklin, Northwest Territories. Canadian Journal of Earth Sciences.

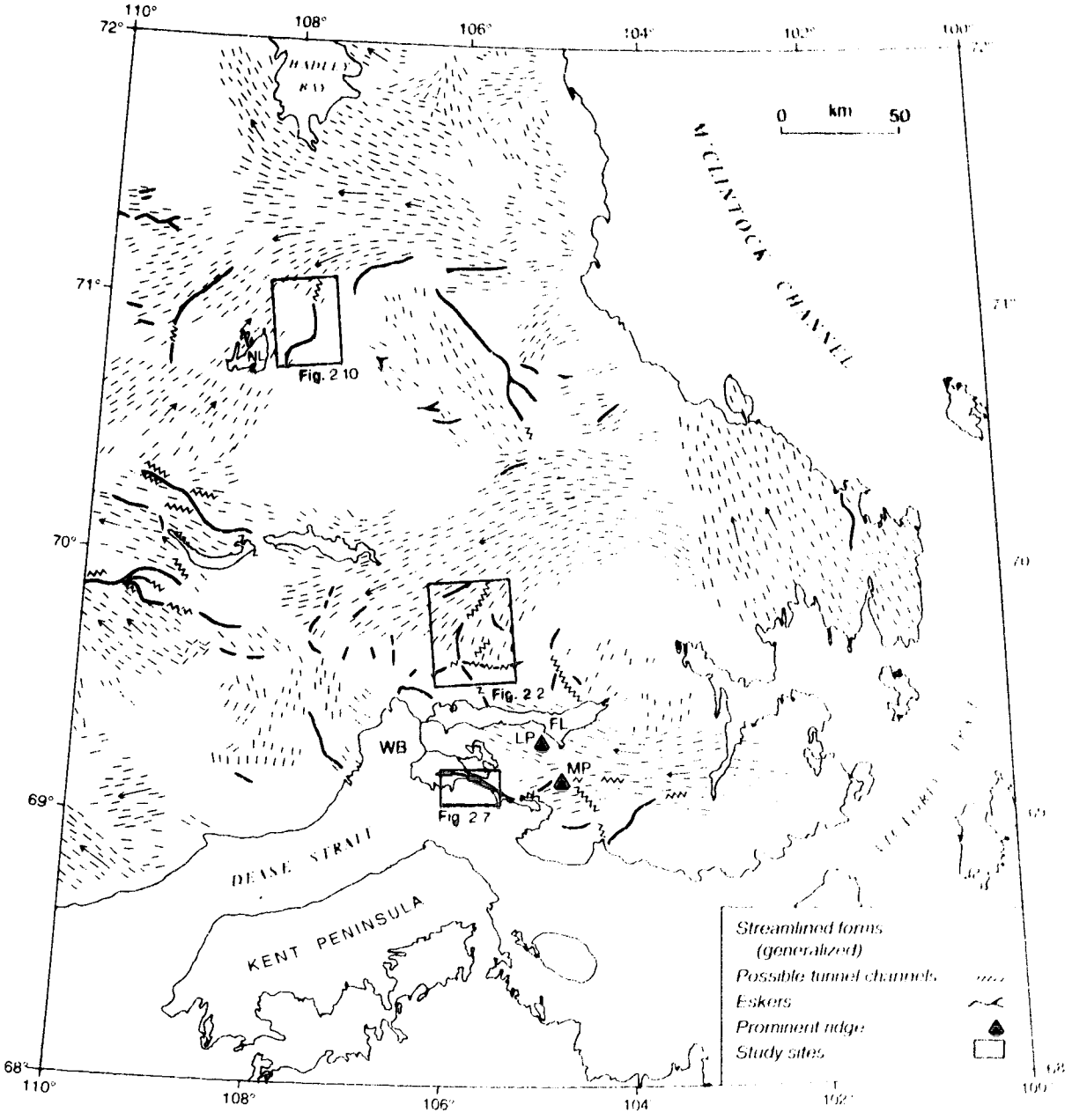

Figure 2.1. Location map showing generalized patterns of streamlined forms, tunnel channels, and eskers on southern and eastern Victoria Island, Northwest Territories. Boxes show location of Augustus Hills glaciofluvial system (Fig. 2.7), Ferguson Lake glaciofluvial complex (Fig. 2.2), and Namaycush Lake glaciofluvial system (Fig. 2.10). FL, Ferguson Lake; LP, Lady Pelly; MP, Mount Pelly; NL, Namaycush Lake; WB, Wellington Bay. Modified from Fyles (1963) and Sharpe (1992*c*).

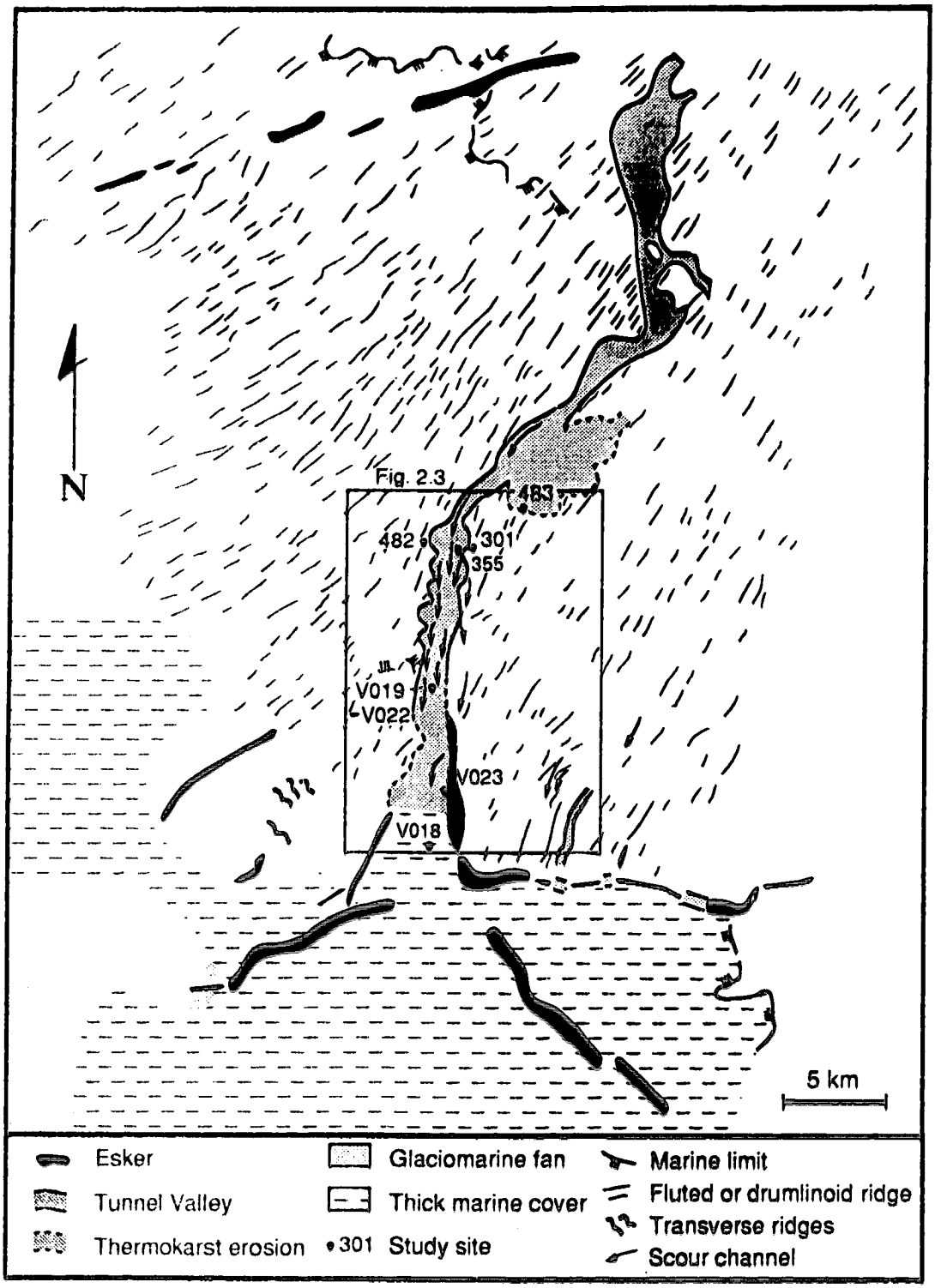

Figure 2.2. Map of Ferguson Lake glaciofluvial complex showing landform associations, study sites, and location of Figure 2.3. See Figure 2.1 for location.

Figure 2.3. Air photograph mosaic of Ferguson Lake glaciofluvial complex with section locations (V018-V023). Flow from the north-northeast. CL, crescentic lakes within tunnel channel; D, drumlinoid ridges; DCR, double-crested ridges; F, flutes; L, lobe adjacent to tunnel channel; ME, major esker; R, residual hills within tunnel channel; S, subdued streamlined forms; SE, smaller eskers within tunnel channel; TC, tunnel channel with scalloped margins. Air photographs A16170-186, A16170-187 and A16170-188 copyright 16 July 1958 Her Majesty the Queen in Right of Canada, reproduced from the collection of the National Air Photo Library with permission of Energy, Mines and Resources Canada.

-tunnel channel system trends obliquely to the major system (Figs. 2.1 and 2.2). South of this intersection, streamlined forms are less obvious and forms transitional between streamlined and transverse ridges are draped by marine sediments (Fig. 2.2). Marine limit crosses the area irregularly at ~150 m asl.

A sparsity of natural exposures and a possible bias toward sandy sections necessitates interpretation from description of each landform, the landform associations (Figs. 2.1-2.3) and limited sedimentary logs (Figs. 2.4 and 2.5). Each landform is described and interpreted separately. Finally, the most probable sequence of events is proposed.

Streamlined forms: observations

Streamlined forms (drumlinoid and fluted ridges) cover most of the area surrounding Ferguson Lake glaciofluvial complex (Figs. 2.2 and 2.3). Although these landforms are spatially gradational, flutes are more frequent in the north of the study area, whereas drumlins dominate the southern portion. Within the predominantly drumlinized zone, flutes occur downflow of the upflow-facing main channel wall (Fig. 2.3). Crescentic lakes, streamlined forms, and ice-marginal fans indicate a flow from the north-northeast.

Flutes separate elongate ridges up to 2.5 km long, 150 m wide, and 8 m high (Fig. 2.3). They are often occupied by elongate lakes. Crescentic lakes wrap around the proximal ends (north-northeast end) of some fluted ridges. These ridges differ from those described elsewhere (e.g., Shaw 1988); they are less clearly defined, and their crest lines often appear broken, or exhibit irregular low sinuosity (Figs. 2.2 and 2.3). Underlying stratified, interbedded, and undeformed glacigenic sediments are up to 40 m thick (Sharpe 1985) (Fig. 2.5*a*, sections 482 and 483).

Drumlinoid ridges are relatively straight-crested but generally shorter (< 1.5 km) and wider (150 to 300 m) than the fluted ridges (Fig. 2.3). They are predominantly spindle-shaped. The lakes associated with the drumlinized landscape vary in shape, but are generally elongate parallel with ridge orientation. The sediments within the drumlinoid ridges are similar to those in the fluted ridges, exhibiting undeformed, interbedded sand, gravel, and diamicton (Sharpe 1985, 1987).

Streamlined forms: interpretation

Elongate and crescentic lakes associated with streamlined fields are inferred to fill scour zones. A lack of deformation in the sediments of streamlined forms, the presence of crescentic lakes that wrap around their proximal ends, and enhanced fluting downflow of a positive step (channel wall) have been used to infer formation by erosive catastrophic meltwater sheets (cf. Shaw and Sharpe 1987). However, a complete absence of deformation in the streamlined sediments at the Ferguson Lake site cannot be claimed, as there were no laterally extensive exposures.

The crest lines of streamlined forms, unlike those described elsewhere, exhibit irregular low

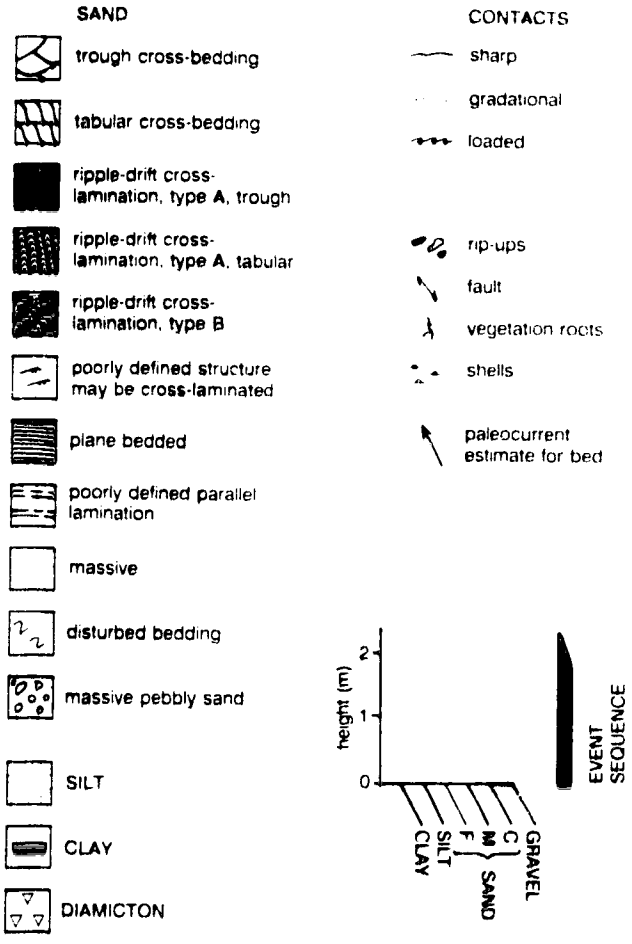

Figure 2.4. Legend for sedimentary logs.

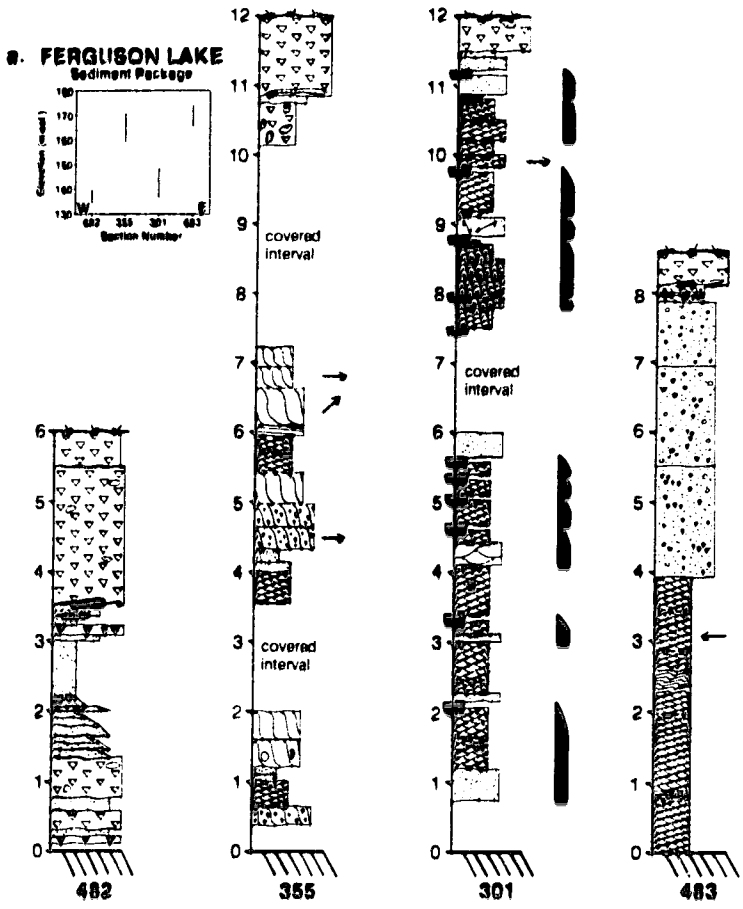

Figure 2.5. Sedimentary logs from the Ferguson Lake site, with paleocurrent estimates, event-sequence symbols, and elevation above sea level. See Figure 2.4 for legend. *a*. Landforms adjacent to and associated with the tunnel channel: fluted ridges (482, 483); residual hill in tunnel channel (355); and lobe adjacent to tunnel channel (301).

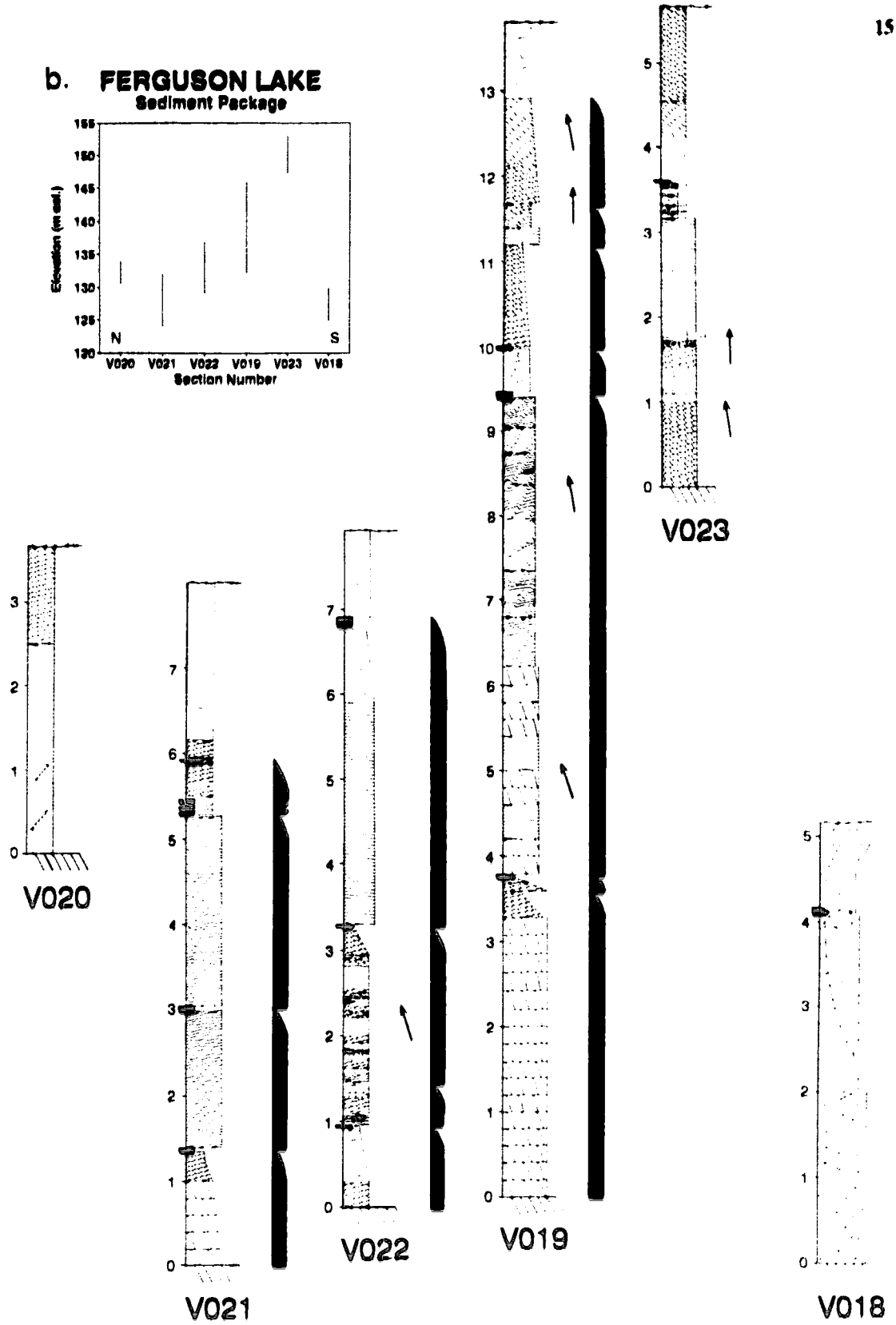

Figure 2.5. (*concluded*) *b*. Esker ridge (V019-V023) and double-crested ridge (V018).

sinuosity. There are a number of possible explanations for this. First, streamlined forms near Ferguson Lake may be immature forms, the formative flow having ceased prior to form completion. Second, forms may have been modified by mass wasting, melting of buried ice, or thermokarst erosion. Elsewhere on Victoria Island, massive ground ice has been observed (Sharpe 1992*a*). If the flutings at this site were eroded into ice-rich sediment, subsequent melting of that ice could impart low-sinuosity crest lines to streamlined forms. The inference of ice-rich sediment beneath the ice sheet would necessitate cold-based ice conditions at this site. Such conditions are favourable precursors to catastrophic meltwater events, as cold-based ice would prevent meltwater drainage until threshold conditions were reached (Shoemaker 1991). The source of such meltwater is uncertain. It may have been generated basally and up-ice from the Ferguson Lake site, ponded supraglacially in depressions in the ice surface, or included connected supraglacial and subglacial reservoirs (Shoemaker 1992*b*). The inferred event does not necessitate a gradual change to warm-based conditions at the study site either prior to or after catastrophic release (Shoemaker 1992*b*).

It is the intent of this paper to focus on the genesis of channelized glaciofluvial landforms rather than streamlined forms. We interpret streamlined forms as products of erosion by catastrophic meltwater sheets, as (*i*) our observations are consistent with those made by proponents of that hypothesis (cf. Shaw *et al.* 1989), and (*ii*) by espousing this hypothesis certain details of tunnel channel morphology may be explained, which would otherwise remain enigmatic.

Tunnel channels: observations

The main channel (45 km long, 1 to 2 km wide, and about 30 m deep) north of Ferguson Lake is sinuous, as are other smaller channels adjacent to it (Fig. 2.2). These channels cross-cut the streamlined field and are incised into glacigenic sediment (sections 482 and 483, Fig. 2.5*a*). Immediately downflow of the channel margins (to the southwest) flutes persist in a zone otherwise predominantly occupied by drumlinoid ridges (Fig. 2.3). A fluted sedimentary lobe appears to extend from the eastern margin of the main channel. Section 301 is exposed in this lobe (Fig. 2.2). Twelve or 13 rhythmic sequences (0.2 to 1.5 m thick) of cross-laminated medium to fine sand, fining up to silt or clay, are observed. Paleoflow was toward the east. The section is capped by diamicton and is below marine limit.

The morphology of the main channel is complex. Its thalweg is discontinuous and the channel margins are not parallel, but rather exhibit pronounced scallops along the western wall (Fig. 2.3). Within the scallops, crescentic lakes fill the deepest channel sections, and residual hills occur at their geometric focus, or offset slightly to the north (Fig. 2.3). Inset streamlined hills occur at a lower elevation than the surrounding land surface. Section 355 (Figs. 2.2 and 2.5*a*) is exposed in one such feature and exhibits tabular and trough cross-bedded sand indicating paleoflows towards the east and

northeast. The eastern side of the channel is less scalloped and exhibits more residuals (or less erosion) than the western side. Shallow inset channels, rather than deep scours, dissect the eastern portion of the channel (Figs. 2.2 and 2.3).

Tunnel channels: interpretation

The channels do not appear to be part of a connected fluvial system, which may have existed prior to the last glaciation. In addition, postglacial fluvial activity has been minor (cf. Jenness 1952). Tunnel channels are commonly observed to cross-cut streamlined fields and contain eskers (e.g., Wright 1973). This is the case for the channels at Ferguson Lake. Consequently, the channels at this site are considered to be tunnel channels. Form, sedimentology, and context of the main tunnel channel also support this interpretation.

Tunnel channels: form, sedimentology, and context

Given that flutes occur downflow of the western channel wall, it is probable that the channel existed prior to the formation of the streamlined forms. In addition, flutes on the lobe adjacent to the eastern channel wall are oriented parallel to those in the adjacent streamlined field. The sedimentary lobe was, therefore, modified by the event that produced the streamlined field. Consequently, the lobe must predate the formation of this field. Fining-upward rhythmites in this lobe are inferred to represent "overbank" deposits, each rhythmite associated with episodic broadening of the ice tunnel over the tunnel channel prior to fluting formation. The diamicton cap may have been deposited before or after the fluting event and may have also been reworked or winnowed by later marine inundation (section 301 is below marine limit), or reworked by solifluction. However, the presence of interbedded sand and diamicton within section 482 necessitates their deposition prior to fluting formation. The diamicton cap has a similar composition to underlying diamictons. In addition, the meltwater event inferred to have eroded the flutes may have also left basal ice relatively debris poor (cf. Shaw *et al.* 1989). Consequently, the diamicton cap was most likely deposited prior to fluting formation.

The scalloped tunnel channel walls are interpreted to be the product of scour, both associated with the meltwater sheet flood event, and during later channelized flow. The deepest scours are along the western side of the channel and are now filled by crescentic lakes (Fig. 2.3). Inset streamlined hills are inferred to be residuals, either of older glacigenic sediments (Sharpe 1985), or of glaciofluvial sediments deposited during the formation of the streamlined field. The eastern side of the scalloped portion of the tunnel channel exhibits more residuals (or less erosion) than the western side. Flow from the north-northeast, which produced streamlined forms, cut across the preexisting tunnel channel. Preferential deposition of the coarsest material carried by the subglacial sheet flow, at points of flow separation or negative steps (channel wall), is inferred for the eastern side of the channel. In addition, cross-beds in a within-channel residual indicate easterly and northeasterly paleoflows. These are

interpreted as dunes that may have been deposited by a return eddy generated at the channel wall during the sheet-flow event.

At the Ferguson Lake site, the angle of skew (α) of the negative step (channel wall) is about 160° to the inferred sheet flow. For $135° < \alpha < 180°$, the flow-separation bubble produced at a negative step forms a vortex that adds both axial velocity and rotational components to flow (cf. Allen 1982). The length of the separation zone (distance to the point of flow reattachment) is primarily controlled by the relative roughness at the step, determined by the ratio of flow depth (h) to step height (H). At this site ($H \approx 30$ m, $h \approx 10$ m; cf. Shaw 1989), the separation bubble would have been approximately 255 m (160 m if $H \approx 20$; cf. Allen 1982, p. 111, fig. 3-10). The tunnel channel now has a width on the order of 1 km, but was presumably narrower during the proposed sheet-flow event. The channel is inferred to have been narrower, as sediment was preferentially deposited at the eastern side of the channel during the sheet-flow event, and the channel would also have been eroded by later channelized flow. However, it is probable that the zone of flow reattachment occurred within the tunnel channel. Scour along the reattachment zone may account for the deepest scours at the western side of the channel. In addition, streaming of vortices in a subglacial sheet between streamlined forms upflow would have concentrated scour at intervals across the sheet. This could account for the scalloping of the western wall. Hence, the distribution of scallops may be related to the angle of impingement of the vortices on the western wall and the arrangement of vortices in streams within the formative flow.

Deeper scours at the western side of the tunnel channel are explained primarily as the imprint of vortices within the tunnel channel, contemporaneous with the formation of the streamlined forms. By contrast, the shallower scour channels at the eastern side may have been eroded by subsequent channelized meltwater. In addition, such sediment-charged, high-velocity flows would have enhanced the scallops in the western wall by mechanical erosion and melting of ice-rich sediment (cf. Mathews 1973). Channel walls may have also been modified by later thermokarst erosion.

Scouring by channelized meltwater has produced a complex tunnel channel morphology. A combined substrate (N-channel; Nye 1973) and ice tunnel (R-channel; Röthlisberger 1972) could explain the observation of a discontinuous thalweg, by allowing intertwined vortices in the channelized flow to impinge upon the base of the ice sheet, as well as upon the basal substrate. Alternatively, or in addition, repeated reoccupation of the tunnel channel after the formation of the streamlined forms, and possibly during successive lesser discharge events, may have further complicated tunnel channel morphology.

Depositional ridges: observations

The depositional ridges are primarily eskerine, although they may include deposits at the eastern margin of the tunnel channel as previously described. The ridges occur at a number of scales, from a major esker running south of the tunnel channel, to smaller discontinuous esker segments within the

tunnel channel, to small double-crested ridges west of the major esker (Fig. 2.3).

The broad-crested, major esker at this site is about 500 m wide and it exhibits kettle holes and erratic boulders (Fig. 2.3). It extends south from the eastern margin of the tunnel channel, continuously for 8.5 km, at which point it is intersected obliquely by a second esker-tunnel channel complex (Fig. 2.2). It is bounded to the west by a string of lakes. To the east, the topographic gradient is more gradual.

Few natural exposures exist within the major esker (Figs. 2.3 and 2.5*b*). Surficial materials are mainly pebble-sized clasts, whereas underlying beds have a maximum grain size of coarse sand. Section V023 is primarily composed of ripple-drift cross-lamination types A and B (subsequently referred to as RDXL A and RDXL B, respectively), parallel-laminated, and massive sand. One clay drape was noted (Fig. 2.5*b*). A longer sedimentary record was acquired from the major esker as it extends from the tunnel channel (sections V019-V022, Figs. 2.3 and 2.5*b*). The maximum grain size in these sections is coarse sand. The sections are rhythmically bedded. Each rhythmite is a fining-upward sequence from coarse, medium or fine sand, to silt or clay (see event sequences, Fig. 2.5*b*). No extensive faulting was observed. Paleocurrents were towards the north (Fig 2.5*b*; Appendix 1). All sections were located near the western flank of the esker.

Double-crested ridges occur mainly to the west of the Ferguson Lake esker (Fig. 2.3). Some of these are short, solitary segments up to 100 m long. Others form a dendritic pattern about 2 km long, adjacent to the esker and possibly associated with the west side of the expanded tunnel channel zone (Figs. 2.2 and 2.3). The double-crested style is enhanced by small lakes infilling a centre-line depression. Section V018 is a sedimentary sequence from the eastern side of a double-crested ridge (Figs. 2.2 and 2.5*b*). The sedimentary package fines upward and is capped by a rubbly diamicton. Interbedded coarse and medium sand overlies massive coarse sand and granules. The whole section is disturbed by folding and a series of curvilinear reverse faults (Fig. 2.5*b*) with displacement towards the centre-line depression.

Depositional ridges: interpretation

Most of the sediments in the main esker form fining-upward rhythmites. Each rhythmite is inferred to represent a waning-flow sequence. Sedimentary structures indicate relatively low energy conditions. Within-rhythmite repetition of structural sequences is inferred to represent responses to pulsed meltwater velocity or suspended sediment supply (cf. Lowe 1988). The clay drapes suggest that the meltwater system completely shut down from time to time, although the conduit (R-channel) remained water-filled during esker formation. The rhythmic sedimentary packages, the thinness of some rhythmites, and the presence of clay drapes suggest possible seasonal control on sedimentation and, thus, a supraglacial meltwater source (cf. Weertman and Birchfield 1983; Hebrand and Åmark 1989). The ice sheet must have been warm based or polythermal at this time.

Sections were exposed only in the upper and marginal portions of the main ridge. The relatively low-energy conditions inferred from the sediments may be explained either in terms of lateral deposition within a subglacial conduit during waning or low-discharge events, or as the product of subaqueous deposition within an ice-walled channel or reentrant. Marked textural differences between surficial sediments and those exposed within the ridge question the validity of inferring esker genesis primarily from the texture of surficial materials (e.g., St-Onge 1984).

Northward paleoflow in the major esker was approximately opposite to the flow direction inferred for the streamlined forms. Following flooding and bed separation, extremely low ice-surface gradients are expected (Shoemaker 1991). Thus, local piezometric surfaces may have driven subglacial meltwater northward (cf. Shreve 1985). Alternately, meltwater flow within enlarged subglacial conduits (broad R-channels at atmospheric pressure; Hooke 1989) or ice-walled reentrants with embayments (i.e. geometrically nonuniform conduits) may have effected local northward currents now recorded in sediments toward the western esker flank.

Double-crested ridges with sediment displacement toward a centre-line depression were probably initially deposited over ice or ice-rich sediment as single ridges within ice-walled channels. Melting of the underlying ice resulted in a faulted, double-crested ridge (cf. McDonald and Shilts 1975). The rubbly diamicton cap may be a till, which would indicate the existence of an ice roof to the channels. However, it contains very little clay, so may be better explained as the product of marine reworking and solifluction of glaciofluvial sand and gravel, particularly as the exposure is well below marine limit.

The relatively small size of the eskers and double-crested ridges suggests that they were probably some of the last depositional products of the glaciofluvial system. Lack of features indicating former ice-marginal positions, the well preserved nature of the landform elements, and the variable paleocurrent directions suggest regional ice stagnation toward the end of deglaciation (Sharpe 1992*a*, 1992*b*). Therefore, both eskers and double-crested ridges likely represent deposition in ice-walled channels (with or without an ice roof) under stagnant ice conditions.

Inferred sequence of events

Formative processes for the Ferguson Lake glaciofluvial complex have been inferred from landform associations and morphology, and sedimentary logs. The event sequence is complicated by the existence of a channel prior to the formation of the streamlined field. This channel was likely cut by earlier channelized subglacial meltwater flow (Fig. 2.6*a*). Under high meltwater discharges, localized lifting of the ice from the bed resulted in the deposition of glaciofluvial sediment in a splay lobe. Beyond this complication, a parsimonious interpretation of the observed landform suite is adopted. A subglacial meltwater sheet is invoked to explain the streamlined forms as surficial elements eroded into

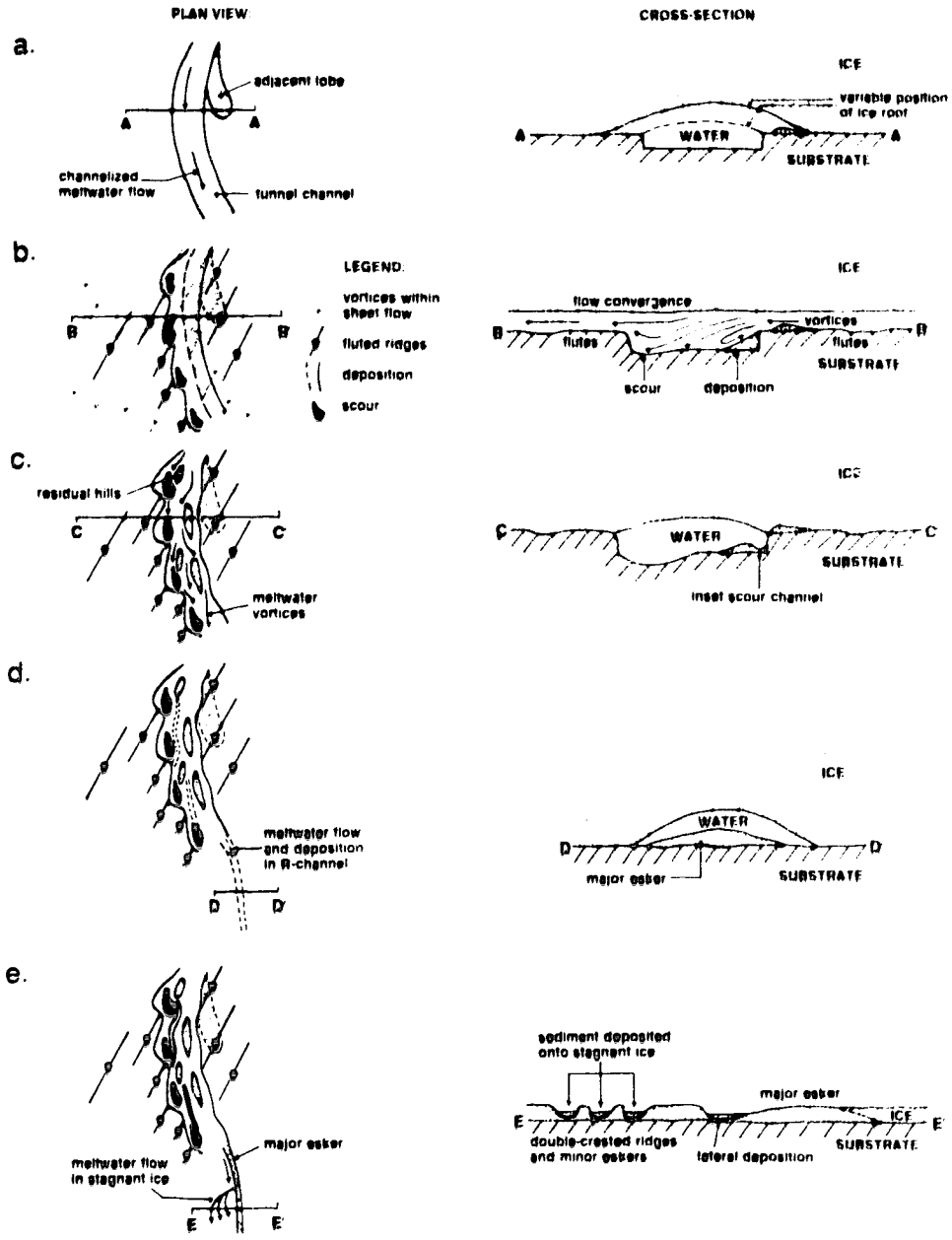

Figure 2.6. Schematic illustration of the temporal (*a-e*) sequence of events at the Ferguson Lake site (note scale changes). *a*. Tunnel channel cut into preexisting glacial sediments by earlier catastrophic subglacial meltwater flow in R/N-channel. Overbank deposition of splay lobe. *b*. Formation of streamlined terrain, and scalloped margins, crescentic scours and return-eddy deposits of tunnel channel, by catastrophic subglacial meltwater sheet flow. *c*. Further erosion of tunnel channel and formation of shallower scour channels and residual hills by catastrophic subglacial meltwater flow in R/N-channel. *d*. Ice stagnation and formation of major esker by seasonally controlled, subglacial meltwater flow in R-channel. *e*. Formation of double-crested ridges and minor eskers in open conduits (presence of ice roof unknown).

thick, ice-rich sediment (Fig. 2.6*b*). Such a catastrophic meltwater release may have been accompanied by ice-sheet surging along the path of the meltwater sheet (cf. Shoemaker 1992*a*). A meltwater-sheet event would have included flow separation and sediment deposition in the obliquely oriented channel. Impingement of vortices on and below the downflow channel wall may have initiated the scalloped margin. Crescentic scours were also eroded at this time, at points of flow reattachment within the tunnel channel. Under waning flow, a reduced meltwater discharge was confined to the tunnel channel, resulting in shallow scours and low residual hills within the channel. It is probable that meltwater also cut upward into the ice at this time, forming a combined R, N-channel (Fig. 2.6*c*). When a threshold was reached in the supplying meltwater reservoir, flow within the tunnel channel ceased (cf. Shoemaker 1992*b*) and ice may have invaded the channel. It is probable that the ice-surface gradient was drastically altered by decoupling of the ice sheet from its bed; the decoupled section carried virtually no shear stress. Later, within stagnant ice, seasonally controlled meltwater drained subglacially by way of an R-channel within the tunnel channel (cf. Shreve 1985). The esker formed in this R-channel (Fig. 2.6*d*). Discontinuous eskers within the tunnel channel may be the result of localized conduit closure against obstacles (residual hills), nondeposition, or a downflow connected N- and R-channel meltwater system. Double-crested ridges were deposited in open conduits (Hooke 1989) or cracks (King and Buckley 1969) in stagnant ice (Fig. 2.6*e*).

The above sequence is simplified. It is likely that the tunnel channel carried several separate discharge events. In addition, meltwater discharge through an R-channel is inferred to fluctuate over time, contingent upon whether supraglacial to subglacial meltwater routing was direct or indirect (cf. Willis *et al.* 1990). Seasonal influence is suggested by rhythmicity and clay drapes in the esker sediments.

Augustus Hills glaciofluvial system

Landform associations

Augustus Hills is part of a broad, flat-topped ridge with an approximate east-southeast – west-northwest trend (Figs. 2.1 and 2.7). This ridge is part of a discontinuous glaciofluvial system that may extend from Mount Pelly in the east to about 10 km west-northwest of Augustus Hills, or possibly beyond Wellington Bay (Fig. 2.1). East of Mount Pelly, a bedrock channel now containing elongate lakes that wrap around residuals, and a field of streamlined forms trending east-west, may also be associated with the ridge (Fig. 2.1). The channel is inferred to be a tunnel channel. At Augustus Hills, the ridge is up to 3.75 km wide, with a maximum elevation of about 100 m asl (Fig. 2.7). It exhibits asymmetric cross profiles, an irregular long profile and a sinuous crest line. The southern portion of the ridge has raised strandlines. The whole feature was drowned by marine incursion to about 157 m asl after about 9 ka BP (Sharpe 1992*c*).

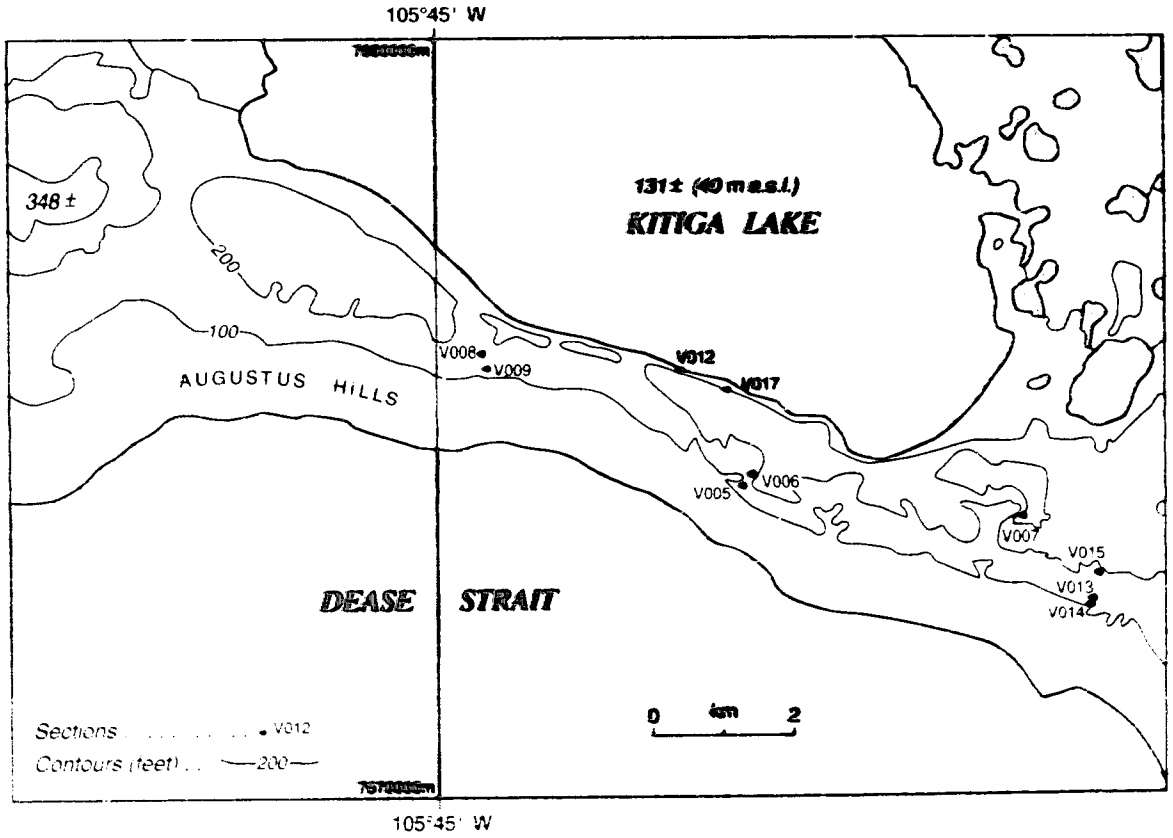

Figure 2.7. Map of section locations and morphology at the Augustus Hills site. See Figure 2.1 for location.

Sedimentary package

Ten recorded sections, ranging in height from 5.00 to 22.74 m, document sediment over about 52 m of the ridge height (Fig. 2.8). The sedimentary sequence is unknown below approximately 47 m asl at the crest and 34 m asl at the flanks of the ridge. Where exposed, the sediment comprises glaciofluvial sand, silt and clay, capped in places by shelly deposits and aeolian sand. Lone gravel clasts occur within medium and coarse sand units. Only toward the top of section V007 does gravel constitute the dominant grain size. Here, the cobbles are striated. To the west end of Augustus Hills, isolated boulders are perched on the surface.

Sedimentary architecture is broadly parallel or sheet-like and gently undulatory (Fyles 1963). However, a pronounced undulatory surface is observed towards the top of sections V014 and V015. Section V005, situated on the ridge flank, exhibits faulting, although no one fault extends through the entire section (Fig. 2.8).

Most sections exhibit a number of fining-upward sequences, from very coarse, coarse, medium, or fine sand to fine sand, silt, or clay. Sedimentary sequences are delimited by event-sequence symbols on Figure 2.8. Some sequences coarsen and then fine upward. Sequence thickness varies from about 0.05 to 4.60 m. One sequence in excess of 20 m constitutes most of section V007. Clay drapes are generally thin (<0.01 m), but thick clay units (>0.1 m) are observed. Sedimentary sequences may begin with plane-bedded, cross-bedded, or cross-laminated sand, or sand with a poorly defined structure that may be cross laminated, progress up to cross-laminated sand, sand with a poorly defined structure, or massive sand and silt, and most are draped by parallel-laminated silt or clay. Some cross-bedded cosets in medium sand are abruptly punctuated by clay. In places, tabular cross beds and RDXL A alternate (section V017, Fig. 2.8). No oscillatory wave cross lamination was observed. Paleocurrent measurements from 28 cross-bedded and cross-laminated cosets show a mean direction of 273° (Fig. 2.8; Appendix 1).

Most of the contacts between cosets and event sequences at Augustus Hills are sharp and undulatory. However, gradational contacts exist at transitions between RDXL A and RDXL B, or where massive sand and sand with a poorly defined structure repeat. Other contacts are irregular and faulted (section V005; Fig. 2.8), or loaded with convolutions and flame structures (cf. section V009; Fig. 2.8). Loaded contacts are particularly associated with the more massive and texturally differentiated sequences.

Trends in grain size, sedimentary structure, and event-sequence thickness are shown in Figure 2.9. It should be noted that (*i*) section V008 has been omitted, as the sediments in this section appear to have been reworked by marine and aeolian processes; (*ii*) section V007 has been omitted, as most of the section represents a single event sequence, which is at a higher elevation and noncorrelative with

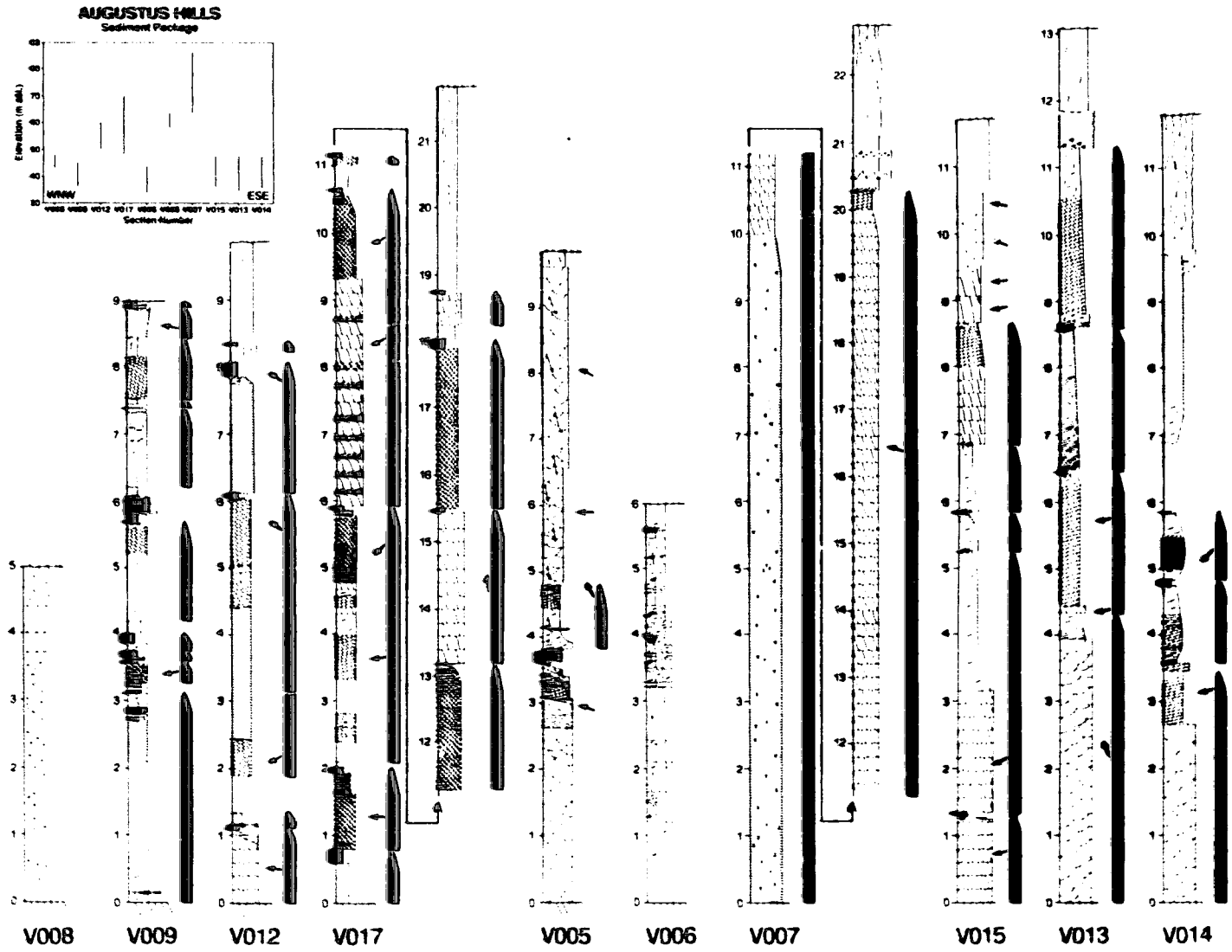

Figure 2.8. Sedimentary logs from the Augustus Hills site, with paleocurrent estimates, event-sequence symbols, and elevation above sea level. See Figure 2.4 for legend.

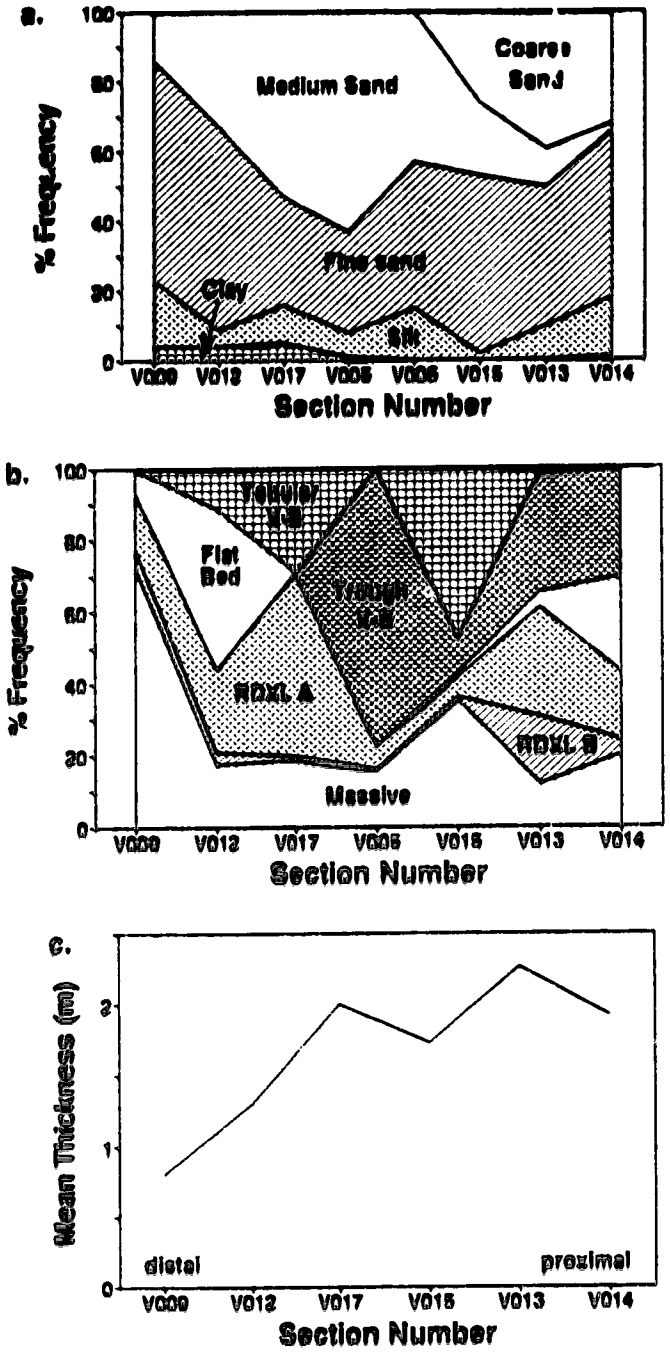

Figure 2.9. Augustus Hills. *a*. Grain-size frequency by section. *b*. Structural frequency by section (flat beds include primarily proximal plane beds and primarily distal draped lamination). *c*. Mean event-sequence thickness by section. Sections arranged in order, from proximal (right) to distal. Note sections represent point data, but connecting lines are drawn to aid visual clarity. See text for sections omitted.

the other sections (discussed on page 28); and (*iii*) section V006 has been omitted from Figures 2.9*b* and 2.9*c*, as the sediments have been disturbed by slope movement and exhibit no primary structures. Only sections with more than one recognizable event sequence are included in Figure 2.9*c*. In general, coarse sand is observed only in the more proximal sections, whereas fine sand, silt, and clay accounted for about 70% of the sediment in the more distal sections (Fig. 2.9*a*). Trough cross-beds are more frequent proximally and are replaced by tabular cross-beds downflow. Massive sand dominates the most distal section (Fig. 2.9*b*). Syndepositional deformation in the form of flame structures and convolutions is also more prevalent distally. The mean thickness of event sequences decreases distally (Fig. 2.9*c*).

Interpretation/discussion

Depositional environment

A sinuous ridge morphology, strong unidirectional flow inferred from sedimentary structures and paleocurrent estimates, and a lack of bidirectional forms, which may have resulted from waves or tidal currents at Augustus Hills, suggest that this ridge is an esker rather than a beach ridge, baymouth bar, or spit. The coastal location, strandlines, and presence of marine shells confirm later marine reworking.

As soon as the ice retreated during deglaciation, the isostatically depressed land surface was immediately inundated by a postglacial sea. As there was minimal postformational disturbance of the sediments, it is unlikely that they were deposited onto ice. This rules out supraglacial and englacial sites of deposition (cf. Banerjee and McDonald 1975). Indeed, Powell (1983) has reported that supraglacial streams are absent and englacial streams rarely flow from tidewater glacier fronts because of their highly crevassed nature. The ridge must, therefore, have been deposited subglacially or ice-marginally. In either case, meltwater would have likely debouched subaqueously into high standing water which was probably brackish.

The sediments are generally similar to subaqueous outwash deposits (e.g., Rust and Romanelli 1975). First, they exhibit proximal to distal fining, which argues for a continuity of sedimentation along the length of the ridge. Second, depositional processes inferred from the frequency of sedimentary structures indicate that deposition from suspension dominated the most distal section. Load structures also indicate high rates of sedimentation from suspension (e.g., Cheel and Rust 1986). It may be expected that RDXL B would be more common than RDXL A in distal locations. This is not the case, but may be accounted for by the high frequency of massive units, and units with poorly defined structure, in distal sections. In this case, the rate of deposition from suspension is inferred to be so rapid that ripples rarely formed in the under-loose bed. Hydrodynamically, the distal transition from trough to tabular cross-beds may be attributed to a reduction in stream power or flow velocity and also implies synchronous sedimentation along the ridge. Third, the mean thickness of event sequences

decreases distally.

Subaqueous outwash commonly contains gravel (e.g., Cheel and Rust 1982). Its absence in Augustus Hills has several possible implications. First, the system may have had insufficient velocity or power to entrain and transport gravel. Second, gravel may not have been available to the system. The second possibility seems unlikely, as other smaller eskers in the area and the local till contain gravel. Third, gravel may be present in the ridge core, although it is not exposed. For example, an arched gravel core may exist below 47 m asl at the ridge crest and 34 m asl at the flanks. Surficial gravel units may represent marine winnowed diamicton, which was deposited onto the esker surface from the stagnating ice sheet, or dropstones from icebergs or sea ice.

The irregular crest line is problematic, as deposition into a standing-water body would have produced a surface sloping distally. Some undulatory surfaces within the ridge may have been formed by in-phase waves (Cheel 1991) associated with supercritical density currents (cf. Hand 1974) or supercritical flow exiting a confined system (cf. Rajaratnam and Subramanyan 1986). The undulatory character may be a product of time-transgressive sedimentation, or sedimentation into a closed conduit of nonuniform geometry. However, trends in sedimentary texture and structure and a relatively planar sedimentary architecture argue against these interpretations. The irregular ridge surface may be simply a product of post-depositional gullying. From the available exposure it was not possible to determine whether the full sedimentary package (Fig. 2.8) represents a continuous time (vertical) sequence, or whether vertical and lateral sedimentation were differentiated over time and related to conduit expansion. Such differentiation in vertical and lateral sedimentation over time may account for the anomalous, noncorrelative, thick (20.3 m) single event recorded in section V007 close to the ridge crest.

The question remains as to whether the site of deposition was subglacial or ice marginal. The site of deposition must account for low paleocurrent variability, ridge morphology, and lateral faulting. Taken together, these lines of evidence suggest that sedimentation must have been in an ice-walled channel (Banerjee and McDonald 1975). There is no diagnostic evidence for or against the presence or absence of an ice roof during deposition of the exposed sediments. However, as Augustus Hills is below marine limit, it is reasonable to assume high sea level at the time of ridge formation. High sea level and lateral ice support favour deposition in a broad ice tunnel flowing full of water. It is difficult to imagine the alternative, a very narrow inlet into the ice front.

Meltwater regime

The most significant observation from the exposed sections is sediment rhythmicity. Each of these rhythms may represent one event. The textural and structural progression through each sequence is indicative of waning-flow conditions. Coarsening-upward to fining-upward sequences are inferred to represent turbidity-current activity. The alternation of ripples and dunes within one event sequence is inferred to record spatial differentiation of sedimentary structures within a declining meltwater discharge

sequence, rather than flow-velocity fluctuations. This differentiation may result from ripples climbing up the stoss side of the dunes and supplying sediment to the dune foresets, or to ripples forming in the lee of the dunes before being overridden by dune migration (Allen 1982).

Clay drapes were probably produced in standing water when discharge effectively ceased. If meltwater supply was shut down, sea level would have effectively ponded subglacial meltwater by raising the height of the piezometric surface (Powell 1990), providing an environment suitable for clay deposition. Such shutdown is expected in winter, hence the clay drapes are used to infer a seasonality to the rhythmites with relatively thin clay caps. This implies a supraglacial to subglacial connection in the meltwater system (cf. Hebrand and Åmark 1989) and warm-based ice conditions. Although a seasonal shutdown of meltwater discharge may explain thin clay drapes, it does not account for the relatively great thickness of some of these units (up to 20 cm). In a tidewater setting, salt-water incursion into the conduit during successive winters may have flocculated clays. Thick clay units may have resulted where clay was continuously supplied by low meltwater discharges near the end of the melt season and was flocculated upon contact with salt water.

In addition to the seasonal implications of clay drapes, many of the event sequences are suggestive of quasi-continuous or episodic sedimentation from turbidity currents (cf. Burbidge and Rust 1988). Conversely, the presence of persistent plane-bedded and cross-bedded units is indicative of more steady, uniform flows. Alternatively, these units may indicate very high energy turbidity currents with power to transport coarse sands and deposit them as traction bedforms (Allen 1982). Diurnal or weather-related discharge events affecting subglacial water pressure and subglacial plumbing may have controlled these sediment pulses (Østrem 1975; Willis *et al.* 1990).

To summarize, Augustus Hills is inferred to have formed subaqueously by deposition in an ice-walled channel, probably with an ice roof, in stagnant ice. Closed-conduit conditions are probable if high sea levels are assumed. The sedimentation is rhythmic and was probably seasonally controlled. Pulses within seasonal events may be the result of diurnal or weather-related discharge events, or changes in subglacial plumbing (Gorrell and Shaw 1991). The disturbed sand at the top of most of the sections is the product of later ridge modification by marine, mass-movement, periglacial, pedogenic, and aeolian activity.

Namaycush Lake glaciofluvial complex

Landform associations/ridge morphology

Namaycush Lake glaciofluvial complex provides an example of the association between an esker, subaqueous fans and extended deposits, located at the edge of streamlined terrain, and extending from a channel to the north (Figs. 2.1, 2.10 and 2.11). Extended deposits are defined as a zone of hummocky

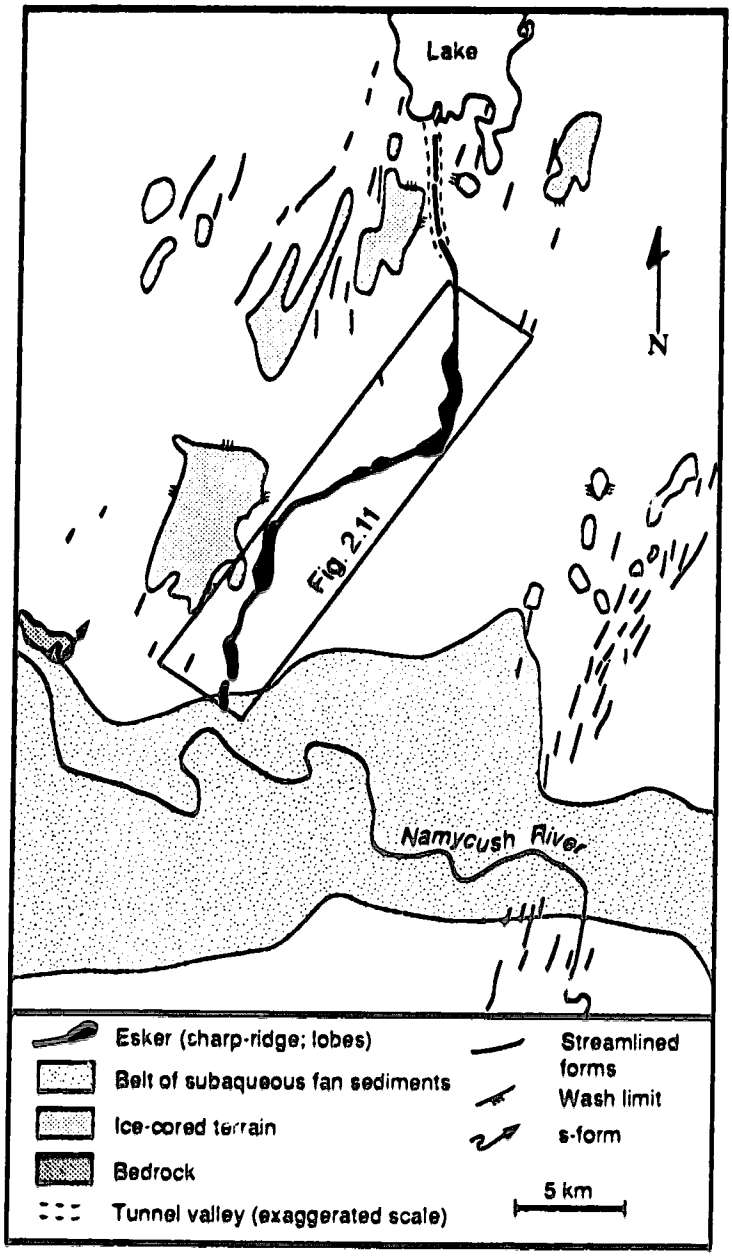

Figure 2.10. Map of landform associations at the Namaycush Lake site, and location of Figure 2.11. See Figure 2.1 for location.

Figure 2.11. Air photograph mosaic showing esker (E), fans (1-3), extended deposits (4), and section locations (V033, V034) at the Namaycush Lake site. See Figure 2.10 for location. Air photographs A16170-49, A16170-109 and A16170-110 copyright 16 July 1958 Her Majesty the Queen in Right of Canada, reproduced from the collection of the National Air Photo Library with permission of Energy, Mines and Resources Canada.

sediments that occur lateral to, and run parallel to, a bend in the esker ridge. Adjacent streamlined terrain, escarpment noses, and comma forms indicate flow from the south-southwest, whereas streamlined terrain to the north indicates divergent flow from the northeast (Fig. 2.1). Ice-cored hills are present within streamlined terrain (e.g., Sharpe 1992*a*). A broad belt of subaqueous fan sediments occurs to the south (Fig. 2.10). The esker is continuous for about 27 km and trends south and southwest across relatively flat terrain, below marine limit. It is a single, sharp-crested, sinuous ridge with no sedimentary exposures (Fig. 2.11). Three lobate fans extend from the esker (1, 2, and 3, Fig. 2.11). In addition, extended deposits appear to underlie the main ridge at site 4 (Fig. 2.11).

Sedimentary sequences in fans: observations

Two sedimentary logs were recorded for fans 1 and 3 (Figs. 2.11 and 2.12). Paleocurrents from RDXL indicate paleoflow with a southward component (130° to 220°; Fig. 2.12; Appendix 1). Fan 1, the smallest fan, contains silt to coarse sand, with fine sand the most common (section V033; Fig. 2.12). A number of fining-upward event sequences, varying in thickness from 1.50 to 0.02 m, are observed. RDXL A dominates the lower 6 m of the section, whereas massive and plane-bedded sand appear to dominate the upper part. No clay is present.

Fan 3 contains sediments with a maximum grain size of medium-fine sand (section V034; Fig. 2.12). In detail, the recorded succession comprises a large number of fining-upward packages in massive sand and silt, with thicknesses varying from a few millimetres to a few centimetres. Only two clay drapes a few millimetres thick were observed.

Fans and extended deposits: interpretation

The sedimentary package in fan 1 (section V033) indicates pulsed flows with traction processes having dominated the lower 6 m of the section, and sedimentation from traction and suspension having dominated the upper part. If clay drapes are interpreted as seasonal markers, their absence in fan 1 suggests that the whole sequence was deposited in a single year (Smith and Ashley 1985). Given the small size of the fan, this suggestion is plausible.

Deposition from suspension with very little traction transport may be inferred from fan 3 sediments. Thin clay drapes imply seasonal control on sedimentation, and deposition of section V034 over three years is favoured. The event sequences between these clay drapes have a much higher frequency than those observed in the Augustus Hills esker. Diurnal or weather-related controls, or changes in subglacial plumbing related to fluctuations in subglacial water pressure within a melt season, may be inferred for these pulses. The record of numerous within-season pulses suggests that fans preserve low-magnitude events better than do eskers (Gorrell and Shaw 1991).

The location of the extended deposits at a bend in the esker path may be critical to their interpretation. When water flows around a bend, a relatively high pressure is created. During high

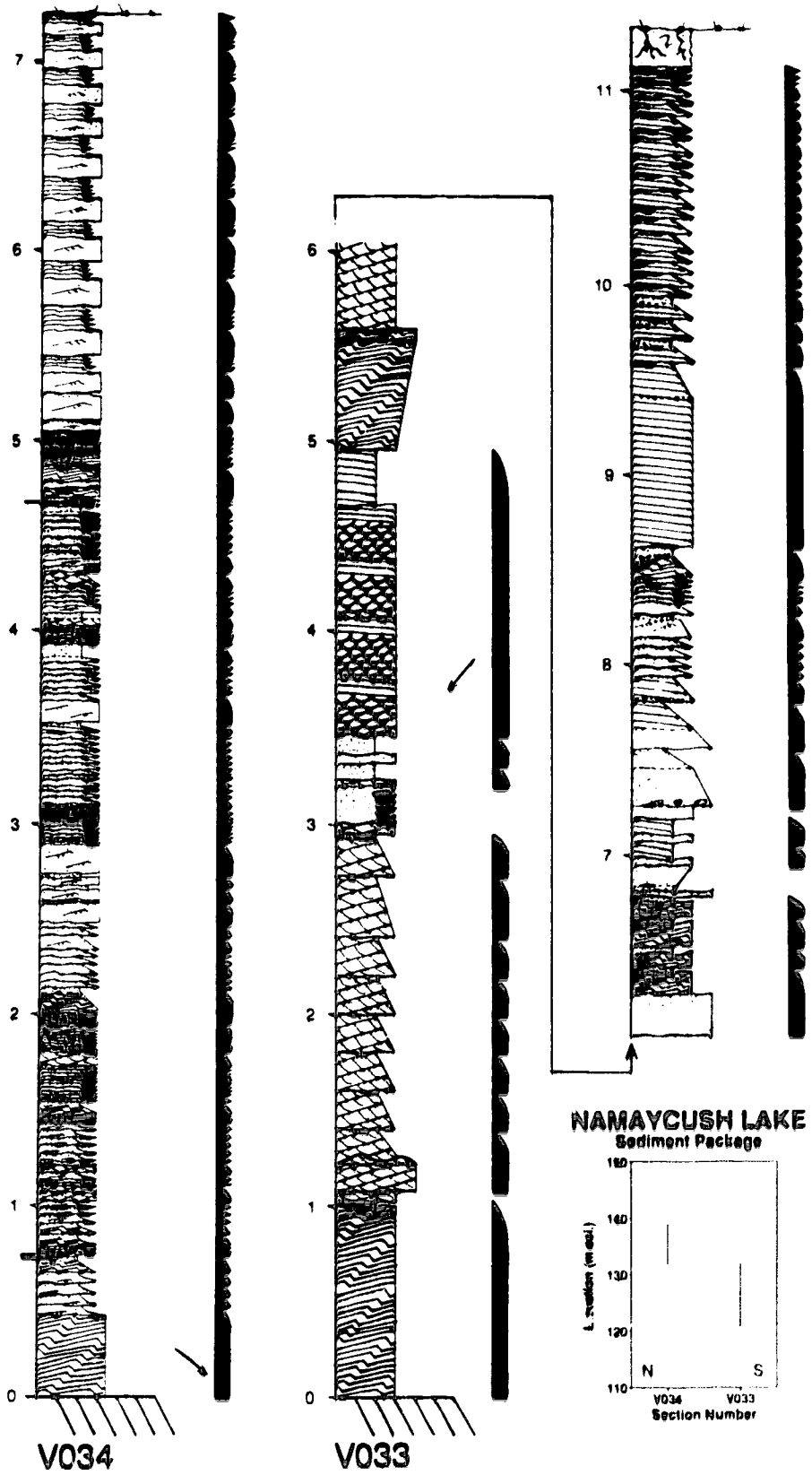

Figure 2.12. Sedimentary logs from the Namaycush Lake site with paleocurrent estimates, event-sequence symbols, and elevation above sea level. See Figure 2.4 for legend.

meltwater discharges this could cause localized hydraulic lifting of the ice sheet. An increase in meltwater discharge causes an increased velocity within a conduit, which results in increased sediment transport. Local uplift at the bend causes local flow expansion and deposition of extended deposits. When discharge declines, normal high-pressure zones are reestablished at the conduit margins, isolating subsequent esker deposits from the extended deposits. The localized ice floatation inferred here may require proximity to a grounding line (Gorrell and Shaw 1991) or ice margin that may be represented by the belt of subaqueous fan sediments further south.

Discussion: depositional environment and meltwater regime

The association of a continuous esker ridge with a possible tunnel channel to the north, and a broad belt of subaqueous fan sediments to the south, suggests a subglacial site of deposition for the esker ridge at the Namaycush Lake site. The thick belt of subaqueous fan sediment to the south, suggests that fan 1 may record an ice-marginal position (cf. Burbidge and Rust 1988). However, the lack of other east-west belts of subaqueous sediments and the landform associations at site 4, argue for subglacial deposition in cavities, perhaps proximal to a grounding line (Gorrell and Shaw 1991), for the remainder of the fans.

Paleoflow patterns present an enigma in event reconstruction at the Namaycush Lake site. Whereas the esker sediments indicate a southerly paleoflow, adjacent streamlined forms indicate earlier northeasterly flow. If streamlined forms, comma scours, and escarpment noses relate to erosive meltwater sheet flows (cf. Shaw *et al.* 1989), such exceptional drainage events would have lowered ice-sheet profiles and may have influenced local distribution of meltwater head, or both, producing a new hydraulic gradient to drive subglacial meltwater in the opposite direction. The time between the formation of the streamlined fields and the eskers is unknown. It is possible that the esker was formed by meltwater that was driven by a hydraulic gradient inherited from the event which produced the streamlined field to the north.

Esker deposits are inferred to record subglacial drainage of meltwater from supraglacial sources. However, the seasonal melt control on esker sedimentation may be either by direct supraglacial to subglacial routing or by indirect filtering through a subglacial meltwater system which may also include linked-cavity or cavity-film drainage (cf. Willis *et al.*, 1990).

Implications for ice-sheet dynamics

Reconstruction of ice-sheet dynamics from landforms requires interpretation of the sediments within them as well as of their morphology and landform associations. The details and vagaries of glacial hydrology and hydraulics for three sites on Victoria Island have been outlined. In general, the landforms produced by erosional events (streamlined forms and tunnel channels) are inferred to record low-frequency, high-magnitude changes in meltwater discharge related to catastrophic drainage in sheets

and combined R/N-channels, whereas depositional landforms (eskers, associated fans, and extended deposits) record the subtleties of lower-magnitude, R-channel drainage of predominantly supraglacial meltwater. Together, these landforms record the activity of subglacial meltwater processes through the course of deglaciation. A temporal disconnection between the different drainage conditions is suggested by possible paleoflow reversals between the formation of the streamlined terrain and eskers. Lateglacial meltwater storage and flow may have locally altered the low ice-sheet profile (Shoemaker 1991, 1992*a*, 1992*b*) to produce cross-cutting relationships and even flow reversals between streamlined forms and eskers. As the streamlined fields exhibit complex cross-cutting relationships (Fig. 2.1), the location of the proposed M'Clintock dome (Dyke 1984) cannot be relevant to any of the landforms discussed here (Sharpe 1992*a*, 1992*b*), whether they were formed by ice or water. Indeed, it is likely that most of these landforms were formed after glacial maximum (Fyles 1963; Sharpe 1992*a*, 1992*b*)

It has been suggested that the eskers at the three sites lack major postdepositional disturbance and have in common a tunnel channel. Consequently, at least an early phase of esker sedimentation may have occurred in a subglacial environment. Although it is not possible to unequivocally determine whether the eskers were formed contemporaneously along their length, or in segments, time-transgressively, textural and structural trends in sediments suggest a continuity of processes along their length. This continuity argues for synchronous sedimentation along the length of the esker ridges, in subglacial conduits, rather than time-transgressive sedimentation at a retreating ice margin. This is supported by a lack of recessional ice-marginal landforms and sediments (Sharpe 1992*a*).

The details of esker sedimentology and morphology have been used to reconstruct local ice-sheet dynamics. The presence of eskers indicates warm-based or polythermal ice conditions. A continuous esker at the Namaycush Lake site records seasonally controlled discharges with localized ice floatation events in a subglacial conduit near a grounding line. The less connected or disconnected ridges at Augustus Hills and Ferguson Lake sites also record seasonally controlled discharge events and were produced by a thinning and stagnating ice mass. They may have been deposited in subglacial R-channels or ice-walled reentrants, the former being more probable.

References

Allen, J.R.L. 1982. Sedimentary structures: their character and physical basis, Vol. II. Developments in Sedimentology 30, Elsevier, Amsterdam.

Arnold, N.S., and Sharp, M. 1992. Influence of glacier hydrology on the dynamics of a large Quaternary ice sheet. Journal of Quaternary Science, 7: 109-124.

Banerjee, I., and McDonald, B.C. 1975. Nature of esker sedimentation. *In* Glaciofluvial and glaciolacustrine sedimentation. *Edited by* A.V. Jopling, and B.C. McDonald. Society of Economic Paleontologists and Mineralogists, Special Publication 23, pp. 132-154.

Barnett, P.J. 1990. Tunnel valleys: evidence of catastrophic release of subglacial meltwater, central-southern Ontario, Canada. Glaciological Society of America, Northeastern Section, Program with Abstracts, 22: A3.

Burbidge, G.H., and Rust, B.R. 1988. A Champlain Sea subwash fan at St-Lazare, Quebec. *In* The late Quaternary development of the Champlain Sea Basin. *Edited by* N.R. Gadd. Geological Association of Canada, Special Publication 35, pp. 47-61.

Cheel, R.J. 1991. Horizontal lamination and the sequence of bed phases and stratification under upper flow regime conditions. Sedimentology, 37: 517-529.

Cheel, R.J., and Rust, B.R. 1982. Coarse-grained facies of glaciomarine deposits near Ottawa, Canada. *In* Research in Glacial, glaciofluvial and glaciolacustrine systems. *Edited by* R. Davidson-Arnott, W. Nickling, and B.D. Fahey. GeoBooks, Norwich, U.K., pp. 279-295.

Cheel, R.J., and Rust, B.R. 1986. A sequence of soft-sediment deformation (dewatering) structures in late Quaternary subaqueous outwash near Ottawa, Canada. Sedimentary Geology, 47: 77-93.

Dyke, A.S. 1984. Quaternary geology of Boothia Peninsula and northern District of Keewatin, central Canadian Arctic. Geological Survey of Canada, Memoir 407.

Fyles, J.G. 1963. Surficial geology of Victoria and Stefansson Islands, District of Franklin. Geological Survey of Canada, Bulletin 101.

Gorrell, G.A., and Shaw, J. 1991. Deposition in an esker, bead and fan complex, Lanark, Ontario, Canada. Sedimentary Geology, 72: 285-314.

Hand, B.M. 1974. Supercritical flow in density currents. Journal of Sedimentary Petrology, 44: 637-648.

Hebrand, M., and Åmark, M. 1989. Esker formation and glacier dynamics in eastern Skåne and adjacent areas, southern Sweden. Boreas, 18: 67-81.

Hooke, R. LeB. 1989. Englacial and subglacial hydrology: a qualitative review. Arctic and Alpine Research, 21: 221-233.

Jenness, J.L. 1952. Problem of glaciation in the western Islands of Arctic Canada. Bulletin of the Geological Society of America, 63: 939-951.

King, C.A.M., and Buckley, J.T. 1969. Geomorphological investigations in west central Baffin Island,

N.W.T., Canada. Arctic and Alpine Research, 1: 105-120.

Lowe, D.R. 1988. Suspended load fallout rate as an independent variable in the analysis of current structures. Sedimentology, 35: 765-776.

Mathews, W.H. 1973. Record of two jökulhlaups. *In* Symposium on the hydrology of glaciers, Proceedings of the Cambridge Symposium, 7-13 Sept. 1969. International Association of Scientific Hydrology, Publication 95, pp. 99-110.

McDonald, B.C., and Shilts, W.W. 1975. Interpretation of faults in glaciofluvial sediments. *In* Glaciofluvial and glaciolacustrine sedimentation. *Edited by* A.V. Jopling, and B.C. McDonald. Society of Economic Paleontologists and Mineralogists, Special Publication 23, pp. 123-131.

Nye, J.F. 1973. Water at the bed of a glacier. *In* Symposium on the hydrology of glaciers, Proceedings of the Cambridge Symposium, 7-13 Sept. 1969. International Association of Scientific Hydrology, Publication 95, pp. 189-194.

Østrem, G. 1975. Sediment transport in glacial meltwater streams. *In* Glaciofluvial and glaciolacustrine sedimentation. *Edited by* A.V. Jopling, and B.C. McDonald. Society of Economic Paleontologists and Mineralogists, Special Publication 23, pp. 101-122.

Paterson, W.S.B. 1981. The physics of glaciers. 2nd ed. Pergamon Press, Oxford.

Powell, R.D. 1983. Glacial-marine sedimentation processes and lithofacies of temperate tidewater glaciers, Glacier Bay, Alaska. *In* Glacial-marine sedimentation. *Edited by* B.F. Molnia. Plenum Press, New York, pp. 185-232.

Powell, R.D. 1990. Glacimarine processes at grounding-line fans and their growth to ice-contact deltas. *In* Glacimarine environments: processes and sediments. *Edited by* J.A. Dowdeswell, and J.D. Scourse. Geological Society Special Publication 53, pp. 53-73.

Rajaratnam, N., and Subramanyan, S. 1986. Plane turbulent denser wall jets and jumps. Journal of Hydraulic Research 24: 281-296.

Röthlisberger, H. 1972. Water pressure in intra- and subglacial channels. Journal of Glaciology, 11: 177-203.

Rust, B.R., and Romanelli, R. 1975. Late Quaternary subaqueous outwash deposits near Ottawa, Canada. *In* Glaciofluvial and glaciolacustrine sedimentation. *Edited by* A.V. Jopling, and B.C. McDonald. Society of Economic Paleontologists and Mineralogists, Special Publication 23, pp. 177-192.

Sharpe, D.R. 1985. The stratified nature of deposits in streamlined glacial landforms on southern Victoria Island, District of Franklin. *In* Current research, part A. Geological Survey of Canada, Paper 85-1A, pp. 365-371.

Sharpe, D.R. 1987. The stratified nature of drumlins from Victoria Island and southern Ontario, Canada. *In* Drumlin symposium. *Edited by* J. Menzies, and J. Rose. A. A. Balkema, Rotterdam,

pp. 185-214.

Sharpe, D.R. 1992*a*. Glacial sediments and landforms, southern Victoria Island, N.W.T., Canada. Ph.D. thesis, University of Ottawa, Ottawa.

Sharpe, D.R. 1992*b*. Quaternary geology of Wollaston Peninsula, Victoria Island. Geological Survey of Canada, Memoir 434.

Sharpe, D.R. 1992*c*. Quaternary geology of Cambridge Bay, Victoria Island. Geological Survey of Canada, Map 1825A, scale 1:250,000.

Shaw, J. 1988. Subglacial erosional marks, Wilton Creek, Ontario. Canadian Journal of Earth Sciences, 25: 1256-1267.

Shaw, J. 1989. Drumlins, subglacial meltwater floods, and ocean responses. Geology, 17: 853-856.

Shaw, J., and Sharpe, D.R. 1987. Drumlin formation by subglacial meltwater erosion. Canadian Journal of Earth Sciences, 24: 2316-2322.

Shaw, J., Kvill, D., and Rains, B. 1989. Drumlins and catastrophic subglacial floods. *In* Subglacial bedforms – drumlins, rogen moraine and associated subglacial bedforms. *Edited by* J. Menzies, and J. Rose. Sedimentary Geology, 62: 177-202.

Shoemaker, E.M. 1991. On the formation of large subglacial lakes. Canadian Journal of Earth Sciences, 28: 1975-1981.

Shoemaker, E.M. 1992*a*. Subglacial floods and the origin of low relief ice sheet lobes. Journal of Glaciology, 38: 105-112.

Shoemaker, E.M. 1992*b*. Water sheet outburst floods from the Laurentide Ice Sheet. Canadian Journal of Earth Sciences, 29: 1250-1264.

Shreve, R.L. 1985. Esker characteristics in terms of glacial physics, Katahdin esker system, Maine. Geological Society of America Bulletin, 96: 639-646.

Smith, N.D., and Ashley, G.M. 1985. Proglacial lacustrine environment. *In* Glacial sedimentary environments. *Edited by* G.M. Ashley, J. Shaw, and N.D. Smith. Society of Economic Paleontologists and Mineralogists Short Course 16, pp. 135-216.

St-Onge, D.A. 1984. Surficial deposits of the Redrock Lake area, District of Mackenzie. *In* Current research, part A. Geological Survey of Canada, Paper 84-1A, pp. 271-278.

Weertman, J., and Birchfield, G.E. 1983. Stability of sheet water flow under a glacier. Journal of Glaciology, 29: 374-382.

Willis, I.C., Sharp, M., and Richards, K.S. 1990. Configuration of the drainage system of Midtalsbreen, Norway, as indicated by dye-tracing experiments. Journal of Glaciology, 36: 89-101.

Wright, H.E., Jr. 1973. Tunnel valleys, glacial surges, and subglacial hydrology of the Superior lobe, Minnesota. *In* The Wisconsinan Stage. *Edited by* R.F. Black, R.P. Goldthwait, and H.B. Willman. Geological Society of America, Memoir 136, pp. 251-276.

CHAPTER 3

Tunnel channels and associated landforms, south-central Ontario: their implications for ice-sheet hydrology[1]

Introduction

Some recent literature on subglacial landscapes (Shaw 1983; Shaw and Kvill 1984; Shaw and Sharpe 1987; Shaw *et al.* 1989; Brennand and Sharpe in press) and on dynamic modelling (Shoemaker 1991, 1992*a*, 1992*b*; Arnold and Sharp 1992) highlights the role of glacial hydrology. With this emphasis on meltwater action, it is timely to enquire more deeply about the hydrologic system of ice sheets. Such enquiry may follow three basic paths: (*i*) theoretical modelling (cf. Shoemaker 1991, 1992*a*, 1992*b*; Arnold and Sharp 1992); (*ii*) studies of the hydrology and hydraulics of contemporary glaciers as an analog for that of former ice sheets (cf. Sharp *et al.* 1989; Willis *et al.* 1990); and (*iii*) inference of process from glaciofluvial landforms and sediment (cf. Shaw *et al.* 1989; Kor *et al.* 1991; Brennand and Sharpe in press). In reality, a comprehensive understanding of the hydrology of Pleistocene ice sheets will only be obtained by combining all of these approaches; contemporary glacial hydrologic theory and observation must be applied in an attempt to explain observed Pleistocene glaciofluvial landforms and landform assemblages. Such an approach should be realist, inferential and broadly uniformitarian (Baker 1988*a*, 1988*b*). Above all, inferences from observed landforms and sediment must constrain theory.

Much recent glacial geomorphic and sedimentologic literature has focused on drumlin genesis (cf. Menzies and Rose 1987; Shaw *et al.* 1989), paying cursory attention to tunnel channels and eskers. Tunnel channels have often been reported to cross-cut drumlin fields (Wright 1973; Grube 1983; Shaw 1983; Dardis and McCabe 1983; Eyles and McCabe 1989; Mooers 1989, 1990; Brennand and Sharpe in press) and contain eskers (cf. Shaw and Gorrell 1991; Brennand in press). Consequently, both tunnel channels and eskers were formed by meltwater after the formation of drumlins. Here we investigate channelized landforms to explore, qualitatively, post-drumlin hydrologic conditions in south-central Ontario.

An anastomosing network of tunnel channels dissects the southern Ontario landscape (Sharpe 1987; Barnett 1990; Gilbert 1990; Shaw and Gilbert 1990; Shaw and Gorrell 1991; Gilbert and Shaw 1992). We prefer the term tunnel channel, rather than tunnel valley, as evidence is presented later which infers bankfull conditions (cf. Mooers 1989). We present detailed maps of the terrestrial tunnel

---

[1] A version of this paper has been submitted for publication as:
Brennand, T. A., and Shaw, J. Tunnel channels and associated landforms, south-central Ontario: their implications for ice-sheet hydrology. Canadian Journal of Earth Sciences.

channel system between Tamworth in the east, Norwood in the west, the Shield margin in the north, and Lake Ontario in the south (Fig. 3.1). All maps were compiled using air photographs of approximate scales: 1:15 000 and 1:50 000. Two previously unreported landforms are also described: elongate scours on drumlinized residuals, and megachannels. We suggest that drumlin fields, the Dummer Moraine, elongate scours within drumlin fields, megachannels, tunnel channels, transverse ridges within tunnel channels, eskers, and the Oak Ridges glaciofluvial complex (Oak Ridges Moraine (cf. Duckworth 1979)), together, record subglacial hydrologic evolution.

Background

The study area includes parts of the Peterborough-Trenton and Quinte-Lake Ontario drumlin fields. The drumlins in the former are oriented north-northeast to south-southwest, those in the latter are oriented parallel to the axis of Lake Ontario (east-northeast to west-southwest). The Peterborough-Trenton drumlin field lies to the south of the Dummer moraine (Barnett *et al.* 1991), is buried by the Oak ridges glaciofluvial complex (Mirynech 1962; G. Gorrell personal communication 1991), and is truncated by the Quinte-Lake Ontario drumlin field (Fig. 3.1; Shaw and Gilbert 1990). Drumlins in these fields have variable composition: (*i*) limestone bedrock, with or without thin diamicton drapes; (*ii*) preexisting sorted and unsorted sediments, including glaciolacustrine rhythmites; and (*iii*) interstratified sand and diamicton (Deane 1950; Gravenor 1957; Sharpe 1987). Crescentic scours are common around the proximal ends of drumlins (Shaw and Sharpe 1987). The variable composition, including bedrock, and the crescentic scours have been used to infer an erosional origin for these fields (Gravenor 1957; Shaw and Sharpe 1987; Shaw and Gilbert 1990; Boyce and Eyles 1991).

While there is general agreement that the drumlins in the Peterborough-Trenton drumlin field are erosional forms, the mechanism of erosion is much debated. Boyce and Eyles (1991) argued that the drumlins were carved beneath an ice stream by subglacially deforming sediment. Others argued for erosion by catastrophically released meltwater sheets (cf. Shaw and Sharpe 1987). We continue to favour the meltwater hypothesis since Boyce and Eyles (1991) provide no substantive evidence to reject it, and their own hypothesis is problematical for the following reasons:

1. The well records they use are crude and, while they may permit reconstruction of a coarse stratigraphy, they do not provide the information needed to determine sediment genesis and age.
2. There is no systematic mapping of deformed sediment over the surface of drumlins or between them. Detailed logs of sedimentary sequences in drumlins of the Peterborough and associated fields indicate undeformed sediment and intact stratigraphy within less than one metre of the landsurface (Shaw 1983; Sharpe 1987; Shaw in press).
3. There is nothing to indicate the margin of the postulated ice stream, and the expected sediment accumulation at its terminus does not exist (Gravenor 1957). In this regard, Boyce and Eyles (1991)

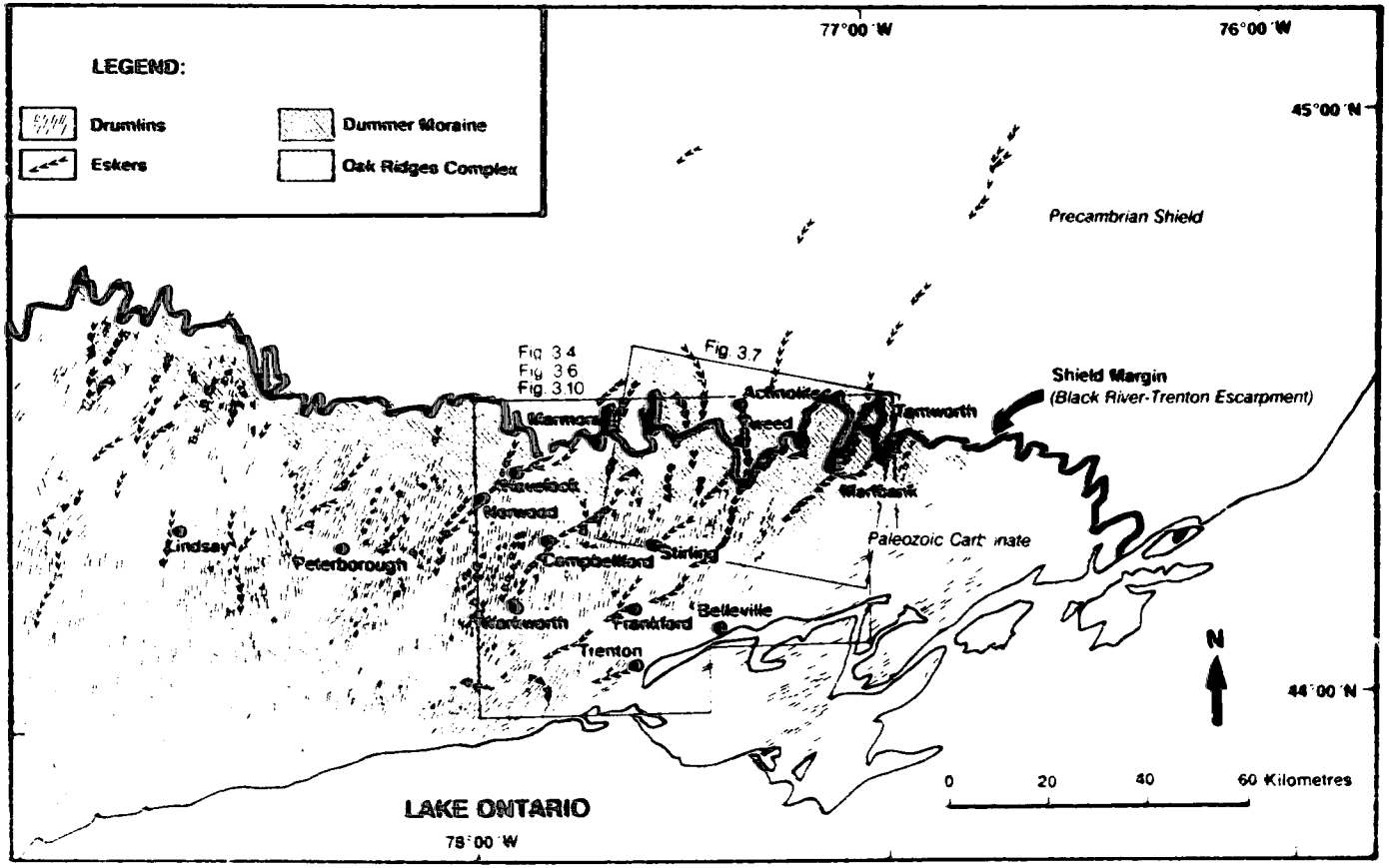

Figure 3.1. Study area showing drumlin fields, eskers, Dummer Moraine, Oak Ridges glaciofluvial complex and locations of Figures 3.4, 3.6, 3.7 and 3.10. Modified from Barnett *et al.* (1991).

present no evidence for their depicted limit of the Simcoe lobe, yet large quantities of sediment are expected at the terminus of an ice stream carrying an enormous flux of subglacial sediment (Alley *et al.* 1989).

4. The flow directions they propose to the south and west of the postulated Simcoe Lobe limit are supported neither by drumlin morphology and orientation, nor by meltwater channels between drumlins.

5. Whereas, Boyce and Eyles (1991) state that there is an absence of eskers in the southern part of the field, Barnett *et al.* (1991) (Fig. 3.1) clearly show linear glaciofluvial deposits through this area.

6. We show that eskers are in tunnel channels that truncate drumlins. Esker conduits may also have fed sediment to the Oak Ridges glaciofluvial complex. Thus, eskers and the Oak Ridges glaciofluvial complex were possibly contemporaneous and the complex is younger than the drumlins. Consequently, Boyce and Eyles (1991) are incorrect in their assertion that a drumlin-forming ice stream overrode the Oak Ridges glaciofluvial complex; the complex actually buries drumlins (Mirynech 1962; G. Gorrell personal communication 1991). As well, the connection that they make between eskers and subglacial drainage at the time of drumlin formation is invalid because the two landforms were created at different times (cf. Shaw 1983; Brennand and Sharpe in press).

By using the meltwater hypothesis and reconstructing flow lines based on drumlin orientation, two catastrophic meltwater sheet events have been proposed for southern Ontario: (*i*) the Algonquin event swinging from the north and northeast, southeastwards across Lake Ontario and diverging over northern New York State, responsible for the Peterborough-Trenton and northern New York State drumlin fields; and (*ii*) the Ontarian event flowing from the northeast along Lake Ontario, responsible for the Quinte-Lake Ontario drumlin field (Shaw and Gilbert 1990).

Our interest here is in subglacial hydrologic evolution in the period following the main drumlin-forming event (Algonquin event, Shaw and Gilbert 1990). Sheet-flow scouring, megachannels, anastomosing tunnel channels, eskers, and transverse ridges originated, or were reactivated, during this period. Each landform type is described and interpreted independently. Landform associations are identified, paying particular attention to cross-cutting and superimposed relationships. From these relationships we elucidate a sequence of hydrologic conditions and events over the course of deglaciation in south-central Ontario. Finally, the Dummer moraine and Oak Ridges glaciofluvial complex are briefly discussed in the context of the proposed sequence. Our findings provide a framework for further field testing.

A subglacial sheet flow with a sculpted bed (drumlins) and confining ice surface describes the initial conditions for landforms formed immediately after drumlins. Thus, the starting conditions for post-drumlin-stage landforms include a drumlin-covered bed and a counterpart ice bed, in phase with the drumlins and separated from them by a high-velocity meltwater sheet. In this model, as the flow

wanes and the ice settles to the bed, local flow conditions depend on the geometry of the meltwater sheet. A geometric model of ice base-bed interaction underpins our explanation of the evolution of tunnel channels and associated landforms.

Modelling of geometric interactions

Brown *et al.* (1986) and Brown (1987, 1989) modelled progressive channelization for fluid flow through rock joints. They brought two rough, mismatched surfaces together and simulated viscous laminar flow between the surfaces over a range of gap widths. At large separation, the flow geometry is little affected by interaction with the surfaces. At small separation, the flow is largely controlled by gap geometry. A similar, but more complicated phenomenon, is considered for the western part of the study area. We assume that the ice and bed had nested morphology - the positive forms (drumlins) on the bed fitted exactly into corresponding inverted erosional marks in the ice bed. A necessary simplification of the model is to assume no erosion or deformation of the ice bed as it approached the drumlinized surface during waning flow.

A real drumlin landscape was digitized and surfaced (BED, Fig. 3.2*a*). A second surface was duplicated with an initial 30 m gap width between this surface and the BED (ICE = BED + 30 m, Fig. 3.2*a*). The surfaces were brought together along a horizontal plane until they interlocked. The new gap width was calculated as (ICE - BED) to generate a RESIDUAL volume (Fig. 3.2*b*). This residual may be represented as a surface (Fig. 3.2*b*). But the low points on this surface are actually points of low gap width, where discharge would be reduced, and the high points are areas of high gap width, where discharge would be greatest. Discharge in these cases being measured per unit width. As it is easiest to visualize zones of high potential flow as low points, the gap width surface is best inverted (Fig. 3.2*c*). A classed contour map of water depths with potential flow lines on the inverted surface (Fig. 3.2*c*) is presented (Fig. 3.3).

Some connected channels (continuous flow lines) may be drawn across the entire model surface (Fig. 3.3). Such connected channels may be the precursors to tunnel channels. Potential flow lines form an anastomosing pattern (Fig. 3.3). In places, to maintain continuity, flow is inferred to have been upslope; in other places, channelized flow may have connected cavities or localized sheet flows to one another and to adjacent channels. These latter flows (dashed arrows in Fig. 3.3) may produce the late-stage sheet flow scours discussed next. Smaller initial gap widths gave similar results and, consequently, they are not presented here.

Late-stage sheet flow scours between drumlins

Description

The western half of the study area lies within Peterborough-Trenton drumlin field, and exhibits numerous elongate, relatively narrow, deep scours (arrows on western portion of Fig. 3.4; Fig. 3.5).

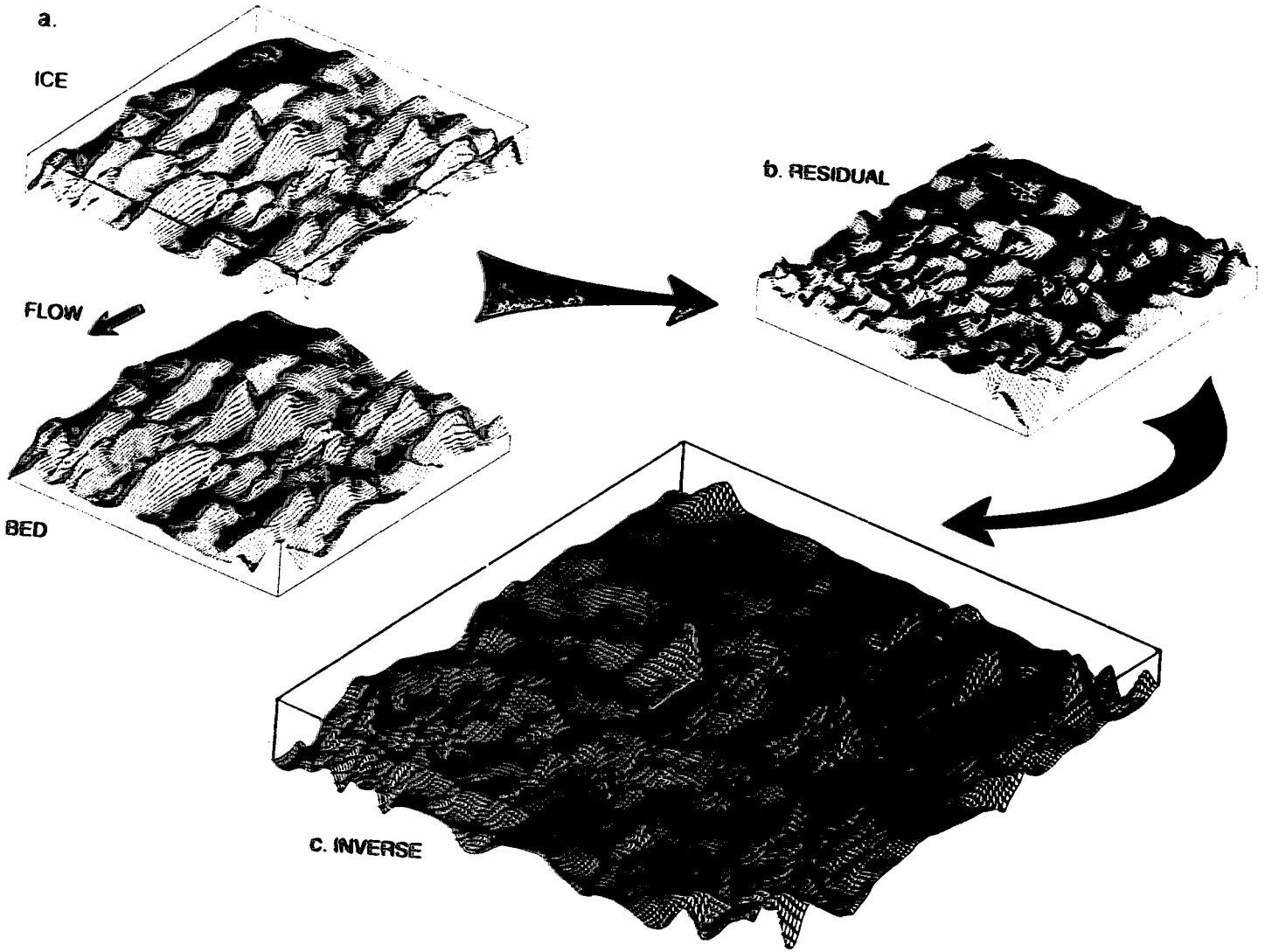

Figure 3.2. Geometric model of the interaction between two mismatched surfaces (ICE base and BED) at 30 m gap width (*a*). Note: gap width between the two surfaces is greatly exaggerated here, to aid visual clarity; *b*. Gap width between the two surfaces in *a*. once they are interlocked (RESIDUAL = ICE - BED); *c*. More visual rendition of residual volume (RESIDUAL × -1); low points are zones of high potential meltwater discharge.

Figure 3.3. Classed contour map of potential water depths on the inverted surface (Fig. 3.2*c*). Grey scale class interval 10 m (white, 0 m to -10 m). Potential channelized flow within declining sheet flow (black arrows); potential channelized flow connecting cavities to other cavities or channels (dashed arrows).

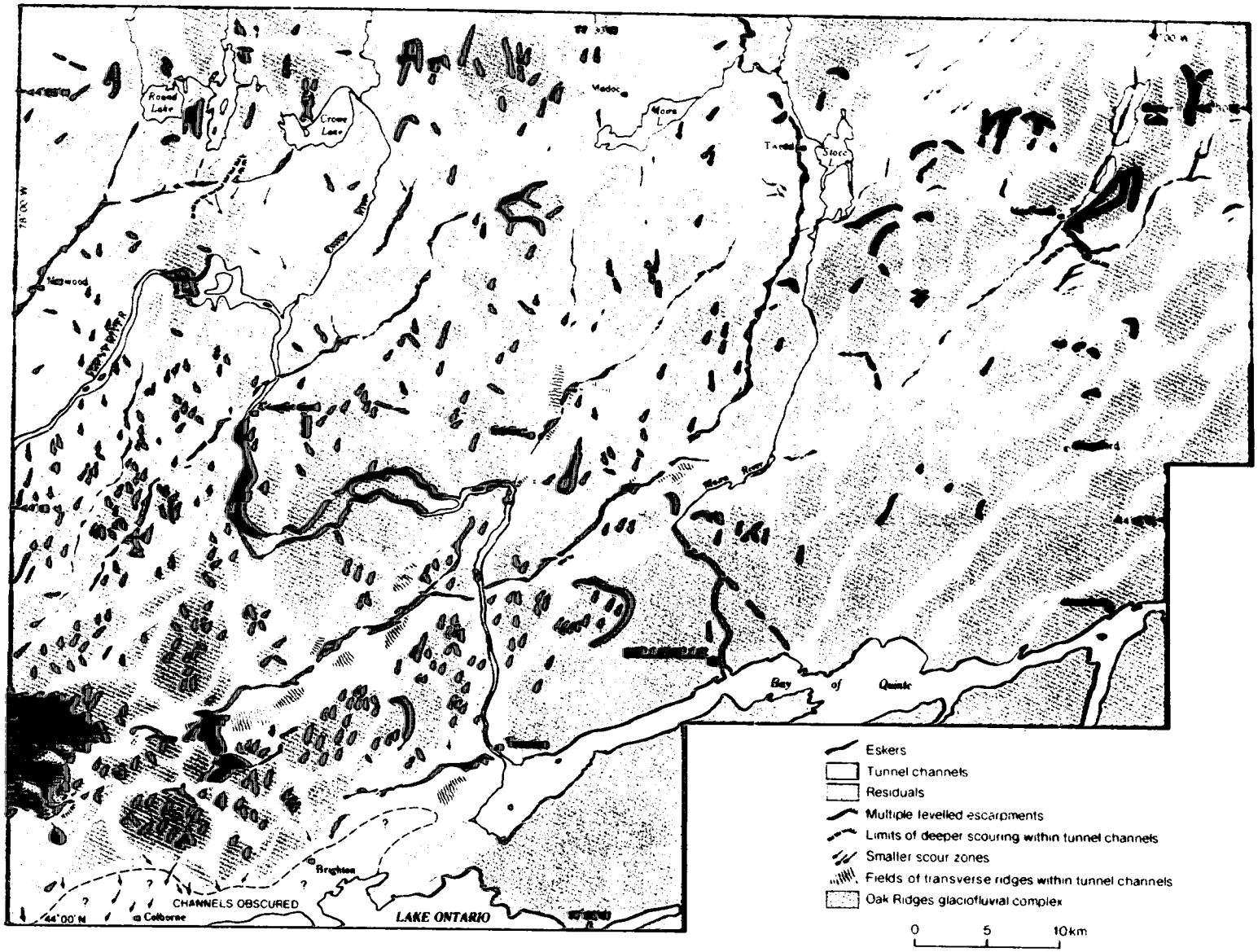

Figure 3.4. Distribution of elongate scours (west), scour zones (east), tunnel channels, transverse ridges in tunnel channels, eskers, and the Oak Ridges glaciofluvial complex in south-central Ontario. See Figure 3.1 for location.

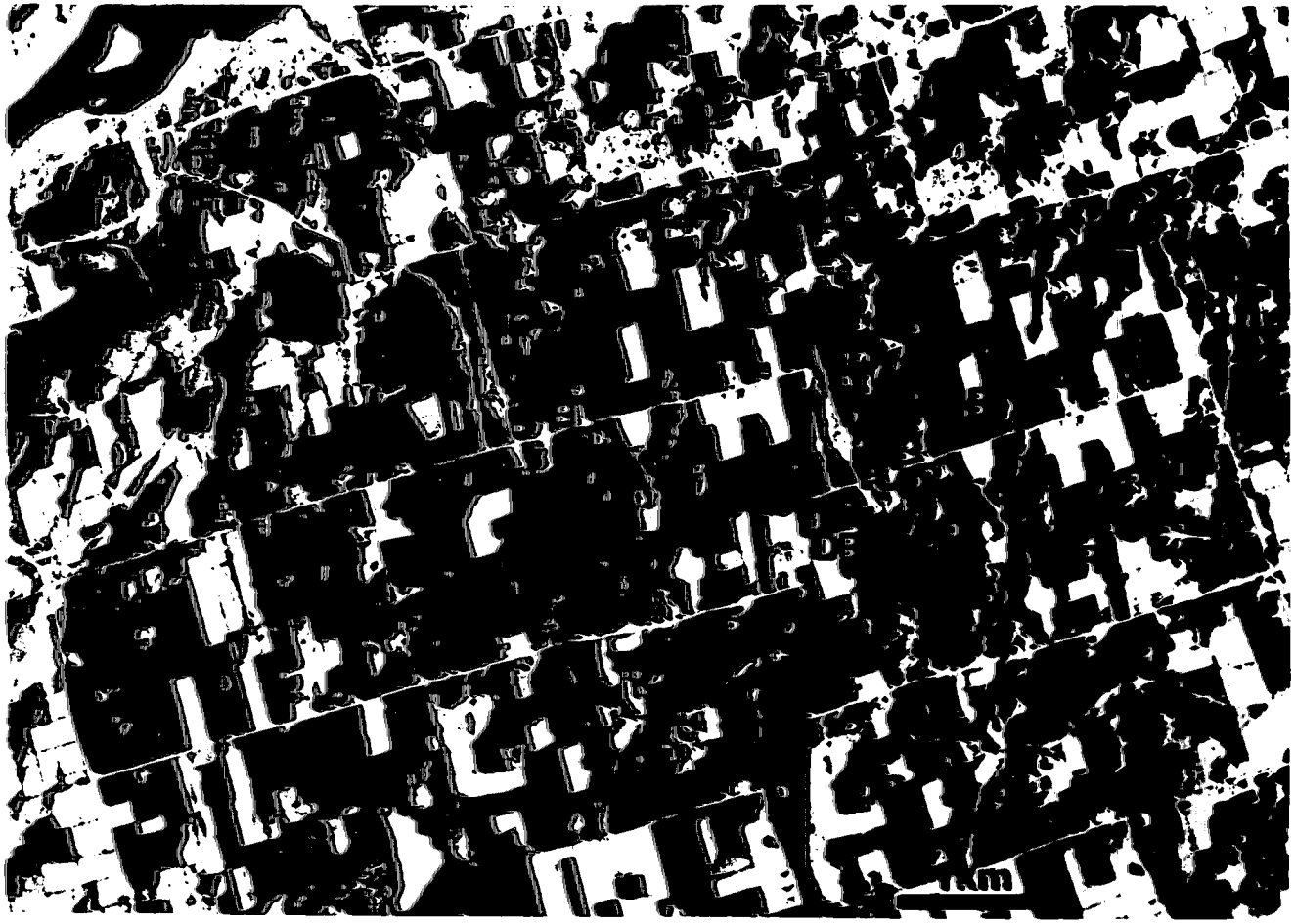

Figure 3.5. Air photograph stereopair showing tunnel channels (TC), an esker (E) in a tunnel channel, drumlinized residuals (DR) between tunnel channels and sinuous late-stage sheet flow scours (thin arrows) on drumlinized residuals. Air photographs A27083-123 and A27083-124 copyright 25 April 1987 Her Majesty the Queen in Right of Cananda, reproduced from the collection of the National Air Photo Library with Permission of Energy, Mines and Resources Canada.

These linear scours are generally less than 1 km long and are differentiated from primary drumlin scours (which, by definition, demarcate each erosional drumlin), in that they are commonly sinuous, do not demarcate drumlins, and may even truncate them. They are less clearly defined, shallower, and discontinuous compared to tunnel channels; they start and end abruptly, and are disconnected. It should be noted that the arrows on the eastern portion of Figure 3.4 represent scour zones, which are primarily associated with blind-ended tunnel channels rather than drumlinized residuals. They are discussed later.

Interpretation

While it is possible that some of the elongate scours marked on the western portion of Figure 3.4 may simply be associated with initial drumlin formation, the fact that most appear to be incised deeper than individual drumlin-demarcating scours, leads to two possible interpretations. First, they may record localized scour at the end of the inferred drumlin-forming, subglacial meltwater sheet flood event. With the initiation of ice-bed recoupling, towards the end of the flood event, the sheet would have begun to break up into discrete streams. Meltwater sheets are inherently unstable due to thickness perturbations (Walder 1982). Spatial variation in meltwater sheet thickness produces greater viscous heat dissipation and melt rates where the sheet is thick. This favours channelization, even when ice and bed surfaces are relatively planar. The added influence of geometric interaction between the ice base and bed on sheet thickness (Figs. 3.2 and 3.3) increases the likelihood of the formation of channels of different magnitude. Initially, channelization would have occurred within a sheet. With further collapse and pinning, a discontinuous sheet or "punctuated water sheet" (Weertman 1972) would have developed. As meltwater was under hydrostatic pressure, it would have been capable of flowing upslope between cavities created by the contact of the two rough surfaces (Figs. 3.2 and 3.3). Depending on local pressure gradients and local meltwater discharge, channels probably connected areas of broad sheet flow in cavities, thereby effecting flow continuum. Elongate scours in the present landscape represent local channelized flow at a late stage in the sheet flood.

As the base of the ice sheet deformed and began to drape the basal topography, some meltwater paths would have been pinched off, diverting flow into others which scoured further. Thus, discontinuous scour zones are observed, on what are now drumlinized residuals, or interfluves, between tunnel channels.

A second explanation for some elongate scours is also plausible: they may record tunnel channel overbank events. In the western, drift-dominated region, such events may have produced localized scour between drumlins on residuals. Greater surface relief in the drumlinized landscape may have inhibited the formation or maintenance of localised sheet flow which is inferred for tunnel channel overbank events in the east (discussed later), where local topography is more subdued. These overbank events may have happened in the waning stages of sheet flows when meltwater discharge was highly nonuniform. If some meltwater paths became locally blocked by ice or sediment, flow would have been

diverted and concentrated in other channels, causing localized high meltwater discharges there. Overbank events are discussed further in connection with the tunnel channel system.

Most scours described here are inferred to record mainly the final stages of a meltwater sheet event (Algonquin event, Shaw and Gilbert 1990). It is possible that scours were initiated as late-stage sheet flow scours, and were later enhanced during localized tunnel channel overbank events. By extension, tunnel channels (discussed later) are inferred to record the culmination of these progressive channelization and flow diversion processes.

Bedrock geology and meganchannels

Description

The study area is divided into two major geologic regions: the Precambrian Shield to the north, and the Paleozoic limestones to the south (Ontario Geological Survey 1991). The Black River-Trenton escarpment marks this lithologic break (Fig. 3.1). The north-facing scarp extends for approximately 290 km; from Midland on Georgian Bay to Kingston at the eastern end of Lake Ontario (Hewitt 1964). This Precambrian-Paleozoic boundary is serrated, exhibiting a number of Precambrian reentrants (for example at Beaver Lake and Stoco Lake, Figs. 3.6 and 3.7; Carson 1981*a*). Precambrian lithologies (Grenville Province) include felsic to ultramafic plutonic, and metasedimentary rocks, that is, granite, granodiorite, migmatite, gabbro, marble, conglomerate and breccia. Quaternary sediments are less than 1 m thick on the Shield (Barnett 1992). Paleozoic rocks are primarily limestones, mudstones and shales of the Gull River, Bobcaygeon, Verulam and Lindsay Formations (Fig. 3.6; Carson 1980*a*, 1980*b*, 1980*c*, 1981*a*, 1981*b*, 1981*c*).

Paleozoic outliers, up to 14 km from the main boundary (Carson 1980*b*), suggest that the Shield margin was north of its present location prior to the last glaciation (Fig. 3.6; Mirynech 1962). These outliers range in size from a few hundred m^2 to 5 km^2; and may stand up to 4 m above the surrounding Precambrian surface (Carson 1981*a*). Paleozoic strata form a south-dipping homocline, inclined at ~3.8 m km^{-1} or ~0.2° (Kay 1942; Winder 1954*a*, 1954*b*; Liberty 1960). However, localized domes (monadnocks; Kay 1942; Liberty 1960) occur in the Paleozoic rocks, associated with buried hills on the Precambrian basement. Such localities may also exhibit Precambrian inliers (e.g., ~12 km east-northeast of Belleville, Fig. 3.6; Carson 1981*a*, 1981*b*, 1981*c*).

Associated with major tunnel channels and Precambrian reentrants in the Kingsford, Beaver Lake-Marlbank, and Stoco Lake areas (eastern portion of study area), are lobate reentrants of Bobcaygeon, and to a lesser extent Gull River, Formations into the younger Verulum Formation (Fig. 3.6). These reentrants are up to 8 km wide and 27 km in length. Bobcaygeon Formation reentrants of a similar scale are not observed in the western portion of the study area. While the reentrants extending through Kingsford and Marlbank are to some extent fault-controlled (Carson 1981*a*; Ontario

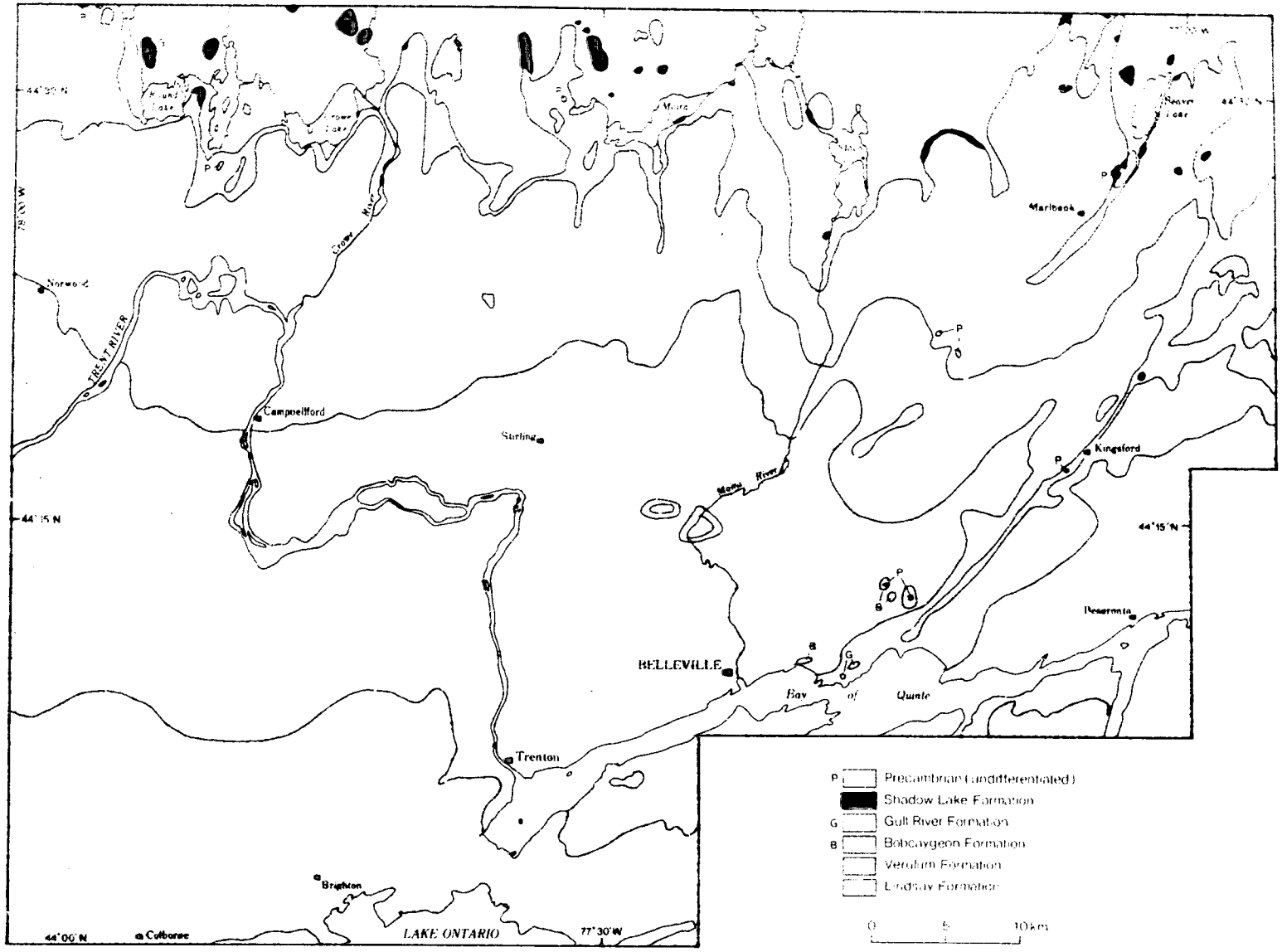

Figure 3.6. Bedrock geology of south-central Ontario with Formation boundaries. Modified from Carson (1980*a*, 1980*b*, 1980*c*, 1981*a*, 1981*b*, 1981*c*). See Figure 3.1 for location.

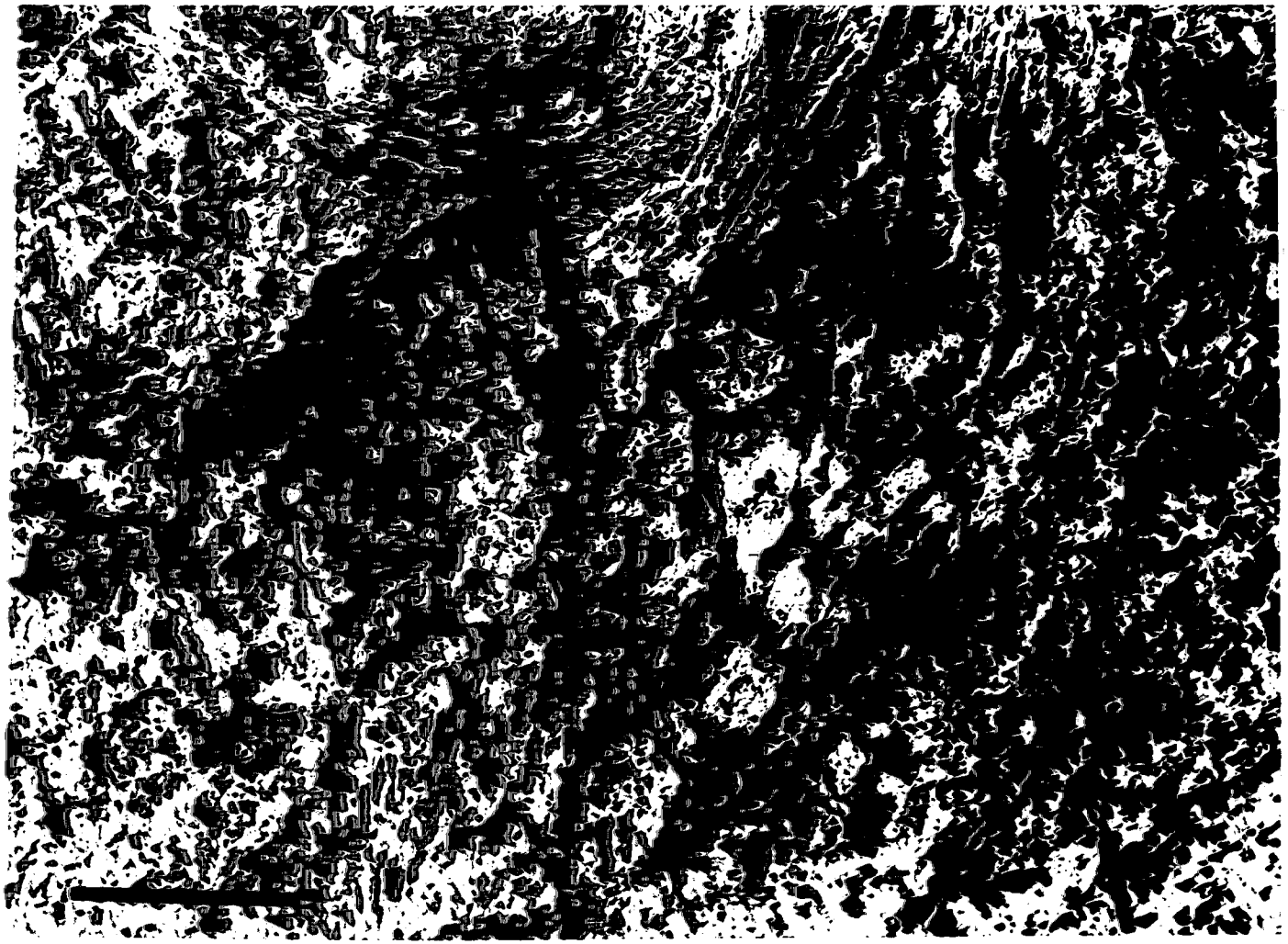

Figure 3.7. Contrast-stretched, edge-enhanced LANDSAT 4 image of part of the tunnel channel system around Tweed (TM 16-29, band 5, 24-Oct-82, Ontario Ministry of Natural Resources, Provincial Remote Sensing Office). scale bar is 10 km. See Figure 3.1 for location. Note: serrated Shield margin with numerous Precambrian reentrants (top); drumlin field (lower left); multiple escarpment levels (upper right); and Marlbank esker passing through Beaver Lake channel (right).

Geological Survey 1991), the one in the Stoco Lake area is not (Fig. 3.6).

Interpretation

The large lobate reentrants of Bobcaygeon and Gull River Formations extending into areas of younger Verulam Formation are interpreted as subparallel scour zones. The agent of scouring may have been: (*i*) preglacial tributaries of the proposed ancient Laurentian River, some of which may have been fault- or joint-controlled (Wilson 1904; Mirynech 1962); (*ii*) glacial erosion; (*iii*) megachannel or narrow sheet flow (Shoemaker 1992*b*) activity associated with meltwater sheet break-up, and perhaps contemporaneous with late-stage sheet flow scouring in the western part of the study area; or (*iv*) scouring associated with episodic overbank flow from tunnel channels. Wilson (1904) proposed preglacial drainage lines along all three major lobate Bobcaygeon reentrants. She also proposed similar drainage lines for other parts of the eastern portion of the study area, but these are not expressed as lobate geologic reentrants. This may be explained by either differential incision by the preglacial rivers, or by some other process, or processes, that have enhanced some channels. Reentrants may have been enhanced by differential glacial erosion along the valleys of preglacial streams. However, the existence and preservation of s-forms in the Kingsford reentrant (at Marysville, ~7 km northwest of Deseronto, Fig. 3.6; Gilbert *et al.* in press) suggest that glacial erosion alone was not responsible for reentrant formation. Indeed, striae are observed only to ornament well-preserved s-forms (cf. Gorrell and Shaw 1991; Gilbert and Shaw 1992). Perhaps preglacial rivers, glacial abrasion, subglacial megachannel flow and tunnel channel overbank flow, all contributed to the erosion exposing the Bobcaygeon and Gull River Formations.

In view of the evidence for sheet floods, a combination of scour in relatively narrow zones as the meltwater sheet became discontinuous and overbank surges from tunnel channels is probable. Thus, during ice-bed recoupling, the ever-changing geometry of the gap between the ice and its bed would have produced continual change in meltwater routing and, consequently, in local meltwater discharge. Megachannel and tunnel channel overbank flow may have occurred in sequence; broad scouring in megachannels or narrow sheets during sheet break up, followed by enhanced scour by tunnel channel overbank flows.

A lack of similar large-scale lobate reentrants in the western portion of the study area is best explained by the greater thickness of glacigenic sediments there. Glacigenic sediment thicknesses are generally less than 10 m in the east (Leyland and Mihychuk 1983), and greater than 60 m in the west (Leyland 1982; Leyland and Mihychuk 1984*a*, 1984*b*). Thus, subglacial meltwater erosion in the east was primarily into bedrock, while in the west erosion was largely of glacigenic sediments, and was influenced by a rough ice base-bed interface geometry (Figs. 3.2 and 3.3). If this were the case, scouring of these megachannels must have post-dated deposition of the thick glacigenic sediments in the west, and may

have been contemporaneous with late-stage sheet flow scouring in the east.

The megachannelized scour zones are interpreted to have been enhanced subglacially because the latest episode of scour is presumed to be younger than subglacial deposits. They are intimately associated with tunnel channels exhibiting paths against regional gradient (Gilbert 1990), and they were likely initiated prior to extensive tunnel channel dissection. In this context, these scour zones may well record transitional subglacial hydrologic conditions between an extensive meltwater sheet and relatively narrow tunnel channels, although their enhancement by scour during tunnel channel overbank events cannot be ruled out.

Tunnel channel system

Description

South of the Shield margin, southern Ontario is dissected by a complex, anastomosing network of channels (Figs. 3.4 and 3.7; cf. Shaw and Gilbert 1990; Shaw and Gorrell 1991). Most channels are connected, and form an integrated system. These channels reach a maximum of ~90 km in length and are 160 to 4200 m wide, in the study area (Fig. 3.4). Where bedrock is exposed, channels are incised up to 30 m below the surrounding land surface (e.g., around Kingsford, and south of Beaver Lake; Figs. 3.4 and 3.8). Major channels are oriented approximately northeast-southwest, but are interconnected by channels lacking a preferential orientation. The orientation of major channels and paleocurrent directions estimated from esker sediments within them (Brennand in press) suggest that both were formed by flows from northeast to southwest. In places, these channels are well defined and incised into bedrock (Fig. 3.8) or glacigenic sediment (Wilson 1904; Mirynech 1962); in others, they are scour zones which truncate drumlins (oriented north-northeast to south-southwest) within the Peterborough-Trenton drumlin field (Fig. 3.9).

The channel system in this study is part of a more extensive system which extends westward to southern Georgian Bay (Barnett 1990), eastward to Kingston (Shaw and Gorrell 1991; Shaw and Gilbert 1990), and southward into Lake Ontario (Gilbert 1990; Shaw and Gilbert 1990; Gilbert and Shaw 1992). Sharpe (1987) noted a complex tunnel channel system in the area between Norwood and Peterborough. There are similar channels within the northeastern part of Lake Ontario (Gilbert 1990; Shaw and Gilbert 1990; Gilbert and Shaw 1992), and northern New York State (Muller and Cadwell 1986; Mullins and Hinchey 1989). These channels are not related to the modern drainage pattern (Fig. 3.4; Gilbert and Shaw 1992). In places they are occupied by underfit creeks, and exhibit well-preserved glacial landforms such as drumlins, eskers and transverse ridges on their floors (Fig. 3.4). Consequently, there can have been little postglacial modification of these channels (Gilbert and Shaw 1992).

East of Tweed, the channels are easily observed on LANDSAT images. Figure 3.7 is a contrast-stretched, edge-enhanced image (portion of LANDSAT 4, TM 16-29, band 5, taken 24-Oct-82) of the northeastern part of the study area. Channels are easily observed in band 5 (mid-infrared, wavelength:

Figure 3.8. View across fault-guided tunnel channel incised into Paleozoic limestone at Kingsford; now occupied by Salmon River. (Photographer: Brennand 1989).

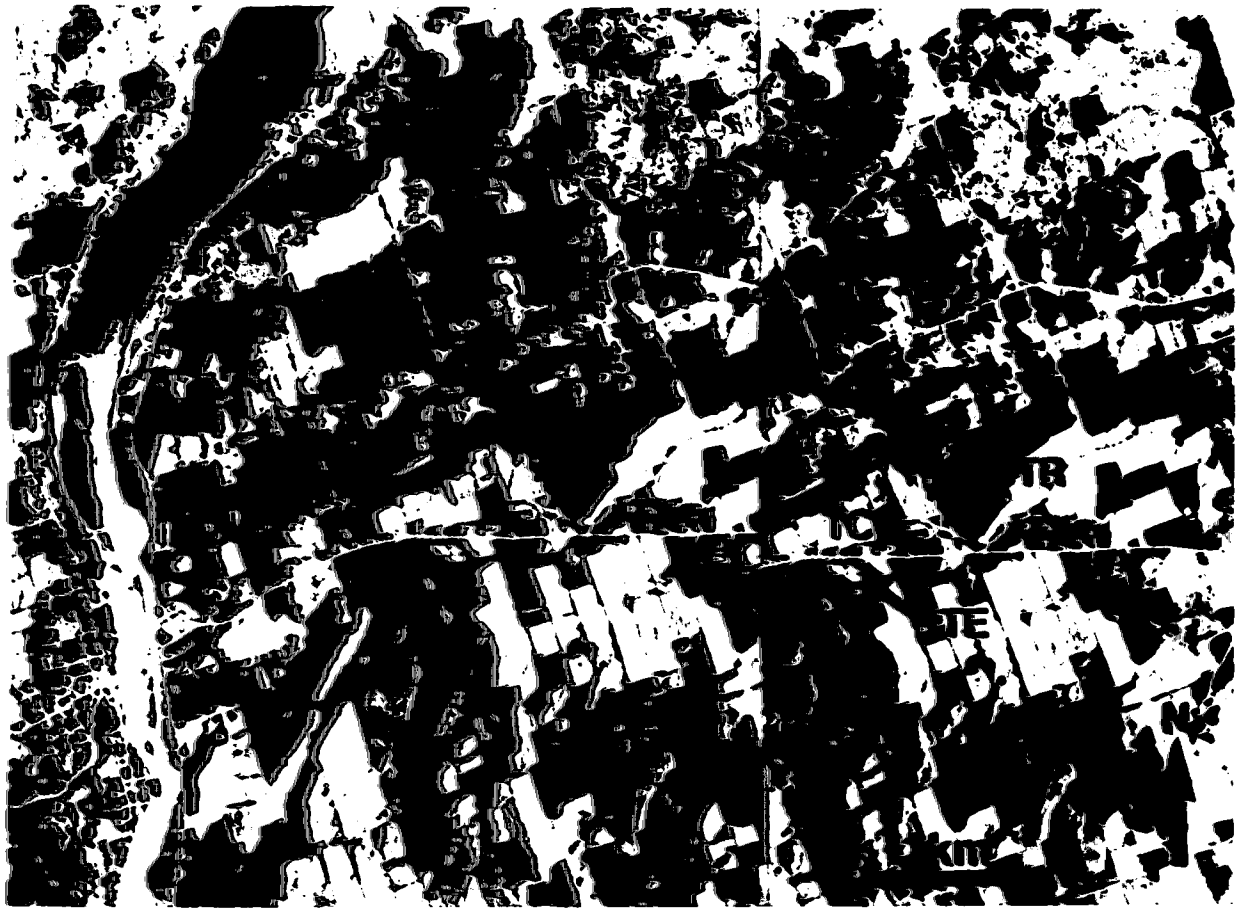

Figure 3.9. Air photograph stereopair showing drumlins truncated (TR) by tunnel channel (TC) containing Tweed esker (TE), ~12 km north of Trenton. Air photographs A27083-189 and A27083-190 copyright 25 April 1987 Her Majesty the Queen in Right of Canada, reproduced from the collection of the National Air Photo Library with permission of Energy, Mines and Resources.

1.55-1.75 μm) as many are now occupied by glaciolacustrine sediments (Leyland 1982; Leyland and Mihychuk 1983, 1984*a*, 1984*b*; Leyland and Russell 1984), are poorly drained or wetter than surrounding residuals, and are marshy. Consequently, they are poor reflectors of band 5 radiation and appear dark on Figure 3.7 (cf. Lillesand and Kiefer 1987, p.567; Gupta 1991, p.31).

Channel path is against contemporary regional gradient (Gilbert 1990). As most of the channels are partly filled with glaciolacustrine sediment, and without drilling or geophysical investigation, it is difficult to determine terrestrial channel long profiles. However, the high-stand shoreline of Glacial Lake Iroquois gives a proxy datum for late-glacial times. If channel profiles are related to this plane they occur below lake level in the east, and occasionally above lake level in the west (Fig. 3.10). As the paleocurrents in the channels were from northeast to southwest, and the channel slopes were towards the northeast, water flow was upslope and must have been subglacial. In addition, undulating long profiles are a result of uneven incision along channels. Some channels even contain a number of lake basins along their axis (e.g., Beaver Lake-Marlbank channel, Figs. 3.4, 3.7, and 3.10). In eastern Lake Ontario, Gilbert (1990) also noted channels with undulating long profiles and deep scour pools. Some channel beds are striated and grooved (Wilson 1904). In places, these grooves have been identified as s-forms using the terminology of Kor *et al.* (1991) (Shaw 1988; Gilbert 1990; Shaw and Gilbert 1990; Gorrell and Shaw 1992; Gilbert and Shaw 1992).

Although channel identification is difficult north of the Black River-Trenton escarpment, Wilson (1904) suggests that some may extend headwards onto the Shield. Channel paths do not seem to have been geologically controlled south of the Shield margin, although some channel walls do follow Formation boundaries. Precambrian reentrants along the Black River-Trenton escarpment, and structures in the Shield to the north, may have facilitated flow channelization (Figs. 3.4, 3.6, and 3.7).

Channels extend through the Dummer Moraine which is mapped as continuous across the northern portion of the channelized landscape in this region (cf. Fig. 3.1; Leyland and Mihychuk 1983, 1984*b*; Leyland and Russell 1984; Barnett *et al.* 1991). However, this relationship is complex; Dummer Moraine is observed in some large and small channels, but not others. Drumlinized residuals, eskers and fields of transverse ridges lie within some of the larger channels (Figs. 3.4 and 3.5). Some small eskers are also observed on residuals (Fig. 3.4). Tunnel channels appear to be buried by the Oak Ridges glaciofluvial complex (Fig. 3.4; Shaw and Gorrell 1991).

There are two distinct morphological sets of tunnel channels, one to the east and one to the west, connected through a central transitional zone. The eastern set coincides with the predominantly bedrock zone, and the western set with thick, drumlinized glacigenic sediment (Barnett *et al.* 1991). Although some channels extend across the entire region (e.g., the Beaver Lake-Marlbank channel, Fig. 3.4) the contrasting morphologies are described separately.

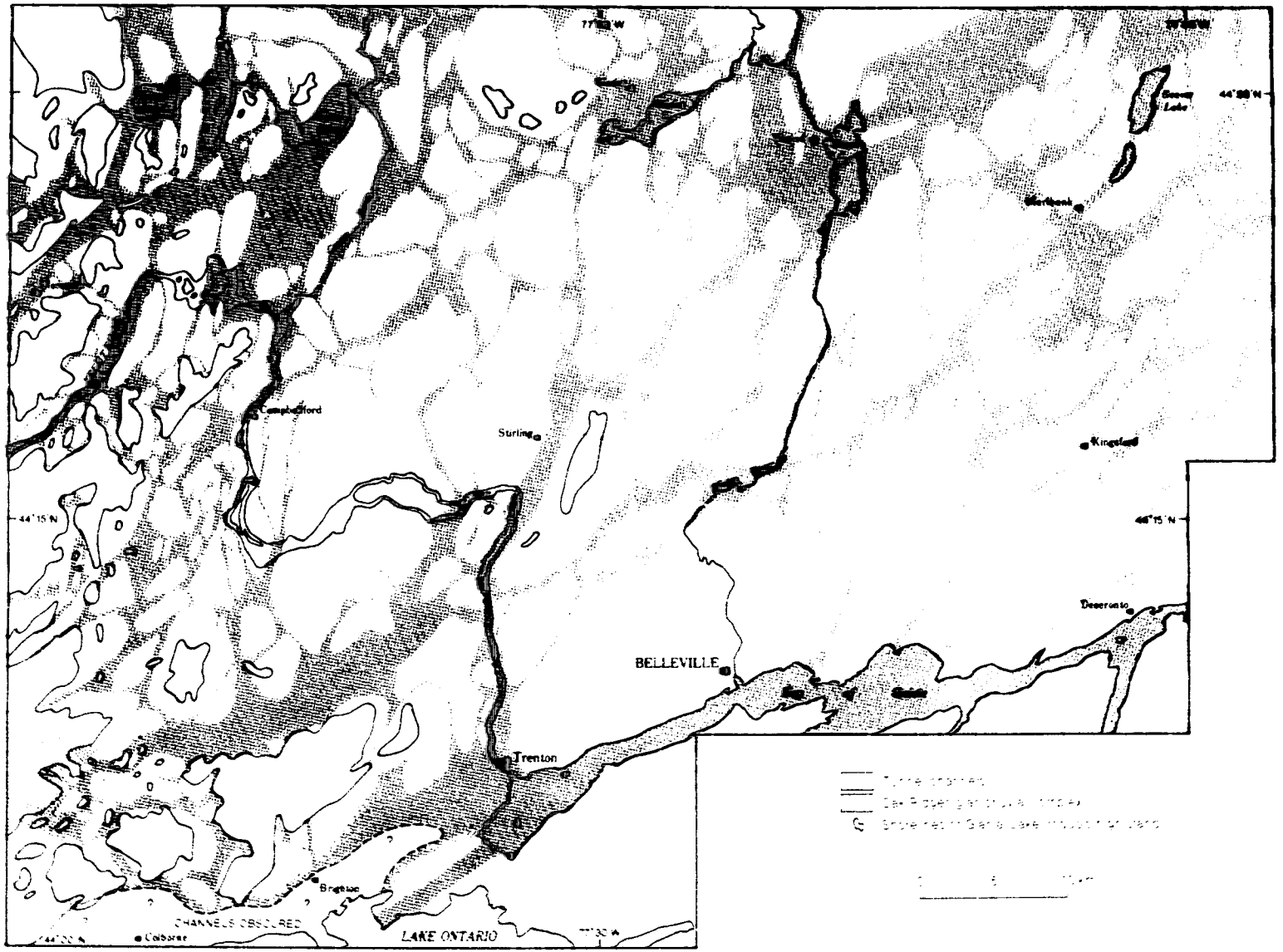

Figure 3.10. Location of the high-stand shoreline of Glacial Lake Iroquois (after Mirynech 1962) in relation to tunnel channel paths. See Figure 3.1 for location.

Eastern channels: description

East of a line between Tweed and Belleville (Fig. 3.4), channels are primarily cut into Paleozoic bedrock. These channels are mostly flat floored and flanked by steep walls (Fig. 3.8; Mirynech 1962). Channel incision left streamlined residuals.

Residual limestone escarpments are often convex upflow, forming streamlined noses (Figs. 3.4 and 3.7). Most escarpments delineate boundaries between limestone Formations or Members (Figs. 3.4 and 3.6). Escarpments formed at a number of levels, in a 'staircase' rising progressively in a downflow (south and southwesterly) direction; each lower level delineating a more confined channel. Inset channels and multiple escarpments are particularly prevalent close to the Shield margin (e.g., around Beaver Lake, Figs. 3.4 and 3.7).

In some locations, shallower, higher channels appear to have been left 'hanging' above deeper, lower channels; in others lower and upper channels are gradationally connected. Hanging tributary valleys are also associated with buried channels on the Scotian Shelf (Boyd *et al.* 1988). Some major channels, such as Tamworth-Kingsford-Salmon River and Beaver Lake-Marlbank channels, follow regional fault systems (cf. Ontario Geological Survey 1991; Gilbert and Shaw 1992). In the southeast, many channels appear to be blind-ended. Headwards or downflow of distinct walls, channels merge into more indistinct and wider scour zones (arrows on the eastern part of Fig. 3.4; Fig. 3.11). Around Marysville (~7 km northwest of Deseronto, Fig. 3.4) some adjacent flutes appear to be aligned parallel to channels, rather than with the flow directions of inferred regional meltwater-sheet events (Shaw and Gilbert 1991; Gilbert *et al.* in press).

Many channels contain bedrock or sediment erosional residuals. Some of these are aligned parallel to drumlins on adjacent interfluves, others are aligned parallel to channel walls (Figs. 3.4, 3.7, and 3.11). The geology of channel floors is highly variable; Paleozoic and Precambrian bedrock, Dummer Moraine, glaciolàcustrine sediment, till, organic sediment and modern alluvial deposits are mapped (Leyland 1982; Leyland and Mihychuk 1983; Leyland and Russell 1984). In addition, some of the larger channels contain esker ridges and associated deposits (Fig. 3.4; Shaw and Gilbert 1990; Shaw and Gorrell 1991; Brennand in press). The geology in the channels is similar to that of the residuals or interfluves; in the northeast residuals are of Precambrian and Paleozoic bedrock, and Dummer Moraine; in the southeast, they contain Paleozoic bedrock and till.

Western channels: description

West of a line between Stirling and Trenton, smaller, more complexly anastomosing channels dissect the Peterborough-Trenton drumlin field (Figs. 3.4 and 3.5). These channels, which are mainly cut into glacigenic sediment, are narrower and are more closely spaced than eastern channels. Nevertheless, there are four larger, northeast to southwest oriented channels in this region: one through

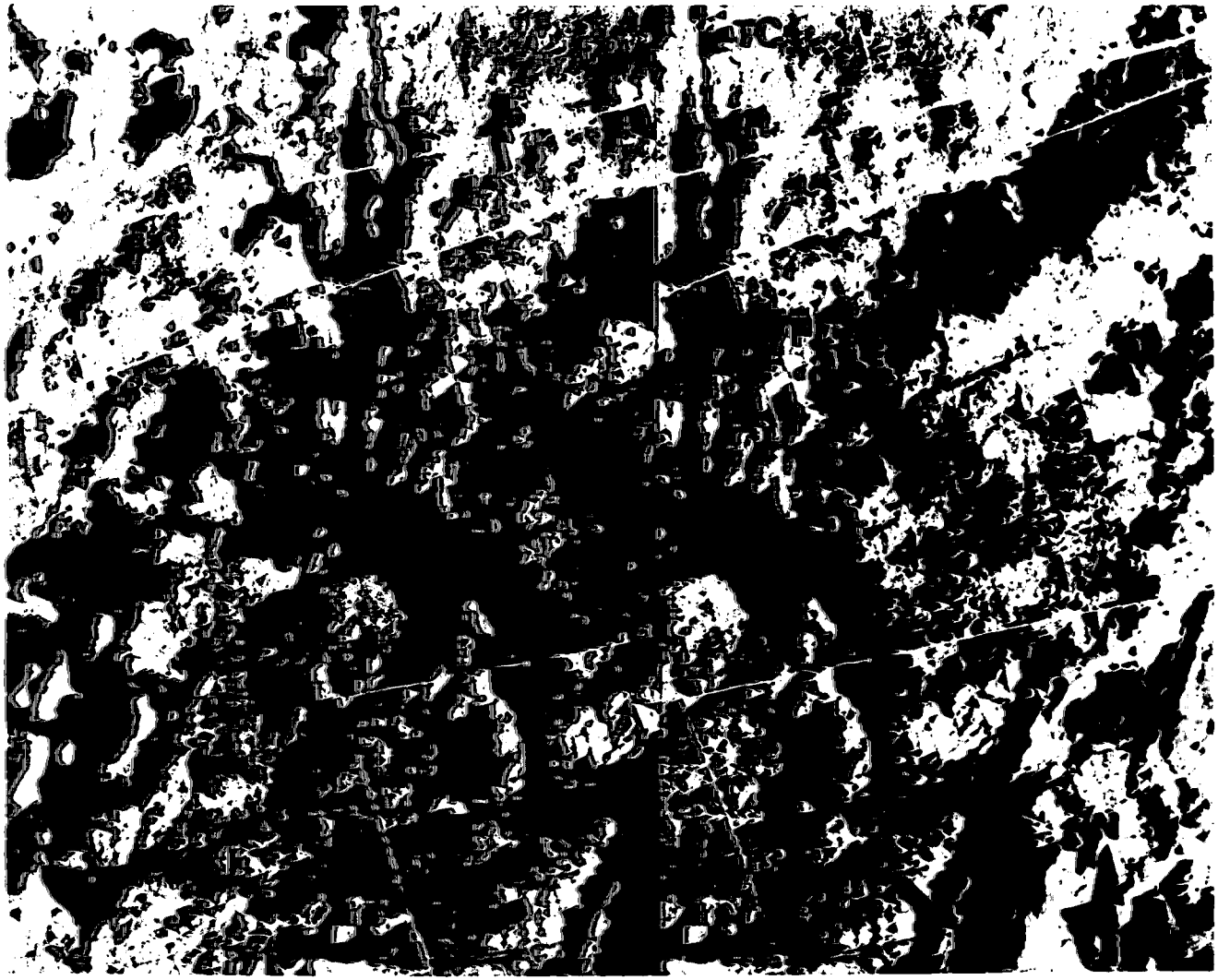

Figure 3.11. Air photograph stereopair showing a potential zone of localized sheet flow (SF) and flow interference (FI) between two tunnel channels (TC), one of which is blind-ended (TCB), ~12 km west-southwest of Marlbank. Streamlined bedrock residual (R) within tunnel channel. Air photographs A27083-104 and A27083-105 copyright 25 April 1987 Her Majesty the Queen in Right of Canada, reproduced from the collection of the National Air Photo Library with permission of Energy, Mines and Resources Canada.

Tweed or Beaver Lake-Marlbank to the Oak Ridges glaciofluvial complex; one through Campbellford; one along the Trent River-Rice Lake axis; and one through Norwood (Fig. 3.4). The channels are not structurally guided, and even the curvilinear westward extension of the Point Anne-Campbellford fault system (Ontario Geological Survey 1991) has not influenced channel location. The major channel extending through Campbellford begins at a Precambrian reentrant (Figs. 3.4 and 3.6).

Northwestern channels dissect residuals composed of Paleozoic bedrock, Dummer Moraine and till (Leyland and Mihychuk 1984*a*). Southwestern channels dissect residuals containing till with a glaciolacustrine drape (Leyland and Mihychuk 1984*b*). Channels in both areas contain or expose glaciolacustrine sediment, organic sediment, and till. In the northwest, channel floors locally reveal Paleozoic bedrock (Leyland and Mihychuk 1984*a*).

Interpretation

Any landscape represents a palimpsest of landforms and environments. The channels of south-central Ontario may have any one, or a combination, of five possible origins. First, they may be related to a preglacial fluvial system. Certainly some channels appear to follow the inferred route of preglacial tributaries of the ancient Laurentian River (Spencer 1891; Wilson 1904; Gravenor 1957; Mirynech 1962). But, observations that channel path is against regional gradient, channel long profiles undulate, channel pattern is integrated and anastomosing, and channels truncate other glacial landforms (such as drumlins and the Dummer Moraine) require further explanation than preglacial fluvial incision alone.

Second, they may be structurally controlled - associated with regional fault or joint patterns (Mirynech 1962), or karstic landform systems (cf. Ford 1987). Yet, the coincidence of some channels with regional fault systems (cf. Ontario Geological Survey 1991) in no way explains their formation, it merely accounts for their location (Barnett and Kelly 1987; Gilbert and Shaw 1992). It should be noted, as well, that not all fault systems are utilized by channels (cf. McFall 1990; Ontario Geological Survey 1991); some channels are cut into thick glacigenic sediment, and their formation was, consequently, unaffected by the structural weakness and resistance to erosion of underlying bedrock.

Third, they may have been eroded by glacier ice alone (Carlson *et al.* 1982; Grube 1983; Krüger 1983). Striae are superimposed on s-forms, suggesting that glacial abrasion caused at least ornamentation. It is also possible that glacial erosion (plucking and abrasion) may have occurred prior to s-form formation. It is, however, difficult to rationalize an anastomosing channel pattern with glacial erosion as a primary formative agent.

Fourth, they may have been ice-marginal spillways or proglacial channels. Subglacial eskers located in the bottom of some channels (Brennand in press), and the upslope flow inferred in channels, preclude these explanations.

Fifth, the favoured origin is that they may be tunnel channels eroded by subglacial meltwater. The integrated, anastomosing network of channels is interpreted as a result of contemporaneous erosion

by catastrophic, channelized subglacial meltwater (Wright 1973; Shaw 1983; Shaw and Kvill 1984; Boyd *et al.* 1988; Shaw 1988; Ehlers and Linke 1989; Shaw *et al.* 1989; Barnett 1990; Gilbert 1990; Shaw and Gilbert 1990; Shaw and Gorrell 1991; Gilbert and Shaw 1992; Loncarevic *et al.* 1992; Shoemaker 1992*b*). A number of observations lead to this inference. First, the anastomosing pattern argues for a meltwater origin. Second, landform relationships dictate erosion in a subglacial environment; channels truncate drumlins and contain eskers, both of which have been interpreted as subglacial landforms in south-central Ontario (cf. Shaw and Sharpe 1987; Shaw and Gilbert 1990; Brennand in press). Third, flow paths were against contemporary regional gradient, and appear to have been upslope in relation to a once-level plane demarcated now by the high-stand shoreline of Glacial Lake Iroquois. In addition, individual channels have undulating long profiles as is evidenced by separate lake basins along the Beaver Lake-Marlbank channel axis (Fig. 3.4). Subaerial fluvial activity cannot produce upslope flow paths. But, such paths and undulating long profiles may be produced by flowing water under hydrostatic pressure beneath an ice sheet (Shreve 1972, 1985*a*, 1985*b*). Fourth, the scale and integration of the system suggest contemporaneous operation, and necessitate catastrophic discharges which were not sustainable for long periods (Wright 1973; Boyd *et al.* 1988; Shaw *et al.* 1989).

It is not our intent to suggest that these channels have resulted solely from subglacial channelized meltwater incision. Subglacial meltwater flow is governed in part by ice surface gradient, but it will tend to favour topographic lows or structural weaknesses (Shreve 1972, 1985*a*, 1985*b*). It is, therefore, plausible that meltwater would make use of preexisting valleys (Gilbert 1990), surficially expressed faults (Gilbert and Shaw 1992), and less resistant bedrock strata or surficial sediment. There may also have been multiple tunnel-channel events. It would be interesting to know if stacked channels exist in the western subsurface record, similar to those reported in the North Sea (cf. Long and Stoker 1986; Cameron *et al.* 1987; Ehlers and Wingfield 1991).

There are three main theories on tunnel channel formation which focus on meltwater as the primary agent of incision. The debate centres around whether meltwater discharge was catastrophic or more steady-state during tunnel channel formation; whether the channels were formed contemporaneously or time-transgressively; and whether the basal substrate had any bearing on their genesis or form. It has been suggested that tunnel channels may have been cut by: (*i*) relatively steady-state, longer-term, subglacial meltwater discharges of basally produced meltwater along the entire length of laterally-migrating R-channels (Röthlisberger 1972), possibly with deformation of subglacial sediments into these channels and removal of this material by fluvial action (Woodland 1970; Boulton and Hindmarsh 1987; Mullins and Hinchley 1989); (*ii*) subglacial meltwater discharges confined to a short distance behind the ice margin and operating seasonally (Mooers 1989, 1990), or formed at the ice margin catastrophically (Wingfield 1990), producing channels time-transgressively with ice retreat; or

(iii) contemporaneous occupation and incision of the entire channel system by catastrophic, channelized subglacial meltwater flow (Wright 1973; Shaw 1983; Boyd *et al.* 1988; Shaw 1988; Shaw *et al.* 1989; Barnett 1990; Gilbert 1990; Shaw and Gilbert 1990; Gilbert and Shaw 1992; Loncarevic *et al.* 1992; Shoemaker 1992*b*). The scale and integration of the system in south-central Ontario refute both *(i)* and *(ii)*. In addition, the tunnel channel system forms a complex anastomosing network which is integrated across changes in basal substrate: bedrock in the east and glacigenic sediment in the west. If subglacial deformation was integral to tunnel channel formation in the west, it would have had to have been laterally constrained (not pervasive), as adjacent drumlins are truncated, not destroyed. Such lateral constraint on subglacial deformation into low pressure channels has been demonstrated in theory by Alley (1992). However, to resolve this question, it is also essential to test the deformation theory by examining sediment adjacent to the channels. In this regard, Barnett (1990) observed no deformation in glacigenic sediments constituting channel walls west of Lake Simcoe. It is perhaps possible to argue that the eastern channels are Nye-channels (Nye 1973), while the western channels are formed by combined R-channel/subglacial deformation processes (cf. Boulton and Hindmarsh 1987). However, as Wingfield (1990) points out

> "The multiplicity and similarity of the incisions would suggest that they were all formed by the same commonplace mechanism in accordance with the tenet of Occam's Razor" (Wingfield 1990, p. 42-43).

Consequently, alternative *(iii)* seems most plausible, and is investigated further.

The concept of catastrophic subglacial meltwater discharges through the entire channel system is a logical extension of inferences about subglacial hydrologic conditions associated with other landforms investigated so far. The tunnel channel system is inferred to represent more constrained channelized conditions following late-stage sheet flow and megachannel scouring. At this time, a reduced meltwater discharge would have resulted in geometric interaction between the ice base and bed, and consequent thermodynamic feedbacks (Walder 1982; Shoemaker 1992*b*) within a punctuated meltwater sheet (zero thickness at some locations; Weertman 1972).

In the east, interaction between a relatively planar bedrock surface with s-forms, and a similar, but inverted, ice base geometry, may be expected to give rise to initial waning stage flow geometries intermediate between sheets and channels - megachannels. Such broad flows are inherently unstable (Walder 1982). As meltwater discharge declined, progressive channelization would have utilized preexisting channels or lines of geologic weakness. In this sense, the location of incipient channelization is stochastic. However, subglacial meltwater is driven by a pressure gradient at the bed and, by continuity, would have flowed to the ice-sheet margin. Thus, incipient channels must be connected. At the commencement of channel incision it is plausible that not all channels were connected; indeed, the observation of blind-ended channels and unconnected channels attest to this process 'frozen in time'

(Figs. 3.4 and 3.11). Connection between such channel segments may have been by relatively wide, shallow sheet flows, which lacked the velocity to incise deeply into the bed. Potential paths of such localized sheet flows are indicated by arrows on the eastern portion of Figure 3.4.

In the west, the effect of the interaction of basal ice and bed geometries on meltwater flow paths would have been more complex. Ice-bed recoupling would have been spatially chaotic, governed primarily by local interactive ice base-bed geometries and meltwater routing (Figs. 3.2 and 3.3). Early drainage would have been by linked channels and broad cavities or sheets. Over time, changes in relative pressures between channels may have created local pressure gradients which facilitated channelization in meltwater sheets over basal highs, thereby dissecting drumlinized residuals, and creating new channels (late-stage sheet flow scours). As discharge declined further, meltwater flow paths would have most probably become blocked where gap widths were smallest, that is along sheet segments, as the ice and bed recoupled. Meltwater would have then been rerouted into connected channels. Such diversion would have increased meltwater discharge along the new path. This may have produced local overbank events during a period of predominantly channelized flow. In this manner, new channels may have been created by avulsion, caused by and causing a concomitant rearrangement of pressure gradients.

In the east, such diversion and overbank flow may have been responsible for flutes aligned parallel to channels rather than to adjacent drumlin axes (Shaw 1988; Shaw and Gilbert 1990; Gilbert and Shaw 1992; Gilbert *et al.* in press), and the enhancement of multiple escarpment levels such as those just south of Beaver Lake (Fig. 3.4). Shoemaker (1992*b*) suggests that tunnel channels cannot develop into sheet flows as ice head will be reduced, due to ice thinning after a catastrophic meltwater sheet-flow event. However, the overbank events suggested here would have been the product of flow diversion and locally increased meltwater discharge. It is equally plausible that these channel-parallel flutes may have been formed at a transitory phase between sheet and full tunnel channel conditions, when the flow was in the process of progressive channelization.

As the tunnel channels, in their present form, are inferred to be end points of a catastrophic subglacial meltwater sheet event, they are not envisaged to be long-lived. Anastomosing tunnel channels are related, by some authors, to extreme discharges that can only be sustained for short periods (Wright 1973; Boyd *et al.* 1988; Shaw *et al.* 1989). In addition, the fact that they contain drumlinized residuals and Dummer Moraine deposits suggests that this final tunnel channel occupation, which along with the inferred meltwater sheet event probably marked the beginning of deglaciation, was not powerful enough to completely remove these landforms. Again, this suggests multiple occupancy of the eastern channels, with the main erosive activity occurring before formation of the Peterborough-Trenton drumlin field (Algonquin event, Shaw and Gilbert 1990). At some time between an earlier tunnel channel phase and

their last occupation, it is likely that channels were filled with glacigenic sediment, most of which was removed during the final tunnel channel phase. This inference is made because western tunnel channels are cut into glacigenic sediment which was drumlinized by the Algonquin event (Shaw and Gilbert 1990), and eastern channels still contain some drumlinized material and Dummer Moraine deposits. In other words, western tunnel channels may have been incised solely by the last tunnel channel phase, while most eastern tunnel channels were simply enhanced and reexcavated at that time, although some minor channels were perhaps added then. It is likely that the multiple-generation, bedrock-incised channels in the east, to some extent, governed the location and pattern of single-generation, drift-incised channels downflow (in the west of the study area). The glacigenic sediments to the west may even bury tunnel channels that were earlier extensions of those to the northeast.

The anastomosing pattern of the tunnel channels deserves comment. In subaerial environments an anastomosing pattern is the product of bank cohesion and elevation of base-level control (or basin subsidence), such that avulsion and crevasse splays result (Smith and Smith 1980; Smith 1983). In the inferred subglacial environment, the anastomosing pattern was primarily an effect of progressive channelization governed by the state (hydrodynamic and thermodynamic) of the meltwater sheet above and locally by the ice base-bed interactive geometry, rather than avulsion of already channelized flow. That is, channel pattern was forced by changes in the meltwater sheet above, rather than by a rise in water level in the channel below. However, some new channels may have been created by a form of avulsion. Adjacent channels may have become connected by a sheet which later became channelized, when pressure gradients were conducive to down-cutting. Most new channels, however, would have been created where basal ice and bed geometries gave rise to R-channels (Röthlisberger 1972) through which water could pass more efficiently than in a sheet; less energy would be required to overcome friction. Over time, erosion of the substrate beneath the R-channel would have created N-channels (Nye 1973), and resulted in combined R/N-channels (Brennand and Sharpe in press). By this mechanism, most new tunnel channels were formed, and existing channels incised further.

As the meltwater reservoir was exhausted, ice would have invaded the tunnel channels. Striae within tunnel channels may have been produced at this time. In some cases, striae superimposed on s-forms have been observed only along the margins of the channels, suggesting that the N-channels or combined R/N-channels continued to operate when the ice was still active (Gorrell and Shaw 1991; Gilbert and Shaw 1992).

Transverse ridges within tunnel channels

Description

Fields of transverse ridges (Fig. 3.12), observed within tunnel channels on both 1:15 000 (Fig. 3.13) and 1:50 000 scale air photographs, are 0.3 to 1.4 km wide and 0.6 to 6.7 km long (Fig. 3.4). They are primarily confined to the western portion of the study area, in the region of thicker glacigenic

Figure 3.12. Transverse ridges adjacent to the southern end of Tweed esker, and within a tunnel channel. (Photographer: Brennand 1989).

Figure 3.13. Air photograph stereopair of part of a field of transverse ridges (TR) within a tunnel channel, adjacent to Tweed esker (TE). ~10 km north-northwest of Brighton. TCM is northern margin of tunnel channel. Air photographs 71-4406-6-151 and 71-4406-6-152 supplied courtesy of the Ontario Ministry of Natural Resources.

sediment, and to larger tunnel channels which also contain eskers. Individual ridges are 2 to 6 m in height, are oriented perpendicular to channel axes, and are aligned subparallel to one another, with spacings of 20 to 100 m (Figs. 3.12, 3.13). Some ridges bifurcate.

Transverse ridges occur in areas mapped as glaciofluvial sand and gravel, glaciolacustrine sand and silt (shallow water) or glaciolacustrine silt and clay (deep water) (Leyland and Mihychuk 1984*a*, 1984*b*). Seismic investigations have revealed 1 to 3 m of sand over sand and gravel in a field of transverse ridges, approximately 10 km north-northwest of Brighton (Fig. 3.4), in Cold Creek valley (G. Gorrell personal communication 1989). This same area was described as "pitted" lacustrine clay plain by Mirynech (1962, p. 101-102, plate 28).

Interpretation

Little substantive work on transverse ridges has appeared in the literature. Løken and Leahy (1964) described morphologically similar small ridges, composed of clay, near Kingston. These were attributed to squeezing of lacustrine clays into basal crevasses during ice readvance. However, Henderson (1967) observed no evidence of forward motion in the sediments within the ridges, and suggested ice-pressing of a crevassed ice shelf into lacustrine clay. Watkins (1992) argued that the regular ridge pattern, perpendicular to channel path, and with local bifurcations, was not readily explained by a crevasse pattern resulting from tension at the ice base. Instead, she drew on observations by Ashton and Kennedy (1972) of erosional forms (ripples) sculpted into the base of river ice by sub-ice water flow. She suggested that such forms may have been eroded into the base of an ice shelf, and would have acted as moulds to underlying glaciolacustrine sediments when the ice was let down during lake lowering (see also Vreeken in Gilbert *et al.* in press). If this hypothesis is correct, it fixes the formation of the transverse ridges to a very late stage of deglaciation.

All of the above hypotheses were formulated for ridges containing glaciolacustrine sediment to the east of the present study area. At two locations south of Campbellford, Shaw and Gorrell (1991) reported large, subglacially-formed gravel dunes within tunnel channels. A number of their sites (Shaw and Gorrell 1991, fig. 2) coincide with fields of transverse ridges mapped in the present project (Fig. 3.4). These dunes may be the product of any of three possible events. First, they may have been active towards the end of the last tunnel channel event when flow velocity was low enough to allow deposition within the channels (Shaw and Gorrell 1991). Such a process may have been facilitated by the availability of local sediment in the drift-dominated, western part of the study area. It is possible that the fields of gravel dunes are more extensive than mapped here, and were later obscured by glaciolacustrine sedimentation. Second, they are preferentially located in the larger channels which also contain eskers (Fig. 3.4). It is possible that episodic flood events through R-channels (esker precursors) may have resulted in localized hydraulic lifting, narrow sheet flow, and dune formation. Third, gravel

dunes may have been the product of meltwater flow from a grounding-line position out under an ice shelf at a relatively late stage of deglaciation. Insufficient information is available to test these hypotheses at present. It is perhaps possible that both ice-pressed, ripple-form ridges and subglacial gravel dunes exist in the study area. Further investigation is required.

Eskers

Description

The description which follows is a summary of more detailed observations presented by Brennand (in press). Esker ridges form a dendritic pattern in the study area and feed into the Oak Ridges glaciofluvial complex (Fig. 3.4). Most are located within tunnel channels incised into bedrock or glacigenic sediment (Figs. 3.5 and 3.8), although some small eskers lie on residuals between tunnel channels (Fig. 3.4). Major esker ridges (Marlbank, Tweed, Campbellford, and Norwood) are regularly spaced, 10 to 15 km apart. In length, these eskers vary from ~40 km (Campbellford and Norwood eskers) to ~70 km (Tweed esker). The width of the main esker ridges increases from east to west. Ridges are relatively continuous, and exhibit upslope long profiles. Measurements from imbricated gravels within esker ridges indicate low variability in paleocurrent direction. Internally, ridge sediments form three styles of macroforms: composite, pseudoanticlinal, and oblique accretion avalanche bed. Sand and gravel couplets may be stacked within each of these macroforms. Esker ridges exhibit minimal postformational disturbance. Seismic investigations (reflection method supplemented by refraction measurements) revealed intercalated till with stratified sand and gravel at one location (G. Gorrell personal communication 1989). At another location diapiric folding was observed at the ridge core. Fans, beads, laterally-fining deposits, anabranched reaches of the main ridge, and extended, hummocky zones are intimately associated with the main esker ridges. Extended, hummocky zones are not mapped on Figure 3.4, but fans, beads and laterally-fining deposits are mapped with main esker ridges, as undifferentiated esker deposits.

Interpretation

The location of esker ridges within tunnel channels, minimal postformational disturbance, and low paleocurrent variability are characteristic of esker deposition in constrained, subglacial conduits (cf. Charlesworth 1957; Flint 1957; Banerjee and McDonald 1975). Ridge continuity and upslope path imply that meltwater was under pressure for it to flow against topographic gradient, and necessitate closed-conduit conditions (Shreve 1972, 1985*a*) during esker ridge formation (Brennand in press). Contemporaneous erosion, transportation, and deposition in an upsloping, subglacial conduit flowing full of water has been inferred for the eskers. Macroforms and large bedforms are the depositional manifestations of these processes (Brennand in press). Sand and gravel couplets have been proposed to record flood events through the conduit with possible seasonal control and, therefore, a connection

between supraglacial and subglacial parts of the glacial meltwater system. From theory, Weertman and Birchfield (1983) have also suggested that R-channels may only be maintained if they are primarily supplied by supraglacial meltwater. In general, the observation that main esker ridges become wider from east to west across the study area is best explained by increased sediment availability, as the thickness of glacigenic sediments increases westwards. For a detailed account of inferred esker genesis and related meltwater regime in the study area, the reader is referred to Brennand (in press).

Esker pattern is more pertinent to this paper. Eskers form a dendritic network within an anastomosing tunnel channel system. Although meltwater is driven by ice-surface gradient it preferentially follows topographic lows (Shreve 1972, 1985*a*, 1985*b*), hence, eskers are in tunnel channels. However, not all tunnel channels contain eskers. Perhaps one explanation for this is the inferred differences in meltwater regime responsible for the formation of these landforms. Tunnel channels were incised by catastrophic, channelized, meltwater flows, whereas rhythmic sedimentation within eskers and associated deposits suggests that supraglacial, seasonally-controlled meltwater dominated the hydrologic system at the time of esker formation (Brennand in press).

Seasonal control on the subglacial hydrologic system necessitates a relatively direct supraglacial to subglacial meltwater connection within the ice sheet. Such connection may have been possible through thick ice via water-filled moulins or crevasses, provided these passageways remained water-filled (Glen 1954; Loewe 1955; Weertman 1973, 1974; Robin 1974). However, if we hypothesise that such connections were made through moulins and/or crevasses, this infers that meltwater could arrive at the bed at any location (in tunnel channels or on residuals); such meltwater would not necessarily connect with the bed at topographic lows. Moulins draining to conduits which remained open (that is, the main esker conduits within tunnel channels) would have been most active and would have developed larger surface catchments. Although supraglacial meltwater may collect and initiate R-channels on a topographic high, the fact that meltwater tends to follow topographic lows (Shreve 1972, 1985*a*) would result in smaller subglacial catchment areas for such R-channels on residuals. Consequently, R-channels would likely have been smaller on residuals than in tunnel channels. The largest R-channels have the lowest pressure, and meltwater flows from high to low pressure (Röthlisberger 1972; Shreve 1972, 1985*a*). Consequently, large R-channels would have tended to capture subglacial meltwater from small R-channels, and would have eventually dominated the subglacial hydrologic system (Shreve 1972, 1985*a*).

Small R-channels on residuals are expected to have low preservation potential; they may have remained open for one season only. Any sediment delivered to them by subglacial deformation or basal erosion may have been flushed directly into the major R-channels where it was eventually deposited. Conversely, Brennand (in press) has argued that the interactive geometries of major R-channels and associated macroforms in tunnel channels may have acted to trap meltwater as conduit pressure fell at

the end of a melt season. The location of such linearly-arranged, water-filled cavities within topographic lows (tunnel channels) may have facilitated repeated reoccupation of these conduits (Brennand in press).

Discussion

Having argued for progressive channelization associated with catastrophic meltwater sheet break-up, followed by later, seasonally-controlled R-channel drainage for meltwater landforms of south-central Ontario, we now attempt to integrate the Dummer Moraine and the Oak Ridges glaciofluvial complex into this sequence of events. Further implications for ice-sheet hydrology are discussed.

The Dummer Moraine

The Dummer Moraine lies along the Shield margin, starting just south of the margin in the west, and just to the north of it in the east of the study area (Fig. 3.1; Mirynech 1962; Barnett *et al.* 1991). It is mainly found on Gull River and Bobcaygeon Formation limestones (Shulmeister 1989), although it extends onto Verulum Formation limestone south of the Precambrian reentrant at Tweed-Stoco Lake (Figs. 3.1 and 3.6). The moraine extends for ~180 km in a broad arcuate belt, generally less than 12 km wide (Mirynech 1962, 1967; Shulmeister 1989). The southern margin appears to merge with the Peterborough-Trenton drumlin field (Mirynech 1962, 1967); in places drumlins are observed within the Dummer Moraine zone (Gravenor 1957; Barnett *et al.* 1991). This moraine is hummocky with low relief (<6 m; Gravenor 1957; Mirynech 1962; Gadd 1980), and is composed primarily of large, angular, limestone boulders in a dominantly sandy matrix (Leyland and Mihychuk 1983, 1984*b*; Finamore 1984; Leyland and Russell 1984). However, Shulmeister (1989) notes a significant Shield-derived component on the northern fringes of the Dummer Moraine. Tunnel channels and eskers cross the Moraine (Figs. 3.1 and 3.4; Gadd 1980). The termination of the Dummer Moraine east of Tamworth (Fig. 3.1; Chapman and Putnam 1966) coincides with the margin of the proposed Ontarian meltwater sheet event (Shaw and Gilbert 1990).

The genesis of this moraine is unclear. It was initially interpreted as a diffuse terminal moraine, deposited during a local readvance towards the end of the last (Wisconsinan) glaciation (Coleman 1937; Gravenor 1957; Mirynech 1962, 1967; Chapman and Putnam 1966). Schlüchter (1979) and Gadd (1980) suggested that a readvance was not necessary to produce the moraine, but rather its formation was related to bedrock structure and the dynamics of ice retreat. Barnett (1992) proposed that the moraine was deposited during ice-marginal stagnation along the Black River-Trenton escarpment during the Two Creeks Interstadial recession (~12 ka BP). Genetically, it has been interpreted as a product of glacial plucking at the Shield margin due to a change in glacial hydrologic conditions across this boundary (Shulmeister 1989). Shulmeister (1989) proposed that meltwater generated at the ice base headward of the Shield margin would have drained through the relatively thin karstified limestone south of the margin, due to an efficient epikarst drainage system (cf. Williams 1983). Freezing of this water would

have resulted in limestone blocks being frozen to the ice base and plucked from the bed. Melting out of this material was suggested to have resulted in the Dummer Moraine.

The conceptual model outlined by Shulmeister (1989) suffers from the same problems faced by other similar megablock entrainment theories (cf. Moran 1971; Aber 1985). If the ice is to be in contact with the bed during megablock entrainment, the incorporation of the block(s) into the ice requires ice or surrounding basal sediment displacement, unless incorporation occurs at a downflow-facing bed step where a cavity may form (cf. Röthlisberger and Iken 1981). In south-central Ontario ice flow encountered an upflow-facing escarpment.

Dummer Moraine deposits in some tunnel channels, indicate that these channels, at least, predate moraine formation, and probably carried several meltwater events. There are three possible explanations for the absence of Dummer Moraine deposits in other channels: (*i*) they were never present; (*ii*) they were subsequently removed; or (*iii*) they have been masked by later glacigenic or modern deposits. The first explanation seems unlikely, as there is no good reason why moraine should be deposited in some channels and not others. The latter two explanations seem more plausible. Masking of some Dummer Moraine deposits is certainly possible. Channels are often filled with Glacial Lake Iroquois sediments or organic deposits (Leyland 1982; Leyland and Mihychuk 1983, 1984*a*, 1984*b*; Leyland and Russell 1984). Conversely, removal of Dummer Moraine deposits suggest that powerful meltwater flows in some channels postdated moraine formation.

These landform relationships suggest that the Dummer Moraine was deposited before the latest flow events in tunnel channels. With respect to the proposed event sequence presented in this paper, and as the moraine and drumlins appear to be intimately associated, Dummer Moraine and drumlin formation may have been roughly contemporaneous. How might this hypothesis assist explanation of block entrainment in the vicinity of an upflow-facing escarpment? According to Shaw and Sharpe (1987), drumlins were formed by turbulent separated meltwater flows of high Reynolds numbers. If the freezing plane of the ice sheet extended into the karstified and thin limestone, quarrying may have been a result of the water sheet migration. The meltwater sheet flood event would have commenced as a wedge migrating out from a reservoir (Shoemaker 1992*b*). As the sheet reached the frozen limestone wedge (over impermeable Shield rocks) some water may have been forced along the limestone-Shield contact, and limestone blocks may have been lifted with the ice bed by hydraulic jacking. Alternatively, the limestone may not have been frozen. In this case, using the Bernoulli principle, low pressure, related to high flow velocities where the flow was constricted over the escarpment, may have caused hydraulic plucking of heavily jointed bedrock. This relatively high-velocity, low-pressure zone would have been localized at the escarpment, so that blocks were deposited soon after they had been entrained into the flow.

It should be noted that the eastward extent of the Dummer Moraine appears to coincide with the margin of the Ontarian event (Shaw and Gilbert 1990). This supports the suggestion that the Dummer Moraine was formed during the Algonquin event, and later truncated by the Ontarian event (cf. Shaw and Gilbert 1990).

The Oak Ridges glaciofluvial complex

The Oak Ridges glaciofluvial complex is also enigmatic. It is approximately 160 km long, up to 14.5 km wide, with sediments up to 215 m thick in places, and primarily composed of glaciofluvial, stratified sand and gravel, with some diamicton and rhythmically laminated silt and clay (Duckworth, 1979). The ridge has a hummocky to flat-topped topography (Gwyn and Cowan 1978). It is geographically related to tunnel channels (Deane 1950; Duckworth 1979), drumlins and eskers (Chapman and Putnam 1966), which have been attributed to subglacial meltwater processes.

Taylor (1913) first interpreted the complex as interlobate. In an attempt to explain the alignment of drumlins in the Peterborough drumlin field north and south of the complex, and espousing the notion that drumlins are a product of glacial action, Chapman and Putnam (1966) proposed that the Oak Ridges complex was overridden from the north. Similarly, Gravenor (1957) interpreted till overlying the complex, and the orientation of drumlins north and south of the complex, as indicating that the complex was overridden. Gwyn and Cowan (1978) proposed that the Oak Ridges complex was deposited by a braided river system as an outwash apron in the front of a northward-flowing Ontario lobe. These deposits were then overridden by the same lobe, burying the braided river deposits beneath Halton till. They argue that if the complex were interlobate, it would have geomorphic and sedimentologic features arranged symmetrically on either side of its longitudinal axis, and sediments would fine towards the central axis. More recently, Duckworth (1979) and Gadd (1980) have again proposed an interlobate origin for the complex. This genesis has been attributed to similar features in Canada (cf. Prest 1983; Veillette 1986) and Scandinavia (cf. Punkari 1980).

However, as the Oak Ridges complex is primarily composed of glaciofluvial stratified sediment, it is likely that its evolution was controlled by the glacial hydrologic system. The convergence of eskers on the eastern end of the complex (Figs. 3.1 and 3.4; Shaw and Gorrell 1991) supports this argument. Original interpretations of sedimentary packages within the complex include deltas which, in light of recent work, may be reinterpreted as large bedforms (Brennand 1991*a*, 1991*b*, 1992, in press; Shaw and Gorrell 1991). In addition, discrete gravel ridges previously interpreted as crevasse-fill deposits (Duckworth 1979), may actually represent an early eskerine phase of deposition. It is, therefore, possible that the complex formed subglacially. Barnett (1992) suggests that material eroded from tunnel channels during the Mackinaw Interstade (~13.2 ka BP) by jökulhlaups may have been deposited in the Oak Ridges complex. However, some tunnel channels are buried by the complex (Fig. 3.4; Shaw and

Gorrell 1991) and must, therefore, be older than it.

Given the glaciofluvial origin for the Oak Ridges complex and its close association with tributary eskers, it is highly likely that the complex and eskers were formed contemporaneously. As the eskers postdate the tunnel channels which truncate drumlins, the eskers are younger than the drumlins. Boyce and Eyles (1991) are, therefore, incorrect in their assertions about the relative timing of, and consequently the necessary subglacial hydrologic conditions for, drumlin, esker and Oak Ridges complex formation.

Implications for ice-sheet hydrology

Boulton and Hindmarsh (1987) proposed that, hydrodynamically, tunnel channels in soft-sediment areas were equivalent to eskers in bedrock areas. Clark (1991) extended this notion to suggest that eskers would only be present where the bed was not deforming. This paper contradicts these assertions at two levels. First, we have demonstrated that the scale and integration of tunnel channels can only be explained by catastrophic drainage through the whole system contemporaneously. Conversely, ridge continuity and the upslope path of eskers, in combination with the sand and gravel couplets within them, suggest seasonally-controlled meltwater discharges, and supraglacial to subglacial connection in the meltwater system. Second, an adequate sediment supply is required for eskers to form. It has been suggested elsewhere that catastrophic meltwater sheet events would tend to result in relatively clean basal ice (cf. Shaw *et al.* 1989). This is also substantiated by the lack of a diamicton drape over eskers in the study area (Brennand in press). Consequently, sediment supply for eskers must initially come from glacigenic sediment adjacent to R-channels. There are lateral constraints on sediment deformation into major R-channels (Alley 1992). Some sediment may be routed from minor R-channels to major R-channels. In either case, local deformation of sediment into R-channels is required for esker formation in this study area.

Table 3.1. Traditional and proposed glacial landform sequences, south-central Ontario

	TRADITIONAL SEQUENCE[1]		PROPOSED SEQUENCE
1.	Oak Ridges Interlobate Moraine	1.	Drumlins & Dummer Moraine (subglacial)
2.	Drumlins	2.	Late-stage Sheet Flow Scours & Latest Megachannel Flow
3.	Eskers	3.	Latest Tunnel Channel Flow
4.	Dummer Moraine (recessional)	4.	Eskers (& Oak Ridges Glaciofluvial Complex?)
5.	Glacial Lake Iroquois Shorelines	5.	Glacial Lake Iroquois Shorelines
		6.	Transverse Ridges within Tunnel Channels

[1] cf. Gravenor (1957)

The landform associations and interpretations presented in this paper point to a new glacial landform sequence for south-central Ontario, which differs substantially from the traditional view (Table 3.1; cf. Gravenor 1957). We feel that the proposed sequence best explains the suite of observations that

are presently available. It is hoped that new field research on the Oak Ridges glaciofluvial complex by the Ontario Geologic Survey and the Geological Survey of Canada will clarify the timing of this feature. Further research on the extent of the Dummer Moraine and on the distribution of the different types of transverse ridges may also prove invaluable.

References

Aber, J.S. 1985. The character of glaciotectonism. Geologie en Mijnbouw, 64: 389-395.

Alley, R.B. 1992. How can low-pressure channels and deforming tills coexist subglacially? Journal of Glaciology, 38: 200-207.

Alley, R.B., Blakenship, D.D., Rooney, S.T., and Bentley, C.R. 1989. Sedimentation beneath ice shelves - the view from ice stream B. Marine Geology, 85: 101-120.

Arnold, N.S., and Sharp, M. 1992. Influence of glacier hydrology on the dynamics of a large Quaternary ice sheet. Journal of Quaternary Science, 7: 109-124.

Ashton, G.D., and Kennedy, J.F. 1972. Ripples on underside of river ice covers. Journal of the Hydraulics Division, Proceedings of the American Society of Civil Engineers, HY 9: 1603-1624.

Baker, V.R. 1988*a*. Geological fluvial geomorphology. Geological Society of America Bulletin, 100: 1157-1167.

Baker, V.R. 1988*b*. Cataclysmic processes in geomorphological systems. Zeitschrift für Geomorphologie, 67: 25-32.

Banerjee, I., and McDonald, B.C. 1975. Nature of esker sedimentation. *In* Glaciofluvial and glaciolacustrine sedimentation. *Edited by* A.V. Jopling, and B.C. McDonald. Society of Economic Paleontologists and Mineralogists, Special Publication 23, pp. 304-320.

Barnett, P.J. 1990. Tunnel valleys: evidence of catastrophic release of subglacial meltwater, central-southern Ontario, Canada. Geological Society of America, Northeastern Section, Program with Abstracts, 22: 3.

Barnett, P.J. 1992. Quaternary geology of Ontario. *In* Geology of Ontario. *Edited by* P.C. Thurston, H.R. Williams, R.H. Sutcliffe, and G.M. Stott. Ontario Geological Survey, Special Volume 4, Part 2, pp. 1011-1088.

Barnett, P.J., and Kelly, R.I. 1987. Quaternary history of southern Ontario. XIIth INQUA congress field excursion A-11, guidebook: Ottawa, National Research Council of Canada, 77 p.

Barnett, P.J., Cowan, W.R., and Henry, A.P. 1991. Quaternary geology of Ontario, southern sheet. Ontario Geological Survey, Map 2556, scale 1:1 000 000.

Boulton, G.S., and Hindmarsh, R.C.A. 1987. Sediment deformation beneath glaciers: rheology and geological consequences. Journal of Geophysical Research, 92: 9059-9082.

Boyce, J.I., and Eyles, N. 1991. Drumlins carved by deforming till streams below the Laurentide Ice Sheet. Geology, 19: 787-790.

Boyd, R., Scott, D.B., and Douma, M. 1988. Glacial tunnel valleys and Quaternary history of the outer Scotian Shelf. Nature, 333 (6168): 61-64.

Brennand, T.A. 1991*a*. Large-scale bedforms in the Harricana glaciofluvial ridge, Québec, and their

implications for meltwater regimes. Geological Association of Canada Annual Meeting, Toronto, Program with Abstracts, 16: A14.

Brennand, T.A. 1991*b*. Form and sedimentology of the Harricana glaciofluvial system, Québec, and their implications for meltwater regimes. Canadian Association of Geographers Annual Meeting, Kingston, Program with Abstracts, 40: 78.

Brennand, T.A. 1992. Large-scale bedforms and macroforms in subglacial eskers: Implications for esker genesis and meltwater regime. Symposium on Subglacial Processes, Sediments and Landforms. University of Ulster, Northern Ireland. [Abstract].

Brennand, T.A. in press. Macroforms, large bedforms and rhythmic sedimentary sequences in subglacial eskers, south-central Ontario: implications for esker genesis and meltwater regime. Sedimentary Geology.

Brennand, T.A., and Sharpe, D.R. in press. Ice-sheet dynamics and subglacial meltwater regime inferred from form and sedimentology of glaciofluvial systems: Victoria Island, District of Franklin, Northwest Territories. Canadian Journal of Earth Sciences.

Brown, S.R. 1987. Fluid flow through rock joints: the effect of surface roughness. Journal of Geophysical Research, 92: 1337-1347.

Brown, S.R. 1989. Transport of fluid and electric current through a single fracture. Journal of Geophysical Research, 94: 9429-9438.

Brown, S.R., Kranz, R.L., and Bonner, B.P. 1986. Correlation between the surfaces of natural rock joints. Geophysical Research Letters, 13: 1430-1433.

Cameron, T.D.J., Storker, M.S., and Long, D. 1987. The history of Quaternary sedimentation in the UK sector of the North Sea Basin. Journal of the Geological Society, London, 144: 43-58.

Carlson, P.R., Bruns, T.R., Molnia, B.F., and Schwab, W.C. 1982. Submarine valleys in the northeastern Gulf of Alaska: characteristics and probable origin. Marine Geology, 47: 217-242.

Carson, D.M. 1980*a*. Paleozoic geology of the Burleigh Falls-Peterborough area, district of southern Ontario. Ontario Geological Survey Preliminary Map P.2337, Geological Series, scale 1:50 000.

Carson, D.M. 1980*b*. Paleozoic geology of the Bannockburn-Campbellford area, southern Ontario. Ontario Geological Survey Preliminary Map P.2374, Geological Series, scale 1:50 000.

Carson, D.M. 1980*c*. Paleozoic geology of the Trenton-Consecon area, southern Ontario. Ontario Geological Survey Preliminary Map P.2375, Geological Series, scale 1:50 000.

Carson, D.M. 1981*a*. Paleozoic geology of the Kaladar-Tweed area, southern Ontario. Ontario Geological Survey Preliminary Map P.2411, Geological Series, scale 1:50 000.

Carson, D.M. 1981*b*. Paleozoic geology of the Belleville-Wellington area, southern Ontario. Ontario Geological Survey Preliminary Map P.2412, Geological Series, scale 1:50 000.

Carson, D.M. 1981c. Paleozoic geology of the Tichborne-Sydenham area, southern Ontario. Ontario Geological Survey Preliminary Map P.2413, Geological Series, scale 1:15 840.

Chapman, L.J., and Putnam, D.F. 1966. The physiography of southern Ontario, 2nd ed. University of Toronto Press, Toronto.

Charlesworth, J.K. 1957. The Quaternary Era: with special reference to its glaciations, Vol. 1. Edward Arnold (Publ.) Ltd., London.

Clark, P.U. 1991. Distribution of eskers deposited by the Laurentide and Eurasian Ice Sheets as an indicator of subglacial bed conditions. Geological Association of Canada, Annual Meeting, Toronto, Program with Abstracts, 16: A24.

Coleman, A.P. 1937. Lake Iroquois. Ontario Department of Mines Annual Report, 45: 1-36.

Dardis, G.F., and McCabe, A.M. 1983. Facies of subglacial channel sedimentation in late-Pleistocene drumlins, Northern Ireland. Boreas, 12: 263-278.

Deane, R.E. 1950. Pleistocene geology of the Lake Simcoe district, Ontario. Geological Survey of Canada, Memoir 256.

Duckworth, P.B. 1979. The late depositional history of the western end of the Oak Ridges Moraine, Ontario. Canadian Journal of Earth Sciences, 16: 1094-1107.

Ehlers, J., and Linke, G. 1989. The origin of deep buried channels of Elsterian age in northwest Germany. Journal of Quaternary Science, 4: 255-265.

Ehlers, J., and Wingfield, R. 1991. The extension of the Late Weichselian/Late Devensian ice sheets in the North Sea Basin. Journal of Quaternary Science, 6: 313-326.

Eyles, N., and McCabe, A.M. 1989. The late Devensian (<22,000 BP) Irish Sea Basin: the sedimentary record of a collapsed ice sheet margin. Quaternary Science Reviews, 8: 307-351.

Finamore, P.F. 1984. The stratigraphical significance of the Dummer Moraine, Bannockburn (31 C/12) and surrounding areas. Engineering Terrain Special Project No. S-15, Ontario Ministry of Natural Resources, pp. 130-131.

Flint, R.F. 1957. Glacial and Pleistocene geology. John Wiley and Sons, New York.

Ford, D. 1987. Effects of glaciations and permafrost upon the development of karst in Canada. Earth Surface Processes and Landforms, 12: 507-521.

Gadd, N.R. 1980. Late-glacial regional ice-flow patterns in eastern Ontario. Canadian Journal of Earth Sciences, 17: 1439-1453.

Gilbert, R. 1990. Evidence for the subglacial meltwater origin and the late Quaternary lacustrine environment of Bateau Channel, eastern Lake Ontario. Canadian Journal of Earth Sciences, 27: 939-945.

Gilbert, R., and Shaw, J. 1992. Glacial and early postglacial lacustrine environment of a portion of

northeastern Lake Ontario. Canadian Journal of Earth Sciences, 29: 63-75.

Gilbert, R., Shaw, J., Sharpe, D.R., Vreeken, W.J., *et al.* in press. A field guide to the glacial and postglacial landscape of southeastern Ontario. Geological Survey of Canada.

Glen, J.W. 1954. The stability of ice-dammed lakes and other water-filled holes in glaciers. Journal of Glaciology, 2: 316-318.

Gorrell, G., and Shaw, J. 1991. Deposition in an esker, bead and fan complex, Lanark, Ontario, Canada. Sedimentary Geology, 72: 285-314.

Gravenor, C.P. 1957. Surficial geology of the Lindsey-Peterborough area, Ontario, Victoria, Peterborough, Durham, and Northumberland counties, Ontario. Geological Survey of Canada, Memoir 288.

Grube, F. 1983. Tunnel valleys. *In* Glacial deposits in north-west Europe. *Edited by* J. Ehlers. A. A. Balkema, Rotterdam, pp. 257-258.

Gupta, R.P. 1991. Remote sensing in geology. Springer-Verlag, Berlin.

Gwyn, Q.H.J., and Cowan, W.R. 1978. The origin of the Oak Ridges and Orangeville moraines of southern Ontario. Canadian Geographer, 22: 345-352.

Henderson, E.P. 1967. Surficial geology of the St. Lawrence River, Kingston to Prescott. *In* The Geological Association of Canada guidebook: geology of parts of eastern Ontario and western Québec. *Edited by* S.E. Jenness, pp. 199-207.

Hewitt, D.F. 1964. Precambrian-Paleozoic contact relationships in eastern Ontario. American Association of Petroleum Geologists guidebook, geology of central Ontario, Toronto convention 1964, pp. 9-12.

Kay, G.M. 1942. Ottawa-Bonnechere graben and Lake Ontario homocline. Geological Society of America Bulletin, 53: 585-646.

Kor, P.S.G., Shaw, J., and Sharpe, D.R. 1991. Erosion of bedrock by subglacial meltwater, Georgian Bay, Ontario: a regional view. Canadian Journal of Earth Sciences, 28: 623-642.

Krüger, J. 1983. Glacial morphology and deposits in Denmark. *In* Glacial deposits in north-west Europe. *Edited by* J. Ehlers. A. A. Balkema, Rotterdam, pp. 181-191.

Leyland, J.G. 1982. Quaternary geology of the Belleville area, southern Ontario. Ontario Geological Survey Preliminary Map P.2540, Geological Series, scale 1:50 000.

Leyland, J.G., and Mihychuk, M. 1983. Quaternary geology of the Tweed area, southern Ontario. Ontario Geological Survey Preliminary Map P.2615, Geological Series, scale 1:50 000.

Leyland, J.G., and Mihychuk, M. 1984*a*. Quaternary geology of the Trenton-Consecon area, southern Ontario. Ontario Geological Survey Preliminary Map P.2586, Geological Series, scale 1:50 000.

Leyland, J.G., and Mihychuk, M. 1984*b*. Quaternary geology of the Campbellford area, southern

Ontario. Ontario Geological Survey Preliminary Map P.2532, Geological Series, scale 1:50 000.

Leyland, J.G., and Russell, T.S. 1984. Quaternary geology of the Sydenham area, southern Ontario. Ontario Geological Survey Preliminary Map P.2587, Geological Series, scale 1:50 000.

Liberty, B.A. 1960. Belleville and Wellington map-areas, Ontario, 30 N/14 and part of 30 N/15 W¼, 31 C/3 and part of 31 C/2 W¼. Geological Survey of Canada, Paper 60-31.

Lillesand, T.M., and Kiefer, R.P. 1987. Remote sensing and image interpretation, 2nd ed. John Wiley and Sons, New York.

Loewe, F. 1955. The depth of crevasses. Journal of Glaciology, 2: 511-512.

Loken, O.H., and Leahy, E.J. 1964. Small moraines in southeastern Ontario. Canadian Geographer, 8: 10-21.

Loncarevic, B.D., Piper, D.J.W., and Fader, G.B.J. 1992. Application of high-quality bathymetry to geological interpretation on the Scotian Shelf. Geoscience Canada, 19: 5-12.

Long, D., and Stoker, M.S. 1986. Channels in the North Sea: the nature of a hazard. Advances in underwater technology, ocean science and offshore engineering, Oceanology, 6: 339-351.

McFall, G.H. 1990. Faulting of a Middle Jurassic, ultramafic dyke in the Picton quarry, Picton, Ontario. Canadian Journal of Earth Sciences, 27: 1536-1540.

Menzies, J., and Rose, J. 1987. (Editors) Drumlin symposium. Proceedings of the drumlin symposium, First international conference on geomorphology, Manchester. A. A. Balkema, Rotterdam.

Mirynech, E. 1962. Pleistocene geology of the Trenton-Campbellford map-area, Ontario. Ph.D. Thesis, University of Toronto, Toronto.

Mirynech, E. 1967. Pleistocene and surficial geology of the Kingston-Coburg-Tweed area, Ontario. *In* The Geological Association of Canada guidebook: geology of parts of eastern Ontario and western Québec. *Edited by* S.E. Jenness, pp. 183-198.

Mooers, H.D. 1989. On the formation of the tunnel valleys of the Superior Lobe, central Minnesota. Quaternary Research, 32: 24-35.

Mooers, H.D. 1990. A glacial-process model: the role of spatial and temporal variations in glacier thermal regime. Geological Society of America Bulletin, 102: 243-251.

Moran, S.R. 1971. Glaciotectonic structures in drift. *In* Till: a symposium. *Edited by* R.P. Goldthwaite. Ohio State University Press, pp. 127-148.

Muller, E.H., and Cadwell, D.H. 1986. Surficial geologic map of New York-Finger Lakes sheet. New York State Museum, Albany, Geologic Survey Map and Chart Series #40, scale 1:250 000.

Mullins, H.T., and Hinchey, E.J. 1989. Erosion and infill of New York Finger Lakes: implications for Laurentide Ice Sheet deglaciation. Geology, 17: 622-625.

Nye, J.F. 1973. Water at the bed of a glacier. *In* Symposium on the hydrology of glaciers, Proceedings

of the Cambridge Symposium, 7-13 Sept. 1969. International Association of Scientific Hydrology, Publication 95, pp. 189-194.

Ontario Geological Survey 1991. Bedrock geology of Ontario, southern sheet. Ontario Geological Survey Map 2544, scale 1:1 000 000.

Prest, V.K. 1983. Canada's heritage of glacial features. Geological Survey of Canada, Miscellaneous Report 28.

Punkari, M. 1980. The ice lobes of the Scandinavian Ice Sheet during the deglaciation in Finland. Boreas, 9: 307-310.

Robin, G. de Q. 1974. Depth of water-filled crevasses that are closely spaced. Journal of Glaciology, 13: 543.

Röthlisberger, H. 1972. Water pressure in intra- and subglacial channels. Journal of Glaciology, 11: 177-203.

Röthlisberger, H., and Iken, A. 1981. Plucking as an effect of water-pressure variations at the glacier bed. Annals of Glaciology, 2: 57-62.

Schlüchter, C. 1979. The Dummer moraine in southern Ontario - its sedimentology and origin. Geological Association of Canada Annual Meeting, Program with Abstracts, 4: 77.

Sharp, M., Gemmell, J.C., and Tison, J-L. 1989. Structure and stability of the former subglacial drainage system of the glacier de Tsanfleuron, Switzerland. Earth Surface Processes and Landforms, 14: 119-134.

Sharpe, D.R. 1987. The stratified nature of drumlins from Victoria Island and southern Ontario, Canada. *In* Drumlin symposium. *Edited by* J. Menzies, and J. Rose. A.A. Balkema, Rotterdam, pp. 185-214.

Shaw, J. 1983. Drumlin formation related to inverted melt-water erosional marks. Journal of Glaciology, 29: 461-478.

Shaw, J. 1988. Subglacial erosional marks, Wilton Creek, Ontario. Canadian Journal of Earth Sciences, 25: 1256-1267.

Shaw, J. in press. A qualitative view of sub-ice-sheet landscape evolution. Progress in Physical Geography.

Shaw, J., and Gilbert, R. 1990. Evidence for large-scale subglacial meltwater flood events in southern Ontario and northern New York State. Geology, 18: 1169-1172.

Shaw, J., and Gorrell, G. 1991. Subglacially formed dunes with bimodal and graded gravel in the Trenton drumlin field, Ontario. Géographie physique et Quaternaire, 45: 21-34.

Shaw, J., and Kvill. D. 1984. A glaciofluvial origin for drumlins of the Livingstone Lake area, Saskatchewan. Canadian Journal of Earth Sciences, 21: 1442-1459.

Shaw, J., and Sharpe, D.R. 1987. Drumlin formation by subglacial meltwater erosion. Canadian Journal of Earth Sciences, 24: 2316-2322.

Shaw, J., Kvill, D., and Rains, B. 1989. Drumlins and catastrophic subglacial floods. Sedimentary Geology, 62: 177-202.

Shoemaker, E.M. 1991. On the formation of large subglacial lakes. Canadian Journal of Earth Sciences, 28: 1975-1981.

Shoemaker, E.M. 1992*a*. Subglacial floods and the origin of low relief ice lobes. Journal of Glaciology, 38: 105-112.

Shoemaker, E.M. 1992*b*. Water sheet outburst floods from the Laurentide Ice Sheet. Canadian Journal of Earth Sciences, 29: 1250-1264.

Shreve, R.L. 1972. Movement of water in glaciers. Journal of Glaciology, 11: 205-214.

Shreve, R.L. 1985*a*. Esker characteristics in terms of glacial physics, Katahdin esker system, Maine. Geological Society of America Bulletin, 96: 639-646.

Shreve, R.L. 1985*b*. Late Wisconsin ice-surface profile calculated from esker paths and types, Katahdin esker system, Maine. Quaternary Research, 23: 27-37.

Shulmeister, J. 1989. A conceptual model for the deposition of the Dummer Moraine, southern Ontario. Geomorphology, 2: 385-392.

Smith, D.G. 1983. Anastomosed fluvial deposits: modern examples from western Canada. *In* Modern and ancient fluvial systems. *Edited by* J. Collinson, and J. Lewin. International Association of Sedimentology, Special Publication 6, pp. 155-168.

Smith, D.G., and Smith, N.D. 1980. Sedimentation in anastomosed river systems: examples from alluvial valleys near Banff, Alberta. Journal of Sedimentary Petrology, 50: 157-164.

Spencer, J.W. 1891. Origin of the basins of the Great Lakes. American Geologist, 7: 86-97.

Taylor, F.B. 1913. The moraine systems of southwestern Ontario. Royal Canadian Institute Transactions, 10: 57-59.

Veillette, J.J. 1986. Former southwesterly ice flows in the Abitibi-Timiskaming region: implications for the configuration of the late Wisconsinan ice sheet. Canadian Journal of Earth Sciences, 23: 1724-1741.

Walder, J.S. 1982. Stability of sheet flow of water beneath temperate glaciers and implications for glacier surging. Journal of Glaciology, 28: 273-293.

Watkins, K.J. 1992. The genesis and morphology of transverse ridges in the Kingston, Ontario region. M.Sc. Thesis, Queen's University, Kingston.

Weertman, J. 1972. General theory of water flow at the base of a glacier or ice sheet. Reviews of Geophysics and Space Physics, 10: 287-333.

Weertman, J. 1973. Can a water-filled crevasse reach the bottom surface of a glacier? *In* Symposium on the hydrology of glaciers, Proceedings of the Cambridge Symposium, 7-13 Sept. 1969. International Association of Scientific Hydrology, Publication 95, pp. 139-145.

Weertman, J. 1974. Depth of water-filled crevasses that are closely spaced. Journal of Glaciology, 13: 544.

Weertman, J., and Birchfield, G.E. 1983. Stability of sheet water flow under a glacier. Journal of Glaciology, 29: 374-382.

Williams, P.W. 1983. The role of the subcutaneous zone in karst hydrology. Journal of Hydrology, 61: 45-67.

Willis, I.C., Sharp, M.J., and Richards, K.S. 1990. Configuration of the drainage system of Midtdalsbreen, Norway, as indicated by dye-tracing experiments. Journal of Glaciology, 36: 89-101.

Wilson, A.W.G. 1904. Trent River and Saint Lawrence outlet. Geological Society of America Bulletin, 15: 221-242.

Winder, C.G. 1954*a* Campbellford map-area, Ontario. Geological Survey of Canada, Paper 54-17, 12 p.

Winder, C.G. 1954*b*. Burleigh Falls and Peterborough map-areas, Ontario. Geological Survey of Canada, Paper 53-27.

Wingfield, R. 1990. The origin of major incursions within the Pleistocene deposits of the North Sea. Marine Geology, 91: 31-52.

Woodland, A.W. 1970. The buried tunnel-valleys of East Anglia. Proceedings of the Yorkshire Geological Society, 37: 521-578.

Wright, H.E., Jr. 1973. Tunnel valleys, glacial surges, and subglacial hydrology of the Superior Lobe, Minnesota. *In* The Wisconsinan Stage. *Edited by* R.F. Black, R.P. Goldthwaite, and H.B. Willman. Geological Society of America, Memoir 136, pp. 251-276.

CHAPTER 4

Macroforms, large bedforms and rhythmic sedimentary sequences in subglacial eskers, south-central Ontario: implications for esker genesis and meltwater regime[1]

Introduction

Previous studies on eskers have been conducted at two levels: (*i*) genetic interpretation based on external morphology (e.g., Shilts 1984; St-Onge 1984); and (*ii*) detailed site observation (e.g., Allen 1971; Denny 1972; Banerjee and McDonald 1975; Saunderson 1975; Diemer 1988). A number of models of esker genesis have been put forward (cf. Banerjee and McDonald 1975). Banerjee and McDonald's (1975) seminal paper related esker morphology and sedimentology to the site of deposition and the nature of the conduit (open or closed). However, their interpretation of fans and deltas as ice-marginal indicators only, led them to conclude that all eskers were time-transgressive. This notion was echoed by Hebrand and Åmark (1989) for some Swedish eskers.

The literature to date describes esker formation in terms of glacial hydrologic theories derived from observations on contemporary glaciers and small eskers, often in the process of formation (cf. Lewis 1949; Stokes 1958). However, esker systems produced by Pleistocene ice sheets tend to be much larger in dimensions than those forming today (cf. Banerjee and McDonald 1975). It is debatable, therefore, whether a modern analog for the formation of large Pleistocene eskers exists and "to what degree modern subaerially exposed eskers should constrain the interpretation of sedimentary sequences in large 'fossil eskers'" (Banerjee and McDonald 1975, p. 133).

The present discussion focuses on the landform associations, morphology and sedimentology, including clast lithology, sphericity and roundness, of late Wisconsinan eskers in south-central Ontario, Canada. Four main eskers passing through Tweed, Marlbank, Campbellford and Norwood are examined in detail (Figs. 4.1 and 4.2). Large bedforms, macroforms and sedimentary sequences are identified, described and interpreted with respect to esker morphology and the meltwater regime responsible for their formation. An attempt is made to relate esker sedimentology systematically to external morphology by invoking formative processes in a uniformitarian manner (cf. Baker 1988*a*, 1988*b*); processes observed in modern environments are preferred as explanation, but these processes may be invoked in different combinations or situations and at very different magnitudes from those observed

---

[1] A version of this paper has been accepted for publication as:
Brennand, T.A. in press. Macroforms, large bedforms and rhythmic sedimentary sequences in subglacial eskers, south-central Ontario: implications for esker genesis and meltwater regime. Sedimentary Geology.

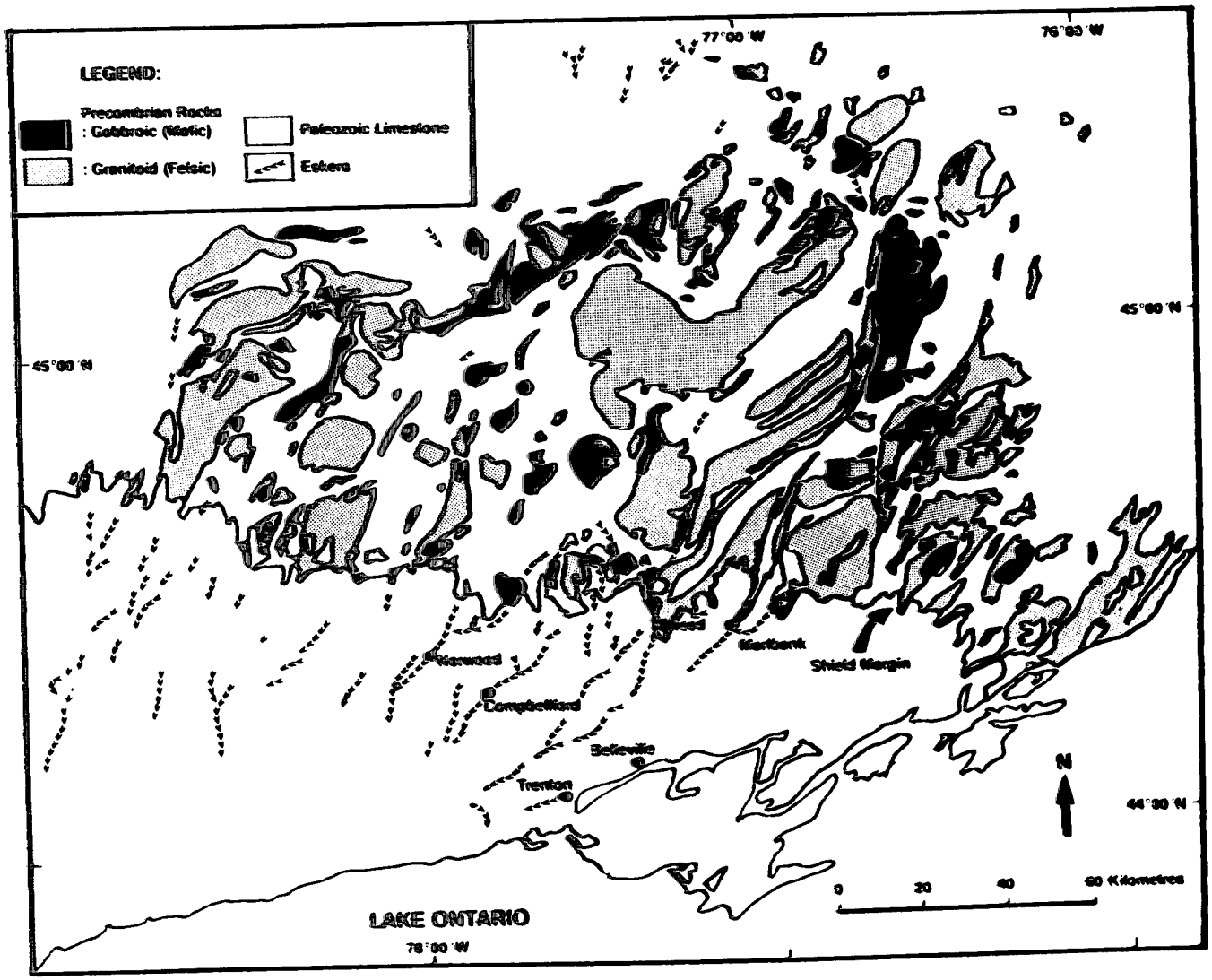

Figure 4.1. Bedrock geology (modified from Ontario Geological Survey 1991) and esker distribution (modified from Barnett *et al.* 1991) in the study area. A, Actinolite.

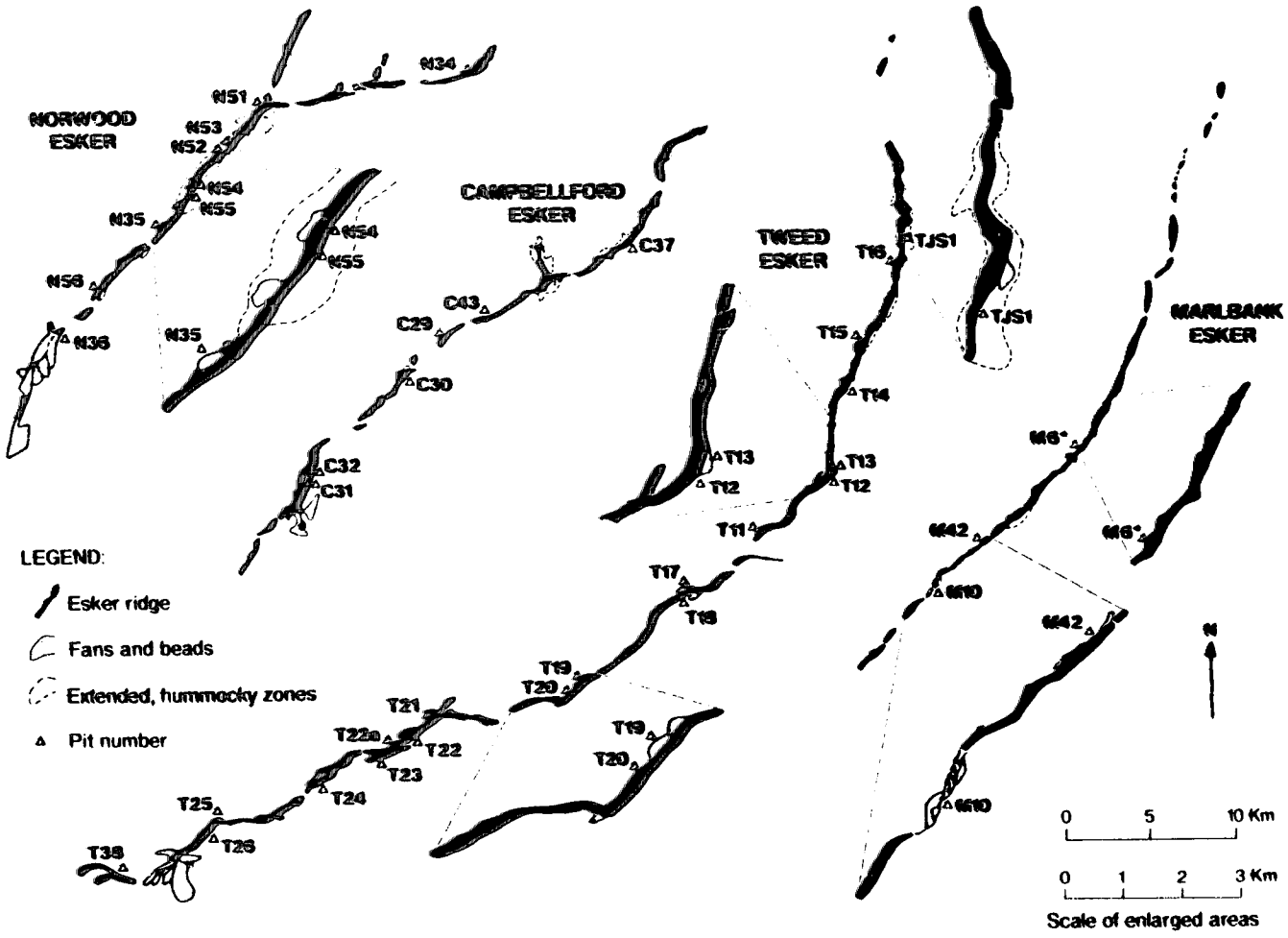

Figure 4.2. Morphologic elements of the main eskers studied. Tributary ridges are not shown. The only obvious bead is mapped at pit N35.

today. A model of synchronous subglacial sedimentation for large Pleistocene eskers, where ice-marginal sedimentation was, at most, a minor (later) component of esker sedimentation is presented. Sediment supply and the dynamics of the glacial hydrologic system necessary to maintain a continuous conduit are investigated.

Theories of esker genesis

There appears to be general agreement that large Pleistocene eskers were formed subglacially or ice marginally in deltaic, fan or reentrant environments (Table 4.1). However, many Pleistocene eskers may have undergone complex genesis (cf. Lundqvist 1979). The eskers of south-central Ontario exhibit little postdepositional sedimentary disturbance. Consequently, supraglacial and englacial depositional environments are not discussed here. Evidence used to determine subglacial and ice-marginal sites of esker deposition in the literature is presented (Table 4.2). There are, however, disagreements as to whether subglacial conduits were flowing full (closed) or partly full (open, at atmospheric or triple-point pressure) at the time of esker sedimentation (cf. Shreve 1972 versus Hooke 1984), and as to whether eskers were deposited in time-transgressive segments (Table 4.1) or synchronously (cf. Shreve 1985; Garbutt 1990). In addition, although conduit drainage may have been continuous along its length, deposition may have occurred in time-transgressive segments (Ashley *et al.* 1991).

Table 4.1. Literature on site of esker deposition.

Subglacial	Pleistocene eskers: Woodworth (1894); Stone (1899); Deane (1950)[1]; Gravenor (1957)[1]; Mirynech (1962)[1]; Lobanov (1967); Frakes *et al.* (1968); Danny (1972); McDonald & Vincent (1972); Banerjee & McDonald (1975)[2]; Shilts & McDonald (1975); Saunderson (1977, 1982)[1]; Ringrose (1982); Shilts (1984)[2]; St-Onge (1984)[1]; Lindstrom (1985); Shilts (1985); Shreve (1985); Terwindt & Augustinus (1985); Shilts & Aylsworth (1987)[2]; Diemer (1988)[2]; Visser *et al.* (1987); Jensen (1988); Aylsworth & Shilts (1989a, 1989b); Garbutt (1990); Ashley *et al.* (1991)[2]; Gorrell & Shaw (1991); Brennand and Sharpe (in press). Contemporary eskers: Stokes (1958); Jewtuchowicz (1965); Szuprynczyński (1965); Price (1966, 1969); Gustavson & Boothroyd (1982, 1987).
Englacial	Pleistocene eskers: Alden (1918); Tanner (1932); Shulmeister (1969). Contemporary eskers: Szuprynczyński (1965); Petrie & Price (1966); Price (1966, 1969); Howarth (1971); Gustavson & Boothroyd (1982, 1987).
Supraglacial	Pleistocene eskers: Crosby (1902); Tanner (1932). Contemporary eskers: Lewis (1949); Szuprynczyński (1965); Petrie & Price (1966); Price (1966, 1969); Fitzsimons (1991).
Ice-marginal delta, fan or reentrant environment	Pleistocene eskers: De Geer (1897); Banerjee (1969); Saunderson & Jopling (1970); Aario (1971*a*, 1971*b*); Danny (1972); Shaw (1972); Rust & Romanelli (1975); Banerjee & McDonald (1975); Saunderson (1975); Saunderson & Jopling (1980); Cheel (1982); Thomas (1984); Cheel & Rust (1986); Burbidge & Rust (1988); Christian (1988); Diemer (1988); Henderson (1988); Sharpe (1988); Hebrand & Åmark (1989). Contemporary eskers: Szuprynczyński (1965); Howarth (1971). Experimental: Hanson (1943).
Crack- or crevasse-fill in stagnant ice	Pleistocene eskers: Upham (1910); Flint (1928, 1930); King & Buckley (1969).

[1] Papers discuss southern Ontario eskers.
[2] Authors specifically infer time-transgressive sedimentation and a subglacial site of deposition.

To add to this confusion, the evidence listed for ice-marginal esker formation (Table 4.2) has also been documented for associated esker beads and fans inferred to have been deposited in a

Table 4.2. Evidence used to determine the site of esker deposition (from Charlesworth (1957), Flint (1957), and Banerjee and McDonald (1975)).

Subglacial	Ice marginal
Bedrock valley association	Typically beaded morphologic expression
Minimal postformational disturbance, especially in the central section of the esker, although diapiric intrusion may exist	Characteristic sedimentological associations related to decelerating flow on entry into a standing-water body. The nature of the associations will differ as a function of: height of water input, salinity of the water body, and sediment concentration of the input
Low variability in paleoflow directions	High variability in paleoflow directions
Diamicton drape	No diamicton drape
Upslope, level or downslope path	Downslope or level path

subglacial, grounding-line position (Gorrell and Shaw 1991). Conversely, the path of an esker up an adverse slope has been explained not only by a hydraulic head in a subglacial environment, but also, theoretically, by time-transgressive sedimentation at the ice margin as the ice retreated (e.g., Banerjee and McDonald 1975; Shilts 1984). The upslope path in the latter case was inferred to be a result of segmental sedimentation over low gradients rather than an active, upslope, water-flow path.

Geologic setting

Bedrock geology

The study area is divided into two major geologic regions: the Precambrian Shield in the north, and the Paleozoic limestones in the south (Fig. 4.1). The north-facing Black River-Trenton escarpment marks the Shield margin. Precambrian rocks (Grenville Province) are felsic to ultramafic plutonic, and metasedimentary, and include: granites, granodiorites, migmatites, gabbros, marbles, conglomerates and breccias (Ontario Geological Survey 1991). Paleozoic outliers (Fig. 4.1) indicate that the Shield margin was north of its present location prior to the last glaciation (Mirynech 1962). Some eskers lie on the Shield and extend onto the Paleozoic carbonate (Marlbank and Tweed eskers; Fig. 4.1), whereas others appear to start at or near the Shield margin (Norwood and Campbellford eskers; Fig. 4.1). Consequently, the Shield margin provides a means to test the provenance of esker sediments.

Quaternary geology/landform associations

All of the main eskers are located in channels cut into glacigenic sediment or bedrock, whereas some minor eskers (<3 km long) occur on interfluves (Brennand and Shaw submitted). These channels are difficult to follow north of the Shield margin. However, Wilson (1904) suggested that some do extend headward onto the Shield. The channels appear to have been occupied and enhanced by subglacial meltwater and follow a path which is against the regional gradient (cf. Gilbert 1990; Brennand and Shaw submitted). Consequently, they are inferred to be tunnel channels formed by catastrophic subglacial meltwater flows (Gilbert 1990; Shaw and Gilbert 1990; Shaw and Gorrell 1991; Gilbert and Shaw 1992; Brennand and Shaw submitted). This does not rule out the possibility that some of the

channels may have predated the last glaciation (Wilson 1904), but it does imply that they were enhanced by subglacial meltwater during the late Wisconsinan (cf. Gilbert 1990; Brennand and Shaw submitted).

Gross morphology

The four eskers studied in detail (Fig. 4.2) exhibit four main morphologic elements: (1) main ridge, (2) fans, (3) beads with minor ridges, and (4) extended, hummocky zones.

Main esker ridges

In general, these are single sinuous ridges, but bifurcation is not uncommon (Fig. 4.2). Obvious anabranched reaches along the Marlbank and Campbellford eskers are 2.0 km and 0.7 km in length, respectively (Fig. 4.2). The width of the main ridges increases from east to west across the study area. The Tweed and Marlbank esker ridges are generally 0.03 to 0.10 km wide, whereas the Campbellford and Norwood esker ridges are up to 0.15 km and 0.40 km wide, respectively. Major and minor (< 1 km long) tributary ridges join the main esker ridges from upflow (Fig. 4.1).

In general, eskers in this region are relatively sharp crested. The Norwood ridge is certainly broader in places, but not flat topped. The term "broad crested" is not applied here, as this term has dynamic implications which may not be directly equivalent to those proposed by Shreve (1985) for the Katahdin esker system. In plan view (Fig. 4.2), the ridges do not exhibit a consistent width along their length. In some places (pit M6*, Fig. 4.2), the main ridge is composed of a number of wider bulbous areas (O'Donnell 1966) joined by narrower sharp-crested ridges.

Crest long profiles of the main ridges are irregularly undulatory (Fig. 4.3). These profiles have been rotated to bring the high-stand shoreline of Glacial Lake Iroquois (750' or 228.6 m) back to a horizontal plane using isobase data (Mirynech 1962). This adjustment (raising the southwest end) was necessary to compensate for greater rebound in the northeast following deglaciation. While it cannot compensate for all isostatic adjustments, that is those prior to the Iroquois high stand, it gives the best approximation at present. The long profiles (Fig. 4.3) show that crest lines trend upslope. The elevational range (climb) of the eskers is between 92 m (Tweed esker) and 53 m (Norwood esker). As the thickness of aggregate deposits in the Tweed esker is 3 to 25 m (Ministry of Natural Resources 1987), and this is considerably less than the crest line elevational change, the upslope paths of the main eskers in this study are considered to be real; upslope paths are not a result of changes in the thickness of aggregate deposits downflow.

Ridge continuity is also demonstrated by crest long profiles (Fig. 4.3). Most of the discontinuities in the ridges are occupied by underfit creeks, the Trent River or the West Ouse River (Fig. 4.3). The Campbellford esker is more continuous northeast of Campbellford to the Shield margin, and relatively discontinuous southwest of Campbellford (Fig. 4.3*b*). Mirynech (1962) suggested that the southern portion of the Campbellford esker is wave modified. The Marlbank esker is the most

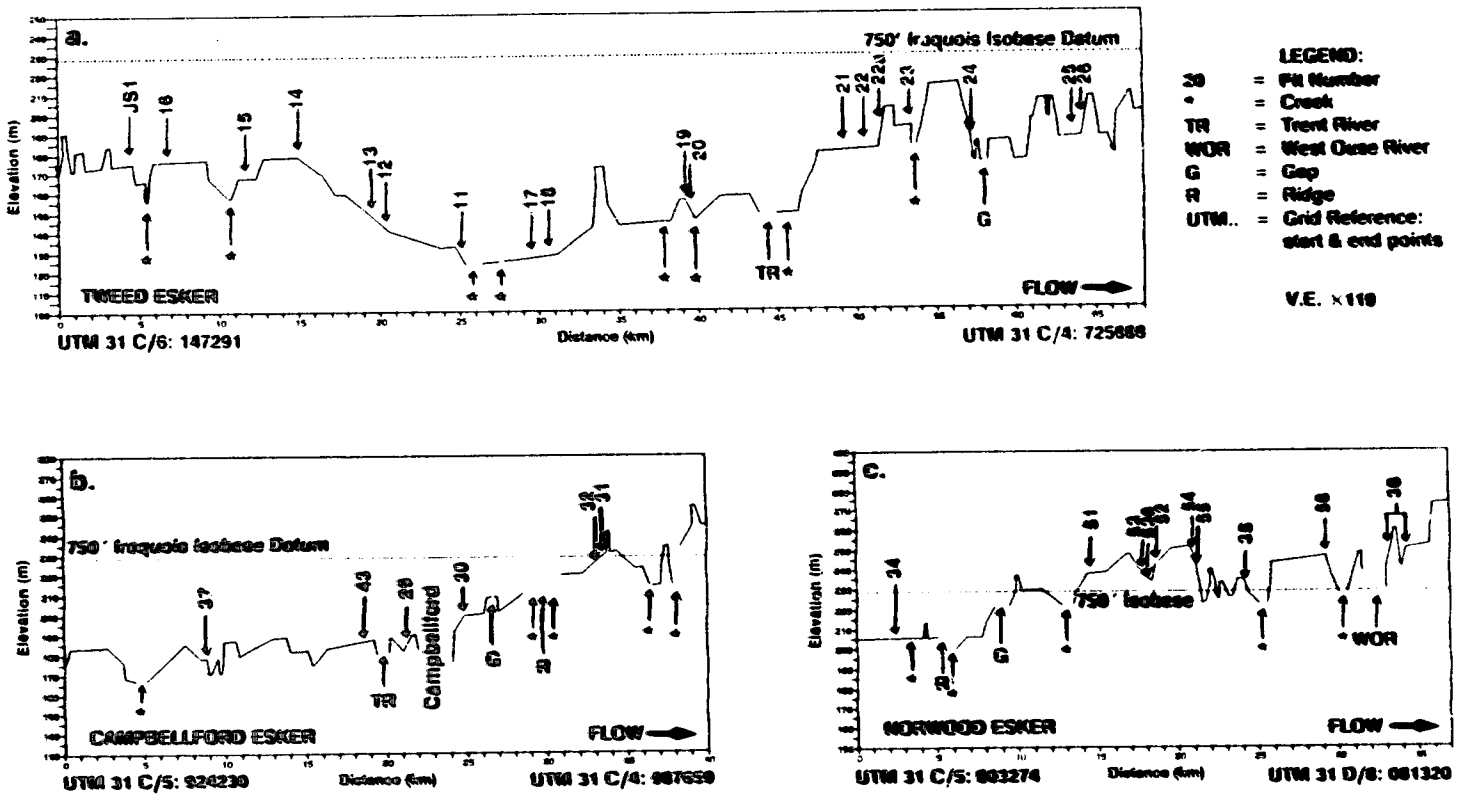

Figure 4.3. Crest long profiles rotated to bring the high-stand shoreline (750' or 228.6 m) of Glacial Lake Iroquois back to a horizontal plane. *a*. Tweed esker. *b*. Campbellford esker. *c*. Norwood esker.

discontinuous of the four eskers studied (consequently, a long profile was not plotted; Fig. 4.2); it is quite discontinuous on the Shield and for 32 km above its junction with the Tweed esker (Fig. 4.1). Some of its inferred path is now occupied by the Moira River.

Fans

Both major and minor fans extend from the main esker ridges in a downflow direction. Major fans are *en echelon*, or overlapping, towards the southern ends of the main eskers (Tweed, Campbellford and Norwood; Fig. 4.2). They reach a maximum of 2.5 km long and 1 km wide. Mirynech (1962) reported a kame-esker complex, interpreted here as a fan complex, at the southern end of the Tweed esker. Minor fans are connected laterally to the main esker ridges. They are mapped on both sides of each ridge and preferentially at bends. They also occur along straighter portions of the ridges. Minor fans are generally less than 1 km long and 0.2 to 0.3 km wide. The Tweed esker exhibits at least 18 minor fans (Fig. 4.2).

Beads with minor ridges

A single bead is located ~1 km southwest of Norwood (pit N35; Fig. 4.2) on Norwood esker. The bead is ~0.25 km wide and ~0.3 km long. This bead is joined to the main ridge by narrow minor ridges. Although it was the only bead mapped in this study, some of the minor fans which run alongside the main ridges may represent a morphological (and functional?) continuum with beads.

Extended, hummocky zones

Long (up to 8.5 km), wide (up to 0.5 km) hummocky zones, previously mapped as proximal sand, gravelly sand and gravel (Leyland and Mihychuk 1983, 1984*a*, 1984*b*; Leyland and Russell 1984), are observed on one or both sides of the main ridges towards the headward (northern) ends of the Tweed, Campbellford and Norwood eskers (Fig. 4.2). These deposits are at lower elevations than the main ridges. This morphologic element is not to be confused with the extended deposits of Hebrand and Åmark (1989). They considered these deposits to include all nonlinear morphologic components: hummocks, plateaus, and terraces. Plateaus and terraces are not recognized in this study. In contrast to the inference of Hebrand and Åmark (1989) that extended deposits occur as downflow extensions of the main ridges, the hummocky, extended zones in this study are lateral to, and run parallel to, the main ridges.

Down-esker trends

Clast lithology, sphericity and roundness

Clast lithology, sphericity and roundness were recorded along the length of the esker ridges. Distance from a datum was determined planimetrically for each ridge. Data collection from the Tweed esker was the most systematic, and is the focus of attention here. Samples were collected from two clast populations: (*i*) unit samples, or *in situ* clasts, from vertical sections; and (*ii*) oversize samples gathered

from the base of slopes under pit faces and from piles of oversize material within the pit. Unit samples include pebbles and cobbles (-4.5ϕ to -7.5ϕ diameter). Oversize samples include cobbles and boulders (-5.5ϕ to -11.0ϕ diameter). The separate treatment of the two samples is a crude attempt to control grain size (Sneed and Folk 1958). Sample size at each location varied from 60 to 120 clasts (Table 4.3; Appendices 2 and 3).

Clast roundness was determined visually in the field (Powers 1953; Appendices 2 and 3). For statistical manipulation, the geometric mean of the visual roundness class (Powers 1953) exhibited by each clast was assigned as its roundness value. Maximum projection sphericity (Ψ_p) was calculated from clast axial lengths (Sneed and Folk 1958; Appendices 2 and 3). The results of the analyses are presented in total (Table 4.3) and graphed selectively (Figs. 4.4, 4.5 and 4.6).

Observations

With distance from the Shield margin, there is an increase in the proportions of limestone clasts and a concomitant decrease in the proportions of Shield clasts for the unit samples taken from Tweed esker (Fig. 4.4*a*; Table 4.3). Limestone clasts dominate unit sample clast counts at each location. Trends in the oversize samples are almost diametrically opposite to those exhibited by the unit samples (Fig. 4.4*b*; Table 4.3). Although Shield lithologies dominate oversize clast counts, downflow (south) from the Shield margin the percentage of Shield clasts increases and that of limestone clasts decreases. The percentage of gabbro clasts in both unit and oversize samples, increases away from the Shield margin.

Mean Ψ_p (Sneed and Folk 1958) of unit sample clasts decreases with distance down esker for most lithologies (Fig. 4.5*a*; Table 4.3). Similar trends are observed in the oversize samples (Fig. 4.5*b*; Table 4.3). Excluding lithologies only represented by one clast, grand mean Ψ_p ranges (Figs. 4.5*c* and 4.5*d*; Table 4.3) are similar for both unit and oversize samples. Limestone has one of the lowest grand mean Ψ_p in both oversize and unit samples (Table 4.3).

Grand mean roundness classes for most clast lithologies, in both unit and oversize samples, are rounded to subrounded (Fig. 4.6*c* and 4.6*d*; Table 4.3; Powers 1953). Unit samples exhibit a general increase in the mean roundness of Shield clasts with distance downflow, while the mean roundness of limestone clasts remains relatively constant (Fig. 4.6*a*; Table 4.3). Oversize samples show no consistent downflow trends (Fig. 4.6*b*; Table 4.3) and large confidence intervals on closely grouped means (Table 4.3) restrict further generalization.

Interpretations

The divergence of clast lithology trends down esker for unit and oversize samples suggests that these groups may be recording two different processes. Unit samples exhibit a decrease in Shield clasts with distance from the Shield margin (Figs. 4.1 and 4.4*a*). This is expected fluvial transport behaviour

Table 4.3. Lithologic frequency and mean roundness and mean sphericity by lithology for clast samples from the Tweed esker[1].

Analysis	Pit	Distance (km)	N	Limestone (L)	Mudstone (M)	Granite (GT)	Granodiorite (GD)	Gabbro (GB)	Meta-sedimentary[2]	Migmatite (MG)	Basalt (B)	Granitoid[3] (GR444)	Shield[4] (SHIELD)
Lithologic frequency (%)[5]: unit samples	T14	21.56	60	50.0 ± 12.7	5.0 ± 5.5	[illegible]	8.3 ± 7.0	1.7 ± 3.2	18.3 ± 9.8	0.0	0.0	25.0 ± 11.0	45.0 ± 12.6
	T23	58.95	60	58.3 ± 12.5	0.0	[illegible]	11.7 ± 8.1	18.3 ± 9.8	1.7 ± 3.2	0.0	0.0	21.7 ± 10.4	41.7 ± 12.5
	T24	63.57	60	73.3 ± 11.2	0.0	1.7 ± 3.2	3.3 ± 4.5	21.7 ± 10.4	0.0	0.0	0.0	5.0 ± 5.5	26.7 ± 11.2
	T26	70.13	60	58.3 ± 12.5	0.0	5.0 ± 5.5	6.7 ± 6.3	20.0 ± 10.1	6.7 ± 6.3	1.7 ± 3.2	1.7 ± 3.2	11.7 ± 8.1	41.7 ± 12.5
Lithologic frequency (%)[5]: oversize samples	TJS1	11.63	120	20.8 ± 3.3	10.0 ± 1.7	44.2 ± 5.9	11.7 ± 2.0	4.2 ± 0.7	9.2 ± 1.6	0.0	0.0	55.8 ± 6.6	69.2 ± 6.0
	T14	21.56	60	45.0 ± 8.4	6.7 ± 1.6	18.3 ± 4.2	8.3 ± 2.0	1.7 ± 0.4	20.0 ± 4.5	0.0	0.0	28.7 ± 5.8	48.3 ± 8.8
	T24	63.57	60	43.3 ± 8.3	0.0	15.0 ± 3.5	20.0 ± 4.5	5.0 ± 1.2	3.3 ± 0.8	13.3 ± 3.1	0.0	35.0 ± 7.1	58.7 ± 9.4
	T26	70.13	60	31.7 ± 6.6	0.0	15.0 ± 3.5	16.7 ± 3.8	26.7 ± 5.8	10.0 ± 2.4	0.0	0.0	31.7 ± 6.6	68.3 ± 8.7
Mean sphericity[6]: unit samples	T14	21.56	60	0.699 ± 0.039	0.585 ± 0.109	0.742 ± 0.053	0.727 ± 0.053	0.707 ± NS	0.703 ± 0.077			0.737 ± 0.053	0.722 ± 0.040
	T23	58.95	60	0.691 ± 0.035		0.701 ± 0.045	0.729 ± 0.053	0.670 ± 0.057	0.654 ± NS			0.721 ± 0.053	0.696 ± 0.036
	T24	63.57	60	0.621 ± 0.030		0.692 ± NS	0.702 ± 0.209	0.6.1 ± 0.079				0.619 ± 0.209	0.691 ± 0.074
	T26	70.13	60	0.633 ± 0.042		0.713 ± 0.209	0.749 ± 0.069	0.690 ± 0.058	0.772 ± 0.047	0.776 ± NS	0.472 ± NS	0.733 ± 0.068	0.695 ± 0.045
	GRAND MEAN SPHERICITY			0.655 ± 0.019	0.585 ± 0.109	0.733 ± 0.046	0.742 ± 0.035	0.695 ± 0.036	0.717 ± 0.056	0.776 ± NS	0.472 ± NS	0.737 ± 0.035	0.702 ± 0.023
Mean sphericity[6]: oversize samples	TJS1	11.63	120	0.741 ± 0.040	0.758 ± 0.052	0.777 ± 0.025	0.707 ± 0.052	0.835 ± 0.051	0.747 ± 0.051			0.762 ± 0.024	0.765 ± 0.021
	T14	21.56	60	0.693 ± 0.048	0.651 ± 0.069	0.765 ± 0.056	0.737 ± 0.109	0.870 ± NS	0.636 ± 0.051			0.756 ± 0.048	0.710 ± 0.044
	T24	63.57	60	0.597 ± 0.043		0.719 ± 0.052	0.760 ± 0.042	0.479 ± 0.206	0.776 ± 0.132	0.719 ± 0.029		0.742 ± 0.033	0.716 ± 0.037
	T26	70.13	60	0.616 ± 0.056		0.769 ± 0.052	0.753 ± 0.053	0.599 ± 0.049	0.745 ± 0.069			0.761 ± 0.048	0.691 ± 0.040
	GRAND MEAN SPHERICITY			0.662 ± 0.026	0.731 ± 0.054	0.768 ± 0.021	0.737 ± 0.031	0.636 ± 0.062	0.705 ± 0.038	0.719 ± 0.029		0.758 ± 0.017	0.731 ± 0.016
Mean roundness[6]: unit samples	T14	21.56	60	0.495 ± 0.055	0.697 ± 0.281	0.275 ± 0.049	0.532 ± 0.165	0.410 ± NS	0.589 ± 0.103			0.361 ± 0.068	0.480 ± 0.061
	T23	58.95	60	0.476 ± 0.056		0.352 ± 0.169	0.327 ± 0.094	0.638 ± 0.121	0.590 ± NS			0.339 ± 0.084	0.480 ± 0.065
	T24	63.57	60	0.479 ± 0.048		0.300 ± NS	0.410 ± NS	0.505 ± 0.110				0.373 ± 0.072	0.461 ± 0.063
	T26	70.13	60	0.453 ± 0.040		0.470 ± 0.116	0.500 ± 0.192	0.595 ± 0.126	0.733 ± 0.221	0.210 ± NS	0.410 ± NS	0.467 ± 0.071	0.590 ± 0.061
	GRAND MEAN ROUNDNESS			0.478 ± 0.026	0.697 ± 0.281	0.329 ± 0.050	0.432 ± 0.071	0.562 ± 0.057	0.612 ± 0.092	0.210 ± NS	0.410 ± NS	0.377 ± 0.045	0.489 ± 0.043
Mean roundness[6]: oversize samples	TJS1	11.63	120	0.524 ± 0.072	0.521 ± 0.076	0.330 ± 0.026	0.699 ± 0.097	0.594 ± 0.134	0.580 ± 0.095			0.407 ± 0.048	0.442 ± 0.042
	T14	21.56	60	0.427 ± 0.049	0.518 ± 0.211	0.413 ± 0.080	0.569 ± 0.155	0.410 ± NS	0.425 ± 0.029			0.461 ± 0.070	0.444 ± 0.041
	T24	63.57	60	0.447 ± 0.053		0.443 ± 0.118	0.597 ± 0.080	0.410 ± 0.000	0.445 ± 0.284	0.658 ± 0.151		0.525 ± 0.073	0.541 ± 0.053
	T26	70.13	60	0.480 ± 0.054		0.329 ± 0.055	0.503 ± 0.104	0.643 ± 0.088	0.422 ± 0.074			0.421 ± 0.071	0.508 ± 0.058
	GRAND MEAN ROUNDNESS			0.465 ± 0.030	0.520 ± 0.074	0.354 ± 0.024	0.602 ± 0.055	0.595 ± 0.069	0.481 ± 0.041	0.658 ± 0.151		0.437 ± 0.032	0.475 ± 0.026

[1] Raw data in Appendices 2 and 3.
[2] Metasedimentary abbreviated to 'MS' in Figures 4.5 and 4.6.
[3] Granitoid class includes granites and granodiorites.
[4] Shield class includes granites, granodiorites, gabbros, migmatites, basalts and metasedimentary rocks.
[5] Data presentation: % frequency ± sampling error at 95 % confidence interval. Calculation modified from Dryden (1931) using 95 % confidence interval.
[6] Data presentation: mean ± 95 % confidence interval for the sample mean.
NS Insufficient data for calculation of confidence limits

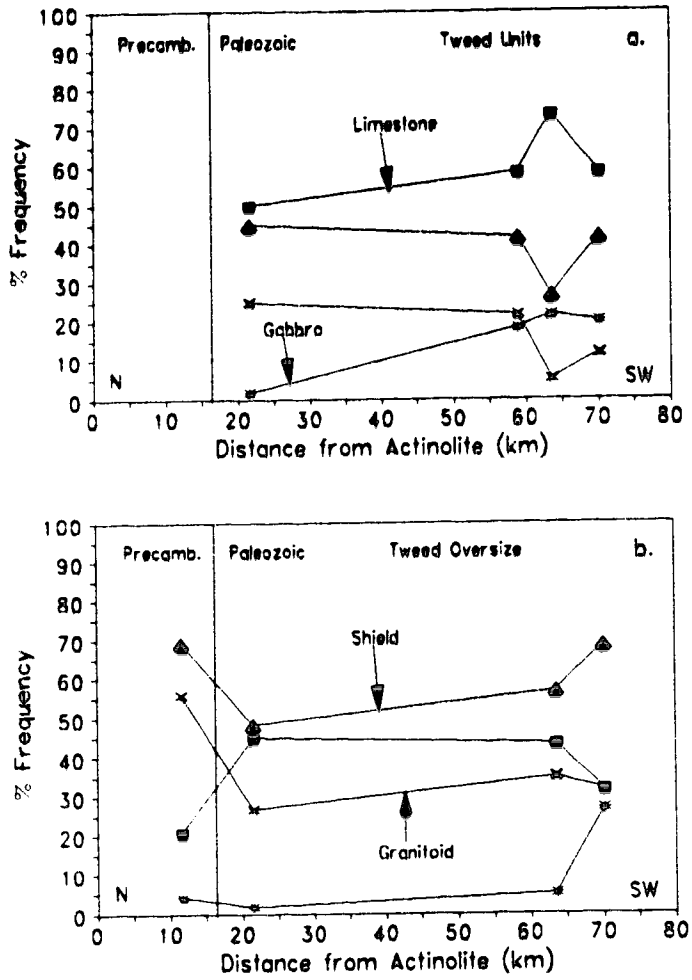

Figure 4.4. Clast lithology for the Tweed esker unit (*a*) and oversize (*b*) samples. Lines connecting points are not meant to imply continuous variation, but merely to aid in graphical interpretation. The vertical line is the location of the Shield margin. Actinolite is located on Figure 4.1.

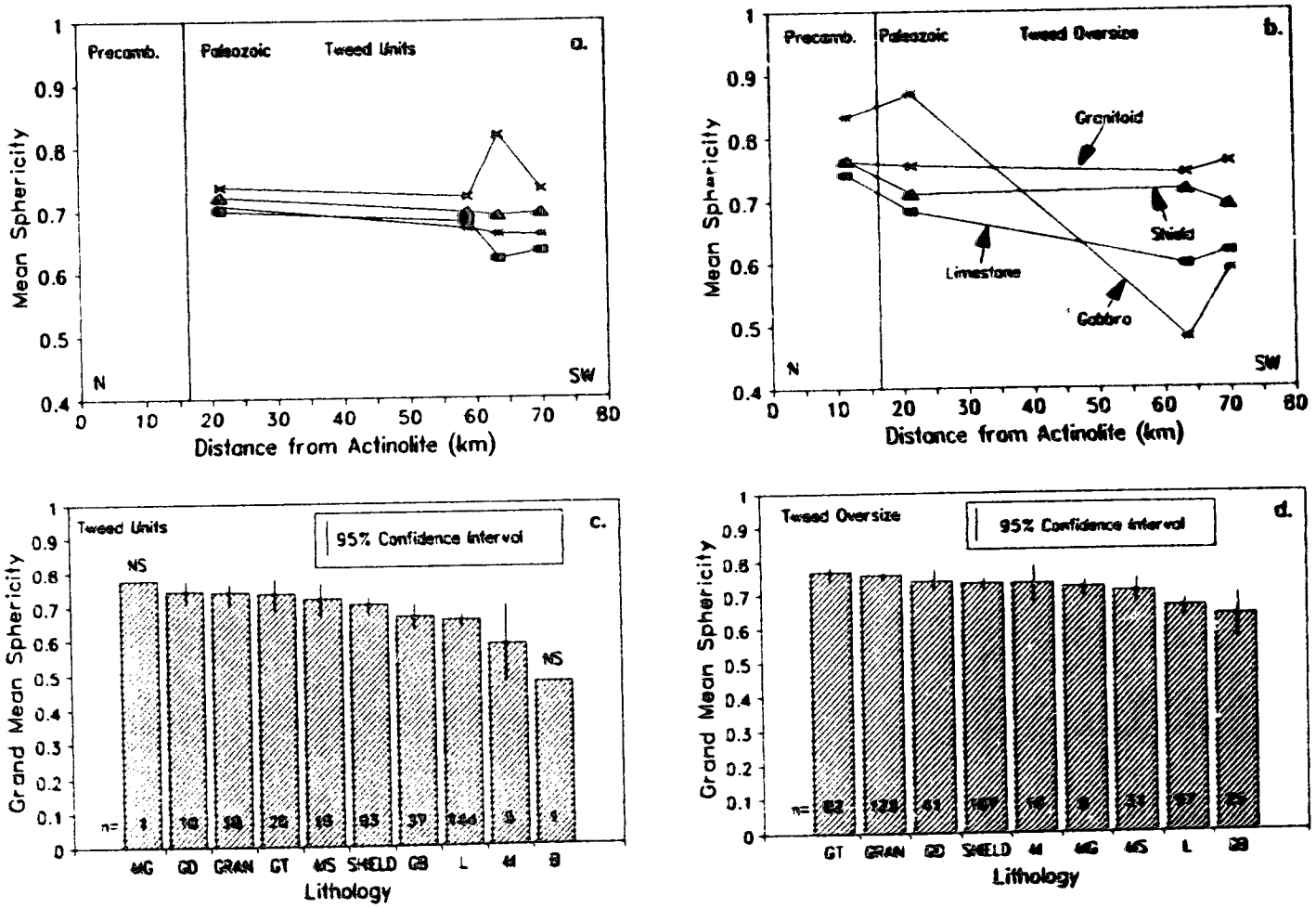

Figure 4.5. Mean and grand mean maximum projection sphericity (Ψ_p, Sneed and Folk 1958) for the Tweed unit (*a*, *c*) and oversize (*b*, *d*) clasts. Lines connecting points are not meant to imply continuous variation, but merely to aid graphical interpretation. The vertical line is the location of the Shield margin. For lithologic abbreviations see Table 4.3. Actinolite is located on Figure 4.1.

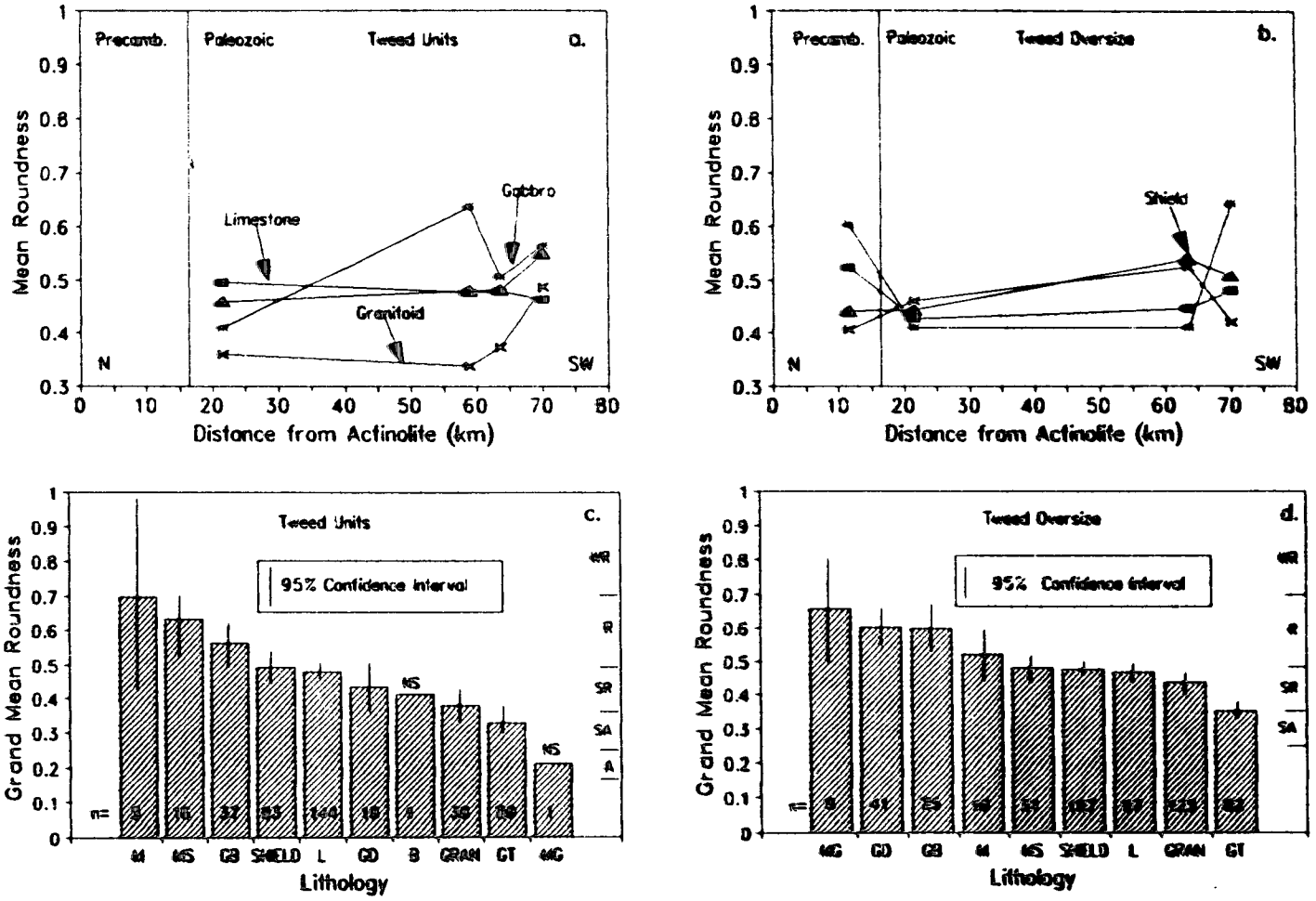

Figure 4.6. Mean and grand mean roundness for the Tweed esker unit (*a*, *c*) and oversize (*b*, *d*) clasts. Lines connecting points are not meant to imply continuous variation, but merely to aid graphical interpretation. The vertical line is the location of the Shield margin. Roundness classes after Powers (1953): WR, well rounded; R, rounded; SR, subrounded; SA, subangular; A, angular. For lithologic abbreviations see Table 4.3. Actinolite is located on Figure 4.1.

(cf. Sneed and Folk 1958). However, the increased percentage of Shield clasts in oversize samples and of gabbro in both samples, away from their source (Figs. 4.1 and 4.4), cannot be explained by regular fluvial processes. Possible sources of sediment deposited in an esker include allogenic sediment, sediment melted out from debris-rich ice, bedrock eroded by flowing water, adjacent deformable sediment squeezed into the conduit (cf. Shoemaker 1986; Shoemaker and Leung 1987; Alley 1991), sediment flushed from cavities into the conduit, and/or fluvially reworked or episodically transported sediment from within the conduit system. The most likely cause of an increase in exotic lithologies with distance from source in the oversize samples, is squeezing of local deformable substrate (containing both exotic and local lithologies) into the conduit or melt out of sediment from debris-rich ice. Moreover, gabbro is potentially the most far-travelled lithology (Fig. 4.1), and towards the southern end of Tweed esker the percentage of gabbro clasts increases whereas that of granitoid clasts declines (Fig. 4.4). This observation is consistent with a spatially controlled, incremental freeze on and melt out of debris in the subglacial environment. Such material may be consequently delivered to the conduit through local subglacial deformation or ice transport and melt-out processes. The appearance of limestone clasts north (upflow) of the Shield margin in an oversize sample (Fig. 4.4*b*) is explained by the presence of a limestone outlier (Fig. 4.1). The lower percentage of large limestone clasts within these oversize samples (Fig. 4.4*b*) may be explained by the poor preservation of large, relatively soft limestone clasts.

Past research has suggested that clast sphericity is primarily controlled by lithology and grain size (cf. Sneed and Folk 1958). An overall decrease in sphericity with distance for the Tweed unit samples (Fig. 4.5*a*) may be explained by the mode of fluvial transport. Clast fabric data (discussed later) from gravels within the esker ridge record imbricate clasts with a-axes dominantly transverse to flow direction. It is inferred from this that clasts were primarily transported by tractional rolling as bedload (cf. Johansson 1963, 1965, 1976; Rust 1972). Consequently, a decrease in sphericity downflow is interpreted as the effect of clast abrasion by rolling along the bed, thus producing prolate clast forms. In addition, limestone clasts increase in frequency down esker in the unit samples (Fig. 4.4*a*) and exhibit the most pronounced decrease in sphericity with distance along the ridge (Fig. 4.5*a*). Limestone tends to be removed from outcrop in tabular fragments, preferentially breaks parallel to bedding planes (cf. Sneed and Folk 1958), and forms discs or rods during the abrasion process. Similar trends are also evident for the oversize samples and deserve comment. Trends in oversize clast lithology suggest that these clasts were transported primarily by ice, and only secondarily by water. If the continuous decrease in sphericity with distance (Fig. 4.5*b*) is real, it must be explained by coherent processes rather than stochastic inference. While it is possible that a decrease in sphericity may be explained by fluvial transportational vigour over short distances, this does not explain the apparent consistent down-esker trend. It is possible that grain size may have been a controlling factor. The data set was inadequate

to investigate this hypothesis as confidence limits are too large (Table 4.3). Mean sphericity trends in the Tweed oversize sample remain enigmatic.

The dominance of rounded to subrounded clasts in both the unit and oversize samples (Figs. 4.6*c* and 4.6*d*) is consistent with fluvial transport processes (cf. Sneed and Folk 1958). Clast roundness in a fluvial system is primarily governed by transportational distance and vigour, and sedimentation rates (cf. Sneed and Folk 1958). An increase in the mean roundness of far-travelled clasts (Shield clasts) with distance from source for unit samples (Fig. 4.6*a*) suggests relatively long transport distances, vigorous flows, and low sedimentation rates in a continuous meltwater conduit. A constant mean roundness for limestone clasts downflow (~ 0.48) in the same data set (Fig. 4.6*a*) may indicate the effects of preferential cleavage parallel to bedding planes, thus cancelling out the expected effects of attrition (cf. Sneed and Folk 1958). Alternatively, it could indicate a continual addition of limestone clasts to the system by melt out of debris from the conduit walls or squeezing of local deformable substrate into the conduit. The grand mean roundness of limestone clasts in the unit samples (0.478 ± 0.026, Table 4.3) is significantly less than the asymptotes reported elsewhere (e.g., 0.63, Sneed and Folk 1958). This may be attributed to the use of a synthetic class geometric mean (Powers 1953) in calculations of mean roundness, operator error, variations in the type and regime of the fluvial environment, differences in physical characteristics of the limestone in each study (cf. Sneed and Folk 1958), and/or continual influx of limestone clasts into the subglacial conduit system. The erratic nature of downflow changes in the mean roundness of the oversize samples (Fig. 4.6*b*) is perhaps consistent with the inferred deformation and melt-out origin for the larger clasts. That is, these clasts are inferred to have been transported by ice for most of the distance from their source, and fluvially for only a short distance before deposition in the Tweed esker.

To summarize, down-esker trends in clast lithology, sphericity and roundness suggest sediment supply to the Tweed esker was mainly from squeezing of adjacent sediment into the main conduit or tributary conduits, melt out of sediment from conduit walls, and fluvial reworking of that sediment within the conduit system. Fluvial transport processes within the continuous, closed conduit are suggested to have been dominated by tractional rolling as bedload.

Paleoflow direction estimates

Paleoflow direction measurements were taken from gravel fabrics, cross beds in gravel and sand, and cross laminae in sand at a number of localities along the length of the eskers (Fig. 4.7; Tables 4.4 and 4.5; Appendices 4 and 5). Bulk gravel fabrics (azimuth and dip of clast a-b planes) were recorded in: heterogeneous, unstratified gravel; plane-bedded gravel; massive, imbricate, clast-supported gravel; and pseudoanticlinal macroforms in the esker ridges (Fig. 4.7; Table 4.4). The statistics for pit TJS1 (Fig. 4.7; Table 4.4) include one sample from each side of a pseudoanticlinal macroform which

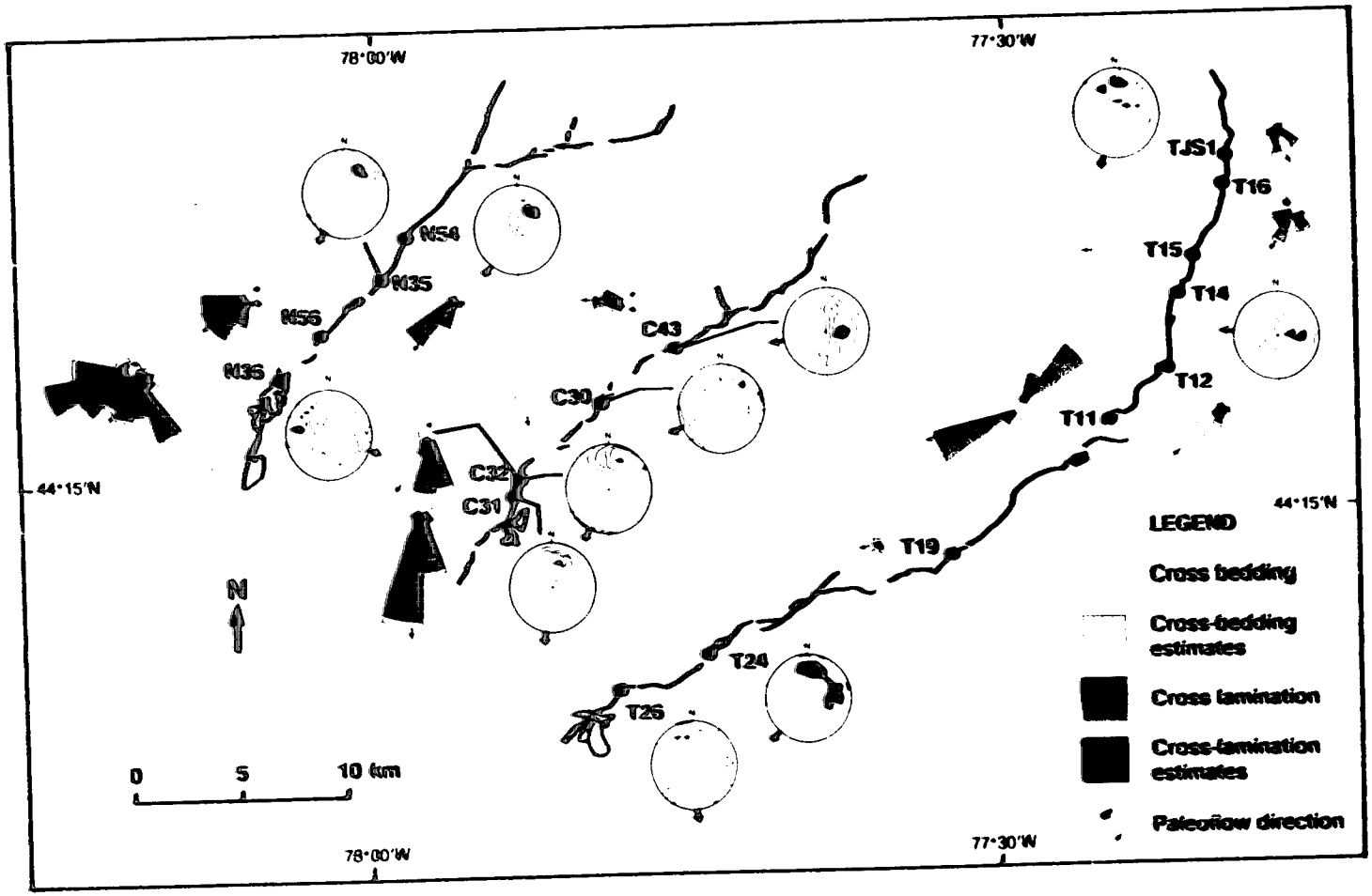

Figure 4.7. Paleoflow direction measurements for the Tweed (T), Campbellford (C) and Norwood (N) eskers. TJS1, C43, etc. are pit locations. Gravel fabrics presented as lower-hemisphere projections (contour interval is 2 standard deviations), and cross-lamination and cross-bed measurements as rose diagrams. Rose diagrams are plots of actual number of observations. Longest segment at pit C31 represents 37 observations; the same scale is used for all rose diagrams except at pit N36 (displayed at 50%; longest segment represents 71 observations).

Table 4.4. Gravel fabric statistics[1].

Pit Number	Sedimentary Facies/Structures	Sample Number	Flow Azimuth	Mean Dip	Vector Strength (S_1)	Significance Level[2]
TJS1	Plane-bedded gravel; pseudoanticlinal macroform[3]	180	198°	52°	0.5887	99.0%
T14	Eastern side of pseudoanticlinal macroform only	60	277°	55°	0.6203	99.0%
T24	Heterogeneous, unstratified gravel	60	221°	49°	0.5137	99.0%
T26	Heterogeneous, unstratified gravel	110	178°	38°	0.5803	99.0%
C43	Heterogeneous, unstratified gravel	60	260°	57°	0.6520	99.0%
C30	Heterogeneous, unstratified gravel	133	246°	27°	0.5946	99.0%
C32	Heterogeneous, unstratified gravel	25	208°	28°	0.6666	99.0%
C31	Plane-bedded gravel; massive, imbricate, clast-supported gravel	120	189°	49°	0.6804	99.0%
N54	Heterogeneous, unstratified gravel; massive, imbricate, clast-supported gravel	50	218°	46°	0.7695	99.0%
N35	Heterogeneous, unstratified gravel	30	209°	39°	0.6004	99.0%
N36	Heterogeneous, unstratified gravel; massive, imbricate, clast-supported gravel	100	109°	33°	0.5261	99.0%

[1] Raw data in Appendix 4.
[2] Significance level of sample being nonrandom, according to test statistic (S_1/S_2) of Woodcock and Naylor (1983).
[3] Both sides of pseudoanticlinal macroform included.

together produce an inferred paleoflow down the esker ridge. Data for pit T14 (Fig. 4.7) are from only the eastern side of a pseudoanticlinal macroform. Because secondary vortices responsible for the formation of the pseudoanticlinal macroform produced imbrication downflow, and towards the crest of the anticline (discussed later), the stereonet and statistics for pit T14 (Fig. 4.7; Table 4.4) are interpreted to be the result of deposition within a constrained conduit. In most cases, flow azimuths deviate very

Table 4.5. Paleoflow direction statistics from cross-bed and cross-lamination measurements[1].

Pit Number	Depositional environment	Sample Number (N)	Vector mean ($\bar{\theta}$)	Mean resultant magnitude ($\bar{R}$)	Standard Error (S_e)	Significance level of $\bar{R}$[2]	Deviation of $\bar{\theta}$ from main ridge axis
TJS1	Laterally-fining deposit	23	154°	0.9187	4.8743°	99.0%	22°
T16	Laterally-fining deposit	35	210°	0.7168	7.8130°	99.0%	20°
T15	Minor fan	21	276°	0.9199	5.0978°	99.0%	76°
T12	Laterally-fining deposit	43	229°	0.9504	2.7985°	99.0%	1°
T11	Minor fan	76	254°	0.1661	27.4508°	70.0%	25°
T19	Minor fan	14	256°	0.9028	6.9972°	99.0%	26°
C43	Laterally-fining deposit	24	273°	0.8428	6.8309°	99.0%	23°
C30	Laterally-fining deposit	6	171°	0.7162	18.8783°	95.0%	59°
C32	Laterally-fining deposit	61	212°	0.8166	4.5793°	99.0%	12°
C31	Laterally-fining deposit	62	182°	0.9709	1.7950°	99.0%	18°
N35	Lateral bead	31	221°	0.9594	2.5405°	99.0%	5°
N56	Laterally-fining deposit	54	221°	0.8591	4.2564°	99.0%	5°
N36	Major fan or fan complex	352	201°	0.6309	2.9977°	99.0%	0° - 60°

[1] Raw data in Appendix 5.
[2] Significance level determined from critical values of $\bar{R}$ for Rayleigh's test for the presence of a preferred trend (Curray 1956; Davis 1986)

little from the ridge axis and are significant at the 99 % level (Table 4.4). The flow azimuth for pit N36 (Fig. 4.7; Table 4.4) appears to be at ~90° to the axis of the main ridge. These data are from a major fan or fan complex (Fig. 4.2) towards the distal end of the esker.

Paleoflow directions inferred from paleocurrent measurements on cross beds and cross laminations exhibit a much higher degree of deviation from the ridge axis (Fig. 4.7; Table 4.5). This is expected given the smaller scale of the structures, the lower flow regime inferred for their formation, and the greater influence of local bed topography on their formative flow direction (Allen 1966). Statistically, most are unidirectionally significant at the 95% level (Table 4.5). Data for pit T11 (Fig. 4.7) include regressive, type B, ripple-drift cross-lamination (cf. Jopling and Walker 1968) in a minor fan. Fans are characterized by inferred paleoflow directions with over 25° deviation from the main ridge axis (Table 4.5). In general, paleoflow directions inferred from laterally-fining deposits within the ridge deviate by less than 25° from the ridge axis. A possible exception is pit C30 (Fig. 4.7), where the sample size is so small that its deviation of 59° (Table 4.5) cannot be accepted with confidence. Data for pit N36 (Fig. 4.7) may include measurements from more than one fan. However, up to 360° variation in paleocurrent measurements could be consistent with deposition in a single subaqueous fan (cf. Cheel 1982).

General depositional environment

The general environmental constraints on esker sedimentation must first be determined before sedimentological interpretation of esker deposits, in terms of detailed genesis and hydrodynamic controls on sedimentation, can be attempted. This first step is vital as many sedimentary structures within eskers are common to both open-channel and closed-conduit systems (Saunderson 1977, 1982; Ringrose 1982). Landform associations, esker morphology, and down-esker trends in clast characteristics and paleoflow direction estimates, in combination, suggest a continuous, subglacial, closed-conduit depositional environment. Location of esker ridges within tunnel channels, upslope paths and low variability in paleoflow directions are characteristic of eskers deposited in subglacial conduits (Table 4.2). Ridge continuity combined with upslope paths imply that water must have been under considerable pressure to flow against the topographic gradient. This would have necessitated closed-conduit conditions, where water was driven to the ice margin by excess pressure over hydrostatic pressure (cf. Shreve 1972). Discontinuities in esker ridges have been attributed to postdepositional erosion or time-transgressive sedimentation (e.g., De Geer 1897; Henderson 1988). For closed-conduit, steady-state conditions, Shreve (1985) stated that equipotential contours would be closest over bump crests. This would have resulted in high transportational capacities in the subglacial streams crossing them. Therefore, discontinuities may have been zones of nondeposition that were synchronous with esker sedimentation elsewhere in continuous conduits. Saunderson (1977) suggested that gaps were erosional zones that were contemporaneous with sliding bed deposition. The notion of nondepositional zones within

continuous conduits will be discussed later.

Sedimentology of the main esker ridges

The sedimentologic characteristics of 37 pits were investigated (Fig. 4.2). Each observed unit was given a number in the form: pit number/face number-unit number (e.g., T24/1-1). Paleoflow direction estimates from cross-bedded sand and gravel, cross-laminated sand (Appendix 5), and imbricate clast ab-planes (Appendix 4), were recorded together with clast a-axis orientations (Appendix 2). An architectural approach towards esker ridge sedimentology was taken (cf. Miall 1985).

On the scale of the esker ridge, gravel architecture may be tabular or pseudoanticlinal. Normal faults are common towards the lateral flanks of the main ridges, but there is minimal postformational disturbance at the ridge cores (Fig. 4.8*a*). This corroborates the inference of a subglacial environment of deposition with lateral ice support (cf. McDonald and Shilts 1975) for the esker ridges. At one location along the Tweed esker, a diapiric fold is observed at the ridge core (Fig. 4.8*b*), and a seismic investigation (reflection method supplemented by refraction measurements) northeast of pit T24 (Fig. 4.2) revealed diamicton, possibly till, intercalated with glaciofluvial sand and gravel (G. Gorrell personal communication 1989). The formation of a diapiric fold would have required relatively low pressure conditions to have been established within the conduit. Under similar meltwater discharge (Q_w) conditions, large conduits would have had relatively lower pressures than small conduits (cf. Röthlisberger 1972). Since a pressure gradient must have existed between adjacent ice and the water within the conduit, till creep or injection into the conduit would have occurred (cf. Hoppe 1952; Shoemaker 1986; Shoemaker and Leung 1987; Alley 1991). Sediment may have been squeezed into conduits during low pressure conditions in the winter (cf. Alley 1991; Gorrell and Shaw 1991) or during transient very low pressure conditions during a rise in Q_w (cf. Röthlisberger 1972). In the latter case, invoking Bernoulli's Principle, basal sediment and ice would have been sucked into the conduit, the sediment forming the diapiric fold and the ice being removed by melting.

No diamicton drape was observed over the esker ridges, but this is not problematic to a subglacial interpretation as clast lithology, sphericity and roundness trends, and diamicton, possibly till, intercalated with ridge sand and gravel, suggest that the primary source of esker sediment was from adjacent basal sediment. This implies that the ice was relatively clean at the time of esker formation. These sediment supply considerations may explain the relatively narrow ridge and discontinuous nature of the Marlbank esker (Fig. 4.2) which is located in a bedrock channel.

Within the main esker ridges, three types of macroforms, or ridge-scale sedimentary structures, are identified: composite, pseudoanticlinal, and oblique accretion avalanche bed. The sedimentology of these macroforms is discussed next.

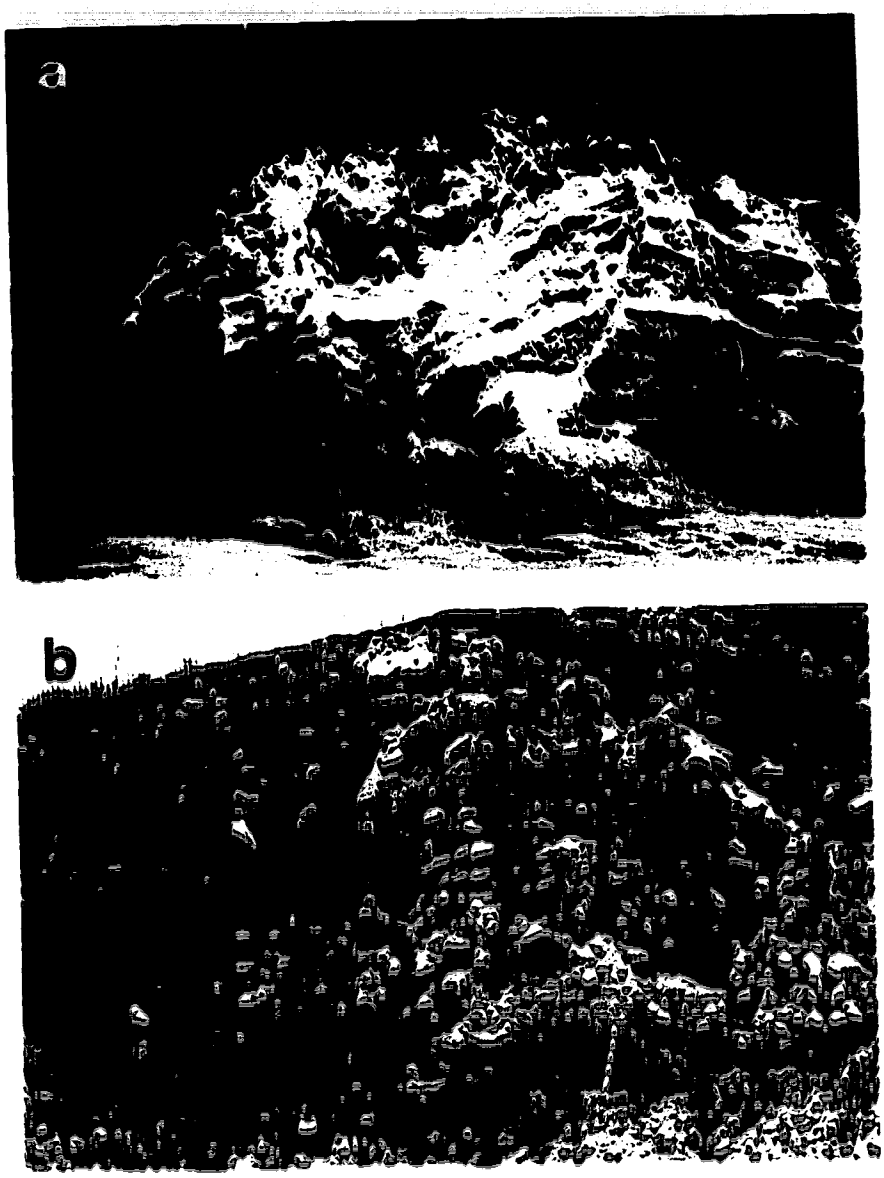

Figure 4.8. *a*. Normal faults lateral to an undisturbed ridge core, Campbellford esker (pit C32; Fig. 4.2). Note alternating sand and gravel units. *b*. Diapiric fold at the core of Tweed esker (pit T14; Fig. 4.2). Metre rods for scale.

Composite macroforms

Composite macroforms (cf. Hoey 1992; e.g., expansion bars, Baker 1978) on the scale of the ridge exhibit a number of different sand and gravel facies (described and interpreted below), including climbing dunes in gravel (Fig. 4.9). These macroforms are over 10 m in height. They are interpreted to be products of deposition in zones of flow expansion where conduits widen. This mechanism is discussed later.

Heterogeneous, unstratified gravel

Heterogeneous, unstratified gravel (Fig. 4.10) is the dominant sedimentary facies in the esker ridges and is the primary gravel facies at their cores. Bed geometry may be tabular or pseudoanticlinal. Lower contacts are erosional. Units are 0.5 to 5.0 m thick, and may exhibit a maximum grain size of boulders (generally $<-10\phi$ diameter), cobbles or pebbles. This facies is polymodal (Figs. 4.11*a* and 4.11*c*), ungraded, and framework-supported by clasts over -1ϕ diameter (Fig. 4.10; cf. Rust and Koster 1984). Material finer than 4ϕ constitutes less than 5% by weight of each unit (Fig. 4.11; Appendix 6).

Standard deviations calculated from grain size data on some of the finer (pebble-dominated) heterogeneous, unstratified gravels (Table 4.6), suggest that, *en masse*, this facies is very poorly sorted (standard deviation $>2\phi$; Table 4.6) (Folk and Ward 1957). This is misleading as gravel structure includes vaguely delineated lenses of bimodal clast-supported, bimodal matrix-supported, polymodal, and unimodal/openwork gravel (Fig. 4.10). The arrangement of these lenses vertically or laterally follows no consistent pattern. This structure is problematic when collecting representative samples for grain size analysis. For example, samples T23/1-1a and T23/1-1b (Table 4.6) were taken from the same unit in close proximity. Their grain size distributions are markedly different (Fig. 4.11*b*). Sample T23/1-1* (Figs. 4.11*a* and 4.11*b*; Table 4.6) is an amalgamation of samples T23/1-1a and T23/1-1b.

Table 4.6. Grain-size statistics[1] from heterogeneous, unstratified gravel.

Sample number	Graphic mean	Inclusive graphic standard deviation
T19/6-7	-3.00 ϕ	2.58 ϕ
T19/9-1	-3.53 ϕ	2.76 ϕ
T23/1-1a	-4.72 ϕ	1.75 ϕ
T23/1-1b	-0.07 ϕ	1.75 ϕ
T23/1-1*	-2.28 ϕ	2.82 ϕ
C43/1-1	-2.12 ϕ	2.13 ϕ

[1] after Folk and Ward (1957) from raw data in Appendix 6

Larger clasts (boulders, cobbles and/or pebbles) often occur in imbricate clusters, within gravel with an otherwise visually random fabric (Fig. 4.10). Although the dominant orientation of imbricate clasts is with their a-axis transverse to flow direction (a(t)), a high proportion of clasts are oriented with

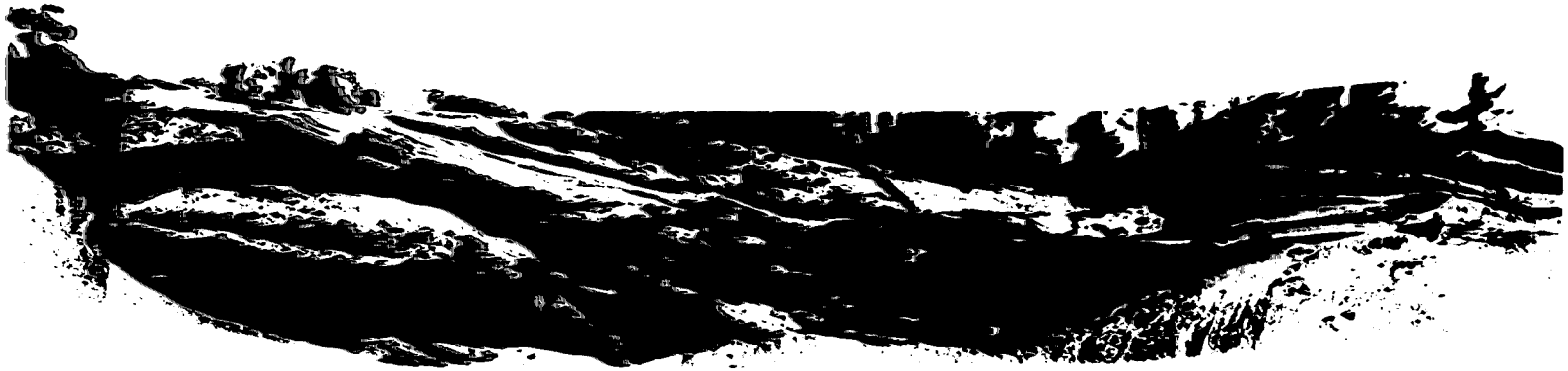

Figure 4.9. Part of a composite macroform, Norwood esker (pit N36; Fig. 4.2). Note climbing gravel dunes (right). Flow to the left. Metre rods for scale.

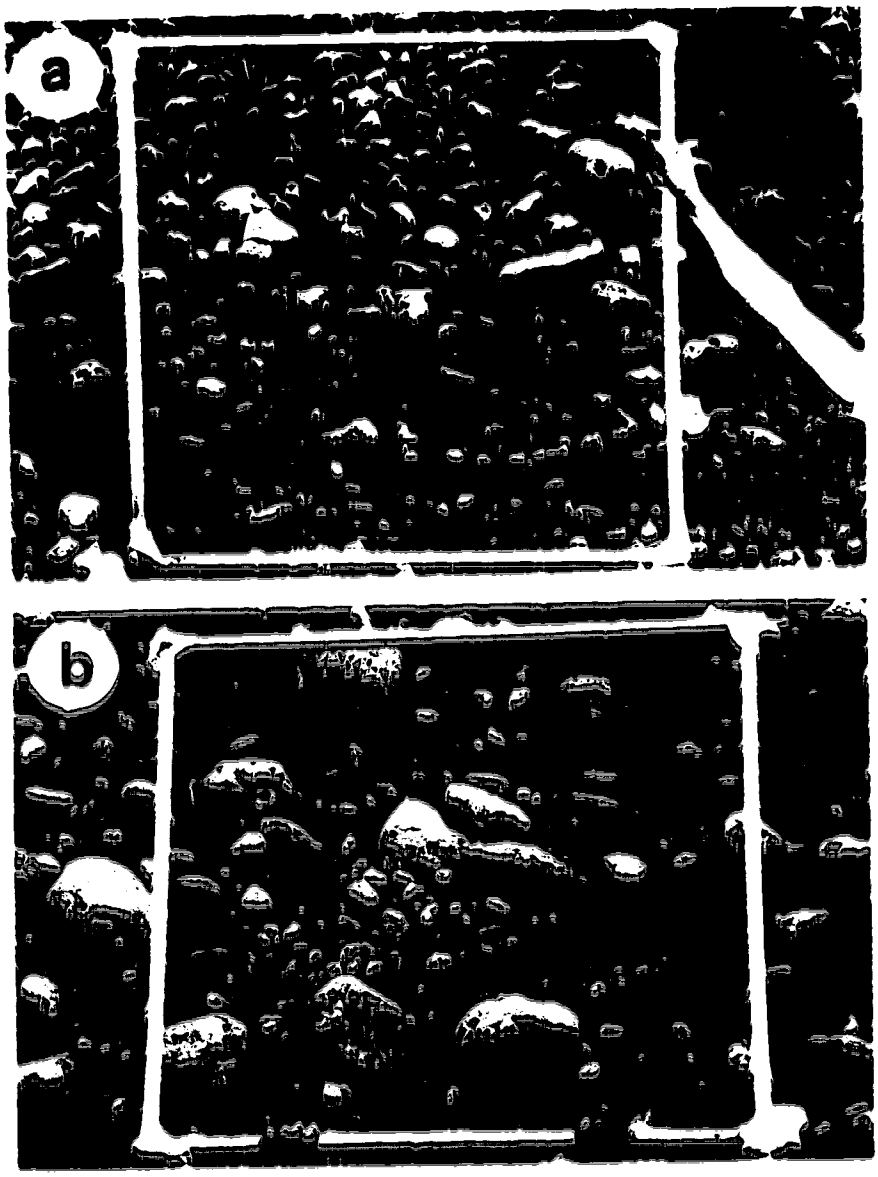

Figure 4.10. Heterogeneous, unstratified gravel facies: *a*. Poorly delineated lenses of bimodal clast-supported, polymodal and openwork gravel. Visually chaotic fabric, Campbellford esker (pit C30; Fig. 4.2). *b*. Vaguely delineated lenticular organization and cluster imbrication of larger clasts, Norwood esker (pit N36; Fig. 4.2). Metre grid for scale.

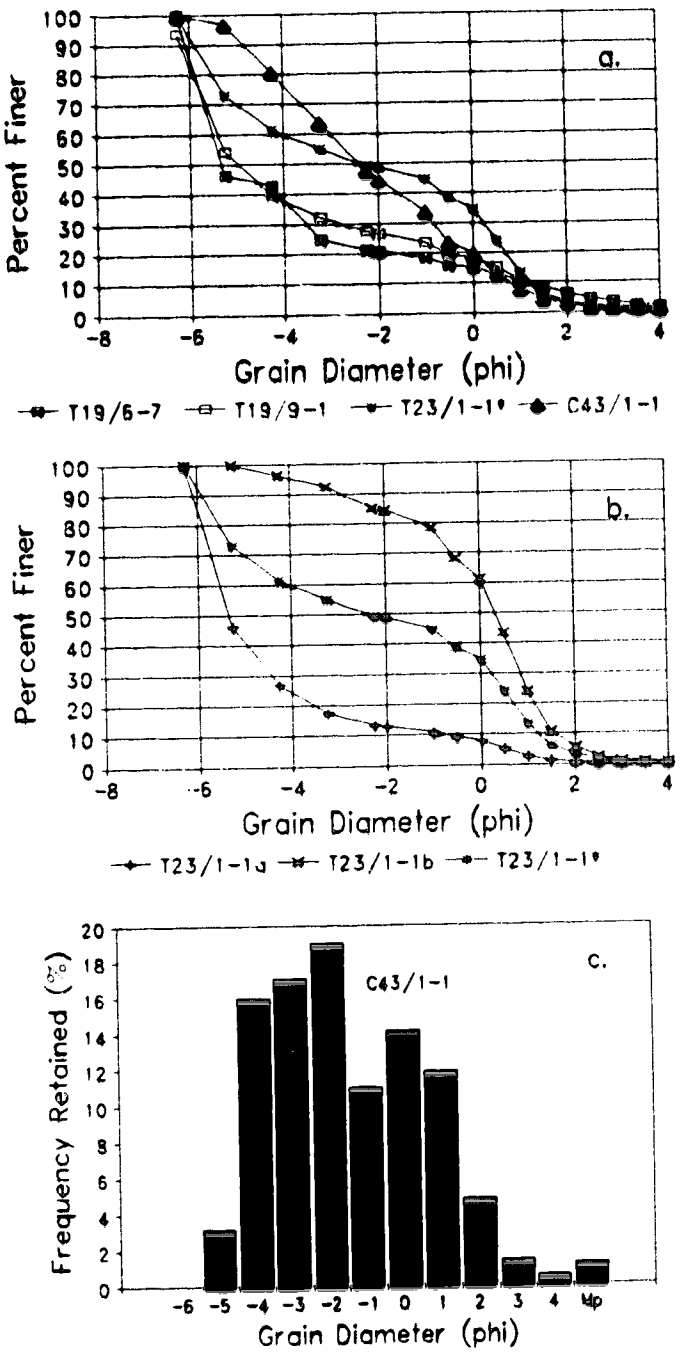

Figure 4.11. Heterogeneous, unstratified gravel facies: *a*. Grain-size distributions. *b*. Partitioning of facies. Grain-size data for sample T23/1-1* are an amalgamation of samples T23/1-1a and T23/1-1b. *c*. Grain-size histogram demonstrating polymodal texture (unit C43/1-1; Table 4.6; Appendix 6).

their a-axis parallel to flow direction (a(p)) (Table 4.7). In most cases, the dominant orientation of both cobbles and pebbles is a(t) (Table 4.7). The mean dip of the imbricate plane of clasts ranges from 14° to 57°, with most over 30°. The unit (unit N36/1-1; Table 4.7) exhibiting a mean dip of 14° has a higher proportion of fines than the other heterogeneous, unstratified gravels. Vector strength (eigenvalue S_1) is variable (Table 4.7).

Table 4.7. Summary fabric and transport orientation data for individual gravel facies[1]

Unit Number	Sedimentary Facies/Structure	Sample Number	Flow Azimuth	Mean Dip	Vector Strength (S_1)	Significance Level [2]	Transport Orientation Data			
							a(t)	a(p)	Cobbles[3]	Pebbles[3]
T24/1-1	Heterogeneous, unstratified gravel	60	221°	49°	0.5137	99.0%	48.3%	43.3%	a(t)	a(p)
C43/1-1	Heterogeneous, unstratified gravel	60	260°	57°	0.6590	99.0%	53.3%	41.7%	a(t)	a(t)
C30/7-1	Heterogeneous, unstratified gravel	50	230°	37°	0.4708	97.5%	47.5%	50.0%	a(p)	a(t)
C32/3-5	Heterogeneous, unstratified gravel	25	208°	28°	0.8665	99.0%	N/A	N/A	N/A	N/A
N54/1-7	Heterogeneous, unstratified gravel	25	220°	42°	0.8112	99.0%	N/A	N/A	N/A	N/A
N35/2-2	Heterogeneous, unstratified gravel	30	209°	39°	0.8004	99.0%	N/A	N/A	N/A	N/A
N36/1-1 (1990)	Heterogeneous, unstratified gravel (with higher % fines)	60	302°	14°	0.4233	90.0%	53.3%	43.3%	a(t)	a(t)
C31/6-2	Massive, imbricate, clast-supported, gravel	60	188°	50°	0.8312	99.0%	56.7%	40.0%	a(t)	a(t)
N54/1-5	Massive, imbricate, clast-supported, gravel	25	215°	51°	0.7777	99.0%	N/A	N/A	N/A	N/A
N36/18-1	Massive, imbricate, clast-supported, gravel	40	115°	42°	0.8163	99.0%	55.0%	45.0%	N/A	N/A
TJS1/1-3	Plane-bedded gravel	60	194°	35°	0.6305	99.0%	53.3%	25.0%	N/A	N/A
C31/10-1	Plane-bedded gravel	60	191°	47°	0.5303	99.0%	41.7%	55.0%	N/A	N/A
TJS1/2-3	Pseudoanticlinal macroform (west)	60	155°	50°	0.7955	99.0%	73.3%	21.7%	N/A	N/A
TJS1/2-1	Pseudoanticlinal macroform (east)	60	255°	45°	0.7258	99.0%	61.7%	31.7%	N/A	N/A
T14/1-3	Pseudoanticlinal macroform (east)	60	277°	55°	0.6208	99.0%	55.0%	35.0%	a(t)	a(t)
N36/22-1	Pseudoanticlinal macroform (east)	30	297°	37°	0.5247	90.0%	40.0%	40.0%	a(t)	a(p)
N36/22-5	Pseudoanticlinal macroform (west)	100	120°	39°	0.5760	99.0%	52.0%	44.0%	none	a(t)
M6°/1-centre	Oblique accretion avalanche bed macroform	60	270°	13°	0.4078	90.0%	38.3%	55.0%	N/A	N/A
M6°/1-LHS	Oblique accretion avalanche bed macroform	59	236°	44°	0.4565	95.0%	55.0%	41.7%	N/A	N/A
N36/7-6 (1989)	In-phase wave structure, gravel	50	88°	25°	0.7529	99.0%	N/A	N/A	N/A	N/A
N36/7b-1	In-phase wave structure, gravel	60	107°	25°	0.4386	99.0%	50.0%	40.0%	N/A	N/A
N36/7b-9	In-phase wave structure, sand	30	53°	27°	0.5737	99.0%	39.1%	52.2%	a(t)	a(p)
N36/17-8	In-phase wave structure, gravel	100	122°	11°	0.4707	99.0%	49.0%	38.0%	a(p)	a(t)
N36/19-5	In-phase wave structure, gravel	60	116°	29°	0.5508	99.0%	62.7%	23.7%	equal	a(t)
N36/17-10	Water-escape structure in a gravel in-phase wave structure	30	15°	29°	0.6191	99.0%	30.0%	70.0%	N/A	N/A

[1] Raw data in Appendices 2 and 4.
[2] Significance level of sample being nonrandom, according to test statistic (S_1/S_2) of Woodcock and Naylor (1983).
[3] Dominant a-axis orientation for cobble and pebble grain sizes.
N/A No data available.

Deposition from fluidal flows is inferred from the presence of imbricate clast clusters with a-

axis orientations dominantly transverse to flow direction. Large clasts were primarily transported by tractional rolling as bedload (cf. Johansson 1963, 1965, 1976; Rust 1972). A-axis parallel clasts suggest that transport by suspension and saltation also occurred prior to deposition (cf. Johansson 1963). High clast dips are attributed to the high frequency of clast-to-clast contacts during deposition of this framework-supported facies (cf. Rust 1972). This is consistent with lower clast dips recorded for more matrix-rich members of this facies, where clast-to-clast contacts would have been less frequent (unit N36/1-1, Table 4.7).

Sediment support mechanisms in a fluid flow with traction, saltation and suspension transport would have included support from the bed and from fluid turbulence. The absence of grading and the dominance of clast-to-clast contacts indicate that dispersive pressure within a highly concentrated sediment dispersion (cf. Smith 1986; Costa 1988) or a sliding bed (Saunderson 1977, 1982) was not important.

Deficiency of very coarse sand to granule grain sizes (-0ϕ to -2ϕ diameter) in open-channel fluvial sediments imparts a natural bimodality to gravel deposits (cf. Shaw and Kellerhals 1982). This deficiency may be the result of preferential transport of this size range (cf. Russell 1968) or, more likely, of selective crushing and abrasion of the smallest sizes carried as bedload (Shaw and Kellerhals 1982). Obvious deficiency in this size range is not exhibited in the frequency histograms for the heterogeneous, unstratified gravel within the eskers (Fig. 4.11). The preservation of this grain size range in esker and subaqueous fan sediments may have been the result of relatively rapid rates of sedimentation in these systems.

In flume experiments, longitudinal sediment sorting was observed in poorly-sorted gravel (McBride *et al.* 1975; Iseya and Ikeda 1987; Whiting *et al.* 1988). Here, gravel travelled as sheets with distinctive longitudinal sorting related to differential transport velocities. Large clasts had higher velocities than smaller ones, where shear velocities were well above critical values for all grain sizes present (cf. Meland and Norrman 1969; Shaw 1969). Gravel sorting with a congested, openwork zone, a smooth, matrix-rich zone and a transitional, half matrix-filled zone resulted (Iseya and Ikeda 1987). This sequence was produced in flume experiments under steady flow discharge but involving nonuniform and unsteady bedload transport. If the rate of sediment deposition was relatively rapid, such longitudinal sorting may have been preserved in the sedimentary record. In vertical section, such a mechanism may have produced a vaguely lenticular organization in the resulting gravel facies. In addition, the structure may have been complicated by pulses in flow velocity during a depositional event. This is perhaps corroborated by the transport data for unit C30/7-1 (Table 4.7), where cobbles have dominant a(p) orientations and pebbles have dominant a(t) orientations. This suggests that cobbles were primarily transported in suspension, while pebbles were transported as traction bedload. Clearly, if flow discharge

was steady this would not be sensible. The apparent anomaly may be accounted for by unsteady flow or, alternatively, by reorientation of clasts about obstacles as they came to rest (Johansson 1963, 1976).

An alternative to the relatively regular sorting produced by the above mechanism is reported in the literature on cluster bedforms (cf. Brayshaw *et al.* 1983; Brayshaw 1984, 1985). Here, obstacle clasts act as the focus for entrapment of clasts which become tightly packed and imbricate on the stoss side of obstacles. Finer material 'hides' in the wake of obstacle clasts (downflow separation bubble on their lee side; Brayshaw *et al.* 1983). Such cluster bedforms have been reported to vary in length from 0.1 to 1.2 m, and be twice as wide as they are long (Brayshaw 1984). Clast clusters are generally offset from one another downflow, less frequent towards channel walls, more frequent on bars, and are reported to vary in frequency downflow from zero to over 4 clusters per m^2 (Hassan and Reid 1990). Such clusters tend towards an equilibrium spacing for the prevailing flow conditions and are perhaps a gravel-bed analog for the ripple and dune bedforms of sand-bed streams (Hassan and Reid 1990). Clusters are believed to be deposited during the waning stages of floods (Brayshaw 1984). Their break-up can produce short-term pulses in bedload transport (Brayshaw 1985), as they tend to delay incipient motion and limit the availability of bed material for transport (Brayshaw 1984). Preservation of this bedform in vertical section, where sedimentation rates were rapid, may also have been responsible for producing the vaguely lenticular organization of the heterogeneous, unstratified gravel facies. Longitudinal sediment sorting, and sorting attributed to the development of cluster bedforms, are the most probable mechanisms responsible for the formation of the heterogeneous, unstratified gravel facies.

The coarse grain size of heterogeneous, unstratified gravel suggests relatively powerful flows. Entrainment velocities (U) on the order of 2.1 to 14.5 ms^{-1} are estimated for the largest clasts in this facies (-10ϕ diameter; cf. Williams 1983). These velocities are comparable to those reported for the drainage of ice-dammed lakes (cf. Elfstrõm 1987; Lord and Kehew 1987). Assuming closed-conduit conditions, an estimated conduit cross-sectional area (A_{est}) of 8849 m^2 (where height ~ 30 m and half width ~ 200 m, estimated from the maximum width of Norwood esker) for a conduit with the geometry of a segment defined by the space between the arc of a circle and its chord (Hooke *et al.* 1990), and the continuity equation $Q_w = U \times A_{est}$; discharge (Q_w) is calculated at 1.3×10^5 m^3s^{-1}, if U = 14.5 ms^{-1}, during the events responsible for depositing the coarsest members of this facies. The polymodal, framework-dominant character of the facies suggests that although all grain sizes were available in transport, most fines were transported away from the sites of heterogeneous, unstratified gravel deposition. Banerjee and McDonald (1975) reported an esker ridge gravel with a disrupted framework, which may be similar to the heterogeneous, unstratified gravel facies described here.

Massive, imbricate, clast-supported gravel

This facies is texturally and structurally gradational with the heterogeneous, unstratified gravel

facies. It is dominated by boulders (<-10ϕ diameter; Fig. 4.12*a*) and cobbles or cobbles, with a matrix of small pebbles, granules and sand, and is relatively bimodal and clast-supported (Fig. 4.12*a*). Unit thicknesses are generally less than 2 m. Imbrication is pervasive rather than clustered (Fig. 4.12*a*). There is a mixture of a(t) and a(p) clast imbrication, with a(t) being dominant (Table 4.7). Mean dips are high (>40°; Table 4.7) and imbrication is strong (Table 4.7). Units are generally ungraded, although one exhibits inverse grading (unit C31/6-2, Table 4.7).

This facies is similar to the heterogeneous, unstratified gravel facies, and is also interpreted as the product of deposition from fluidal flows. However, there is less matrix, stronger and more pervasive imbrication, and a more massive structure than for the heterogeneous, unstratified gravel. These differences suggest that transport was primarily by traction, and that deposition was perhaps more gradual for massive, imbricate, clast-supported gravel than for heterogeneous, unstratified gravel. Traction transport is consistent with the observation that both cobble and pebble a-axis orientations are transverse to flow direction. Some transport by suspension and saltation is recorded by a(p) clasts. Dispersive pressure within a suspension may account for the inverse grading observed in unit C31/6-2 (Table 4.7). Alternatively, and more probably, this coarsening-upwards sequence may represent the rising limb of a flood hydrograph. Entrainment velocities of 2.1 to 14.5 ms^{-1} are estimated for clasts of -10ϕ diameter (Williams 1983).

Imbricate, polymodal gravel

Visually, this facies is structurally and texturally gradational with the previous two facies (Figs. 4.10, 4.12*a* and 4.12*b*). In general, bed geometry is tabular in lateral, upflow portions of the ridge, while it is more lenticular in downflow locations, and has a pronounced undulatory surface (in-phase wave structure) in proximity to the major downflow fans (pit N36; Fig. 4.2). Unit thicknesses rarely exceed 1.5 m, except in the major fans. The facies may be ungraded or weakly inverse-to-normally graded (Fig. 4.12*b*). An increased proportion of sand often effects a matrix-supported character, although the facies is texturally polymodal (Fig. 4.12*b*). Maximum clast size does not usually exceed -6.5ϕ diameter.

This facies is inferred to have been rapidly deposited from a highly concentrated dispersion (cf. Smith 1986; Costa 1988). Entrainment velocities of 0.6 to 4.4 ms^{-1} are estimated for clasts of -6.5ϕ diameter (Williams 1983). Further observations and interpretations are presented in the section on in-phase wave structures.

Plane-bedded gravel

This is the least frequently observed facies in the main esker ridges. Observed unit thicknesses vary from 1.5 to 4 m. Plane beds have tabular geometry and are variously polymodal to graded (Fig. 4.12*c*). Stratification is less obvious (less well developed, Walker 1975; Smith 1990) in the coarser units. This facies is dominated by small boulders (<-8.2ϕ diameter) with cobbles and pebbles, cobbles with pebbles (Fig. 4.12*c*), or pebbles with granules. Pebbles, granules and sand fill the void spaces (Fig.

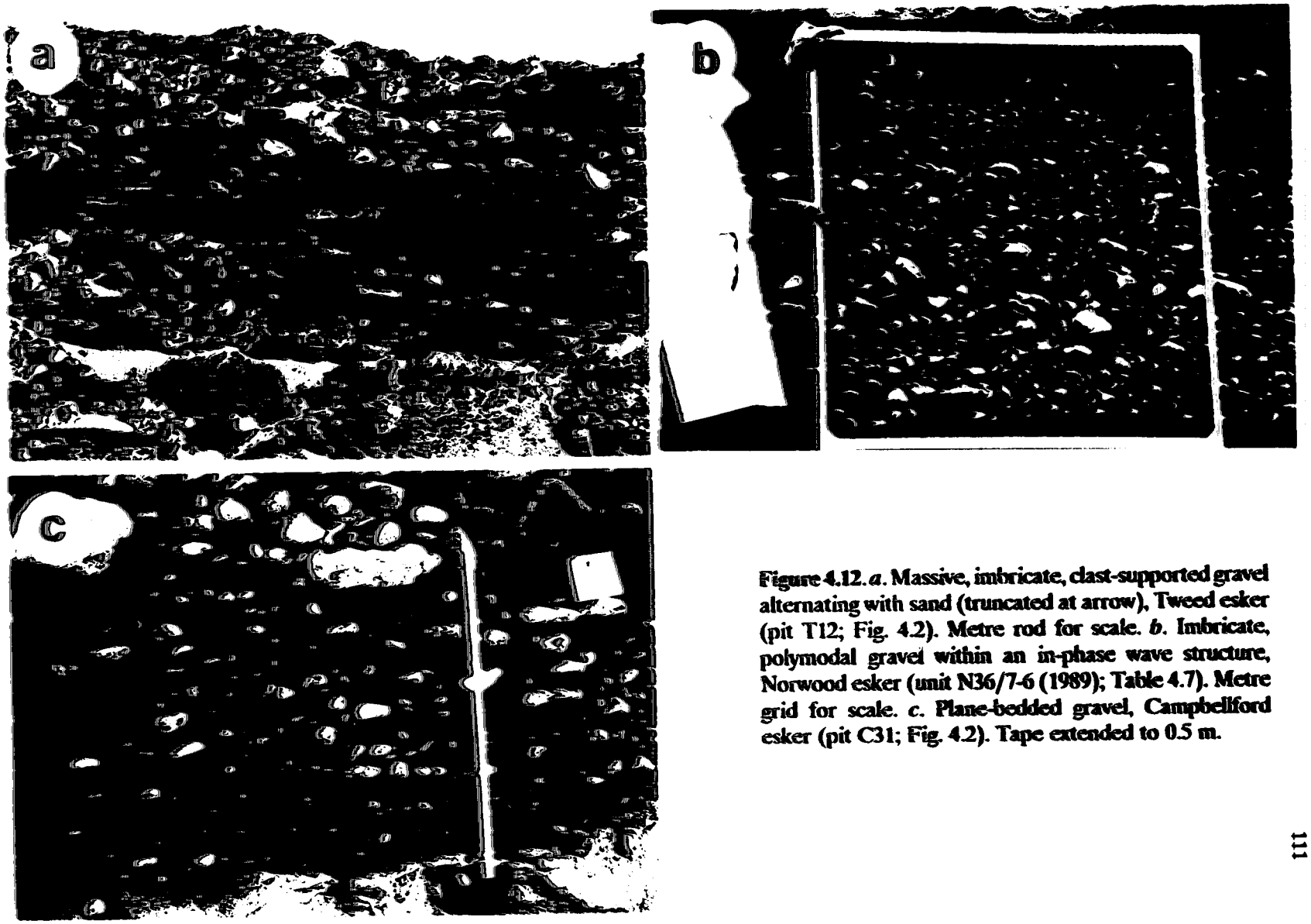

Figure 4.12. *a*. Massive, imbricate, clast-supported gravel alternating with sand (truncated at arrow), Tweed esker (pit T12; Fig. 4.2). Metre rod for scale. *b*. Imbricate, polymodal gravel within an in-phase wave structure, Norwood esker (unit N36/7-6 (1989); Table 4.7). Metre grid for scale. *c*. Plane-bedded gravel, Campbellford esker (pit C31; Fig. 4.2). Tape extended to 0.5 m.

4.12*c*). Clast imbrication is a mixture of a(t) and a(p) (Table 4.7), with mid-range vector strengths (Table 4.7), and mean dips comparable to those of heterogeneous, unstratified and massive, imbricate, clast-supported gravels (Table 4.7).

Stratification within this facies is indicative of deposition from traction transport in fluidal flows. Entrainment velocities of 1.1 to 8.0 ms^{-1} are estimated for clasts of -8.2ϕ diameter (Williams 1983). Plane bedding may be attributed to the downflow migration of bed waves which formed by interaction between eddies in the flow and the bed (Allen 1984*a*), or to the effects of the burst/sweep process on local rates and modes of sediment transport in a turbulent flow (cf. Cheel and Middleton 1986). Transport in a turbulent suspension prior to deposition is inferred for unit C31/10-1 (Table 4.7), where a(p) orientations are dominant.

Cross-bedded gravel

Trough and tabular cross-bedded gravel (Figs. 4.13*a* and 4.13*b*) is observed in all of the main esker ridges, and more frequently with distance down esker. Individual foreset beds are generally <50 cm thick, cross-bed sets are generally <2.5 m thick, and cosets are generally <3 m thick. Foresets dip at approximately 26° to 30° downflow. Cross-bedded gravel is dominated by cobbles and pebbles (Fig. 4.13*a*), with small boulders (<-8.2ϕ diameter) at the base of some rhythmically-graded foreset beds (Fig. 4.13*b*). A typical rhythmically-graded bed starts with bimodal, clast-supported boulders, cobbles or pebbles with a sandy matrix which often exhibits convolute laminations (part A; Figs. 4.13*c* and 4.14). Part A usually accounts for 50 to 60% of the bed thickness, and passes up-sequence into relatively openwork cobbles or pebbles (part B; Figs. 4.13*c* and 4.14), then into openwork granules (part C; Fig. 4.13*c*). Occasionally foreset beds are polymodal with poorly defined cross bedding. However, larger clasts often occur in imbricate clusters towards the base of such foreset beds. Similar rhythmically-graded gravel sequences, but in vaguely delineated lenticular packages, are observed within single gravel units on the scale of the esker ridges. Such units are up to 10 m thick and continue laterally over the width of the esker, while rhythmic packages are 0.5 to 1.0 m thick and 1.0 to 2.0 m wide. Some packages have downflow-inclined lower contacts (Shulmeister 1989).

The cross-bedded gravels are products of bedform migration (cf. McDonald and Vincent 1972). Traction was the dominant transport mechanism. Longitudinal sediment sorting during transport of heterogeneous gravels, and lee-side deposition of suspended load in return flow beneath a separation eddy, contributed to the characteristic foreset grading (Shaw and Gorrell 1991). Shaw and Gorrell (1991) described a basal matrix-supported gravel and reported a concomitant fining of clasts and a coarsening, or decrease in the volume of matrix, up-sequence in each foreset bed within large subglacially formed dunes. Such gradual up-sequence changes are not observed within the foreset beds in south-central Ontario eskers; rather, a basal clast-supported gravel passes up-sequence into openwork

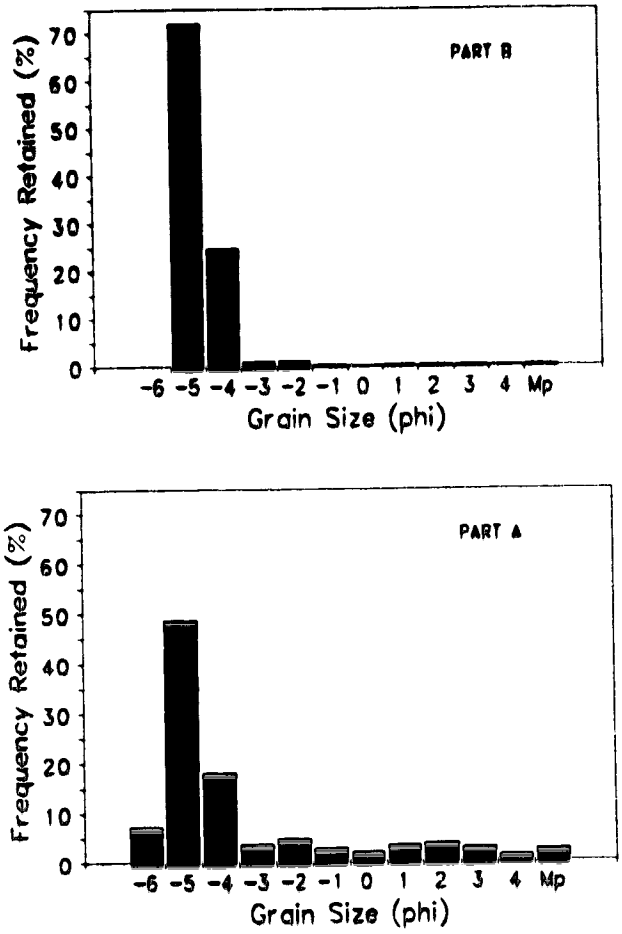

Figure 4.14. Grain-size histograms for rhythmically-graded gravel, Campbellford esker (pit C30; Fig. 4.2). Parts A and B show fining-upward sequence and a reduction in the percentage of matrix. Raw data in Appendix 6.

gravel. Overall, the cross-bedded gravel facies (in addition to heterogeneous, unstratified and massive, imbricate, clast-supported gravel facies) in south-central Ontario eskers is relatively matrix-poor. The constrained nature of flow within conduits may be responsible for the lack of fines, as fines remained in suspension and were transported downflow. The occasional occurrence of a polymodal gravel foreset bed may indicate that the heterogeneous gravel mixture feeding the foreset had only poorly developed longitudinal sorting. In addition, continuous deposition from bedload and suspended load may have produced the polymodal texture (Shaw and Gorrell 1991).

Continuous upslope flow paths for the eskers of south-central Ontario suggest closed-conduit conditions during esker formation. Flow depths of 5 to 25 m at the time of dune formation are estimated from dune heights of 2.5 m (McDonald and Vincent 1972). Entrainment velocities are estimated to have ranged from 1.1 to 8.0 ms^{-1}, for clasts of -8.2ϕ diameter (Williams 1983).

Traditionally, bimodal gravel has been interpreted as a sliding bed facies, associated with high Q_w events in eskers (e.g., Saunderson 1977, 1982; Ringrose 1982; Lindström 1985; Shulmeister 1989), or as the product of a change in flow power, such that there was initial deposition of gravel and later deposition of sand in open channels (e.g., Baker 1973; Smith 1974). Openwork gravel has been interpreted as a winnowed (e.g., Lundqvist 1979) or waning-flood (e.g., Shulmeister 1989) deposit. However, rhythmically-graded, vaguely-lenticular gravel packages with downflow-inclined lower contacts, within units on the scale of an esker, may be more appropriately attributed to deposition in the lee of a bedform (Anketell and Rust 1990: Shaw and Gorrell 1991), a negative step (cf. Carling and Glaister 1987), or a macroform, and related to longitudinal sediment sorting during transport of heterogeneous gravel to the brink of the form (Shaw and Gorrell 1991). Alternatively, rhythmic grading within these downflow-inclined packages may have been a product of the migration of smaller gravel bedforms, themselves possessing rhythmically-graded foreset beds, over the brink of a larger bedform or macroform (Anketell and Rust 1990).

Similar grading in tabular beds arranged in sets on the scale of an esker, and observed in sections cut perpendicular to flow direction (Fig. 4.13*d*), may also be interpreted as cross beds related to bedform migration or macroform progradation. However, without observation of downflow-inclined lower contacts between beds, it is equally possible that such units could be graded, plane-bedded gravels (cf. Cheel and Middleton 1986; Smith 1990).

Pseudoanticlinal macroforms

Pseudoanticlinal macroforms (or coarse gravel anticlinal macroforms, Garbutt 1990) are composed of low-angled, arched or anticlinal bedding in gravel up to -10ϕ diameter, on the scale of the main esker ridges (Fig. 4.15). They are generally observed where a ridge is narrow and geometrically uniform. Facies within this macroform include heterogeneous, unstratified gravel (Fig. 4.15) and

Figure 4.15. Pseudoanticlinal macroform composed of heterogeneous, unstratified gravel with a crest-convergent fabric, Tweed esker (pit TJS1; Fig. 4.2). Fabric data in Appendix 4, statistics in Table 4.7. Metre rods (arrows) for scale. Primary flow was into the photograph (southward).

massive, imbricate, clast-supported gravel. Occasionally, sand units, which may be continuous or discontinuous, alternate with gravel facies to form this macroform. Paleoflow azimuths inferred from gravel fabrics (Appendix 4), are downflow and convergent on the crest of the anticline (Fig. 4.15; Table 4.7). Clast orientations are dominantly a(t) (Table 4.7).

Powerful flows were required to move the boulders and cobbles which make up this macroform. Entrainment velocities of 2.1 to 14.5 ms^{-1} are estimated for clasts of -10ϕ diameter (Williams 1983). The formation of a primary pseudoanticlinal macroform with crest-convergent fabrics is inferred to have been the product of secondary currents or vortices. Secondary currents have been reported for flow in closed conduits (Rouse 1961). Here, circulation was set up in the plane of a cross section and superimposed on primary longitudinal flow; mean motion formed a spiral or vortex moving downflow. Whereas double helicoidal vortices can form in long, straight, deep, narrow, open-channel flow (Matthes 1947), closed-conduit conditions have been inferred during the formation of the main esker ridges from continuous, upslope crest long profiles (Fig. 4.3). Pseudoanticlinal macroforms are observed where the esker ridges are fairly narrow and geometrically uniform, and not where they pinch and swell, laterally and vertically. By inference, narrow, subglacial, closed conduits of uniform geometry may have been a prerequisite for the maintenance of strong secondary vortices (Shreve 1972, 1985; Garbutt 1990).

Dominance of a(t) clast orientations is consistent with observations from both heterogeneous, unstratified gravel facies, and massive, imbricate, clast-supported gravel facies which form the bulk of this macroform. Tractive forces generated by fluidal secondary flows as they converged on the crest of the anticline are inferred to be responsible for this orientation.

Oblique accretion avalanche bed macroforms

Oblique accretion avalanche bed (OAAB) macroforms exhibit high-angled inclined surfaces (~30°), or avalanche beds, dominated by pebbles (<-6ϕ diameter; Fig. 4.16). They were only observed in the Marlbank esker. Morphologically these macroforms occur at zones of slight expansion along an otherwise relatively continuous, narrow esker ridge.

At pit M6* (~6 m vertical exposure; Fig. 4.2), the angle of inclination of the beds decreases upward (32° to 14° dip towards ~280° orientation) and reactivation surfaces are observed. Fabrics from different locations within the structure exhibited both weak a(t) and a(p) imbrication, downflow and oblique to the esker ridge crest (Table 4.7). Facies within this structure include polymodal gravelly sand (Fig. 4.17), openwork cobbles and openwork pebbles. Immediately lateral to the gravel avalanche beds and at a lower elevation, the sedimentary sequence (~2 m thickness) is composed of fining-upward sets (0.25 to 0.30 m thick) of massive, cross-laminated, parallel-laminated and penecontemporaneously-deformed coarse or medium sand to silt or clay.

At pit M42 (~8 m vertical exposure; Fig. 4.2), steeply inclined avalanche beds (~30°) are observed directly on bedrock (Fig. 4.16*a*). Each bed is 0.5 to 1.5 m thick and composed of graded

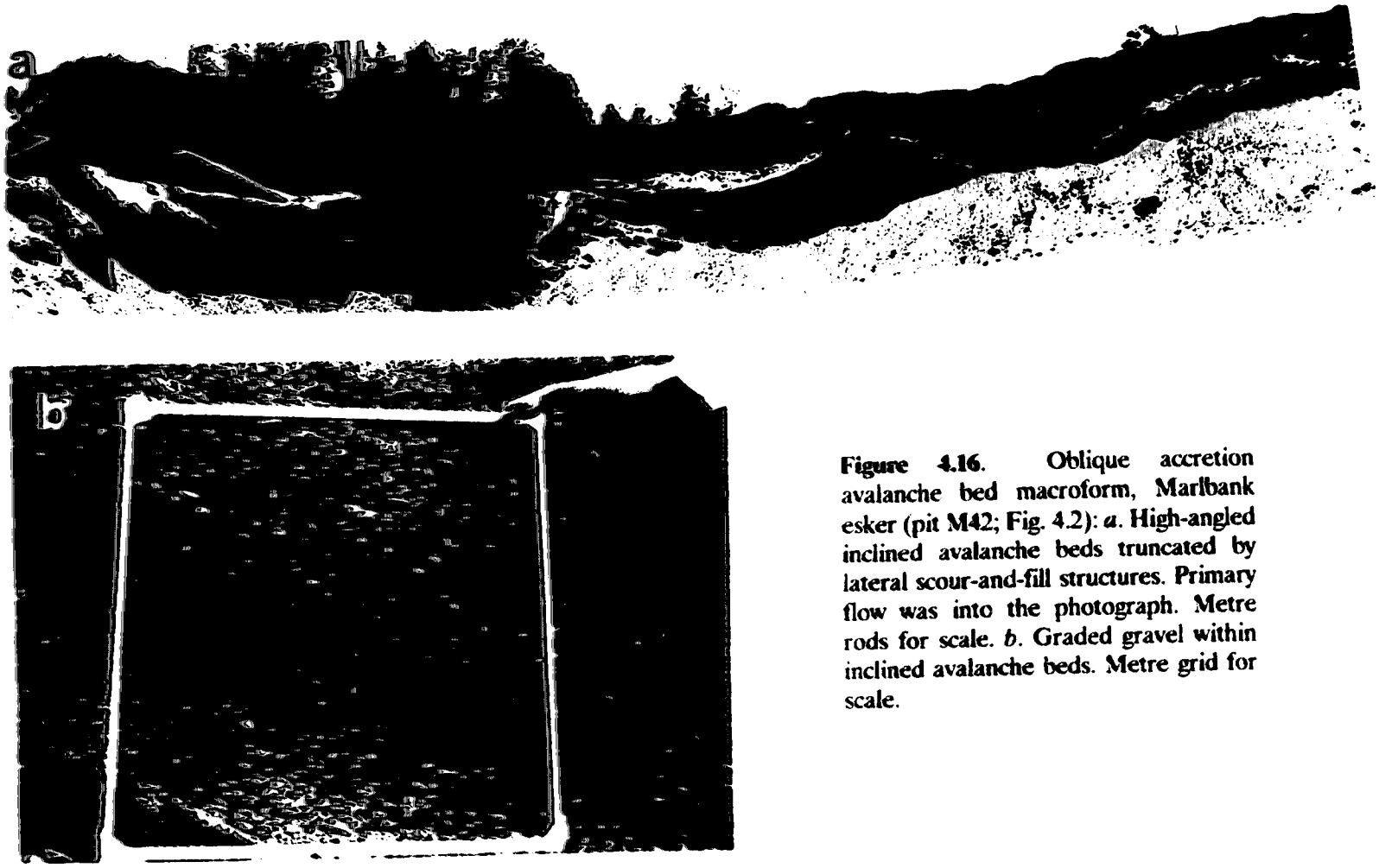

Figure 4.16. Oblique accretion avalanche bed macroform, Marlbank esker (pit M42; Fig. 4.2): *a*. High-angled inclined avalanche beds truncated by lateral scour-and-fill structures. Primary flow was into the photograph. Metre rods for scale. *b*. Graded gravel within inclined avalanche beds. Metre grid for scale.

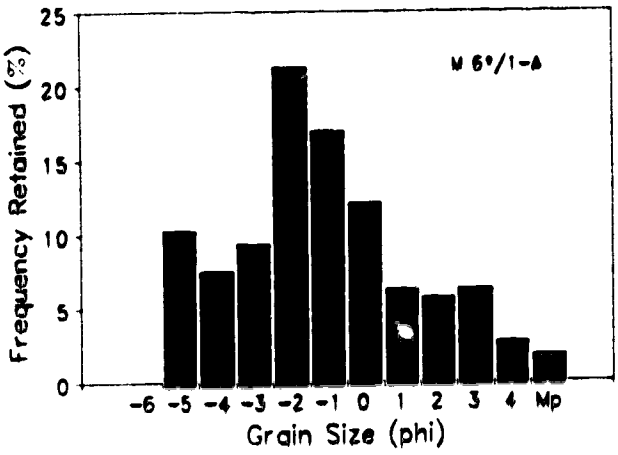

Figure 4.17. Grain-size histogram for polymodal gravelly sand within an oblique accretion avalanche bed macroform, Marlbank esker (pit M6*; Fig. 4.2), unit M6*/1−A. Raw data in Appendix 6.

pebbles and granules (Fig. 4.16*b*) with a maximum grain size of -5.6ϕ diameter. The grading in each bed is relatively uniform, making differentiation of the top and bottom difficult (Fig. 4.16*b*). Three gravel structures are observed within most avalanche beds: polymodal, matrix-rich pebbly sand; polymodal, framework-supported pebbly sand; and openwork pebbles (Fig. 4.16*b*). If this sequence is correctly ordered, the proportion of matrix decreases up-sequence in each avalanche bed. The ab-planes of the larger clasts tend to parallel the avalanche beds. Scour-and-fill structures truncate these beds on the lateral flank of the ridge (Fig. 4.16*a*). Fills have a maximum grain size of small boulders (<-8.2ϕ diameter).

Although structures similar to OAAB macroforms have been interpreted as esker deltas (cf. Banerjee and McDonald 1975; Thomas 1984), some of their characteristics distinguish them from previously described esker deltas. First, no obvious topset/foreset/bottomset relationships (cf. Clemmensen and Houmark-Nielsen 1981) are observed, and fines lateral to the avalanche beds at pit M6* (Fig. 4.2) may be later glaciolacustrine deposits associated with Glacial Lake Iroquois (cf. Mirynech 1962). The avalanche beds at pit M42 (Figs. 4.2 and 4.16) lie directly on bedrock; no bottomsets exist. Second, OAAB macroforms do not punctuate segments of the Marlbank esker, but rather occur at zones of morphologic expansion within a continuous ridge. Third, lateral scour-and-fill structures truncate the earlier avalanche beds and run parallel to the esker axis (Fig. 4.16*a*).

Flow separation and expansion of a secondary current vortex, from the main conduit into a lateral cavity, is inferred for the formation of OAAB macroforms. Avalanche beds are interpreted as

prograding avalanche fronts into a subglacial cavity connected to the main conduit. Similar large avalanche beds have been reported within flood-related expansion bars (Baker 1973). Sliding and rolling of clasts down the avalanche surfaces may have contributed to weak a(t) and a(p) clast orientations parallel to the inclined beds observed at pit M6* (Fig. 4.2; cf. Johansson 1976). Fluctuation of discharge over time may have accounted for the pseudo-inverse grading of avalanche beds at pit M42 (Figs. 4.2 and 4.16). Alternatively, the grading may be attributed to the delivery of longitudinally sorted sediment to the brink of the macroform as described previously for gravel cross beds (Shaw and Gorrell 1991).

Lack of bottomset beds at pit M42 (Figs. 4.2 and 4.16) is interpreted to be the result of a relatively rapid rate of cavity opening or exposure, and rapid sedimentation and progradation in a subglacial environment. Fine sediment would have been carried off downflow within a continuous conduit. The lateral scours may have been eroded during higher flow velocities caused either by a decrease in conduit cross-sectional area during sedimentation, or by a reduction in the sediment load carried by the flow. The larger clast size in scour fills may be attributed to a higher flow velocity during a later event, or to a change in the clast size available to the flow.

Reduction in the angle of inclination of foreset beds towards the ridge crest at pit M6* (Fig. 4.2), suggests aggradation and indicates that there may have been a process link between pseudoanticlinal and OAAB macroforms; that is, both may have required the operation of secondary vortices for their formation.

Vertically alternating sand and gravel units

A secondary signal of the hydrodynamic conditions within a subglacial conduit may be inferred from vertically alternating sand and gravel units (Figs. 4.8, 4.9, 4.12*a* and 4.18) within the macroforms. Gravel units may be members of any of the facies previously discussed. Although sand units are predominantly cross laminated, they also may be plane bedded, cross bedded, parallel laminated/draped, or massive. The contacts between gravel and sand units are often very sharp (Fig. 4.18). Occasionally, truncation of a sand unit (Fig. 4.12*a*) highlights the probability of amalgamated gravel units (events) which may not be obvious from vertical sections of heterogeneous, unstratified gravel, or massive, imbricate, clast-supported gravel. Between one and seven couplets are observed at most exposures in the esker ridges.

Couplets similar to those described above are common to many eskers (e.g., Jewtuchowicz 1965; Lobanov 1967; Allen 1971; Shaw 1972; Banerjee and McDonald 1975; Ringrose 1982). They have been attributed to changes in depositional conditions on seasonal or annual time scales, suggesting a supraglacial to subglacial connection in the glacial hydrologic system (cf. Banerjee and McDonald 1975; Ringrose 1982). However, couplets may equally represent episodic flood deposition caused by lake (cf. Whalley 1971; Nye 1976; Haeberli 1983) or subglacial cavity drainage (cf. Iken *et al.* 1983; Kamb *et al.*

Figure 4.18. Vertically alternating sand and gravel units with sharp contacts (couplets), Norwood esker (pit N36; Fig. 4.2). Metre rod for scale.

1985; Walder 1986; Kamb 1987). What is certain, is that the sequences may involve: (*i*) a temporal or spatial change in sediment supply (cf. Shaw 1972); (*ii*) a spatial change in flow conditions, that is, the headward growth of the main conduits and capture of smaller conduits and cavities (cf. Willis 1990); or (*iii*) a temporal change in flow competence. The latter may be directly related to seasonal melting, producing a direct connection between the supraglacial and subglacial meltwater subsystems or, indirectly related by the influence of seasonal meltwater on subglacial water pressure, effecting periodic capture of subglacial, water-filled cavities. In this sense, possibilities (*ii*) and (*iii*) may be related. Alternatively, temporal change may be episodic (jökulhlaups), related to the drainage of large supraglacial lakes or subglacial water bodies.

While the migration of large bedforms and progradation of macroforms within a conduit may explain some vertically alternating sand and gravel sequences (e.g., related to flow separation zones in the lee of these forms), the pervasive occurrence of these couplets argues for a flow-dynamic control. Peaked or flood-type (jökulhlaup) hydrographs (Fig. 4.19*a*) may be invoked to explain both rhythmicity and the sharp contacts between sand and gravel units. Most deposition occurs on the falling limb of a flood hydrograph. Whalley (1971) reported a 93% reduction in meltwater discharge (Q_w) over a 10 minute period associated with a jökulhlaup shutoff. Assuming a conduit of uniform area, such a reduction in Q_w would effect a concomitant reduction in mean flow velocity ($\bar{U}$), and consequently shear velocity (U_*) (Fig. 4.19*b*). A 93% reduction in $\bar{U}$ from 11.25 ms^{-1} to 0.75 ms^{-1} would result in a reduction in U_* from 75 cms^{-1} to 5 cms^{-1} (Fig. 4.19*b*). At $U_* \sim 75$ cms^{-1}, all clasts smaller than medium pebbles (<30 mm diameter) would have been in suspension, large pebbles to small boulders (30 to 600 mm diameter) would have been transported as bedload, and medium to large boulders (>600 mm diameter) would have been stationary (Fig. 4.19*b*). Within minutes U_* may have fallen to ~5 cms^{-1}, such that material finer than medium sand (<0.4 mm diameter) was in suspension, medium to very coarse sand (0.4 to 2 mm diameter) was transported as bedload, and all gravel clasts (>2 mm diameter) were stationary (Fig. 4.19*b*). Therefore, on the falling limb of a flood discharge within a subglacial conduit, a rapid reduction in U_* may have been responsible for the sharp contact between the sand and gravel units. Consequently, a sand and gravel couplet may be interpreted as the product of a single flood event.

Caution should be exercised when interpreting all apparent couplets as the product of a seasonally-induced flood (cf. Banerjee and McDonald 1975) as gravel units may have been amalgamated. In addition, it is possible that either: more than one flood event may have occurred in any one season, if the occurrence was controlled by the capture of conduits, water-filled cavities or large subglacial water bodies due to changes in subglacial water pressure; or, no flood of appreciable magnitude may have occurred in a particular season. This emphasises the notion that esker ridge sediments are a very coarse

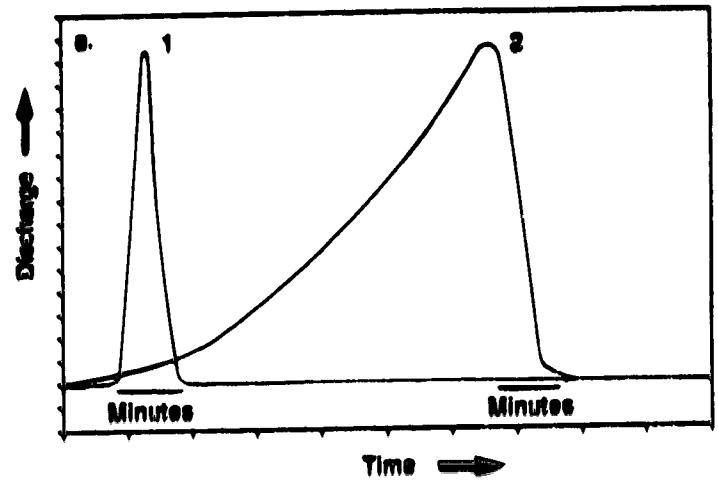

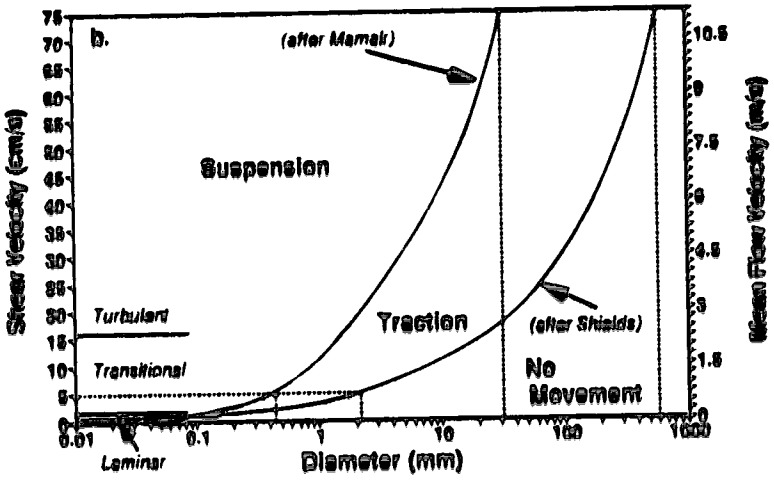

Figure 4.19. *a*. Schematic jökulhlaup hydrographs. 1. Sudden meltwater release associated with the drainage of a large water body. 2. Progressive enlargement of the catchment area of a main conduit associated with capture of minor conduits and cavities. Both show a rapid reduction in meltwater discharge on the falling limb (modified from Haeberli 1983). *b*. Critical shear velocities (U_*) for traction and suspension transport. Data for critical suspension criterion ($U_*/w > 1.0$, where w = settling velocity) and flow regime from Mamak (1964, cited in Graf and Acaroglu 1966). Data for critical traction criterion (Shields' criterion) from Blatt *et al.* (1980) and Walker (1975), and for diameter (d) > 100 mm U_* calculated from $U = 0.46d^{0.50}$ (Williams 1983) and $15U_* \approx \bar{U}$ (Walker 1975), assuming $U \approx \bar{U}$.

record of sediment and meltwater discharge fluctuations within a conduit, and possibly only record the most powerful events within that conduit (Gorrell and Shaw 1991).

Discussion: esker ridge macroforms

Subglacial conduits are unlikely to have uniform geometry; they may bend (cf. Hagen *et al.* 1983) and/or pinch and swell, laterally and vertically (cf. Walder and Hallet 1979; Hallet and Anderson 1980). Studies on slow-flowing contemporary glaciers have suggested that with an increase in meltwater discharge, the drainage system evolves from a linked-cavity network into an integrated conduit system (cf. Willis *et al.* 1990). Some of the bulges in pre-esker conduits may have been cavity remnants (Hooke 1989, fig. 4). Alternatively, with increased meltwater discharge, conduits may have enlarged by melting or localized floatation (Gorrell and Shaw 1991) to capture adjacent water-filled cavities with which they coexisted (Iken and Bindshadler 1986; Walder 1986; Fowler 1987). In this manner, the location and spacing of expansion zones may have changed over time within conduits.

Esker macroforms should not be viewed as normal fluvial bedforms (e.g., large dunes or mesoforms, cf. Hoey 1992) migrating down a conduit of uniform geometry and responding solely to flow power (variation in the fluid-dynamic regime of the boundary layer, Hoey 1992). Rather, they are envisaged as being initially spatially controlled by the preexisting geometry of the conduit. Deposition and augmentation of composite and OAAB macroforms are inferred to have occurred in zones of conduit expansion and concomitant flow expansion; the style of the macroform having been controlled by local conduit geometry downflow from the point of expansion. Macroforms are believed to scale to flow width (cf. Hoey 1992). Later, as the macroform developed, feedback between macroform and conduit geometries may have ensued. On occasion, progradation of macroforms may have temporarily blocked constricted portions of conduits and acted as possible internal (autogenic) controls on sediment availability and flow resistance (cf. Ashmore 1991). More constricted zones of the conduits would have experienced relatively higher flow velocities than expanded zones. Pseudoanticlinal macroforms are inferred to be products of relatively constricted, geometrically uniform conduit segments. Very constricted conduit segments may have experienced erosion, or simply transportation, along their length during high discharges. Some minimal deposition may have occurred along these segments during lower meltwater discharges. Consequently, conditions along a continuous conduit are inferred to have changed downflow from erosional to transportational to depositional, controlled by conduit geometry.

Although exposure was not extensive enough to reveal the spatial dimensions of the macroforms, vertical exposures suggest they attain heights of at least 10 m; crest line undulations (Fig. 4.3) are on the order of 20 m maximum relief. Longitudinally, the macroforms are inferred to conform to the wavelength of crest line undulations (1 to 5 km; Fig. 4.3). However, the construction of the long profiles (Fig. 4.3) was constrained by the contour interval of the topographic maps (10 m on 1:50 000 NTS sheets), so it is possible that shorter wavelengths may be differentiated on larger-scale maps.

The presence of macroforms within eskers may not be restricted to the examples from south-central Ontario reported here. Hebrand and Åmark (1989, p. 77) inferred for some Swedish eskers that "deposition took place only in restricted parts of the conduit at one and the same time". They proposed a large and orderly reduction in meltwater competence at the ice margin, with this sequence repeated time-transgressively in an up-glacier direction as the ice margin retreated. Spatial constraints on erosion, transportation and deposition within a continuous conduit, imposed by conduit geometry, may provide an alternative explanation. Hebrand and Åmark (1989, p. 73-74, fig. 9D) also noted undisturbed, undulating bedding in longitudinal section, which can be related to esker morphology. In addition, Saunderson (1977) alluded to the presence of macroforms in the Guelph esker, Ontario, when he speculated that cross beds may have been deposited in the lee of a core of sliding-bed deposits. Bedforms related to flow expansion in a conduit have been investigated experimentally by Johansson (1976). He describes simple delta-like forms with backsets, topsets, foresets and bottomsets. Large backset beds were not observed in the esker ridges of this study, but they have been observed in the Peterborough esker (Banerjee and McDonald 1975) and in expansion zones in the Harricana glaciofluvial complex, Québec (Brennand 1991*a*, 1991*b*).

Sedimentology of major and minor fans, beads with minor ridges, and laterally-fining deposits

Observations

In major and minor fans, massive, plane-bedded, cross-bedded, cross-laminated (ripple-drift cross-lamination types A, B, C and S, Jopling and Walker 1968) and draped sand, silt and clay are observed in proximal-to-distal and upward-fining sequences. Cross-laminated and massive sand and silt dominate these sequences. Fining-upward rhythms decrease in thickness upward from metres to millimetres. Coarse gravels are limited to basal and proximal locations, while clay is, in general, limited to upper rhythmites, some of which may be related to later sedimentation in Glacial Lake Iroquois (cf. Mirynech 1962). However, thin clay drapes (1 to 2 mm thick) are also observed in some fining-upward rhythms within fans. Towards the top of some minor fan deposits, fine sand and silt units exhibit ball-and-pillow structures (Fig. 4.20*a*). Microfaults, convolute laminations, flame structures, drag structures, and rip-ups are common throughout the fan deposits. Sedimentary architecture is tabular, gently inclined (Fig. 4.20*b*) or undulatory.

Similar sequences to those described above are observed in beads and laterally-fining deposits. Beads tend to exhibit more rapid downflow fining, and normal and thrust faulting (pit N35; Fig. 4.2; cf. Banerjee and McDonald 1975; Gorrell and Shaw 1991). Minor ridges, distributary from the main esker ridge to the beads, are composed of sand and gravel couplets which have been faulted and overfolded (pit N35; Fig. 4.2). Laterally-fining deposits display more pervasive normal faulting than minor fans. All of these observations have been made by previous authors (e.g., Banerjee and McDonald 1975;

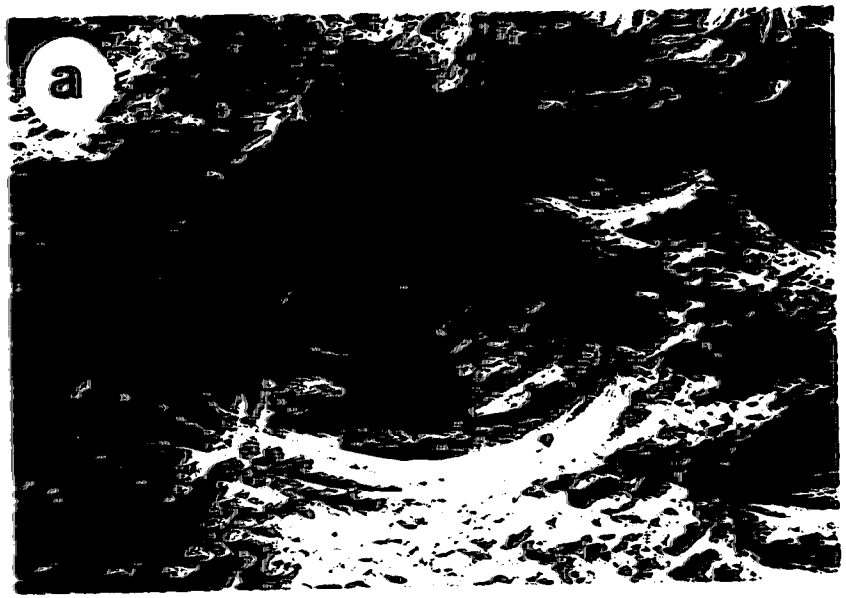

Figure 4.20. *a*. Ball-and-pillow structures in the upper part of a minor fan along the Tweed esker (pit T17; Fig. 4.2). Scraper is 20 cm long. *b*. Tabular, gently inclined architecture of a minor fan along the Tweed esker (pit T17; Fig. 4.2). Arrow marks the location of Figure 4.20*a*. Shovel handle is ~ 1 m long.

Diemer 1988; Henderson 1988; Gorrell and Shaw 1991). Consequently, further description is limited to a new observation which has significance for the interpretation of these deposits as depositional components of continuous subglacial conduits.

Hummocky or in-phase wave structures

Hummocky or in-phase wave structures are observed: (1) at zones of morphologic expansion along the main esker ridges; (2) near the base of some minor fans and laterally-fining deposits; and (3) toward the downflow ends of the main esker ridges in major fans (Fig. 4.21). These structures are composed of diffusely-graded sand or granules (Fig. 4.21*a*) or imbricate, polymodal gravel (Fig. 4.21*b*), exhibit undulatory surfaces between beds (Fig. 4.21), and are often draped by fine sand and silt (Fig. 4.21). In some cases, a single in-phase wave structure is observed; in others, in-phase wave structures are stacked and offset, effecting an overall repetitive lenticular geometry in vertical section (Fig. 4.21). These structures have similar morphologies in sections perpendicular to one another, consequently, they are inferred to be three-dimensional forms.

Sandy in-phase wave structures are 5 to 20 m in wavelength and 0.5 to 2.5 m in height (Fig. 4.21*a*). Internally, sediments are well sorted, and may be massive or diffusely graded. Diffusely-graded sand exhibits diffuse or wispy laminae (Fig. 4.21*a*). In places these laminae are concordant with the upper surface, in others they are truncated by that surface. That is, in-phase wave surfaces may be erosional or depositional. Pebbles and cobbles are dispersed, or 'suspended', within the diffusely-graded deposit (Fig. 4.21*a*), often with their a-axes parallel to flow (Table 4.7); vector strength is weak (Table 4.7). Clasts are commonly concentrated along surfaces internal to the hummock (Fig.21*a*). Occasionally, scours (up to 0.5 m in width) truncate an in-phase wave surface and are filled with bimodal cobbles or pebbles and sand (Fig. 4.21*a*). Fine sand and silt rafts, or soft-sediment clasts, are also observed within the hummocks. In-phase wave structures are separated by fine sand and silt drapes (0.1 to 0.6 m thick; Fig. 4.21*a*), which may be cross laminated, parallel laminated, or massive, and exhibit microfaulting, flames and other penecontemporaneous deformation structures.

Gravel in-phase wave structures are up to 12 m in wavelength and 1 m in height (Fig. 4.21*b*). Truncation of these structures has produced an elongate, low-angled, lenticular architecture in vertical section (Fig. 4.21*b*). Gravel in-phase wave structures are bounded above and below by sandy in-phase wave structures at pit N36 (Fig. 4.2), and are composed of imbricate, polymodal pebble and cobble gravel (Fig. 4.12*b*). In places low-angled beds are observed to dip upflow or downflow within the hummocks. Some hummocks exhibit inverse-to-normal or normal grading, others have clast concentrations along bedding surfaces within the hummock. Occasionally, larger clasts form weakly imbricate, a(t) clusters (Table 4.7). Soft sediment clasts and discrete openwork pebble pods (possibly representing frozen rafts of openwork pebbles) are observed within the hummocks. Again, gravel in-

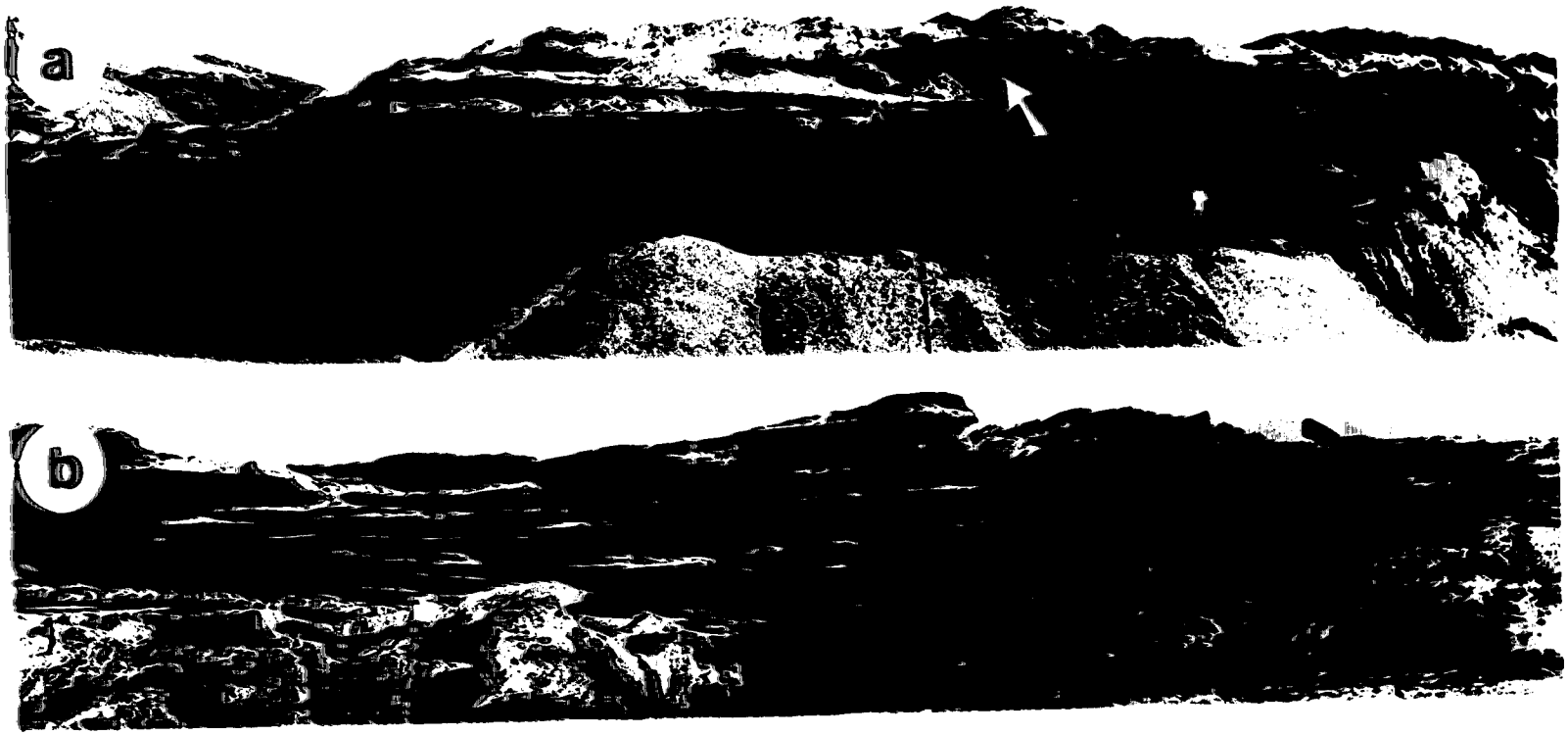

Figure 4.21. In-phase wave structures within a major fan or fan complex at pit N36 (Fig. 4.2) *a*. Diffusely-graded sandy in-phase wave structures draped by fine sand and silt, with a scour-and-fill structure (arrow) and dispersed clasts within hummocks. *b*. Gravel in-phase wave structures draped by fine sand and silt. Note water-escape/load structure (arrow), and drag and load structures at base of gravel hummocks. Metre rods for scale.

phase wave structures are draped by coarse to fine sand and silt in fining-upward rhythms (Fig. 4.21*b*), with cross lamination, parallel lamination, massive beds and penecontemporaneous deformation structures. In one case, clay (1 mm thick) drapes a fining-upward rhythm. Draped rhythms are often truncated and exhibit load structures associated with the formation of subsequent gravel in-phase wave structures (Fig. 4.21*b*). In another case, a water-escape structure in gravel (Fig. 4.21*b*) disrupts the overlying sandy drape; clasts within it are aligned parallel to the direction of water escape, with mean dips equivalent to the angle of drape disruption (Table 4.7).

The three-dimensional, lenticular geometry of these structures resembles that of smaller in-phase wave structures (often termed antidunes) reported for open channels (e.g., Middleton 1965; Shaw and Kellerhals 1977; Rust and Gibling 1990), coasts (e.g., Allen 1984*b*; Barwis and Hayes 1985) and turbidity currents (e.g., Skipper 1971; Hand 1974; Prave and Duke 1990), and larger in-phase wave structures reported for volcaniclastic sediments (e.g., Pierson and Scott 1985; Boudon and Lajoie 1989; Charland and Lajoie 1989; Fisher 1990).

With increasing flow velocity, bedforms in open-conduit flow develop from ripples to dunes, to plane beds, to in-phase waves (cf. Ashley 1990; Cheel 1990). It has been suggested that in-phase waves would not form under closed-conduit conditions, since surface waves are suppressed by the conduit roof (e.g., Banerjee and Mcdonald 1975; Saunderson 1977, 1982; Ringrose 1982). However, an interfacial in-phase wave may form at any density interface (cf. Hand 1974). In addition, in closed-conduit flume experiments, McDonald and Vincent (1972) reported undulations on the bed similar to the hummocky surfaces described here. They hesitantly suggested that these may have been related to standing waves.

Necessary conditions for the formation of in-phase wave structures may occur in subglacial environments where meltwater with high sediment concentrations flows from a constricted to an expanded reach within a subglacial conduit (including connected lateral cavities) or into standing water in an ice-marginal or grounding-line position (Gorrell and Shaw 1991). During flow expansion, supercritical denser inflow ($Fr_d > 1$, where Fr_d is the densimetric Froude number) may become subcritical ($Fr_d < 1$). Near the transition, in-phase waves at the density interface and on the bed are probable. These conditions may have produced in-phase wave structures (cf. Cheel 1990) in the south-central Ontario eskers.

Hummocky surfaces may be concordant with internal laminae (drape laminae, Cheel 1990), or truncate backset or foreset cross-laminae. In these cases, the complete lenticular deposit may be explained as the product of upper-flow-regime, in-phase wave deposition (and migration). For such structures to be preserved in the sediment record would have required net sediment deposition (cf. Skipper 1971). Diffusely-graded sediments, penecontemporaneous deformation structures (cf. Aario 1971*b*), dewatering structures (cf. Lowe 1975) and preservation of soft-sediment rafts, within in-phase

wave structures, attest to high sedimentation rates. In other cases, massive sand or gravel with little internal lamination or bedding is topped by a hummocky surface. While it may be possible that sedimentation rates were so rapid during in-phase wave formation that internal laminae or beds were not preserved, it is also possible that massive sediments were first deposited, and later eroded by in-phase waves.

The sediments within in-phase wave structures are inferred to have been deposited from hyperconcentrated flood flows (e.g., McCutcheon and Bradley 1984; Smith 1986; Costa 1988). Such flows are non-Newtonian and have sediment concentrations between 40 and 80% by weight (20 and 47% by volume) (cf. Smith 1986; Costa 1988). In-phase wave structures have previously been reported in hyperconcentrated flood-flow deposits (e.g., Pierson and Scott 1985). Weak stratification and imbrication, framework-supported, poorly-sorted gravel, and normal grading are characteristic of hyperconcentrated flood-flow deposits (cf. Smith 1986). Similarly, the presence of both weak a(p) and a(t) imbrication has been reported and attributed to grain-by-grain deposition from traction and suspension (cf. Smith 1986). The anomalous observation of a(p) cobbles and a(t) pebbles within one gravel hummock (unit N36/17-8, Table 4.7) suggests that flow may have been unsteady during the deposition of this facies. Weak inverse grading towards the base of some hummocks may be explained by the sediment support mechanisms within hyperconcentrated flood flows; primary sediment support is from fluid turbulence, with secondary support from dispersive pressure, buoyancy and hindered settling (cf. Smith 1986).

Sand and silt drapes over single in-phase wave trains or vertically stacked in-phase wave structures in sand or gravel are inferred to be the result of waning flow events, some of which may have been associated with the sand and gravel couplets, or flood deposits, in the main esker ridges. In general, conduits enlarge by melting to accommodate increased meltwater discharge (Q_w) (cf. Röthlisberger 1972; Shreve 1972). However, during a flood event, conduits may have been unable to accommodate the rapidly increasing Q_w. High water pressures, particularly at bends, would have resulted, locally exceeding the high ice overburden pressures along the margins of subglacial conduits and connecting the main conduits to adjacent water-filled cavities, with or without minor connecting conduits. As meltwater with a high sediment concentration expanded into a lateral cavity, it may have also undergone transition from supercritical to subcritical flow. This is inferred to have created the hydraulic jump ($Fr_d \approx 1$) necessary to form in-phase wave trains. Gorrell and Shaw (1991) have inferred similar denser wall jets with hydraulic jumps to explain the morphology and sedimentary characteristics of subaqueous (subglacial) fan and bead deposits. Indeed, they showed diffusely-graded sand with in-phase wave surfaces filling a scour (Gorrell and Shaw 1991, fig. 17.A.). Jensen (1988, fig. 3a) also showed in-phase wave structures within scours in a Danish esker.

Approximations for flow velocity (U) and depth (h) are made from measurements of the

wavelength (L) of in-phase waves and estimates of the density of hyperconcentrated inflow (ρ_1) and ambient fluid (ρ_2), using equations from Allen (1984*b*, p. 407, equations 10.29 and 10.30) (Table 4.8). This method provides similar results to the equations of Hand *et al.* (1972) and Hand (1974). In-phase wave surfaces have wavelengths (L) of 5 to 20 m. Costa (1988) suggested a bulk density (ρ_1) range of 1330 to 1800 kgm^{-3} for hyperconcentrated flood flows. The density of the ambient fluid (ρ_2) is assumed to be ~1000 kgm^{-3}. Flow velocity estimates (U, Table 4.8) fall within the range (0.6 to 4.4 ms^{-1}; Williams 1983) estimated from the maximum clast size (-6.5ϕ diameter) in gravel in-phase wave structures.

Table 4.8. Estimates of flow depth and velocity for in-phase wave structures.

	ρ_1 = 1330 kgm^{-3}		ρ_1 = 1800 kgm^{-3}	
L (m)	h (m)	U (ms^{-1})	h (m)	U (ms^{-1})
20	1.82	2.10	2.04	2.08
5	0.45	1.05	0.51	1.49

Interpretations/discussion

Major fan complexes are inferred to have been deposited at a subglacial grounding line (cf. Gorrell and Shaw 1991), whereas a subglacial conduit/cavity environment is inferred for minor fans, beads and laterally-fining deposits; all lack the pervasive deformation characteristic of sediments which have been let down from supraglacial or englacial positions (cf. Charlesworth 1957). Where fans and beads punctuate esker segments, they have been traditionally interpreted as products of ice-marginal, time-transgressive sedimentation (cf. Banerjee and McDonald 1975). In south-central Ontario, the main esker ridges were deposited in continuous, closed conduits, and minor fans and beads do not punctuate depositional esker segments. Downstream continuation of distributary ridges and beads as contributory ridges to the main esker, and smooth continuation of minor fans upflow and downflow with the esker ridges, argue for synchronous subglacial deposition of the main esker ridges, beads and fans. Removal of lateral ice support after deposition in a subglacial conduit may be invoked to explain faulting within beads and laterally-fining deposits (cf. McDonald and Shilts 1975).

Rapid fining of sediment in the minor fans and beads is attributed to a reduction in flow competence during flow expansion, or differential transport of coarse and fine sediment caused by rapid aggradation (cf. Gorrell and Shaw 1991). It is suggested that as meltwater discharge declined on the falling limb of a flood hydrograph, the normal high-pressure zones at the conduit margins were reestablished. These zones would have acted as the controlling valves (cf. Willis *et al.* 1990) which sealed water-filled cavities and minor conduits (Gorrell and Shaw 1991). Overfolding and faulting in distributary ridges at pit N35 (Fig. 4.2) may be explained by deformation as ice locally reattached to the

bed, causing cavities and minor conduits to be pinched off from the main esker ridge at the cessation of a high Q_w event. Cessation of flow in cavities would have produced standing-water bodies which may have resulted in deposition of thin clay drapes in minor fans. The fact that cavities and minor conduits remained water-filled, provided a zone of weakness such that the same flow path was reutilized during succeeding high Q_w events (Gorrell and Shaw 1991). This repetition is inferred to have produced repeated fining-upward sequences in beads and minor fans. A similar Q_w controlled grounding-line environment may account for the presence of, and rhythmicity within, sand and silt drapes over sand and gravel in-phase wave structures in major downflow fans (pit N36; Figs. 4.2 and 4.21).

Whereas the valve or conduit-avulsion mechanism (primarily changes in meltwater discharge over time) may account for most of the pulsations observed in the sedimentary record of fans and beads (Gorrell and Shaw 1991), some may be attributed to a second mechanism. It has been suggested that within-conduit macroforms may have temporarily stored sediment, providing a spatial control on sediment availability. If macroforms indeed acted as temporary sediment storage features, some of the rhythmic sedimentary sequences in the minor, lateral and major, downflow fans, may be related to internally generated pulses (autopulses, Ashmore 1991) in the bedload transportation rate (e.g., Ashmore 1988, 1991; Gomez *et al.* 1989; Hoey and Sutherland 1991; Young and Davies 1991; Hoey 1992).

Whereas laterally-fining deposits may simply represent deposition during the waning stages of conduit operation, in reality, similar sedimentary sequences in minor fans and laterally-fining deposits make distinction between them difficult. In this paper, the distinction has been made primarily on morphologic grounds. Minor fans and beads are both intimately associated with the main ridge. It is likely that they represent a morphologic and sedimentologic continuum related to the tunnel avulsion mechanism proposed.

Sedimentology of anabranched reaches of the main esker ridges and hummocky, extended zones

Observations

Few exposures are available in these morphologic elements. A section exposed in the Marlbank esker (pit M10, Fig. 4.2) is the only example of sediments within an anabranched reach in this study. Sand and gravel couplets are intensely faulted (normal and reverse). Pebbles and cobbles exhibit heterogeneous, unstratified, massive and openwork structures. Sand units are primarily massive or diffusely graded and range texturally from coarse to fine sand.

Observations from pits N53 and N52 (Fig. 4.2) provide some insight into the characteristics and context of sediments within hummocky, extended zones. Faulted and folded, sand and gravel couplets occur adjacent to the esker ridge (pit N52, Fig. 4.2). Facies include heterogeneous, unstratified and cross-bedded gravel, and cross-laminated and massive sand and silt. Further from the ridge, sand and gravel couplets are still observed, but sand units are thicker (pit N53, Fig. 4.2).

Interpretations

Multiple-crested eskers and esker nets have long been reported in the literature (e.g., Crosby 1902; Price 1966, 1969; Shaw *et al.* 1989). Three main theories have been advanced for their formation. First, it has been suggested that such eskers are the product of glaciofluvial deposition in supraglacial channels (e.g., Crosby 1902; Price 1966). It has been proposed that topographic inversion caused by differential ice melting resulted in sediments capping an ice ridge. With time these deposits are inferred to have slid down the ice ridge flanks to form double-crested eskers. Repetition of this process is believed to result in multiple-crested eskers (e.g., Crosby 1902; Price 1966). This suggestion is difficult to rationalize for the eskers of south-central Ontario, as most other observations favour sedimentation in continuous subglacial closed conduits. Second, development of kettle-holes, due to ice-block disintegration within a ridge, may have also resulted in a multiple-crested appearance (e.g., Howarth 1971). The intricate pattern of anabranched reaches (Fig. 4.2) argues against such a stochastic control in this study. Third, under steady-state, closed-conduit conditions and along gently ascending esker paths, Shreve (1985*a*) suggested that a relatively low rate of conduit roof melting during ridge aggradation may have caused flow to be concentrated at low points lateral to the main ridge. Pseudo-separation of the flow into two parallel channels, subsequent deposition in these channels and repetition of this process, may have produced multiple-crested eskers. Hooke (1984) suggested a similar mechanism for subglacial open-channel flow. In Pleistocene eskers, the flow separation mechanism has the advantage of exploiting subglacial sediment sources, rather than requiring large volumes of supraglacial or englacial sediment. Whereas this process may be appropriate for anabranched reaches in this study where subglacial, closed-conduit, ascending conditions have been inferred, the mechanism falls short of explaining the complex anabranched pattern.

An alternate mechanism, consistent with subglacial, continuous, closed-conduit conditions inferred for the main esker ridges, is presented here. Hummocky, extended deposits and anabranched reaches are inferred to be further responses to rapid changes in meltwater discharge (Q_w) and water pressure within a conduit. Shaw *et al.* (1989) suggested that anabranched eskers may indicate subglacial floods. If melt rates within a conduit were inadequate to accommodate a rapid increase in Q_w, high-pressure zones at the conduit margins may have been locally breached and a broad zone of minor conduits established. Close proximity of these conduits may have aided further breaches between them, producing complex interconnections. Multiple conduits would have effectively increased the cross-sectional area and reduced the flow velocity. A concomitant decrease in flow competence would have resulted in rapid deposition. Some minor conduits may have become choked with sediment, while others may have opened to accommodate diverted meltwater. With a decrease in Q_w during the waning stages of a high-discharge event, the normal pressure field at the margins of the main conduit would have

reestablished and this conduit would have regained dominance (cf. Röthlisberger 1972).

In some cases, the increased cross-sectional area created by a multiple-conduit system may have been inadequate. With a very rapid increase in Q_w, larger breaches in the marginal high-pressure seal to the main conduit may have ensued. Here, localized floatation or hydraulic lifting over a broad zone either side of the main conduit may have occurred. This plane of separation may have been at a frozen bed. In addition, the associated high Q_w and conduit rupture may have contributed ice blocks to the flow. Meltwater flow within this broader zone may have approximated a narrow sheet. Flow expansion would have resulted in loss of competence and enhanced sedimentation. As Q_w declined, the main conduit would have been rapidly reestablished (cf. Nye 1976). Alternatively, a transitional multiple, perhaps anabranched, conduit system may have formed due to thermodynamic feedbacks within a nonuniform sheet (Walder 1982).

In both cases, ice is inferred to have settled back down onto the bed adjacent to the main conduit and may have experienced minor forward motion. This recoupling may account for the shearing and folding deformation observed within the deposits. Subsequent melting of buried ice blocks (or frozen ground) and removal of lateral ice support on ice-sheet disintegration explains the intense faulting and hummocky topography of the extended zones. The presence of sand and gravel couplets necessitate repetition of this process at the same location. The reasons for the location and repetition of channel avulsion responsible for the anabranched reaches of the main eskers and the extended, hummocky zones are enigmatic at present. While the mechanism described here is not directly equivalent to that proposed for anastomosed subaerial rivers (cf. Smith and Putnam 1980; Smith 1983), both invoke channel avulsion.

Discussion: implications for esker genesis and meltwater regime

Subglacial, closed-conduit flow and macroforms

By concentrating on the morphologic and sedimentologic characteristics of the main esker ridges, it has been possible to infer the mode of esker genesis. Synchronous erosion, transportation and deposition by pulsed meltwater discharges in up-sloping, subglacial, closed conduits has been inferred. The depositional products of these processes are the large bedforms, macroforms, and sand and gravel couplets. By extension, minor fans, beads with minor ridges, anabranched reaches of the main esker ridges, and hummocky, extended zones have been interpreted primarily as consequences of subglacial deposition in cavities or minor conduits connected to the main conduit, in response to elevated subglacial water pressures and flood discharges through the main conduit. Sediment supply for esker formation was primarily from squeezing in of adjacent sediment, either during low meltwater discharges in the winter (Shaw and Gorrell 1991), or during a high Q_w event with high melt rates and low local pressures.

It is, perhaps, interesting to speculate on the effects of the progradation of macroforms and the

migration of large bedforms to conduit margins which feed into standing-water bodies. It is likely that the arrival of macroforms and bedforms at the end of a conduit would have produced a high-magnitude, episodic sediment delivery to the margin. Flow expansion into a standing-water body would have resulted in a reduction in flow power and would have favoured the preservation of macroforms and bedforms at the margin. Jet inertia may have caused these forms to be transported a short distance away from the end of the conduit. Stacking of such macroforms and bedforms at a stable conduit margin may have contributed to grounding-line or ice-marginal subaqueous fan sequences. South-central Ontario eskers appear to feed into the Oak Ridges glaciofluvial complex (cf. Barnett *et al.* 1991). Earlier interpretations of sedimentary packages (Duckworth 1979) within the complex include reference to small deltas (~3 m in height); these look (Duckworth 1979, fig. 7) remarkably similar to large gravel bedforms. Interpretations presented here suggest that in cases where foresets are observed within, lateral to, or downflow from large subglacial eskers, former interpretations of these foresets as deltas (e.g., Shaw 1972) may need to be reconsidered.

Subglacial, closed-conduit conditions are primarily inferred here from continuous upslope paths and lack of postdepositional disturbance, particularly at the centre of the main esker ridges. No obvious sliding-bed facies was observed, despite the common use of the presence of this facies as the main criterion for inferring closed-conduit conditions (e.g., Saunderson 1977, 1982; Ringrose 1982; Lindström 1985; Henderson 1988). This apparent omission requires further comment.

The sliding-bed facies

The sliding-bed facies has been described as a poorly-sorted, massive, matrix-supported sand and gravel (Saunderson 1977, 1982; Ringrose 1982). It has been attributed to flows with shear stresses between those required for plane beds and heterogeneous suspensions in pipes; the result being an *en bloc* moving bed, during full-conduit flow (cf. Newitt *et al.* 1955; Saunderson 1977, 1982). Proposed conditions necessary for sliding include excess hydrostatic pressure from proximal to distal ends of the conduit, and seepage flow through the gravel due to surface waves being suppressed by the conduit roof (Saunderson 1977, 1982). The buoyant effect of sand on gravel and dispersive pressure in a heterogenous (poorly sorted) sediment are invoked as sediment support mechanisms (Saunderson 1977). The sliding-bed facies, then, has been associated with high-discharge events, probably of flood magnitude, in closed conduits (Saunderson 1977, 1982).

Unfortunately, similar massive, matrix-supported, poorly-sorted facies have been reported in open-channel deposits (cf. Ringrose 1982), in proximal outwash deposits (e.g., Boulton and Eyles 1979), and in hyperconcentrated flood-flow deposits (e.g., Lord and Kehew 1987) - a problem of equifinality. Saunderson (1977, 1982) suggested that the sliding-bed facies may replace in-phase wave structures in closed-conduit flows. Clearly, in-phase wave structures can occur where interfacial in-phase waves are

established in closed-conduit/cavity environments. Similar gravels to those described as sliding beds, and with in-phase wave surfaces, are described here and explained by deposition from hyperconcentrated dispersions, the surfaces resulting from interfacial in-phase waves. Further problems exist in the description of the sliding-bed facies as matrix-supported. First, by definition, this infers a bimodal grain size. In reality, photographs of this facies display polymodal sediments (Saunderson 1977, fig. 4; Saunderson 1982, fig. 6). This problem of semantics has had further implications, namely that bimodal, matrix-supported gravels have been, perhaps incorrectly, attributed to the sliding-bed mechanism (e.g., Lindström 1985). It is necessary to question how this facies becomes bimodal, when all sediment sizes were probably available in transport (cf. Saunderson 1977). As discussed previously, bimodality would appear to necessitate conditions of flow separation over bedforms or macroforms, and longitudinal sediment sorting during transport. Further, with dispersive pressure as the primary sediment support mechanism, inverse grading may be expected in a sliding-bed facies. Presumably, as sand shears past gravel clasts in a sliding bed (Saunderson 1977) a(p) clast orientations should result. This type of information has not been recorded for so-called sliding-bed deposits.

The heterogeneous, unstratified gravel facies (Fig. 4.10) present in the main esker ridges in south-central Ontario is a close visual equivalent to Saunderson's (1977, 1982) sliding-bed facies. Predominant a(t) clast orientations (Table 4.7) and its characteristic structure are explained by deposition from fluidal flows, where sediment support was provided by fluid turbulence and the bed.

Engineering literature indicates that sliding beds may form in closed conduits. This has been demonstrated experimentally for slurry flow through narrow pipes (e.g., Newitt *et al.* 1955). Its absence in the esker ridges of south-central Ontario indicates that the necessary conditions for its formation were not attained. That is, water was not forced into the bed upflow and/or a pressure head of sufficient magnitude necessary to drive the coarse bed was not realized.

Conduit maintenance between seasons/events

Stacked sand and gravel couplets suggest that multiple flood events are recorded in the main esker ridges. In addition, the ridges are relatively undeformed. If each sand and gravel couplet represents an annual flood, and more than one couplet is observed without deformation, the conduits must have remained open between events. Further, esker deposits are often transitional to lacustrine rhythmites (cf. Hebrand and Åmark 1989). This suggests a strong seasonal control on meltwater supply to the conduits and a supraglacial to subglacial connection in the meltwater system. In contemporary glaciers, conduits appear to close down in the winter; the system redevelops in the following spring (cf. Willis *et al.* 1990). Conduit closure would have resulted in deformation of esker sediments. Intense deformation was not observed; several explanations are possible. First, if conduits fed into a standing-water body, as appears to have been the case for those draining the Laurentide Ice Sheet, they may have

remained open when the meltwater supply was shut down in the winter, at least to the height of the piezometric surface formed by the water body (cf. Powell 1990). Second, closure rate by plastic deformation of ice may have been insufficient to cause the conduit walls to impinge upon esker gravels. Third, the inferred nonuniform geometry of the conduits may have been the key. Constricted segments of the conduit may have pinched off as pressure within the conduits fell, thereby trapping water within expanded segments and creating linearly arranged water-filled cavities. Reestablishment of conduit flow between cavities in the next melt season may have been facilitated by the location of these repeatedly occupied conduits in topographically low tunnel channels (Brennand and Shaw submitted).

The explanations above assume that the couplets approximate to single seasonal events. A divergent hypothesis is that eskers were deposited in a single year, the couplets representing multiple flood events within a single melt season. However, the complexity and number of finer grained rhythmic sequences in adjacent fans and beads, and downflow fans and glaciolacustrine rhythmites argue against this. In this paper, multiple discharge events have been preferred as explanation of morphologic and sedimentologic observations. Esker ridges are coarse records of the most powerful pulses, whereas fans and beads record flow events in finer detail; they are primarily depositional reservoirs.

References

Aario, R. 1971*a*. Associations of bedforms and palaeocurrent patterns in an esker delta, Haapajärvi, Finland. Annales Academiae Scientiarum Fennicae, Series A, III. Geologica-Geographica.

Aario, R. 1971*b*. Syndepositional deformation in the Kurkiselkä esker, Kiiminki, Finland. Bulletin of the Geological Society of Finland, 43: 163-173.

Alden, W.C. 1918. The Quaternary geology of southeastern Wisconsin. United States Geological Survey, Professional Paper 106.

Allen, J.R.L. 1966. On bed forms and palaeocurrents. Sedimentology, 6: 153-190.

Allen, J.R.L. 1971. A theoretical and experimental study of climbing-ripple cross-lamination, with a field application to the Uppsala esker. Geografiska Annaler, Series A, 53:157-187.

Allen, J.R.L. 1983. River bedforms: progress and problems. *In* Modern and ancient fluvial systems. *Edited by* J.D. Collinson, and J. Lewin. International Association of Sedimentologists, Special Publication 6, pp. 19-33.

Allen, J.R.L. 1984*a*. Parallel lamination developed from upper-stage plane beds: a model based on the larger coherent structures of the turbulent boundary layer. Sedimentary Geology, 39: 227-242.

Allen, J.R.L. 1984*b*. Sedimentary structures: their character and physical basis. Developments in Sedimentology 30. Vol. I. Elsevier, Amsterdam.

Alley, R.B. 1991. Deforming-bed origin for southern Laurentide till sheets? Journal of Glaciology, 37: 67-76.

Anketell, J.M., and Rust, B.R. 1990. Origin of cross-stratal layering in fluvial conglomerates, Devonian Malbaie Formation, Gaspé, Quebec. Canadian Journal of Earth Sciences, 27: 1773-1782.

Ashley, G.M. 1990. Classification of large-scale subaqueous bedforms: a new look at an old problem. Journal of Sedimentary Petrology, 60: 160-172.

Ashley, G.M., Boothroyd, J.C., and Borns, H.W., Jr. 1991. Sedimentology of late Pleistocene (Laurentide) deglacial-phase deposits, eastern Maine; an example of a temperate marine grounded ice-sheet margin. *In* Glacial marine sedimentation; paleoclimatic significance. *Edited by* J.B. Anderson, and G.M. Ashley. Geological Society of America, Special Paper 261, pp. 107-125.

Ashmore, P.E. 1988. Bed load transport in braided gravel-bed stream models. Earth Surface Processes and Landforms, 13: 677-695.

Ashmore, P.E. 1991. Channel morphology and bed load pulses in braided, gravel-bed streams. Geografiska Annaler, Series A, 73: 37-52.

Aylsworth, J.M., and Shilts, W.W. 1989*a*. Glacial features around the Keewatin Divide: Districts of Mackenzie and Keewatin. Geological Survey of Canada, Paper 88-21.

Aylsworth, J.M., and Shilts, W.W. 1989*b*. Bedforms of the Keewatin Ice Sheet, Canada. Sedimentary Geology, 62: 407-428.

Baker, V.R. 1973. Paleohydrology and sedimentology of Lake Missoula flooding in eastern Washington. Geological Society of America, Special Paper 144.

Baker, V.R. 1978. Large-scale erosional and depositional features of the Channeled Scabland. *In* The Channeled Scabland: a guide to the geomorphology of the Columbia Basin, Washington. *Edited by* V.R. Baker, and D. Nummedal. National Aeronautics and Space Administration, Washington, pp. 81-115.

Baker, V.R. 1988*a*. Geological fluvial geomorphology. Geological Society of America Bulletin, 100: 1157-1167.

Baker, V.R. 1988*b*. Cataclysmic processes in geomorphological systems. Zeitschrift für Geomorphologie, Neue Folge Supplementbände, 67: 25-32.

Banerjee, I. 1969. Sedimentology of an esker north of Peterborough, Ontario. Geological Survey of Canada, Paper 69-1B, pp. 61-62.

Banerjee, I., and McDonald, B.C. 1975. Nature of esker sedimentation. *In* Glaciofluvial and glaciolacustrine sedimentation. *Edited by* A.V. Jopling, and B.C. McDonald. Society of Economic Paleontologists and Mineralogists, Special Publication 23, pp. 304-320.

Barnett, P.J., Cowan, W.R., and Henry, A.P. 1991. Quaternary geology of Ontario, southern sheet. Ontario Geological Survey, Map 2556, scale 1:1 000 000.

Barwis, J.H., and Hayes, M.O. 1985. Antidunes on modern and ancient washover fans. Journal of Sedimentary Petrology, 55: 907-916.

Blatt, H., Middleton, G., and Murray, R. 1980. Origin of sedimentary rocks, 2nd ed. Prentice-Hall, Inc., New Jersey.

Boudon, G., and Lajoie, J. 1989. The 1902 Peléean deposits in the Fort Cemetery of St. Pierre, Martinique: a model for the accumulation of turbulent nuées ardentes. Journal of Volcanology and Geothermal Research, 38: 113-129.

Boulton, G.S., and Eyles, N. 1979. Sedimentation by valley glaciers; a model and genetic classification. *In* Moraines and varves. *Edited by* Ch. Schlüchter. Balkema, Rotterdam, pp. 11-24.

Brayshaw, A.C. 1984. Characteristics and origin of cluster bedforms in coarse-grained alluvial channels. *In* Sedimentology of gravels and conglomerates. *Edited by* E.H. Koster, and R.J. Steel. Canadian Society of Petroleum Geologists, Memoir 10, pp. 77-85.

Brayshaw, A.C. 1985. Bed microtopography and entrainment thresholds in gravel-bed rivers. Geological Society of America Bulletin, 96: 218-223.

Brayshaw, A.C., Frostick, L.E., and Reid, I. 1983. The hydrodynamics of particle clusters and sediment

entrainment in coarse alluvial channels. Sedimentology, 30: 137-143.

Brennand, T.A. 1991*a*. Large-scale bedforms in the Harricana glaciofluvial ridge, Québec, and their implications for meltwater regimes. Geological Association of Canada, Program with Abstracts, 16: A14.

Brennand, T.A. 1991*b*. Form and sedimentology of the Harricana glaciofluvial system, Québec, and their implications for meltwater regimes. Canadian Association of Geographers, Program with Abstracts, 40: 78.

Brennand, T.A., and Sharpe, D.R. in press. Ice-sheet dynamics and subglacial meltwater regime inferred from form and sedimentology of glaciofluvial systems: Victoria Island, District of Franklin, Northwest Territories. Canadian Journal of Earth Sciences.

Brennand, T.A., and Shaw, J. submitted. Tunnel channels and associated landforms, south-central Ontario: their implications for ice-sheet hydrology. Canadian Journal of Earth Sciences.

Burbage, G.H., and Rust, B.R. 1988. A Champlain Sea subwash fan at St. Lazare, Quebec. *In* The late Quaternary development of the Champlain Sea Basin. *Edited by* N.R. Gadd. Geological Association of Canada, Special Paper 35, pp. 47-61.

Carling, P.A., and Glaister, M.S. 1987. Rapid deposition of sand and gravel mixtures downstream of a negative step: the role of matrix-infilling and particle-overpassing in the process of bar-front accretion. Journal of the Geological Society, London, 144: 543-551.

Charland, A., and Lajoie, J. 1989. Characteristics of pyroclastic deposits at the margin of Fond Canonville, Martinique, and implications for the transport of the 1902 nuées ardentes of Mt. Pelée. Journal of Volcanology and Geothermal Research, 38: 97-112.

Charlesworth, J.K. 1957. The Quaternary Era: with special reference to its glaciation, Vol. I. Edward Arnold (Publ.) Ltd., London.

Cheel, R.J. 1982. The depositional history of an esker near Ottawa, Canada. Canadian Journal of Earth Sciences, 19: 1417-1427.

Cheel, R.J. 1990. Horizontal lamination and the sequence of bed phases and stratification under upper flow regime conditions. Sedimentology, 37: 517-529.

Cheel, R.J., and Middleton, G.V. 1986. Horizontal laminae formed under upper flow regime plane bed conditions. Journal of Geology, 94: 489-504.

Cheel, R.J., and Rust, B.R. 1986. A sequence of soft-sediment deformation (dewatering) structures in late Quaternary subaqueous outwash near Ottawa, Canada. Sedimentary Geology, 47: 77-93.

Christian, K.W. 1988. The Monro esker complex: ice-contact sedimentation within a bedrock valley. M.Sc. Thesis, Queen's University, Kingston.

Clemmensen, L.B., and Houmark-Nielsen, M. 1981. Sedimentary features of a Weichselian

glaciolacustrine delta. Boreas, 10: 229-245.

Costa, J.E. 1988. Rheologic, geomorphic, and sedimentologic differentiation of water floods, hyperconcentrated flows, and debris flows. *In* Flood geomorphology. *Edited by* V.R. Baker, R.C. Kochel, and P.C. Patton. John Wiley and Sons, Inc., London. pp. 113-122.

Crosby, W.O. 1902. Origin of eskers. The American Geologist, 30: 1-39.

Curray, J.R. 1956. The analysis of two-dimensional orientation data. Journal of Geology, 64: 117-131.

Davis, J.C. 1986. Statistics and data analysis in geology, 2nd ed. John Wiley and Sons, New York.

Deane, R.E. 1950. Pleistocene geology of the Lake Simcoe District, Ontario. Geological Survey of Canada, Memoir 256.

De Geer, G. 1897. Om rullstensåsarnas bildningssätt. Geologiska Föreningens i Stockholm Förhandlingar, 19: 366-388.

Denny, C.S. 1972. The Ingraham esker, Chazy, New York. United States Geological Survey, Paper 800-B, pp. B35-B41.

Diemer, J.A. 1988. Subaqueous outwash deposits in the Ingraham ridge, Chazy, New York. Canadian Journal of Earth Sciences, 25: 1384-1396.

Dryden, A.L., Jr. 1931. Accuracy in percentage representation of heavy mineral frequencies. Proceedings of the National Academy of Sciences, 17: 233-238.

Duckworth, P.B. 1979. The late depositional history of the western end of the Oak Ridges Moraine, Ontario. Canadian Journal of Earth Sciences, 16: 1094-1107.

Elfström, Å. 1987. Large boulder deposits and catastrophic floods: a case study of the Bäldakatj area, Swedish Lapland. Geografiska Annaler, Series A, 69: 101-121.

Fisher, R.V. 1990. Transport and deposition of a pyroclastic surge across an area of high relief: the 18 May 1980 eruption of Mount St. Helens, Washington. Geological Society of America Bulletin, 102: 1038-1054.

Fitzsimons, S.J. 1991. Supraglacial eskers in Antarctica. Geomorphology, 4: 293-299.

Flint, R.F. 1928. Eskers and crevasse fillings. American Journal of Science, 15-16: 410-416.

Flint, R.F. 1930. The origin of the Irish eskers. Geographical Review, 20: 615-630.

Flint, R.F. 1957. Glacial and Pleistocene geology. John Wiley and Sons, New York.

Folk, R., and Ward, W.C. 1957. Brazos River bar: a study in the significance of grain-size parameters. Journal of Sedimentary Petrology, 27: 3-27.

Fowler, A.C. 1987. A theory of glacier surges. Journal of Geophysical Research, 92: 9111-9120.

Frakes, L.A., Figueiredo, F.P.M. de, and Fulfaro, U. 1968. Possible fossil eskers and associated features from the Paraná, Brazil. Journal of Sedimentary Petrology, 38: 5-12.

Garbutt, M.D. 1990. Full and open conduit sedimentation within a large-scale esker system in

southwestern Finland. Geological Society of America, Northeastern Section, Program with Abstracts, 22: 19.

Gilbert, R. 1990. Evidence for the subglacial meltwater origin and the late Quaternary lacustrine environment of Bateau Channel, eastern Lake Ontario. Canadian Journal of Earth Sciences, 27: 939-945.

Gilbert, R., and Shaw, J. 1992. Glacial and early postglacial lacustrine environment of a portion of northeastern Lake Ontario. Canadian Journal of Earth Sciences, 29: 63-75.

Gomez, B., Naff, R.L., and Hubbell, D.W. 1989. Temporal variations in bedload transport rates associated with the migration of bedforms. Earth Surface Processes and Landforms, 14: 135-156.

Gorrell, G., and Shaw, J. 1991. Deposition in an esker, bead and fan complex, Lanark, Onatrio, Canada. Sedimentary Geology, 72: 285-314.

Graf, W.H., and Acaroglu, E.R. 1966. Settling velocities of natural grains. Bulletin of the International Association of Scientific Hydrology, 11: 27-43.

Gravenor, C.P. 1957. Surficial geology of the Lindsay-Peterborough area, Ontario, Victoria, Peterborough, Durham, and Northumberland counties, Ontario. Geological Survey of Canada, Memoir 288.

Gustavson, T.C., and Boothroyd, J.C. 1982. Subglacial fluvial erosion: a major source of stratified drift, Malaspina glacier, Alaska. *In* Research in glacial, glaciofluvial and glaciolacustrine systems. *Edited by* R. Davidson-Arnott, W. Nickling, and B.D. Fahey. Proceedings of the 6th Guelph symposium on geomorphology. GeoBooks, Norwich, pp. 93-117.

Gustavson, T.C., and Boothroyd, J.C. 1987. A depositional model for outwash sediment sources and hydrologic characteristics, Malaspina Glacier, Alaska: a modern analog of the south-eastern margin of the Laurentide Ice Sheet. Geological Society of America Bulletin, 99: 187-200.

Haeberli, W. 1983. Frequency and characteristics of glacier floods in the Swiss Alps. Annals of Glaciology, 4: 85-90.

Hagen, J.O., Wold, B., Liestøl, O., 1983. Subglacial processes at Bondhusbreen, Norway: preliminary results. Annals of Glaciology, 4: 91-98.

Hallet, B., and Anderson, R.S. 1980. Detailed glacial geomorphology of a proglacial bedrock area at Castleguard Glacier, Alberta, Canada. Zeitschrift für Gletscherkunde und Glazialgeologie, 16: 171-184.

Hand, B.M. 1974. Supercritical flow in density currents. Journal of Sedimentary Petrology, 44: 637-648.

Hand, B.M., Middleton, G.V., and Skipper, K. 1972. Antidune cross-stratification in a turbidite sequence, Chloridorme formation, Gaspé, Québec. Discussion. Sedimentology, 18: 135-138.

Hanson, G.F. 1943. A contribution to experimental geology: the origin of eskers. American Journal of Science, 241: 447-452.

Hassan, M.A., and Reid, I. 1990. The influence of microform bed roughness elements on flow and sediment transport in gravel bed rivers. Earth Surface Processes and Landforms, 15: 739-750.

Hebrand, M., and Åmark, M. 1989. Esker formation and glacier dynamics in eastern Skåne and adjacent areas, southern Sweden. Boreas, 18: 67-81.

Henderson, P.J. 1988. Sedimentation in an esker system influenced by bedrock topography near Kingston, Ontario. Canadian Journal of Earth Sciences, 25: 987-999.

Hoey, T.R. 1992. Temporal variations in bedload transport rates and sediment storage in gravel-bed rivers. Progress in Physical Geography, 16: 319-338.

Hoey, T.R., and Sutherland, A.J. 1991. Channel morphology and bedload pulses in braided rivers: a laboratory study. Earth Surface Processes and Landforms, 16: 447-462.

Hooke, R. LeB. 1984. On the role of mechanical energy in maintaining subglacial water conduits at atmospheric pressure. Journal of Glaciology, 30: 180-187.

Hooke, R. LeB. 1989. Englacial and subglacial hydrology: a qualitative review. Arctic and Alpine Research, 21: 221-233.

Hooke, R. LeB., Laumann, T., and Kohler, J. 1990. Subglacial water pressures and the shape of subglacial conduits. Journal of Glaciology, 36: 67-71.

Hoppe, G. 1952. Hummocky moraine regions with special reference to the interior of Norrbotten. Geografiska Annaler, 34: 1-71.

Howarth, P.J. 1971. Investigations of two eskers at eastern Breidamerkurjökull, Iceland. Arctic and Alpine Research, 3: 305-318.

Iken, A., and Bindschadler, R.A. 1986. Combined measurements of subglacial water pressure and surface velocity of Findelengletscher, Switzerland: conclusions about drainage system and sliding mechanism. Journal of Glaciology, 32: 101-119.

Iken, A., Röthlisberger, H., Flotron, A., and Haeberli, W. 1983. The uplift of Unteraargletscher at the beginning of the melt season - a consequence of water storage at the bed. Journal of Glaciology, 29: 28-47.

Iseya, F., and Ikeda, H. 1987. Pulsations in bedload transport rates induced by longitudinal sediment sorting: a flume study using sand and gravel mixtures. Geografiska Annaler, Series A, 69: 15-27.

Jensen, J.P. 1988. Lateral accretion features (epsilon cross-bedding) and point bars in the Weichselian Køge esker, East-Sjælland, Denmark. Bulletin of the Geological Society of Denmark, 37: 11-19.

Jewtuchowicz, S. 1965. Description of eskers and kames in Gåshamnöyra and on Bungebreen, south of Hornsund, Vestspitsbergen. Journal of Glaciology, 5: 719-725.

Johansson, C.E. 1963. Orientation of pebbles in running water. Geografiska Annaler, 45: 85-112.

Johansson, C.E. 1965. Structural studies of sedimentary deposits. Geologiska Föreningens i Stockholm Föhandlingar, 87: 3-61.

Johansson, C.E. 1976. Structural studies of frictional sediments. Geografiska Annaler, 58: 201-300.

Jopling, A.V., and Walker, R.G. 1968. Morphology and origin of ripple-drift cross-lamination, with examples from Pleistocene Massachusetts. Journal of Sedimentary Petrology, 38: 971-984.

Kamb, B. 1987. Glacier surge mechanisms based on linked cavity configuration of the basal water conduit system. Journal of Geophysical Research, 92: 9083-9100.

Kamb, B., Raymond, C.F., Harrison, W.D., *et al.* 1985. Glacier surge mechanism: 1982-1983 surge of Variegated Glacier, Alaska. Science, 227: 469-479.

King, C.A.M., and Buckley, J.T. 1969. Geomorphological investigations in west-central Baffin Island, N.W.T., Canada. Arctic and Alpine Research, 1: 105-120.

Lewis, W.V. 1949. An esker in the process of formation: Böverbreen, Jotunheimen, 1947. Journal of Glaciology, 1: 314-319.

Leyland, J.G., and Mihychuk, M. 1983. Quaternary geology of the Tweed area, southern Ontario. Ontario Geological Survey, Preliminary Map P2615, scale 1:50 000.

Leyland, J.G., and Mihychuk, M. 1984*a*. Quaternary Geology of the Trenton-Consecon area, southern Ontario. Ontario Geological Survey, Preliminary Map P2586, scale 1:50 000.

Leyland, J.G., and Mihychuk, M. 1984*b*. Quaternary geology of the Campbellford area, southern Ontario. Ontario Geological Survey, Preliminary Map P2532, scale 1:50 000.

Leyland, J.G., and Russell, T.S. 1984. Quaternary geology of the Sydenham area, southern Ontario. Ontario Geological Survey, Preliminary Map P2587, scale 1:50 000.

Lindström, E. 1985. The Uppsala esker: The Åsby-Drälinge Exposures. *In* Glaciofluvium. *Edited by* L.-K. Königsson. Striae, 22: 27-32.

Lobanov, N. 1967. Structure and lithology of an esker ridge near Kuznechnaya station on the Karel'skii Isthmus. Lithology and Mineral Resources, 2: 462-468.

Lord, M.L., and Kehew, A.E. 1987. Sedimentology and paleohydrology of glacial-lake outburst deposits in southeastern Saskatchewan and northwestern Dakota. Geological Society of America Bulletin, 99: 663-673.

Lowe, D.R. 1975. Water escape structures in coarse-grained sediments. Sedimentology, 22: 157-204.

Lundqvist, J. 1979. Morphogenic classification of glaciofluvial deposits. Sveriges Geologiska Undersökning, Series C, 767, 72 pp.

Matthes, G.H. 1947. Macroturbulence in natural stream flow. Transactions of the American Geophysical Union, 28: 255-265.

McBride, E.F., Shepherd, R.G., and Crawley, R.A. 1975. Origin of parallel, near-horizontal laminae by

migration of bed forms in a small flume. Journal of Sedimentary Petrology, 45: 132-139.

McCutcheon, S.C., and Bradley, J.B. 1984. Effects of high sediment concentrations on velocity and sediment distributions. *In* Water for resource development. *Edited by* D.L. Schreiber. American Society for Civil Engineers, New York, pp. 43-47.

McDonald, B.C., and Shilts, W.W. 1975. Interpretation of faults in glaciofluvial sediments. *In* Glaciofluvial and glaciolacustrine sedimentation. *Edited by* A.V. Jopling, and B.C. McDonald. Society of Economic Paleontologists and Mineralogists, Special Publication 23, pp. 123-131.

McDonald, B.C., and Vincent, J.S. 1972. Fluvial sedimentary structures formed experimentally in a pipe, and their implications for interpretation of subglacial sedimentary environments. Geological Survey of Canada, Paper 72-27.

Meland, N., and Norrman, J.O. 1969. Transport velocities of individual size fractions in heterogeneous bed load. Geografiska Annaler, Series A, 51: 127-144.

Miall, A.D. 1985. Architectural-element analysis: a new method of facies analysis applied to fluvial deposits. Earth-Science Reviews, 22: 261-308.

Middleton, G.V. 1965. Antidune cross-bedding in a large flume. Journal of Sedimentary Petrology, 35: 922-927.

Ministry of Natural Resources 1987. Aggregate resources inventory of the county of Hastings, southern Ontario: Ontario Geological Survey, Open File Report 5582.

Mirynech, E. 1962. Pleistocene geology of the Trenton-Campbellford map-area, Ontario. Ph.D. Thesis, University of Toronto, Toronto.

Newitt, D.M., Richardson, J.F., Abbott, M., and Turtle, R.B. 1955. Hydraulic conveying of solids in horizontal pipes. Transactions of the Institution of Chemical Engineers, 33: 93-113.

Nye, J.F. 1976. Water flow in glaciers: jökulhlaups, tunnels and veins. Journal of Glaciology, 17: 179-207.

O'Donnell, N.D. 1966. A study of the Marlbank esker near Marlbank, Ontario. B.Sc. Thesis, Queen's University, Kingston.

Ontario Geological Survey 1991. Bedrock geology of Ontario, southern sheet. Ontario Geological Survey Map 2544, scale 1:1 000 000.

Petrie G., and Price, R.J. 1966. Photogrammetric measurements of the ice wastage and morphological changes near the Casement Glacier, Alaska. Canadian Journal of Earth Sciences, 3: 827-840.

Pierson, T.C., and Scott, K.M. 1985. Downstream dilution of a lahar: transition from debris flow to hyperconcentrated streamflow. Water Resources Research, 21: 1511-1524.

Powell, R.D. 1990. Glaciomarine processes at grounding-line fans and their growth to ice-contact deltas. *In* Glaciomarine environments: processes and sediments. *Edited by* J.A. Dowdeswell, and J.D. Scourse. Geological Society of London, Special Publication 53, pp. 53-73.

Powers, M.C. 1953. A new roundness scale for sedimentary particles. Journal of Sedimentary Petrology, 23: 117-119.

Prave, A.R., and Duke, W.L. 1990. Small-scale hummocky cross-stratification in turbidites: a form of antidune stratification. Sedimentology, 37: 531-539.

Price, R.J. 1966. Eskers near the Casement Glacier, Alaska. Geografiska Annaler, Series A, 48: 111-125.

Price, R.J. 1969. Moraines, sandur, kames and eskers near Breidamerkurjökull, Iceland. Transactions of the Institute of British Geographers, 46: 17-43.

Ringrose, S. 1982. Depositional processes in the development of eskers in Manitoba. *In* Research in glacial, glaciofluvial and glaciolacustrine systems. *Edited by* R. Davidson-Arnott, W. Nickling, and B.D. Fahey. Proceedings of 6th Guelph symposium on geomorphology. Geo Books, Norwich, pp. 117-137.

Röthlisberger, H. 1972. Water pressure in intra- and subglacial channels. Journal of Glaciology, 11: 177-203.

Rouse, H. 1961. Fluid mechanics for hydraulic engineers. Dover Publications, Inc., New York.

Russell, R.J. 1968. Where most grains of very coarse sand and fine gravel are deposited. Sedimentology, 11: 31-38.

Rust, B.R. 1972. Pebble orientation in fluvial sediments. Journal of Sedimentary Petrology, 42: 384-388.

Rust, B.R., and Gibling, M.R. 1990. Three-dimensional antidunes as HCS mimics in a fluvial sandstone: the Pennsylvanian South Bar Formation near Sydney, Nova Scotia. Journal of Sedimentary Petrology, 60: 540-548.

Rust, B.R., and Koster, E.H. 1984. Coarse alluvial deposits. *In* Facies models, 2nd ed. *Edited by* R.G. Walker. Geoscience Canada Reprint Series 1, pp. 53-69.

Rust, B.R., and Romanelli, R. 1975. Late Quaternary subaqueous outwash deposits near Ottawa, Canada. *In* Glaciofluvial and glaciolacustrine sedimentation. *Edited by* A.V. Jopling, and B.C. McDonald. Society of Economic Paleontologists and Mineralogists, Special Publication 23, pp. 177-192.

Saunderson, H.C. 1975. Sedimentology of the Brampton esker and its associated deposits: an empirical test of theory. *In* Glaciofluvial and glaciolacustrine sedimentation. *Edited by* A.V. Jopling, and B.C. McDonald. Society of Economic Paleontologists and Mineralogists, Special Publication 23, pp. 155-176.

Saunderson, H.C. 1977. The sliding bed facies in esker sands and gravels: a criterion for full-pipe (tunnel) flow? Sedimentology, 24: 623-638.

Saunderson, H.C. 1982. Bedform diagrams and the interpretation of eskers. *In* Research in glacial, glaciofluvial and glaciolacustrine systems. *Edited by* R. Davidson-Arnott, W. Nickling, and B.D.

Fahey. Proceedings of 6th Guelph symposium on geomorphology. Geo Books, Norwich, pp. 139-150.

Saunderson, H.C., and Jopling, A.V. 1970. Glaciofluvial sedimentation of the Brampton esker, Ontario. Geological Survey of Canada, Paper 70-1A, pp. 200-201.

Saunderson, H.C., and Jopling, A.V. 1980. Paleohydraulics of a tabular, cross-stratified sand in the Brampton esker, Ontario. Sedimentary Geology, 25: 169-188.

Sharpe, D.R. 1988. Glaciomarine fan deposition in the Champlain Sea. *In* The late Quaternary development of the Champlain Sea Basin. *Edited by* N.R. Gadd. Geological Association of Canada, Special Paper 35, pp. 63-82.

Shaw, J. 1969. Aspects of glaciogenic sedimentation, with special reference to the area around Shewsbury. Ph.D. Thesis, University of Reading, Reading.

Shaw, J. 1972. Sedimentation in the ice-contact environment, with examples from Shropshire (England). Sedimentology, 18: 23-62.

Shaw, J., and Gilbert, R. 1990. Evidence for large-scale subglacial meltwater flood events in southern Ontario and northern New York State. Geology, 18: 1169-1172.

Shaw, J., and Gorrell, G. 1991. Subglacially formed dunes with bimodal and graded gravel in the Trenton drumlin field, Ontario. Géographie physique et Quaternaire, 45: 21-34.

Shaw, J., and Kellerhals, R. 1977. Paleohydraulic interpretation of antidune bedforms with application to antidunes in gravel. Journal of Sedimentary Petrology, 47: 257-266.

Shaw, J., and Kellerhals, R. 1982. The composition of recent alluvial gravels in Alberta river beds. Alberta Research Council, Bulletin 41.

Shaw, J., Kvill, D., and Rains, B. 1989. Drumlins and catastrophic subglacial floods. Sedimentary Geology, 62: 177-202.

Shilts, W.W. 1984. Esker sedimentation models, Deep Rose Lake map area, District of Keewatin. Geological Survey of Canada, Paper 84-1B, pp. 217-222.

Shilts, W.W. 1985. Geological models for the configuration, history and style of disintegration of the Laurentide Ice Sheet. *In* Models in geomorphology. *Edited by* M.J. Woldenburg. The Binghamton symposium on geomorphology, international series 14. Allen and Unwin, Boston. pp. 74-91.

Shilts, W.W., and Aylsworth, J.M. 1987. Glacial geomorphology of northwestern Canadian Shield. *In* Canadian Shield. *Edited by* W.W. Shilts, J.M. Aylsworth, C.A. Kaszycki, and R.A. Klassen. Geological Society of America, Centennial Special Volume 2, pp. 126-142.

Shilts, W.W., and McDonald, B.C. 1975. Dispersal of clasts and trace elements in the Windsor esker, southern Quebec. Geological Survey of Canada, Paper 75-1A, pp. 495-499.

Shoemaker, E.M. 1986. Subglacial hydrology for an ice sheet resting on a deformable aquifer. Journal of Glaciology, 32: 20-30.

Shoemaker, E.M., and Leung, H.K.N. 1987. Subglacial drainage for an ice sheet resting on a layered deformable bed. Journal of Geophysical Research, 92: 4935-4946.

Shreve, R.L. 1972. Movement of water in glaciers. Journal of Glaciology, 11: 205-214.

Shreve, R.L. 1985. Esker characteristics in terms of glacial physics, Katahdin esker system, Maine. Geological Society of America Bulletin, 96: 639-646.

Shulmeister, J. 1989. Flood deposits in the Tweed esker (southern Ontario, Canada). Sedimentary Geology, 65: 153-163.

Skipper, K. 1971. Antidune cross-stratification in a turbidite sequence, Chloridorme Formation, Gaspé, Québec. Sedimentology, 17: 51-68.

Smith, D.G. 1983. Anastomosed fluvial deposits: modern examples from Canada. *In* Modern and ancient fluvial systems. *Edited by* J. Collinson, and J. Lewin. International Association of Sedimentologists, Special Publication 6, pp. 155-168.

Smith, D.G., and Putnam, P.E. 1980. Anastomosed river deposits: modern and ancient examples in Alberta, Canada. Canadian Journal of Earth Sciences, 17: 1396-1406.

Smith, G.A. 1986. Coarse-grained nonmarine volcaniclastic sediment: terminology and depositional process. Geological Society of America Bulletin, 97: 1-10.

Smith, N.D. 1974. Sedimentology and bar formation in the Upper Kicking Horse River, a braided outwash stream. Journal of Geology, 82: 205-224.

Smith, S.A. 1990. The sedimentology and accretionary styles of an ancient gravel-bed stream: the Budleigh Salterton Pebble Beds (Lower Cretaceous), southwest England. Sedimentary Geology, 67: 199-219.

Sneed, E.D., and Folk, R.L. 1958. Pebbles in the lower Colorado River, Texas: a study in particle morphogenesis. Journal of Geology, 66: 114-150.

St-Onge, D.A. 1984. Surficial deposits of the Redrock Lake area, District of Mackenzie. Geological Survey of Canada, Paper 84-1A, pp. 271-278.

Stokes, J.C. 1958. An esker-like ridge in the process of formation, Flatisen, Norway. Journal of Glaciology, 3: 286-289.

Stone, G.H. 1899. The glacial gravels of Maine. United States Geological Survey, Monograph 34.

Szupryczyński, J. 1965. Eskers and kames in the Spitsbergen area. Geographia Polonica, 6: 127-140.

Tanner, V. 1932. The problems of the eskers: the esker-like gravel ridge of Cahpatoaiv, Lapland. Bulletin de la Commission Géologique de Finlande, 99: 1-13.

Terwindt, J.H.J., and Augustinus, P.E.G.F. 1985. Lateral and longitudinal successions in sedimentary

structures in the Middle Mause esker, Scotland. Sedimentary Geology, 45: 161-188.

Thomas, G.S.P. 1984. Sedimentation of a sub-aqueous esker-delta at Strabathie, Aberdeenshire. Scottish Journal of Geology, 20: 9-20.

Upham, W. 1910. Birds Hill, an esker near Winnipeg, Manitoba. Geological Society of America Bulletin, 21: 407-432.

Visser, J.N.J., Loock, J.C., and Collison, W.P. 1987. Subaqueous outwash fan and esker sandstones in the Permo-Carboniferous Dwyka formation of South Africa. Journal of Sedimentary Petrology, 57: 467-478.

Walder, J.S. 1986. Hydraulics of subglacial cavities. Journal of Glaciology, 32: 439-445.

Walder, J.S., and Hallet, B.H. 1979. Geometry of former subglacial channels and cavities. Journal of Glaciology, 23: 335-346.

Walker, R.G. 1975. Generalized facies models for resedimented conglomerates of turbidite association. Geological Society of America Bulletin, 86: 737-748.

Whalley, W.B. 1971. Observations of the drainage of an ice-dammed lake - Strupvatnet, Troms, Norway. Norsk Geografisk Tidsskrift, 25: 165-174.

Whiting, P.J., Dietrich, W.E., Leopold, L.B., *et al.* 1988. Bedload sheets in heterogeneous sediment. Geology, 16: 105-108.

Williams, G.P. 1983. Paleohydrological methods and some examples from Swedish fluvial environments. Geografiska Annaler, Series A, 65: 277-243.

Willis, I.C. 1990. Water storage and its effects on the motion of Midtalsbreen, Norway. (Abstract). Geological Society of America, Northeastern Section, Program with Abstracts, 23: 78.

Willis, I.C., Sharp, M.J., and Richards, K.S. 1990. Configuration of the drainage system of Midtdalsbreen, Norway, as indicated by dye-tracing experiments. Journal of Glaciology, 36: 89-101.

Wilson, A.W.G. 1904. Trent River system and Saint Lawrence outlet. Geological Society of America Bulletin, 15: 211-242.

Woodcock, N.H., and Naylor, M.A. 1983. Randomness testing in three-dimensional orientation data. Journal of Structural Geology, 5: 539-548.

Woodworth, J.B. 1894. Some typical eskers of southern New England. Boston Natural History Society, 26: 197-220.

Young, W.J., and Davies, T.R.H. 1991. Bedload transport processes in a braided gravel-bed river model. Earth Surface Processes and Landforms, 16: 499-511.

CHAPTER 5

Geomorphology, sedimentology, stratigraphic context, and landform associations of the Harricana glaciofluvial complex, Abitibi region, Québec: implications for genesis, meltwater regime and ice-sheet dynamics.[1]

Introduction

The Harricana-Lake McConnell glaciofluvial complex is a linear accumulation of stratified sand and gravel which may extend semi-continuously from a chain of islands in James Bay (Low 1888; Wilson 1938; Hardy 1976, 1977) to the vicinity of Lake Simcoe, southern Ontario (Veillette 1986; Figs. 5.1 and 5.2). It traverses the northward sloping Lake Barlow-Ojibway clay belt, and the fluted Cochrane terrain (Fig. 5.2; Allard 1974; G. Tremblay 1974; Hardy 1976; Chauvin 1977; Veillette 1986). Adjacent glacigenic landforms include eskers, moraines (Fig. 5.1), streamlined forms in glacigenic sediment and bedrock, s-forms, and striae (Fig. 5.2; Veillette 1986). Between Val d'Or (~48°N) and latitude 50°N, the complex has been called the Abitibi or Matagami esker (Allard 1974; Hardy 1976). The complex is presently interpreted as an interlobate moraine formed at the ice front during active retreat of the Hudson and New Quebec ice masses during deglaciation (cf. Hardy 1976; Veillette 1986). It has been suggested that the northern portion of the feature, the Harricana glaciofluvial complex, was deposited time-transgressively between retreating Hudson and New Quebec ice masses, ~11.0 - ~8.5 ka BP (the latter date marking the start of the proposed Cochrane events) (Hardy 1976; Veillette 1989).

During a brief field excursion led by Jean Veillette (Geological Survey of Canada) in the Fall of 1988 to the Abitibi-Timiskaming region of Québec, we were impressed by the similarity of sedimentary facies, facies architecture and facies associations in the Harricana complex, to those observed in the eskers of south-central Ontario. For geomorphic and sedimentologic reasons, these eskers were inferred to have been deposited synchronously in subglacial conduits (Brennand in press). This research on the Harricana complex grew out of these observations, and is an attempt to elucidate the genesis, hydrologic significance and implications for ice-sheet dynamics of this extensive glaciofluvial deposit. Although the complex has been called the Harricana-Lake McConnell interlobate moraine, observations and interpretations presented here bring into question the interlobate nature of this landform. Consequently, a less genetic-laden name, the Harricana glaciofluvial complex, or Harricana complex, is proposed for the northern portion of this system.

---

[1] A version of this paper will be submitted for publication as:
Brennand, T.A., and Shaw, J. Geomorphology, sedimentology, and landform associations of the Harricana glaciofluvial complex, Abitibi region, Québec: implications for genesis, meltwater regime and ice-sheet dynamics. Canadian Journal of Earth Sciences.

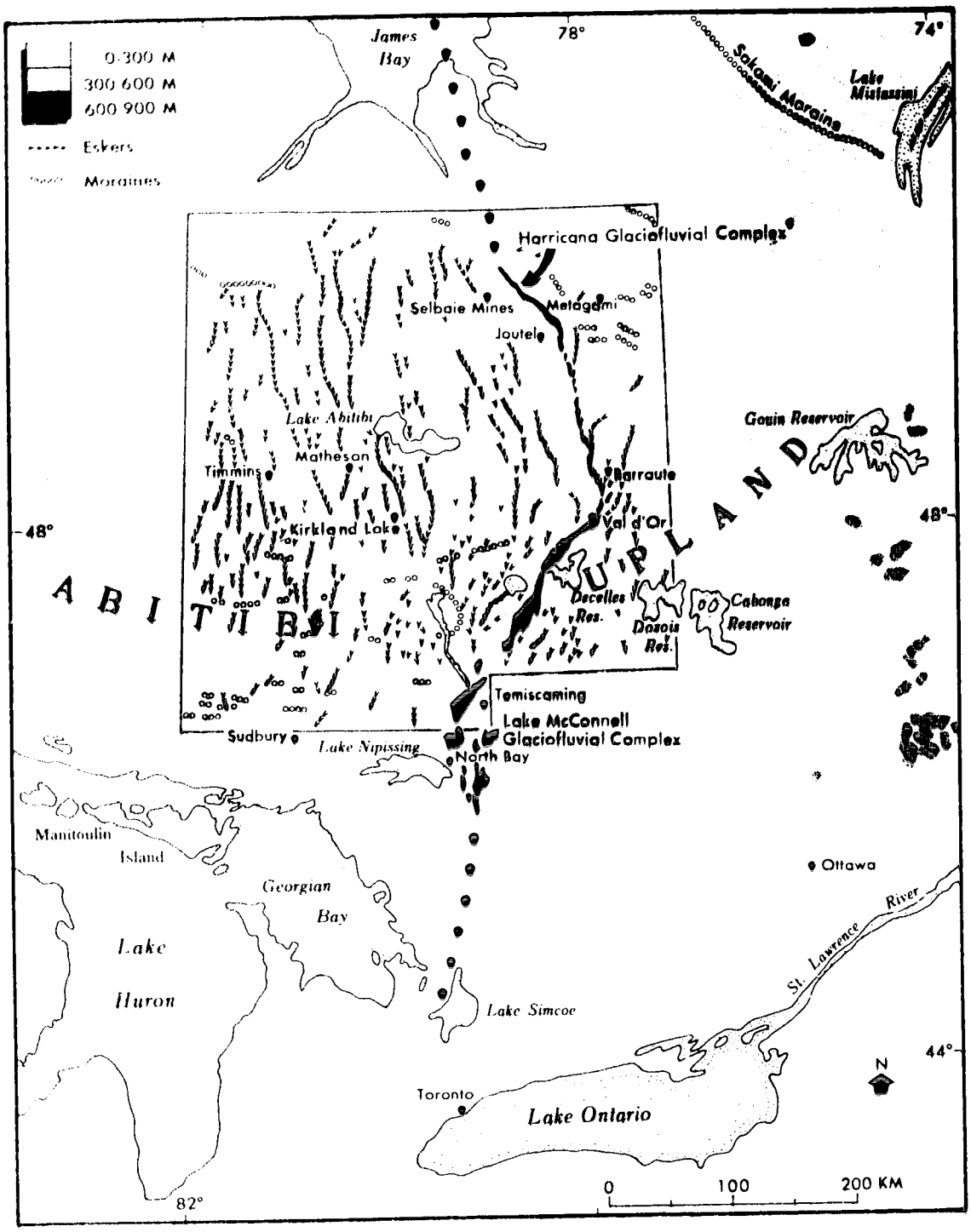

Figure 5.1. Pattern of eskers and moraines adjacent to the Harricana glaciofluvial complex mapped within boxed area with the exception of the Sakami Moraine. Data sources: (1) relief simplified from Yelle (1976); (2) eskers mapped from G. Tremblay (1974), Chauvin (1977), Veillette (1986, 1990), Sado and Carswell (1987); (3) moraines mapped from Hardy (1976), Veillette (1986), Sado and Carswell (1987) and Vincent (1989). Dots are proposed northern (Hardy 1976) and southern (Veillette 1986) extensions of the Harricana complex. The proposed northern island chain part of the Harricana complex (Wilson 1938) extends beyond the mapped area.

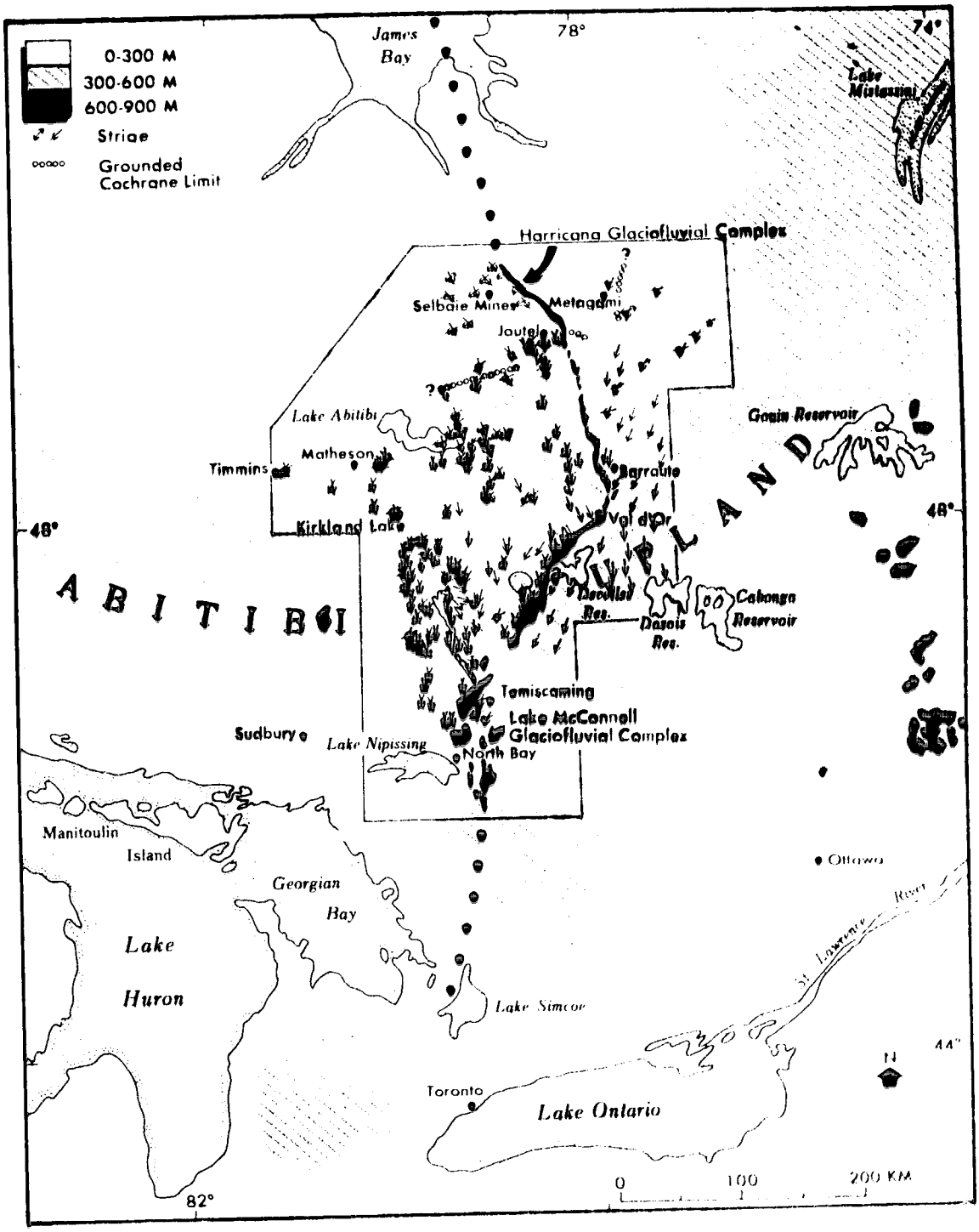

Figure 5.2. Cross-striated sites mapped in dissected zone of Abitibi Uplands, and adjacent to the Harricana glaciofluvial complex (boxed area). Data sources: (1) relief simplified from Yelle ( ); (2) striae mapped from Veillette (1986); (3) proposed grounded Cochrane limit mapped from Veillette *et al.* (1991).

Interlobate moraines

So-called interlobate moraines have been identified in Europe (cf. Aario 1977; Punkari 1980), as well as North America where the Burntwood-Etawney, Knife, and Leaf Rapids complexes in Manitoba (Klassen 1983, 1986; Dredge *et al.* 1986; Kaszychi and DiLabio 1986; Shilts *et al.* 1987; Dredge and Cowan 1989; Dredge and Nixon 1992), the Harricana-Lake McConnell complex in Ontario and Québec (cf. Veillette 1986), and the Oak Ridges complex in Ontario (cf. Duckworth 1979) are regionally significant examples. They are described as broad, semi-continuous ridges and indefinitely-shaped mounds composed mainly of stratified sand and gravel, rising up to 80 m above the surrounding terrain (Punkari 1980). Esker ridges, kettle holes, kames and pitted outwash plains may be associated with these complexes (Zoltai 1965). Striae are commonly observed to converge on the axes of complexes (Punkari 1980; Veillette 1986).

Large, semi-continuous, linearly-arranged glaciofluvial deposits have been inferred to be interlobate moraines primarily on the basis of the characteristics of adjacent indicators of ice-flow direction, landforms and deposits: converging striae, orientation of adjacent end moraines (genesis assumed), esker networks and streamlined bedforms (assumed to be a product of direct glacial action), and analysis of adjacent till geochemistry and pebble lithology (e.g., Allard 1974; Hardy 1976; Chauvin 1977; Kaszycki and DiLabio 1986; Veillette 1986). Three hypotheses as to the regional significance of interlobate moraines have been proposed: (*i*) they were formed along a line of separation where two coalescent ice masses split during deglaciation (Dyke *et al.* 1982; Shilts *et al.* 1987); (*ii*) they developed between ice lobes within a major ice mass (e.g., Hayes lobe, Manitoba, has been reported to have been bounded by the Limestone and Sachigo interlobate moraines (Dredge and Cowan 1989)) which may have been stagnant (Aario 1977; Punkari 1980); (*iii*) they were deposited time-transgressively at sutures within a single ice mass during deglaciation, the sutures resulting from ice-marginal configuration and dynamics during retreat and not inherited from ice mass convergence (Veillette 1986, 1990). The lobes they are said to delimit have been pivotal in the development of continent-scale ice-sheet models, and their deglacial chronology and pattern (e.g., Dyke and Prest 1987). However, to comprehend the genesis and significance of these features requires detailed sedimentologic and morphologic observation and inference from the features themselves, but in the context of constraining observations on surrounding landforms and sedimentary/stratigraphic sequences. Only then will assertions of genesis and regional significance be appropriate. Yet, little research has been reported on a genetic interpretation of these features based, first, on their inherent sedimentology and morphology and, second, on their associations with adjacent landforms and deposits. Allard's (1974) geomorphic analysis of the Harricana glaciofluvial complex and Duckworth's (1979) investigation of the sediments within the Oak Ridges complex are the only examples of this type of study in North America. Indeed, even where good exposures have been

available basic sedimentologic data, such as paleoflow direction estimates, have not been reported (cf. Klassen 1986).

This paper presents results of a detailed morphologic and sedimentologic study of 250 km of the Harricana glaciofluvial complex, between latitudes 48°N and 50°N, in the Abitibi region of Québec. Genetic inferences are viewed in terms of the current understanding of adjacent stratigraphy and landform associations. Implications for ice-sheet hydrology and dynamics are then proposed. But first, an overview of previous research on the Harricana glaciofluvial complex is presented.

Background research on the Harricana glaciofluvial complex

An interlobate origin for the Harricana glaciofluvial complex was first suggested by Wilson (1938). He proposed that the complex marked a zone of separation of two ice masses that he named Labradorean and Western. He considered the north-south oriented island chain in James Bay, described by Low (1888) as being composed of unstratified boulders, sand, and clay and originally interpreted as an end moraine deposited from Labradorean ice, as a northern extension of the Harricana glaciofluvial complex (Figs. 5.1 and 5.2). Wilson traced this feature as far south as 48°N, and noted converging striae in the vicinity of the Harricana complex. L. P. Tremblay (1950), mapping bedrock geology in the Fiedmont area of Québec, also reported converging striae and eskers on either side of a larger north-south trending esker (the Harricana complex). He attributed these landform associations to glacial movement during retreat, and proposed a reentrant in the retreating ice front coinciding with the location of the Harricana complex. Hardy (1976) proposed the name "Harricana Moraine" for the complex then believed to extend for ~630 km from the islands in James Bay to a few kilometres south of Val d'Or, Québec. He also favoured an interlobate origin, based on the orientation of adjacent striae, end moraines (genesis assumed), streamlined bedforms and eskers, and the ridge dimensions, composition and kettle density (Hardy 1976). Similar reasoning was also proposed by Allard (1974), G. Tremblay (1974) and Chauvin (1977). Veillette (1983*a*, 1986, 1988, 1989, 1990) extended the glaciofluvial complex to the south, connecting it with the Lake McConnell complex in the vicinity of North Bay, Ontario (Figs. 5.1 and 5.2; Boissonneau 1968). He also suggested that the complex, although discontinuous, may be connected to a major spillway system between Lake Nipissing and Lake Simcoe, Ontario (Figs. 5.1 and 5.2; Chapman and Putnam 1984). If these proposed extensions are, indeed, part of a single glaciofluvial system with a common origin, the Harricana-Lake McConnell complex extends for almost 1000 km! The interlobate hypothesis was furthered by meticulous analysis of the distribution of adjacent cross-cutting striae (Fig. 5.2), grooves (s-forms?), crag-and-tail features, dispersion of indicator lithologies in tills, and orientations of eskers and moraines (Fig. 5.1; Veillette 1983*a*, 1983*b*, 1986, 1988, 1989, 1990, Veillette *et al.* 1989). Radiocarbon dates from basal postglacial organic material in small lakes and ponds were used to support the idea of a reentrant in the ice front at the Harricana-

Lake McConnell complex (Veillette 1983*a*, 1988, 1990; Richard *et al.* 1989). A reentrant corresponding to the Lake McConnell complex had earlier been proposed by Harrison (1972) on the basis of converging striae in the North Bay-Mattawa region.

Part of the Harricana glaciofluvial complex has been referred to as the Matagami or Abitibi esker (Allard 1974; G. Tremblay 1974; Chauvin 1977). Hardy (1976) and Veillette (1983*a*, 1986, 1990) also noted its esker-like characteristics. Indeed, in his thesis Veillette (1990) was moved to describe the Harricana complex, south of latitude 48°N, as "un énorme complexe d'eskers comprenant une grande variété de dépôts fluvioglaciaires" (p. 72), and as "un méga-esker en position interlobaire" (p. 86). Allard (1974) classified segments of the Harricana complex and adjacent eskers between latitudes 48°N and 50°N into 6 morpho-genetic types based on factor analysis: sand plain, De Geer, retrogressive, strandmark, short segments and structurally controlled (Table 5.1; Allard 1974). North of Lake Obalski (latitude 48°45'N, Fig. 5.3), De Geer and strandmark morpho-genetic segments were reported to alternate. This part of the complex was interpreted as a number of time-transgressive subglacial esker segments, with superimposed subaqueous fans and punctuating deltas (Table 5.1; Allard 1974). East and south of Lake Obalski the complex was classified into sand plain, retrogressive and structurally-controlled segments. These segments were suggested to represent a transition from subglacial to supraglacial sedimentation, with some topographic control on deposit location (Table 5.1). Allard suggested that they were indicative of quasi-continuous, yet non-periodic sedimentation. Eskers to the east of the Harricana complex were mostly classified as De Geer type with some retrogressive and sand-plain segments (Allard 1974).

Table 5.1. Morpho-genetic classification of the Harricana glaciofluvial complex between latitudes 50°N and 48°N, after Allard (1974).

Location	Morpho-genetic classification	Description	Interpretation
North of Lake Obalski to latitude 50°N	De Geer	Beaded	Proglacial deltas formed during retreat
	Strandmark	Linear segments with rounded crests, flanking kettles and some flanking aprons of glaciofluvial sediment	Subglacial eskers with superimposed subaqueous fans deposited time-transgressively during ice retreat
	Structurally controlled	Diabase dike just north of Lake Obalski	Structural control on complex location
East of Lake Obalski	Sand plain	Wide segments with low crests	Represents transition between subglacial and supraglacial/subaerial sedimentation
South of Lake Obalski to latitude 48°N	Structurally controlled	Mount Video and surrounding bedrock knobs within dissected Abitibi Uplands	Topographic control on complex location
	Retrogressive	Continuous ridge with high crest and glaciolacustrine wave-reworked sides	Represents transition between subglacial and supraglacial/subaerial sedimentation

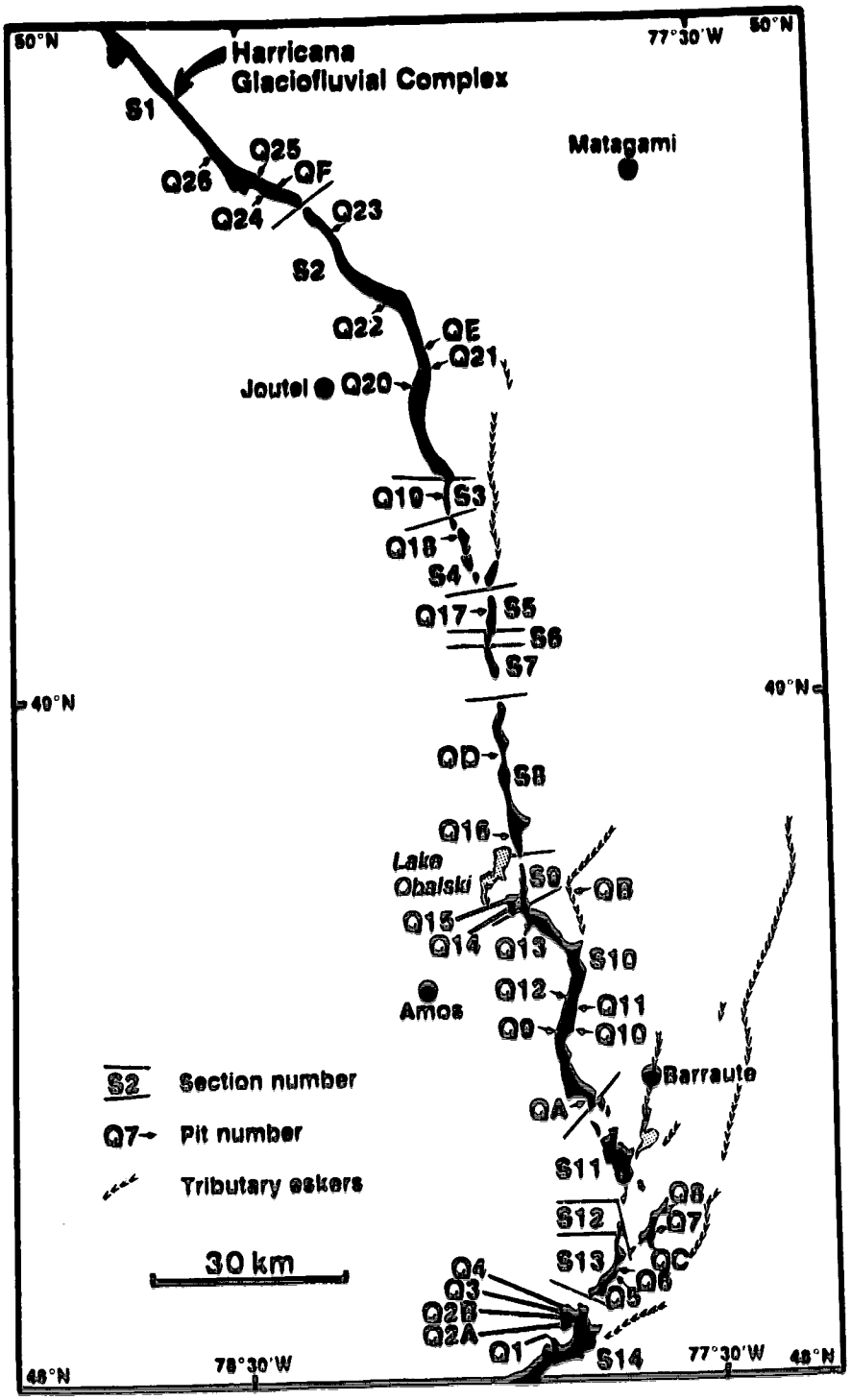

Figure 5.3. Harricana complex divided into depositional segments separated by "gaps". Location of pits, tributary eskers, and Lake Obalski.

While Allard's (1974) classification is based on geomorphic observation, he also presented the most detailed sedimentologic description of the Harricana complex to date. He described stratified and rhythmically bedded sand and gravel, large arched structures in gravel (pseudoanticlinal macroforms (Brennand in press)), and cut-and-fill structures near the surface of the complex. Hardy (1976) stated that the Harricana complex overlies bedrock and underlies Cochrane deposits north of latitude 50°N. Vincent *et al.* (1987) described Cochrane I till overlying stratified sediments as far south as pit Q20 (latitude 49°27'N) in the present study (Fig. 5.3). Further south, Chauvin (1977) suggested that glaciofluvial deposits may overlie glacigenic sediments.

In the context of this previous research the question as to whether the Harricana glaciofluvial complex was synchronously or time-transgressively deposited is central to both a detailed genetic interpretation of the complex itself and to its implications for ice-sheet dynamics. Consequently, expected characteristics of a linear glaciofluvial complex deposited in segments time-transgressively in a reentrant into the ice front, and synchronously in a subglacial conduit are first summarized (Table 5.2).

Morphology, clast characteristics and paleoflow direction estimates

Down-complex trends in morphology, clast characteristics and paleoflow direction estimates are considered and general environmental constraints on sedimentation are proposed. The detailed genesis of the complex is then inferred from its sedimentology.

Morphology

The crest line of the Harricana glaciofluvial complex between the coast of James Bay and latitude 48°N, constructed from contours and spot heights on 1:250 000 scale NTS sheets, rises from north to south (Fig. 5.4). Even at this small scale, the crest line may be described as broadly undulatory. At a larger scale (1: 50 000), most long profile undulations depicted on Figure 5.4 possess their own smaller-amplitude undulations.

Between latitudes 48°N and 50°N the Harricana complex may be split into 14 depositional segments based on air photograph interpretation (Figs. 5.3 and 5.4; Table 5.3). These segments are not identical to those classified by Allard (1974). North of latitude 49°N (segments 1-7, Fig. 5.3) the ridge is mainly relatively high with an undulatory crest line and variable width (Table 5.3). It rises up to 62 m above the surrounding Cochrane terrain and Lake Ojibway clay plain, although this height is generally less than 40 m. Narrow parts of the ridge have rounded crests and side slopes approximating 15° to 20°, locally up to 30° (Allard 1974). Wide sections have broader, flatter crests and side slopes approximating 3° to 10°. Lake-filled depressions ('kettles'?), up to 2 km long and often elongated parallel to the complex, are numerous along its central axis and flanks. Segment lengths range from 1.83 to 56.60 km, with intervening "gap" lengths ranging from approximately 0.50 to 4.47 km. "Gaps" are usually mantled by glaciolacustrine sand, silt and clay, with some organic material (Chauvin 1977). Some

Table 5.2. Expected characteristics[1] of linear synchronous and time-transgressive glaciofluvial deposits.

	Synchronous deposition in a subglacial conduit	Time-transgressive deposition in a reentrant into the ice front
Morphology	Relatively linear accumulation of sediment which may include "gaps" resulting from postdepositional erosion or nondeposition in a continuous conduit Depositional segments not punctuated by deltas or fans although lateral fans may occur Broadening of the deposit towards its downflow end Upslope, level or downslope path	Discrete depositional segments punctuated by deltas or fans; typically beaded morphologic expression Downslope or level path
Down-complex trends in clast characteristics	Lithology: Trends depend upon the sediment source, and may be complicated by a mixture of lateral and local addition of sediment to the system	
	Roundness: *Relatively narrow conduit (upflow)*: Long transport distances and vigorous flows (particularly in a closed conduit) produce high sediment transport rates and low sedimentation rates, such that a mixture of well-rounded (long transport distance) and poorly-rounded (very angular to subrounded; local and laterally derived) clasts are favoured *Broad conduit (downflow)*: Under thinner ice the rate of conduit closure would decrease and the melting rate would adjust accordingly by decreasing flow velocity as the conduit became wider. Also, near a grounding line changes in subglacial water pressure cause local opening and closure of cavities adjacent to conduits. Both circumstances favour lower flow velocities, higher sedimentation rates and poorer clast rounding (a dominance of subrounded clasts).	There should be no gross clast roundness trends down the length of the complex. Rather, each segment should show upflow zones with poor rounding, and the proportion of rounded clasts should increase down-segment. Unless the segments are very long or there are numerous phases of fluvial reworking in a short segment (both of which are unlikely), a time-transgressive complex is unlikely to exhibit well-rounded clasts. In addition, a reentrant environment is by definition subaerial, again suggesting less vigorous flows and favouring poorer clast roundness.
	Sphericity: Trends depend upon the transportational processes and dynamics	
Paleoflow direction estimates	Low variability in paleoflow direction estimates, although variability should increase at lateral fans	High variability in paleoflow direction estimates where segments terminate in fans or deltas
Sedimentology	Minimal postformational disturbance, especially in the central section of the complex, although diapiric intrusion may exist Coarse gravel macroforms along the length of the complex Sand may alternate with gravel facies in vertical section at any location along the complex Sand and silt deposits increase in thickness and frequency downflow, and particularly in proximity to the ice margin or grounding line, where characteristic sedimentological associations related to decelerating flow on entry into a standing-water body may be observed.	Assuming a relatively static ice margin during deposition within a reentrant, the contact between gravel (proximal) and sand (more distal) units should be interfingered in vertical section. The distal ends of each segment should exhibit characteristic sedimentological associations related to decelerating flow on entry into a standing-water body. The nature of the associations will differ as a function of: height of water input, salinity of water body, and sediment concentration of the input.

[1] derived from Banerjee and McDonald (1975), Gorrell and Shaw (1991), and Brennand (in press).

are presently occupied by rivers or lakes (Table 5.3).

In the south (segments 8-14, Fig. 5.3), the complex is generally wider (up to 3.5 km) although its width is variable; some sections are wide (>2 km), low (<10 m above the surrounding Lake Ojibway clay plain) spreads (G. Tremblay 1974), while others form high (>50 m above the surrounding terrain), steep-sided ridges (side slopes up to 17°) (Table 5.3). South of latitude 48°N, its width increases locally to 10 km (Veillette 1986, 1990). Segment are 1.60 to 39.15 km long, with intervening "gap" lengths of 0.18 to 3.19 km. Gaps are mantled by glaciolacustrine sediments and organics, expose bedrock, or are occupied by rivers (Table 5.3). Depressions ('kettles'?) along the central axis of the complex in the south are smaller and less numerous than in the north. Shorelines and spits along the flanks of the complex are more prevalent in the south where sediment was reworked by waves during the Angliers

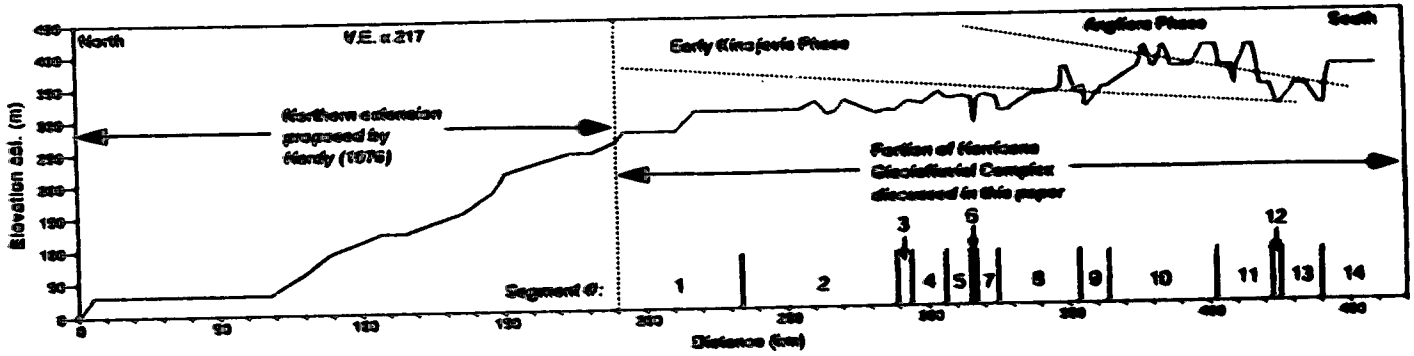

Figure 5.4. Crest long profile along the axis of the Harricana glaciofluvial complex from Point de la Fougère Rouge on the coast of James Bay (51°48'54"N 79°21"18"W) to just south of Val d'Or (48°00'00"N 77°56'30"W), constructed from contours and spot heights on 1:250 000 scale NTS sheets. High-water levels of Angliers and Early Kinojévis phases of Glacial Lake Ojibway approximated from Vincent and Hardy (1979).

Table 5.3. Morphology of the Harricana glaciofluvial complex.

Segment # ordered from north	Associated pits	Length (km)	Width range (km)	Elevation est. (m)[1]	Height above surrounding terrain (m)[1]	Morphologic description	"Gap" length (km) (occupying feature)
1	Q26, Q25, Q24, QF	43.12	0.6-2.0	335 (344)	30 (52)	High, undulatory crest with occasional lateral lobes; side slopes[2] 5°-30°; "kettles" along central axis and flanks	1.16? (none obvious)
2	Q23, Q22, QE, Q21, Q20	56.60	0.4-1.5	320 (344)	45 (55)	High, undulatory crest; variable ridge width; side slopes[2] <5°-16°; "kettles" along central axis but diminishing in number south of pit Q21	0.50 (none obvious)
3	Q19	5.29	0.4-0.5	315 (325)	27 (35)	Short, narrow, undulatory ridge; some "kettles" along central axis; side slopes[2] ~4°	1.00 (none obvious)
4	Q18	11.11	0.5-1.5	320 (331)	30 (41)	Segmented section (~1-3 km segments) dissected by streams; side slopes[2] <7°; elongate lakes adjacent to complex; small "kettles" within complex	2.50 (String of lakes at junction with tributary esker)
5	Q17	6.19	0.3-1.0	323 (340)	23 (40)	Short, narrow ridge, broadening at south end; side slopes[2] 5°-16°	0.80 (River Colgny)
6	None	1.83	~0.5	320 (330)	20 (30)	Short, narrow ridge; side slopes[2] ~5°	0.50 (none obvious)
7	None	5.10	0.4-1.0	325 (340)	25 (40)	Short, narrow, undulatory ridge, broadening and thickening at south end; side slopes[2] 6°-12°	4.47 (none obvious)
8	Q0, Q16	25.17	0.1-2.0	North: 320 (324) South: 366 (391)	North: 15 (19) South: 61 (76)	Wide, low areas connected by narrow, low areas in north ("beaded"); relatively wide and high in south; side slopes[2] 1°-12°; some "kettles" within complex in north, but most lakes adjacent to complex	2.10 (River Obatéki)
9	Q14, Q15	7.05	0.3-0.9	320 (335)	15 (30)	Variable ridge width (lateral fans?); undulatory crest; side slopes[2] ~2.5°	0.70 (none obvious)
10	Q13, Q12, Q11, Q10, Q9, QA	39.15	0.7-2.6	335 (395)	15 (61)	2 streamlined mounds (~5 km long) within complex (? some bedrock association at flank of one), and complex diverted to east of hill. Video bedrock knob; side slopes[2] 4°-17°; shorelines and spit along flank; aeolian dunes adjacent to ridge south of pit Q9	0.80 (Bedrock knobs)
11	Q8, Q7, QC along eastern tributary	17.14	0.5-2.5	365 (395)	45 (75)	Western complex: segmented; diverted and wrapped around bedrock knobs; side slopes[2] 9°-17°; some "kettles" along crest line; fan complex towards south end of segment?. Eastern tributary: exhibits stacked fans and "kettles" along ridge	3.19 (River Senneville)
12	None	1.60	~0.15	335	8	Short, narrow segment; sharp crest	0.18 (River Baudemaque)
13	Q6, Q5	10.76	0.1-2.0	335 (351)	38 (53)	Narrow, undulating ridges connecting expansions in the width of the complex; side slopes[2] 5°-12°; shorelines	2.00 (Val d'Or - some exposed bedrock)
14	Q4, Q3, Q2B, Q2A, C1	17.09+	1.3-3.5	351 (395)	45 (61)	Number of esker ridges within complex, separated by "kettles"; slopes[2] 6°-12°; small bead with contributary and distributary ridges joins complex from east; shorelines; hooked spit	End of NTS sheet 32 C/4

[1] (...) Maximum elevations est. and height above surrounding terrain taken from 1:50 000 scale NTS sheets.

[2] Slopes calculated from contours on 1:50 000 scale NTS sheets.

and Early Kinojévis phases of Glacial Lake Ojibway (Fig. 5.4; Vincent and Hardy 1979).

From the above details the Harricana complex is seen to be a relatively continuous body of glaciofluvial sediment. "Gap" lengths along the complex nowhere exceed 4.5 km, and most are mantled by younger sediments or traversed by streams. Gaps in linear glaciofluvial deposits may result from discontinuous, time-transgressive sedimentation (cf. De Geer 1897), postdepositional erosion (e.g., stream incision), or zones of nondeposition, related to conduit geometry along a synchronously forming deposit (Brennand in press). However, it is by no means certain that all gaps represent sediment discontinuities in this complex. Indeed, both Allard (1974) and Hardy (1976) suggested that some glaciofluvial deposits may be buried by Glacial Lake Ojibway or Tyrrell Sea sediments; locally, glaciolacustrine rhythmites are up to 30 m thick near the Cochrane limit, and Tyrrell Sea sediments are approximately 22 m thick southeast of James Bay (Hardy 1982). Where the complex appears to be dissected by streams and rivers, two explanations are possible: modern drainage may simply be utilizing preexisting gaps or low points; or supraglacial streams may have eroded the complex as the ice surface was lowered (B. Rains personal communication 1992).

Down-complex trends in in situ *clast characteristics*

Clast lithology, roundness, sphericity and shape were recorded from gravel facies exposed in gravel pits along the Harricana glaciofluvial complex. Sample size ranged from 30 to 294 *in situ* clasts per pit; clasts were only taken from gravel facies in fresh vertical exposures. Clast size ranged from pebbles to small boulders (-4.04ϕ to -8.79ϕ), with cobbles (~6.75ϕ) being the most common. Distance from the datum (start of geologic transect, 51°15'N 79°00'W) was measured planimetrically along the axis of the complex for each sample (pit) location.

Clast roundness was determined visually in the field (Powers 1953). For statistical manipulation, the geometric mean of the visual roundness class (Powers 1953) exhibited by each clast was assigned as its roundness value. Maximum projection sphericity (Ψ_p) was calculated from clast axial lengths (Sneed and Folk 1958). Raw data are presented in Appendix 7, and the results of the analyses are presented in Tables 5.4-5.7 and Figures 5.5-5.8. To increase confidence in our interpretations, discussion is mostly limited to the characteristics of the most abundant lithologic classes: granitoid and metabasaltic (Table 5.4; Figs. 5.5 and 5.6). Very few metasedimentary clasts were recorded (Table 5.4); presumably these relatively soft lithologies are poorly preserved (J.J. Veillette personal communication 1993). To provide a context for the interpretation of down-complex trends in clast characteristics the regional bedrock geology is first described.

Bedrock geology of the study area

The Harricana glaciofluvial complex traverses the Abitibi greenstone belt of the Precambrian (Neoarchean) Superior Province (MERQ-OGS 1983). This belt consists of regionally deformed and

Table 5.4. Clast lithology in percent[1] for *in situ* samples from the Harricana glaciofluvial complex.

Pit #	Distance (km)	N	Andesite (AD)	Argillite (AG)	Diorite (D)	Gabbro (GB)	Granodiorite (GD)	Gneiss (GN)	Granite (GT)	Greywacke (GY)	Metabasalt (MB)	Granitoid[A] (GR)
Q1	294.15	120	0.0	0.8 ± 1.6	17.5 ± 6.8	2.5 ± 2.8	41.7 ± 8.8	0.0	0.8 ± 1.6	0.0	36.7 ± 8.6	42.5 ± 8.8
Q3	287.13	180	0.0	0.0	27.2 ± 6.5	0.0	26.7 ± 6.5	0.0	3.9 ± 2.8	0.0	42.2 ± 7.2	30.6 ± 6.7
Q4	286.85	120	0.0	0.0	10.8 ± 5.6	0.0	19.2 ± 7.0	0.0	3.3 ± 3.2	0.0	66.7 ± 8.4	22.5 ± 7.5
Q6	276.62	60	0.0	0.0	26.7 ± 11.2	0.0	20.0 ± 10.1	0.0	3.3 ± 4.5	0.0	50.0 ± 12.7	23.3 ± 10.7
Q8	263.93	120	0.0	0.0	17.5 ± 6.8	0.0	32.5 ± 8.4	0.0	5.8 ± 4.2	0.0	44.2 ± 8.9	38.3 ± 8.7
QA	241.11	60	0.0	8.3 ± 7.0	33.3 ± 11.9	0.0	5.0 ± 5.5	1.7 ± 3.2	5.0 ± 5.5	0.0	46.7 ± 12.6	10.0 ± 7.5
Q11	223.47	120	0.0	7.5 ± 4.7	25.0 ± 7.7	0.0	20.0 ± 7.2	0.0	4.2 ± 3.6	0.0	43.3 ± 8.9	24.2 ± 7.7
Q12	222.95	240	3.8 ± 2.4	9.6 ± 3.7	23.3 ± 5.4	0.0	22.9 ± 5.3	0.0	11.7 ± 4.1	0.0	28.8 ± 5.7	34.6 ± 6.0
Q16	191.99	120	0.0	0.0	28.3 ± 8.1	0.0	37.5 ± 8.7	0.8 ± 1.6	26.7 ± 7.9	0.0	6.7 ± 4.5	64.2 ± 8.6
Q17	153.60	180	1.7 ± 1.9	1.7 ± 1.9	22.8 ± 6.1	0.0	48.3 ± 7.3	0.6 ± 1.1	8.3 ± 4.0	0.0	16.7 ± 5.4	56.7 ± 7.2
Q18	139.86	59	0.0	0.0	37.3 ± 12.3	0.0	30.5 ± 11.7	0.0	8.5 ± 7.1	0.0	23.7 ± 10.9	39.0 ± 12.4
Q19	132.62	60	0.0	0.0	16.7 ± 9.4	0.0	45.0 ± 12.6	1.7 ± 3.2	5.0 ± 5.5	0.0	31.7 ± 11.8	50.0 ± 12.7
Q20	114.05	60	0.0	1.7 ± 3.2	20.0 ± 10.1	0.0	43.3 ± 12.5	0.0	1.7 ± 3.2	0.0	33.3 ± 11.9	45.0 ± 12.6
Q21	109.62	120	0.0	7.5 ± 4.7	29.2 ± 8.1	0.0	15.8 ± 6.5	1.7 ± 2.3	6.7 ± 4.5	0.0	39.2 ± 8.7	22.5 ± 7.5
Q23	80.52	294	0.0	0.0	11.2 ± 3.6	12.6 ± 3.8	43.5 ± 5.7	0.3 ± 0.7	12.9 ± 3.8	0.0	19.4 ± 4.5	56.5 ± 5.7
QF	68.30	60	0.0	0.0	3.3 ± 4.5	15.0 ± 9.0	35.0 ± 12.1	0.0	15.0 ± 9.0	0.0	31.7 ± 11.8	50.0 ± 12.7
Q24	67.59	60	0.0	0.0	8.3 ± 7.0	6.7 ± 6.3	16.7 ± 9.4	0.0	33.3 ± 11.9	3.3 ± 4.5	31.7 ± 11.8	50.0 ± 12.7
Q25	64.68	30	0.0	0.0	20.0 ± 14.3	6.7 ± 8.9	53.3 ± 17.9	0.0	6.7 ± 8.9	10.0 ± 10.7	3.3 ± 6.4	60.0 ± 17.5
Q26	57.19	38	0.0	0.0	15.8 ± 11.6	5.3 ± 7.1	44.7 ± 15.8	0.0	18.4 ± 12.3	0.0	15.8 ± 11.6	63.2 ± 15.3

[A] Granitoid: granite and granodiorite clasts.

[1] Data presentation: % Frequency ± sampling error at 95 % confidence interval. Calculation modified from Dryden (1931) using 95% confidence interval.

Table 5.5. Mean Roundness[1] by lithology for *in situ* clasts from the Harricana glaciofluvial complex.

Pit #	Distance (km)	N	Andesite (AD)	Argillite (AG)	Diorite (D)	Gabbro (GB)	Granodiorite (GD)	Gneiss (GN)	Granite (GT)	Greywacke (GY)	Metabasalt (MB)	Granitoid[a] (GR)
Q1	294.15	120		0.41 ± NS	0.588 ± 0.079	0.517 ± 0.323	0.556 ± 0.054		0.640 ± NS		0.495 ± 0.045	0.561 ± 0.054
Q3	287.13	180			0.580 ± 0.056		0.535 ± 0.052		0.436 ± 0.504		0.468 ± 0.041	0.522 ± 0.047
Q4	286.85	120			0.612 ± 0.096		0.485 ± 0.059		0.400 ± 0.134		0.518 ± 0.038	0.472 ± 0.054
Q6	276.62	60			0.669 ± 0.071		0.533 ± 0.098		0.715 ± 0.245		0.462 ± 0.049	0.559 ± 0.377
Q8	263.93	120			0.608 ± 0.085		0.525 ± 0.054		0.610 ± 0.131		0.551 ± 0.049	0.538 ± 0.050
QA	241.11	60		0.446 ± 0.071	0.575 ± 0.079		0.577 ± 0.306	0.840 ± NS	0.553 ± 0.281		0.479 ± 0.071	0.565 ± 0.186
Q11	223.47	120		0.413 ± 0.073	0.565 ± 0.070		0.609 ± 0.075		0.582 ± 0.206		0.497 ± 0.042	0.604 ± 0.070
Q12	222.95	240	0.506 ± 0.186	0.386 ± 0.053	0.574 ± 0.050		0.561 ± 0.052		0.489 ± 0.054		0.505 ± 0.042	0.537 ± 0.040
Q16	191.99	120			0.595 ± 0.074		0.589 ± 0.064	0.590 ± NS	0.486 ± 0.063		0.515 ± 0.156	0.546 ± 0.047
Q17	153.60	180	0.613 ± 0.244	0.613 ± 0.244	0.713 ± 0.053		0.699 ± 0.035	0.840 ± NS	0.654 ± 0.078		0.606 ± 0.068	0.692 ± 0.032
Q18	139.86	59			0.707 ± 0.059		0.774 ± 0.061		0.740 ± 0.120		0.690 ± 0.097	0.767 ± 0.053
Q19	132.62	60			0.754 ± 0.112		0.652 ± 0.062	0.410 ± NS	0.613 ± 0.244		0.633 ± 0.094	0.648 ± 0.059
Q20	114.05	60		0.590 ± NS	0.783 ± 0.076		0.811 ± 0.031		0.840 ± NS		0.674 ± 0.082	0.812 ± 0.030
Q21	109.62	120		0.697 ± 0.125	0.716 ± 0.057		0.774 ± 0.051	0.410 ± 0.000	0.778 ± 0.080		0.607 ± 0.057	0.775 ± 0.042
Q23	80.52	294			0.812 ± 0.032	0.785 ± 0.040	0.779 ± 0.023	0.590 ± NS	0.728 ± 0.054		0.624 ± 0.052	0.767 ± 0.022
QF	68.30	60			0.840 ± 0.000	0.764 ± 0.102	0.760 ± 0.058		0.606 ± 0.100		0.642 ± 0.086	0.714 ± 0.056
Q24	67.59	60			0.740 ± 0.120	0.643 ± 0.252	0.480 ± 0.081		0.600 ± 0.082	0.500 ± 0.176	0.513 ± 0.083	0.560 ± 0.064
Q25	64.68	30			0.673 ± 0.103	0.840 ± 0.000	0.766 ± 0.068		0.715 ± 0.245	0.367 ± 0.225	0.410 ± NS	0.761 ± 0.064
Q26	57.19	38			0.798 ± 0.082	0.840 ± 0.000	0.653 ± 0.063		0.804 ± 0.070		0.625 ± 0.188	0.697 ± 0.056
GRAND MEAN ROUNDNESS			0.533 ± 0.098	0.469 ± 0.049	0.651 ± 0.018	0.761 ± 0.041	0.654 ± 0.015	0.584 ± 0.142	0.607 ± 0.027	0.420 ± 0.150	0.542 ± 0.014	0.644 ± 0.013

[a] Granitoid: granite and granodiorite clasts.

[1] Data presentation: mean roundness ± 95 % confidence interval for the sample mean.
NS, insufficient data for calculation

Table 5.6. Percent frequency of visual roundness classes by pit for *in situ* clasts from the Harricana glaciofluvial complex.

Pit #	Distance (km)	N	Well Rounded	Rounded	Subrounded	Subangular	Angular	Very Angular
Q1	294.15	120	20.83 ± 3.32	29.17 ± 4.39	39.17 ± 5.47	10.00 ± 1.70	0.83 ± 0.15	0.00
Q3	287.13	180	20.56 ± 2.68	20.56 ± 2.68	42.22 ± 4.69	14.44 ± 1.95	2.22 ± 0.32	0.00
Q4	286.85	120	16.67 ± 2.72	26.67 ± 4.09	46.67 ± 6.10	9.17 ± 1.56	0.83 ± 0.15	0.00
Q6	276.62	60	20.00 ± 4.53	36.67 ± 7.38	36.67 ± 7.38	6.67 ± 1.63	0.00	0.00
Q8	263.93	120	24.17 ± 3.77	27.50 ± 4.19	41.67 ± 5.69	6.67 ± 1.15	0.00	0.00
QA	241.11	60	21.67 ± 4.85	20.00 ± 4.53	45.00 ± 8.44	11.67 ± 2.77	1.67 ± 0.42	0.00
Q11	223.47	120	19.17 ± 3.08	30.83 ± 4.59	37.50 ± 5.30	11.67 ± 1.96	0.83 ± 0.15	0.00
Q12	222.95	240	19.58 ± 2.22	24.58 ± 2.70	41.67 ± 4.03	12.08 ± 1.43	2.08 ± 0.26	0.00
Q16	191.99	120	30.00 ± 4.49	24.17 ± 3.77	25.83 ± 3.98	17.50 ± 2.84	2.50 ± 0.44	0.00
Q17	153.60	180	49.44 ± 5.14	35.00 ± 4.12	11.67 ± 1.60	3.33 ± 0.48	0.56 ± 0.08	0.00
Q18	139.86	59	61.02 ± 9.72	32.20 ± 6.77	5.08 ± 1.26	1.69 ± 0.43	0.00	0.00
Q19	132.62	60	46.67 ± 8.62	26.67 ± 5.78	25.00 ± 5.48	1.67 ± 0.42	0.00	0.00
Q20	114.05	60	73.33 ± 9.59	18.33 ± 4.19	6.67 ± 1.63	1.67 ± 0.42	0.00	0.00
Q21	109.62	120	53.33 ± 6.52	25.83 ± 3.98	15.83 ± 2.60	5.00 ± 0.87	0.00	0.00
Q23	80.52	294	71.77 ± 4.36	16.67 ± 1.74	9.18 ± 1.00	2.38 ± 0.27	0.00	0.00
QF	68.30	60	56.67 ± 9.44	28.33 ± 6.07	13.33 ± 3.14	1.67 ± 0.42	0.00	0.00
Q24	67.59	60	23.33 ± 5.17	38.33 ± 7.62	26.67 ± 5.78	8.33 ± 2.02	3.33 ± 0.83	0.00
Q24	64.68	30	56.67 ± 13.35	30.00 ± 8.98	6.67 ± 2.30	3.33 ± 1.17	3.33 ± 1.17	0.00
Q26	57.19	38	55.26 ± 11.75	34.21 ± 8.82	10.53 ± 3.17	0.00	0.00	0.00

Table 5.7. Mean Sphericity[1] by lithology for *in situ* clasts from the Harricana glaciofluvial complex.

Pit #	Distance (km)	N	Andesite (AD)	Argillite (AG)	Diorite (D)	Gabbro (GB)	Granodiorite (GD)	Gneiss (GN)	Granite (GT)	Greywacke (GY)	Metabasalt (MB)	Granitoid[a] (GR)
Q1	294.15	120		0.637 ± NS	0.693 ± 0.038	0.670 ± 0.115	0.698 ± 0.026		0.781 ± NS		0.682 ± 0.026	0.700 ± 0.026
Q3	287.13	180			0.640 ± 0.028		0.676 ± 0.027		0.631 ± 0.041		0.629 ± 0.019	0.670 ± 0.024
Q4	286.85	120			0.645 ± 0.070		0.664 ± 0.030		0.589 ± 0.121		0.610 ± 0.021	0.653 ± 0.032
Q6	276.62	60			0.684 ± 0.044		0.647 ± 0.050		0.715 ± 0.013		0.691 ± 0.033	0.657 ± 0.045
Q8	263.93	120			0.670 ± 0.041		0.684 ± 0.028		0.636 ± 0.104		0.647 ± 0.030	0.677 ± 0.029
QA	241.11	60		0.574 ± 0.085	0.631 ± 0.038		0.672 ± 0.091	0.787 ± NS	0.591 ± 0.151		0.612 ± 0.047	0.632 ± 0.086
Q11	223.47	120		0.605 ± 0.036	0.691 ± 0.032		0.700 ± 0.036		0.732 ± 0.073		0.679 ± 0.025	0.706 ± 0.032
Q12	222.95	240	0.658 ± 0.043	0.645 ± 0.045	0.709 ± 0.023		0.723 ± 0.020		0.709 ± 0.034		0.658 ± 0.022	0.719 ± 0.018
Q16	191.99	120			0.701 ± 0.029		0.704 ± 0.026	0.622 ± NS	0.677 ± 0.041		0.675 ± 0.067	0.692 ± 0.023
Q17	153.60	180	0.508 ± 0.042	0.679 ± 0.214	0.707 ± 0.029		0.713 ± 0.018	0.800 ± NS	0.682 ± 0.043		0.652 ± 0.034	0.709 ± 0.017
Q18	139.86	59			0.628 ± 0.049		0.716 ± 0.044		0.699 ± 0.156		0.588 ± 0.059	0.710 ± 0.046
Q19	132.62	60			0.644 ± 0.090		0.702 ± 0.029	0.708 ± NS	0.683 ± 0.017		0.607 ± 0.052	0.700 ± 0.027
Q20	114.05	60		0.764 ± NS	0.703 ± 0.043		0.751 ± 0.029		0.682 ± NS		0.714 ± 0.039	0.748 ± 0.028
Q21	109.62	120		0.699 ± 0.062	0.660 ± 0.044		0.702 ± 0.038	0.628 ± 0.150	0.712 ± 0.061		0.644 ± 0.030	0.705 ± 0.032
Q23	80.52	294			0.696 ± 0.032	0.658 ± 0.029	0.705 ± 0.015	0.634 ± NS	0.710 ± 0.029		0.620 ± 0.028	0.706 ± 0.014
QF	68.30	60			0.797 ± 0.063	0.633 ± 0.055	0.743 ± 0.035		0.713 ± 0.031		0.600 ± 0.043	0.734 ± 0.026
Q24	67.59	60			0.791 ± 0.074	0.551 ± 0.193	0.677 ± 0.094		0.720 ± 0.033	0.481 ± 0.095	0.620 ± 0.055	0.708 ± 0.036
Q25	64.68	30			0.712 ± 0.066	0.818 ± 0.023	0.712 ± 0.048		0.729 ± 0.108	0.553 ± 0.197	0.533 ± NS	0.714 ± 0.044
Q26	57.19	38			0.682 ± 0.066	0.651 ± 0.234	0.704 ± 0.051		0.767 ± 0.076		0.619 ± 0.103	0.723 ± 0.043
GRAND MEAN SPHERICITY			0.621 ± 0.051	0.645 ± 0.029	0.680 ± 0.010	0.653 ± 0.027	0.704 ± 0.007	0.687 ± 0.067	0.696 ± 0.014	0.524 ± 0.117	0.642 ± 0.009	0.702 ± 0.006

[a] Granitoid: granite and granodiorite clasts.

[1] Data presentation: mean sphericity ± 95% confidence interval for the sample mean.

NS: insufficient data for calculation

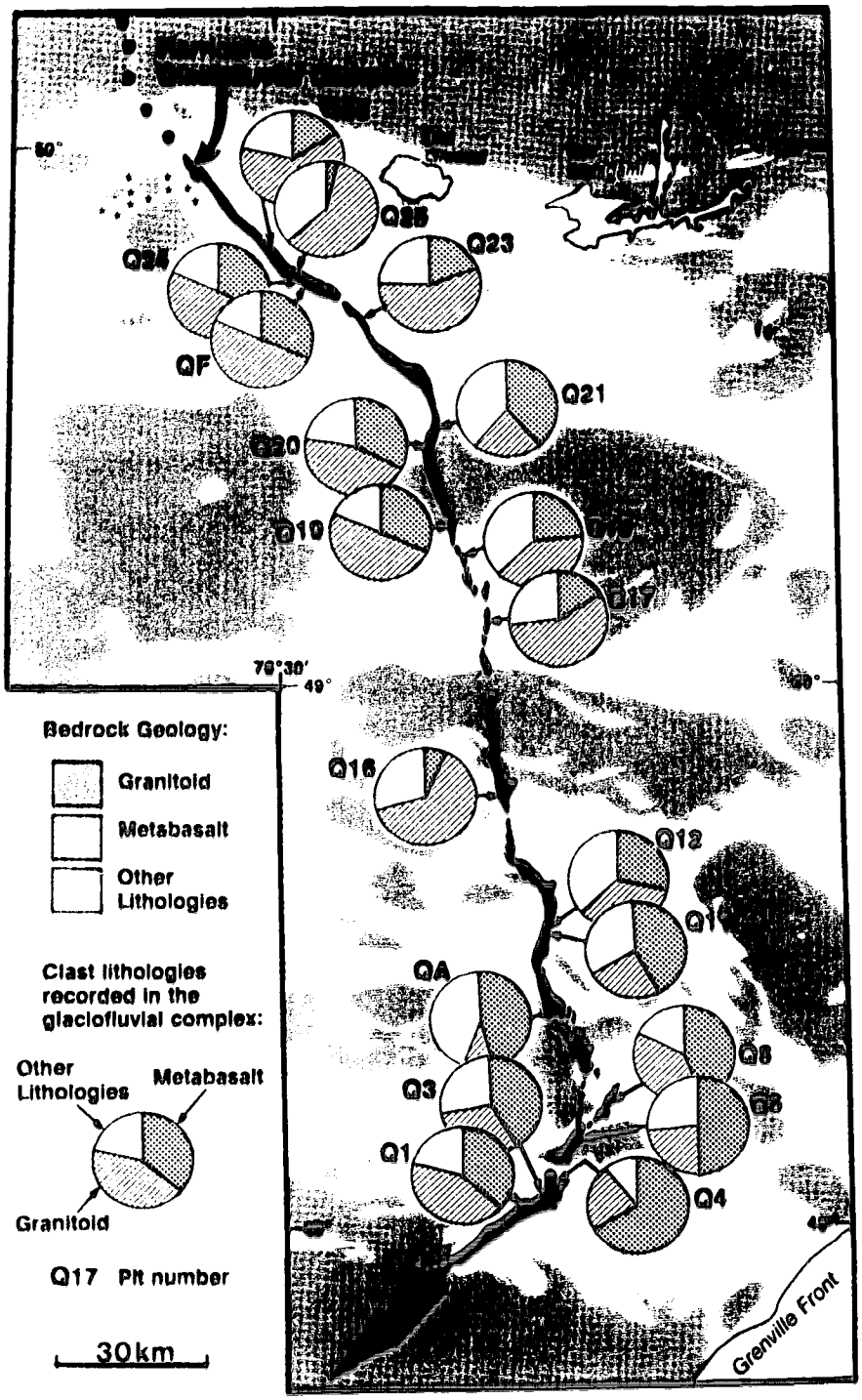

Figure 5.5. Proportion of clast lithologies from *in situ* samples recorded in the Harricana glaciofluvial complex presented as pie graphs (see Table 5.4 for percentage values and 95% confidence limit sampling errors) and superimposed over adjacent Abitibi sub-province (Superior province) bedrock geology (modified from MERQ-OGS 1983). Stars are location of gabbroic bedrock discussed in the text.

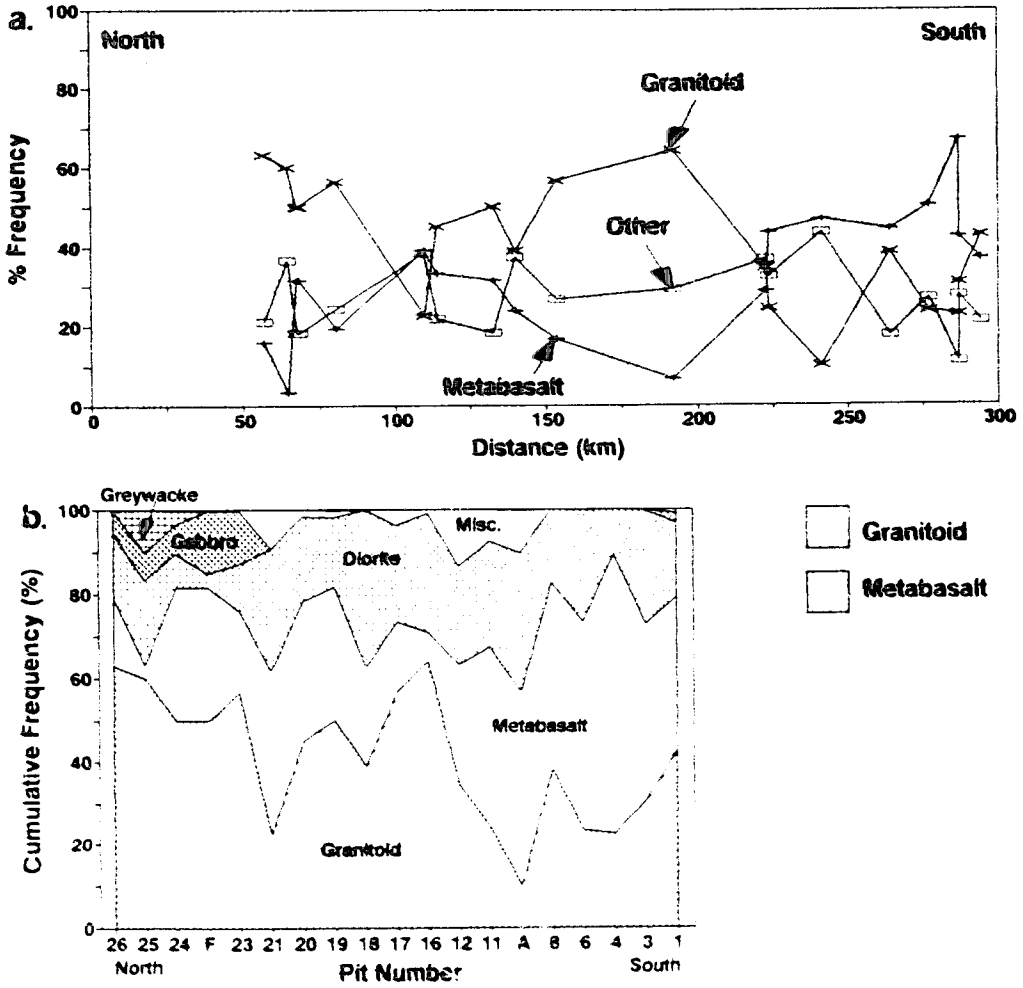

Figure 5.6. *a*. Percent frequency of granitoid and metabasaltic clasts in *in situ* samples superimposed over bedrock geology along the axis of the Harricana glaciofluvial complex. Geologic transect starts at 51°15′N 79°00′W and ends at 48°01′N 77°06′W. *b*. Cumulative frequency of lithologies recorded in each pit (prefixed with "Q" in text) presented in downflow order. See Table 5.4 for numeric data and confidence intervals. Lines connecting points are not meant to imply continuous variation, but merely to aid visual interpretation.

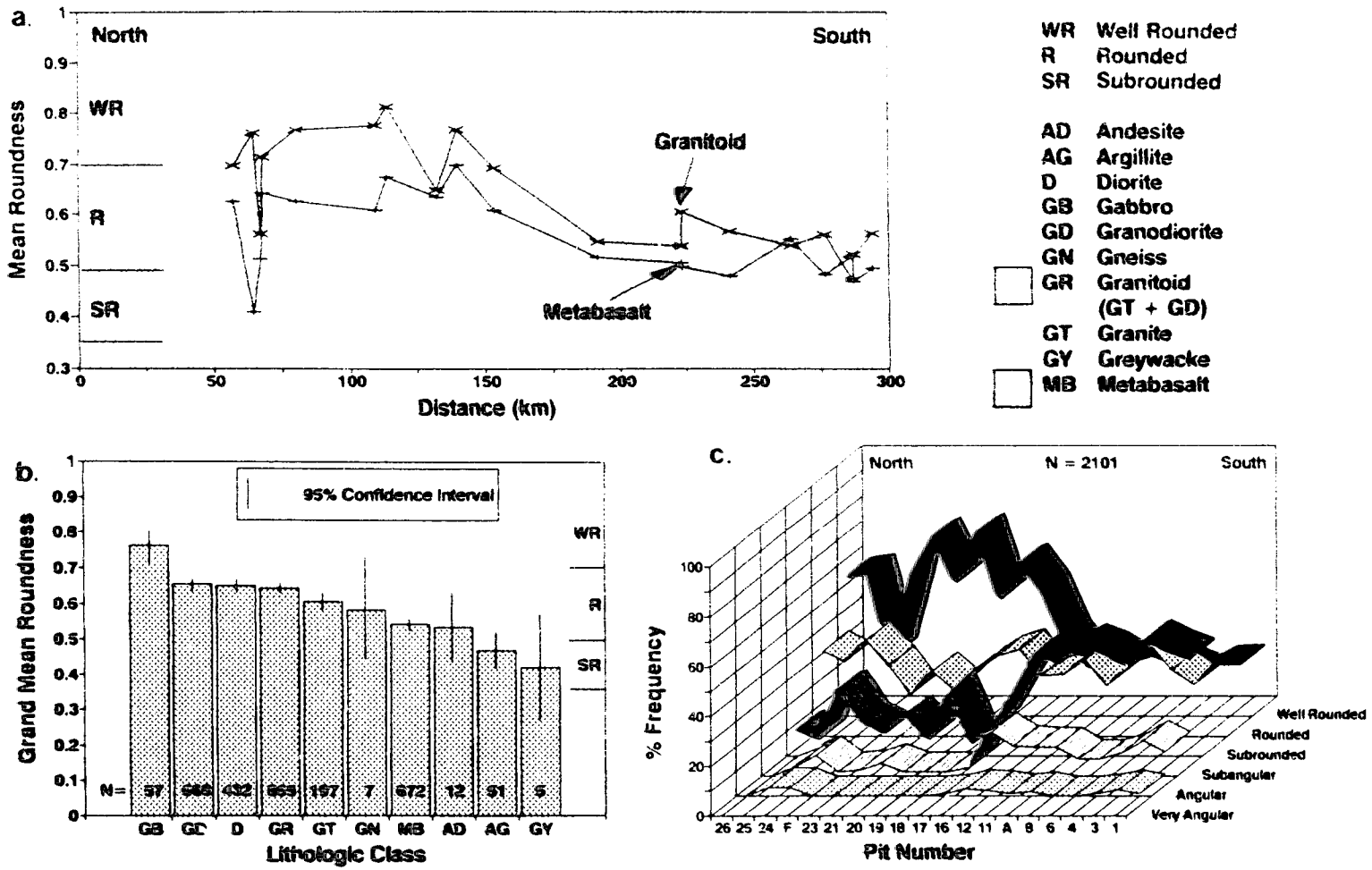

Figure 5.7. *a*. Downflow trend in the mean roundness (Powers 1953) of granitoid and metabasaltic clasts in *in situ* samples; geologic transect same as Figure 5.5. *b*. Grand mean roundness for each lithologic class recorded. *c*. Frequency of occurrence of each visual roundness class by pit. Pits (prefixed with "Q" in text) arranged in downflow order. See Tables 5.5 and 5.6 for numeric data and confidence intervals. Lines connecting points are not meant to imply continuous variation, but merely to aid visual interpretation.

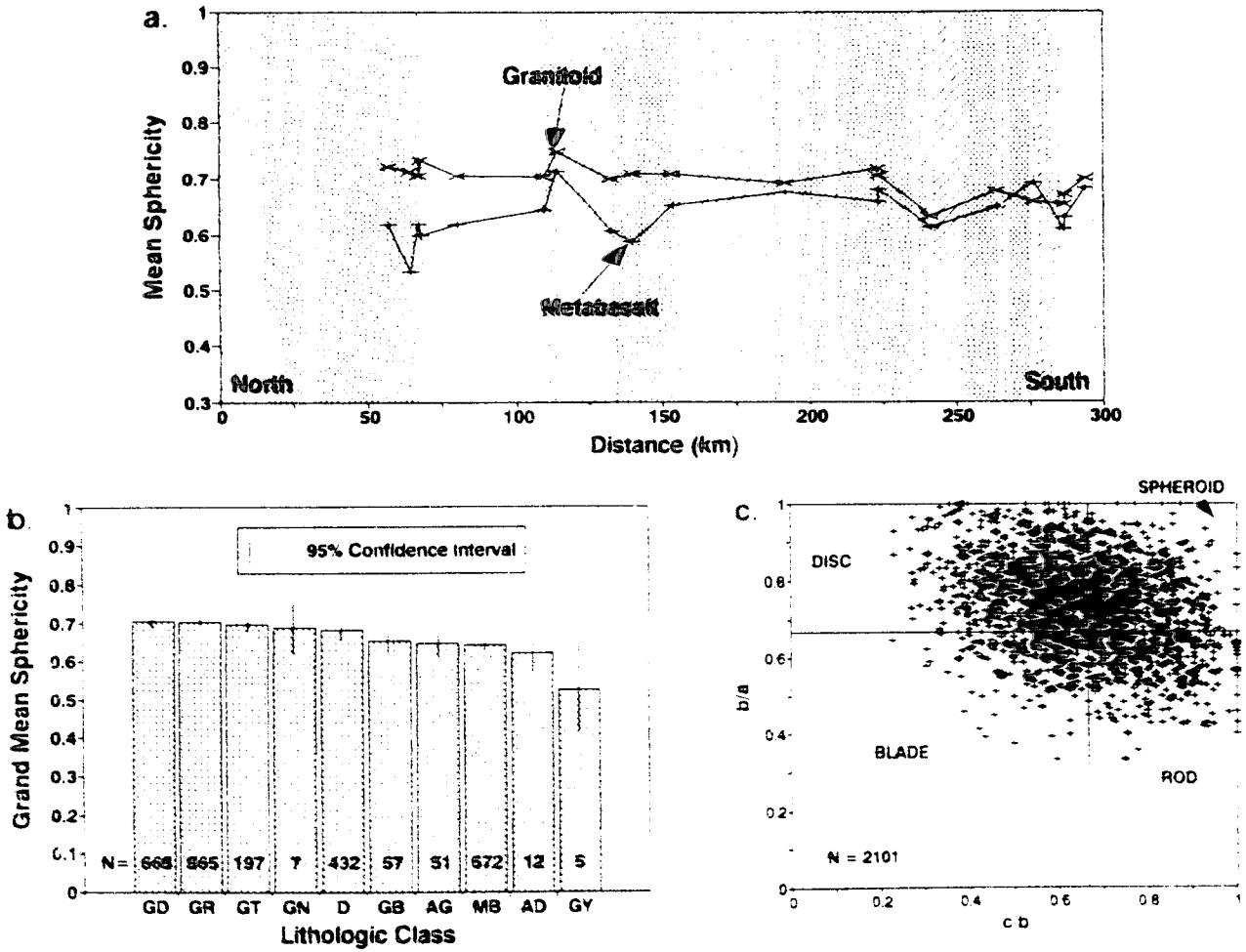

Figure 5.8. *a*. Downflow trends in the mean sphericity (Ψ_p, Sneed and Folk 1958) of granitoid and metabasaltic clasts in *in situ* samples; geologic transect same as Figure 5.5. Lines connecting points are not meant to imply continuous variation, but merely to aid visual interpretation. *b*. Grand mean sphericity for each lithologic class recorded. See Table 5.7 for numeric data and confidence intervals, and Figure 5.7 for legend. *c*. Zingg (1935) shape classification for all clasts measured. a, clast long axis; b, clast intermediate axis; c, clast short axis.

metamorphosed volcanic and sedimentary rocks (e.g., basalts, gabbros, andesites, gneisses). Granitoid intrusions occur as discrete batholiths (Fig. 5.5). Numerous younger Precambrian diabase dikes transect the region. Precambrian (Neoarchean) granitoid and metasedimentary (gneisses, wackes, siltstones) rocks of the Opatica subprovince occur north of the Abitibi Subprovince. Paleozoic (Silurian) rocks (carbonates, sandstones, shales and conglomerates) occur in the James Bay Lowland, further north. Pitted greywackes, or "Omars", from the Omarolluk Formation outcrop on the Belcher Islands, southeastern Hudson Bay (cf. Prest and Nielsen 1987; Prest 1990).

Clast lithology

Metabasaltic and granitoid clasts dominate gravel lithologies in the Harricana complex (Figs. 5.5 and 5.6; Table 5.4). Other than at pit Q21 where metabasalt is the local bedrock, granitoid clasts dominate clast counts in the northern part of the complex, while metabasaltic clasts dominate the complex south of pit Q11 (Figs. 5.5 and 5.6; Table 5.4). The preponderance of granitoid clasts in the north and of metabasaltic clasts in the south follows trends in the regional bedrock geology in the vicinity of the complex (Fig. 5.5). It may also reflect long transport distances and vigorous flows in the north, and shorter transport distances and less vigorous flows in the south; metabasaltic clasts would have undergone greater attrition than granitoid clasts in vigorous flows over long transport distances.

Interpretation of clast counts recorded in individual pits with respect to local bedrock geology is more difficult. Explanation must relate to the source of Harricana glaciofluvial sediment. Sediment deposited within a subglacial conduit system or a reentrant may be derived by: erosion of bedrock or sediment by flowing water; meltout from debris-rich ice in the channel walls (and roofs of conduits); squeezing-in of adjacent deformable substrate (Shoemaker 1986; Shoemaker and Leung 1987; Alley 1992); flushing of stored sediment from adjacent cavities; or fluvial reworking of sediment within a conduit or reentrant (cf. Brennand in press). If sediment was derived from erosion of bedrock upflow and reworking of that sediment by fluvial processes alone, then peaks in a particular lithology may be expected in the vicinity of and just downflow from its local bedrock source. Most relatively high granitoid clast counts occur where the complex overlies granitoid bedrock, or just downflow (south) of a granitoid bedrock source (Figs. 5.5 and 5.6). However, some small peaks occur in locations where granitoid bedrock does not underlie, nor is immediately upflow from the sample location (Fig. 5.6). This observation may be explained by the derivation of granitoid clasts from adjacent bedrock, surrounding debris-rich ice, or adjacent or underlying glacigenic sediment. In this regard, if gabbroic clasts present in some northern pits originated directly from a local bedrock source, lateral transport of sediment to the Harricana complex must have occurred; gabbroic bedrock is present adjacent to, but not below, the complex in the north (pits Q23 to Q26; stars, Fig. 5.5). During an investigation of boulder transport in the James Bay Lowlands, Bouchard and Salonen (1989) recorded a boulder lithology count from the surface of the Harricana complex, approximately 1 km south of pit Q23 (Fig. 5.5). Using the transport

distance distribution method, they suggested that a high chi-square value for the sample indicated a wide range of dispersal directions. This corroborates the inference of lateral transport of sediment into the Harricana complex proposed here.

The downflow transport distance of a particular lithology from its bedrock source depends on the duration and vigour of the transporting flow and the rate of sedimentation or burial. Sediment cover or nonerosional flows may explain observations such as relatively low counts of metabasaltic clasts despite a local metabasaltic bedrock (e.g., pits Q17 to Q19, Figs. 5.5 and 5.6; Table 5.4).

The presence of pitted greywackes from the Omarolluk Formation ("Omars", cf. Prest and Nielsen 1987; Prest 1990) in southeastern Hudson Bay, in some northern pits (pits Q24 and Q25; Fig. 5.6*b*; Table 5.4) deserves comment. Omars have not been observed within the Matheson or New Quebec tills which lie adjacent to the Harricana complex for most of its length (Veillette 1990). However, Hardy (1976) suggested that the complex extended to the chain of islands in James Bay, approximately 250 km south of the Belcher Islands. Glacial transport followed by glaciofluvial transport of "Omars" from the Belcher Islands may account for their presence in the northern part of the Harricana complex.

The complicated spatial distribution of bedrock lithologies in the Abitibi region and uncertainty as to whether the source material was bedrock or glacigenic sediment limit the potential for interpretation of lithologic frequency data alone to assist in differentiation between time-transgressive and synchronous sedimentation of the Harricana complex. However, knowledge of lithologic variation from pit to pit is a necessary precursor to roundness and sphericity investigations (cf. Sneed and Folk 1958). In addition, clast lithology counts suggest lateral transport of sediment into the Harricana complex and provide some insight into possible sediment sources.

Clast roundness

Grand mean roundness values for all clasts, irrespective of lithology, range from subrounded to well rounded (Fig. 5.7*b*; Tables 5.5 and 5.6; Powers 1953). This is consistent with fluvial transport processes (Sneed and Folk 1958). Granitoid clasts are well rounded to rounded north of pit Q17, and rounded to subrounded south of pit Q12 (Fig. 5.7*a*; Table 5.5). Although mean roundness in metabasaltic clasts is generally lower than that of granitoid clasts, similar trends also occur; in general, metabasaltic clasts have mean roundness values >0.6 in the north and <0.6 in the south (Fig. 5.7*a*; Table 5.5). For both lithologies, the change in mean roundness classification occurs between pits Q17 and Q12 (Fig. 5.3). Similar trends are observed in the full data set, disregarding clast lithology (Fig. 5.7*c*; Table 5.6). The break in roundness classification coincides with a gross change in the width of the complex (Fig. 5.3; Table 5.3).

The morphology of the northern part of the Harricana complex suggests a relatively narrow

conduit. Vigorous transport and relatively long distances of transport, in association with low sedimentation rates, promoted greater rounding. The high roundness values for the northern part suggest relatively high velocities which also give rise to the inferred transport characteristics. The relatively narrow and uniform width of the northern part of the complex indicates that, despite increasing discharge downflow, the closure rate resulting from ice thickness was sufficiently high to maintain a narrow conduit and sufficiently uniform that there was no appreciable increase in width over a long distance. Note that a downstream increase in discharge and decrease in ice thickness should result in an increase in conduit width.

By contrast, the southern part of the complex is often wider than the northern part. As there is no reason why discharge should have dramatically increased, it is probable that ice thickness was decreasing. This is to be expected as the margin of an ice sheet is approached. Thus, the widening to the south perhaps indicates that the closure rate decreased and the melting rate was adjusted accordingly by decreasing velocity as the conduit became wider. In addition, sedimentologic evidence (preserved later) suggests that the ice sheet was probably close to floatation near to a grounding line. In such an environment changes in subglacial water pressure cause local opening and closure of cavities adjacent to conduits (Gorrell and Shaw 1991). Both arguments favour southward increases in sedimentation and decreases in transport distance and vigour. The decreased roundness in the southern portion of the complex is explained by this combination of circumstances producing a less efficient system.

Thus, the characteristics of the complex in the north are best explained by deposition under thick ice with a relatively low surface gradient. In the south, the morphology and clast roundness suggest deposition under thinner ice in proximity to a grounding line. This makes most sense if the northern and southern parts were formed synchronously beneath an ice sheet; their characteristics are related simply to their distance from the grounding line. In an alternative recessional model, a conduit with the characteristics of the southern part should progressively develop northwards and the northern and southern parts of the complex would have similar characteristics. This is clearly not the case and we reject the recessional model in favour of a continuous and synchronous conduit with nonuniform downflow geometry.

Clast sphericity and shape

Previous research has suggested that clast sphericity is primarily governed by lithology and grain size (Sneed and Folk 1958). The mean maximum projection sphericity (Ψ_p, Sneed and Folk 1958) of clasts at a particular pit, and the grand mean Ψ_p of clasts grouped by lithology remain relatively constant down-complex (~0.6), irrespective of lithology (Figs. 5.8*a* and 5.8*b*; Table 5.7). The affect of grain size at 0.5ϕ intervals on the sphericity of both granitoid and metabasaltic clasts was investigated. Such trends as larger clasts having lower Ψ_p (cf. Sneed and Folk 1958) and down-complex changes were explored

and none was obvious. Our data suggest that grain size, in the cobble range, did not govern Ψ_p. However, these tests are not rigorous because sample numbers were small and confidence limits large; consequently, this analysis is not presented.

Relatively constant mean Ψ_p down-complex, irrespective of lithology and possibly grain size, may indicate that all clasts have not travelled far (Sneed and Folk 1958). This conclusion may be consistent with a segmental, time-transgressive origin for the Harricana complex. But, Sneed and Folk (1958) demonstrated that, irrespective of lithology, clasts which are close to their source showed similar shape. Plotting all clast shape data on a simple Zingg diagram (Fig. 5.8c; Zingg 1935) illustrates a wide divergence of form: spheroids, discs, rods and blades are represented. In a continuous conduit a relatively constant Ψ_p suggests that 'terminal' sphericity was achieved rapidly for any particular lithology with respect to a particular transport process or set of processes. Once this was achieved the clasts did not become more spheroidal. Changes in transport processes for individual clasts (tractional rolling, saltation and suspension) as indicated by gravel fabrics and transport orientation data (presented later) may complicate downflow sphericity trends. That is, if a clast was only rolled downflow it may be expected to become increasingly prolate. However, this tendency would be disrupted if flow conditions resulted in periodic saltation or suspension transport.

Generally, this investigation suggests that sphericity is less informative than roundness with respect to differentiating deposition in time-transgressive segments and synchronously down-complex. Clast sphericity and shape are related more to transportational processes and dynamics than to gross depositional environment.

Paleoflow direction estimates

Paleoflow direction measurements were recorded from gravel fabrics (clast ab-planes; Appendix 8) and cross-bedded and cross-laminated sand (Appendix 9) along the length of the Harricana complex (Figs. 5.9 and 5.10; Tables 5.8 and 5.9). Mean paleoflow directions, or flow azimuths, were determined from bulk measurements on gravel clasts or sand structures; they do not necessarily represent measurements from a single unit within a pit. The number of measurements at one pit range from 30 to 170 for gravel fabrics and from 5 to 110 for cross beds and cross laminations in sand (Tables 5.8 and 5.9). Statistically all flow azimuths are unidirectionally significant at the 99% level (Tables 5.8 and 5.9).

Gravel fabrics

Fabrics were measured in a variety of gravel facies: plane bedded; imbricate, polymodal; bimodal, massive, clast-supported (in large-scale, downflow-dipping, rhythmically-graded, tabular beds); and heterogeneous, unstratified (Table 5.8), many of which were components of composite macroforms (Brennand in press). Fabrics were also measured in oblique accretion avalanche bed macroforms (pits Q3 and Q4; Fig. 5.9), in the downflow accretion avalanche beds of what may be a composite macroform

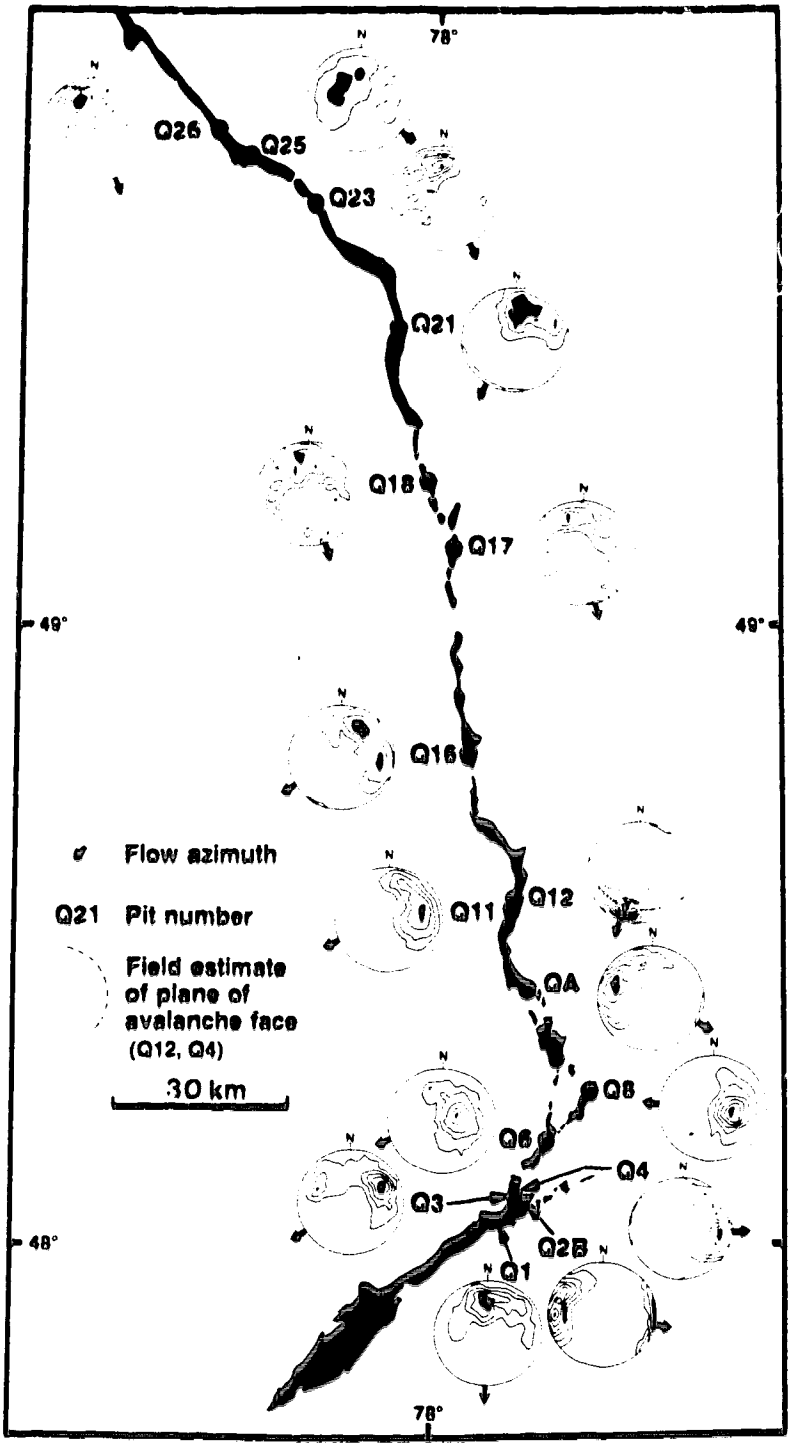

Figure 5.9. Paleoflow direction estimates from gravel fabric measurements. Fabrics displayed as equal area lower hemisphere plots. Statistics presented in Table 5.8.

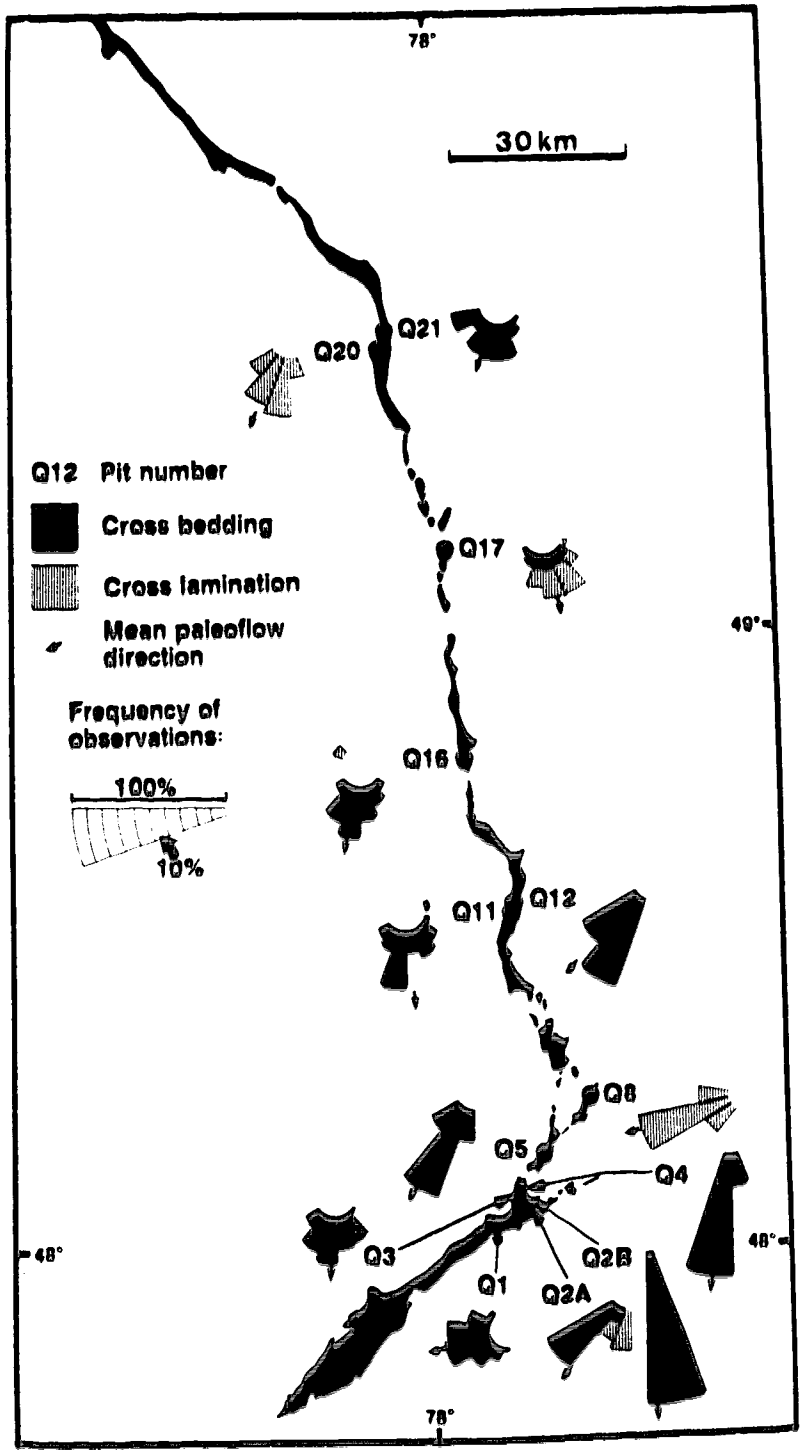

Figure 5.10. Paleoflow direction estimates from cross-bed and cross-lamination measurements in sand. Statistics presented in Table 5.9.

Table 5.8. Gravel fabric statistics.

Pit #	Sedimentary Facies/Structures	Sample Number	Flow Azimuth	Mean Dip	Vector Strength (S_1)	Significance Level[1]
Q1	Plane-bedded gravel	120	183°	44°	0.5870	99.0%
Q2B	Imbricate, polymodal fine gravel	60	100°	16°	0.7762	99.0%
Q3	Alternating oblique accretion avalanche bed macroform ('flipped' clasts[2] from both east and west sets)	120	238°	41°	0.5477	99.0%
Q4	Oblique accretion avalanche bed macroform; east side of complex ('parallel' clasts[3])	42	(271°) 91°	28°	0.7431	99.0%
Q6	Bimodal, massive, clast-supported gravel from large-scale, downflow-dipping, rhythmically-graded beds ('flipped' clasts)	60	250°	67°	0.6465	99.0%
Q8	East side of pseudoanticlinal macroform	60	275°	56°	0.7031	99.0%
QA	Heterogeneous, unstratified gravel	60	115°	37°	0.6397	99.0%
Q11	Imbricate, polymodal, matrix-rich gravel	60	246°	41°	0.6485	99.0%
Q12	Large cross-bedded gravel or south-dipping avalanche beds of macroform ('parallel' clasts[3])	97	(8°) 188°	33°	0.8158	99.0%
Q16	Heterogeneous, unstratified gravel	60	240°	38°	0.5573	99.0%
Q17	Bimodal, massive, clast-supported gravel from large-scale, downflow-dipping, rhythmically-graded beds ('flipped' clasts)	60	163°	36°	0.5318	99.0%
Q18	Heterogeneous, unstratified gravel	149	161°	41°	0.5176	99.0%
Q21	Imbricate gravel lag	63	181°	37°	0.5663	99.0%
Q23	Upflow-inclined, plane-bedded gravel	160	143°	39°	0.5848	99.0%
Q25	Bimodal, massive, clast-supported gravel from exposure-scale, downflow-dipping, rhythmically-graded beds ('flipped' clasts)	30	126°	59°	0.4870	99.0%
Q26	Heterogeneous, unstratified gravel; imbricate, polymodal, matrix-rich coarse gravel	170	157°	42°	0.7001	99.0%

[1] Significance level of sample being non-random, according to test statistic (S_1/S_2) of Woodcock and Naylor (1983).
[2] Clast ab-planes dip upflow with respect to the field estimated avalanche face
[3] Clast ab-planes dip downflow and are approximately parallel to the field estimated avalanche face. Flow azimuth (no brackets) assumed to be 180° to azimuth if imbrication inferred (brackets).

(pit Q12; Fig. 5.9), and in a pseudoanticlinal macroform (pit Q8; Fig. 5.9). Paleoflow estimates are unidirectional with a component towards the south (Table 5.8; Fig. 5.9). However, unless macroform type is known for gravel fabric measurements, flow azimuths can be misleading. Paleoflows from gravel fabric measurements in pseudoanticlinal macroforms were downflow and converge on the crest of the complex (cf. Brennand in press). Thus, the disparity between the orientation of the complex axis and the flow azimuth for pit Q8 occurs because the fabric was measured on clasts to the east of the axis of a pseudoanticlinal macroform (Table 5.8; Fig. 5.9). Conversely, paleoflow estimates (flow azimuths) from oblique accretion avalanche bed macroforms are downflow and diverge from the axis of the complex (Brennand in press), and those from downflow accretion avalanche beds are downflow and parallel to the axis of the complex (Table 5.8; Fig. 5.9).

Measurement and interpretation of gravel fabric from oblique or downflow accretion avalanche beds is complicated. For the most part these avalanche beds are like large gravel cross beds (Fig. 5.11). It was tempting to estimate flow direction simply from the maximum dip direction of the avalanche face. However, the large size of the macroform, in excess of 10 m in vertical exposure within a single form,

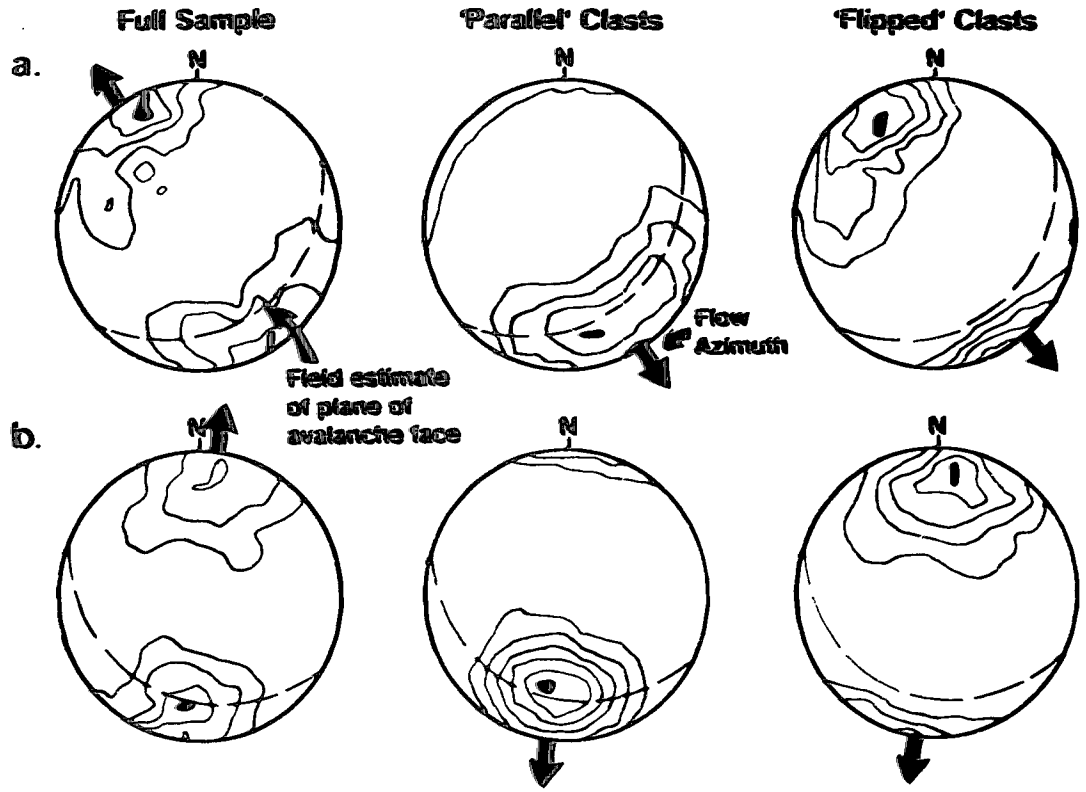

Figure 5.11. Examples of gravel fabric plots for southeast dipping cross-bedded gravel (*a*. Q23/1-1) and a large downflow dipping avalanche bed macroform (*b*. Q12/1-1aLHS) with 'parallel' and 'flipped' clasts. All plots are equal area lower hemisphere projections. Statistics presented in Table 5.11.

Table 5.9. Paleoflow direction statistics derived from cross-bed and cross-lamination measurements.

Pit Number	Sample Number (n)	Vector Mean ($\bar{\theta}$)	Mean Resultant Magnitude ($\bar{R}$)[1]	Standard Error ($S_{\bar{\theta}}$)	Approximate deviation of $\bar{\theta}$ from the axis of the complex
Q1	80	257°	0.9138	2.7700°	17°
Q2A	6	177°	0.9979	3.3035°	7°
Q2B	18	219°	0.9596	3.8585°	49°
Q3	65	187°	0.9957	3.0868°	7°
Q4	15	189°	0.9917	2.0958°	19°
Q5	5	211°	0.9787	5.1594°	9°
Q8	5	253°	0.9622	7.3109°	48°
Q11	34	176°	0.8422	5.7404°	24°
Q12	10	222°	0.9876	2.5721°	22°
Q16	65	191°	0.8059	4.5703°	31°
Q17	110	168°	0.9299	2.0789°	1°
Q20	31	204°	0.9561	2.9455°	19°
Q21	45	200°	0.8579	4.6631°	10°

[1] All samples show a preferred trend at $\alpha = 0.01$. Significance level (α) determined from critical values of $\bar{R}$ for Rayleigh's test for the presence of a preferred trend (Curray 1956; Davis 1986).

renders such estimates difficult and uncertain. Consequently, field estimates of the plane of the avalanche face were recorded, and clast fabric was measured independently. The results of this procedure are presented for large gravel cross beds and downflow accretion avalanche beds (Fig. 5.11). Lower hemisphere stereonets display two discrete clast populations: clasts approximately parallel to the estimated plane of the avalanche face, both in dip and azimuth, and clasts which are 'flipped' and dip upflow at a high angle relative to the avalanche face (Fig. 5.11; cf. Rust 1984). 'Parallel' clasts slid down the avalanche face, whereas 'flipped' clasts may record imbricate clusters, or clasts which were reoriented (flipped up) by return eddies or secondary vortices in the lee of the avalanche face (cf. Shaw and Gorrell 1991). Gravel fabrics from 'flipped' clasts were measured from both east and west sides of an alternating oblique accretion avalanche bed macroform at pit Q3. By combining these two opposing data sets, a complex-parallel flow azimuth results (Fig. 5.9; Table 5.8).

At first glance paleoflow direction estimates from gravel fabrics appear to fall into two groups. North of pit Q17 flow directions closely follow the axis of the complex, and deposition within an ice-walled channel is favoured. At pits Q23 and Q18 (Fig. 5.9), imbricate gravel fabrics were measured in composite macroforms (Brennand in press). South of pit Q17 flow directions diverge more from the axis of the complex. Here, deposition within a less confined, broad conduit or reentrant may be inferred. However, the apparent paleoflow divergence in pits Q8 and Q4 is related to the processes responsible for the formation of particular gravel macroforms. It is possible that apparent paleoflow

divergence at other southern pits may also be related to large three-dimensional gravel macroforms, however, exposure was not extensive enough to identify such forms at these pits. Gravel fabric at pit Q2B was measured in an in-phase wave structure, later attributed to deposition in a grounding-line environment.

If gravel structure is accounted for in terms of bedforms and macroforms (discussed later; Brennand, in press), paleoflow estimates from gravel fabrics are unidirectional towards the south and favour deposition in an ice-walled channel, either a subglacial conduit (cf. Brennand, in press) or tightly constrained reentrant (cf. Cheel 1982).

Cross-bedded and cross-laminated sand

Mean paleoflow direction estimates from cross-bedded and cross-laminated sand are again strongly unidirectional; estimates are generally within 30° of the orientation of the axis of the complex (Table 5.9; Fig. 5.10). At pit Q16 (Fig. 5.10), paleoflow direction measurements in cross-laminated sand were from regressive ripples in the lee of a dune. Paleoflow direction estimates suggest a relatively constrained depositional environment and unidirectional formative flow along the length of the complex. Measurements at pits Q2B, Q4 and Q16 (Fig. 5.10; Table 5.9) were made in subaqueous fans or grounding-line deposits (discussed later).

Environmental constraints inferred from down-complex trends

Inferences from clast lithology counts suggest lateral transport of sediment into the Harricana complex, delivered by tributary conduits or transported in ice or by local deformation of adjacent sediment into the Harricana or tributary conduits. Relatively constant clast sphericity, irrespective of lithology and possibly grain size, suggests continual changes in the mode of transportation of clasts within the complex. Clast lithology and sphericity are not readily interpreted in terms of gross depositional environment along the complex.

Segmental trends in morphology, clast roundness and paleoflow direction estimates (cf. Table 5.2) were not detected in the portion of the Harricana glaciofluvial complex studied. Rather, the complex is shown to be a relatively continuous body of upsloping glaciofluvial sediment which increases in width downflow towards an ice margin or grounding line. Although gaps in the complex may be attributed to time-transgressive sedimentation, nondeposition within a continuous conduit or post-depositional erosion are preferred explanations: a down-complex decrease in clast mean roundness and low variability in paleoflow direction estimates favour synchronous deposition in a subglacial conduit. As the Harricana complex follows an upslope path (Fig. 5.4), meltwater within the "Harricana conduit" must have been under hydrostatic pressure; this necessitates subglacial, closed-conduit conditions (Shreve 1972), and reinforces the suggestion that gaps in the complex may be related to nondepositional zones within a continuous system (or post-depositional erosion) rather than time-transgressive sedimentation. However, some superimposed subaqueous fans and some grounding-line sedimentary assemblages are

identified in the south and are discussed later.

Having proposed general environmental conditions for the deposition of the Harricana complex, it is now appropriate to describe and interpret its detailed sedimentology. The aim here is to better understand the detailed processes and subenvironments within such enormous conduits. Establishing the broad environment first is essential because many bedforms and their associated structures are common to both open channels and closed conduits (Table 5.10).

Sedimentology of the Harricana glaciofluvial complex

The scale of the complex makes an architectural approach to its sedimentology appropriate (cf. Miall 1985; Brennand in press). To simplify description and interpretation of macroforms and sedimentary environments in general, individual gravel facies and sandy in-phase wave structures are first briefly described and interpreted. These facies and structures were investigated at 31 sites (Fig. 5.3). Each site was an area of extensive exposure in gravel quarries. Each observed unit was given a number in the form: pit number/face number-unit number, for example, Q2B/1-9. Paleoflow direction estimates from cross-bedded and cross-laminated sand, and imbricate clast ab-planes were recorded together with clast a-axis orientations (Tables 5.9 and 5.11; Appendices 7, 8 and 9). In the portion of the Harricana complex studied, cobbles and boulders dominate, and little post-depositional disturbance of the sediments was observed. Sand and silt beds are thicker and more frequent in the south. Sedimentary structures in sand and silt units include plane beds, cross beds, cross laminations, parallel laminations, in-phase wave stratification and massive beds. In some vertical exposures gravel and sand facies alternate. Composite, pseudoanticlinal and oblique accretion avalanche bed macroforms are identified (Brennand in press). Occasionally, sediments fine laterally towards the flanks of the Harricana complex.

Heterogeneous, unstratified gravel

Heterogeneous, unstratified gravel (Figs. 5.12*a* and 5.12*b*) is the most common individual facies within the Harricana complex. It is texturally polymodal, with grain sizes ranging from boulders to fine sand and silt; the dominant grain sizes being cobbles and boulders (-7ϕ to -9ϕ). Units are 1 to 5 m thick and lower contacts are erosional. Bed geometry may be tabular or pseudoanticlinal. This facies is mostly framework-supported (cf. Rust and Koster 1984) and ungraded (Figs. 5.12*a* and 5.12*b*). Vaguely delineated lenses of polymodal, bimodal clast-supported, bimodal matrix-supported, and openwork gravel may all be observed within the same unit (Fig. 5.12*a*; Brennand in press). The arrangement of these lenses follows no consistent vertical or lateral pattern. Imbricate clusters of larger clasts are common within gravels with an otherwise visually random fabric (Fig. 5.12*b*). Although imbricate cobbles are generally oriented with their a-axis transverse to flow direction (a(t)), a large number of a-axis parallel (a(p)) clasts, particularly pebbles, are also present (Table 5.11). Mean dip angles of the imbricate plane of clasts are generally high (36°to 44°, Table 5.11).

Table 5.10. Gravel facies deposited under closed-conduit and open-channel conditions.

Facies	Structural characteristics[1]	Main sediment support mechanisms	Origin of structure	Interpretation	
				Closed conduit[3]	Open channel
Heterogeneous, unstratified gravel	Vaguely lenticular, tectural organization of heterogeneous gravel; ungraded; framework supported; cluster imbrication with a(t) b(i) and a(p) a(i) and high dips; tabular or pseudoanticlinal bed geometry	Fluid turbulence; bed	(i) Longitudinal sediment sorting during tractional transport; (ii) Sorting associated with the development of cluster bedforms	Facies within a composite or pseudoanticlinal macroform; deposition during the waning stages of floods	(ii) Expansion bar[4]; (iii) Waning flood-flow deposit[5]
Massive, imbricate, clast-supported gravel[2]	Massive; relatively bimodal and clast-supported; generally ungraded; pervasive imbrication with a(t) b(i) and a(p) a(i) and high dips; tabular or pseudoanticlinal bed geometry	Fluid turbulence; bed	Deposition primarily from traction transport with minor suspension and saltation transport	Facies within a composite or pseudoanticlinal macroform	(i) Longitudinal bar[4, 6]
Plane-bedded gravel	Plane bedded, becoming more massive in coarser units; polymodal, graded or longitudinally sorted beds; a(t) b(i) imbrication dominant; tabular bed geometry	Bed; fluid turbulence	Deposition primarily from traction transport	Facies within a composite macroform	(i) Longitudinal gravel bar (Expansion bar?)[4, 7]; (iii) Diffuse gravel sheets[8]
Imbricate, polymodal gravel	Texturally polymodal although some may be more matrix-rich; ungraded or weak normal or inverse-to-normal grading; a(p) a(i) and a(t) b(i) imbrication; tabular or lenticular bed geometry	Fluid turbulence; dispersive pressure; buoyancy; hindered settling	Deposition from highly concentrated dispersion (homogenous or heterogenous)	May form in-phase wave structures associated with the establishment of a density interface at points of flow expansion	(i) Hyperconcentrated flood-flow deposit[9]; (iii) Longitudinal bar with later infiltration[4]
Cross-bedded gravel	Graded foreset beds: (A) Base - bimodal, clast-supported gravel occasionally with convoluted laminae in sand (B) Middle - Openwork gravel (C) Upper - Openwork gravel (smaller grain size)	Fluid turbulence; bed	Bedform migration or macroform progradation; longitudinal sediment sorting during transport of heterogeneous gravel, and lee-side deposition of suspended load in return flow beneath a separation eddy	Large gravel dunes; facies within composite macroform, associated with bedform migration or macroform progradation	(i) Longitudinal gravel bar4, 7; (ii) Transverse bar[4]

[1] a(t) b(i): clast a-axis transverse to flow direction, b-axis imbricate; a(p) a(i): clast a-axis parallel to flow direction and imbricate.

[2] Not identified in the Hamicana complex

Interpretations derived from: [3]Brennand (in press); [4]Baker (1973); [5]Fraser and Bleuer (1988); [6]Ringrose (1992); [7] Rust (1984); [8]S.A. Smith (1990); [9]G.A. Smith (1986).

Table 5.11. Fabric and transport orientation data for gravel facies and structures

Unit Number	Sedimentary Facies/Structure	Sample Number	Flow Azimuth	Mean Dip	Vector Strength (S_r)	Significance Level [1]	Transport Orientation Data			
							a(t)	a(p)	Cobbles[2]	Pebbles[3]
QA/1-1	Heterogeneous, unstratified gravel	60	115°	37°	0.6397	99.0%	63.3%	31.7%	a(t)	[a(p)]
Q16/4-2	Heterogeneous, unstratified gravel	60	240°	38°	0.5573	99.0%	48.3%	50.0%	a(t)	a(p)
Q18/1-4	Heterogeneous, unstratified gravel	99	152°	42°	0.5329	99.0%	54.2%	42.4%	a(t)	[a(p)]
Q18/1-1	Heterogeneous, unstratified gravel	50	176°	36°	0.5051	99.0%	N/A	N/A	N/A	N/A
Q23/2-1	Heterogeneous, unstratified gravel	60	152°	38°	0.6507	99.0%	45.0%	48.3%	equal	[a(p)]
Q26/1-2	Heterogeneous, unstratified gravel	110	162°	44°	0.6795	99.0%	N/A	N/A	N/A	N/A
Q1/1-2RHS	Plane-bedded gravel	60	190°	45°	0.7013	99.0%	50.0%	43.3%	a(t)	equal
Q1/1-3LHS	Plane-bedded gravel	60	162°	41°	0.4688	99.0%	45.0%	53.3%	[a(t)]	a(p)
Q23/1-2	Inclined, plane-bedded gravel	160	149°	39°	0.5848	99.0%	56.8%	35.6%	a(t)	[a(p)]
Q28/2-1	Imbricate, polymodal gravel with in-phase wave surfaces	60	100°	16°	0.7762	99.0%	N/A	N/A	N/A	N/A
Q11/1-1	Imbricate, polymodal, matrix-rich gravel with tabular geometry	60	246°	41°	0.6485	99.0%	48.3%	51.7%	[a(t)]	a(p)
Q26/1-1LHS	Imbricate, polymodal, matrix-rich gravel with poorly defined convex-up bedding surfaces	60	151°	38°	0.7496	99.0%	63.2%	34.2%	a(t)	none
Q23/1-1: Full sample	Large cross-bedded gravel	59	326°	2°	0.6016	99.0%	42.4%	49.2%	[a(p)]	a(p)
Q23/1-1: 'Parallel' clasts[3]	Large cross-bedded gravel	28	(328°) 148°	29°	0.6986	99.0%	15.3%	27.1%	[a(p)]	a(p)
Q23/1-1: 'Flipped' clasts[4]	Large cross-bedded gravel	31	140°	23°	0.7445	99.0%	27.1%	22.0%	[a(t)]	[a(t)]
Q6/1-2: 'Flipped' clasts[4]	Bimodal, massive, clast-supported gravel from large-scale, downflow-dipping, rhythmically-graded, tabular beds	60	250°	67°	0.6465	99.0%	43.3%	53.3%	a(p)	[a(p)]
Q17/1-7RHS: 'Flipped' clasts[4]	Bimodal, massive, clast-supported gravel from large-scale, downflow-dipping, rhythmically-graded, tabular beds	60	163°	36°	0.5318	99.0%	38.3%	60.0%	a(p)	equal
Q25/1-1b: 'Flipped' clasts[4]	Bimodal, massive, clast-supported gravel from large-scale, downflow-dipping, rhythmically-graded, tabular beds	30	126°	59°	0.4870	99.0%	36.7%	56.7%	a(p)	none
Q12/1-1aRHS (east): Full sample	Large cross-bedded gravel or south-dipping avalanche beds of macroform	60	29°	18°	0.5063	99.0%	45.0%	53.3%	equal	a(p)
Q12/1-1aRHS (east): 'Parallel' clasts[3]	Large cross-bedded gravel or south-dipping avalanche beds of macroform	35	(35°) 215°	29°	0.7752	99.0%	25.0%	33.3%	[a(p)]	a(p)
Q12/1-1aRHS (east): 'Flipped' clasts[4]	Large cross-bedded gravel or south-dipping avalanche beds of macroform	25	205°	48°	0.5998	99.0%	20.0%	20.0%	[a(t)]	[a(p)]
Q12/1-1aLHS (west): Full sample	Large cross-bedded gravel or south-dipping avalanche beds of macroform	60	8°	0.08°	0.6096	99.0%	45.0%	55.0%	a(p)	equal
Q12/1-1aLHS (west): 'Parallel' clasts[3]	Large cross-bedded gravel or south-dipping avalanche beds of macroform	26	(6°) 186°	32°	0.8620	99.0%	16.7%	26.7%	[a(p)]	a(p)

Unit Number	Sedimentary Facies/Structure	Sample Number	Flow Azimuth	Mean Dip	Vector Strength (S_1)	Significance Level [1]	Transport Orientation Data			
							a(l)	a(p)	Cobbles[2]	Pebbles[2]
Q12/1-1aLHS (west): 'Flipped' clasts[4]	Large cross-bedded gravel or south-dipping avalanche beds of macroform	34	168°	29°	0.7424	99.0%	26.3%	26.3%	a(p)	a(l)
Q12/1-1bLHS (west): Full sample	Large cross-bedded gravel or south-dipping avalanche beds of macroform	60	17°	19°	0.6959	99.0%	33.3%	63.3%	equal	a(p)
Q12/1-1bLHS (west): 'Parallel' clasts[3]	Large cross-bedded gravel or south-dipping avalanche beds of macroform	36	(14°) 194°	36°	0.8624	99.0%	20.0%	38.3%	equal	a(p)
Q12/1-1bLHS (west): 'Flipped' clasts[4]	Large cross-bedded gravel or south-dipping avalanche beds of macroform	24	202°	17°	0.7802	99.0%	13.3%	25.0%	equal	a(p)
Q3/2-4LHS (East): 'Flipped' clasts[4]	Oblique accretion avalanche bed macroform (East set of alternating sequence)	60	131°	36°	0.5783	99.0%	46.3%	46.3%	[a(p)]	[a(l)]
Q3/2-4RHS (West): 'Flipped' clasts[4]	Oblique accretion avalanche bed macroform (West set of alternating sequence)	60	241°	37°	0.7852	99.0%	60.0%	31.7%	a(l)	none
Q4/3-3 (East): Full sample	Oblique accretion avalanche bed macroform dipping to east	60	275°	18°	0.6145	99.0%	33.3%	66.7%	a(p)	a(p)
Q4/3-3 (East): 'Parallel' clasts[3]	Oblique accretion avalanche bed macroform dipping to east	42	(271°) 91°	28°	0.7431	99.0%	18.3%	51.7%	a(p)	a(p)
Q4/3-3 (East): 'Flipped' clasts[4]	Oblique accretion avalanche bed macroform dipping to east	18	99°	25°	0.5590	99.0%	15.0%	15.0%	equal	equal
Q21/5-1LHS: Full sample	Oblique accretion avalanche bed macroform dipping to south-southeast	60	339°	24°	0.5158	99.0%	46.3%	41.7%	a(l)	[a(l)]
Q21/5-1LHS: 'Parallel' clasts[3]	Oblique accretion avalanche bed macroform dipping to south-southeast	36	(344°) 164°	43°	0.7193	99.0%	31.7%	28.3%	[a(l)]	equal
Q21/5-1LHS: 'Flipped' clasts[4]	Oblique accretion avalanche bed macroform dipping to south-southeast	24	140°	27°	0.7056	99.0%	16.7%	13.3%	[a(l)]	equal
Q8/1-1LHS (east)	East side of pseudoanticlinal macroform	60	275°	56°	0.7031	99.0%	53.3%	43.3%	[a(l)]	[a(p)]

N/A No data available

[1] Significance level of sample being non-random, according to test statistic (S_1/S_2) of Woodcock and Naylor (1983).

[2] Dominant a-axis orientation for cobble and pebble grain sizes; [...] indicates < 5% difference in dominant orientation of a-axes.

[3] 'Parallel' clasts: ab-planes dip downflow and are approximately parallel to field estimated dip of avalanche face or foreset. Flow azimuth (no brackets) assumed to be 180° to azimuth if imbrication inferred (brackets).

[4] 'Flipped' clasts: ab-planes dip upflow with respect to avalanche face or foreset.

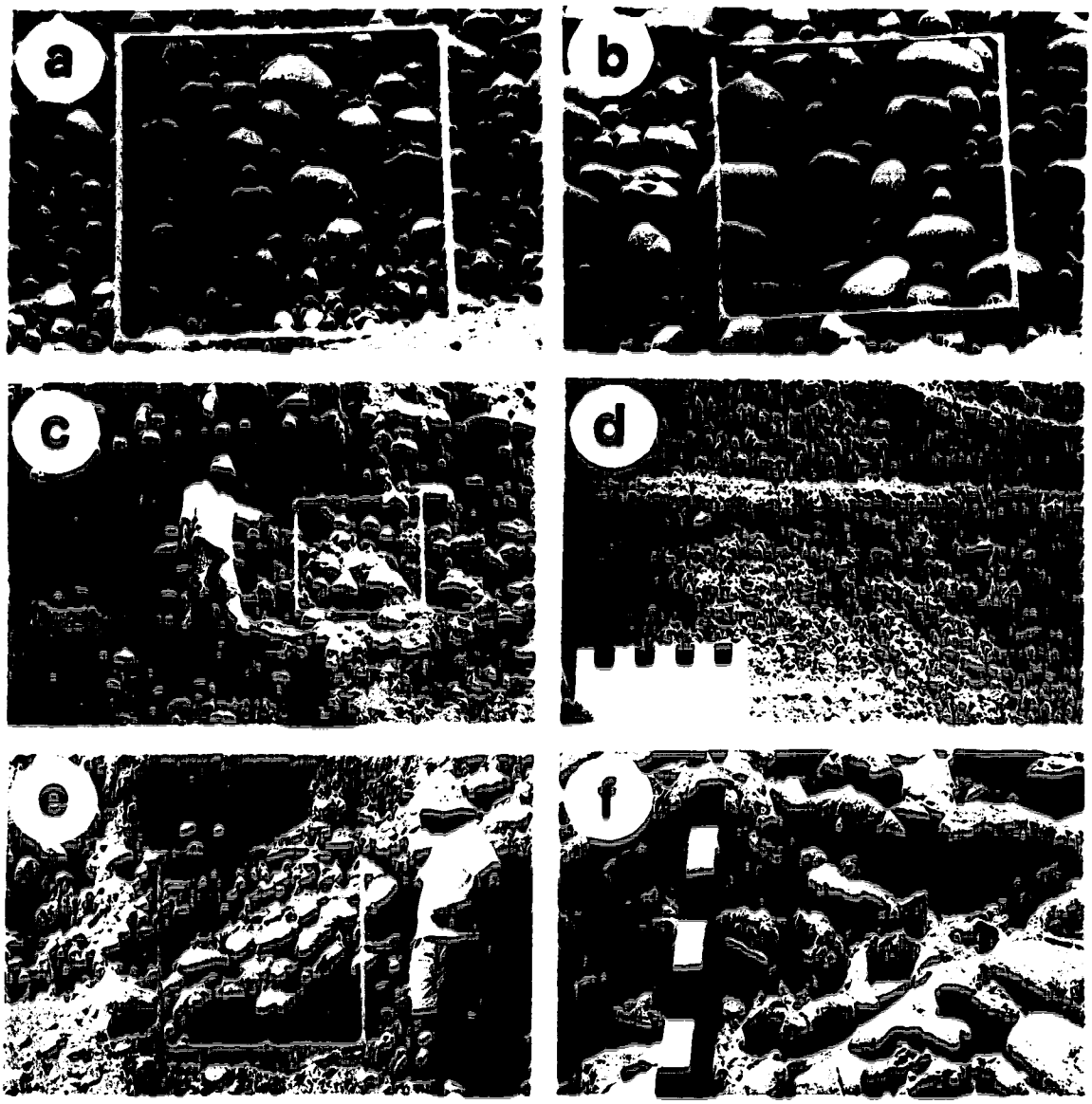

Figure 5.12. Individual facies within the Harricana complex. *a*. Heterogeneous, unstratified gravel exhibiting vaguely lenticular, textural organization (unit Q21/1-1aRHS). Grid is 1 m^2. *b*. Heterogeneous, unstratified gravel with imbricate clast clusters (unit Q23/1-3). *c*. Imbricate, polymodal, matrix-rich coarse gravel with clasts occurring preferentially along poorly defined convex-up bedding surfaces (unit Q26/1-1LHS; Table 5.11). *d*. Imbricate, polymodal fine gravel with diffusely-graded laminae (unit Q2B/2-1; Table 5.11). *e*. Grading in cross-bedded gravel (unit Q23/1-1; Table 5.11). *f*. Bimodal, clast-supported gravel with contorted laminae in sand (unit Q5/3-1) at the base of large-scale, downflow-inclined, tabular beds. Ten centimetre intervals on scale.

Deposition from fluidal flows is inferred from imbricate clast clusters. Cobbles were primarily transported by tractional rolling as bedload, whereas pebbles were primarily transported by saltation and suspension (Johansson 1963, 1965, 1976; Rust 1972). Sediment support would have been mainly by the bed and fluid turbulence. High clast dips are attributed to the high frequency of clast-to-clast contacts during deposition of this framework-supported facies (Rust 1972).

The vaguely lenticular organization in heterogeneous, unstratified gravel may result from preservation of longitudinal sediment sorting during transport (Iseya and Ikeda 1987). Longitudinal sorting results from larger clasts having higher transport velocities than smaller ones where shear velocities are well above critical values for all grain sizes present (cf. Meland and Norrman 1969). Flume experiments have produced gravel sorting with an openwork zone, a matrix-rich zone and a half matrix-filled zone under steady flow discharge, but involving nonuniform and unsteady bedload transport (Iseya and Ikeda 1987). Such longitudinal sorting may be preserved in the sedimentary record if the rate of sedimentation was relatively rapid, as is expected for the waning stages of a jökulhlaup. In addition, some imbricate gravel clusters may record the preservation of cluster bedforms, formed during the waning stages of floods (cf. Brayshaw 1984).

The coarse grain size indicates relatively powerful flows, with entrainment velocities on the order of 1.5 to 10.3 ms^{-1} estimated for some of the largest clasts in this facies (-9ϕ diameter; Williams 1983). Such velocities are comparable to those reported for flood flows (jökulhlaups) resulting from the drainage of ice-dammed lakes (cf. Elfström 1987).

Plane-bedded gravel

Plane-bedded gravel is composed of polymodal cobble and pebble gravel with granules and sand. Units (cosets) are 2 to 6 m thick, and individual beds are 0.1 to 0.5 m thick. Bed geometry is tabular and beds may be inclined upflow (Fig. 5.13). In places this facies is sorted into openwork, matrix-supported, clast-supported and polymodal lenses along bedding planes (Fig. 5.13). Larger clasts are often arranged into imbricate clusters with mainly a(t) and dips comparable to those exhibited by the heterogeneous, unstratified gravel facies (Table 5.11). Some pebbles were oriented with their a-axes parallel to flow direction (Table 5.11).

Stratification and imbrication within these facies is indicative of deposition from traction transport in fluidal flows. Some smaller clasts may have been transported in turbulent suspension or saltation. Plane beds may be attributed to the downflow migration of bed waves which formed by interaction between eddies in the flow and the bed (cf. Allen 1984), or to the effects of the burst/sweep process on local rates and modes of sediment transport in a turbulent flow (cf. Cheel and Middleton 1986). Upflow-inclined, plane-bedded gravel (Fig. 5.13) is interpreted as a product of deposition in diffuse gravel sheets (cf. S.A. Smith 1990) with well preserved longitudinal sediment sorting (cf. Iseya and Ikeda 1987).

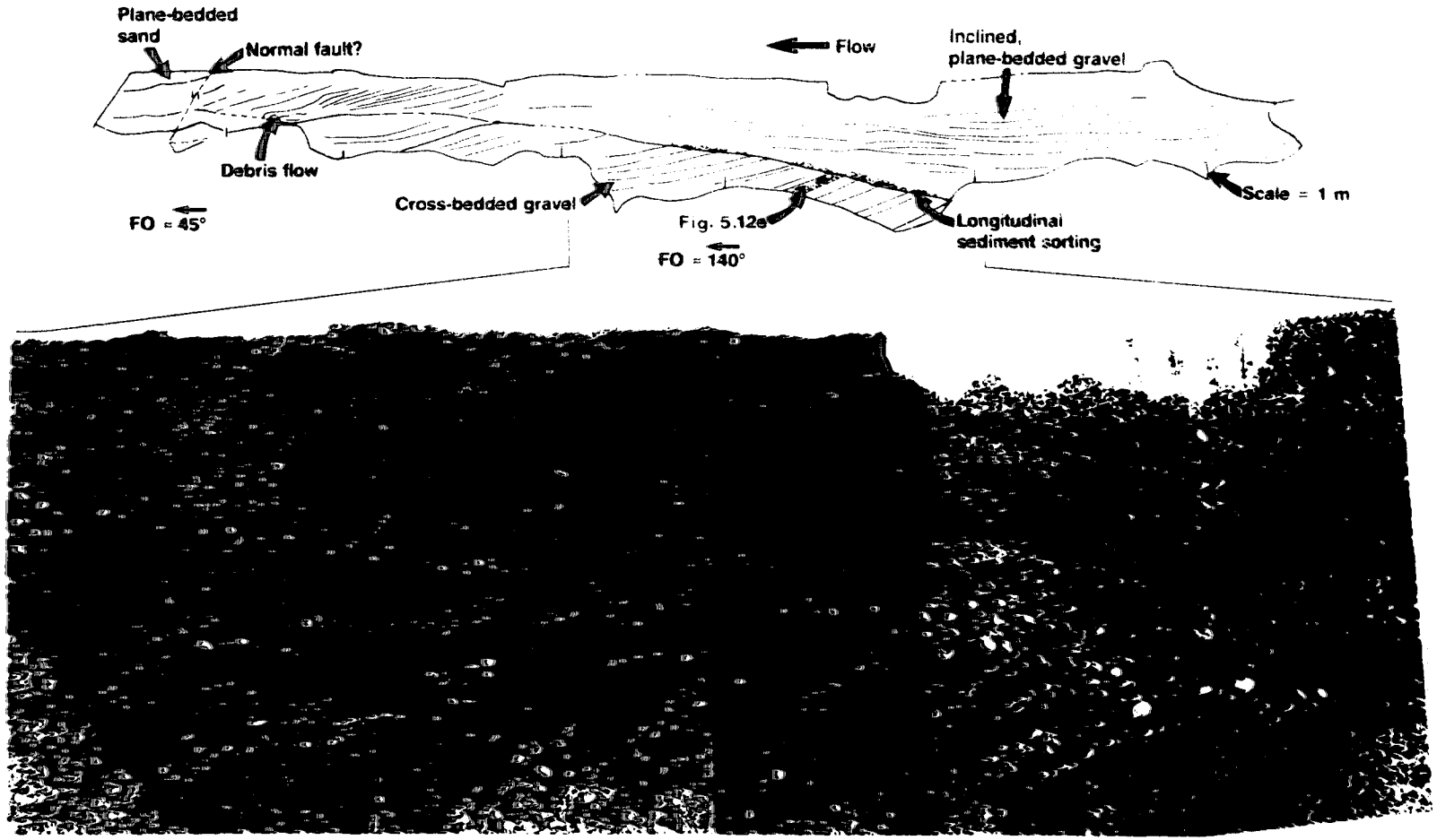

Figure 5.13. Sediments exposed in long axis of part of a composite macroform at pit Q23 (Fig. 5.3). FO, approximate pit face orientation.

Imbricate, polymodal gravel and sandy in-phase wave structures

Imbricate, polymodal gravel may be composed of matrix-rich pebbles to coarse sand with cobbles or boulders (Fig. 5.12*c*), or coarse sand and granules with imbricate pebbles (Fig. 5.12*d*). Exposed units are 2 to 4 m thick. Bed geometry may be tabular or lenticular. Finer units often exhibit pronounced wavy surfaces, diffusely-graded laminae which may be concordant with or truncated by the upper surface, small scour-and-fill structures, and silty rip-up clasts or tabular rafts of unconsolidated sediment (pit Q20, Fig. 5.14). In the coarser units, clasts tend to be concentrated along poorly defined bedding surfaces (Fig. 5.12*c*) forming imbricate clusters with a-axes oriented both parallel and transverse to flow, and with high clast mean dips (units Q11/1-1 and Q26/1-1LHS, Table 5.11). Some sets exhibit normal or inverse-to-normal grading.

This facies is inferred to have been deposited from a heterogeneous, highly concentrated dispersion (cf. G.A. Smith 1986). Weak stratification, imbrication, poor sorting, and normal grading are characteristic of hyperconcentrated flood-flow deposits (G.A. Smith 1986). Both a(p) and a(t) imbrication have been reported in such deposits and attributed to grain-by-grain deposition from traction and suspension (G.A. Smith 1986). Sediment support may have been from fluid turbulence, dispersive pressure, buoyancy and hindered settling (cf. G.A. Smith 1986). In finer units, diffusely-graded laminae are suggestive of rapid sedimentation from suspension.

The lenticular geometry of some members of this facies resembles that of smaller in-phase wave structures reported in open-channels (cf. Shaw and Kellerhals 1977) and turbidity currents (cf. Skipper 1971), and larger in-phase wave structures reported in volcaniclastic deposits (cf. Fisher 1990). In the latter case, in-phase wave structures have been identified in hyperconcentrated flood-flow deposits (e.g., Pierson and Scott 1985). Where imbricate, polymodal gravel exhibits a lenticular geometry, it is inferred to record in-phase wave structures deposited from hyperconcentrated flood flows (Brennand in press).

The characteristics of this facies at pit Q20 are particularly intriguing. Matrix-rich gravel (~2 m thick) is truncated by ~8 m of tabular cross-bedded medium-coarse sand with pebbles concentrated near the base and with occasional reactivation surfaces (Fig. 5.14). The contact between these two units is sharp with broad convex-up and concave-up segments (Fig. 5.14). Within the matrix-rich gravel facies clasts are concentrated along low-angled, upflow-dipping beds or backset beds (Fig. 5.14; cf. Banerjee and McDonald 1975). In addition, large tabular rafts of contorted medium-fine sand lie along these backset beds (Fig. 5.14). At pit Q20, the matrix-rich gravel (with large rafts of unconsolidated sediment) is inferred to have been deposited from a hyperconcentrated flood flow as a large antidune, the rafts coming to rest on the upflow side, or backset beds, of this bedform. These unconsolidated sediment rafts may have been frozen during transport (cf. Shaw 1972; Allen 1982), or have been transported for

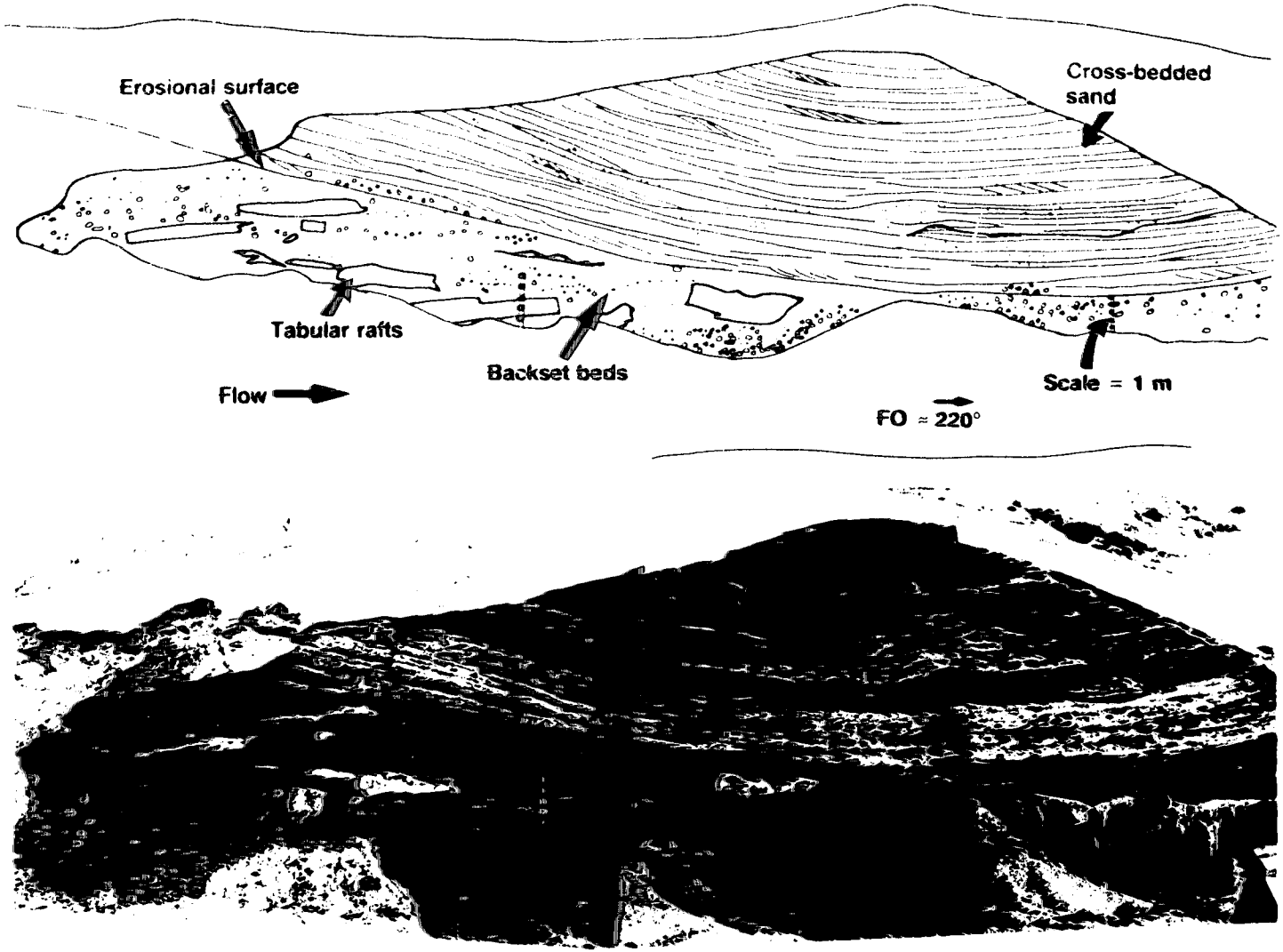

Figure 5.14. Large antidune backset beds with tabular rafts of unconsolidated sediment below tabular cross-bedded medium-coarse sand at pit Q20 (Fig. 5.3). FO, approximate pit face orientation.

a short distance only in an unfrozen state. In this latter case, blocks of unconsolidated sediment may have been eroded by turbulent flow upflow, but turbulence may have been dampened by high sediment concentration downflow. Thus, rafts may have been buoyed up by the flow, not abraded by it (Postma *et al.* 1988).

Sandy in-phase wave structures are composed of well-sorted and diffusely-graded coarse to medium sand (Fig. 5.15). Bed geometry is lenticular. Within sets, low-angled swaley laminations marked by diffuse grading and concentrations of small pebbles or granules may be concordant with, or truncated by, the upper swaley surface of the set (Fig. 5.15). Pebbles and silty rip-up clasts are dispersed or 'suspended' within the diffusely-graded sand. Most sets are draped by medium-fine sand, fine sand and silt, which may be massive, parallel laminated or cross laminated, and exhibit microfaults, flame structures and other penecontemporaneous deformation structures (Fig. 5.15). Occasionally both the drape and the swaley-laminated, diffusely-graded sand below are truncated by small scour-and-fill structures (Fig. 5.15).

Sandy in-phase wave structures were observed at pits Q16 and Q21, in locations where the complex increases in width (Table 5.3; Fig. 5.3). The most laterally extensive example of this facies was observed at pit Q2B (Fig. 5.15), in deposits flanking interconnected esker ridges and beads, and where the complex is particularly wide (Table 5.3; Fig. 5.3). Here, in-phase wave structures in diffusely-graded medium and coarse sand are stacked and offset, effecting an overall repetitive lenticular geometry in vertical section (Fig. 5.15). Some in-phase wave surfaces are erosional; that is they truncate internal laminae. Others are depositional or concordant with internal laminae (Fig. 5.15). Wave amplitudes range from 0.8 to 1.5 m, and wavelengths (L) range from 14 to 22 m. Approximations for flow velocity (U) and depth (h) are calculated from measurements of L and estimates of the density of a hyperconcentrated inflow (ρ_1) (Costa 1988) and an ambient fluid (ρ_2), using equations from Allen (1984, p. 407: $U^2 = gh(\rho_1 - \rho_2)/\rho_1$ and $L = 2\pi h\,(\rho_1 + \rho_2)/\rho_1$), where g is the acceleration due to gravity (Table 5.12).

Table 5.12. Estimates of flow depth and velocity for sandy in-phase wave structures.

	ρ_1 = 1330 kgm^{-3}		ρ_1 = 1800 kgm^{-3}	
L (m)	h (m)	U (ms^{-1})	h (m)	U (ms^{-1})
22	2.00	2.21	2.25	3.13
14	1.27	1.76	1.43	2.50

ρ_1 range of hyperconcentrated flood flow from Costa (1988)
ρ_2 assumed to be 1000 kgm^{-3} (clear water)

In-phase wave structures are inferred to have been deposited from hyperconcentrated flood

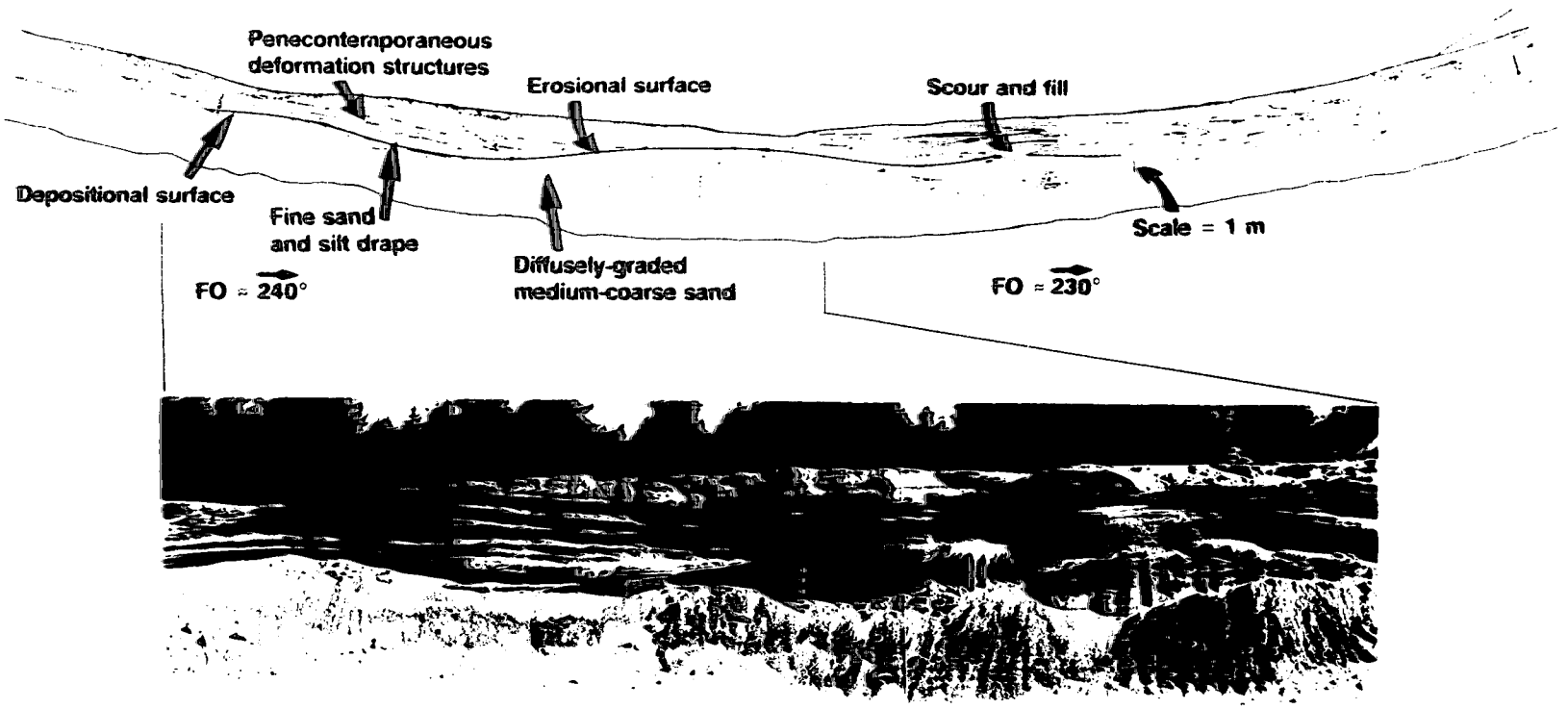

Figure 5.15. Sandy in-phase wave structures at pit Q2B (Fig. 5.3). Note: the metre scale is in different locations in the sketch and the photographic panorama. FO, approximate pit face orientation.

flows under powerful upper-flow-regime conditions (cf. Cheel 1990). Diffusely-graded sediments, penecontemporaneous deformation structures, and the preservation of soft-sediment rafts within in-phase wave structures, indicate high rates of deposition from suspension. In some cases, diffusely-graded or massive sand and gravel may have been first deposited then eroded by in-phase waves. Such relationships suggest a delicate balance between erosion and deposition, that is between meltwater and sediment discharge. Sand and silt 'drapes' over in-phase wave structures at pits Q2B (Fig. 5.15) and Q20 (Fig. 5.14) are inferred to be the result of waning-flow events, some of which may be associated with vertically alternating sand and gravel deposits observed elsewhere within the body of the complex (discussed later).

In-phase waves develop at density interfaces between fluids when flow undergoes a transition from supercritical ($Fr_d > 1$, where Fr_d is the densimetric Froude number) to subcritical ($Fr_d < 1$). Near the transition an in-phase wave may be established at the density interface. In a glacial environment such conditions may occur in a subglacial conduit, where meltwater with high sediment concentration flows from a constricted to an expanded reach (Brennand in press), or in an ice-marginal or grounding-line position where meltwater with a high sediment concentration flows into standing water (Gorrell and Shaw 1991). In the northern portion of the Harricana complex, an undulatory crest line in the vicinity of pit Q26 (Fig. 5.3; Table 5.3), and lateral expansion of the complex at pit Q20 (Fig. 5.3) favour formation in a subglacial conduit. In contrast, the presence of a number of interconnected esker ridges within the laterally extensive complex, the identification of a nearby bead with a contributory and a distributary ridge, and the lateral position of the facies with respect to the esker ridges at pit Q2B (Table 5.3; Fig. 5.3) favour deposition in a grounding-line environment (Gorrell and Shaw 1991).

Cross-bedded gravel

Both trough and tabular cross-bedded gravel are observed within the Harricana complex. Tabular cross-beds are generally observed as single sets which are 3 to 5 m thick, whereas individual foreset beds are 0.4 to 1.0 m thick (Figs. 5.12*e* and 5.13). Trough cross-beds may occur as single sets, but more often occur as fining-upward cosets. At pit Q1 (Fig. 5.3), trough cross-bedded sets range from 0.2 to 0.3 m thick, with a coset thickness of 6 m.

Texturally, these facies are dominated by boulders and cobbles, or cobbles and pebbles. Tabular foreset beds usually exhibit rhythmic grading. A typically rhythmically-graded bed starts with bimodal boulder/cobble or cobble gravel with a small pebble-granule-sand matrix which often exhibits convolute laminations (Fig. 5.12*e* and 5.12*f*). This passes up-sequence to cobble-pebble then pebble gravel which may be openwork or include a small amount of fine matrix (Figs. 5.12*e* and 5.13). Occasionally matrix-rich polymodal beds replace the rhythmically-graded triplet. Clast orientation data (unit Q23/1-1, Table 5.11) suggests that 'parallel' clasts became emplaced by sliding down the foreset,

whereas a(t) 'flipped' clasts rolled down the foreset and lodged as imbricate clusters, and a(p) 'flipped' clasts became reoriented by return eddies in the lee of the foreset (cf. Shaw and Gorrell 1991). Similar rhythmic grading is observed in some trough cross-beds, and in large (up to 2 m thick) downflow-dipping, tabular beds on the scale of the exposure. In the latter, clasts are mainly a(p) with high upflow dips ('flipped') (units Q6/1-2, Q17/1-7RHS, Q25/1-1b, Table 5.11).

Cross-bedded gravel is a product of bedform migration (cf. McDonald and Vincent 1972) with traction having been the dominant transport mechanism. Longitudinal sediment sorting during transport of heterogeneous gravel, and lee-side deposition of suspended load in the return flow beneath a separation eddy are inferred to have produced the foreset grading (Shaw and Gorrell 1991). At pit Q23, such longitudinal sorting is preserved along the stoss slope of a large gravel dune (Fig. 5.13). Given the probability of a closed-conduit during the formation of the Harricana complex, flow depths in excess of 10 m are estimated from a dune height of 5 m (McDonald and Vincent 1972). Large-scale rhythmically-graded, downflow-dipping, tabular beds may be attributed to macroform progradation.

Composite macroforms

Composite macroforms are architecturally complex and composed of numerous gravel facies. These macroforms have obvious stoss and lee sides. Stoss slopes dip upflow at approximately 5°-10°, whereas lee slopes may dip downflow at approximately the angle of rest of the constituting sediment. Downflow and lateral fining, and vertically alternating sand and gravel are observed within some composite macroforms. These macroforms can only be identified with certainty in places where exposure is excellent: pits Q23 and Q18 (Fig. 5.3). A composite macroform may also exist at pit Q12 (Fig. 5.3).

Pit Q23 is located in a relatively narrow portion of the Harricana complex, with a high crest and relatively steep slopes (segment 2, Table 5.3; Fig. 5.3). Vertical exposures are up to 12 m high, and one exposure extends for over 100 m cutting a portion of a composite macroform along its flow-parallel axis (Fig. 5.13). A 5 m thick set of cross-bedded gravel (unit Q23/1-1, Table 5.11) with rhythmically-graded foreset beds, is overlain unconformably by plane-bedded gravel, inclined upflow at approximately 5° and exhibiting subtle convex-up surfaces between beds (Fig. 5.13). Diffuse gravel sheets are inferred for the upflow-inclined, plane-bedded gravel facies. Longitudinal sediment sorting, resulting from differential bedload transport is preserved in the gravel sheets (Fig. 5.13) and suggests that deposition rates were rapid. Clast orientations (unit Q23/1-2, Table 5.11) suggest that smaller pebbles may have been transported in suspension or saltation, while larger pebbles and cobbles were transported by tractional rolling as bedload. Downflow and lateral to the diffuse gravel sheets finer gravel cross beds are exposed. Sediment remobilization down the northeast flank of the macroform, as a debris flow with a pronounced flow nose is visible at the base of these cross beds (Fig. 5.13). Lateral to the core of the macroform, heterogeneous, unstratified, well-rounded gravel is normally faulted. Heterogeneous,

unstratified gravel displays a similar proportion of a(t) and a(p) clasts with high dips (unit Q23/2-1, Table 5.11), suggesting deposition from traction, suspension or saltation depending on grain size. Towards the northeastern flank of the macroform, massive gravel interfingers with massive, cross-bedded and plane-bedded medium-fine sand. Numerous normal faults are observed. Interfingering suggests periodic gravel remobilization down the flank of the macroform. In the lowest flanking position, a sandy, matrix-supported diamicton with sandy shear planes and folds is interpreted as a debris flow diamicton (Fig. 5.16). This diamicton and the lateral normal faults are inferred to have formed towards the end of the construction of the Harricana complex, when supporting lateral ice (conduit walls) or buried ice melted (cf. McDonald and Shilts 1975).

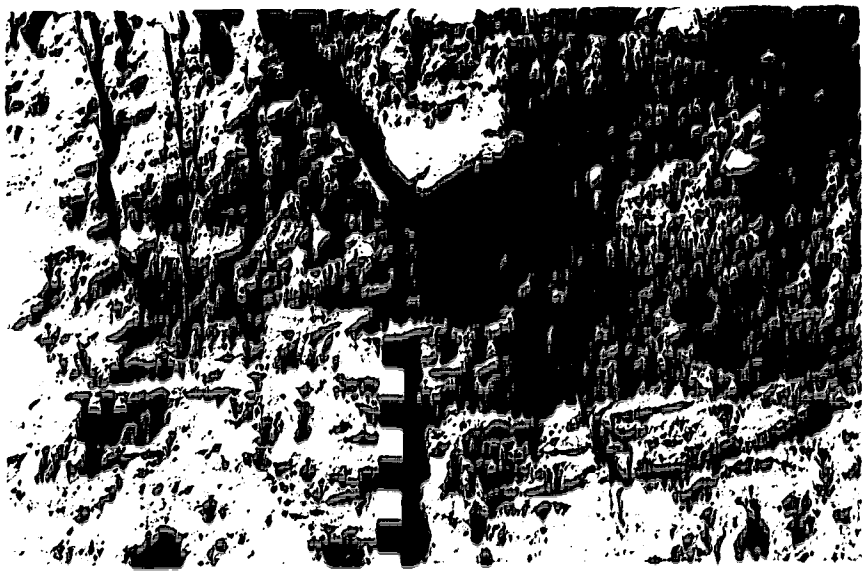

Figure 5.16. Shear planes and folds within debris-flow diamicton along the flank of the Harricana complex at pit Q23 (Fig. 5.3). Ten centimetre intervals on scale.

Pit Q18 is located in a short elongated segment (part of segment 4, Fig. 5.3) west of Lac Paradis. Approximately 100 m of flow-parallel exposure with a maximum vertical thickness of ~9 m is exposed (Fig. 5.17). Beds dip gently upflow and are interpreted as climbing sets on the stoss side of a macroform. Plane-bedded gravel, heterogeneous, unstratified gravel and tabular cross-bedded gravel alternate with cross-bedded and cross-laminated sand. The lowermost sand has been folded and sheared in a downflow direction, and is truncated by possible in-phase wave structures, including backset beds in gravel (Fig. 5.17). High shear stress exerted by the upper-flow-regime conditions responsible for formation of in-phase wave structures in an expanding conduit may explain downflow shearing and

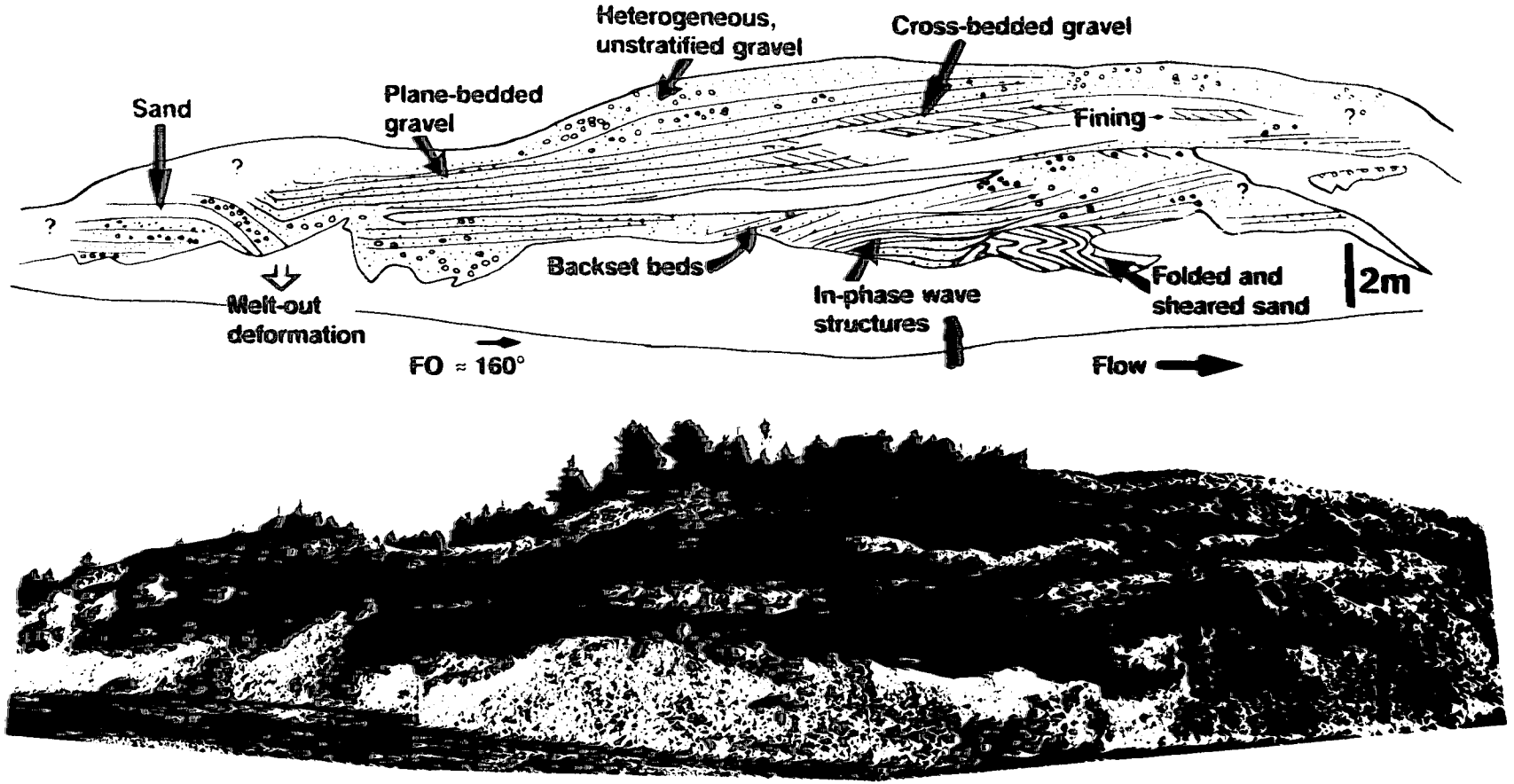

Figure 5.17. Composite macroform at pit Q18 (Fig. 5.3). FO, approximate pit face orientation.

truncation of the underlying sand. Downflow fining in the upper part of the section is attributed to flow expansion in a conduit which locally increased in height downflow. In vertical section, sheared sand and in-phase wave structures are observed below downflow-fining cross beds. This relationship may indicate upflow enlargement of an expanded portion of a subglacial conduit over time, and/or during subsequent events as sediment was deposited in that expanded portion, a form of paragenesis. Faulting and deformation of sand and gravel facies at the upflow end of the exposure (Fig. 5.17) suggest meltout of locally buried ice at this location (cf. McDonald and Shilts 1975). Sedimentary architecture and facies relationships at pit Q18 are inferred to record a large portion of a composite macroform, consistent with formation in an expanded portion of a subglacial conduit (Brennand in press), the size of which increased in an upflow direction over time and/or during successive events. The gravel backset beds in the lower part of the section also suggests flow expansion in a conduit (Johansson 1976).

Pit Q12 occurs in segment 10 (Fig. 5.3) and is dug into the second of two streamlined mounds within this segment of the Harricana complex (Table 5.3). Each mound is approximately 5 km long. A 10 m vertical exposure of downflow accreting avalanche beds or large cross beds is observed (Fig. 5.18*a*). Bedding planes are convex-up in transverse section, and downflow dipping in long profile (Fig. 5.18*a*). Some beds are truncated; truncation may record reactivation surfaces (cf. Shaw and Gorrell 1991). From this architecture and geomorphic expression, these downflow accreting avalanche beds are inferred to be part of a longitudinal (Rust 1984) or expansion (Baker 1978) macroform. Individual beds are 0.1 to 2.0 m thick. Beds of polymodal, framework-supported gravel, and granules with dispersed pebbles and cobbles alternate (Fig. 5.18*b*) and may be attributed to longitudinal sediment sorting prior to sediment delivery to the avalanche face (Iseya and Ikeda 1987). Some predominantly granule beds exhibit inverse grading characteristic of grain flows with dispersive pressure. Measurement of gravel fabric from avalanche beds reveals two clast populations: 'parallel' and 'flipped' (Table 5.11; Fig. 5.18*b*; Rust 1984). Clast orientations (units Q12/1-1aLHS, Q12/1-1aRHS, Q12/1-1bLHS, Table 5.11) suggest that 'parallel' clasts slid down the avalanche face, while 'flipped' clasts rolled down the face and lodged as imbricate clusters, or became reoriented by return eddies in the lee of the avalanche face (cf. Shaw and Gorrell 1991). These avalanche beds, or large dune foresets, truncate underlying trough cross-bedded coarse sand and are truncated by littorally reworked sand and gravel in gently inclined sheets. As pit Q12 is located towards the distal end of the streamlined mound, we suggest that the exposed sediments are lee-side deposits of a composite longitudinal or expansion macroform which may also exhibit alternating sand and gravel units.

Oblique accretion avalanche bed (OAAB) macroforms

OAAB macroforms exhibit steeply inclined avalanche beds which have accreted downflow and obliquely to the axis of the complex (Brennand in press). The best example of this type of macroform

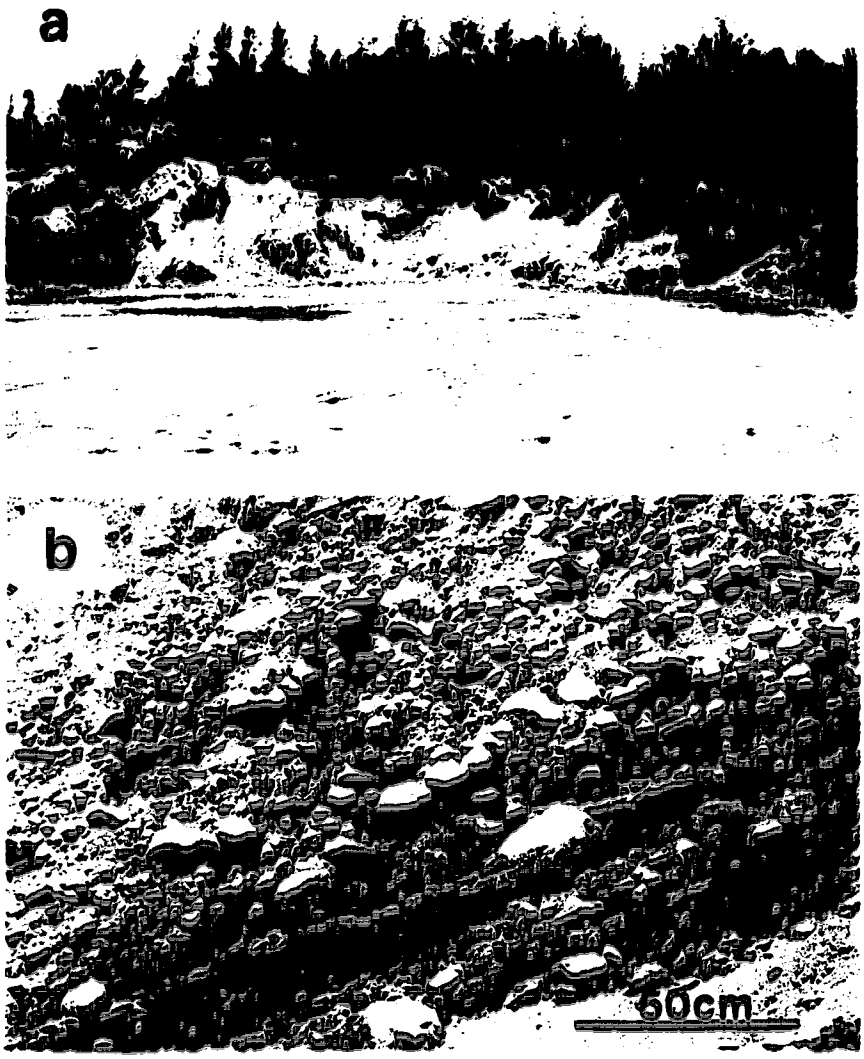

Figure 5.18. *a*. Downflow accreting avalanche bed macroform at pit Q12 (Fig. 5.3). Section is ~ 10 m high. Flow out of face. *b*. Close-up of avalanche beds at pit Q12 showing 'parallel' and 'flipped' clasts.

is observed at pit Q3 (Figs. 5.3 and 5.19), and extends through pit Q2A (Fig. 5.3). At pit Q3, the long axis of the Harricana complex is oriented north-south (Fig. 5.3). Three sets of avalanche beds truncate one another. One OAAB set dips at ~30° towards the southwest (set A), and is truncated by a similar set dipping towards the southeast (set B), which is in turn truncated by a set dipping towards the southwest (set C; Fig. 5.19). Individual avalanche beds, ranging in thickness from 0.5 to 1.0 m, are composed of polymodal gravel with 'flipped' (imbricate) clast clusters (Fig. 5.20*a*) or rhythmically-graded gravel (Fig. 5.20*b*). Rhythmically-graded gravel beds fine up-sequence from relatively bimodal, clast-supported cobbles and pebbles in a matrix of medium-coarse sand, to openwork pebbles, to openwork granules (Fig. 5.20*b*).

Gravel fabric measurements from 'flipped' clasts in OAAB sets are downflow and away from the crest of the macroform (units Q4/3-4LHS and Q3/2-4RHS, Table 5.11). Clast orientations with respect to flow direction are both a(p) and a(t), with a(t) orientations the most common (units Q4/3-4LHS and Q3/2-4RHS, Table 5.11). Consequently, clast emplacement by rolling down the avalanche slope is inferred to dominate over reorientation by a second helicoidal vortex or return flow eddy along the avalanche slope.

The formation of this macroform is attributed to the operation of two major helicoidal vortices within a conduit. Initial dominance of one vortex over another may be associated with bends in the conduit, the shape of the conduit, and the shape and roughness of the bed. When a helicoidal vortex was dominant along the western side of the complex, sediment was transported obliquely up the western side of the growing macroform. As sediment avalanched over the eastern side, southeast dipping avalanche beds were formed (set B). Unless melting of the conduit walls kept pace with deposition of the southeast dipping avalanche beds, the cross-sectional area of the conduit would have been reduced along the eastern side due to sedimentation, and possibly increased along the western side due to erosion. The eastern vortex would have become smaller and rotated faster and have had more erosive power. The upper, southwest-dipping avalanche beds (set C) are inferred to have been formed at that time. The boulder lag truncating the southeast dipping avalanche beds may also be a product of this event. Longitudinal sediment sorting during transport up the "stoss" side of the macroform may explain the rhythmic grading observed in some avalanche beds. In addition, the position of the conduit may have shifted or the conduit may have enlarged during this process due to differential melting of the conduit walls. The alternating OAAB macroform is draped by 6 m of plane-bedded and cross-bedded granules and coarse sand with dispersed pebbles (Fig. 5.19). The sequence is truncated in the east by gently inclined sheets of gravel and sand which may be attributed to littoral reworking during occupation of the area by Glacial Lake Ojibway.

Similar macroforms are observed at pits Q4 and Q21 (Fig. 5.3). In both cases, only a single

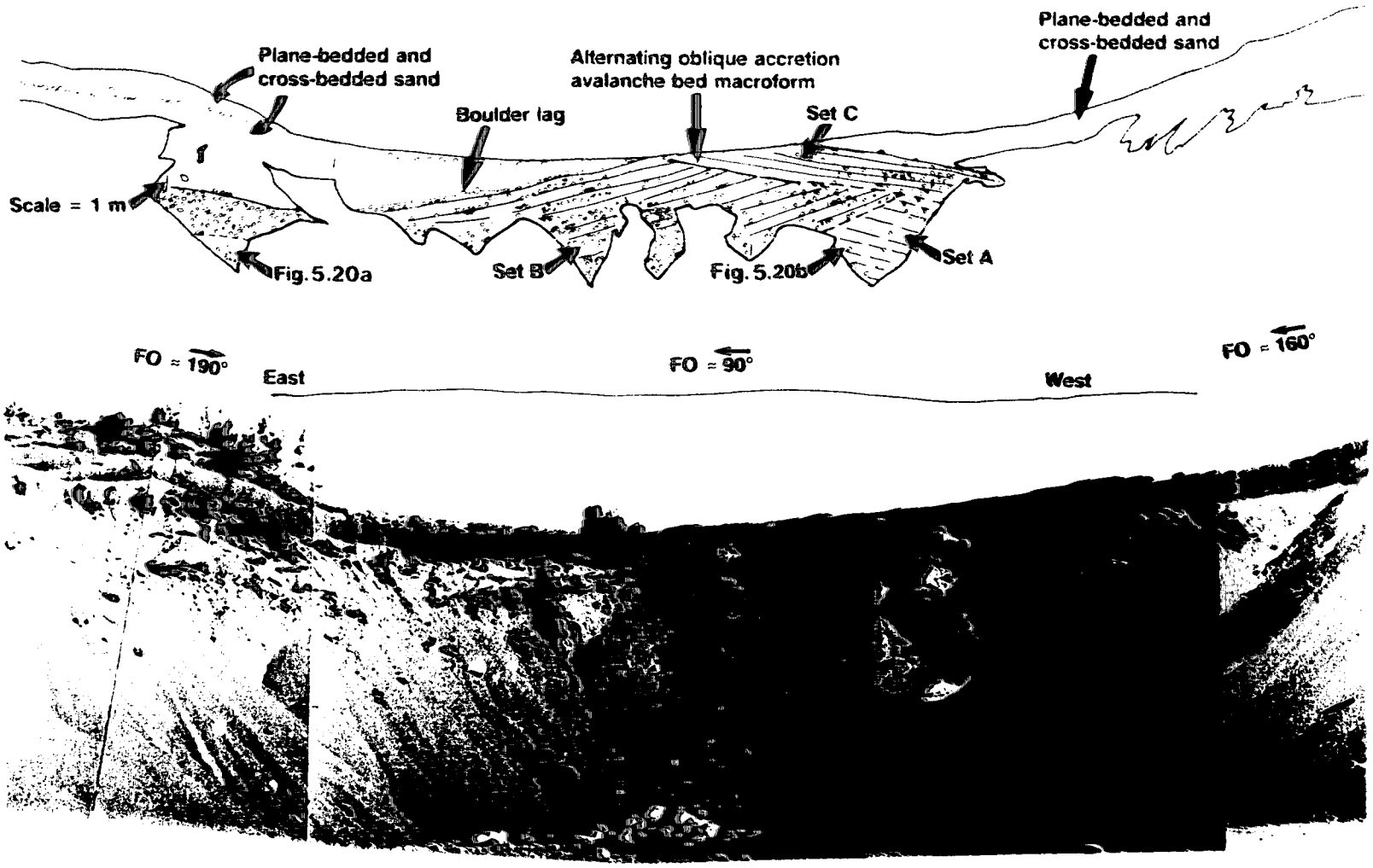

Figure 5.19. Alternating oblique accretion avalanche bed macroform at pit Q3 (Fig. 5.3). Flow into face. FO, approximate pit face orientation.

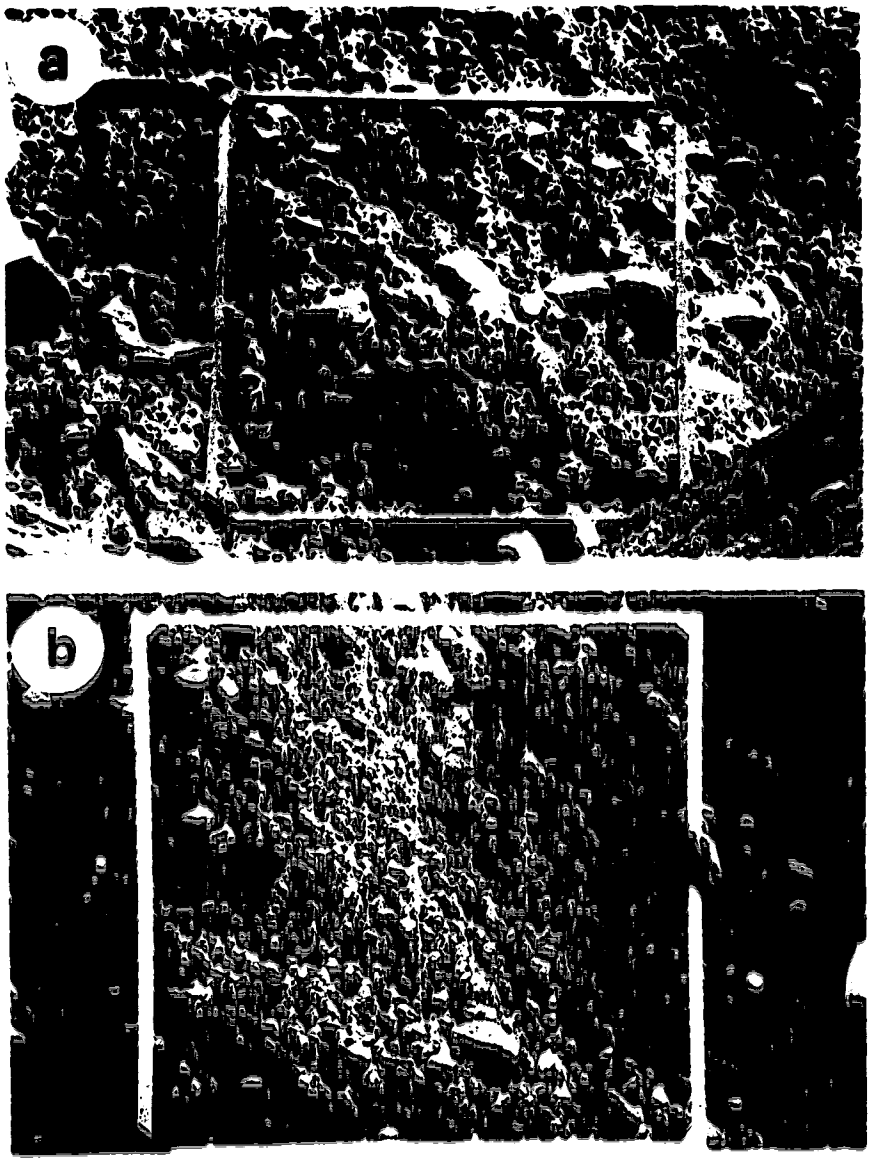

Figure 5.20. Close-ups of sedimentary style within alternating oblique accretion avalanche bed macroform at pit Q3 (Fig. 5.3). *a*. Clast clusters along beds. *b*. Rhythmic grading of finer gravel. Grid is 1 m^2.

OAAB set was observed and paleoflow direction estimates from gravel fabrics were away from the crest of the Harricana complex (down the avalanche face) and obliquely downflow (units Q4/3-3 and Q21/5-1, Table 5.11; Fig. 5.3). Clasts were either 'flipped' or 'parallel' to the plane of the avalanche face (units Q4/3-3 and Q21/5-1, Table 5.11). Clast orientations suggest that 'parallel' clasts became emplaced both by slipping and rolling down the avalanche face, while 'flipped' clasts mostly rolled down the face, some coming to rest as imbricate clusters.

Flow separation and expansion of a secondary current vortex, from a narrow conduit into an expanded zone of that conduit or a lateral cavity, is suggested for the formation of single OAAB sets (cf. Brennand in press). At pit Q4 (Fig. 5.3), this macroform underlies inclined plane-bedded and low-angle cross-bedded coarse to medium sand, with occasional in-phase wave structures and diffusely-graded scour-and-fill structures. Parallel-laminated, cross-laminated and massive fine sand, silt and clay overlie these sediments. The overall sedimentary association south of Val d'Or, with gravel cores (esker ridges), lateral fining, and in-phase wave structures, and the complexity of geomorphic expression (segment 14, Table 5.3), suggest that sedimentary associations at pit Q4 define a subaqueous fan built obliquely from an esker ridge. A grounding-line environment is inferred from these associations (cf. Gorrell and Shaw 1991) and is discussed later.

Pseudoanticlinal macroforms

Pseudoanticlinal macroforms are broad, low-angled, arched structures on the scale of the complex (Fig. 5.21; Brennand in press). With the available exposures only one of these macroforms was identified with certainty, at pit Q8 (Figs. 5.3 and 5.21). However, sediments at pit Q19 (Fig. 5.3) may also form one limb of a pseudoanticlinal macroform. In both of these locations the complex is narrow (Table 5.3; Fig. 5.3). At pit Q8 (Fig. 5.3), the macroform is composed of heterogeneous, unstratified cobble and pebble gravel (Fig. 5.21). Paleoflow direction estimated from imbricated clast clusters is downflow and convergent on the crest of the macroform/Harricana complex (unit Q8/1-1LHS, Table 5.11; Fig. 5.3). Deposition from tractional rolling, suspension and saltation are inferred from clast orientation with respect to paleoflow direction estimates (unit Q8/1-1LHS, Table 5.11).

The formation of a pseudoanticlinal macroform with crest-convergent fabric is inferred to be the product of secondary currents or vortices in a narrow, geometrically-uniform conduit (cf. Rouse 1961; Brennand in press). Unlike OAAB macroforms, the paired helicoidal vortices responsible for the formation of pseudoanticlinal macroforms are inferred to have been of similar power.

Vertically alternating sand and gravel facies

Vertically alternating sand and gravel facies are common along the length of the Harricana complex (Figs. 5.14, 5.17 and 5.22). The sand unit is commonly truncated by the overlying gravel facies and appears discontinuous. Generally, a pit contains only two to three couplets, however, couplets are numerous at pits Q16 and Q7 (Fig. 5.3) where sedimentary assemblages resemble those of subaqueous

Figure 5.21. Low-angled pseudoanticlinal structure at pit Q8 (Fig. 5.3). Arrow is location of fabric from unit Q8/1-1LHS (Table 5.11). Flow into face. Section is 5.5 m high.

Figure 5.22. Vertically alternating sand and gravel facies at pit Q21 (Fig. 5.3). Scale is 1 m.

fans. These sedimentary assemblages are discussed later.

Vertically alternating sand and gravel facies may result from: (*i*) temporal or spatial change in sediment supply, related to the formation of large bedforms and macroforms within a conduit; (*ii*) spatial change in flow conditions, such as the headward growth and capture of conduits and cavities; or (*iii*) temporal change in flow competence (cf. Brennand in press). The latter may relate to seasonal melting and a supraglacial to subglacial connection in the meltwater system, or to the episodic drainage of supraglacial or subglacial water bodies. At pit Q20 (Figs. 5.3 and 5.14), 2 m of matrix-rich gravel with backset beds and an in-phase wave surface is overlain by ~8 m of cross-bedded medium-coarse sand. This complete sequence was probably deposited during a single meltwater discharge event, possibly related to a jökulhlaup. Conversely, Allard (1974) attributed vertically alternating sand and gravel to annual meltwater discharge cycles.

Sedimentary macroforms and environments: discussion

Eskers of south-central Ontario contain macroforms similar to those described here (Brennand in press). Geomorphic and sedimentologic reasoning suggests that these macroforms record the effects of spatially and temporally differentiated erosion, transportation and deposition in a nonuniform conduit (Brennand in press). Trends in clast roundness, paleoflow direction estimates, and the relative continuity and downflow broadening of the Harricana complex along an upslope path favour a synchronous subglacial closed-conduit origin (cf. Table 5.2) for the portion of the complex studied.

Consequently, macroforms in the Harricana complex are also interpreted as sedimentary responses to a nonuniform subglacial conduit. A subglacial conduit not only bends but also pinches and swells, laterally and vertically (cf. Walder and Hallet 1979). Some of these bulges in the pre-complex conduit may have been cavity remnants (cf. Hooke 1989, fig. 4). Alternatively, with increased meltwater discharge, the conduit may have enlarged by melting or localized floatation (cf. Gorrell and Shaw 1991) to capture adjacent water-filled cavities with which it coexisted (cf. Iken and Bindshadler 1986). In this manner, the location and spacing of expansion zones may have changed over time within the conduit (Brennand in press). High velocity meltwater flow inferred from gravel facies and macroforms may have carried ice blocks, the burial and subsequent meltout of which may account for the numerous kettle holes observed within the complex.

We infer that the style of macroform at a particular location was controlled by local conduit geometry. Thus, composite and OAAB macroforms were deposited in conduit expansions. Over time, or during successive meltwater discharge events, the geometry of an expansion zone would have changed as a result of sedimentation. The effects of an accreting macroform may have increased conduit sinuosity, or have extended the expansion zone upflow. By contrast, pseudoanticlinal macroforms appear to have developed where the conduit was relatively narrow and geometrically uniform (Brennand in press). By extension, where the conduit was very narrow, deposition may only have occurred at periods of low flow. Indeed, nondeposition or even erosion along narrow segments may have created some of the "gaps" in the Harricana complex (Fig. 5.3; Table 5.3). In addition, the operation of paired helicoidal vortices within the "Harricana conduit" may have scoured the landsurface alongside the Harricana complex; elongate lakes are now observed to parallel the northern portion of the complex.

Subaqueous fan and grounding-line sedimentary assemblages

Subaqueous fan or grounding-line sedimentary assemblages were exposed at three locations along the Harricana complex. South of Val d'Or, sedimentary associations and their geomorphic expression suggest a grounding-line environment with beads, fans and esker ridges (Fig. 5.3; Table 5.3). An esker ridge, composed of an alternating OAAB macroform laterally draped by plane-bedded and cross-bedded coarse sand and granules is exposed in pits Q2A (Fig. 5.3) and Q3 (Figs. 5.3 and 5.19). An OAAB macroform, overlain by subaqueous fan sediments, is inferred for pit Q4 (Fig. 5.3). Downflow-inclined subaqueous fan sediments exhibit scoured surfaces filled by diffusely-graded or massive medium sand with dispersed pebbles, and plane-bedded, cross-bedded and diffusely-graded sand with some in-phase wave surfaces. Glaciolacustrine parallel-laminated, cross-laminated and massive fine sand, silt and clay overlie these deposits. Thick sequences of cross-laminated sand were not observed (Gorrell and Shaw 1991) but may exist downflow from pit Q4 (Fig. 5.3). An extensive sequence of in-phase wave structures in both granules and medium sand have been described at pit Q2B (Figs. 5.3 and 5.15). These are related to the effects of denser wall jets with hydraulic jumps (cf. Gorrell and Shaw

1991; Brennand in press). Erosional and depositional in-phase wave surfaces, and fine sand and silt drapes over in-phase wave trains, imply rapid changes in meltwater and sediment discharge and a delicate balance between them. These observations and interpretations, taken together with the complex geomorphology of segment 14 (Table 5.3), suggest a grounding-line depositional environment where subglacial water pressure was delicately poised close to the floatation point of the ice sheet (Gorrell and Shaw 1991) composed of cold ice except near the bed and near the surface in summer.

Fining-upward gravel to coarse sand units, 0.1 to 1.0 m thick, and vertically alternating gravel and medium sand are exposed at pit Q7 (Fig. 5.3). Gravel is plane bedded, cross bedded or massive. Coarse sand is generally plane bedded or massive and has numerous pebbles dispersed within it. Medium sand is plane bedded, cross bedded and cross laminated. All units are gently inclined downflow. In pit QC (Fig. 5.3), downflow from pit Q7 (Fig. 5.3), 3 m of plane-bedded and cross-bedded medium and coarse sand are exposed. Together, both of these pits occur within a geomorphically expressed lobe superimposed over the Harricana complex (Table 5.3). Sediments at pits Q7 and QC are therefore interpreted as subaqueous-fan sediments, likely deposited in a grounding-line or ice-marginal environment during ice retreat.

At pit Q16 (Fig. 5.3), 5 m of heterogeneous, unstratified gravel is exposed near the surface at the crest of the Harricana complex. Below this, a small exposure shows two heterogeneous, unstratified gravel units separated by cross-bedded medium-coarse sand. In a flanking position, six rhythmically alternating units of polymodal clast-supported gravel and plane-bedded, cross-laminated or diffusely-graded coarse to fine sand are observed (face Q16/4). In a more flanking position, and downflow from face Q16/4, 2 m of plane-bedded, cross-bedded and diffusely-graded medium to coarse sand are exposed. Paleoflow direction estimates from gravel fabrics, cross beds and cross laminations are oblique to the axis of the Harricana complex (Figs. 5.9 and 5.10). A lateral, low-angled, subaqueous-fan environment is inferred for most of the sediments exposed at pit Q16. Such a fan may have formed in an ice-marginal or grounding-line position, or in a subglacial cavity (Gorrell and Shaw 1991; Brennand in press). As the sediments form the upper package in flanking locations, while heterogeneous, unstratified gravel is exposed near the surface at the crest of the complex, it is likely that this subaqueous fan was superimposed over earlier, coarser Harricana complex deposits, however, the actual depositional environment (grounding line, ice margin or subglacial cavity) cannot be determined.

Discussion: stratigraphic context, landform associations and implications for ice-sheet hydrology and dynamics

Morphology, sedimentology, clast characteristics and paleoflow direction estimates from the Harricana complex, between latitudes 48°N and 50°N, favour an origin by synchronous deposition of a subglacial esker in a continuous, closed conduit (Table 5.2). Some subaqueous fans rest on, or lie lateral to, these primary deposits. Such fans may have been deposited in subglacial cavities during esker

formation, or superimposed over esker deposits (cf. Wilson 1938) at a grounding-line or ice-marginal position during ice retreat or downwasting. If most of the sediments within the Harricana complex are indeed eskerine and approximately synchronous, this new interpretation must be rationalized with event-sequences determined from adjacent stratigraphy and landforms.

Stratigraphic context

Stratigraphic correlation for Abitibi-Timiskaming and surrounding areas has been attempted (cf. Veillette 1986, 1989; Thorleifson *et al.* 1992). Regional correlations as proposed in the literature, together with reported ice-flow directions and evidence used to infer those directions are presented in Table 5.13. Few natural exposures of till older than Matheson till exist in this region (cf. McClenaghan 1989); most older stratigraphic sequences have been constructed from analysis of rotosonic drill cores and cross-cutting striae (e.g., Veillette 1986; McClenaghan *et al.* 1987, 1988, 1992; S.L. Smith 1992). Two ice-free intervals have been reported: the Missinaibi formation, and the Abitibi River sediments and Owl Creek Beds (Table 5.13). Depending on the chronologic technique used, Wisconsinan glacial inception (O^{18} stage 5) may have commenced after deposition of the Missinaibi Formation with an ice centre in central Québec, or after deposition of the Abitibi River sediments and Owl Creek Beds with an ice centre in northern Québec (Table 5.13; Wyatt 1989; Thorleifson *et al.* 1992). The Adam, Matheson and New Quebec tills have been attributed to southwest flow of Labrador sector ice, related to a northern Québec ice centre (Thorleifson *et al.* 1992, 1993), and based primarily on till composition, fabric, and striae data (Table 5.13). This inferred southwest flow would have crossed the area now occupied by the Harricana complex (Veillette 1986).

Changes in till composition, cross-cutting striae, bedrock erosion marks, and esker and end moraine (genesis assumed) distribution have been interpreted as indicating a shift in ice-flow direction to the south-southeast at the time of deposition of the upper parts of the Matheson and Sandy tills (Table 5.13). Although some intermediate striae between southwest and south-southeast are reported, cross-cutting southwest and south-southeast striae are more common, and no differential weathering between surfaces exhibiting these striae is described (Veillette 1986, 1989, 1990). It has been proposed that the earlier southwesterly flow relates to ice advance from northern Québec, whereas later south-southeast flow relates to conditions during ice retreat (Veillette 1986, 1989). Veillette (1990) suggested that this latter flow was relatively short-lived.

To the east of the Harricana complex, streamlined landforms, striae and till composition have been inferred to record southwesterly ice flow (New Quebec till, Table 5.13). Southwesterly orientations may record coincident ice advance and retreat directions, or reflect incomplete field data (Veillette 1986). Some cross-cutting striae record ice flow deflected to the south within a 65 km band east of the Harricana complex (Fig. 5.2; Hardy 1976). This deflection was attributed to interaction of the proposed

Hudson and New Quebec ice masses (Hardy 1976).

The change in ice flow direction recorded in the upper part of the Matheson till has been attributed to the break-up of the Labrador sector of the Laurentide Ice Sheet into New Quebec and Hudson ice masses during deglaciation (Hardy 1976; Veillette 1986, 1989), with time-transgressive deposition of the Harricana complex at this time (Table 5.13). Veillette (1990) attributed break-up of the Labrador sector to rapid ice flow initiated by a deforming substrate in the Great Lakes region at the ice margin. He suggested that downdraw in this zone of rapid ice flow would have lowered the ice-sheet profile, caused a reentrant to form at the ice-sheet margin, which extended to the northeast, and concentrated sedimentation in the Harricana-Lake McConnell complex (Veillette 1986, 1990). He also thought that a calving bay into Glacial Lake Algonquin and Post-Algonquin, combined with the inferred corridor of rapid ice flow, controlled development of the early deglacial reentrant axis in the North Bay region (Veillette 1986, 1990). This deglacial corridor has been corroborated by radiocarbon dates on basal postglacial organics from small lakes and ponds (Veillette 1988; Richard *et al.* 1989). Hickock and Dreimanis (1992) argued recently for widespread deformation of till in the Great Lakes region. Conversely, Clayton *et al.* (1989) reported a lack of widespread pervasive deformation of sediment along the southern margin of the Laurentide Ice Sheet. In addition, others (e.g., Shaw and Sharpe 1987) have suggested that rapid ice flow may have been initiated by meltwater flood events, which do not necessarily exclude subsequent subglacial deformation (cf. Hickock and Dreimanis 1992).

Some authors have proposed that the Kipling and Cochrane tills are equivalent, based on core stratigraphy, till composition and ice-flow indicators (Skinner 1973; Veillette 1989; S.L. Smith 1992); others state that the Kipling till is correlated with the regionally extensive Severn and Sky Pilot tills of Ontario and Manitoba deposited during southwesterly ice flow, and therefore cannot be correlated with the Cochrane till (Thorleifson 1989; Thorleifson *et al.* 1993). The Cochrane till may record deposition from a series of surges (Hardy 1976; Veillette 1989). Although Cochrane till has been reported to drape the Harricana complex in the north (cf. Hardy 1976; Vincent *et al.* 1987), this till was not identified in exposure during the present field study. Consequently, our research cannot help elucidate the origin of the Cochrane till or the timing of the Cochrane event.

The most pertinent stratigraphic information, with respect to the genesis of the Harricana complex, is the change in flow direction associated with the Matheson till (Table 5.13). In most cases it would appear that this change in flow direction was relatively abrupt; cross-cutting southwest and south-southeast oriented striae are observed and the geochemistry and lithologic composition of the upper and lower parts of the till are quite distinct (cf. Veillette *et al.* 1989; McClenaghan *et al.* 1992). In a continuously grounded, wet-based ice mass, it is hard to explain such an abrupt change in flow direction. We propose that decoupling of the ice sheet from its bed during a meltwater-flood event,

accompanied by a concomitant change in regional ice-surface profiles, may more appropriately explain the abrupt change in ice-flow direction at the regional scale. This is discussed later.

Landform associations

Regional landform associations of the Harricana complex include: the Abitibi Uplands, eskers, moraines, streamlined landforms, and bedrock erosional forms (striae, grooves or s-forms, rat-tails and crag-and-tail features) (some of which are shown on Figs. 5.1 and 5.2; cf. Allard 1974; Hardy 1976; Veillette 1986, 1989, 1990).

Most of the Harricana complex is located in a dissected portion of the Abitibi Uplands. Its path appears to be diverted as it moves up against the margin of the dissected zone south of Val d'Or (Figs. 5.1 and 5.2). This change in orientation of the complex, from south-southeast to southwest, was attributed to time-transgressive formation of the Harricana-Lake McConnell complex; the portion south of Val d'Or related to earlier southwesterly ice flow, and that to the north associated with later southeasterly ice flow (Veillette 1986). However, it may also be argued that the bend in the path of the Harricana-Lake McConnell complex was simply a result of topographic control on local hydraulic gradients.

A number of well preserved fluting fields, or fields of streamlined forms, are observed at the landsurface adjacent to the Harricana complex (cf. Prest *et al.* 1968). Traditionally, such fields have been interpreted as products of direct glacial action (cf. Menzies 1979). With this assumption, Hardy (1976) proposed time-transgressive formation of streamlined terrain within 100 km of the ice margin, in front of and behind the Sakami Moraine (Fig. 5.1). Currently, the possibility of fluting formation by subglacial meltwater sheet-flood events is being discussed (cf. Shaw *et al.* 1989; Shaw in press). There is general agreement, however, that these fields were produced in a subglacial environment (cf. Menzies 1989). Moreover, the excellent preservation of these subglacial bedforms implies that they represent the last major geomorphic activity of the continental ice sheet (Shaw in press). By extension this suggests that, "the bulk of erosion and transport of debris and deposition of till by continental ice sheets preceded or accompanied formation of these landforms" (Shaw in press). In support, meltout till is only locally identified in the region (Bouchard 1989) and may even have been formed prior to fluting, suggesting that the ice sheet may have been relatively debris poor after formation of the streamlined forms and during formation of the Harricana complex. The formation of streamlined forms by subglacial floods (cf. Shaw *et al.* 1989) remains a possibility.

The Harricana complex is generally aligned obliquely to adjacent fields of streamlined forms (cf. Prest *et al.* 1968). Excluding the enigmatic Cochrane events, the complex is believed to have been deposited after the formation of the streamlined forms (cf. Veillette 1986). These inferred temporal and spatial relationships of eskers and streamlined forms have been reported elsewhere (cf. Wright 1973;

Shaw 1983). Such relationships in south-central Ontario and southern and eastern Victoria Island indicate that eskers are not related to events which produced streamlined forms but, rather, are influenced by the ice-sheet and topographic geometry resulting from the events that formed these features (Brennand and Sharpe in press; Brennand and Shaw, submitted).

To the east of the Harricana complex, relatively short tributary eskers converge on the complex in the north (Figs. 5.1 and 5.3). Short eskers appear to diverge from the complex over the eastern Abitibi Upland in the south (Fig. 5.1). Between Matagami and the Sakami Moraine eskers are absent (Hardy 1976). To the west of the complex an integrated esker network, including the Harricana complex, converges on the dissected portion of the Abitibi Upland (Fig. 5.1). The sedimentary architecture of one of these eskers, the Lac Berry esker, includes elements similar to the pseudoanticlinal and alternating OAAB macroforms reported in the Harricana complex (Rondot 1982, figs. 11 and 12). Where eskers cross the Upland they appear to be shorter and more discontinuous. Invoking subglacial, steady-state, closed conduits as precursors to esker formation, Shreve (1972, 1985) concluded that subglacial eskers may be discontinuous along upslope paths.

Very few ice-marginal deposits are observed throughout the Abitibi-Timiskaming region and north to the central James Bay Lowlands (Thorleifson *et al.* 1993). Exceptions include: the Laverlochère and Roulier moraines southwest of Val d'Or (cf. Veillette 1986); discontinuous morainic deposits west of Lake Timiskaming (Boissonneau 1968); a moraine oriented east-northeast to the west of the Harricana complex at latitude 50°27'N (Hardy 1976); and some discontinuous moraines between Matagami and the Sakami Moraine (Hardy 1976; Vincent 1989) (Fig. 5.1). Most of these moraines are composed of glaciofluvial sediments (cf. Boissonneau 1968; Vincent 1989; Veillette 1990). Retreat of an active Hudson ice mass to the northwest, and of an active New Quebec ice mass to the northeast have been proposed as the deglacial model for this region (Hardy 1976; Veillette 1986, 1989, 1990). Retreat of a debris-poor ice sheet by calving into the deep water of Glacial Lake Barlow-Ojibway may explain the sparsity of ice-marginal deposits (Hardy 1976). Alternately, lack of ice-marginal deposits may be interpreted as evidence of regional ice stagnation or perhaps stagnation-zone retreat (cf. Koteff and Pessl 1981) following the last flute-forming event south of the proposed Cochrane limit (Fig. 5.2; Veillette *et al.* 1991). West of the Harricana complex, the integrated esker system may be inferred to drain a stagnant ice sheet. Between the Harricana complex and the Sakami Moraine, more numerous morainic deposits may favour a more active retreat. It is possible that this ice mass may have drained via cavities and bedrock channels; very few eskers are mapped (Vincent 1989).

The latest striae appear to converge on the Harricana complex at both regional (as far west as Timmins, Ontario, S.L. Smith 1992; Table 5.8) and local scales (Veillette 1986). Some striae are parallel to the Harricana complex (Vincent 1989) and converge on other large eskers such as the

Roulier and Moffett eskers (Veillette 1986). Convergence of striae on eskers may be explained by local indraw of ice caused by melting at conduit walls (cf. Shreve 1972, 1985; Shilts *et al.* 1987). This process does not reflect activity in the ice sheet as a whole. Indraw of ice also explains lateral transport of sediment to the Harricana complex. In addition, thermal and fluvial erosion in marginal areas of thinner ice would have eventually resulted in the development of a reentrant at the downflow end of a large conduit.

Regional convergence of striae on the Harricana complex is perhaps more interesting. While Veillette (1986, 1989, 1990) argues that these striae were formed perpendicular to the retreating Hudson ice margin, we find little evidence to corroborate active ice-marginal retreat in this region. Rather, we suggest that following a subglacial meltwater-flood event through the breach in the Abitibi Uplands (Kor *et al.* 1991) striae may have been produced during a period of readjustment of ice-sheet profiles within a coherent ice mass. Southeast of Val d'Or, striae appear to diverge at the margin of the breach in the Abitibi Upland (Fig. 5.2); a similar divergence to that shown by the eskers (Fig. 5.1). This divergence may be attributed to topographic funnelling and reorientation of equipotential contours in the ice sheet as it flowed over the Abitibi Upland.

Bedrock erosion marks, or s-forms (Kor *et al.* 1991), and rat-tails have been reported to parallel striae and flutings in the region (Veillette 1983*b*, 1986, 1989, 1990). Kor *et al.* (1991) invoke a meltwater-flood event to explain similar s-forms along the shore of Georgian Bay. They suggest that this meltwater may have originated in the James Bay/Hudson Bay area and passed through the breach in the Abitibi Uplands before continuing to Georgian Bay. Indeed, such a flood may have enhanced or created the breach in the Abitibi Uplands (Kor *et al.* 1991). The Harricana complex is located along the path of that proposed subglacial flood. If this complex was formed after changes in the ice-sheet geometry created by such a flood, then, unless the flood fanned out or bifurcated in the vicinity of North Bay, it is possible that the Lake McConnell glaciofluvial complex is temporally unrelated to the Harricana complex.

Implications for ice-sheet hydrology and dynamics

The consequences of a subglacial meltwater flood along a James Bay-Abitibi Upland breach-Georgian Bay path would have been dramatic (cf. Shoemaker 1992*a*). Flood discharges for meltwater sheets less than 150 km wide and over 10 m deep may have been of the order 10^6-10^7 m^3s^{-1} (Shoemaker 1992*b*). The ice surface along the path of such a flood would have been lowered (perhaps aided by surging), resulting in a broad depression or a number of irregular basins along this axis (Shoemaker 1992*a*). Recoupling of the ice to its bed may have been accompanied by some forward motion of the ice along the flood path. Striae parallel to the Harricana complex (Vincent 1989) may have been produced at this time.

After recoupling the ice-surface gradient would have been increased at the margins of the flood path; the ice surface would have sloped with components towards the ice margin and towards the flood path. Ice flow would have been established in the coherent ice mass obliquely towards the depression axis (the present location of the Harricana glaciofluvial complex). Such convergent ice flow may have produced convergent striae. In addition, changes in the ice-surface profile would have resulted in new hydraulic gradients, and subglacial meltwater would have been driven towards an area of low potential corresponding to the depression in the ice surface, likely collecting in a large subglacial conduit. These processes would have occurred on both sides of the linear depression in the ice surface, creating flow paths traditionally ascribed to the New Quebec and Hudson ice masses (cf. Hardy 1976). In addition, any supraglacial meltwater would have also tended to accumulate in the supraglacial depression (Shoemaker 1992*a*), perhaps in a string of basins. Periodic discharge of this supraglacial meltwater, or ponded subglacial meltwater, through the subglacial drainage system may explain the vertically alternating gravel and sand units at some locations along the Harricana glaciofluvial complex. However, the body of the complex is primarily composed of coarse gravel macroforms, suggesting very powerful flows which would have melted conduit walls. Depending on the rate of melt and the rate of ice indraw to the conduit, it is probable that the formation of some striae and the Harricana glaciofluvial complex, and/or a conduit precursor, may have been contemporaneous. If conduit wall melting (very large conduit) was rapid, local ice flow towards the conduit would be maintained. At this time, stagnant ice to the west of the complex appears to have been drained by an integrated esker system (Hardy 1976), while more active ice to the east may have been drained by a cavity-bedrock tunnel system.

As deglaciation progressed, the Harricana complex followed a zone of relatively thin ice. The large conduit would have been the focus for rapid melting, resulting in a lobate appearance to the deglacial ice-sheet margin. This geometry is corroborated by radiocarbon data, and possibly the location of the Roulier, Laverlochère (Veillette 1986), and associated western moraines (Boissonneau 1968), although these may be grounding-line moraines (cf. Sharpe and Cowan 1991). This geometry may also have been facilitated by topographic funnelling of meltwater through the dissected portion of the Abitibi Uplands. Some ice-marginal or grounding-line sedimentation may have been superimposed over the eskerine core of the Harricana complex during this phase, particularly in the southern part of the study area.

Observations in the present study cannot elucidate the impact of the Cochrane event on the Harricana complex. However, littoral reworking of glaciofluvial sediments by Glacial Lake Ojibway was identified in the southern part of the Harricana complex.

A fundamental question raised by this discussion is: What caused the apparent change in geometry of the ice sheet in this region, prior to 11 ka BP (cf. Dyke and Prest 1987)? We believe that

there are three possible answers: (*i*) the geometry was a product of earlier convergence of two separate ice masses (cf. Dyke *et al.* 1982); (*ii*) it was initiated by downdraw resulting from subglacial deformation and associated higher flow rates at the margin in the southern part of the Laurentide Ice Sheet (Veillette 1986, 1990); or (*iii*) it was the result of a meltwater-flood event. For the Harricana complex, suggestion (*i*) cannot be substantiated (Table 5.13; Veillette 1986). The second suggestion requires pervasive deformation near the southern margin of the Laurentide Ice Sheet to have triggered downdraw, and implies time-transgressive formation of the suture and of the Harricana complex. The present research favours synchronous formation of the portion of the Harricana complex studied. Development of a deglacial corridor along the Harricana complex axis is readily explained by thinner ice associated with a large subglacial conduit. Our observations favour synchronous regional changes in ice sheet geometry related to the effects of a meltwater-flood event.

References

Aario, R. 1977. Classification and terminology of morainic landforms in Finland. Boreas, 6: 87-100.

Allard, M. 1974. Geomorphologie des eskers Abitibiens. Cahiers de Géographie de Québec, 18: 271-296.

Allen, J.R.L. 1982. Late Pleistocene (Devensian) glaciofluvial outwash at Banc-Y-Warren, near Cardigan (west Wales). Geological Journal, 17: 31-47.

Allen, J.R.L. 1984. Sedimentary structures: their character and physical basis. Developments in Sedimentology 30. Vol. I. Elsevier, Amsterdam.

Alley, R.B. 1992. How can low-pressure channels and deforming tills coexist subglacially. Journal of Glaciology, 38: 200-207.

Baker, V.R. 1973. Paleohydrology and sedimentology of Lake Missoula flooding in eastern Washington. Geological Society of America, Special Paper 144.

Baker, V.R. 1978. Large-scale erosional and depositional features of the Channeled Scabland. *In* The Channeled Scabland: a guide to the geomorphology of the Columbia Basin, Washington. *Edited by* V.R. Baker, and D. Nummedal. National Aeronautics and Space Administration, pp. 81-115.

Banerjee, I., and McDonald, B.C. 1975. Nature of esker sedimentation. *In* Glaciofluvial and glaciolacustrine sedimentation. *Edited by* A.V. Jopling, and B.C. McDonald. Society of Economic Paleontologists and Mineralogists, Special Publication 23, pp. 304-320.

Boissonneau, A.N. 1968. Glacial history of northeastern Ontario II. The Timiskaming-Algoma area. Canadian Journal of Earth Sciences, 5: 97-109.

Bouchard, M.A. 1989. Subglacial landforms and deposits in central and northern Québec, Canada, with emphasis on Rogen moraines. *In* Subglacial bedforms - drumlins, rogen moraine and associated subglacial bedforms. *Edited by* J. Menzies, and J. Rose. Sedimentary Geology, 62: 293-308.

Bouchard, M.A., and Salonen, V.-P. 1989. Glacial dispersal of boulders in the James Bay Lowlands of Québec, Canada. Boreas, 18: 189-199.

Brayshaw, A.C. 1984. Bed microtopography and entrainment thresholds in gravel-bed rivers. Geological Society of America Bulletin, 96: 218-233.

Brennand, T.A. in press. Macroforms, large bedforms and rhythmic sedimentary sequences in subglacial eskers, south-central Ontario: implications for esker genesis and meltwater regime. Sedimentary Geology.

Brennand, T.A., and Sharpe, D.R. in press. Ice-sheet dynamics and subglacial meltwater regime inferred from form and sedimentology of glaciofluvial systems: Victoria Island, District of Franklin, Northwest Territories. Canadian Journal of Earth Sciences.

Brennand, T.A., and Shaw, J. submitted. Tunnel channels and associated landforms, south-central Ontario: their implications for ice-sheet hydrology. (Canadian Journal of Earth Sciences).

Chapman, L.J., and Putnam, D.F. 1984. Physiography of southern Ontario. Ontario Geological Survey, Map P.2715, scale 1:600 000.

Chauvin, L. 1977. Géologie des dépôts meubles de la région de Joutel-Matagami. Ministére des richesses naturelles, dossier public 539, 106 p.

Cheel, R.J. 1982. The depositional history of an esker near Ottawa, Canada. Canadian Journal of Earth Sciences, 19: 1417-1427.

Cheel, R.J. 1990. Horizontal lamination and the sequence of bed phases and stratification under upper flow regime conditions. Sedimentology, 37: 517-529.

Cheel, R.J., and Middleton, G.V. 1986. Horizontal laminae formed under upper flow regime plane bed conditions. Journal of Geology, 94: 489-504.

Clayton, L., Mickelson, D.M., and Attig, J.W. 1989. Evidence against pervasively deformed bed material beneath rapidly moving lobes of the southern Laurentide Ice Sheet. Sedimentary Geology, 62: 203-208.

Costa, J.E. 1988. Rheologic, geomorphologic, and sedimentologic differentiation of water floods, hyperconcentrated flows, and debris flows. *In* Flood geomorphology. *Edited by* V.R. Baker, R.C. Kochel, and P.C. Patton. John Wiley and Sons, London, pp. 113-122.

Curray, J.R. 1956. The analysis of two-dimensional orientation data. Journal of Geology, 64: 177-131.

Davis, J.C. 1986. Statistical and data analysis in geology. 2nd ed. John Wiley and Sons, New York.

De Geer, G. 1897. Om rullstensåsarnas bildningssätt. Geologiska Föreningens i Stockholm Förhandlingar, 19: 366-388.

DiLabio, R.N.W., Miller, R.F., Mott, R.J., and Coker, W.B. 1988. The Quaternary stratigraphy of the Timmins area, Ontario, as an aid to mineral exploration by drift prospecting. *In* Current research, part C. Geological Survey of Canada, Paper 88-1C, pp. 61-65.

Dredge, L.A., and Cowan, W.R. 1989. Quaternary geology of the southwestern Canadian Shield. *In* Quaternary geology of Canada and Greenland. *Edited by* R.J. Fulton. Geological Survey of Canada, Geology of Canada, no. 1, pp. 214-249.

Dredge, L.A., and Nixon, F.M. 1992. Glacial and environmental geology of northeastern Manitoba. Geological Survey of Canada, Memoir 432.

Dredge, L.A., Nixon, F.M., and Richardson, R.J. 1986. Quaternary geology and geomorphology of northwestern Manitoba. Geological Survey of Canada, Memoir 418.

Dryden, A.L. Jr. 1931. Accuracy in percentage representation of heavy mineral frequencies. National Academy of Science, 17: 233-238.

Duckworth, P.B. 1979. The late depositional history of the western end of the Oak Ridges moraine, Ontario. Canadian Journal of Earth Sciences, 16: 1094-1107.

Dyke, A.S., and Prest, V.K. 1987. Late Wisconsinan and Holocene history of the Laurentide Ice Sheet. Géographie physique et Quaternaire, 41: 237-263.

Dyke, A.S., Dredge, L.A., and Vincent, J.-S. 1982. Configuration and dynamics of the Laurentide Ice Sheet during the Late Wisconsin maximum. Géographie physique et Quaternaire, 36: 5-14.

Elfström, Å. 1987. Large boulder deposits and catastrophic floods: a case study of the Bäldkatj area, Swedish Lapland. Geografiska Annaler, Series A, 69: 101-121.

Fisher, R.V. 1990. Transport and deposition of a pyroclastic surge across an area of high relief: the 18 May 1980 eruption of Mount St. Helens, Washington. Geological Society of America Bulletin, 102: 1038-1054.

Fraser, G.S., and Bleuer, N.K. 1988. Sedimentological consequences of two floods of extreme magnitude in the late Wisconsinan Wabash Valley. Geological Society of America, Special Paper 229, pp. 111-125.

Gorrell, G., and Shaw, S. 1991. Deposition in an esker, bead and fan complex, Lanark, Ontario, Canada. Sedimentary Geology, 72: 285-314.

Hardy, L. 1976. Contribution à l'étude géomorphologique de la portion québecoise des basses terres de la baie de James. Thèse de doctorat, Université McGill, Montréal.

Hardy, L. 1977. La déglaciation et les épisodes lacustre et marin sur le versant québécois des basses terres de la Baie de James. Géographie physique et Quaternaire, 31: 261-273.

Hardy, L. 1982. Le Wisconsinien supérieur à l'est de la Baie James (Québec). Naturaliste Canadien, 109: 333-351.

Harrison, J.E. 1972. Quaternary geology of the North Bay-Mattawa region. Geological Survey of Canada, Paper 71-26.

Hickock, S.R., and Dreimanis, A. 1992. Deformation till in the Great Lakes region: implications for rapid flow along the south-central margin of the Laurentide Ice Sheet. Canadian Journal of Earth Sciences, 29: 1565-1579.

Hooke, R. LeB. 1989. Englacial and subglacial hydrology: a qualitative review. Arctic and Alpine Research, 21: 221-233.

Iken, A., and Bindshadler, R.A. 1986. Combined measurements of subglacial and surface velocity of Findelengletscher, Switzerland: conclusions about drainage system and sliding mechanism. Journal of Glaciology, 32: 101-119.

Iseya, F., and Ikeda, H. 1987. Pulsations in bedload transport rates induced by longitudinal sediment sorting: a flume study using sand and gravel mixtures. Geografiska Annaler, Series A, 69: 15-27.

Johansson, C.E. 1963. Orientation of pebbles in running water. Geografiska Annaler, 45: 85-112.

Johansson, C.E. 1965. Structural studies of sedimentary deposits. Geologiska Föreningens i Stockholm Föhandlingar, 87: 3-61.

Johansson, C.E. 1976. Structural studies of frictional sediments. Geografiska Annaler, 58: 201-300.

Kaszychi, C.A., and DiLabio, R.N.W. 1986. Surficial geology and till geochemistry, Llyn Lake-Leaf Rapids region, Manitoba. *In* Current research, part B. Geological Survey of Canada, Paper 86-1B, pp. 245-256.

Klassen, R.W. 1983. Lake Agassiz and the late glacial history of northern Manitoba. *In* Glacial Lake Agassiz. *Edited by* J.T. Teller, and L. Clayton. Geological Association of Canada, Special Paper 26, pp. 97-116.

Klassen, R.W. 1986. Surficial geology of north-central Manitoba. Geological Survey of Canada, Memoir 419.

Kor, P.S.G., Shaw, J., and Sharpe, D.R. 1991. Erosion by subglacial meltwater, Georgian Bay, Ontario: a regional view. Canadian Journal of Earth Science, 28: 623-642.

Koteff, C., and Pessl, F., Jr. 1981. Systematic ice retreat in New England. United States Geological Survey, Professional Paper 1179.

Low, A.P. 1888. Report on explorations in James' Bay and country east of Hudson Bay, drained by the Big, Great Whale and Clearwater rivers. Geological Survey of Canada, Annual Report 3 (2-J), pp. 1J-94J.

McClenaghan, M.B. 1989. Quaternary geology and geochemical exploration in the Matheson area, Northeastern Ontario. M.Sc. Thesis, Queen's University, Kingston.

McClenaghan, M.B., Lavin, O.P., Nichol, I., and Shaw, J. 1987. Quaternary geology and geochemical exploration in the Matheson area. *In* Geoscience research grant program, summary of research 1986-87. *Edited by* V.G. Milne. Ontario Geological Survey, Miscellaneous Paper 136, pp. 200-214.

McClenaghan, M.B., Lavin, O.P., Nichol, I., and Shaw, J. 1988. Quaternary geology and geochemical exploration in the Matheson area, northeastern Ontario. *In* Prospecting in areas of glaciated terrain-1988. *Edited by* D.R. MacDonald, and K.A. Mills. Canadian Institute of Mining Metallurgy, pp. 1-20.

McClenaghan, M.B., Lavin, O.P., Nichol, I., and Shaw, J. 1992. Geochemistry and clast lithology as an aid to till classification, Matheson, Ontario, Canada. Journal of Geochemical Exploration, 42: 237-260.

McDonald, B.C., and Shilts, W.W. 1975. Interpretation of faults in glaciofluvial sediments. *In* Glaciofluvial and glaciolacustrine sedimentation. *Edited by* A.V. Jopling, and B.C. McDonald. Society of Economic Paleontologists and Mineralogists, Special Publication 23, pp. 123-131.

McDonald, B.C., and Vincent, J.S. 1972. Fluvial sedimentary structures formed experimentally in a pipe, and their implications for interpretation of subglacial sedimentary environments. Geological

Survey of Canada, Paper 72-27.

Meland, N., and Norrman, J.O. 1969. Transport velocities of individual size fractions in heterogeneous bed load. Geografiska Annaler, Series A, 51: 127-144.

Menzies, J. 1979. A review of the literature on the formation and location of drumlins. Earth Science Reviews, 14: 315-359.

Menzies, J. 1989. Drumlins - products of controlled or uncontrolled glaciodynamic response? Quaternary Science Reviews, 8: 151-158.

MERQ-OGS 1983. Lithostratigraphic map of the Abitibi Subprovince. Ontario Geological Survey/Ministère de l'Énergie et des Ressources, Québec, 1:500 000. Catalogued as "Map 2484" in Ontario and "DV 83-16" in Québec.

Miall, A.D. 1985. Architectural-element analysis: a new method of facies analysis applied to fluvial deposits. Earth Sciences Reviews, 22: 261-308.

Pierson, T.C., and Scott, K.M. 1985. Downstream dilution of a lahar: transition from debris flow to hyperconcentrated streamflow. Water Resources Research, 21: 1511-1542.

Postma, G., Nemec, W., and Kleinspehn, K.L. 1988. Large floating clasts in turbidites: a mechanism for their emplacement. Sedimentary Geology, 58: 47-61.

Powers, M.C. 1953. A new roundness scale for sedimentary particles. Journal of Sedimentary Petrology, 23: 117-119.

Prest, V.K. 1990. Laurentide ice-flow patterns: a historical review, and implications of the dispersal of Belcher Island erratics. Géographie physique et Quaternaire, 44: 113-136.

Prest, V.K., and Nielsen, E. 1987. The Laurentide Ice Sheet and long distance transport. Geological Survey of Finland, Special Paper 3, pp. 91-101.

Prest, V.K., Grant, D.R., and Rampton, N. 1968. Glacial map of Canada. Geological Survey of Canada Map 1253A, scale 1:5 000 000.

Punkari, M. 1980. The ice lobes of the Scandinavian Ice Sheet during the deglaciation in Finland. Boreas, 9: 307-310.

Richard, P.J.H., Veillette, J.J., and Larouche, A.C. 1989. Palynostraitgraphie et chronologie du retrait glaciaire au Témiscamingue: évaluation des âges ^{14}C et implications paléoenvironmentales. Canadian Journal of Earth Sciences, 26: 627-641.

Ringrose, S. 1982. Depositional processes in the development of eskers in Manitoba. *In* Research in glacial, glaciofluvial and glaciolacustrine systems. *Edited by* R. Davidson-Arnott, W. Nickling, and B.D. Fahey. Proceedings of the 6th Guelph symposium on geomorphology. Geo-Books, Norwich, U.K., pp. 117-137.

Rondot, J. 1982. L'esker du Lac Berry. Ministère de l'Énergie et des Ressources, Direction de la

Géologie.

Rouse, H. 1961. Fluid mechanics for hydraulic engineers. Dover Publications Inc., New York.

Rust, B.R. 1972. Pebble orientation in fluvial sediments. Journal of Sedimentary Petrology, 42: 384-388.

Rust, B.R. 1984. Proximal braidplain deposits in the Middle Devonian Malbaie Formation of Eastern Gaspé, Quebec, Canada. Sedimentology, 31: 675-695.

Rust, B.R., and Koster, E.H. 1984. Coarse alluvial deposits. *In* Facies Models. 2nd ed. *Edited by* R.G. Walker. Geoscience Canada Reprint Series 1, Toronto, pp. 53-69.

Sado, E.V., and Carswell, B.F. 1987. Surficial geology of northern Ontario. Ontario Geological Survey Map 2518, scale 1:1 200 000.

Saunderson, H.C. 1977. The sliding bed facies in esker sands and gravels: a criterion for full-pipe (tunnel) flow? Sedimentology, 24: 623-638.

Sharpe, D.R., and Cowan, W.R. 1991. Moraine formation in northwestern Ontario: product of subglacial fluvial and glaciolacustrine sedimentation. Canadian Journal of Earth Sciences, 27: 1478-1486.

Shaw, J. 1972. Sedimentation in the ice-contact environment, with examples from Shropshire (England). Sedimentology, 18: 23-62.

Shaw, J. 1983. Drumlin formation related to inverted melt-water erosion marks. Journal of Glaciology, 29: 461-478.

Shaw, J. in press. A qualitative view of sub-ice-sheet landscape evolution. Progress in Physical Geography.

Shaw, J., and Gorrell, G. 1991. Subglacially formed dunes with bimodal and graded gravel in the Trenton drumlin field, Ontario. Géographie physique et Quaternaire, 45: 21-34.

Shaw, J., and Kellerhals, R. 1977. Paleohydraulic interpretation of antidune bedforms with application to antidunes in gravel. Journal of Sedimentary Petrology, 47: 257-266.

Shaw, J., and Sharpe, D.R. 1987. Drumlin formation by meltwater erosion. Canadian Journal of Earth Sciences, 24: 2316-2322.

Shaw, J., Kvill, D., and Rains, B. 1989. Drumlins and catastrophic subglacial floods. Sedimentary Geology, 62: 177-202.

Shilts, W.W., and Wyatt, P.H. 1988. Aminostratigraphy of marine and associated nonglacial beds of the Hudson Bay Lowland. *In* Institute of arctic and alpine research, 17th annual workshop, University of Colorado, Boulder, Abstracts, p. 49.

Shilts, W.W., Aylsworth, J.M., Kaszycki, C.A., and Klassen, R.A. 1987. Canadian Shield. *In* Geomorphic systems of North America. *Edited by* W.L. Graf. Geological Society of America, Centennial Special Volume 2, pp. 119-161.

Shoemaker, E.M. 1986. Subglacial hydrology for an ice sheet resting on a deformable aquifer. Journal

of Glaciology, 32: 20-30.

Shoemaker, E.M. 1992*a*. Water sheet outburst floods from the Laurentide Ice Sheet. Canadian Journal of Earth Sciences, 29: 1250-1264.

Shoemaker, E.M. 1992*b*. Subglacial floods and the origin of low relief ice sheet lobes. Journal of Glaciology, 38: 105-112.

Shoemaker, E.M., and Leung, H.K.N. 1987. Subglacial drainage for an ice sheet resting on a layered deformable bed. Journal of Geophysical Research, 92: 4935-4946.

Shreve, R.L. 1972. Movement of water in glaciers. Journal of Glaciology, 11: 205-214.

Shreve, R.L. 1985. Esker characteristics in terms of glacial physics, Katahdin esker system, Maine. Geological Society of America Bulletin, 96: 639-646.

Skinner, R.G. 1973. Quaternary stratigraphy of the Moose River Basin, Ontario. Geological Survey of Canada, Bulletin 225.

Skipper, K. 1971. Antidune cross-stratification in a turbidite sequence, Chloridorme Formation, Gaspé, Québec. Sedimentology, 17: 51-68.

Smith, G.A. 1986. Coarse-grained nonmarine volcaniclastic sediment: terminology and depositional process. Geological Society of America Bulletin, 97: 1-10.

Smith, S.A. 1990. The sedimentology and accretionary styles of an ancient gravel-bed stream: the Budleigh Salterton Pebble Beds (Lower Triassic), southwest England. Sedimentary Geology, 67: 199-219.

Smith, S.L. 1992. Quaternary stratigraphic drilling transect, Timmins to the Moose River Basin, Ontario. Geological Survey of Canada, Bulletin 415, 94 p.

Sneed, E.D., and Folk, R.L. 1958. Pebbles in the lower Colorado River, Texas: a study in particle morphogenesis. Journal of Geology, 66: 114-150.

Steele, K.G., Baker, C.L., and McClenaghan, M.B. 1989. Models of glacial stratigraphy determined from drill core, Matheson area, northeastern Ontario. *In* Drift prospecting. *Edited by* R.N.W. DiLabio, and W.B. Coker. Geological Survey of Canada, Paper 89-20, pp. 127-138.

Thorleifson, L.H. 1989. Quaternary stratigraphy of the central Hudson Bay Lowland, northern Ontario, Canada. Ph.D. thesis, University of Colorado, Boulder.

Thorleifson, L.H., Wyatt, P.H., Shilts, W.W., and Nielsen, E. 1992. Hudson Bay lowland Quaternary stratigraphy: evidence for early Wisconsinan glaciation centred in Quebec. *In* The last interglacial-glacial transition in North America. *Edited by* P.U. Clark, and P.D. Lea. Geological Society of America, Special Paper 270, pp. 207-221.

Thorleifson, L.H., Wyatt, P.H., and Warman, T.A. 1993. Quaternary stratigraphy of the Severn and Winsk drainage basins, Northern Ontario. Geological Survey of Canada, Bulletin 442.

Tremblay, G. 1974. Géologie du Quaternaire, régions de Rouyn-Noranda et d'Abitibi, comtés d'Abitibi-est et d'Abitibi-ouest, Québec. Ministére des richesses naturelles, dossier public 236.

Tremblay, L.P. 1950. Fiedmont map area, Abitibi county, Quebec. Geological Survey of Canada, Memoir 253.

Veillette, J.J. 1983*a*. Déglaciation de la vallée supérieure de l'Outaouais, le lac Barlow et le sud be lac Ojibway, Québec. Géographie physique et Quaternaire, 37: 67-84.

Veillette, J.J. 1983*b*. Les polis glaciaires au Témiscamigue: une chronologie relative. *In* Current research, part A. Geological Survey of Canada, Paper 83-1A, pp. 187-196.

Veillette, J.J. 1986. Former ice flows in the Abitibi-Timiskaming region: implications for the configuration of the late Wisconsinan ice sheet. Canadian Journal of Earth Sciences, 23: 1724-1741.

Veillette, J.J. 1988. Déglaciation et évolution des lacs proglaciaires post-Algonquin et Barlow au Témiscaningue, Québec et Ontario. Géographie physique et Quaternaire, 42: 7-31.

Veillette, J.J. 1989. Ice movements, till sheets and glacial transport in Abitibi-Timiskaming, Quebec and Ontario. *In* Drift prospecting. *Edited by* R.N.W. DiLabio, and W.B. Coker. Geological Survey of Canada, Paper 89-20, pp. 139-154.

Veillette, J.J. 1990. Le Dernier Glaciaire au Témagamingue, Québec et Ontario. Thèse de doctotat, Université Libre de Bruxelles, Belgique.

Veillette, J.J., Averill, S.A., LaSalle, P., and Vincent, J.-S. 1989. Quaternary geology of Abitibi-Témiscamingue and mineral exploration. Field trip B1 of the Geological Association of Canada, guidebook, 122 p.

Veillette, J.J., Paradis, S.J., Thibaudeau, P., and Pomares, J.-S. 1991. Distribution of distinctive Hudson Bay erratics and the problem of the Cochrane limit in Abitibi, Quebec. *In* Current research, part C. Geological Survey of Canada, Paper 91-1C, pp. 135-142.

Vincent, J.-S. 1989. Quaternary geology of the southeastern Canadian Shield. *In* Quaternary geology of Canada and Greenland. *Edited by* R.J. Fulton. Geological Survey of canada, Geology of Canada, no. 1, pp. 249-274.

Vincent, J.-S., and Hardy, L. 1979. The evolution of glacial lakes Barlow and Ojibway, Quebec and Ontario. Geological Survey of Canada, Bulletin 316.

Vincent, J.-S., Veillette, J.J., Allard, M., Richard, P.J.H., *et al*. 1987. The last glacial cycle and ice-retreat from the upper Ottawa river valley to southeast Hudson Bay. XIIth INQUA congress field excursion C-10 guidebook.

Walder, J., and Hallet, B.H. 1979. Geometry of former subglacial water channels and cavities. Journal of Glaciology, 23: 335-346.

Williams, G.P. 1983. Paleohydrological methods and some examples from Swedish fluvial environments. Geografiska Annaler, Series A, 65: 227-243.

Wilson J.T. 1938. Glacial geology of part of north-western Quebec. Transactions of the Royal Society of Canada, Section 4, 32: 49-59.

Woodcock, N.H., and Naylor, M.A. 1983. Randomness testing in three-dimensional orientation data. Journal of Structural Geology, 5: 539-548.

Wright, H.E. Jr. 1973. Tunnel valleys, glacial surges and subglacial hydrology of the Superior lobe, Minnesota. *In* The Wisconsinan Stage. *Edited by* R.F. Black, R.P. Goldthwaite, and H.B. Willman. Geological Society of America, Memoir 136: 251-276.

Wyatt, P.H. 1989. The stratigraphy and amino acid chronology of Quaternary sediments in central Hudson Bay Lowland. M.Sc. thesis, University of Colorado, Boulder.

Yelle, J.S. 1976. Physiographic map of eastern Canada and adjacent areas. Geological Survey of Canada, Map 1399A (SW), scale 1:2 000 000.

Zingg, T. 1935. Beiträge zur Schotteranalyse. Schweizerische Mineralogosche und Petrographische Mitteilungen, 15: 39-140.

Zoltai, S.C. 1965. Glacial features of the Quetico-Nipigon area, Ontario. Canadian Journal of Earth Sciences, 2: 247-269.

CHAPTER 6

Summary, discussion, and future research avenues

Two questions were posed at the outset of this thesis:

1. How did tunnel channels and eskers form?
2. Are the processes responsible for their formation related and do they record an evolution in the ice sheet drainage system?

Using an integrated approach, combining landform associations, geomorphic and sedimentologic investigation and glacial hydrologic theory, the observations and interpretations presented contribute some partial answers to the questions posed. What follows is a summary and discussion of the major findings of this thesis, and suggestions for future research avenues in light of these findings.

Tunnel channel genesis

Laurentide tunnel channels truncate fields of streamlined forms (drumlins and flutings) and contain eskers. In south-central Ontario, tunnel channels have upslope, undulatory flow paths, and form an integrated, anastomosing pattern in bedrock and glacigenic sediment over an area of at least 60 km^2 (this thesis). These characteristics suggest synchronous operation of a large subglacial N-channel system. A combined R/N-channel flow is inferred from the discontinuous thalweg of the tunnel channel at Ferguson Lake. In both cases, formation by multiple flow events is suggested by: flutes that have developed downflow from the upflow facing channel wall at Ferguson Lake, favouring the existence of the wall before the event that formed the streamlined field; the coincidence of some channel paths with inferred preglacial drainage paths (cf. Wilson 1904); and the depth of incision into bedrock and the presence of Dummer Moraine on the floor of some channels in south-central Ontario.

For both Ontario and Victoria Island associated streamlined fields were interpreted as the products of erosion by turbulent separated flows within catastrophically released subglacial meltwater sheets (cf. Shaw and Gilbert 1990; Sharpe 1992). Chapters 2 and 3 present reasons for accepting this hypothesis. Thus, subglacial sheet flow with a sculpted bed (streamlined forms) and confining ice surface describes the initial conditions for landforms formed immediately after drumlins and flutings. Consequently, the starting conditions for post-drumlin and post-fluting landforms include a streamlined bed and counterpart ice bed, in phase with the streamlined forms and separated from them by a high velocity meltwater sheet. In south-central Ontario, the identification of elongate, relatively narrow, deep scours on drumlinized residuals (late-stage sheet flow scours) in the western part of the study area, and broad scour zones or megachannels in the eastern part, both in close association with the tunnel channels, suggest progressive channelization and flow diversion processes. Such processes may be governed by the geometric interactions between the recoupling ice base and bed and the thermodynamic

feedbacks within an increasingly discontinuous meltwater sheet.

If the geometric model of progressive channelization of meltwater during the collapse of a meltwater sheet presented here is correct, then why are tunnel channels on Victoria Island isolated, rather than integrated, anastomosing systems as modelled? Perhaps the answer lies in the nature of the reservoir feeding the meltwater sheet event, and the magnitude and duration of that event. Meltwater for the Algonquin event may have been subglacially generated in Québec, following a coherent path over Lake Mistassini, over the Algonquin Highlands and into the Finger Lakes region of New York State (Shaw and Gilbert 1990; J. Shaw personal communication 1993). In contrast, streamlined fields on Victoria Island are relatively short and record numerous cross-cutting relationships (cf. Fyles 1963). It is possible that these small streamlined fields may have been eroded by meltwater released from relatively small subglacial or supraglacial reservoirs. Perhaps, such events were shorter-lived and collapsed more rapidly than the larger Algonquin event, rendering insufficient meltwater and time to form complex anastomosing tunnel channel systems.

Tunnel channels: future research avenues

1. Although a general qualitative model of tunnel channel genesis from the progressive collapse and channelization of a catastrophically released meltwater sheet has been suggested, the mechanics of formation have not been addressed. The question as to whether tunnel channels were directly incised by meltwater as N-channels or whether subglacial deformation of sediment into R-channels was responsible for their formation has not been tested. Careful investigation of sediments in tunnel channels walls, including geophysical profiling, is required to answer this question.
2. Numerical modelling of turbulent flow between rough surfaces may be attempted as a quantitative partner of the qualitative model presented in Chapter 3.
3. Detailed description and interpretation of the morphology of the tunnel channels in terms of within-channel residuals, scour zones and fields of transverse ridges is necessary to infer the meltwater flow regime responsible for tunnel channel formation and evolution. In areas where sedimentary exposures in transverse ridges are not available, remote sensing methods such as ground-penetrating radar may assist in a genetic interpretation of within-channel bedforms.

Esker genesis

Subglacial or grounding-line depositional environments are inferred for all of the Laurentide eskers investigated in this thesis. In south-central Ontario and on Victoria Island the eskers lie in or extend from tunnel channels, favouring a subglacial origin, at least for the early phases of esker sedimentation. In south-central Ontario, sedimentation in a synchronous, subglacial, closed conduit is also inferred from: continuous upslope flow paths, minimal postformational disturbance in esker sediments, down-esker trends in clast roundness, and low variability in paleoflow direction estimates.

Gaps along esker ridges are attributed to nondepositional zones along a continuous conduit or postdepositional erosion. Esker sediment records powerful, pulsed flows, perhaps controlled by episodic drainage of subglacial cavities or supraglacial water bodies, or seasonal changes in meltwater production. Seasonal control may suggest that each sand-gravel couplet records a supraglacial to subglacial connection in the meltwater system. However, more indirect seasonal changes in subglacial water pressures may have effected episodic drainage of subglacial cavities into conduits.

An architectural approach to esker sedimentology in the context of a constraining depositional environment, provides a useful tool for reconstructing the mechanics of esker formation. Gravel facies and macroforms have been identified, described and interpreted. They reflect powerful flows down nonuniform conduits, with the style of sedimentation controlled by conduit geometry. By extension, fans, beads with minor ridges, and extended, hummocky zones are interpreted as sedimentation related to high discharge events which caused localized floatation to capture adjacent cavities or allow localized (narrow), short-lived, sheet-flow events.

Time-transgressive formation in an interlobate position has been inferred for the Harricana glaciofluvial complex from the arrangement of adjacent landforms and sediments (cf. Veillette 1986). However, inferences from the complex itself question this interpretation. The complex is a relatively continuous body of upsloping glaciofluvial sediment which increases in width and complexity downflow towards an ice margin or grounding line. Thus, the complex is interpreted as a large esker deposited in a subglacial, closed conduit. The identification of gravel facies, macroforms, and sand-gravel couplets similar to those in the south-central Ontario eskers also support this interpretation and again suggest powerful, pulsed flows through a nonuniform conduit.

In contrast to the coarse-grained, integrated esker systems investigated in south-central Ontario and Québec, those investigated on Victoria Island were isolated and fine grained, their sediments resembling those reported in subaqueous fans. This perhaps represents a bias resulting from the natural gullying process rather than a dominance of fine-grained eskers on Victoria Island, as many eskers adjacent to those investigated exhibited cobbles over their surfaces. However, the differences in sedimentary styles suggests that late on during deglaciation there was less meltwater production, less energetic conditions and possibly very much lower and thinner ice sheet profiles than in Ontario and Québec. Rhythmites with clay drapes suggest seasonally-governed meltwater discharges and a warm-based or polythermal ice sheet. At Namaycush Lake, a continuous esker with fans and extended deposits suggests deposition in a subglacial conduit with localized floatation events in proximity to a grounding line. The more disconnected eskers at Ferguson Lake and Augustus Hills further south, were probably deposited in a thinning and stagnating ice mass, although their association with tunnel channels, and continuity in the textural and structural characteristics of the sediments at Augustus Hills, combined with probable high sea levels, still favour synchronous sedimentation in subglacial conduits, rather than

time-transgressive sedimentation in reentrants.

Eskers: future research avenues

1. While the descriptions and interpretations of gravel facies and macroforms presented in this thesis are rigorous, as in all realist science, the necessary link to processes and controls is tenuous. The main problem lies in the dearth of research on the mechanics of sediment movement of extreme grain sizes in unsteady flows (cf. Allen 1983) and the flow dynamics, sedimentation mechanisms and potential sedimentary structures expected in nonuniform, closed conduits. Engineering literature has furnished information on slurry flow through pipelines (e.g., Newitt *et al.* 1955). However, concern has been with maintaining sediment movement rather than with depositional consequences, and with uniform rather than nonuniform conduits (excluding bends, Rouse 1961). Flume studies may assist in refining or refuting the interpretations presented here.
2. Macroforms have been identified based on detailed sedimentologic analysis. It may be possible to define the three-dimensional morphology and sedimentary variation of these macroforms using remote-sensing methods such as ground-penetrating radar. Having done so, in areas where sedimentary exposures are poor and limited, as in the Northwest Territories, such remotely-sensed data may facilitate the identification of similar macroforms. The presence or absence of these forms may assist in a genetic interpretation of other Laurentide eskers.

Laurentide meltwater systems: implications for ice-sheet models

Having interpreted both tunnel channels and eskers in terms of radically different Laurentide meltwater drainage systems, landform associations and stratigraphic context provide a key to speculating on changes in the Laurentide meltwater system over the course of deglaciation. In south-central Ontario and on Victoria Island landform associations suggest catastrophically released sheet flow events which collapsed to channelized flows (recorded in the streamlined fields and tunnel channels) followed by the establishment of seasonally controlled drainage systems (recorded in eskers, fans, beads and extended, hummocky zones). Thus, a smooth evolution in the ice sheet drainage system recorded by streamlined forms, tunnel channels and eskers is not suggested, based on the differences in their scales, the rhythmicity of esker sediments and, on Victoria Island, possible paleoflow reversals between streamlined fields and cross-cutting eskers. However, the question as to whether tunnel channels were completely invaded by ice after a sheet flow event, or whether residual R-channels remained has not been answered. In south-central Ontario, meltwater flowed upslope to the ice margin. The collapse of a meltwater sheet would have caused the ice and bed to recouple in northern New York State, funnelling the remaining meltwater through the Finger Lakes. With regressive recoupling, it is likely that R-channel or N-channel flows were pinched off in south-central Ontario leaving elongate water-filled cavities in tunnel channels.

However, this is, perhaps, a moot point as the depositional manifestation of the R-channels - eskers - record seasonally controlled drainage established some time after the catastrophic event(s).

For catastrophic meltwater sheet events to have occurred required large meltwater reservoirs which may have been supraglacial or subglacial. If subglacial, it is likely that the ice was cold based downflow from the reservoir. At Ferguson Lake, the streamlined forms are inferred to have been eroded into ice-rich sediment, and one possible mechanism suggested for the formation of the Dummer Moraine in south-central Ontario involves ice frozen into karstified limestone before the Algonquin event. In contrast, eskers suggest later warm-based or polythermal ice conditions. In addition, on Victoria Island, in south-central Ontario, and in the region adjacent to the Harricana glaciofluvial complex, the sparsity of ice-marginal indicators and the well preserved morphology and sedimentology of eskers suggest that after meltwater sheet events the Laurentide Ice Sheet stagnated or underwent stagnation zone retreat in these regions. At Namaycush Lake, in south-central Ontario and towards the southern part of the Harricana glaciofluvial complex (latitude 48°N), grounding-line environments are inferred. Potential geographic differences and temporal changes in the thermal conditions of the Laurentide Ice Sheet, as inferred from geomorphic and sedimentary evidence, must be addressed in future ice-sheet models.

The regional implications of the interpretation of the Harricana glaciofluvial complex as a large, synchronously deposited, subglacial esker have been discussed in context of landform associations and relevant stratigraphic interpretations. The location of the complex is attributed to changes in the ice sheet and topographic geometry resulting from the meltwater event(s) inferred to have created adjacent streamlined forms. If this hypothesis is correct, then a similar inference may be appropriate in other areas exhibiting streamlined forms (including s-forms), regionally converging striae, and so-called interlobate moraines. One such area is in northern Manitoba. A potential flood route from Hudson Bay, over the Lake Winnipeg basin and south to Minnesota follows a low-relief, dissected tract, and may be responsible for similar landform assemblages to those described in association with the Harricana complex. It is, perhaps, interesting to note that the Leaf Rapids interlobate moraine, Manitoba (Kaszychi and DiLabio 1986), which has many of the characteristics of the Harricana complex, was earlier interpreted as a subglacial esker by Ringrose (1982).

Laurentide meltwater systems: future research avenues

1. Until recently the tunnel channels in south-central Ontario were unmapped. It is likely that comparable systems remain unmapped elsewhere. In places where eskers cross-cut streamlined fields, tunnel channels are expected.
2. Detailed and integrated investigations of other so-called interlobate moraines are required to determine their genesis and their implications for Laurentide deglacial models. This is particularly vital in northern Manitoba as Shoemaker (1992) has suggested the possibility of

reversed drainage of Glacial Lake Agassiz towards Hudson Bay through the interlobate complexes. In south-central Ontario the Oak Ridges complex has also been interpreted as an interlobate moraine. However, this feature remains enigmatic and should be investigated in detail.

3. The implications of the detailed hydrodynamic reconstructions presented in this thesis necessitate reassessment of the current models of ice-sheet dynamics inferred for the regions investigated, as meltwater and ice sheet dynamics are inter-related. The feedback between these systems affected the rate and style of deglaciation, and may have contributed to apparently climatically unrelated rises in sea level (Shaw 1989; Blanchon and Shaw 1993). Dynamic reconstructions of ice sheet disintegration are used as inputs to models of global atmospheric circulation patterns (e.g. Kutzbach, 1987). The sensitivity of these models to the dynamics of the ice sheet, makes any reassessment of the glacial hydrologic system associated with that ice sheet of prime importance. Therefore, integrated investigations similar to those presented here must be undertaken elsewhere within the limits of all Wisconsinan continental ice sheets.

References

Allen, J.R.L. 1983. River bedforms: progress and problems. *In* Modern and ancient fluvial systems. *Edited by* J.D. Collinson, and J. Lewin. International Association of Sedimentologists, Special Publication 6, pp. 19-33.

Blanchon, P., and Shaw, J. 1993. Catastrophic sea-level rise during deglaciation: evidence from submerged terraces and glacial landforms. Geological Association of Canada, Program with Abstracts, 18: A10.

Fyles, J.G. 1963. Surficial geology of Victoria and Steffansson Islands, District of Franklin. Geological Survey of Canada, Bulletin 101.

Kaszycki, C.A., and DiLabio, R.N.W. 1986. Surficial geology and till geochemistry, Llyn Lake-Leaf Rapids region, Manitoba. *In* Current Research, part B. Geological Survey of Canada, Paper 86-1B, pp. 245-256.

Kutzbach, J.E. 1987. Model simulations of the climatic patterns during the deglaciation of North America. *In* North America and adjacent oceans during the last deglaciation. *Edited by* W.F. Ruddiman, and H.E. Wright, Jr. Geological Society of America, Boulder, Colorado, The Geology of North America, K-3: 425-446.

Newitt, D.M., Richardson, J.F., Abbott, M., and Turtle, R.B. 1955. Hydraulic conveying of solids in horizontal pipes. Transactions of the Institution of Chemical Engineers, 33: 93-113.

Ringrose, S. 1982. Depositional processes in the development of eskers in Manitoba. *In* Research in glacial, glaciofluvial and glaciolacustrine systems. *Edited by* R. Davidson-Arnott, W. Nickling., and B.D. Fahey. Proceedings of 6th Guelph symposium on geomorphology. Geo Books, Norwich, pp. 117-137.

Rouse, H. 1961. Fluid mechanics for hydraulic engineers. Dover Publications, Inc., New York.

Sharpe, D.R. 1992. Glacial sediments and landforms, southern Victoria Island, N.W.T., Canada. Ph.D. Thesis, University of Ottawa, Ottawa.

Shaw, J. 1989. Drumlins, subglacial meltwater floods, and ocean responses. Geology, 17: 853-856.

Shaw, J., and Gilbert, R. 1990. Evidence for large-scale subglacial meltwater flood events in southern Ontario and northern New York State. Geology, 18: 1169-1172.

Shoemaker, E.M. 1992. Water sheet outburst floods from the Laurentide Ice Sheet. Canadian Journal of Earth Sciences, 29: 1250-1264.

Veillette, J.J. 1986. Former ice flows in the Abitibi-Timiskaming region: implications for the configuration of the late Wisconsinan ice sheet. Canadian Journal of Earth Sciences, 23: 1724-1741.

Wilson, A.W.G. 1904. Trent River and St-Lawrence outlet. Geological Society of America Bulletin, 15: 221-242.

APPENDIX 1

Paleoflow direction estimates from cross-bedded and cross-laminated sand within eskers and fans, Victoria Island, Northwest Territories.

Section number	Paleoflow estimates[1]	Sedimentary structure[2]	Individual measurements (in degrees)
Ferguson Lake (estimates used in Figure 2.5b)			
V023	0°	RDXL A	
	350°	RDXL A	
V019	350°	RDXL B	
	0°	RDXL B	
	350°	RDXL B	
	340°	Tabular cross bedding	
V022	340°	RDXL A	
Augustus Hills (estimates used in Figure 2.8)			
V014	225°	RDXL A	
	260°	RDXL A	
V013	260°	RDXL A	
	260°	Tabular cross bedding	
	336°[3]	Trough cross bedding	295 315 7 330 321 317 325 5 15 32 297
V015	280°	Trough cross bedding	
	290°	Trough cross bedding	
	260°	Tabular cross bedding	
	260°	Tabular cross bedding	
	245°	Tabular cross bedding	
	255°	Tabular cross bedding	
V007	290°	Tabular cross bedding	
V005	300°	Trough cross bedding	
	270°	Trough cross bedding	
	335°	RDXL A	
	293°	RDXL B	
V017	355°	Tabular cross bedding	
	240°	RDXL A	
	240°	Tabular cross bedding	
	225°	RXDL A	
	263°	RDXL A	
	270°	RDXL A	
V012	300°	RDXL B	
	308°	RDXL A	
	240°	RDXL A	
	278°[3]	Tabular cross bedding	283 241 320 225 342 293 102 259 130 257 274 280 165 340 357 271
V009	280°	RDXL B	
	260°	RDXL A	
Namaycush Lake (estimates used in Figure 2.12)			
V033	220°	RDXL A	
V034	130°	RDXL A	

[1] Paleoflow direction estimates arranged in order from the top to the bottom of the section.
[2] RDXL A, ripple drift cross-lamination, type A; RDXL B, ripple drift cross-lamination, type B (Jopling and Walker 1968).
[3] Vector mean.

APPENDIX 2

Clast size, lithology, sphericity, roundness and a-axis orientation data for unit clasts within the Tweed esker.

Axial dimensions (cm)			Clast/sieve size[1] (mm)	Clast/sieve size[2] (ϕ)	Lithology[3]	Maximum Projection Sphericity[4]	Visual Roundness Class[5]	Clast a-axis Orientation[6]
a	b	c						
T16 (21.56 km)								
13.7	10.4	6.4	122.11	-6.93	MS	0.663	VR	P
12.0	11.0	7.0	130.38	-7.03	L	0.721	SA	T
14.2	13.6	8.2	158.61	-7.31	GT	0.706	A	P
7.7	6.0	4.2	73.24	-6.19	L	0.728	SR	T
15.0	10.0	7.0	122.07	-6.93	L	0.691	SR	T
12.7	8.8	8.3	120.97	-6.92	L	0.852	VR	T
12.4	10.0	7.0	122.07	-6.93	GD	0.736	SR	T
11.0	6.0	4.8	76.84	-6.26	GB	0.707	SR	O
6.8	4.0	3.0	50.00	-5.64	GD	0.694	SR	T
8.0	4.2	3.0	51.61	-5.69	M	0.647	VR	T
12.0	11.5	7.0	134.63	-7.07	L	0.711	SR	P
8.0	5.8	4.0	70.46	-6.14	GT	0.704	SA	P
6.1	4.7	2.0	51.08	-5.67	L	0.522	SR	P
10.8	8.7	7.3	113.57	-6.83	MS	0.829	SA	P
6.4	4.8	3.7	60.61	-5.92	L	0.766	VR	P
9.2	8.4	4.4	94.83	-6.57	MS	0.633	SR	T
10.5	7.6	7.0	103.32	-6.69	MS	0.851	R	T
10.0	7.0	3.5	78.26	-6.29	GT	0.563	A	P
11.7	8.8	6.5	109.40	-6.77	L	0.745	R	T
7.0	5.1	3.0	59.17	-5.89	L	0.635	R	T
9.3	6.4	2.4	68.35	-6.09	MS	0.463	VR	T
7.0	5.8	4.8	75.29	-6.23	GT	0.829	SA	T
5.8	4.8	3.0	56.60	-5.82	L	0.689	R	P
13.4	9.4	6.4	113.72	-6.83	L	0.690	SR	T
8.4	6.2	3.8	72.72	-6.18	L	0.655	SR	T
6.8	5.5	3.0	62.65	-5.97	L	0.625	R	P
5.7	4.0	3.0	50.00	-5.64	MS	0.736	R	P
7.1	4.8	3.4	58.82	-5.88	L	0.700	SR	T
9.0	7.6	6.2	98.08	-6.62	L	0.827	SR	P
5.2	3.6	3.2	48.17	-5.59	L	0.819	SR	T
5.8	4.0	2.3	46.14	-5.53	L	0.614	SA	T
6.5	4.4	3.7	57.49	-5.85	MS	0.784	R	P
5.6	3.8	2.3	44.42	-5.47	M	0.632	VR	T
11.5	8.8	7.2	113.70	-6.83	GT	0.802	SA	T
5.8	3.7	1.5	39.92	-5.32	M	0.475	SR	T
8.3	6.3	2.8	68.94	-6.11	MS	0.535	R	T
8.5	6.3	6.2	88.39	-6.47	GT	0.896	A	P
8.7	4.5	3.7	58.26	-5.86	L	0.707	SA	O
6.0	5.0	4.2	65.30	-6.03	GT	0.839	SA	T
4.9	3.4	2.0	39.45	-5.30	MS	0.624	SR	T
3.8	3.4	2.4	41.62	-5.38	L	0.768	R	T
4.5	3.0	2.6	39.70	-5.31	GD	0.795	R	P
5.4	3.7	3.5	50.93	-5.67	MS	0.851	R	P
6.5	5.0	4.4	66.60	-6.06	L	0.843	VR	T
7.9	3.5	1.8	39.36	-5.30	L	0.493	VR	P
5.0	4.0	1.4	42.38	-5.41	L	0.465	SA	O
5.7	4.2	2.5	48.88	-5.61	GD	0.642	SR	T
14.0	8.5	5.7	102.34	-6.68	GT	0.652	SA	T

Axial dimensions (cm)			Clast/sieve size[1] (mm)	Clast/sieve size[2] (ϕ)	Lithology[3]	Maximum Projection Sphericity[4]	Visual Roundness Class[5]	Clast a-axis Orientation[6]
a	b	c						
8.4	6.3	4.5	77.42	-6.27	L	0.728	SA	T
7.5	7.0	3.5	78.26	-6.29	L	0.619	SA	T
14.5	11.5	10.0	152.40	-7.25	L	0.845	SR	T
7.0	7.0	4.7	64.31	-6.00	GD	0.769	VR	N
9.5	8.2	4.0	91.24	-6.51	L	0.593	R	P
7.7	5.4	4.3	69.03	-6.11	MS	0.766	VR	O
10.8	5.0	4.7	68.62	-6.10	GT	0.745	A	O
6.8	6.4	3.0	70.68	-6.14	L	0.594	VR	T
8.0	6.0	3.7	70.49	-6.14	L	0.661	SR	P
8.2	5.0	4.7	68.62	-6.10	L	0.815	SR	P
7.8	7.5	6.0	96.05	-6.59	L	0.852	SR	P
7.5	5.5	3.8	65.73	-6.04	GT	0.682	SR	T
T23 (58.08 km)								
10.0	9.0	4.0	98.49	-6.62	L	0.566	SA	T
7.2	5.0	4.0	64.03	-6.00	GT	0.765	SA	T
5.7	3.4	3.0	45.34	-5.50	GB	0.776	VR	P
10.0	7.0	3.0	76.16	-6.25	L	0.508	A	T
9.3	6.5	3.4	73.36	-6.20	GB	0.579	SR	T
7.8	6.1	2.7	66.71	-6.06	L	0.538	SR	T
9.8	8.5	5.2	99.64	-6.64	GB	0.690	VR	P
7.5	4.2	3.2	52.80	-5.72	L	0.690	SR	T
5.5	4.7	3.4	58.01	-5.86	L	0.767	VR	T
9.5	7.0	6.2	93.51	-6.55	GD	0.835	SR	T
15.3	10.0	9.4	137.24	-7.10	GD	0.834	SA	P
12.7	5.5	4.5	71.06	-6.15	L	0.665	SA	P
6.6	4.7	4.2	63.03	-5.98	L	0.830	SR	T
6.7	4.8	2.6	54.59	-5.77	L	0.598	R	T
7.8	4.1	2.8	49.65	-5.63	L	0.629	SR	P
6.8	5.0	3.0	58.31	-5.87	GD	0.845	VA	T
6.2	5.2	4.0	65.60	-6.04	L	0.794	R	P
8.0	6.0	4.2	73.24	-6.19	L	0.719	R	T
5.6	5.1	2.3	55.95	-5.81	L	0.573	SR	P
5.8	4.5	3.2	55.22	-5.79	GT	0.734	SA	T
5.2	5.2	2.4	57.27	-5.84	GT	0.600	A	N
8.4	5.0	4.7	68.62	-6.10	L	0.809	R	P
8.3	6.9	2.7	74.09	-6.21	L	0.507	SA	P
4.9	3.7	2.8	46.40	-5.54	L	0.758	SR	P
8.2	5.1	3.8	63.60	-5.99	L	0.704	SR	T
6.8	4.6	4.3	62.97	-5.98	GB	0.841	SR	T
5.3	4.4	3.5	56.22	-5.81	L	0.809	VR	T
5.9	5.3	2.8	59.94	-5.91	L	0.633	R	T
11.5	7.0	5.0	86.02	-6.43	L	0.680	SR	T
8.1	6.4	2.6	69.08	-6.11	GB	0.511	R	T
5.5	3.5	2.7	44.20	-5.47	L	0.726	SR	O
5.4	4.0	2.8	48.83	-5.61	GT	0.716	R	T
6.0	4.8	2.8	55.57	-5.80	GB	0.651	R	T
7.1	5.8	2.8	64.40	-6.01	L	0.578	VR	P
4.4	3.2	1.7	36.24	-5.18	L	0.593	SA	T
5.4	3.6	2.3	42.72	-5.42	L	0.651	SR	T
5.3	3.9	3.2	50.45	-5.66	L	0.793	SR	T
4.9	3.8	3.5	51.66	-5.69	L	0.871	SR	T
6.0	5.0	3.2	59.36	-5.89	GB	0.701	SR	P
9.7	5.6	5.0	75.07	-6.23	L	0.774	R	O
6.1	4.8	2.1	52.39	-5.71	L	0.535	VR	O
7.2	7.0	5.0	86.02	-6.43	GB	0.793	VR	T

Axial dimensions (cm)			Clast/sieve size[1] (mm)	Clast/sieve size[2] (ϕ)	Lithology[3]	Maximum Projection Sphericity[4]	Visual Roundness Class[5]	Clast a-axis Orientation[6]
a	b	c						
6.3	4.5	3.1	54.64	-5.77	GT	0.700	SR	P
5.3	3.1	2.2	38.01	-5.26	GB	0.668	VR	P
8.5	7.4	3.3	81.02	-6.34	L	0.561	R	P
6.0	5.0	3.8	82.80	-5.97	L	0.786	SR	P
6.5	2.7	2.2	34.83	-5.12	MS	0.654	R	P
6.8	5.5	2.0	58.52	-5.87	GB	0.478	SR	P
4.5	3.3	3.0	44.60	-5.48	L	0.848	R	T
7.0	5.3	4.2	67.62	-6.08	GD	0.782	SR	P
4.5	4.0	2.3	46.14	-5.53	GD	0.668	SR	O
4.2	3.2	2.1	38.28	-5.26	GT	0.692	SA	T
5.2	3.8	2.5	45.49	-5.51	GB	0.684	VR	T
4.1	3.7	2.8	46.40	-5.54	L	0.804	SR	P
6.7	5.4	3.2	82.77	-5.97	L	0.659	A	T
7.8	6.0	3.5	69.46	-6.12	GD	0.643	A	P
5.7	3.4	2.8	44.05	-5.46	L	0.742	SR	O
8.5	8.0	5.4	98.52	-6.59	GD	0.756	SR	T
7.4	6.8	3.8	77.90	-6.28	L	0.662	SR	P
12.4	8.4	3.4	90.62	-6.50	L	0.484	SR	P
T24 (63.57 km)								
13.5	12.8	4.0	134.10	-7.07	L	0.456	R	T
6.6	5.8	2.4	62.77	-5.97	L	0.535	VR	P
9.2	6.6	4.8	83.23	-6.38	L	0.719	R	P
9.5	7.4	3.8	83.19	-6.38	L	0.593	SR	T
8.7	5.6	4.3	70.60	-6.14	GB	0.792	R	T
8.3	6.8	5.0	84.40	-6.40	L	0.764	VR	P
7.8	5.8	3.8	69.34	-6.12	L	0.686	VR	P
10.0	8.2	4.6	94.02	-6.55	L	0.640	R	T
9.9	9.1	4.0	99.40	-6.64	L	0.565	R	T
12.8	11.0	4.2	117.75	-6.88	L	0.504	SR	P
12.4	11.5	7.8	138.96	-7.12	L	0.755	R	P
11.0	8.3	7.0	108.58	-6.76	L	0.814	R	P
10.0	7.8	5.2	93.74	-6.55	L	0.705	SA	P
5.7	5.3	2.4	58.18	-5.86	GB	0.579	VR	P
9.4	8.8	4.1	97.08	-6.60	L	0.591	R	T
12.0	9.8	4.3	107.02	-6.74	L	0.543	SR	P
12.8	9.5	6.2	113.44	-6.83	L	0.684	SA	P
10.5	9.0	7.8	119.10	-6.90	GB	0.865	SA	T
5.3	4.4	4.0	59.46	-5.89	L	0.883	SR	P
8.4	6.2	4.0	73.78	-6.21	L	0.677	SR	T
10.1	5.4	1.9	57.25	-5.84	L	0.408	SA	T
6.2	4.0	2.4	46.65	-5.54	L	0.618	SA	T
8.0	6.0	3.4	68.96	-6.11	GB	0.625	SR	P
8.3	5.8	3.0	65.30	-6.03	L	0.575	SR	P
5.3	4.4	2.8	52.15	-5.70	GB	0.698	SR	T
5.8	4.5	2.6	51.97	-5.70	L	0.640	A	T
4.9	4.2	1.6	44.94	-5.49	L	0.503	SA	T
12.2	9.5	9.0	130.86	-7.03	GD	0.888	SR	P
7.4	5.4	3.4	63.81	-6.00	L	0.664	SR	P
8.1	5.4	2.7	60.37	-5.92	L	0.554	R	T
12.0	9.0	4.8	102.00	-6.67	L	0.601	R	T
8.2	6.5	3.4	73.36	-6.20	L	0.604	R	O
10.8	7.5	4.0	85.00	-6.41	L	0.586	SR	T
5.8	5.0	1.8	53.14	-5.73	GB	0.485	SR	T
8.8	7.6	4.0	85.88	-6.42	L	0.624	SR	T
7.0	4.7	3.5	58.60	-5.87	L	0.722	VR	P

Axial dimensions (cm)			Clast/sieve size[1] (mm)	Clast/sieve size[2] (ϕ)	Lithology[3]	Maximum Projection Sphericity[4]	Visual Roundness Class[5]	Clast a-axis Orientation[6]
a	b	c						
6.2	5.1	2.8	58.18	-5.86	L	0.631	R	P
4.9	3.1	1.1	32.89	-5.04	L	0.434	SA	P
9.0	5.0	3.1	58.63	-5.88	L	0.601	SA	P
11.2	11.0	6.0	126.30	-6.97	L	0.686	R	N
16.7	10.7	7.2	128.97	-7.01	L	0.685	SR	T
5.7	5.4	3.0	61.77	-5.95	L	0.668	SR	T
6.3	6.0	4.1	72.67	-6.18	L	0.765	SR	T
7.8	5.7	2.1	60.75	-5.92	L	0.469	R	T
9.8	7.8	4.3	89.07	-6.48	L	0.630	SA	T
6.4	4.1	1.8	44.76	-5.48	L	0.501	SR	Q
6.4	4.4	2.2	49.19	-5.62	L	0.559	SR	T
4.1	4.1	3.4	53.26	-5.74	GB	0.884	VR	N
8.0	6.2	3.0	68.68	-6.11	L	0.560	R	P
12.0	8.0	5.0	94.34	-6.56	GB	0.641	SR	P
5.8	4.4	3.3	55.00	-5.78	L	0.755	SA	P
4.6	3.2	1.2	34.16	-5.09	GB	0.464	SR	P
7.2	5.2	2.7	58.59	-5.87	GB	0.583	SR	P
6.3	5.9	2.8	65.31	-6.03	L	0.598	SR	T
7.1	6.0	3.6	69.97	-6.13	GD	0.675	SR	Q
5.2	4.3	2.2	48.30	-5.59	L	0.603	SR	P
9.0	8.3	3.8	91.20	-6.51	GB	0.581	VR	T
9.8	7.5	3.3	81.04	-6.36	GB	0.533	SA	T
7.4	6.2	5.7	84.22	-6.40	GT	0.892	SA	T
10.2	6.7	6.6	94.05	-6.56	GB	0.862	SR	T
T26 (70.13 km)								
9.7	7.8	3.5	85.49	-6.42	L	0.548	SR	P
6.6	4.0	3.5	53.15	-5.73	MG	0.776	A	P
6.5	4.2	3.8	56.64	-5.82	L	0.810	SA	T
16.0	11.0	9.0	142.13	-7.15	L	0.774	R	P
6.1	4.6	3.1	55.47	-5.79	L	0.702	R	P
5.4	3.9	1.9	43.38	-5.44	L	0.559	SR	P
4.1	3.3	2.2	39.66	-5.31	GD	0.712	R	T
9.1	6.4	3.7	73.93	-6.21	GB	0.620	SR	P
7.8	7.2	2.4	75.69	-6.25	B	0.472	SR	P
5.7	5.3	3.1	61.40	-5.94	L	0.685	R	T
5.3	4.4	2.7	51.62	-5.69	L	0.681	R	P
5.0	3.3	2.3	40.22	-5.33	L	0.687	R	P
14.4	9.0	6.7	112.20	-6.81	L	0.705	SR	T
7.0	5.0	4.1	64.66	-6.01	GB	0.785	R	P
9.5	6.0	3.0	67.08	-6.07	L	0.544	SR	P
5.5	4.5	3.9	59.55	-5.90	L	0.852	R	T
5.8	4.5	2.1	49.66	-5.63	GB	0.556	SR	P
10.0	6.7	1.7	69.12	-6.11	L	0.354	R	T
12.3	9.2	6.0	109.84	-6.78	GD	0.685	SR	T
5.4	4.5	4.0	60.21	-5.91	L	0.871	R	T
5.4	4.2	3.4	54.04	-5.76	MS	0.801	VR	T
3.7	2.5	1.2	27.73	-4.79	L	0.541	SR	P
6.5	5.7	2.5	62.24	-5.98	L	0.568	SR	T
5.5	4.5	2.8	53.00	-5.73	GB	0.684	VR	P
9.2	7.7	5.0	91.81	-6.52	MS	0.709	SR	T
6.4	5.0	2.0	53.85	-5.75	GT	0.503	SR	T
9.0	4.8	3.9	61.85	-5.95	L	0.709	SR	O
6.0	5.1	3.0	59.17	-5.89	GB	0.668	SA	T
9.0	6.5	4.8	80.80	-6.34	GB	0.735	VR	T
6.6	4.8	4.2	63.78	-6.00	L	0.824	SA	T

Axial dimensions (cm)			Clast/sieve size[1] (mm)	Clast/sieve size[2] (ϕ)	Lithology[3]	Maximum Projection Sphericity[4]	Visual Roundness Class[5]	Clast a-axis Orientation[6]
a	b	c						
4.1	3.5	2.8	43.60	-5.45	GT	0.780	R	T
9.0	7.3	4.0	83.24	-6.38	GB	0.627	SR	T
10.0	6.8	2.5	72.45	-6.18	GB	0.455	VR	P
10.3	9.2	2.6	96.80	-6.59	L	0.418	SR	P
7.8	4.9	1.7	51.87	-5.70	L	0.427	SR	T
3.8	3.0	1.3	32.70	-5.03	L	0.533	R	T
6.3	4.7	3.8	60.44	-5.92	GB	0.789	R	T
7.0	4.2	3.1	52.20	-5.71	L	0.691	SA	T
6.0	4.2	3.7	55.97	-5.81	MS	0.818	VR	T
8.2	6.7	3.2	74.26	-6.21	L	0.574	SR	T
6.6	4.1	3.0	50.80	-5.67	L	0.680	SA	P
5.0	3.3	2.5	41.40	-5.37	L	0.726	SR	T
6.7	4.2	3.0	51.61	-5.69	L	0.686	VR	P
5.4	4.1	2.4	47.51	-5.57	GB	0.641	SR	T
8.5	4.7	1.4	49.04	-5.62	L	0.404	SR	O
5.8	5.1	4.2	66.07	-6.05	GD	0.843	R	P
4.4	3.3	3.0	44.60	-5.48	GT	0.854	SR	P
7.0	4.3	2.4	49.24	-5.62	GB	0.579	VR	O
6.2	3.6	2.2	42.19	-5.40	L	0.604	SA	T
5.7	4.1	2.0	45.62	-5.51	L	0.558	R	P
6.0	4.4	3.4	55.61	-5.80	MS	0.761	VR	T
4.8	2.8	1.8	33.20	-5.05	L	0.625	SR	P
5.0	3.6	2.2	43.91	-5.46	L	0.603	SR	O
4.8	4.6	2.8	53.85	-5.75	L	0.711	SR	P
5.3	3.5	2.4	42.44	-5.41	L	0.680	R	O
4.8	2.8	2.5	37.54	-5.23	GB	0.777	SA	P
5.3	3.5	2.8	44.82	-5.49	L	0.753	SR	O
6.2	4.8	2.4	53.67	-5.75	L	0.582	SR	P
4.3	3.1	1.2	33.24	-5.05	L	0.480	SR	T
5.3	4.0	3.0	50.00	-5.64	GD	0.754	SR	P

[1] Clast/sieve size (x) in mm: $x = \sqrt{(b^2 + c^2)}$, where clast b-axis and c-axis dimensions are converted to mm.

[2] Clast/sieve size (z) in ϕ: $z = (-\log_{10}x)/(\log_{10}2)$.

[3] Lithology: B, basalt; GB, gabbro; GD, granodiorite; GT, granite; L, limestone; M, mudstone; MG, migmatite; MS, metasedimentary.

[4] Sphericity: Values calculated using Maximum Projection Sphericity (Ψ_p, Sneed and Folk, 1958).

[5] Roundness: Data collected in the form of visual roundness classes (Powers, 1953). Calculations in the Table 4.3 are based on the geometric means (GM) of the visual roundness classes. VR, very rounded (GM = 0.84); R, rounded (GM = 0.59); SR, subrounded (GM = 0.41); SA, subangular (GM = 0.30); A, angular (GM = 0.21); VA, very angular (GM = 0.14).

[6] Orientation: Orientation of the clast a-axis with respect to the orientation of the maximum dip of its ab-plane. N, no obvious a-axis; O, a-axis oblique; P, a-axis parallel; T, a-axis transverse.

APPENDIX 3

Clast size, lithology, sphericity, and roundness data for oversize clasts from the Tweed esker.

Axial dimensions (cm)			Clast/sieve size[1] (mm)	Clast/sieve size[2] (ϕ)	Lithology[3]	Maximum Projection Sphericity[4]	Visual Roundness Class[5]
a	b	c					
TJS1 (11.83 km)							
105.0	47.0	40.0	617.17	-9.27	L	0.600	SR
66.0	49.0	35.0	602.16	-9.23	GD	0.726	R
65.0	51.0	42.0	660.68	-9.37	GD	0.812	SA
62.0	58.0	54.0	792.46	-9.63	GT	0.933	SA
54.0	37.0	19.0	415.93	-8.70	L	0.569	SR
45.0	35.0	35.0	494.97	-8.96	L	0.920	SR
39.0	26.0	22.0	340.59	-8.41	L	0.763	SR
41.0	34.0	25.0	422.02	-8.72	L	0.767	R
58.0	53.0	40.0	664.00	-9.38	GT	0.816	SA
59.0	46.0	26.0	528.39	-9.05	MS	0.632	R
85.0	66.0	54.0	852.76	-9.74	L	0.608	SR
99.0	90.0	64.0	1104.36	-10.11	GT	0.774	A
71.0	64.0	35.0	729.45	-9.51	GT	0.649	SR
38.0	33.0	22.0	396.61	-8.63	L	0.730	VR
51.0	50.0	41.0	646.61	-9.34	MS	0.872	R
43.0	41.0	15.0	436.58	-8.77	GD	0.507	R
43.0	32.0	31.0	445.53	-8.80	MS	0.888	R
67.0	36.0	30.0	468.61	-8.87	L	0.722	R
44.0	40.0	25.0	471.70	-8.88	GT	0.711	A
58.0	46.0	28.0	538.52	-9.07	MS	0.668	VR
32.0	27.0	26.5	378.32	-8.56	L	0.934	SR
43.0	26.0	23.0	347.13	-8.44	GD	0.781	R
83.0	53.0	45.0	695.27	-9.44	GB	0.774	SR
66.0	59.0	37.0	698.42	-9.44	GT	0.708	SA
94.0	80.0	70.0	1053.01	-10.05	GT	0.868	SA
57.0	46.0	32.0	560.36	-9.13	MS	0.733	R
62.0	42.0	40.0	580.00	-9.18	GT	0.852	A
46.0	37.0	21.0	425.44	-8.73	L	0.640	SR
43.0	40.0	25.0	471.70	-8.88	L	0.716	R
47.0	47.0	24.0	527.73	-9.04	L	0.642	SR
57.0	40.0	34.0	524.98	-9.04	GT	0.799	SR
63.0	39.0	38.0	544.52	-9.09	M	0.839	R
40.0	38.0	28.0	472.02	-8.88	GD	0.804	VR
34.0	34.0	25.0	422.02	-8.72	GD	0.816	VR
37.0	27.0	21.0	342.05	-8.42	L	0.763	A
54.0	49.0	46.0	672.09	-9.39	M	0.929	SR
74.0	59.0	45.0	742.02	-9.54	GT	0.776	SA
63.0	42.0	23.0	478.85	-8.90	GT	0.588	SA
59.0	46.0	32.0	560.36	-9.13	GT	0.725	SA
45.0	45.0	24.0	510.00	-8.99	GD	0.860	VR
42.0	35.0	30.0	460.98	-8.85	GD	0.851	VR
79.0	51.0	45.0	680.15	-9.41	MS	0.707	R
80.0	61.0	60.0	855.63	-9.74	GT	0.904	A
57.0	40.0	24.0	486.48	-8.87	MS	0.635	R
89.0	51.0	41.0	654.37	-9.35	MS	0.721	SR
76.0	56.0	31.0	640.08	-9.32	GT	0.612	SA
69.0	59.0	55.0	805.60	-9.66	GT	0.907	SR
50.0	38.0	37.0	530.38	-9.05	M	0.897	SR
91.0	60.0	50.0	781.02	-9.61	GT	0.773	SA

Axial dimensions (cm)			Clast/sieve size[1] (mm)	Clast/sieve size[2] (ϕ)	Lithology[3]	Maximum Projection Sphericity[4]	Visual Roundness Class[5]
a	b	c					
100.0	84.0	60.0	877.27	-9.78	GT	0.827	A
59.0	40.0	37.0	544.69	-9.09	GT	0.636	R
45.0	35.0	28.0	448.22	-8.81	L	0.704	SR
50.0	24.0	23.0	332.42	-8.38	L	0.763	SR
53.0	40.0	28.0	468.26	-8.93	MS	0.790	SR
102.0	70.0	68.0	975.91	-9.93	GT	0.868	A
69.0	56.0	26.0	617.41	-9.27	GT	0.563	SR
38.0	33.0	24.0	408.04	-8.67	GD	0.787	VR
66.0	47.0	36.0	592.03	-9.21	MS	0.750	R
61.0	49.0	20.0	569.39	-9.15	L	0.658	R
49.0	25.0	24.0	346.55	-8.44	L	0.780	VR
78.0	67.0	42.0	790.76	-9.63	GT	0.699	SR
62.0	44.0	23.0	496.49	-8.96	M	0.582	R
68.0	56.0	38.0	676.76	-9.40	GT	0.726	SR
84.0	59.0	48.0	760.59	-9.57	GT	0.777	SR
53.0	45.0	35.0	570.09	-9.16	MS	0.803	R
64.0	47.0	33.0	574.28	-9.17	GT	0.715	SA
64.0	43.0	42.0	601.08	-9.23	GT	0.863	A
91.0	79.0	49.0	929.62	-9.86	GT	0.696	SR
76.0	63.0	42.0	757.17	-9.56	GT	0.719	SA
61.0	44.0	24.0	501.20	-8.97	GD	0.602	VR
77.0	70.0	60.0	921.95	-9.85	GT	0.875	SR
80.0	63.0	55.0	836.30	-9.71	GT	0.845	SR
68.0	49.0	29.0	569.39	-9.15	GT	0.635	SR
70.0	48.0	38.0	612.21	-9.26	GT	0.757	A
100.0	62.0	41.0	743.30	-9.54	GT	0.632	SR
78.0	59.0	44.0	736.00	-9.52	GB	0.751	R
97.0	94.0	91.0	1308.32	-10.35	GT	0.969	SR
83.0	67.0	40.0	780.32	-9.61	M	0.663	R
85.0	71.0	65.0	962.60	-9.91	GB	0.889	R
80.0	67.0	27.0	722.36	-9.50	L	0.518	SR
48.0	38.0	29.0	478.92	-8.90	L	0.775	VR
100.0	63.0	50.0	804.30	-9.65	GT	0.737	SA
77.0	72.0	48.0	865.33	-9.76	L	0.748	VR
100.0	78.0	60.0	984.07	-9.94	M	0.775	R
93.0	59.0	56.0	813.45	-9.67	GT	0.631	SR
91.0	77.0	59.0	970.05	-9.92	GT	0.794	A
83.0	54.0	30.0	617.74	-9.27	GD	0.589	SR
71.0	59.0	33.0	676.02	-9.40	L	0.641	VR
79.0	56.0	38.0	676.76	-9.40	L	0.691	SR
55.0	48.0	40.0	624.82	-9.29	GB	0.848	R
123.0	120.0	90.0	1500.00	-10.55	M	0.820	SR
70.0	60.0	51.0	787.46	-9.62	GT	0.854	R
61.0	46.0	41.0	616.20	-9.27	L	0.844	SR
68.0	68.0	55.0	874.59	-9.77	GT	0.869	SA
96.0	58.0	51.0	772.33	-9.59	GT	0.778	SR
78.0	56.0	42.0	700.00	-9.45	M	0.741	R
80.0	58.0	49.0	744.11	-9.54	GD	0.814	VR
77.0	64.0	58.0	863.71	-9.75	GT	0.882	A
78.0	50.0	42.0	652.99	-9.35	GT	0.770	SR
75.0	61.0	37.0	713.44	-9.48	GT	0.672	SR
86.0	70.0	67.0	968.97	-9.92	GT	0.908	SR
84.0	60.0	47.0	762.17	-9.57	GT	0.762	SA
120.0	73.0	70.0	1011.39	-9.98	M	0.826	VR
143.0	60.0	45.0	750.00	-9.55	M	0.621	SR
58.0	41.0	40.0	572.80	-9.16	GT	0.877	A

Axial dimensions (cm)			Clast/sieve size[1] (mm)	Clast/sieve size[2] (ϕ)	Lithology[3]	Maximum Projection Sphericity[4]	Visual Roundness Class[5]
a	b	c					
85.0	38.0	28.0	456.07	-8.83	GT	0.697	A
84.0	45.0	31.0	548.44	-9.09	GT	0.668	SR
56.0	47.0	45.0	650.69	-9.35	L	0.917	R
72.0	69.0	37.0	782.04	-9.61	M	0.654	SR
72.0	53.0	40.0	664.00	-9.38	GT	0.751	SA
66.0	41.0	38.0	559.02	-9.13	M	0.765	SR
92.0	58.0	50.0	765.77	-9.58	GT	0.770	SA
66.0	58.0	42.0	716.10	-9.48	GT	0.774	SA
90.0	70.0	48.0	848.76	-9.73	L	0.718	SR
80.0	61.0	33.0	693.54	-9.44	GD	0.610	R
90.0	67.0	50.0	836.00	-9.71	GT	0.748	SA
80.0	55.0	50.0	743.30	-9.54	GB	0.912	VR
77.0	54.0	41.0	676.01	-9.41	GT	0.742	A
91.0	60.0	60.0	848.53	-9.73	GT	0.672	SR
77.0	53.0	25.0	586.00	-9.19	GD	0.538	VR
T14 (31.56 km)							
150.0	94.0	62.0	1126.08	-10.14	MS	0.651	SR
67.0	45.0	35.0	576.28	-9.17	L	0.757	R
40.0	35.0	23.0	418.81	-8.71	L	0.678	R
68.0	53.0	42.0	676.24	-9.40	MS	0.700	SR
62.0	49.0	46.0	685.93	-9.42	GT	0.913	SR
29.0	23.0	22.0	318.28	-8.31	L	0.900	R
45.0	41.0	39.0	565.86	-9.14	L	0.938	R
90.0	61.0	60.0	855.63	-9.74	GB	0.870	SR
46.0	43.0	36.0	560.80	-9.13	L	0.870	R
44.0	38.0	33.0	503.29	-8.98	GT	0.868	SR
52.0	48.0	18.0	512.64	-9.00	MS	0.510	SR
70.0	52.0	24.0	572.71	-9.16	L	0.544	SR
52.0	45.0	22.0	500.90	-8.97	M	0.595	VR
59.0	52.0	32.0	610.57	-9.25	GT	0.698	SR
73.0	46.0	32.0	580.36	-9.13	L	0.676	SA
43.0	35.0	18.0	393.57	-8.62	L	0.602	SA
41.0	39.0	25.0	463.25	-8.86	M	0.733	SR
79.0	48.0	28.0	555.70	-9.12	L	0.594	A
48.0	37.0	23.0	435.66	-8.77	L	0.680	SR
71.0	61.0	31.0	684.25	-9.42	L	0.608	SR
50.0	33.0	28.0	432.76	-8.76	MS	0.782	SR
100.0	50.0	40.0	640.31	-9.32	M	0.687	SR
139.0	84.0	75.0	1126.10	-10.14	L	0.786	SR
77.0	47.0	38.0	604.40	-9.24	L	0.738	SR
68.0	37.0	31.0	482.70	-8.91	L	0.728	R
64.0	38.0	37.0	530.38	-9.05	L	0.827	SA
72.0	39.0	24.0	457.93	-8.84	MS	0.593	R
75.0	70.0	53.0	878.01	-9.78	GD	0.814	SR
48.0	42.0	30.0	516.14	-9.01	GT	0.766	SR
47.0	41.0	30.0	508.04	-8.99	GD	0.778	R
85.0	60.0	24.0	646.22	-9.34	L	0.487	SR
40.0	39.0	30.0	492.04	-8.94	GT	0.834	SR
95.0	88.0	30.0	929.73	-9.86	L	0.479	R
70.0	55.0	20.0	585.23	-9.19	L	0.474	A
82.0	59.0	30.0	661.89	-9.37	MS	0.574	SR
68.0	56.0	31.0	640.08	-9.32	L	0.635	R
119.0	119.0	82.0	1445.16	-10.50	GT	0.782	R
74.0	51.0	42.0	660.68	-9.37	GT	0.778	SA
117.0	107.0	43.0	1153.17	-10.17	L	0.532	SA

Axial dimensions (cm)			Clast/sieve size[1] (mm)	Clast/sieve size[2] (ϕ)	Lithology[3]	Maximum Projection Sphericity[4]	Visual Roundness Class[5]
a	b	c					
107.0	71.0	46.0	845.99	-9.72	L	0.656	SA
114.0	87.0	27.0	910.93	-9.83	MS	0.423	SR
144.0	90.0	53.0	800.56	-9.64	MS	0.600	SR
80.0	67.0	33.0	746.86	-9.54	M	0.591	SR
93.0	68.0	64.0	919.35	-9.84	GD	0.875	R
121.0	82.0	56.0	992.98	-9.96	MS	0.684	SR
81.0	60.0	35.0	694.62	-9.44	GD	0.635	SR
100.0	80.0	38.0	885.66	-9.79	GT	0.568	R
100.0	87.0	50.0	836.00	-9.71	MS	0.722	SR
118.0	70.0	43.0	821.52	-9.68	L	0.610	SA
74.0	60.0	33.0	684.76	-9.42	MS	0.620	SR
63.0	55.0	33.0	641.40	-9.33	GT	0.683	SR
80.0	69.0	34.0	769.22	-9.59	L	0.597	SR
73.0	43.0	40.0	587.28	-9.20	GT	0.801	SA
66.0	49.0	30.0	574.54	-9.17	L	0.656	SR
107.0	66.0	56.0	855.56	-9.76	L	0.765	SA
68.0	68.0	30.0	743.24	-9.54	GD	0.583	VR
116.0	87.0	45.0	979.49	-9.94	MS	0.585	SR
70.0	46.0	37.0	590.34	-9.21	GT	0.725	SA
100.0	90.0	70.0	1140.18	-10.16	L	0.818	R
119.0	85.0	71.0	1107.52	-10.11	L	0.795	SR
T24 (63.57 km)							
66.0	63.0	43.0	762.76	-9.58	GT	0.765	SR
93.0	65.0	36.0	743.03	-9.54	L	0.602	SR
37.0	22.0	17.0	278.03	-8.12	MG	0.711	R
29.5.0	22.0	17.0	278.03	-8.12	GT	0.766	A
27.0	17.5	10.5	204.08	-7.67	L	0.619	SR
24.5	17.0	9.5	194.74	-7.61	L	0.604	SR
24.0	22.5	13.8	263.95	-8.04	MS	0.709	R
30.0	19.5	14.8	244.80	-7.94	GT	0.723	SR
24.6	21.5	12.0	246.22	-7.94	L	0.651	SR
25.0	13.4	10.0	167.20	-7.39	L	0.671	SR
52.0	31.5	20.0	373.13	-8.54	L	0.628	SR
31.0	20.5	11.0	232.65	-7.86	L	0.578	R
22.0	19.0	11.5	222.09	-7.80	L	0.684	SR
30.0	19.0	8.5	208.15	-7.70	L	0.508	SR
25.0	14.7	13.0	196.24	-7.62	L	0.774	SR
28.2	21.7	6.4	226.24	-7.82	GB	0.410	SR
50.0	18.0	16.5	244.18	-7.93	L	0.674	SA
36.0	24.0	12.0	268.33	-8.07	GT	0.554	VR
28.0	28.0	5.5	285.35	-8.16	GB	0.342	SR
29.0	22.0	20.0	297.32	-8.22	L	0.857	VR
36.0	29.0	23.0	370.14	-8.53	GD	0.799	SR
32.0	24.0	11.5	266.13	-8.06	L	0.560	SR
41.0	36.0	21.0	416.77	-8.70	GD	0.671	R
31.5	22.5	16.0	276.09	-8.11	MG	0.715	VR
39.0	33.5	18.0	380.30	-8.57	GD	0.631	R
33.0	31.0	10.0	325.73	-8.35	L	0.464	SR
33.0	26.0	12.0	286.36	-8.16	L	0.555	SR
55.0	33.5	16.0	371.25	-8.54	L	0.521	SA
70.0	68.0	53.0	862.15	-9.75	GT	0.840	SR
54.0	38.0	27.0	466.15	-8.86	L	0.711	VR
63.0	26.0	19.0	322.02	-8.33	L	0.607	SR
27.0	24.0	19.0	306.10	-8.26	GD	0.824	SR
30.5	29.0	17.0	336.15	-8.39	GT	0.691	R

Axial dimensions (cm)			Clast/sieve size[1] (mm)	Clast/sieve size[2] (ϕ)	Lithology[3]	Maximum Projection Sphericity[4]	Visual Roundness Class[5]
a	b	c					
31.0	28.0	15.0	317.65	-8.31	GD	0.640	R
33.5	26.0	17.0	310.64	-8.28	GT	0.686	SR
35.0	23.0	12.0	259.42	-8.02	L	0.587	SR
50.0	43.0	35.0	554.44	-9.11	GD	0.831	R
41.0	32.0	27.5	421.93	-8.72	GD	0.834	VR
60.0	40.0	19.0	526.55	-9.04	L	0.501	SA
47.0	38.0	28.0	480.10	-8.91	GT	0.756	SR
37.0	34.0	20.0	394.46	-8.62	GB	0.685	SR
34.0	27.0	20.5	339.01	-8.41	MG	0.773	VR
28.5	18.0	15.0	234.31	-7.87	GD	0.762	R
31.5	30.0	8.0	310.48	-8.28	L	0.411	R
56.0	37.0	23.0	435.66	-8.77	MG	0.637	SR
29.0	27.0	21.0	342.05	-8.42	GD	0.827	R
52.0	28.0	21.5	353.02	-8.46	GT	0.685	SA
39.0	28.5	22.0	360.03	-8.49	MG	0.760	VR
36.0	26.5	16.0	309.56	-8.27	L	0.648	SR
28.0	24.0	20.0	312.41	-8.29	MS	0.843	SA
38.0	33.0	23.0	402.24	-8.65	GD	0.768	SR
33.0	30.0	19.0	355.11	-8.47	MG	0.717	R
64.0	41.0	24.0	475.08	-8.89	L	0.606	SR
47.0	43.0	16.0	458.80	-8.84	L	0.506	SR
20.5	20.0	19.0	346.70	-8.44	GD	0.752	VR
61.5	49.0	10.0	500.10	-8.97	L	0.325	SA
77.0	46.0	38.0	595.66	-9.22	MG	0.744	VR
58.0	47.0	30.0	557.58	-9.12	L	0.694	R
93.0	75.0	48.0	880.45	-9.80	MG	0.694	SA
49.0	42.0	31.0	522.02	-9.03	GD	0.778	R
T3[6] (70.13 km)							
35.0	24.0	21.0	318.90	-8.32	GD	0.808	SR
24.0	18.0	13.0	222.04	-7.79	GB	0.734	R
23.0	20.0	10.0	223.61	-7.80	L	0.604	SR
16.0	12.0	9.5	153.05	-7.26	GD	0.770	R
32.0	26.0	16.0	305.29	-8.25	GT	0.676	SR
24.0	17.0	16.0	233.45	-7.87	GD	0.857	R
21.0	15.0	14.0	205.18	-7.68	MS	0.855	R
20.0	20.0	16.0	256.12	-8.00	GT	0.863	SA
23.0	19.0	6.0	199.25	-7.64	L	0.439	VR
14.0	11.0	10.0	148.66	-7.22	GT	0.867	A
47.0	26.0	24.0	353.84	-8.47	GD	0.780	R
17.0	12.0	10.0	156.20	-7.29	L	0.790	R
19.5	13.5	5.5	145.77	-7.19	GB	0.490	SR
15.0	12.0	9.0	150.00	-7.23	GT	0.768	SR
17.0	13.0	7.0	147.65	-7.21	GB	0.608	VR
15.3	12.8	5.0	137.42	-7.10	GB	0.507	VR
14.0	11.0	4.0	117.05	-6.87	GB	0.474	VR
37.0	30.0	25.0	390.51	-8.61	GD	0.827	SA
21.0	12.5	11.0	166.51	-7.38	L	0.774	SR
24.0	19.0	5.0	196.47	-7.62	GB	0.384	R
17.0	17.0	6.0	180.28	-7.49	GT	0.503	SR
21.0	17.0	9.0	192.35	-7.59	L	0.613	SR
13.5	10.0	2.5	103.08	-6.69	L	0.363	SR
27.0	17.0	14.0	220.23	-7.78	MS	0.755	SR
22.0	19.0	8.0	206.16	-7.69	GD	0.538	R
20.0	17.0	8.0	187.88	-7.55	GB	0.576	R
16.0	14.0	7.0	156.52	-7.29	GD	0.608	VR

Axial dimensions (cm)			Clast/sieve size[1] (mm)	Clast/sieve size[2] (ϕ)	Lithology[3]	Maximum Projection Sphericity[4]	Visual Roundness Class[5]
a	b	c					
23.0	19.0	14.0	235.01	-7.88	GB	0.768	SR
21.0	18.0	11.0	210.95	-7.72	L	0.697	SR
21.0	13.0	10.0	164.01	-7.36	GB	0.716	R
22.0	18.0	9.0	201.25	-7.65	L	0.592	SR
17.0	14.0	12.0	184.39	-7.53	GT	0.847	SR
12.0	9.0	8.5	123.79	-6.95	GT	0.876	SA
11.8	10.7	5.0	118.11	-6.88	L	0.588	R
8.0	5.0	3.0	58.31	-5.87	L	0.611	R
21.0	15.0	9.0	174.93	-7.45	L	0.639	SR
16.0	12.0	7.0	138.92	-7.12	MS	0.651	SA
13.5	10.2	6.0	116.34	-6.89	GB	0.642	VR
20.0	12.0	11.0	182.79	-7.35	L	0.798	SR
14.5	13.0	9.0	158.11	-7.30	GD	0.757	SR
15.0	12.0	10.0	156.20	-7.29	MS	0.824	SR
12.0	11.8	6.0	132.38	-7.05	GB	0.638	R
17.5	14.0	6.0	152.32	-7.25	GB	0.531	SA
19.5	18.0	8.0	196.98	-7.62	GB	0.570	VR
18.0	14.5	7.0	161.01	-7.33	L	0.576	R
15.0	13.5	9.0	162.25	-7.34	MS	0.730	SR
15.0	13.0	8.0	152.64	-7.25	L	0.692	R
13.0	12.0	6.2	135.07	-7.08	GB	0.630	VR
19.0	14.0	11.0	176.04	-7.46	GD	0.771	SA
24.0	17.0	8.0	187.88	-7.55	L	0.543	SR
21.0	13.0	11.0	170.29	-7.41	L	0.765	SR
14.5	11.0	9.5	145.34	-7.18	GT	0.829	A
19.0	18.0	8.0	195.98	-7.62	GB	0.575	R
19.0	16.0	10.0	188.68	-7.56	GT	0.693	SA
15.0	13.0	10.0	164.01	-7.36	GD	0.802	SR
15.0	13.0	8.0	152.64	-7.25	L	0.692	SR
14.0	13.0	7.0	147.65	-7.21	MS	0.649	SR
19.0	13.0	4.0	136.01	-7.09	L	0.405	SR
16.3	9.5	5.5	109.77	-6.78	GB	0.583	R
18.0	15.0	6.5	163.48	-7.35	L	0.542	SR

[1] Clast/sieve size (x) in mm: $x = \sqrt{(b^2 + c^2)}$, where clast b-axis and c-axis dimensions are converted to mm.

[2] Clast/sieve size (z) in ϕ: $z = (-\log_{10}x)/(\log_{10}2)$.

[3] Lithology: GB, gabbro; GD, granodiorite; GT, granite; L, limestone; M, mudstone; MG, migmatite; MS, metasedimentary.

[4] Sphericity: Values calculated using Maximum Projection Sphericity (ψ_p, Sneed and Folk, 1958).

[5] Roundness: Data collected in the form of visual roundness classes (Powers, 1953). Calculations in the Table 4.3 are based on the geometric means (GM) of the visual roundness classes. VR, very rounded (GM = 0.84); R, rounded (GM = 0.59); SR, subrounded (GM = 0.41); SA, subangular (GM = 0.30); A, angular (GM = 0.21); VA, very angular (GM = 0.14).

APPENDIX 4

Fabric data[1] from gravel facies and structures within south-central Ontario eskers[2].

M6°/1-centre (Oblique accretion avalanche bed macroform)

130	40	80	48	190	32	0	50	100	42	315	57	245	21	280	31	225	53	310	15	330	70	30	55
180	38	200	40	35	50	15	57	265	30	80	42	145	31	90	58	80	36	160	47	90	55	5	48
90	37	30	52	285	22	185	17	85	5	80	28	140	6	255	38	90	42	315	32	180	14	230	42
80	24	235	32	260	50	70	27	345	40	283	15	252	16	210	32	110	71	100	34	95	4	80	45
200	41	285	3	265	27	285	32	287	13	165	49	175	64	170	46	100	38	255	30	300	30	170	47

M6°/1-LHS (Oblique accretion avalanche bed macroform)

20	9	100	33	350	49	5	34	235	17	55	33	40	10	340	42	110	24	100	47	90	45	280	34
20	28	190	55	285	15	310	45	190	38	80	53	340	63	100	21	330	30	10	80	310	45	210	25
200	57	310	30	90	38	340	17	65	16	140	18	245	80	90	17	70	61	100	44	270	17	310	28
45	54	270	25	50	17	85	48	40	31	345	25	170	3	85	10	90	50	75	57	20	43	50	4
75	3	150	2	80	24	270	48	100	61	280	64	230	50	110	40	300	72	200	65	30	44		

YJS1/1-3 (Plane-bedded gravel)

0	27	10	33	35	6	35	10	65	68	0	27	272	6	45	70	310	7	25	0	60	22	10	18
15	14	335	42	40	62	20	44	10	36	10	67	30	23	120	55	290	10	5	14	12	25	10	44
0	26	35	48	40	40	30	31	20	48	0	12	15	37	0	33	130	16	10	10	312	58	350	36
50	42	325	9	205	73	65	4	50	67	80	35	125	39	5	28	350	26	355	38	180	18	20	42
30	22	330	7	195	39	20	40	235	64	260	2	75	46	310	11	200	45	320	30	90	50	25	30

YJS1/3-1 (Pseudosynclinal macroform - east side)

70	55	80	25	65	65	20	65	30	26	60	35	55	67	95	52	95	35	75	37	115	21	100	30
65	48	60	46	45	25	280	85	80	32	45	16	90	53	115	37	85	70	230	5	185	14	80	37
65	58	40	24	60	55	90	64	55	66	100	51	105	17	30	42	260	20	290	15	115	31	120	40
50	27	60	9	90	35	50	60	10	37	85	68	60	89	20	21	305	28	100	30	75	88	110	34
50	22	80	24	80	52	85	62	70	45	290	3	90	26	60	26	50	45	130	60	90	34	110	58

YJS1/3-3 (Pseudosynclinal macroform - west side)

330	33	310	41	25	74	10	40	60	77	300	75	310	35	25	35	350	54	330	28	345	67	340	28
290	74	275	48	275	30	25	67	340	74	325	53	315	49	0	31	5	65	50	15	280	42	10	10
320	15	325	38	305	10	340	38	330	38	315	68	310	55	340	46	5	35	320	65	290	30	325	35
350	54	325	71	350	50	25	64	315	54	65	38	355	23	330	35	335	54	340	50	10	49	270	35
300	68	10	74	320	19	328	35	320	42	355	14	320	54	5	62	0	22	355	36	330	40	355	64

Y14/1-3 (Pseudosynclinal macroform - east side)

30	50	100	25	75	18	285	50	90	34	170	19	20	17	160	22	50	74	85	50	90	50	340	19
100	38	15	75	145	38	190	40	100	73	285	62	160	37	140	65	235	79	80	76	30	25	100	64
60	11	70	30	110	30	80	30	80	44	90	73	40	65	180	50	190	7	260	42	210	22	145	37
65	42	45	32	120	60	95	23	80	51	90	53	110	57	25	50	115	32	115	65	80	63	185	42
80	27	210	64	135	28	110	28	245	35	10	34	110	45	120	31	155	42	100	68	80	40	45	40

Y36/1-1 (Heterogeneous, unstratified gravel)

25	15	300	33	15	17	80	22	40	84	195	44	63	43	32	36	355	30	275	60	100	58	15	32
110	45	190	76	355	55	50	28	5	13	340	25	68	30	70	27	300	47	35	55	330	39	85	74
158	14	355	51	335	16	225	32	85	10	15	35	114	61	30	59	100	38	5	69	60	4	170	28
168	28	350	20	8	14	255	30	135	42	72	40	113	61	90	15	250	74	40	41	142	78	150	24
0	46	30	23	80	25	310	10	345	28	30	35	104	36	100	36	85	34	45	5	120	33	350	35

Y26/D-c/p (Heterogeneous, unstratified gravel)

270	30	275	13	305	11	60	33	325	53	227	50	350	15	5	35	95	22	250	49	10	36	130	4
20	65	55	50	330	16	120	4	300	26	170	5	30	30	90	26	0	35	50	30	135	7	150	10
45	60	195	2	235	8	10	11	345	25	20	55	350	20	155	57	310	3	65	20	270	30	100	10
265	19	195	32	340	37	20	17	330	25	50	30	345	27	45	44	335	70	240	9	255	44	310	31
295	25	240	11	320	5	330	38	60	32	220	15	220	3	140	8	60	19	65	14	60	20	70	58

T36/1-2 (1988) (Heterogeneous, unstratified gravel)

20	15	337	40	334	36	4	37	39	28	9	65	9	72	19	72	21	42	34	49	44	75	19	54
104	35	54	68	4	55	354	12	69	45	334	42	89	26	20	56	334	68	329	21	337	39	4	35
159	31	309	36	321	26	337	24	275	28	337	62	4	16	19	28	327	34	315	24	20	22	15	32
24	14	327	10	341	12	354	26	24	10	301	45	359	40	39	14	284	32	19	18	320	16	39	20
343	26	335	32																				

C43/1-1 (Heterogeneous, unstratified gravel)

70	40	45	42	85	49	25	60	100	73	25	28	75	63	110	48	145	42	0	31	165	48	90	35
70	65	85	67	185	28	110	60	350	44	80	58	20	5	30	68	255	34	120	60	130	25	140	24
20	45	150	48	212	51	60	74	105	62	45	42	145	53	82	62	163	16	75	22	15	50	110	44
10	30	25	48	212	54	62	58	25	45	75	20	95	53	25	38	90	30	95	48	75	31	40	22
90	67	25	58	35	38	200	30	150	35	65	34	100	62	125	25	170	38	130	40	105	38	40	30

C30/3-1 (1988) (Heterogeneous, unstratified gravel)

252	30	148	22	226	27	104	34	32	20	34	8	248	20	35	31	32	1	39	8	38	68	62	9
50	33	74	40	132	49	104	40	72	44	117	32	67	32	55	26	67	7	16	1	167	9	92	17
40	13																						

C30/3-5 (1988) (Heterogeneous, unstratified gravel)

67	48	137	30	102	25	42	15	44	21	52	29	62	29	52	29	220	8	51	16	74	18	95	12
353	13	80	12	46	22	47	10	75	32	172	34	96	21	109	21	92	7	57	38	82	15	81	3

C30/3-6 (1988) (Heterogeneous, unstratified gravel)

47	26	72	12	72	15	180	25	62	36	98	41	48	38	42	26	77	31	60	50	132	31	105	38
32	31	47	24	98	41	67	49	118	2	90	41	103	25	259	54	94	32	54	5	82	8	78	16
98	25																						

C30/7-1 (Heterogeneous, unstratified gravel)

263	9	255	15	50	55	5	32	120	13	150	46	280	22	305	36	248	25	35	22	162	58	264	56
270	56	60	45	25	16	75	51	125	39	228	32	32	24	45	30	275	46	15	11	345	35	10	75
50	40	0	45	330	45	65	34	115	24	195	68	275	32	55	18	52	48	38	12	75	15	268	45
280	14	20	37	35	38	120	14	65	1	115	46	325	44	35	40	120	50	55	32	334	65	90	28
10	18	40	42	300	42	275	17	140	61	355	28	138	52	238	28	285	6	25	14	20	6		

C33/3-5 (Heterogeneous, unstratified gravel)

50	33	30	15	0	28	40	35	70	22	50	16	350	23	350	28	30	10	30	35	35	14	355	25
20	17	10	25	10	32	30	32	40	25	40	33	35	25	50	16	25	27	40	47	345	32	60	37
0	28																						

C31/6-2 (Massive, imbricate, clast-supported gravel)

0	57	0	81	10	58	20	33	20	32	50	74	25	36	325	48	348	38	10	75	8	45	305	50
350	37	30	72	35	47	345	42	25	22	340	37	355	58	15	44	55	78	60	72	25	64	15	35
5	41	10	75	340	31	40	56	330	24	20	38	18	38	16	55	355	42	35	22	35	80	315	30
20	40	30	45	5	53	340	38	335	40	335	49	55	35	5	45	310	28	48	34	345	46	45	75
10	48	55	71	40	47	20	38	85	38	335	20	352	28	10	35	5	55	42	28	0	60	25	28

C31/10-1 (Plane-bedded gravel)

10	27	75	4	355	21	320	24	120	73	335	24	322	45	80	18	315	36	120	40	275	70	138	35
35	35	30	60	355	68	10	29	90	45	90	22	35	44	115	38	245	18	338	38	132	20	14	34
30	41	180	17	35	48	35	11	5	33	110	57	55	22	54	15	335	50	328	35	315	52	264	32
340	20	100	52	310	20	350	14	315	28	145	46	15	63	35	32	125	42	340	64	175	54	235	25
110	54	315	14	100	22	355	24	330	44	30	33	352	64	95	28	358	35	65	35	22	45	335	44

N54/1-5 (Massive, imbricate, clast-supported gravel)

70	41	345	22	65	26	5	22	358	28	350	35	25	45	10	30	355	53	40	60	50	45	35	38
45	80	60	55	350	80	55	48	30	70	48	86	54	70	65	15	10	23	58	25	75	78	64	48
72	36																						

N54/1-7 (Heterogeneous, unstratified gravel)

80	28	68	42	25	46	86	52	88	18	54	26	105	32	15	64	45	42	46	37	37	46	25	37
60	60	0	50	50	13	25	28	35	38	28	30	25	42	10	15	350	68	35	43	30	32	330	24
50	34																						

N35/2-2 (Heterogeneous, unstratified gravel)

356	34	340	80	328	26	300	63	40	22	60	36	335	33	29	21	0	45	50	64	47	40	35	35
67	54	60	25	28	44	355	38	10	16	36	36	40	38	15	42	5	32	355	24	45	18	80	52
56	34	22	56	36	28	54	14	38	18	55	24												

N36/1-1 (1980) (Heterogeneous, unstratified gravel)

170	37	223	69	320	25	66	16	295	19	190	43	95	25	190	50	30	18	160	50	340	65	95	25
215	45	310	14	265	12	345	39	144	23	150	40	70	20	65	28	335	45	30	24	250	10	245	40
155	40	230	35	40	20	352	88	335	8	148	21	30	15	310	40	135	34	210	35	275	25	150	34
120	15	140	43	90	21	315	22	300	8	260	10	340	12	95	30	85	22	190	20	230	30	285	10
190	61	170	26	155	24	143	47	240	30	222	28	120	30	326	25	275	45	110	20	265	25	40	15

N36/7-6 (1980) (In-phase wave structure, gravel)

175	35	202	27	225	47	226	14	265	24	235	29	205	19	250	30	270	30	287	34	275	42	285	36
258	18	226	22	243	14	276	18	282	35	248	64	290	28	285	28	270	18	276	30	252	16	296	18
284	22	292	36	264	23	254	13	244	28	268	34	256	10	234	22	272	52	256	14	248	5	135	7
298	14	125	14	298	16	39	12	264	6	308	18	312	54	314	24	294	15	98	15	294	18	242	16
276	34	94	14																				

N36/7b-1 (In-phase wave structure, gravel)

165	32	50	35	355	26	255	57	222	15	275	53	35	44	305	48	5	40	285	45	290	20	295	25
345	23	50	10	15	19	55	10	245	17	170	13	355	24	250	18	325	45	235	40	325	36	80	18
15	20	60	37	275	28	240	38	140	12	250	31	70	18	175	32	50	25	275	15	265	26	85	16
250	24	30	30	300	10	30	45	15	8	165	20	5	15	85	35	335	25	215	40	135	12	295	14
60	61	88	12	270	18	295	10	5	54	20	43	155	22	310	42	310	50	330	48	95	28	275	25

N36/7b-9 (In-phase wave structure, sand)

276	20	252	40	280	36	215	42	28	28	280	11	270	25	180	16	160	5	272	17	235	5	165	11
265	15	285	40	175	21	210	20	260	36	110	29	175	19	155	6	260	12	175	30	255	23	255	28
236	28	260	20	185	16	185	12	195	33	190	24												

N36/17-8 (In-phase wave structure, gravel)

153	25	90	11	335	16	265	25	35	25	135	26	210	10	125	27	165	33	75	16	115	17	190	50
120	17	220	16	160	29	275	12	315	5	300	16	15	22	140	31	275	45	192	20	305	42	10	22
280	54	352	21	135	15	292	20	25	15	308	28	162	14	320	21	230	20	250	15	285	13	225	18
300	30	300	21	192	12	290	42	268	16	305	2	70	20	130	48	135	32	280	27	220	17	0	15
330	55	310	32	88	20	230	13	320	28	315	24	215	10	206	35	140	40	240	14	308	30	310	17
235	20	240	18	300	22	312	38	335	33	225	25	130	32	220	24	115	20	20	18	200	28	305	20
290	24	130	30	125	40	15	34	355	10	310	30	304	6	355	42	205	32	305	35	65	10	210	13
15	12	280	24	280	18	130	14	260	8	205	15	210	8	340	16	195	15	190	20	90	24	225	28
25	25	275	22	330	10	65	28																

N36/17-10 (Water-escape structure in a gravel in-phase wave structure)

215	38	140	16	215	42	235	24	85	28	95	17	195	66	255	32	218	24	165	13	125	16	218	20
185	15	184	28	245	32	170	14	185	45	80	32	135	14	115	24	196	36	195	16	225	58	176	13
202	11	165	12	198	24	110	10	204	16	238	25												

N36/18-1 (Massive, imbricate, clast-supported gravel)

273	78	278	65	280	38	334	42	290	23	320	15	262	18	258	45	255	65	344	68	298	32	328	18
278	48	296	50	298	34	260	52	340	29	296	36	274	12	290	24	275	12	285	38	268	52	290	60
306	48	268	36	278	74	315	26	288	15	335	30	315	28	272	24	323	67	330	57	325	24	312	45
265	20	275	58	285	40	315	25																

N36/19-8 (In-phase wave structure, gravel)

283	55	295	50	0	30	266	34	265	14	335	50	275	10	102	8	50	18	245	31	345	34	258	16
340	24	135	36	257	44	350	21	252	40	280	26	315	14	322	28	305	6	285	30	315	45	300	36
270	17	272	40	252	16	350	38	90	24	260	43	285	16	358	25	190	26	200	13	30	8	25	12
290	36	300	21	275	31	250	41	100	17	185	16	335	5	125	32	290	22	275	42	198	24	355	10
25	20	338	23	105	75	344	43	268	26	82	26	345	21	85	28	325	38	300	17	355	42	208	24

N36/22-1 (Pseudosynclinal macroform - east side)

10	15	300	35	20	68	145	24	263	16	185	35	145	16	130	19	130	34	180	39	143	18	180	34
50	45	90	18	200	76	120	28	90	36	165	48	255	17	25	40	305	7	255	21	125	47	85	88
100	28	80	32	35	14	85	51	10	52	120	29												

N36/22-6 (Pseudosynclinal macroform - west side)

290	53	280	59	325	30	355	15	0	62	280	28	110	46	285	28	300	30	355	52	330	40	350	33
285	25	295	30	305	52	315	43	72	15	290	23	280	11	255	49	335	27	350	57	315	23	325	84
305	25	300	47	342	44	275	14	275	30	282	28	295	26	325	26	80	22	305	72	80	26	325	22
300	42	280	25	310	86	80	47	320	54	337	32	225	15	0	46	82	29	80	42	300	32	143	32
185	48	302	16	225	36	200	25	325	55	205	35	305	26	310	43	165	14	310	30	220	20	205	55
335	14	305	34	255	45	15	34	210	48	225	42	290	20	130	26	275	30	285	14	150	18	15	28
350	58	235	48	325	52	285	26	205	15	248	15	5	26	255	25	315	20	265	12	295	55	305	28
315	74	305	25	235	24	240	28	195	16	220	25	15	30	235	35	330	12	165	18	20	32	320	35
205	30	315	65	285	20	355	30																

[1] Data format: azimuth dip of clast ab-plane (in degrees).

[2] Fit fabrics reported in Table 4.4 were calculated from the above data sets as:

TJS1 = TJS1/1-3 + TJS1/2-1 + TJS1/2-3
T14 = T14/1-3
T24 = T24/1-1
T26 = T26/D-c/p + T26/1-2 (1989)
C43 = C43/1-1
C30 = C30/2-1 (1988) + C30/2-5 (1988) + C30/2-6 (1988) + C30/7-1
C32 = C32/3-5
C31 = C31/6-2 + C31/10-1
N54 = N54/1-5 + N54/1-7
N35 = N35/2-2
N36 = N36/1-1 (1990) + N36/18-1

APPENDIX 5

Paleoflow direction measurements from cross-bedded and cross-laminated sand and gravel within south-central Ontario eskers.

Pit number	Sedimentary Structure	Measurements (in degrees)
TJ51	Cross-bedding estimates	180 162
	Cross lamination	180 178 160 166 166 180 174 142 170 184 190 126 128 160 116
		136 136 124 132 128 124
T16	Cross-bedding estimates	315 142 209
	Cross lamination	295 310 228 210 250 218 220 220 220 164 250 250 150 146 184
		138 244 218 216 234 144 214 162 174 180 220 260 148 164 230
		240 228
T15	Cross bedding	290 270 288 294 244 262 268 274 308 282 275 245 210 270 282
		270 305 280 280 298 312
T12	Cross bedding	224 262 232 240 233 228 230 230 215 244 255 240 238 202 250
		260 252 224 214 246 245 220 222 252 232 226 248 237 208 224
	Cross-bedding estimates	210 190
	Cross lamination	248 232 226 217 210 208 208 220 222 228
	Cross-lamination estimate	175
T11	Cross bedding	207 204 164 200 215 204 216 200 215 213 212 202 205 208 210
	Cross lamination	238 240 246 242 250 244 246 260 234 234 245 245 245 246 248
		240 250 254 247 240 250 243 245 250 245 240 252 235 242 240
		40 42 40 40 40 45 40 44 45 45 45 47 47 48 46
		48 48 45 44 44 40 42 44 45 44 42 45 42 40 38
	Cross-lamination estimate	23
T19	Cross-bedding estimates	255 240 255 255 290 300 270 270 305 290 240
	Cross-lamination estimates	220 255 240
C43	Cross-bedding estimate	270
	Cross lamination	240 250 280 270 280 280 290 275 280 290 275 290 275 285 275
		280 250 280 290 290
	Cross-lamination estimates	25 150 235
C30	Cross bedding	160 165 165 165 155
	Cross-bedding estimate	300
C32	Cross bedding	280 250 225 240 240 295 240 270 245 225 240 245 240 245 280
		250 260 245 230 260
	Cross-bedding estimates	225 270 270 180
	Cross lamination	200 225 205 178 190 195 195 195 190 200 220 195 180 178 170
		205 175 185 195 185 175 195 200 215 175 190 180 195 185 170
	Cross-lamination estimates	205 180 180 180 180 0 180
C31	Cross-bedding estimates	110 185 200 180
	Cross lamination	195 195 182 202 195 190 185 192 186 182 186 193 182 175 192
		200 185 195 185 202 175 192 176 182 174 185 190 187 168 182
		175 185 176 180 180 182 180 175 165 180 185 185 170 185 190
		180 170 190 150 185 185 160 160 195 170 165
	Cross-lamination estimates	200 200
N35	Cross lamination	190 205 175 215 225 205 220 230 235 230 250 225 222 215 222
		225 230 222 227 220 222 225 230 235 225 220 235 215 200 207
	Cross-lamination estimate	235
N56	Cross-bedding estimates	180 155 200
	Cross lamination	190 200 190 215 210 185 205 190 200 205 190 220 215 210 206
		240 230 205 230 240 255 245 260 225 245 245 250 230 255 245
		245 250 245 230 235 240 210 225 238 255 245 240 215 230 220
	Cross-lamination estimates	140 140 220 225 220 40
N36	Cross bedding	150 110 105 280 282 280 288 282 270 265 65 290 280 200 190
		158 185 170 170 156 163 95 160 165 165 170 180 155 160 170
		185 175 150 195 175 155 170 130 155 160 85 150 170 327 280
		330 160 148 155 154 165 155 170 170 160 145 140 135 155 155

Fit number	Sedimentary Structure	Measurements (in degrees)														
		165	150	150	165	175	170	165	150	145	190	180	155	160	165	160
		150	180	170	180	175	180									
	Cross-bedding estimates	162	125	5	340	340	290	270	190	220	215	280	210	150	100	270
		220	190	235	255	270										
	Cross lamination	240	245	245	248	244	220	215	245	230	222	220	240	245	270	248
		265	270	275	270	280	255	225	230	230	250	270	270	268	280	265
		245	270	258	280	265	265	267	270	245	255	275	265	255	280	280
		275	270	265	220	280	155	148	162	180	165	170	165	157	150	175
		150	160	155	165	150	175	165	160	165	163	155	165	155	150	145
		150	160	145	150	150	113	110	100	107	120	110	105	118	124	115
		120	195	235	220	248	223	165	190	190	170	195	200	210	230	240
		210	180	220	193	170	215	193	180	175	165	155	190	150	140	195
		155	190	135	195	140	195	180	144	180	180	180	175	167	180	140
		130	150	135	155	153	138	153	152	150	145	155	230	255	230	235
		230	240	245	235	260	250	220	230	265	275	225	240	245	250	275
		255	260	275	260	270	265	245	260	235	215	260	250	255	255	252
		240	258	270	255	250	255	255	270	260	250	248	248	245	240	240
		245	240	238	235	240	240	240	245	235	230	238	245	195	210	260
		265	258	270	263	130	190	190	180	160	210	195	172	170	145	210
		210	212	215	200	208	195	180	200	205						
	Cross-lamination estimates	125	145	145	145	305	130	40	150	200	200	200	200	200	220	220
		320	195													

APPENDIX 6

Grain-size data for gravel facies and structures within south-central Ontario eskers.

	Sieve size (phi)	Sieve size (mm)	Percent passing							
Unit number			T19/6-7	T19/6-1	T33/1-1a	T33/1-1b	C43/1-1	C30/6-1	C30/6-2	M6°/1-4
Sedimentary facies/structure[1]			*HU gravel*	*HU gravel*	*HU gravel*	*HU gravel*	*HU gravel*	*RG gravel part A*	*RG gravel part B*	*OAAB macroform*
	-7.25	152.319	100.00	100.00	100.00	100.00	100.00	100.00	100.00	100.00
	-6.25	76.109	100.00	93.43	100.00	100.00	100.00	92.80	100.00	100.00
	-5.25	38.055	46.43	54.20	46.15	100.00	96.81	44.17	28.10	89.72
	-4.25	19.027	42.86	39.64	26.92	96.30	80.85	26.16	3.32	82.24
	-3.25	9.514	25.00	32.36	17.31	92.59	63.83	22.58	2.38	72.90
	-2.25	4.757	21.43	27.50	13.46	85.19	47.87	18.96	1.44	56.07
	-2.00	4.000	20.83	26.87	12.98	84.42	44.83	16.01	1.25	51.65
	-1.00	2.000	16.59	23.52	11.08	76.57	33.84	15.40	1.00	34.68
	-0.50	1.414	15.04	19.61	9.01	68.19	23.41	13.91	0.92	24.97
	0.00	1.000	14.90	16.15	7.95	61.38	19.73	13.38	0.90	22.61
	0.50	0.707	12.88	15.17	5.23	43.40	13.02	12.00	0.82	19.22
	1.00	0.500	10.66	10.67	2.69	23.89	7.88	10.04	0.70	16.39
	1.50	0.354	8.31	5.76	1.26	10.86	4.65	8.09	0.56	13.63
	2.00	0.250	6.34	3.27	0.70	5.50	3.08	6.36	0.45	10.71
	2.50	0.177	4.65	1.78	0.38	2.54	2.23	4.61	0.36	7.44
	3.00	0.125	3.32	0.99	0.21	1.11	1.69	3.62	0.30	4.46
	3.50	0.088	2.36	0.60	0.12	0.48	1.38	2.80	0.26	2.56
	4.00	0.063	1.66	0.41	0.07	0.30	1.16	2.33	0.23	1.78
Mean			-3.90	-3.53	-4.72	-0.07	-2.12	-4.13	-5.42	-1.75
Standard deviation			2.58	2.76	1.75	1.75	2.13	2.57	0.59	2.69
Skewness			-0.78	-0.65	-0.67	0.36	-0.17	-0.73	-0.24	-0.10
Kurtosis			1.34	0.73	1.56	-0.17	0.81	1.69	1.05	1.22

[1] *HU gravel*, heterogeneous, unstratified gravel
RG gravel, rhythmically graded gravel within cross-bedded gravel foresets.
OAAB macroform, oblique accretion avalanche bed macroform

APPENDIX 7

Clast size, lithology, sphericity, roundness and a-axis orientation data for *in situ* clasts within the Harricana glaciofluvial complex, Québec.

Axial dimensions (cm)			Clast/sieve size[1] (mm)	Clast/sieve size[2] (ϕ)	Lithology[3]	Maximum Projection Sphericity[4]	Visual Roundness Class[5]	Clast a-axis Orientation[6]
a	b	c						
Q1 (363.22 km)								
12.0	9.0	5.0	102.96	-6.69	GD	0.614	A	T
14.5	7.4	3.0	79.85	-6.32	GD	0.438	SA	T
6.5	5.7	4.3	71.40	-6.16	B	0.703	SR	T
11.0	10.2	7.0	123.71	-6.95	B	0.759	SR	P
15.5	10.0	6.0	116.62	-6.87	GD	0.615	VR	T
10.0	6.5	4.0	76.32	-6.25	D	0.627	SR	T
21.0	11.5	8.5	143.00	-7.16	GD	0.669	SR	T
8.0	5.2	3.0	60.03	-5.91	GD	0.600	R	T
12.0	4.0	3.0	50.00	-5.64	B	0.572	R	P
20.5	14.5	9.0	170.66	-7.41	GD	0.648	SA	T
4.5	3.3	2.2	39.66	-5.31	B	0.688	SR	T
8.5	6.5	4.0	76.32	-6.25	D	0.662	R	P
10.0	5.5	4.3	69.81	-6.13	B	0.695	SR	T
8.5	5.5	4.2	69.20	-6.11	B	0.723	SA	P
7.4	6.0	3.3	68.48	-6.10	GD	0.626	SR	T
6.3	4.5	3.5	57.01	-5.83	GB	0.756	SA	P
6.5	4.0	3.4	52.50	-5.71	B	0.763	SR	P
5.5	4.2	2.0	46.52	-5.54	GB	0.557	SR	P
14.7	10.4	7.2	126.49	-6.98	GB	0.697	VR	P
18.0	13.5	7.5	154.43	-7.27	B	0.614	R	P
14.0	11.5	8.7	144.20	-7.17	GD	0.778	VR	P
19.0	12.0	11.5	166.21	-7.38	B	0.834	SR	O
10.0	9.0	5.0	102.96	-6.69	GD	0.652	SR	T
12.7	12.0	9.0	150.00	-7.23	D	0.810	VR	T
7.4	5.0	4.2	65.30	-6.03	GT	0.781	VR	P
9.8	8.8	5.6	104.31	-6.70	B	0.714	VR	P
11.2	10.3	7.0	124.54	-6.96	GD	0.752	VR	T
6.8	5.4	3.8	66.03	-6.05	GD	0.733	R	P
6.4	4.0	3.0	50.00	-5.64	GD	0.706	SA	O
7.5	6.0	4.5	75.00	-6.23	GD	0.766	SA	P
5.4	5.0	2.3	55.04	-5.78	B	0.581	SA	P
9.8	6.5	5.5	85.15	-6.41	GD	0.780	VR	O
5.0	3.7	2.5	44.65	-5.48	GD	0.698	R	T
4.5	3.8	2.0	42.94	-5.42	B	0.616	R	O
3.5	3.4	2.3	41.05	-5.36	B	0.763	VR	T
6.5	5.2	2.4	57.27	-5.84	GD	0.554	SR	T
9.8	7.5	4.6	87.98	-6.46	GD	0.660	SR	P
7.5	6.5	4.0	76.32	-6.25	D	0.690	VR	T
12.5	8.5	5.8	102.90	-6.69	B	0.682	R	P
6.8	5.5	4.5	71.08	-6.15	GD	0.815	R	T
9.5	6.8	4.2	79.92	-6.32	B	0.649	R	P
11.2	8.5	5.0	98.62	-6.62	D	0.640	VR	P
16.5	10.4	7.2	126.49	-6.98	B	0.671	R	P
12.4	7.8	6.6	102.18	-6.67	GD	0.767	SR	P
8.2	6.5	3.5	73.82	-6.21	B	0.613	SR	T
6.5	5.5	4.8	73.00	-6.19	GD	0.864	VR	P
15.2	13.5	10.4	170.41	-7.41	D	0.808	R	T
12.4	9.5	6.0	112.36	-6.81	B	0.674	R	T
16.2	8.5	5.4	100.70	-6.65	D	0.598	R	P

Axial dimensions (cm)			Clast/sieve size[1] (mm)	Clast/sieve size[2] (ϕ)	Lithology[3]	Maximum Projection Sphericity[4]	Visual Roundness Class[5]	Clast a-axis Orientation[6]
a	b	c						
32.0	19.5	12.5	231.62	-7.85	B	0.630	R	T
9.5	7.4	6.2	98.54	-6.59	B	0.816	SR	T
27.0	19.0	8.5	208.15	-7.70	GD	0.530	VR	T
15.2	10.5	8.5	123.49	-6.95	B	0.642	SR	T
15.5	10.5	8.8	137.00	-7.10	GD	0.781	VR	P
16.8	10.5	9.5	141.60	-7.15	D	0.800	R	T
17.2	10.5	9.5	141.60	-7.15	GD	0.794	VR	T
9.5	5.4	3.5	64.35	-6.01	D	0.620	SR	T
21.0	17.5	15.4	233.11	-7.86	GD	0.884	SR	P
15.5	12.8	7.5	148.35	-7.21	GD	0.657	SR	P
13.5	11.4	9.5	148.39	-7.21	GD	0.837	SR	T
16.0	9.5	5.7	110.79	-6.79	GD	0.598	SR	T
10.3	10.3	4.0	110.49	-6.79	B	0.532	SR	N
10.6	5.3	4.8	71.51	-6.16	GD	0.743	R	T
8.6	6.3	3.6	72.56	-6.18	D	0.621	SR	T
5.5	4.6	2.0	50.16	-5.65	D	0.541	SA	P
13.7	5.8	5.5	79.93	-6.32	GD	0.725	SR	T
8.0	6.3	5.0	80.43	-6.33	GD	0.792	VR	T
11.0	9.5	5.0	111.83	-6.81	D	0.693	R	P
6.4	5.0	3.2	59.36	-5.89	D	0.684	VR	P
12.5	7.5	6.8	101.24	-6.66	D	0.790	R	P
12.6	11.2	7.0	132.08	-7.05	GD	0.699	VR	P
8.3	5.4	3.2	62.77	-5.97	GD	0.611	SR	P
7.9	7.0	2.8	75.39	-6.24	GD	0.521	VR	T
9.2	4.0	2.5	47.17	-5.56	B	0.554	SR	T
13.0	11.0	9.2	143.40	-7.16	B	0.840	SA	T
7.0	6.3	4.2	75.72	-6.24	B	0.737	VR	T
9.8	7.0	4.0	80.62	-6.33	GD	0.616	R	P
10.2	7.0	4.3	82.15	-6.36	AG	0.637	SR	P
7.1	5.2	4.3	67.48	-6.08	GD	0.794	SR	P
5.7	4.8	4.1	63.13	-5.98	D	0.850	VR	T
9.4	7.0	5.3	87.80	-6.46	B	0.753	SR	P
7.0	3.5	2.7	44.20	-5.47	B	0.668	SR	P
10.2	7.4	4.5	86.61	-6.44	GD	0.645	SR	P
6.2	6.0	2.7	65.80	-6.04	B	0.581	SA	T
11.5	10.0	6.5	119.27	-6.90	B	0.716	SR	P
12.4	6.2	4.8	78.41	-6.29	B	0.669	R	P
5.8	4.5	3.0	54.08	-5.76	B	0.701	SR	T
5.9	4.8	4.0	62.48	-5.97	GD	0.827	SR	T
6.0	2.8	2.0	34.41	-5.10	B	0.620	SR	P
6.6	5.5	3.4	64.66	-6.01	B	0.683	R	T
9.0	7.2	6.2	95.02	-6.57	B	0.840	SR	T
6.4	6.6	4.5	79.88	-6.32	GD	0.715	R	P
9.2	5.0	4.0	64.03	-6.00	D	0.703	SR	P
7.0	5.2	2.8	59.06	-5.88	D	0.599	SR	P
13.0	10.5	4.4	113.85	-6.83	B	0.522	R	T
16.5	8.4	7.5	112.61	-6.82	B	0.740	SR	T
10.5	8.6	4.5	98.84	-6.63	B	0.603	R	T
8.5	6.9	5.4	87.62	-6.45	GD	0.792	VR	T
11.0	8.0	5.8	98.81	-6.63	B	0.726	VR	T
16.5	14.2	8.4	164.98	-7.37	GD	0.670	SR	P
10.5	7.6	5.2	92.09	-6.52	GD	0.697	R	P
7.6	5.5	2.5	60.42	-5.92	B	0.531	SA	P
8.5	5.4	3.5	64.35	-6.01	B	0.644	R	T
7.4	4.6	3.5	57.80	-5.85	B	0.711	R	P
8.0	4.8	4.0	62.48	-5.97	GD	0.747	R	P

Axial dimensions (cm)			Clast/sieve size[1] (mm)	Clast/sieve size[2] (ϕ)	Lithology[3]	Maximum Projection Sphericity[4]	Visual Roundness Class[5]	Clast a-axis Orientation[6]
a	b	c						
14.8	9.0	4.5	100.62	-6.65	GD	0.534	SR	P
11.5	10.4	6.5	122.64	-6.94	D	0.707	SR	T
8.8	6.0	4.5	75.00	-6.23	GD	0.727	SR	T
8.5	6.0	4.2	73.24	-6.19	GD	0.768	VR	T
9.2	6.8	4.5	81.54	-6.35	GD	0.687	R	P
9.8	7.6	6.4	99.36	-6.63	D	0.819	R	P
14.5	7.8	6.5	101.53	-6.67	GD	0.720	R	P
9.6	5.5	4.0	68.01	-6.09	D	0.672	VR	P
7.5	5.2	4.2	66.84	-6.06	B	0.768	SA	T
7.4	6.6	3.8	75.18	-6.23	GD	0.643	R	T
7.4	5.8	3.2	66.24	-6.05	D	0.620	SR	T
12.0	8.5	4.4	95.71	-6.58	B	0.575	SR	P
8.2	5.0	3.8	62.80	-5.97	GD	0.708	SR	P
7.4	5.6	4.2	70.00	-6.13	GD	0.752	R	P
12.5	8.6	7.5	114.11	-6.83	B	0.800	R	P
Q3 (355.11 km)								
10.7	5.7	5.2	77.16	-6.27	B	0.763	SR	T
9.7	6.5	4.3	77.94	-6.28	GD	0.664	SR	T
9.0	4.4	3.5	56.22	-5.81	B	0.676	VR	P
9.0	5.0	2.4	55.46	-5.79	B	0.504	SR	T
7.7	6.5	3.8	75.29	-6.23	B	0.661	SR	P
7.8	3.3	2.9	43.93	-5.46	B	0.609	SR	P
12.1	8.7	5.2	101.38	-6.66	GD	0.636	SR	P
13.0	7.7	4.8	90.74	-6.50	B	0.613	SR	T
14.5	11.5	8.0	140.09	-7.13	GD	0.727	SA	T
5.8	5.4	3.2	62.77	-5.97	D	0.689	R	T
19.5	14.0	6.5	154.35	-7.27	B	0.537	SR	P
5.7	3.4	1.5	37.16	-5.22	D	0.488	R	O
9.8	5.5	3.3	64.14	-6.00	B	0.587	SR	O
11.2	8.8	4.2	97.51	-6.61	B	0.564	SA	T
9.8	7.7	5.2	92.91	-6.54	GT	0.710	SR	T
6.2	4.2	2.5	48.88	-5.61	GD	0.621	SR	P
7.2	3.7	1.7	40.72	-5.35	B	0.477	SA	P
13.2	10.2	7.4	126.02	-6.98	B	0.741	R	T
12.6	10.0	5.8	115.60	-6.85	GT	0.644	SR	P
24.0	16.0	10.0	188.68	-7.56	B	0.639	SR	T
9.2	7.0	4.0	80.62	-6.33	B	0.629	VR	T
12.7	7.5	4.3	86.45	-6.43	D	0.579	R	T
13.0	11.0	4.0	117.05	-6.87	GD	0.482	R	P
13.8	9.4	8.8	128.76	-7.01	GD	0.842	SR	P
9.4	6.5	3.5	73.82	-6.21	B	0.585	SA	P
11.5	9.0	7.0	114.02	-6.83	GD	0.779	VR	T
8.9	6.2	4.5	76.61	-6.26	GD	0.716	VR	T
11.5	9.3	6.5	113.46	-6.83	GD	0.734	VR	T
6.2	4.0	2.1	45.18	-5.50	B	0.562	SA	P
8.3	6.2	3.5	71.20	-6.15	B	0.620	SR	T
6.4	5.5	2.5	60.42	-5.92	B	0.562	VR	P
7.4	6.0	4.5	75.00	-6.23	GD	0.770	SR	T
6.0	5.0	2.8	57.31	-5.84	B	0.639	SR	T
5.6	4.8	3.5	59.41	-5.89	GD	0.770	R	P
11.5	10.5	8.0	132.00	-7.04	D	0.809	VR	T
8.4	6.2	3.0	68.88	-6.11	B	0.557	SR	P
7.5	5.4	3.6	64.90	-6.02	B	0.684	SR	T
7.2	5.6	2.8	62.61	-5.97	GD	0.579	SR	P
7.9	6.6	3.5	74.71	-6.22	B	0.617	SR	O

Axial dimensions (cm)			Clast/sieve size[1] (mm)	Clast/sieve size[2] (ϕ)	Lithology[3]	Maximum Projection Sphericity[4]	Visual Roundness Class[5]	Clast a-axis Orientation[6]
a	b	c						
8.4	5.8	4.2	71.61	-6.16	B	0.713	SR	P
7.5	5.0	2.6	56.36	-5.82	GD	0.565	R	T
9.0	7.5	3.8	84.08	-6.39	GT	0.598	SR	T
7.0	4.2	2.5	48.68	-5.61	B	0.597	SR	P
17.0	12.5	7.8	147.34	-7.20	GD	0.659	R	P
16.0	9.5	5.8	111.31	-6.80	GD	0.605	R	T
11.5	7.8	4.5	90.05	-6.49	B	0.609	VR	P
7.8	5.0	3.2	59.38	-5.89	D	0.640	VR	P
8.6	6.6	4.0	78.89	-6.30	GT	0.649	SR	T
10.6	7.4	3.6	82.29	-6.36	B	0.549	SA	O
11.8	10.0	7.0	122.07	-6.93	GD	0.750	VR	T
8.5	6.0	3.8	71.02	-6.15	B	0.657	SR	P
10.8	8.0	5.4	96.52	-6.59	GD	0.696	R	P
9.6	5.0	3.4	60.46	-5.92	B	0.622	SR	T
11.2	7.4	6.5	98.49	-6.62	B	0.799	SR	T
15.5	8.5	5.8	102.90	-6.69	GD	0.634	SR	P
14.5	11.0	7.5	133.14	-7.06	GD	0.707	VR	T
9.5	5.0	3.4	60.46	-5.92	B	0.624	VR	P
15.5	13.0	6.5	145.34	-7.18	B	0.594	SR	T
11.5	5.5	5.0	74.33	-6.22	B	0.734	SA	T
12.8	8.5	5.5	101.24	-6.66	GD	0.653	R	T
18.3	15.5	8.0	174.43	-7.45	B	0.609	R	T
11.3	7.5	3.6	83.19	-6.38	D	0.535	SR	T
10.3	9.0	5.0	102.96	-6.69	D	0.646	R	T
12.0	10.3	5.5	116.76	-6.87	D	0.626	SR	P
22.5	14.0	7.7	159.78	-7.32	D	0.573	VR	O
16.4	11.0	7.5	133.14	-7.06	B	0.678	SR	T
24.0	18.0	9.4	203.07	-7.67	D	0.589	VR	O
16.7	7.4	5.7	93.41	-6.55	B	0.641	SA	P
30.9	14.2	5.5	152.28	-7.25	D	0.410	SA	T
26.0	17.0	10.3	198.77	-7.63	B	0.621	R	P
16.9	8.0	4.5	91.79	-6.52	B	0.531	SA	T
13.5	9.0	5.0	102.96	-6.69	D	0.590	VR	T
23.0	10.5	10.3	147.09	-7.20	D	0.760	SA	T
11.2	10.0	5.0	111.80	-6.80	B	0.607	R	P
14.5	12.0	9.8	154.93	-7.26	B	0.820	SA	P
11.6	7.6	5.3	92.66	-6.53	D	0.683	R	P
8.9	4.7	4.5	65.07	-6.02	B	0.785	A	P
10.7	6.0	4.4	74.40	-6.22	D	0.671	SA	P
14.2	9.0	5.6	106.00	-6.73	GD	0.626	SR	T
6.7	4.7	2.2	51.89	-5.70	GT	0.536	SR	P
9.9	6.5	6.4	91.22	-6.51	D	0.860	SA	T
10.0	7.5	7.0	102.59	-6.68	B	0.868	SA	P
6.3	4.5	2.5	51.48	-5.69	B	0.604	SA	T
9.9	5.5	3.5	65.19	-6.03	D	0.608	VR	T
13.3	9.0	5.6	106.00	-6.73	B	0.640	A	P
12.4	10.2	5.0	113.60	-6.83	D	0.583	SR	T
19.4	14.0	10.5	175.00	-7.45	GD	0.740	SA	T
10.7	7.0	6.8	97.59	-6.61	GD	0.851	VR	P
11.0	5.8	5.4	79.25	-6.31	GD	0.770	SA	T
10.1	9.7	6.0	114.06	-6.83	B	0.716	SA	P
13.0	9.5	6.0	112.36	-6.81	GD	0.663	SR	T
21.0	17.0	12.0	208.09	-7.70	B	0.739	SR	P
10.5	8.0	6.5	103.08	-6.69	D	0.795	VR	T
10.0	8.0	5.0	94.34	-6.56	D	0.670	R	P
22.0	16.0	5.0	167.63	-7.39	D	0.414	VR	T

Axial dimensions (cm)			Clast/sieve size[1] (mm)	Clast/sieve size[2] (ϕ)	Lithology[3]	Maximum Projection Sphericity[4]	Visual Roundness Class[5]	Clast a-axis Orientation[6]
a	b	c						
9.5	7.5	4.0	85.00	-6.41	B	0.608	VR	T
10.5	4.5	4.0	60.21	-5.91	D	0.697	R	T
12.0	10.0	5.5	114.13	-6.83	GD	0.632	SR	T
9.0	6.0	5.5	81.39	-6.35	GD	0.624	SR	P
13.5	8.0	2.5	83.82	-6.39	D	0.387	A	T
10.0	8.0	6.0	100.00	-6.64	GD	0.766	VR	T
11.0	7.5	5.5	93.01	-6.54	D	0.716	SR	T
22.0	12.0	7.5	141.51	-7.14	GD	0.597	R	P
11.0	6.5	4.0	76.32	-6.25	D	0.607	VR	T
10.5	8.0	5.0	94.34	-6.56	B	0.668	SA	P
10.5	8.0	5.0	94.34	-6.56	B	0.668	SR	P
12.5	7.0	5.5	89.02	-6.48	B	0.702	SR	P
18.5	14.0	7.0	156.52	-7.29	B	0.574	SR	P
10.2	6.8	4.6	82.10	-6.36	B	0.673	SR	P
15.0	12.0	8.0	144.22	-7.17	D	0.709	SR	T
14.5	10.5	9.5	141.60	-7.15	GD	0.840	VR	P
16.5	12.5	5.0	134.63	-7.07	GD	0.495	SR	P
22.0	16.0	12.0	200.00	-7.64	GD	0.742	R	P
25.0	15.0	9.0	174.93	-7.45	B	0.600	SR	P
10.5	5.5	4.5	71.06	-6.15	D	0.705	SR	P
11.4	8.0	5.5	97.08	-6.60	GD	0.692	R	P
12.6	8.0	5.5	97.08	-6.60	D	0.670	SR	T
17.0	12.0	6.0	134.16	-7.07	B	0.561	SR	P
12.5	11.5	6.0	129.71	-7.02	D	0.630	VR	T
14.0	11.0	5.0	120.83	-6.92	B	0.546	SA	T
34.0	18.0	12.0	216.33	-7.76	B	0.617	SR	P
14.0	12.3	4.8	132.03	-7.04	B	0.511	SA	T
13.8	11.0	6.5	127.77	-7.00	GD	0.653	VR	T
11.8	10.5	6.0	120.93	-6.92	B	0.662	R	T
19.5	11.0	7.0	130.38	-7.03	GD	0.611	SR	T
12.5	8.0	7.0	106.30	-6.73	D	0.788	SR	P
21.5	11.0	7.5	133.14	-7.06	B	0.620	VR	P
15.0	13.0	3.0	133.42	-7.06	B	0.359	SA	T
8.3	5.8	3.4	67.23	-6.07	D	0.622	SR	T
25.5	15.5	8.5	176.78	-7.47	GD	0.568	SA	T
20.5	13.0	9.5	161.01	-7.33	D	0.697	R	P
13.0	13.0	5.0	139.28	-7.12	B	0.529	VR	N
13.8	13.5	5.0	143.98	-7.17	D	0.512	R	T
18.0	13.0	12.0	176.92	-7.47	GD	0.851	R	P
12.5	8.7	5.2	101.36	-6.66	B	0.629	SR	P
6.2	5.9	4.0	71.28	-6.16	D	0.759	SR	T
11.0	8.5	5.2	99.64	-6.64	D	0.661	R	P
10.7	8.3	5.4	99.02	-6.63	D	0.690	SR	P
12.4	8.3	6.4	104.81	-6.71	D	0.736	VR	T
12.8	8.4	5.0	97.75	-6.61	GD	0.615	SR	T
13.8	10.3	4.9	114.06	-6.83	D	0.553	R	O
15.0	12.0	7.3	140.46	-7.13	GT	0.666	SR	T
18.4	14.1	8.1	162.61	-7.35	B	0.632	R	P
15.5	15.0	5.2	158.76	-7.31	B	0.488	SR	T
11.3	8.9	4.4	99.28	-6.63	D	0.577	SR	T
18.5	13.3	9.0	160.59	-7.33	B	0.690	SR	P
7.5	6.3	4.5	77.42	-6.27	B	0.754	VR	P
11.6	7.7	2.6	81.27	-6.34	GD	0.423	A	O
10.2	8.0	4.0	89.44	-6.48	D	0.581	VR	T
16.0	9.0	4.2	99.32	-6.63	B	0.497	R	T
22.5	13.5	8.0	156.92	-7.29	D	0.595	SR	P

Axial dimensions (cm)			Clast/sieve size[1] (mm)	Clast/sieve size[2] (ϕ)	Lithology[3]	Maximum Projection Sphericity[4]	Visual Roundness Class[5]	Clast a-axis Orientation[6]
a	b	c						
16.0	11.0	7.5	133.14	-7.06	B	0.684	SR	P
12.5	9.5	5.5	100.77	-6.78	B	0.634	VR	T
20.5	13.0	8.5	146.34	-7.19	B	0.541	SR	O
14.0	11.5	7.5	137.30	-7.10	GD	0.704	SR	T
12.0	9.5	6.5	115.11	-6.85	GD	0.719	SR	T
21.5	13.0	7.5	150.08	-7.23	D	0.586	R	P
16.5	14.0	9.0	166.43	-7.38	B	0.670	R	T
14.5	10.5	7.0	126.19	-6.98	D	0.685	VR	T
19.0	16.0	11.0	210.95	-7.72	D	0.707	R	T
26.0	19.0	11.0	219.54	-7.78	GD	0.626	SR	O
14.0	10.5	7.0	126.19	-6.98	D	0.693	VR	T
14.0	12.0	6.5	136.47	-7.09	GD	0.631	SR	T
18.0	15.0	9.5	177.55	-7.47	GD	0.694	SR	T
18.0	13.0	9.0	158.11	-7.30	D	0.702	SR	T
21.0	16.0	10.0	188.68	-7.56	B	0.668	SA	P
11.0	9.5	6.0	112.38	-6.81	GD	0.701	VR	T
23.0	14.0	8.0	161.25	-7.33	GD	0.584	SR	P
16.0	10.0	6.8	120.93	-6.92	B	0.661	VR	P
9.5	6.5	4.0	76.32	-6.25	B	0.638	VR	T
10.5	8.0	5.0	94.34	-6.56	D	0.668	R	T
13.0	10.5	6.0	120.93	-6.92	B	0.641	R	T
14.5	9.0	7.0	114.02	-6.83	B	0.721	SR	P
11.5	10.0	4.5	109.66	-6.78	D	0.561	SR	T
10.5	8.5	4.5	95.18	-6.63	GT	0.610	R	T
22.0	16.0	10.0	188.68	-7.56	B	0.657	SA	P
12.0	10.0	5.5	114.13	-6.83	D	0.632	VR	T
21.0	19.0	11.0	219.54	-7.78	GD	0.672	R	T
19.0	13.0	7.0	147.65	-7.21	GD	0.583	R	T
12.0	10.0	3.5	105.95	-6.73	B	0.467	SR	T
Q4 (354.83 km)								
7.2	6.5	2.8	70.77	-6.15	B	0.551	VR	T
7.6	5.5	2.4	60.01	-5.91	GD	0.517	SR	P
8.6	6.5	2.8	70.77	-6.15	GD	0.520	SR	P
8.4	5.6	4.8	73.76	-6.20	GD	0.788	SR	T
7.4	5.8	2.0	61.35	-5.94	B	0.453	R	P
17.5	10.5	7.8	130.80	-7.03	B	0.692	R	T
8.8	4.6	2.8	53.85	-5.75	B	0.579	SR	P
8.0	7.5	3.2	81.54	-6.35	B	0.555	VR	T
12.5	5.5	3.8	66.85	-6.06	B	0.594	SR	P
8.5	5.8	3.8	69.34	-6.12	D	0.664	VR	P
15.5	10.5	6.6	124.02	-6.95	GD	0.644	R	P
8.4	6.8	3.9	78.39	-6.29	B	0.643	SR	P
5.4	2.6	2.1	33.42	-5.06	B	0.680	R	P
7.2	6.6	4.2	78.23	-6.29	GD	0.719	R	P
13.6	8.8	7.2	113.70	-6.83	B	0.757	R	T
8.2	4.6	2.8	53.85	-5.75	B	0.592	SR	O
26.0	16.5	10.5	195.58	-7.61	GD	0.636	R	O
11.0	8.0	4.5	91.79	-6.52	B	0.613	SR	P
9.2	7.4	5.5	92.20	-6.53	GD	0.763	SR	T
9.5	6.8	5.2	85.60	-6.42	B	0.748	SR	P
6.0	4.9	3.4	59.64	-5.90	B	0.733	SR	T
10.2	8.6	3.6	93.23	-6.54	B	0.529	VR	T
8.5	4.5	3.0	57.63	-5.85	GD	0.697	SR	P
17.0	9.5	7.8	122.92	-6.94	D	0.722	SR	P
7.2	5.4	3.6	64.90	-6.02	B	0.693	SR	P

Axial dimensions (cm)			Clast/sieve size[1] (mm)	Clast/sieve size[2] (ϕ)	Lithology[3]	Maximum Projection Sphericity[4]	Visual Roundness Class[5]	Clast a-axis Orientation[6]
a	b	c						
17.6	9.8	5.4	111.89	-6.81	GD	0.553	SR	T
15.6	13.5	6.5	149.83	-7.23	B	0.585	SR	T
9.0	6.6	2.8	70.94	-6.15	B	0.485	R	P
5.4	4.6	2.4	51.88	-5.70	B	0.614	R	T
10.8	7.4	4.6	87.13	-6.45	GD	0.642	SR	T
11.2	10.4	6.0	120.07	-6.91	GD	0.676	R	P
7.8	5.0	3.0	58.31	-5.87	GD	0.613	SR	T
15.2	13.5	5.8	146.93	-7.20	D	0.547	R	T
13.6	7.5	4.0	85.00	-6.41	B	0.539	R	T
9.5	7.5	4.2	85.98	-6.43	D	0.628	SR	P
7.5	6.0	2.8	66.21	-6.05	B	0.559	SR	T
11.2	7.0	5.6	89.64	-6.49	D	0.737	R	P
13.5	10.8	5.5	121.20	-6.92	B	0.592	SR	T
7.0	6.5	3.6	74.30	-6.22	B	0.658	R	T
6.5	4.0	2.4	46.65	-5.54	B	0.605	SR	P
9.8	6.5	3.0	71.59	-6.16	B	0.521	SR	P
10.6	6.6	3.0	72.50	-6.18	D	0.505	R	T
13.2	9.6	4.5	108.02	-6.73	B	0.543	SA	T
9.4	8.0	6.0	100.00	-6.64	B	0.782	VR	P
11.5	8.5	7.0	110.11	-6.78	D	0.794	VR	P
9.6	5.5	3.5	65.19	-6.03	B	0.614	R	P
15.5	7.5	5.6	93.60	-6.55	B	0.646	VR	O
6.4	5.6	3.5	66.04	-6.05	GD	0.699	SR	T
7.6	5.4	3.2	62.77	-5.97	B	0.630	SR	P
7.0	4.8	2.0	52.00	-5.70	B	0.492	R	P
9.4	5.5	4.8	73.00	-6.19	B	0.764	SR	T
31.5	20.0	10.0	223.61	-7.80	B	0.541	R	P
12.2	9.4	5.8	110.45	-6.79	GD	0.664	R	T
12.0	8.5	5.2	99.64	-6.64	B	0.642	SR	T
8.4	6.2	4.5	76.61	-6.26	B	0.730	SR	P
9.6	7.5	5.0	90.14	-6.49	B	0.703	SR	T
17.5	12.5	6.0	138.65	-7.12	B	0.548	R	T
10.5	7.5	2.8	80.06	-6.32	B	0.463	R	P
8.8	5.5	4.2	69.20	-6.11	GD	0.778	SR	P
17.0	12.5	9.6	157.61	-7.30	B	0.757	R	T
10.6	6.2	4.8	78.41	-6.29	B	0.705	VR	P
10.2	6.3	5.0	80.43	-6.33	GD	0.730	SR	P
7.5	5.0	2.5	55.90	-5.80	B	0.550	VR	P
8.0	5.8	2.3	62.39	-5.96	GT	0.485	SR	T
19.5	14.5	9.5	173.35	-7.44	B	0.683	SR	P
11.0	8.5	4.0	93.94	-6.55	D	0.555	R	P
6.8	4.4	1.0	45.12	-5.50	B	0.322	SR	P
7.6	5.9	3.0	66.19	-6.05	B	0.586	SR	P
7.2	5.3	2.9	60.42	-5.92	B	0.604	SA	P
9.8	7.5	4.2	85.96	-6.43	B	0.621	R	P
8.8	4.9	2.4	54.56	-5.77	B	0.511	R	P
8.3	7.8	2.4	81.61	-6.35	B	0.446	SR	P
4.9	4.2	2.0	46.52	-5.54	B	0.579	SA	T
5.6	3.5	2.8	44.82	-5.49	B	0.737	SR	P
10.5	4.8	3.3	58.25	-5.86	B	0.600	VR	T
8.1	4.5	2.4	51.00	-5.67	B	0.541	VR	P
11.1	9.8	6.5	117.60	-6.88	GD	0.730	VR	P
10.5	7.5	6.4	98.60	-6.62	B	0.804	VR	P
9.3	6.8	2.7	73.16	-6.19	B	0.487	VR	P
6.7	5.0	3.0	58.31	-5.87	GD	0.645	SR	P
14.5	10.2	7.0	123.71	-6.95	B	0.692	SR	P

Axial dimensions (cm)			Clast/sieve size[1] (mm)	Clast/sieve size[2] (ϕ)	Lithology[3]	Maximum Projection Sphericity[4]	Visual Roundness Class[5]	Clast a-axis Orientation[6]
a	b	c						
6.6	4.8	3.0	56.60	-5.82	GD	0.657	SR	T
3.3	2.0	1.2	23.32	-4.54	B	0.602	SA	P
4.3	3.5	1.3	37.34	-5.22	GT	0.482	R	P
3.8	2.8	2.0	34.41	-5.10	D	0.722	VR	P
4.8	3.8	2.0	42.04	-5.42	B	0.603	SR	P
12.5	4.2	2.5	48.88	-5.61	B	0.492	SR	P
4.2	3.2	2.0	37.74	-5.24	B	0.668	A	T
4.1	2.0	1.7	26.25	-4.71	B	0.706	SA	P
3.7	2.8	1.9	33.84	-5.08	B	0.704	SR	T
4.3	3.1	1.4	34.01	-5.09	D	0.528	SR	T
6.9	5.5	2.8	61.72	-5.95	B	0.591	VR	P
7.2	5.7	3.0	64.41	-6.01	B	0.603	SR	P
3.6	1.8	1.0	20.59	-4.36	B	0.538	SR	P
3.1	2.4	1.6	28.84	-4.85	B	0.701	SR	P
5.2	3.6	2.4	43.27	-5.44	GD	0.675	VR	T
7.2	7.0	6.0	92.20	-6.53	D	0.694	R	T
4.8	2.5	2.2	33.30	-5.06	B	0.739	SR	P
4.3	3.2	2.2	38.63	-5.28	B	0.705	R	P
6.3	4.5	3.2	55.22	-5.79	D	0.650	VR	T
4.9	2.3	1.2	25.94	-4.70	B	0.504	SA	P
6.2	4.1	2.5	48.02	-5.59	B	0.626	SR	T
3.0	2.0	1.5	25.00	-4.64	GT	0.721	SA	T
3.6	2.7	1.6	31.38	-4.97	B	0.641	R	P
6.1	4.6	2.0	50.16	-5.65	B	0.522	SA	T
5.6	4.5	2.4	51.00	-5.67	B	0.611	SR	T
4.6	2.4	1.5	28.30	-4.82	GD	0.588	SA	P
6.3	6.3	2.5	67.78	-6.08	B	0.493	R	T
9.7	7.2	4.8	88.53	-6.44	GD	0.691	SA	T
3.6	2.1	0.8	22.47	-4.49	B	0.431	VR	T
3.8	2.8	1.7	32.76	-5.03	GD	0.648	R	P
8.1	5.9	2.0	62.30	-5.96	B	0.437	SR	P
3.5	2.6	2.0	32.80	-5.04	B	0.760	SR	T
4.9	4.0	1.8	43.86	-5.45	B	0.549	R	T
4.4	4.2	2.2	47.41	-5.57	B	0.640	SR	P
2.8	2.6	1.7	31.08	-4.96	B	0.735	VR	P
6.7	4.0	1.5	42.72	-5.42	D	0.439	SR	P
2.7	1.5	1.1	18.60	-4.22	GT	0.669	SA	P
4.6	2.9	2.3	37.01	-5.21	B	0.735	SR	T
6.9	4.2	2.4	48.37	-5.60	B	0.584	SR	P
Q6 (244.51 km)								
14.0	11.2	5.5	124.78	-6.96	GD	0.578	VR	P
15.3	11.5	8.8	144.81	-7.18	B	0.761	R	P
14.2	10.0	7.3	123.81	-6.95	GT	0.721	R	T
7.2	5.1	4.7	69.35	-6.12	B	0.844	R	O
10.7	9.8	5.7	113.37	-6.82	D	0.677	SR	T
17.0	13.5	7.5	154.43	-7.27	D	0.626	R	P
19.0	12.0	10.0	156.20	-7.29	B	0.760	VR	P
20.5	14.5	9.8	175.01	-7.45	GD	0.686	VR	P
18.0	12.8	7.3	147.35	-7.20	GD	0.614	SR	T
17.7	14.5	11.0	182.00	-7.51	GD	0.778	R	P
9.0	8.8	5.2	102.22	-6.68	B	0.699	R	P
12.0	11.8	5.5	130.19	-7.02	B	0.598	SR	T
19.0	17.0	8.5	190.07	-7.57	GD	0.607	SR	O
17.6	10.2	7.5	126.61	-6.98	D	0.579	R	P
26.0	20.0	11.0	228.25	-7.83	B	0.615	SR	P

Axial dimensions (cm)			Clast/sieve size[1] (mm)	Clast/sieve size[2] (ϕ)	Lithology[3]	Maximum Projection Sphericity[4]	Visual Roundness Class[5]	Clast a-axis Orientation[6]
a	b	c						
11.0	10.2	7.0	123.71	-6.95	D	0.759	VR	T
18.0	13.5	7.0	152.07	-7.25	GD	0.586	SA	P
9.8	5.5	5.0	74.33	-6.22	D	0.774	VR	T
9.0	8.5	4.5	98.18	-6.59	B	0.642	VR	P
8.0	6.0	5.2	79.40	-6.31	B	0.826	R	P
16.0	9.3	6.5	113.46	-6.83	B	0.657	SR	P
15.0	13.0	13.0	183.85	-7.52	B	0.953	SR	P
10.2	7.8	5.5	96.44	-6.58	B	0.724	SR	P
22.0	15.5	11.0	190.07	-7.57	GT	0.708	VR	P
11.8	10.2	9.2	137.38	-7.10	D	0.894	VR	P
18.0	15.5	6.8	169.26	-7.40	B	0.571	SA	T
11.5	7.8	4.5	90.05	-6.49	B	0.609	SR	T
12.0	11.8	4.5	126.29	-6.98	D	0.523	R	T
10.4	7.2	4.0	82.37	-6.36	B	0.588	R	P
16.5	12.0	8.5	147.05	-7.20	D	0.715	R	T
12.8	11.0	5.8	124.35	-6.96	B	0.621	R	T
15.8	9.5	7.4	120.42	-6.91	D	0.715	VR	P
14.4	9.6	6.0	113.21	-6.82	D	0.639	R	T
12.5	9.6	5.5	110.64	-6.79	D	0.632	R	T
12.8	6.8	3.6	76.94	-6.27	GD	0.530	SR	P
14.6	13.5	8.4	159.00	-7.31	B	0.710	SR	T
18.4	9.5	5.6	110.28	-6.78	GD	0.564	R	P
13.0	11.2	6.5	129.50	-7.02	D	0.662	R	P
6.8	4.5	3.2	55.22	-5.79	B	0.694	SR	P
8.8	5.5	4.2	69.20	-6.11	B	0.720	SR	T
13.8	10.5	6.5	123.49	-6.95	B	0.666	R	T
9.5	5.8	3.6	68.26	-6.09	B	0.617	SR	P
11.5	9.5	4.0	103.08	-6.69	B	0.527	SA	T
22.5	15.0	9.0	174.93	-7.45	D	0.621	R	P
13.5	8.8	6.5	109.40	-6.77	B	0.708	SR	T
7.4	5.8	3.5	67.74	-6.08	GD	0.658	SR	P
7.0	5.0	3.5	61.03	-5.93	GD	0.705	R	P
19.5	14.0	12.0	184.39	-7.53	B	0.808	SR	P
21.0	16.0	10.5	191.38	-7.58	B	0.690	R	P
13.4	11.0	7.8	134.85	-7.08	B	0.745	SR	T
21.0	11.5	7.8	138.96	-7.12	GD	0.632	R	P
8.6	6.0	3.5	69.46	-6.12	D	0.619	VR	P
11.4	7.0	5.5	89.02	-6.48	B	0.724	SR	T
25.5	19.0	16.5	251.64	-7.98	GD	0.825	SR	T
14.0	11.6	5.5	128.38	-7.00	B	0.571	SR	T
13.6	12.2	7.5	143.21	-7.16	B	0.697	SA	T
13.0	8.5	7.5	113.36	-6.82	D	0.798	VR	P
16.5	13.0	9.0	158.11	-7.30	B	0.725	SR	T
13.0	10.0	5.8	115.60	-6.85	B	0.637	R	T
33.0	27.0	14.5	308.47	-8.26	D	0.618	VR	T
Q8 (231.57 km)								
23.5	16.5	4.5	171.03	-7.42	B	0.374	VR	T
31.5	25.0	9.5	267.44	-8.06	B	0.488	SR	T
21.0	20.8	7.0	219.46	-7.78	GD	0.482	R	P
14.2	13.8	5.0	146.78	-7.20	B	0.503	VR	T
7.9	5.5	3.5	65.19	-6.03	B	0.656	VR	P
17.0	13.7	6.0	149.56	-7.22	B	0.537	VR	T
11.2	7.0	6.5	95.52	-6.58	GT	0.814	SR	P
28.7	19.5	11.5	226.38	-7.82	GD	0.618	SR	O
31.0	24.0	14.0	277.85	-8.12	B	0.641	R	T

Axial dimensions (cm)			Clast/sieve size[1] (mm)	Clast/sieve size[2] (ϕ)	Lithology[3]	Maximum Projection Sphericity[4]	Visual Roundness Class[5]	Clast a-axis Orientation[6]
a	b	c						
20.5	14.7	8.0	167.38	-7.39	D	0.597	VR	P
34.0	16.5	11.0	198.31	-7.63	D	0.600	SR	T
10.5	9.0	5.5	105.48	-6.72	B	0.684	R	T
29.0	18.5	9.0	206.73	-7.68	B	0.532	SR	T
20.0	17.5	9.5	199.12	-7.64	D	0.636	VR	T
12.0	8.5	6.0	104.04	-6.70	B	0.707	VR	T
12.3	9.0	3.5	96.57	-6.59	B	0.480	VR	P
8.8	7.0	4.8	84.88	-6.41	GT	0.721	VR	T
11.7	9.7	5.0	109.13	-6.77	GD	0.604	SA	T
13.5	11.3	5.2	124.39	-6.96	D	0.562	VR	P
7.6	5.0	3.8	62.80	-5.97	B	0.724	R	T
13.0	9.2	6.3	111.50	-6.80	B	0.692	SA	P
7.7	4.7	3.5	58.60	-5.87	b	0.697	R	P
26.0	20.0	12.5	235.85	-7.88	B	0.670	SR	T
35.0	25.0	10.0	269.26	-8.07	GD	0.485	SR	T
17.3	11.0	6.0	125.30	-6.97	B	0.574	R	T
28.0	27.0	13.0	299.67	-8.23	GD	0.607	SR	T
19.5	13.0	11.5	173.57	-7.44	B	0.805	R	O
11.7	7.0	4.0	80.62	-6.33	GT	0.580	R	P
10.2	8.0	3.5	87.32	-6.45	B	0.531	VR	P
10.0	8.4	5.2	98.79	-6.63	B	0.685	VR	T
22.0	14.5	11.5	185.07	-7.53	B	0.746	SR	P
23.5	21.0	8.5	226.55	-7.82	B	0.527	VR	T
16.2	15.5	4.8	162.26	-7.34	B	0.451	R	T
21.2	15.5	4.2	160.59	-7.33	GT	0.377	SR	T
10.5	6.8	5.6	88.09	-6.46	GD	0.760	R	P
18.6	13.5	11.6	177.99	-7.48	B	0.812	SR	T
27.5	21.0	12.5	244.39	-7.93	GD	0.647	SR	T
29.0	25.0	17.0	302.32	-8.24	GD	0.736	SR	T
21.5	14.5	8.0	165.60	-7.37	B	0.590	SR	T
26.0	21.5	13.0	251.25	-7.97	B	0.671	SR	P
21.0	13.4	9.2	162.54	-7.34	B	0.670	VR	P
28.0	18.0	16.5	244.18	-7.93	GD	0.814	R	P
30.0	19.5	17.5	262.01	-8.03	GD	0.806	R	P
23.0	15.5	13.5	205.55	-7.68	B	0.800	SR	P
13.5	10.8	7.0	128.70	-7.01	D	0.695	VR	P
14.5	11.0	5.5	122.98	-6.94	B	0.575	SR	P
11.4	7.5	5.6	93.60	-6.55	GD	0.716	SR	P
9.8	6.8	4.8	83.23	-6.38	GD	0.702	SR	T
8.8	7.2	5.0	87.66	-6.45	D	0.733	SR	P
11.0	10.0	5.8	115.60	-6.85	GT	0.674	VR	T
17.5	14.2	8.5	165.50	-7.37	GD	0.662	SR	T
16.8	13.5	9.5	165.08	-7.37	B	0.736	SR	T
17.5	13.0	8.5	155.32	-7.28	B	0.682	R	P
17.5	10.5	5.8	119.95	-6.91	B	0.568	R	T
11.0	7.5	5.5	93.01	-6.54	GD	0.716	R	P
18.0	12.5	6.5	140.89	-7.14	GT	0.573	R	P
22.0	15.0	8.0	170.00	-7.41	B	0.579	SR	T
18.0	16.5	11.0	198.31	-7.63	GD	0.741	SR	P
14.0	8.2	5.0	96.04	-6.59	GD	0.602	R	P
51.0	33.0	29.5	442.63	-8.79	B	0.803	SR	T
16.5	10.5	6.5	123.49	-6.95	GD	0.625	SR	P
14.0	11.5	5.4	127.05	-6.99	GD	0.566	SR	P
7.0	5.0	4.5	67.27	-6.07	GD	0.833	VR	T
9.8	8.0	4.0	89.44	-6.48	GD	0.589	VR	P
11.8	6.8	6.0	90.69	-6.50	B	0.766	SA	T

Axial dimensions (cm)			Clast/sieve size[1] (mm)	Clast/sieve size[2] (ϕ)	Lithology[3]	Maximum Projection Sphericity[4]	Visual Roundness Class[5]	Clast a-axis Orientation[6]
a	b	c						
8.0	3.6	3.4	49.52	-5.63	D	0.738	VR	P
7.5	7.2	3.6	80.50	-6.33	B	0.621	SR	T
6.7	5.0	3.4	60.46	-5.92	B	0.701	SA	T
8.7	7.0	4.3	82.15	-6.36	D	0.672	R	O
13.0	12.0	7.8	143.12	-7.16	B	0.731	SA	P
5.0	3.8	1.4	40.50	-5.34	B	0.469	R	P
13.2	12.0	7.5	141.51	-7.14	D	0.708	SR	T
9.0	6.5	4.0	76.32	-6.25	GD	0.649	R	T
8.3	4.3	2.8	51.31	-5.68	B	0.603	R	T
6.2	5.2	3.4	62.13	-5.96	GT	0.710	R	T
15.2	11.3	8.8	143.22	-7.16	D	0.787	R	T
12.7	11.5	7.0	134.63	-7.07	GD	0.695	VR	T
10.3	9.4	3.5	100.30	-6.65	D	0.502	VR	T
18.0	13.0	5.0	152.64	-7.25	GD	0.649	SR	P
9.0	6.2	5.5	82.88	-6.37	B	0.815	SR	T
13.5	10.5	8.8	137.00	-7.10	D	0.817	VR	P
15.5	12.0	6.8	137.93	-7.11	GD	0.629	SA	P
14.5	11.5	9.0	146.03	-7.19	GD	0.786	SR	T
13.5	9.2	4.5	102.42	-6.68	GD	0.546	SR	T
9.4	7.5	5.3	91.84	-6.52	B	0.736	R	T
9.5	6.8	3.5	76.48	-6.26	B	0.575	SR	P
9.2	7.5	6.0	96.05	-6.59	B	0.805	R	P
13.2	9.5	8.2	125.50	-6.97	GD	0.812	SR	T
12.7	8.8	5.2	102.22	-6.68	D	0.623	R	P
20.9	8.2	4.8	95.02	-6.57	D	0.512	VR	P
9.2	5.8	5.4	79.25	-6.31	D	0.818	SR	P
13.6	9.4	7.6	120.88	-6.92	GD	0.767	VR	T
12.2	9.4	5.6	109.42	-6.77	GD	0.649	SR	T
5.2	3.0	2.5	39.05	-5.29	D	0.737	SR	P
11.2	9.5	6.5	115.11	-6.85	GD	0.735	VR	T
9.5	6.2	5.4	82.22	-6.36	B	0.791	VR	T
9.8	7.5	4.4	86.95	-6.44	GD	0.645	SR	P
7.0	4.8	2.6	54.59	-5.77	B	0.588	SR	T
8.5	6.0	4.5	75.00	-6.23	GD	0.735	R	P
14.0	11.5	4.5	123.49	-6.95	D	0.501	SR	P
12.5	7.6	6.0	96.83	-6.60	B	0.724	R	T
15.5	9.5	7.8	122.92	-6.94	GD	0.745	R	T
10.4	8.5	4.4	95.71	-6.58	B	0.603	SR	P
10.4	6.2	4.2	74.89	-6.23	B	0.649	SR	T
10.2	8.4	5.5	100.40	-6.65	D	0.707	R	P
11.4	10.0	7.8	126.82	-6.99	B	0.811	SA	T
10.6	7.5	4.0	85.00	-6.41	B	0.586	SR	T
11.0	7.0	5.5	89.02	-6.48	GD	0.732	R	P
14.0	10.2	7.5	126.61	-6.98	D	0.733	SR	P
13.2	10.0	4.2	108.46	-6.76	B	0.511	SR	P
11.0	9.8	7.5	123.41	-6.95	GD	0.805	SR	T
15.5	9.5	9.0	130.86	-7.03	GD	0.819	SA	T
8.2	7.0	4.4	82.68	-6.37	B	0.698	R	T
9.4	8.0	6.5	103.08	-6.69	B	0.826	VR	T
15.5	12.0	7.5	141.51	-7.14	GD	0.671	SR	T
13.2	7.4	3.5	81.86	-6.36	B	0.501	R	P
11.5	7.4	5.1	89.87	-6.49	GD	0.674	VR	P
17.6	9.5	7.0	118.00	-6.88	D	0.664	SR	P
13.8	10.5	7.8	130.80	-7.03	D	0.749	SR	T
9.0	8.5	4.4	95.71	-6.58	GD	0.633	VR	T

Axial dimensions (cm)			Clast/sieve size[1] (mm)	Clast/sieve size[2] (ϕ)	Lithology[3]	Maximum Projection Sphericity[4]	Visual Roundness Class[5]	Clast a-axis Orientation[6]
a	b	c						
QA (209.56 km)								
38.0	26.0	10.0	269.26	-8.07	D	0.472	SR	T
17.0	14.0	10.0	172.05	-7.43	D	0.749	VR	P
40.0	26.0	10.0	269.26	-8.07	B	0.464	SR	T
20.0	20.0	12.0	233.24	-7.87	B	0.711	VR	N
21.0	17.5	6.5	166.68	-7.54	D	0.486	SA	T
26.0	14.0	11.0	178.04	-7.48	GD	0.693	VR	T
11.0	6.6	2.5	70.58	-6.14	B	0.442	SA	P
13.3	13.3	5.3	143.17	-7.16	B	0.542	VR	N
17.0	14.0	8.0	161.25	-7.33	D	0.645	R	T
11.0	9.0	5.5	105.48	-6.72	B	0.674	VR	P
14.5	11.0	5.5	122.98	-6.94	D	0.575	R	T
15.0	12.0	5.0	130.00	-7.02	AG	0.516	SR	T
8.2	7.3	5.4	90.80	-6.50	GN	0.787	VR	T
13.2	11.0	7.0	130.38	-7.03	D	0.696	SR	T
12.3	8.5	4.5	96.18	-6.59	B	0.579	SR	T
13.0	7.5	5.0	90.14	-6.49	D	0.635	R	T
10.5	7.0	3.0	76.16	-6.25	B	0.497	SA	T
23.0	9.5	4.0	103.08	-6.69	B	0.418	A	P
18.5	12.5	5.0	134.63	-7.07	GT	0.476	SR	P
15.0	10.0	7.0	122.07	-6.93	B	0.689	SR	P
38.0	21.0	19.0	283.20	-8.15	B	0.782	SR	T
13.0	11.0	7.0	130.38	-7.03	B	0.700	VR	T
20.0	17.0	10.0	197.23	-7.62	B	0.665	VR	T
16.5	13.0	10.0	164.01	-7.36	D	0.775	R	T
18.0	15.0	8.0	170.00	-7.41	D	0.619	VR	T
18.5	14.0	6.0	152.32	-7.25	B	0.518	SR	P
17.5	16.5	8.5	185.61	-7.54	D	0.630	SR	T
23.0	12.0	7.0	138.92	-7.12	AG	0.582	SR	T
20.0	13.5	4.5	142.30	-7.15	B	0.422	SA	T
20.0	12.5	3.8	130.65	-7.03	B	0.387	SR	T
7.8	4.2	3.8	56.64	-5.82	B	0.761	R	P
10.5	6.5	5.2	83.24	-6.38	AG	0.734	SR	T
10.6	8.2	4.5	93.54	-6.55	B	0.615	R	T
7.0	6.5	3.8	75.29	-6.23	D	0.682	SR	T
6.6	5.2	3.5	62.68	-5.97	D	0.709	SR	T
16.5	11.0	5.5	122.98	-6.94	B	0.550	SR	P
12.8	10.0	4.8	110.92	-6.79	B	0.585	SR	P
21.5	19.0	9.0	210.24	-7.72	D	0.583	SA	T
15.0	12.0	9.5	153.05	-7.26	B	0.794	R	P
13.8	10.5	6.5	123.49	-6.95	D	0.663	SR	T
33.0	20.5	11.5	235.06	-7.88	D	0.580	VR	T
23.0	15.0	8.5	172.41	-7.43	D	0.594	R	T
20.0	15.0	11.0	186.01	-7.54	GD	0.739	R	T
17.5	12.0	7.0	138.92	-7.12	B	0.616	SR	P
21.0	9.0	7.5	117.15	-6.87	B	0.668	SR	P
10.5	9.0	4.8	102.00	-6.67	D	0.625	VR	P
10.2	7.5	3.4	82.35	-6.36	B	0.533	SA	T
9.4	6.5	5.5	85.15	-6.41	B	0.821	SR	T
13.0	7.0	5.8	90.91	-6.51	D	0.718	VR	T
22.0	21.0	9.0	228.47	-7.84	GT	0.560	SR	N
16.5	13.5	5.0	143.96	-7.17	AG	0.482	R	T
26.0	17.0	8.5	190.07	-7.57	D	0.547	R	T
14.0	7.5	6.5	99.25	-6.63	GT	0.738	VR	P
15.5	8.5	4.0	93.94	-6.55	D	0.496	SR	P
16.0	9.5	7.5	121.04	-6.92	B	0.718	SR	P

Axial dimensions (cm)			Clast/sieve size[1] (mm)	Clast/sieve size[2] (ϕ)	Lithology[3]	Maximum Projection Sphericity[4]	Visual Roundness Class[5]	Clast a-axis Orientation[6]
a	b	c						
14.8	11.0	6.5	118.85	-6.89	B	0.499	SR	T
12.5	9.0	6.5	111.02	-6.79	D	0.721	R	T
7.0	5.0	3.8	82.80	-5.97	B	0.744	SR	P
18.5	14.0	7.0	156.52	-7.29	AG	0.574	SR	T
14.2	8.8	7.5	115.62	-6.85	B	0.786	SA	P
Q11 (193.31 km)								
14.0	11.0	5.5	122.98	-6.94	B	0.581	SR	P
11.5	8.5	4.5	96.18	-6.59	B	0.592	SR	P
9.5	7.5	4.5	87.46	-6.45	GD	0.657	SR	P
13.0	9.0	7.8	119.10	-6.90	B	0.804	SR	T
6.5	3.0	2.4	38.42	-5.26	GD	0.666	R	P
11.0	8.0	4.5	91.79	-6.52	B	0.613	SR	T
12.0	11.0	6.0	125.30	-6.97	GD	0.649	VR	T
7.5	5.8	4.5	73.41	-6.20	D	0.775	VR	T
7.2	4.5	3.5	57.01	-5.83	B	0.723	SR	P
12.0	10.0	3.5	105.95	-6.73	D	0.467	VR	T
12.0	9.0	7.5	117.15	-6.87	D	0.805	R	P
8.5	5.5	4.0	68.01	-6.09	B	0.699	SR	P
9.0	6.0	3.5	69.46	-6.12	B	0.610	SA	T
8.0	6.5	4.5	79.06	-6.30	D	0.730	VR	P
10.5	7.8	5.5	95.44	-6.58	B	0.717	SR	T
12.0	9.0	5.0	102.98	-6.69	D	0.614	R	P
18.5	11.5	10.0	152.40	-7.25	B	0.778	R	P
11.5	6.5	5.6	85.80	-6.42	B	0.749	R	P
10.5	7.8	4.5	90.05	-6.49	D	0.628	VR	T
6.0	4.8	3.4	58.82	-5.88	B	0.738	SA	P
6.5	4.5	2.6	51.97	-5.70	D	0.614	SR	P
12.0	8.5	6.0	104.04	-6.70	GT	0.707	SR	T
6.8	4.5	3.5	57.01	-5.83	B	0.737	SR	P
11.0	8.0	4.5	91.79	-6.52	D	0.613	A	P
15.0	10.5	6.5	123.49	-6.95	AG	0.645	R	P
9.0	7.8	5.5	95.44	-6.58	D	0.755	SR	T
9.2	5.6	4.5	71.84	-6.17	B	0.733	SR	P
5.6	3.0	2.4	38.42	-5.26	D	0.700	R	P
10.0	7.0	3.5	78.26	-6.29	B	0.559	SR	T
8.0	6.0	3.8	71.02	-6.15	B	0.670	SR	T
31.0	14.0	10.0	172.05	-7.43	B	0.613	SA	P
10.2	9.7	4.5	106.93	-6.74	D	0.589	SR	P
9.3	6.5	5.0	82.01	-6.36	B	0.745	R	P
11.0	8.5	6.3	105.80	-6.73	B	0.752	R	P
20.0	10.0	10.0	141.42	-7.14	D	0.794	R	T
11.7	9.2	4.0	100.32	-6.65	B	0.530	SR	P
7.7	6.5	2.0	68.01	-6.09	B	0.431	SR	P
9.0	5.2	3.5	62.68	-5.97	AG	0.640	SR	P
4.6	2.6	1.5	30.02	-4.91	B	0.573	R	P
6.3	5.4	4.0	67.20	-6.07	B	0.778	R	P
13.0	12.0	9.5	153.05	-7.26	GD	0.833	VR	T
5.0	3.3	2.5	41.40	-5.37	B	0.724	SR	T
13.0	10.3	5.0	114.49	-6.84	GD	0.572	R	T
12.5	9.0	5.4	104.98	-6.71	B	0.638	R	P
15.5	10.0	8.5	131.24	-7.04	GD	0.775	VR	T
6.5	5.4	3.0	61.77	-5.95	AG	0.635	SR	T
11.2	10.0	7.0	122.07	-6.93	GD	0.759	R	P
18.0	15.0	6.0	161.55	-7.34	AG	0.511	SR	T
11.5	9.0	4.3	99.74	-6.64	AG	0.563	SR	P

Axial dimensions (cm)			Clast/sieve size[1] (mm)	Clast/sieve size[1] (ϕ)	Lithology[2]	Maximum Projection Sphericity[3]	Visual Roundness Class[4]	Clast a-axis Orientation[5]
a	b	c						
7.3	5.0	2.7	56.62	-5.83	AG	0.585	SA	P
15.8	15.5	9.0	179.23	-7.49	AG	0.692	R	T
11.0	6.5	4.0	76.32	-6.25	B	0.607	SR	T
11.2	6.7	5.8	88.62	-6.47	B	0.765	R	P
17.0	12.0	6.5	136.47	-7.09	GD	0.592	SR	T
8.3	6.7	3.5	75.59	-6.24	B	0.604	VR	P
9.9	6.0	3.2	68.00	-6.09	AG	0.557	SA	T
11.8	5.3	4.2	67.62	-6.08	B	0.656	R	P
5.2	3.9	2.2	44.76	-5.48	AG	0.620	SA	T
7.0	4.6	3.5	57.60	-5.85	B	0.726	VR	T
7.5	5.5	2.5	60.42	-5.92	GD	0.533	SR	T
18.0	7.5	7.0	102.59	-6.68	B	0.713	SA	T
14.0	12.0	6.0	134.16	-7.07	GT	0.598	VR	T
8.0	6.3	5.4	82.98	-6.37	B	0.833	SR	P
16.0	10.5	6.5	123.49	-6.95	D	0.631	R	T
12.0	8.0	8.0	113.14	-6.82	D	0.874	R	T
15.2	12.0	10.5	159.45	-7.32	GD	0.846	VR	P
11.0	10.2	7.3	125.43	-6.97	B	0.780	SA	T
10.8	7.2	7.0	100.42	-6.65	B	0.857	R	T
10.6	7.7	4.3	88.19	-6.46	D	0.610	R	T
6.0	3.9	3.4	51.74	-5.69	D	0.791	SR	P
7.0	4.4	4.0	59.46	-5.89	B	0.804	R	P
10.0	9.5	6.4	114.55	-6.84	GD	0.755	R	P
6.7	6.5	3.0	71.59	-6.16	B	0.591	VR	T
7.3	6.0	4.0	72.11	-6.17	GD	0.715	R	P
9.1	7.0	3.6	78.71	-6.30	GD	0.588	R	P
8.7	6.3	4.5	77.42	-6.27	B	0.716	SR	T
15.8	11.0	7.0	130.38	-7.03	GD	0.656	SA	P
13.0	11.0	8.3	137.80	-7.11	GT	0.784	VR	P
11.8	9.5	7.0	118.00	-6.88	GT	0.759	SR	P
9.5	7.8	2.5	81.91	-6.36	B	0.439	VR	T
9.1	7.0	5.2	87.20	-6.45	B	0.752	SA	T
5.5	4.7	2.8	54.71	-5.77	B	0.672	SA	P
5.8	4.0	2.5	47.17	-5.56	B	0.646	SA	P
8.2	7.0	6.0	92.20	-6.53	GD	0.856	SR	P
13.4	7.8	5.7	98.61	-6.59	D	0.677	SA	P
15.0	9.0	7.5	117.15	-6.87	GD	0.747	SR	T
9.0	7.8	3.5	85.49	-6.42	D	0.559	SR	P
6.8	6.6	2.7	71.31	-6.16	B	0.546	R	P
12.5	8.0	7.3	108.30	-6.76	GT	0.811	SR	T
14.4	12.0	6.5	136.47	-7.09	GD	0.625	VR	P
12.0	8.5	7.2	111.40	-6.80	D	0.798	VR	T
8.5	7.5	5.0	90.14	-6.49	GD	0.732	VR	T
12.5	8.5	6.0	104.04	-6.70	GD	0.697	R	P
13.0	10.5	7.4	128.46	-7.01	D	0.738	SR	P
7.5	5.0	4.4	66.60	-6.06	B	0.802	R	P
8.4	7.5	4.8	89.04	-6.48	GD	0.715	SR	T
21.0	12.5	10.0	160.08	-7.32	D	0.725	VR	T
10.5	8.5	4.5	98.18	-6.59	D	0.610	R	P
11.5	8.5	7.0	110.11	-6.78	D	0.794	VR	P
6.5	5.5	3.5	65.19	-6.03	B	0.700	R	T
12.8	6.8	5.5	87.46	-6.45	D	0.703	R	T
10.8	8.0	4.5	91.79	-6.52	B	0.617	R	T
10.5	9.0	5.5	105.48	-6.72	B	0.684	SR	T
12.8	9.5	6.0	112.36	-6.81	D	0.666	SA	T
9.2	7.0	4.0	80.62	-6.33	GD	0.629	R	P

Axial dimensions (cm)			Clast/sieve size[1] (mm)	Clast/sieve size[2] (ϕ)	Lithology[3]	Maximum Projection Sphericity[4]	Visual Roundness Class[5]	Clast a-axis Orientation[6]
a	b	c						
11.5	8.0	4.8	93.30	-6.54	GD	0.630	SR	P
14.0	10.0	7.0	122.07	-6.93	B	0.705	R	T
7.5	6.8	4.0	78.89	-6.30	D	0.679	SR	T
12.5	10.0	7.8	126.82	-6.99	GD	0.787	VR	P
15.0	9.5	7.0	118.00	-6.88	D	0.701	SR	T
8.0	7.5	4.0	85.00	-6.41	B	0.644	SR	T
16.5	11.5	9.0	146.03	-7.19	D	0.753	VR	P
11.8	8.0	6.0	100.00	-6.64	B	0.725	R	P
8.0	6.5	4.0	76.32	-6.25	B	0.675	SR	T
15.0	12.0	5.8	133.28	-7.06	B	0.572	R	P
13.0	8.0	5.5	97.08	-6.60	D	0.663	SR	T
9.5	7.5	6.0	96.06	-6.59	GD	0.796	VR	T
9.5	7.5	4.8	89.04	-6.48	B	0.686	VR	P
12.0	7.5	5.8	94.81	-6.57	B	0.720	SR	P
8.5	6.5	4.0	76.32	-6.25	D	0.662	SR	P
Q12 (192.81 km)								
13.0	10.2	6.8	122.59	-6.94	GD	0.704	VR	P
21.5	13.5	7.0	152.07	-7.25	D	0.553	VR	P
10.9	8.0	5.5	97.08	-6.60	D	0.703	R	P
6.4	3.8	3.6	52.35	-5.71	D	0.811	SA	P
9.0	5.4	4.7	71.59	-6.16	B	0.769	SA	P
7.4	7.0	3.7	79.18	-6.31	AD	0.642	R	P
9.2	8.2	4.7	94.51	-6.56	D	0.664	VR	P
10.0	6.0	3.5	69.46	-6.12	GD	0.589	VR	T
10.8	9.5	8.0	124.20	-6.96	B	0.854	R	P
12.0	9.8	8.4	129.07	-7.01	GT	0.843	R	T
14.2	12.7	11.1	168.67	-7.40	GD	0.881	VR	T
9.8	5.0	4.0	64.03	-6.00	GT	0.689	SR	T
7.2	6.8	5.3	86.21	-6.43	D	0.831	SR	P
15.2	11.3	8.0	138.45	-7.11	GD	0.720	SR	T
9.2	7.8	6.5	101.53	-6.67	AG	0.838	SA	T
3.8	3.7	2.0	42.08	-5.39	B	0.658	SA	T
6.6	4.2	3.8	56.64	-5.82	D	0.805	SR	T
6.4	4.0	3.0	50.00	-5.64	AG	0.706	SR	P
5.8	4.9	3.5	60.22	-5.91	GT	0.755	SR	T
6.5	4.8	3.4	58.82	-5.88	B	0.718	SR	T
6.0	4.2	3.2	52.80	-5.72	GT	0.741	R	P
5.8	5.0	2.4	55.46	-5.79	B	0.583	VR	P
9.2	9.2	3.5	98.43	-6.62	AG	0.525	VR	N
6.0	5.4	5.1	74.28	-6.21	GT	0.929	R	T
6.0	4.5	3.0	54.08	-5.76	AD	0.693	R	P
18.0	15.5	9.5	181.80	-7.51	GD	0.686	SR	T
9.0	6.0	6.0	84.85	-6.41	GD	0.874	VR	P
14.7	9.0	8.3	109.86	-6.78	D	0.689	SR	T
7.5	6.2	3.8	72.72	-6.18	B	0.677	SA	T
7.3	4.5	2.3	50.54	-5.66	AG	0.544	SA	T
7.0	5.5	3.8	66.85	-6.06	GD	0.721	VR	P
9.2	5.2	5.0	72.14	-6.17	D	0.805	R	P
6.5	3.8	2.5	45.49	-5.51	B	0.633	SR	P
9.5	7.5	5.5	93.01	-6.54	B	0.752	VR	P
8.8	5.5	4.5	71.06	-6.15	GD	0.748	SR	P
10.2	6.5	4.8	80.80	-6.34	GD	0.703	R	P
5.5	4.5	3.5	57.01	-5.83	D	0.791	SR	T
5.5	4.5	3.8	58.90	-5.88	D	0.836	SR	P
6.2	5.2	3.5	62.68	-5.97	D	0.724	R	T

Axial dimensions (cm)			Clast/sieve size[1] (mm)	Clast/sieve size[2] (ϕ)	Lithology[3]	Maximum Projection Sphericity[4]	Visual Roundness Class[5]	Clast a-axis Orientation[6]
a	b	c						
5.5	4.2	2.8	50.48	-5.66	D	0.698	SR	P
8.5	6.0	4.5	75.00	-6.23	D	0.735	SR	P
7.0	5.5	5.0	74.33	-6.22	GD	0.866	SR	T
7.0	4.8	4.0	62.48	-5.97	GD	0.781	SR	P
8.4	6.0	5.0	78.10	-6.29	D	0.792	R	T
9.5	8.5	6.0	104.04	-6.70	B	0.764	SR	T
9.0	5.5	4.5	71.06	-6.15	B	0.742	SR	P
7.0	5.5	3.5	65.19	-6.03	D	0.683	SR	P
4.5	3.0	2.5	39.05	-5.29	GT	0.774	R	P
6.6	5.5	3.8	66.85	-6.06	GD	0.735	SR	T
4.0	2.8	1.8	33.29	-5.06	B	0.661	SR	P
4.5	3.0	2.2	37.20	-5.22	B	0.710	SR	P
7.2	5.2	4.4	68.12	-6.09	GD	0.803	SR	T
7.2	6.0	3.5	69.46	-6.12	D	0.657	R	T
17.0	14.5	7.5	163.25	-7.35	GD	0.611	VR	T
9.5	8.0	4.5	91.79	-6.52	GT	0.643	R	T
8.0	5.5	4.5	71.06	-6.15	GD	0.772	R	P
6.6	4.5	4.0	60.21	-5.91	GD	0.814	SR	P
9.8	7.0	3.5	78.26	-6.29	B	0.563	SR	T
12.5	8.0	5.0	94.34	-6.56	D	0.630	VR	T
14.0	12.0	7.5	141.51	-7.14	D	0.694	R	P
17.5	11.0	8.0	136.01	-7.09	B	0.693	R	P
10.0	5.5	3.5	65.19	-6.03	GD	0.606	R	T
21.3	11.3	10.0	150.89	-7.24	D	0.746	VR	P
7.8	5.4	4.3	69.03	-6.11	GT	0.760	R	P
5.8	5.2	4.0	65.60	-6.04	D	0.810	VR	T
8.2	5.0	3.5	61.03	-5.93	AD	0.669	VR	P
7.0	5.2	4.0	65.60	-6.04	GD	0.760	SR	P
12.3	6.0	3.2	68.00	-6.09	D	0.518	VR	P
5.5	3.1	2.8	41.77	-5.38	GD	0.772	SR	P
5.0	3.2	1.6	35.78	-5.16	AG	0.543	SA	P
3.5	3.3	2.1	39.12	-5.29	GT	0.725	SR	P
9.0	6.8	5.3	86.21	-6.43	GT	0.771	SR	P
5.8	4.3	3.5	55.44	-5.79	GD	0.789	R	P
7.0	3.0	2.8	41.04	-5.36	GD	0.720	SR	T
6.5	4.0	2.0	44.72	-5.48	D	0.536	VR	P
4.0	3.2	1.6	35.78	-5.16	D	0.585	SA	T
5.7	4.5	3.0	54.08	-5.76	AD	0.705	R	T
17.0	11.0	10.0	148.66	-7.22	GD	0.812	VR	P
8.8	7.2	5.5	90.60	-6.50	GD	0.782	VR	T
10.8	6.3	4.3	76.28	-6.25	AD	0.648	SR	P
7.0	6.0	4.0	72.11	-6.17	D	0.725	R	T
11.8	6.8	5.5	87.46	-6.45	B	0.722	SR	P
9.5	6.0	2.7	65.80	-6.04	B	0.504	VR	P
9.0	5.4	4.0	67.20	-6.07	B	0.690	SR	P
18.0	12.7	10.2	162.89	-7.35	AG	0.769	SR	P
9.8	5.5	4.5	71.06	-6.15	B	0.722	R	T
11.3	6.3	6.0	87.00	-6.44	B	0.797	R	P
7.2	3.2	2.4	40.00	-5.32	B	0.630	VR	P
8.3	2.8	2.1	35.00	-5.13	B	0.575	SR	T
3.7	3.3	2.2	39.66	-5.31	GT	0.735	SR	T
4.2	2.6	2.1	33.42	-5.06	GT	0.739	SR	P
7.2	5.4	4.0	67.20	-6.07	GD	0.744	R	P
4.2	3.5	2.8	44.82	-5.49	GT	0.811	SR	T
9.5	8.0	3.2	86.16	-6.43	D	0.513	VR	T
14.0	10.0	7.5	125.00	-6.97	GT	0.738	VR	T

Axial dimensions (cm)			Clast/sieve size[1] (mm)	Clast/sieve size[2] (ϕ)	Lithology[3]	Maximum Projection Sphericity[4]	Visual Roundness Class[5]	Clast a-axis Orientation[6]
a	b	c						
5.5	3.0	2.5	39.05	-5.29	AG	0.724	SR	P
3.0	2.5	1.8	20.68	-4.89	GT	0.699	SA	T
5.0	2.5	1.8	30.81	-4.95	AG	0.618	SR	P
6.8	5.0	3.0	58.31	-5.87	AG	0.649	SA	T
12.5	8.5	5.0	98.62	-6.62	D	0.617	VR	P
14.5	9.5	6.5	115.11	-6.85	D	0.674	R	P
8.2	6.4	4.5	78.24	-6.29	D	0.728	SR	T
4.5	3.0	2.5	39.05	-5.29	GD	0.774	SR	P
7.6	4.8	3.5	59.41	-5.89	B	0.696	R	P
9.5	7.0	4.6	83.76	-6.39	D	0.683	R	T
10.0	7.5	5.5	93.01	-6.54	D	0.739	SA	T
10.0	8.2	4.0	91.24	-6.51	D	0.580	R	P
7.5	6.4	4.5	78.24	-6.29	D	0.750	SR	T
9.5	6.5	5.5	85.15	-6.41	GD	0.788	R	P
8.4	5.0	4.0	64.03	-6.00	GD	0.725	VR	P
16.5	10.5	9.5	141.60	-7.15	B	0.805	SR	P
13.5	9.6	8.0	124.96	-6.97	D	0.790	SR	P
9.5	7.0	4.5	83.22	-6.38	GD	0.673	VR	T
8.0	4.5	3.5	57.01	-5.83	B	0.698	SR	P
12.0	9.5	4.6	105.55	-6.72	GT	0.570	VR	P
6.0	5.2	2.5	57.70	-5.85	GD	0.585	SR	T
4.8	3.6	2.5	43.83	-5.45	D	0.712	R	P
5.5	3.0	2.0	36.06	-5.17	AG	0.624	SR	P
6.5	4.0	2.8	48.83	-5.61	B	0.671	SR	P
8.5	7.0	4.5	83.22	-6.38	B	0.698	SR	P
22.0	19.5	14.0	240.05	-7.91	D	0.770	VR	T
20.5	17.0	14.0	220.23	-7.78	GD	0.825	VR	P
15.3	11.0	5.0	120.83	-6.92	B	0.530	VR	P
12.5	12.0	8.0	144.22	-7.17	GD	0.753	VR	P
20.0	18.0	15.0	234.31	-7.87	AG	0.855	R	T
8.2	5.7	4.0	69.63	-6.12	D	0.700	R	T
13.0	11.0	5.5	122.98	-6.94	B	0.598	R	P
9.5	8.0	6.2	101.21	-6.66	D	0.797	VR	P
6.6	5.0	3.5	61.03	-5.93	GT	0.719	R	T
6.8	5.5	3.0	62.65	-5.97	B	0.622	VR	T
10.0	9.7	6.0	114.06	-6.83	GT	0.719	R	P
13.0	8.5	8.0	116.73	-6.87	D	0.834	SR	P
13.5	5.3	2.3	57.78	-5.85	B	0.420	SA	P
9.0	5.8	3.8	69.34	-6.12	B	0.652	R	P
6.3	4.7	4.0	61.72	-5.95	D	0.815	SR	T
14.2	9.3	5.2	106.55	-6.74	D	0.589	VR	T
12.3	11.7	6.3	132.88	-7.05	B	0.651	SA	P
5.7	5.5	3.5	65.19	-6.03	B	0.731	SR	T
7.3	6.3	2.5	67.78	-6.08	AG	0.514	SR	P
22.0	16.5	12.0	204.02	-7.67	D	0.735	VR	T
14.5	10.0	4.0	107.70	-6.75	GT	0.480	SA	T
19.5	14.7	10.0	177.79	-7.47	B	0.704	SR	T
8.8	5.0	4.0	64.03	-6.00	GD	0.714	R	T
4.8	4.5	2.7	52.48	-5.71	GT	0.696	SR	T
16.0	11.0	9.0	142.13	-7.15	B	0.772	SR	P
10.2	8.5	7.3	112.04	-6.81	B	0.850	R	P
10.5	9.0	6.0	108.17	-6.76	GT	0.725	SR	T
9.4	7.3	5.0	88.48	-6.47	GD	0.714	VR	P
15.5	12.0	8.0	144.22	-7.17	B	0.701	SR	T
11.2	8.2	7.6	111.80	-6.80	GD	0.857	VR	T
10.5	8.0	3.8	88.57	-6.47	B	0.556	R	P

Axial dimensions (cm)			Clast/sieve size[1] (mm)	Clast/sieve size[2] (ϕ)	Lithology[3]	Maximum Projection Sphericity[4]	Visual Roundness Class[5]	Clast a-axis Orientation[6]
a	b	c						
7.0	5.8	4.5	73.41	-6.20	B	0.793	VR	P
8.5	6.5	3.4	73.36	-6.20	B	0.594	R	T
8.0	6.0	3.4	68.96	-6.11	B	0.622	SR	P
6.5	5.0	2.8	57.31	-5.84	GD	0.623	SR	P
6.8	4.5	2.6	51.07	-5.70	GT	0.606	SR	P
4.5	3.5	2.4	42.44	-5.41	D	0.715	SR	T
18.0	15.5	9.5	181.60	-7.51	D	0.686	VR	T
9.4	8.0	3.8	71.02	-6.15	B	0.635	R	P
9.8	8.5	4.8	97.62	-6.61	B	0.658	R	P
7.5	6.2	4.5	76.61	-6.26	GD	0.758	SR	P
11.0	9.5	6.8	116.83	-6.87	D	0.762	VR	T
13.6	10.0	6.0	116.62	-6.87	B	0.642	R	T
13.8	9.6	5.0	108.24	-6.76	GD	0.574	VR	P
9.5	6.8	4.8	83.23	-6.38	GD	0.709	VR	P
9.0	7.5	4.5	87.46	-6.45	GD	0.669	SR	P
13.0	7.5	4.5	87.46	-6.45	B	0.592	R	P
7.0	5.4	2.2	58.31	-5.87	D	0.504	SR	P
8.5	4.5	3.5	57.01	-5.83	B	0.684	SR	P
9.5	7.0	4.5	83.22	-6.38	GD	0.673	R	T
5.5	4.4	3.0	53.25	-5.73	GD	0.719	SR	P
9.0	6.5	3.8	75.29	-6.23	D	0.627	SR	P
12.2	8.0	5.5	97.08	-6.60	GD	0.677	SR	P
10.2	6.5	3.0	71.59	-6.16	AD	0.514	SR	T
8.0	6.5	5.2	83.24	-6.38	GD	0.804	SA	T
12.0	9.2	4.5	102.42	-6.68	B	0.568	SR	P
10.5	7.5	5.0	90.14	-6.49	B	0.682	R	T
10.5	7.5	4.0	85.00	-6.41	B	0.588	SR	T
16.0	11.0	8.5	139.01	-7.12	D	0.743	R	P
19.0	13.0	8.5	155.32	-7.28	GT	0.664	R	T
4.2	3.1	0.9	32.28	-5.01	AG	0.398	A	T
6.5	3.0	2.5	39.05	-5.29	AG	0.684	SA	P
11.0	7.0	5.0	86.02	-6.43	B	0.687	VR	T
5.1	2.8	1.5	31.76	-4.99	B	0.540	R	P
4.0	2.4	1.4	27.78	-4.80	AG	0.589	SA	P
4.9	4.0	2.3	46.14	-5.53	AG	0.646	SR	P
2.8	2.4	1.4	27.78	-4.80	AD	0.663	SA	P
10.0	8.0	4.8	93.30	-6.54	AG	0.660	SR	T
8.0	7.0	5.5	89.02	-6.48	D	0.814	VR	T
5.5	4.0	3.8	55.17	-5.79	D	0.869	R	T
5.0	3.0	2.0	36.02	-5.17	GD	0.644	SA	T
9.5	9.3	4.0	101.24	-6.66	B	0.566	VR	N
11.0	6.0	4.0	72.11	-6.17	B	0.624	SA	P
3.8	3.6	2.2	42.19	-5.40	AG	0.707	A	P
6.5	5.0	3.3	59.91	-5.90	GD	0.695	SR	P
2.3	1.7	1.2	20.81	-4.38	GT	0.717	SR	T
2.1	1.5	0.8	17.00	-4.09	B	0.588	SA	T
2.5	1.3	1.0	16.40	-4.04	D	0.675	SA	P
4.0	3.0	1.8	34.99	-5.13	B	0.646	SA	P
4.2	2.2	1.5	26.63	-4.73	B	0.624	VR	O
6.8	3.8	3.4	50.99	-5.67	B	0.765	VR	P
11.5	10.0	5.5	114.13	-6.83	B	0.641	SR	T
3.0	2.1	1.5	25.81	-4.69	GD	0.709	SR	P
3.5	2.8	2.0	34.41	-5.10	D	0.742	SR	P
6.0	5.2	2.0	55.71	-5.80	AG	0.504	SR	P
5.1	3.1	2.6	40.46	-5.34	AG	0.753	SA	P
3.5	2.5	1.8	30.81	-4.95	GT	0.718	SA	P

Axial dimensions (cm)			Clast/sieve size[1] (mm)	Clast/sieve size[2] (ϕ)	Lithology[3]	Maximum Projection Sphericity[4]	Visual Roundness Class[5]	Clast a-axis Orientation[6]
a	b	c						
7.5	7.0	2.0	72.60	-6.19	B	0.424	R	P
5.0	4.5	2.5	51.48	-5.69	D	0.662	R	T
7.1	6.3	2.4	67.42	-6.08	GT	0.505	R	P
3.8	3.5	1.8	39.36	-5.30	B	0.626	R	T
4.0	2.8	1.6	32.26	-5.01	AG	0.611	SR	P
3.8	2.6	1.6	30.53	-4.93	GT	0.638	SA	P
3.2	2.8	1.5	31.76	-4.99	AD	0.631	SR	T
4.2	3.0	2.2	37.20	-5.22	GD	0.727	SR	P
4.5	3.8	2.5	45.49	-5.51	AG	0.715	SR	T
5.8	3.8	1.8	42.05	-5.39	B	0.534	SA	P
4.5	3.6	2.2	42.19	-5.40	D	0.660	SA	P
3.8	3.5	2.5	43.01	-5.43	B	0.777	SR	T
5.2	3.2	2.6	41.23	-5.37	D	0.741	SR	P
9.0	6.0	4.5	75.00	-6.23	D	0.721	SR	P
4.0	2.8	2.2	35.61	-5.15	AD	0.756	SR	P
3.0	1.6	1.2	20.00	-4.32	B	0.669	SR	P
2.8	2.0	1.5	25.00	-4.64	GT	0.738	SR	T
4.5	3.5	2.0	40.31	-5.33	GD	0.633	SA	T
3.6	2.4	1.8	30.00	-4.91	B	0.721	SR	P
4.0	3.0	2.2	37.20	-5.22	D	0.739	R	P
4.5	2.0	1.6	25.61	-4.68	GD	0.658	A	P
3.0	2.8	1.8	33.29	-5.06	B	0.728	A	P
3.2	2.6	2.0	32.80	-5.04	GD	0.763	SR	P
2.5	2.0	0.8	21.54	-4.43	B	0.504	A	P
6.0	4.5	2.5	53.00	-5.73	GD	0.662	R	P
6.4	3.8	2.4	44.94	-5.49	GD	0.619	SR	P
4.5	4.0	2.0	44.72	-5.48	GD	0.606	SR	T
4.0	3.0	1.8	34.99	-5.13	AG	0.646	SR	P
5.0	3.8	2.8	47.20	-5.56	GD	0.744	R	T
3.5	2.2	1.8	28.43	-4.83	B	0.749	SR	T
5.8	3.5	1.5	38.08	-5.25	B	0.480	SR	P
3.6	2.0	1.5	25.00	-4.64	B	0.679	SR	T
5.8	4.4	3.0	53.25	-5.73	GD	0.707	R	P
Q16 (162.38 bm)								
21.0	17.0	12.0	208.09	-7.70	GD	0.739	SR	T
11.0	8.5	6.5	107.00	-6.74	GD	0.767	SR	T
12.5	10.0	7.4	124.40	-6.96	GD	0.759	R	P
20.0	16.5	14.0	216.39	-7.76	GD	0.841	VR	T
13.0	10.5	6.0	120.93	-6.92	D	0.641	SR	T
14.7	8.8	6.2	107.65	-6.75	GD	0.667	SA	P
17.0	12.5	8.5	151.16	-7.24	D	0.698	SA	T
35.0	30.0	13.0	326.98	-8.35	D	0.544	R	T
40.0	32.0	13.0	345.40	-8.43	GD	0.509	R	T
40.0	30.0	21.0	366.20	-8.52	D	0.716	VR	T
28.0	21.0	7.0	221.36	-7.79	GT	0.437	R	P
7.0	7.0	2.5	74.33	-6.22	GT	0.503	R	N
7.5	5.6	2.6	61.74	-5.95	GT	0.544	R	P
9.0	5.7	3.6	67.42	-6.08	GT	0.632	SA	P
7.5	5.7	3.2	65.37	-6.03	GT	0.621	SR	P
12.0	9.0	5.2	103.94	-6.70	GT	0.630	R	P
19.5	17.0	7.0	183.85	-7.52	GD	0.529	VR	T
27.0	20.0	12.0	233.24	-7.87	D	0.644	VR	T
10.0	9.0	8.0	120.42	-6.91	GD	0.893	VR	P
9.0	5.2	4.8	70.77	-6.15	GD	0.780	VR	T
13.0	9.0	5.5	105.48	-6.72	GD	0.637	VR	P

Axial dimensions (cm)			Clast/sieve size[1] (mm)	Clast/sieve size[2] (ϕ)	Lithology[3]	Maximum Projection Sphericity[4]	Visual Roundness Class[5]	Clast a-axis Orientation[6]
a	b	c						
11.4	8.5	7.6	114.02	-6.83	GT	0.842	SR	P
10.5	8.0	5.5	97.08	-6.60	GD	0.711	VR	P
21.0	14.0	7.0	156.52	-7.29	GT	0.550	SA	P
15.0	13.0	8.0	152.64	-7.25	GD	0.690	VR	T
6.0	6.7	5.0	83.60	-6.39	GD	0.776	VR	P
15.2	13.0	10.0	164.01	-7.36	GD	0.797	VR	T
9.2	4.8	4.2	83.78	-6.00	GD	0.736	R	P
12.4	6.8	6.0	90.69	-6.50	GT	0.753	R	P
7.7	5.3	4.8	71.51	-6.16	D	0.826	R	T
32.0	21.0	16.0	264.01	-8.04	D	0.725	VR	P
13.0	10.0	6.5	119.27	-6.90	GT	0.688	SR	P
12.0	7.0	4.5	83.22	-6.38	D	0.622	SA	T
10.5	7.0	3.8	79.65	-6.32	B	0.581	SR	P
12.0	10.0	7.0	122.07	-6.93	GD	0.742	VR	T
9.5	5.5	3.5	65.19	-6.03	D	0.617	R	P
6.5	5.5	2.5	60.42	-5.92	GD	0.559	SA	P
9.0	6.5	5.5	86.15	-6.41	D	0.803	VR	P
8.5	6.5	4.5	79.06	-6.30	GD	0.716	VR	T
8.5	5.0	2.6	56.36	-5.82	GD	0.542	SR	P
12.0	11.0	8.0	138.01	-7.09	GD	0.786	SR	T
9.5	7.8	5.5	96.44	-6.58	D	0.742	R	P
10.5	8.0	5.5	81.39	-6.35	D	0.783	SR	P
17.5	10.5	7.0	126.19	-6.98	GD	0.644	SR	P
9.5	8.0	6.5	103.08	-6.69	GD	0.822	VR	P
10.5	8.5	5.5	101.24	-6.66	D	0.697	SR	P
12.5	10.0	7.5	125.00	-6.97	D	0.766	VR	P
13.5	9.0	6.0	108.17	-6.76	D	0.667	R	P
11.4	8.5	6.2	105.21	-6.72	GT	0.735	R	P
11.0	5.8	3.5	67.74	-6.08	GD	0.577	SR	P
10.0	6.8	3.9	78.39	-6.29	D	0.607	SR	T
7.5	5.5	4.2	69.20	-6.11	B	0.753	VR	P
13.0	11.0	7.5	133.14	-7.06	GT	0.733	SA	T
8.0	3.5	3.0	46.10	-5.53	B	0.685	R	P
24.0	19.0	17.0	254.95	-7.99	D	0.859	VR	T
14.0	11.0	6.5	127.77	-7.00	GD	0.650	VR	T
37.0	23.0	17.0	286.01	-8.16	GD	0.698	VR	P
25.0	22.5	10.5	248.29	-7.96	GD	0.581	R	T
18.5	9.5	8.0	124.20	-6.96	GD	0.714	R	P
39.0	37.0	14.0	395.60	-8.63	B	0.514	SR	T
16.0	14.5	9.5	173.35	-7.44	GD	0.730	R	T
10.0	9.7	5.0	109.13	-6.77	D	0.636	VR	T
10.5	7.5	6.3	97.95	-6.61	GD	0.796	VR	T
9.6	5.5	4.3	69.81	-6.13	B	0.705	VR	T
8.6	8.0	3.2	86.16	-6.43	GT	0.530	VR	P
11.0	7.0	7.0	98.99	-6.63	GT	0.860	A	T
10.6	6.8	4.3	80.45	-6.33	GT	0.635	SA	P
10.2	7.3	5.7	92.62	-6.53	GD	0.758	VR	O
8.5	6.5	5.0	82.01	-6.36	GT	0.768	VR	T
7.5	5.7	3.2	65.37	-6.03	B	0.621	SR	P
7.5	6.0	4.3	73.82	-6.21	D	0.743	VR	T
9.7	7.7	5.0	91.81	-6.52	GT	0.694	SR	T
6.2	4.6	4.1	61.62	-5.95	D	0.838	VR	P
7.2	4.2	2.7	49.93	-5.64	D	0.622	VR	T
6.2	3.2	2.0	37.74	-5.24	D	0.586	SA	P
15.7	11.7	3.9	123.33	-6.95	GT	0.436	SA	P
7.6	6.3	3.7	73.06	-6.19	D	0.659	R	P

Axial dimensions (cm)			Clast/sieve size[1] (mm)	Clast/sieve size[2] (ϕ)	Lithology[3]	Maximum Projection Sphericity[4]	Visual Roundness Class[5]	Clast a-axis Orientation[6]
a	b	c						
9.5	5.0	4.5	67.27	-6.07	GD	0.753	SR	P
5.1	4.8	2.8	55.57	-5.80	GT	0.684	SR	P
9.3	7.2	4.4	84.38	-6.40	GD	0.661	SA	T
5.3	3.8	3.0	48.41	-5.60	GT	0.765	R	T
6.0	4.3	3.7	56.73	-5.83	GT	0.810	SR	T
7.2	6.0	3.6	69.97	-6.13	GD	0.669	VR	T
11.0	8.0	6.0	100.00	-6.64	GT	0.742	VR	P
7.3	7.1	3.3	78.29	-6.29	D	0.594	R	P
8.4	6.5	4.5	79.06	-6.30	GT	0.718	R	P
7.3	4.7	3.8	60.44	-5.92	GD	0.749	SA	T
5.0	2.4	1.7	29.41	-4.88	GN	0.622	R	T
4.2	3.3	2.7	42.64	-5.41	B	0.807	SR	T
8.4	7.7	3.7	85.43	-6.42	GD	0.596	R	P
6.8	4.5	3.0	54.08	-5.76	D	0.665	R	P
5.2	3.5	1.8	39.36	-5.30	GD	0.563	SR	P
13.0	10.5	8.5	135.09	-7.08	GD	0.809	SA	T
8.0	5.8	3.0	65.30	-6.03	GT	0.579	R	P
5.4	3.5	3.1	46.75	-5.55	GT	0.798	SR	T
7.0	4.4	3.6	56.85	-5.83	GD	0.749	SA	T
11.0	6.5	5.5	85.15	-6.41	GT	0.751	R	T
7.0	4.5	4.0	60.21	-5.91	D	0.798	VR	P
5.0	4.5	2.5	51.48	-5.69	GD	0.652	SR	P
8.0	5.5	3.6	65.73	-6.04	GD	0.665	SR	T
10.0	8.5	6.0	104.04	-6.70	GD	0.751	SA	T
7.0	4.8	2.5	54.12	-5.76	GT	0.571	SA	T
7.5	6.0	2.5	65.00	-6.02	D	0.516	SR	T
6.4	4.0	3.2	51.22	-5.68	B	0.737	A	P
7.5	4.6	3.5	57.80	-5.85	D	0.708	VR	T
4.5	3.0	2.8	41.04	-5.36	GT	0.834	SA	P
4.8	4.0	3.2	51.22	-5.68	GT	0.811	SR	P
11.0	9.4	6.6	114.66	-6.84	GT	0.750	VR	
4.5	3.5	2.8	44.62	-5.49	D	0.793	SR	P
6.0	4.4	3.0	53.25	-5.73	GT	0.699	SA	P
18.5	12.0	8.8	148.81	-7.22	D	0.704	SA	P
10.4	8.0	6.0	100.00	-6.64	D	0.756	VR	P
6.8	4.5	4.0	60.21	-5.91	D	0.806	SR	P
4.0	2.8	2.1	35.00	-5.13	D	0.733	A	P
9.0	6.5	5.4	84.50	-6.40	GD	0.793	R	T
5.5	3.0	2.5	39.05	-5.29	GD	0.724	SR	P
8.4	6.0	3.5	69.46	-6.12	GD	0.624	SA	T
7.4	5.2	4.0	65.60	-6.04	GD	0.746	R	P
8.8	4.5	2.6	51.97	-5.70	GT	0.555	SR	T
6.5	4.0	3.0	50.00	-5.64	D	0.702	SA	P
Q17 (124.12 km)								
16.5	12.0	5.5	132.00	-7.04	GD	0.535	VR	T
14.5	8.5	7.0	110.11	-6.78	B	0.735	VR	P
10.5	7.0	6.5	95.52	-6.58	GD	0.831	VR	P
14.0	11.5	6.0	126.71	-7.02	GD	0.607	VR	T
8.5	6.5	5.0	82.01	-6.36	GD	0.768	VR	P
7.5	5.0	3.5	61.03	-5.93	GD	0.689	R	P
8.5	7.5	5.5	93.01	-6.54	GD	0.780	VR	T
12.0	9.5	6.5	115.11	-6.85	GD	0.716	R	P
7.5	6.0	4.0	72.11	-6.17	D	0.708	VR	P
8.5	7.0	3.5	78.26	-6.29	B	0.590	VR	T
14.0	6.5	5.5	85.15	-6.41	B	0.693	R	T

Axial dimensions (cm)			Clast/sieve size[1] (mm)	Clast/sieve size[2] (ϕ)	Lithology[3]	Maximum Projection Sphericity[4]	Visual Roundness Class[5]	Clast a-axis Orientation[6]
a	b	c						
13.5	9.5	6.0	112.36	-6.81	GD	0.656	VR	P
19.0	15.0	9.0	174.93	-7.45	D	0.657	VR	T
7.0	6.0	3.5	69.46	-6.12	GD	0.663	R	T
5.5	4.0	2.8	48.83	-5.61	GD	0.709	VR	P
12.0	10.5	4.5	114.24	-6.84	AD	0.544	SR	P
7.5	5.5	4.0	68.01	-6.09	GD	0.729	R	P
12.5	8.0	4.0	89.44	-6.48	GD	0.547	R	P
11.5	8.0	7.5	109.66	-6.78	GD	0.849	VR	P
16.0	11.0	10.0	148.66	-7.22	D	0.828	VR	P
14.0	11.0	7.5	133.14	-7.06	GD	0.715	VR	T
15.0	13.0	7.5	150.08	-7.23	GD	0.661	R	P
18.0	14.0	12.0	184.39	-7.53	GD	0.830	VR	T
13.5	9.0	6.5	111.02	-6.79	GT	0.703	R	P
13.0	10.0	6.5	119.27	-6.90	GD	0.688	R	P
10.5	6.5	5.5	85.15	-6.41	D	0.762	R	P
10.5	8.5	7.0	110.11	-6.78	D	0.819	VR	P
18.0	14.5	10.0	176.14	-7.46	D	0.726	R	T
13.5	9.0	7.0	114.02	-6.83	B	0.739	SR	P
21.0	15.0	11.0	186.01	-7.54	GD	0.727	R	P
13.0	9.0	6.0	108.17	-6.76	B	0.675	R	T
10.0	8.0	4.5	91.79	-6.52	D	0.633	R	T
7.0	4.5	4.0	60.21	-5.91	D	0.798	R	T
11.5	8.0	5.0	94.34	-6.56	GD	0.648	R	T
11.0	8.5	5.5	101.24	-6.66	GD	0.686	SR	P
9.0	6.0	5.5	81.39	-6.35	D	0.824	VR	P
8.5	7.0	4.0	80.62	-6.33	D	0.645	VR	P
14.0	10.5	6.0	120.93	-6.92	D	0.626	VR	P
7.5	6.0	3.0	67.08	-6.07	GD	0.585	VR	T
13.5	10.5	5.0	116.30	-6.86	GD	0.561	R	P
9.0	7.0	4.5	83.22	-6.38	GD	0.685	SR	P
7.0	6.5	3.0	71.59	-6.16	D	0.583	VR	T
11.5	9.0	4.0	98.49	-6.62	GD	0.537	SA	P
8.0	6.0	3.5	69.46	-6.12	GD	0.634	R	P
5.5	4.5	3.0	54.08	-5.76	D	0.714	VR	T
9.5	7.0	4.5	83.22	-6.38	GT	0.673	VR	P
6.5	4.5	2.5	51.48	-5.69	D	0.598	R	P
16.0	10.0	6.0	116.62	-6.87	GD	0.608	VR	P
7.0	5.5	4.0	68.01	-6.09	GT	0.746	R	T
7.0	5.0	4.0	64.03	-6.00	AG	0.770	R	T
6.5	5.5	3.5	65.19	-6.03	D	0.700	SR	T
8.5	7.0	4.5	83.22	-6.38	B	0.698	SR	P
11.0	11.0	8.5	139.01	-7.12	D	0.842	VR	N
9.0	7.5	4.5	87.46	-6.45	D	0.669	R	T
11.5	8.0	5.0	94.34	-6.56	GD	0.648	VR	P
12.0	9.0	6.5	111.02	-6.79	GD	0.731	VR	T
12.0	10.0	6.5	119.27	-6.90	GD	0.706	VR	P
13.0	12.0	7.0	138.92	-7.12	GD	0.680	VR	T
9.0	7.0	3.5	78.26	-6.29	D	0.579	VR	P
12.0	7.5	6.0	96.05	-6.59	GD	0.737	VR	P
16.5	11.0	8.0	136.01	-7.09	B	0.705	R	P
9.6	7.7	6.0	97.62	-6.61	D	0.787	VR	P
16.0	10.5	7.5	129.03	-7.01	GD	0.694	R	T
26.0	15.0	14.0	205.18	-7.68	GD	0.795	VR	T
10.0	7.5	4.0	85.00	-6.41	GT	0.598	R	T
12.0	8.0	6.5	103.08	-6.69	GD	0.761	VR	P
11.2	8.5	6.0	104.04	-6.70	B	0.723	VR	T

Axial dimensions (cm)			Clast/sieve size[1] (mm)	Clast/sieve size[2] (ϕ)	Lithology[3]	Maximum Projection Sphericity[4]	Visual Roundness Class[5]	Clast a-axis Orientation[6]
a	b	c						
9.5	9.0	3.0	94.87	-6.57	GT	0.472	VR	P
10.2	8.0	6.8	105.00	-6.71	D	0.626	VR	T
7.0	4.5	2.5	51.48	-5.69	GD	0.583	R	T
18.0	13.0	7.0	147.65	-7.21	GD	0.618	VR	P
16.5	11.0	8.5	139.01	-7.12	GT	0.708	VR	P
10.0	4.5	3.0	54.08	-5.76	B	0.585	VR	T
6.5	3.0	2.2	37.20	-5.22	GD	0.628	R	T
8.0	6.0	5.0	78.10	-6.29	GD	0.805	VR	T
6.0	4.5	4.0	60.21	-5.91	D	0.840	VR	T
8.0	5.0	4.8	69.31	-6.12	D	0.832	R	T
8.5	6.5	4.5	79.08	-6.30	GT	0.716	R	T
17.0	13.5	9.0	162.26	-7.34	GD	0.707	SR	P
15.0	8.5	8.5	120.21	-6.91	GD	0.828	VR	P
8.0	6.4	3.8	74.43	-6.22	GD	0.656	R	P
8.0	5.3	3.4	62.97	-5.98	B	0.714	SR	P
10.5	9.0	4.2	99.32	-6.63	B	0.572	SA	T
10.5	7.6	5.5	95.44	-6.58	D	0.717	VR	T
7.0	5.8	3.8	69.34	-6.12	GD	0.709	VR	T
10.3	6.8	5.8	39.38	-6.40	D	0.783	VR	P
11.3	6.0	4.3	73.82	-6.21	B	0.648	SA	T
12.0	10.0	5.5	114.13	-6.83	B	0.632	SR	O
7.5	5.8	5.0	76.58	-6.26	GD	0.831	R	P
8.0	6.5	4.0	76.32	-6.25	D	0.676	SA	T
7.5	5.5	4.5	71.06	-6.15	GD	0.789	R	P
8.0	6.0	5.0	78.10	-6.20	GD	0.805	R	T
6.8	5.5	2.5	60.42	-5.92	B	0.551	VR	P
7.0	5.8	2.5	61.33	-5.94	D	0.542	R	T
6.4	4.0	3.0	50.00	-5.64	B	0.708	VR	P
7.4	5.5	3.2	63.63	-5.99	GD	0.631	VR	P
9.5	8.4	4.0	93.04	-6.54	GD	0.585	R	P
8.0	5.2	3.0	60.03	-5.91	GD	0.600	SR	T
9.5	6.0	6.0	84.85	-6.41	B	0.858	SR	T
9.5	4.0	3.7	54.49	-5.77	GD	0.712	R	T
14.0	11.0	4.8	120.02	-6.91	D	0.531	SR	T
8.5	6.8	4.5	81.54	-6.35	GD	0.705	VR	O
6.1	4.0	2.7	48.26	-5.59	GD	0.660	SA	P
7.1	5.3	2.9	60.42	-5.92	D	0.607	VR	P
7.0	6.3	4.2	75.72	-6.24	GD	0.737	VR	T
10.6	7.2	5.0	87.66	-6.45	GD	0.689	R	P
10.0	6.7	5.0	83.60	-6.39	B	0.730	SR	T
10.2	8.0	5.0	94.34	-6.56	GT	0.674	VR	P
9.2	8.0	6.5	103.08	-6.69	GT	0.831	SA	P
6.8	5.0	5.0	70.71	-6.14	GD	0.828	A	P
8.0	6.0	3.5	69.46	-6.12	B	0.634	VR	T
7.6	6.0	4.5	75.00	-6.23	D	0.763	R	P
5.5	5.0	4.0	64.03	-6.00	D	0.835	VR	P
15.0	8.5	4.5	98.18	-6.59	B	0.542	R	T
10.6	9.5	6.6	115.68	-6.85	GT	0.756	R	T
11.0	9.0	7.0	114.02	-6.83	D	0.791	VR	T
24.0	20.0	8.0	215.41	-7.75	B	0.511	VR	P
11.2	10.5	3.4	110.37	-6.79	AG	0.462	VR	P
10.4	7.2	5.4	90.00	-6.49	GT	0.730	R	P
14.0	10.5	8.0	132.00	-7.04	GD	0.758	VR	T
10.5	8.5	4.0	93.94	-6.55	GD	0.564	VR	P
18.0	10.0	8.5	131.24	-7.04	GD	0.738	VR	P
14.0	11.0	4.0	117.05	-6.87	AD	0.470	VR	T

Axial dimensions (cm)			Clast/sieve size[1] (mm)	Clast/sieve size[2] (ϕ)	Lithology[3]	Maximum Projection Sphericity[4]	Visual Roundness Class[5]	Clast a-axis Orientation[6]
a	b	c						
11.0	9.5	7.0	118.00	-6.88	GD	0.777	VR	T
9.0	6.5	5.5	85.15	-6.41	GD	0.803	R	P
15.5	12.5	11.5	169.85	-7.41	GD	0.880	VR	P
6.5	6.0	4.5	75.00	-6.23	AG	0.804	SR	T
9.0	7.5	3.0	80.78	-6.34	AD	0.511	R	P
18.0	11.0	8.0	136.01	-7.09	GD	0.688	R	P
13.0	9.5	9.0	130.88	-7.03	B	0.889	R	P
18.0	13.0	8.0	152.64	-7.25	GD	0.649	R	T
20.0	12.0	8.0	144.22	-7.17	B	0.644	R	P
9.0	7.0	4.0	80.62	-6.33	D	0.633	R	P
14.0	10.5	5.0	116.30	-6.86	B	0.554	R	P
21.0	16.0	10.0	188.68	-7.56	GD	0.668	VR	P
35.0	23.0	19.0	298.33	-8.22	GD	0.765	R	P
14.0	10.0	8.0	128.06	-7.00	GD	0.770	VR	P
15.0	12.0	7.0	138.92	-7.12	B	0.648	VR	T
13.0	8.0	7.0	106.30	-6.73	GD	0.778	VR	P
15.0	11.0	8.0	136.01	-7.09	GD	0.720	R	T
18.0	16.0	9.0	183.58	-7.52	GD	0.655	VR	T
28.0	20.0	14.0	244.13	-7.93	GD	0.705	SR	P
12.0	9.5	8.0	124.20	-6.96	GD	0.825	R	T
11.0	7.0	4.5	83.22	-6.38	GD	0.641	R	T
19.0	19.0	11.0	219.54	-7.78	D	0.695	VR	N
15.0	14.0	13.0	191.05	-7.58	GD	0.930	VR	T
11.0	7.0	5.0	86.02	-6.43	GT	0.687	R	P
11.0	9.0	4.5	100.62	-6.65	D	0.589	SR	T
12.0	9.0	5.0	102.96	-6.69	GT	0.614	R	T
13.0	10.0	6.0	116.62	-6.87	D	0.652	VR	P
50.0	35.0	26.0	436.00	-8.77	GD	0.728	R	T
32.0	22.0	17.0	278.03	-8.12	GD	0.743	VR	P
47.0	25.0	23.0	339.71	-8.41	GD	0.766	R	P
31.0	23.0	16.0	280.15	-8.13	GD	0.711	R	T
39.0	28.0	24.0	368.78	-8.53	GD	0.808	VR	O
27.0	21.0	12.0	241.87	-7.92	GD	0.633	R	T
50.0	25.0	25.0	353.55	-8.47	D	0.704	SR	T
43.0	25.0	21.0	328.50	-8.35	B	0.743	R	P
35.0	32.0	24.0	400.00	-8.64	GD	0.801	VR	P
30.0	25.0	22.0	333.02	-8.38	D	0.792	SR	P
21.0	16.0	15.0	219.32	-7.78	GD	0.875	VR	P
18.0	13.0	6.0	143.18	-7.16	B	0.538	SR	P
10.5	9.0	6.0	108.17	-6.76	GT	0.725	R	P
13.3	10.2	8.0	129.63	-7.02	GD	0.778	VR	T
13.5	10.2	6.0	118.34	-6.89	B	0.630	R	T
17.5	7.0	5.3	87.80	-6.46	D	0.612	VR	T
10.3	8.0	6.5	103.08	-6.69	GN	0.800	VR	T
13.0	10.0	6.0	116.62	-6.87	B	0.652	VR	P
13.5	9.0	7.5	117.15	-6.87	GD	0.774	VR	T
8.5	7.0	4.5	83.22	-6.38	GD	0.668	VR	T
11.0	10.0	4.8	110.92	-6.70	GT	0.594	VR	T
11.5	10.8	6.0	123.55	-6.95	D	0.662	VR	P
14.5	10.0	5.5	114.13	-6.83	B	0.593	SR	P
14.0	8.5	5.0	98.62	-6.62	D	0.594	VR	P
21.0	20.0	9.0	219.32	-7.78	GD	0.578	SR	P
11.7	10.8	7.8	133.22	-7.06	GD	0.784	VR	P
13.0	11.0	9.0	142.13	-7.15	GD	0.827	VR	T
13.2	13.0	8.0	152.64	-7.25	GD	0.720	VR	T
12.2	8.5	6.5	107.00	-6.74	D	0.741	VR	T

Axial dimensions (cm)			Clast/sieve size[1] (mm)	Clast/sieve size[2] (ϕ)	Lithology[3]	Maximum Projection Sphericity[4]	Visual Roundness Class[5]	Clast a-axis Orientation[6]
a	b	c						
9.8	4.4	2.0	48.33	-5.59	B	0.453	R	T
Q16 (110.23 km)								
22.0	18.0	13.0	222.04	-7.79	GD	0.753	VR	T
28.5	18.0	10.0	205.91	-7.69	GD	0.580	VR	T
10.3	8.0	6.5	103.08	-6.69	D	0.800	VR	T
10.5	9.2	3.8	99.54	-6.64	D	0.531	VR	T
14.0	12.0	10.5	159.45	-7.32	D	0.869	R	P
12.0	10.0	3.0	104.40	-6.71	GT	0.422	R	T
9.0	7.5	3.0	80.78	-6.34	B	0.611	SA	T
		6.0						
14.0	8.5		104.04	-6.70	GD	0.671	VR	P
19.0	13.0	12.0	176.92	-7.47	B	0.835	R	P
8.0	7.8	4.5	90.05	-6.49	D	0.687	VR	T
11.3	7.0	4.0	80.62	-6.33	D	0.587	R	P
14.0	9.0	9.0	127.28	-6.99	D	0.863	VR	P
11.2	7.0	4.5	83.22	-6.38	GD	0.637	VR	T
11.5	8.0	4.5	91.79	-6.52	B	0.604	SR	T
16.5	12.0	7.0	138.92	-7.12	D	0.628	VR	T
17.9	13.0	6.0	143.18	-7.16	J	0.537	R	T
10.5	6.8	3.8	77.90	-6.28	D	0.587	R	T
13.3	7.3	5.7	95.61	-6.59	GD	0.679	VR	T
13.0	8.3	4.0	92.14	-6.53	B	0.529	VR	T
14.0	11.5	11.0	159.14	-7.31	GT	0.909	VR	P
10.5	7.5	5.5	93.01	-6.54	GD	0.727	R	T
10.0	7.4	4.8	88.20	-6.46	D	0.678	VR	P
6.0	3.8	2.6	46.04	-5.52	GT	0.667	VR	T
6.5	5.7	2.4	61.85	-5.95	B	0.538	VR	P
9.5	7.0	7.0	98.99	-6.63	GD	0.903	VR	O
10.7	9.0	6.5	111.02	-6.79	D	0.760	R	T
11.0	7.2	3.4	79.62	-6.32	D	0.527	R	T
19.0	13.0	11.0	170.29	-7.41	GD	0.788	VR	O
14.5	13.5	7.5	154.43	-7.27	D	0.660	VR	T
14.0	7.5	5.5	93.01	-6.54	B	0.660	VR	P
8.5	6.5	3.0	71.59	-6.16	D	0.545	VR	T
9.0	7.0	3.0	76.16	-6.25	D	0.523	VR	T
10.0	8.0	3.8	88.57	-6.47	B	0.565	R	T
16.0	14.0	12.5	187.68	-7.55	GD	0.887	VR	P
12.5	4.5	3.5	57.01	-5.83	D	0.602	R	P
9.5	6.5	3.0	71.59	-6.16	B	0.526	VR	P
8.5	6.5	5.0	82.01	-6.38	B	0.768	R	T
8.5	6.5	2.5	69.64	-6.12	D	0.484	VR	P
16.0	12.5	8.0	148.41	-7.21	GT	0.684	VR	P
14.5	13.5	4.0	140.80	-7.14	B	0.434	R	T
9.0	6.5	4.5	79.06	-6.30	GD	0.702	VR	P
7.0	6.0	3.5	69.46	-6.12	GD	0.663	SR	T
15.0	10.5	7.0	126.19	-6.98	GD	0.676	R	P
17.0	14.0	6.0	152.32	-7.25	GD	0.533	VR	T
8.0	5.0	3.5	61.03	-5.93	GD	0.674	R	P
7.5	5.0	2.0	53.85	-5.75	D	0.474	R	T
11.5	9.0	3.5	96.57	-6.59	B	0.491	VR	P
10.0	9.0	6.0	108.17	-6.76	GD	0.737	VR	P
10.0	8.0	4.0	89.44	-6.48	B	0.585	VR	T
14.5	9.5	6.5	115.11	-6.85	B	0.674	VR	T
21.0	14.0	10.0	172.05	-7.43	GD	0.698	VR	P
11.0	8.5	6.0	104.04	-6.70	D	0.727	VR	P

Axial dimensions (cm)			Clast/sieve size[1] (mm)	Clast/sieve size[2] (ϕ)	Lithology[3]	Maximum Projection Sphericity[4]	Visual Roundness Class[5]	Clast a-axis Orientation[6]
a	b	c						
10.5	9.0	3.5	96.57	-6.59	B	0.509	VR	P
9.5	7.0	6.0	92.20	-6.53	GD	0.815	VR	T
14.0	13.0	9.0	158.11	-7.30	GT	0.763	R	T
6.5	4.5	2.0	49.24	-5.62	D	0.515	R	P
10.0	7.5	3.5	82.76	-6.37	D	0.547	R	P
12.0	9.5	7.0	118.00	-6.88	GD	0.755	VR	T
11.5	7.0	5.0	86.02	-6.43	D	0.677	SR	P
Q19 (103.03 km)								
9.4	8.0	6.0	100.00	-6.64	GD	0.782	VR	T
20.5	13.0	11.0	170.29	-7.41	GD	0.769	VR	T
11.2	7.0	7.0	98.99	-6.63	GD	0.855	R	P
8.3	7.0	3.5	78.26	-6.29	D	0.595	VR	P
9.4	7.0	6.0	92.20	-6.53	D	0.818	SR	P
14.2	6.5	6.5	91.92	-6.52	GD	0.771	R	T
8.3	6.8	4.5	81.54	-6.35	GD	0.711	VR	T
10.2	7.4	4.7	87.66	-6.45	GD	0.664	R	P
10.5	8.0	5.0	94.34	-6.56	GD	0.668	R	T
6.8	3.8	2.3	44.42	-5.47	B	0.589	SR	P
9.5	7.2	4.5	84.91	-6.41	GT	0.666	SR	T
7.5	7.0	4.5	83.22	-6.38	D	0.728	VR	N
7.0	6.2	5.0	79.65	-6.32	B	0.632	SR	P
8.2	5.5	4.0	68.01	-6.09	GN	0.708	SR	P
9.8	6.5	4.3	77.94	-6.28	B	0.662	SR	T
9.0	8.0	3.5	87.32	-6.45	D	0.554	VR	T
5.7	3.9	2.2	44.78	-5.48	GD	0.602	R	P
5.7	4.7	2.5	53.24	-5.73	B	0.616	VR	T
6.1	4.2	2.2	47.41	-5.57	GD	0.574	R	T
5.7	3.3	1.0	34.48	-5.11	D	0.376	VR	T
6.3	5.2	4.0	65.60	-6.04	GD	0.788	VR	P
7.0	4.7	3.2	56.88	-5.83	D	0.678	VR	T
6.1	4.5	2.5	51.48	-5.69	GD	0.611	VR	T
5.3	4.0	2.8	48.83	-5.61	D	0.718	VR	P
6.2	4.3	3.2	53.60	-5.74	B	0.727	SR	T
5.7	4.5	2.0	49.24	-5.62	B	0.538	VR	P
5.4	4.5	1.8	48.47	-5.60	B	0.511	VR	P
6.7	5.5	1.5	57.01	-5.83	B	0.394	VR	P
5.8	3.8	3.2	49.68	-5.63	D	0.775	SR	P
6.2	5.0	1.7	52.81	-5.72	D	0.453	VR	T
5.5	4.0	2.6	47.71	-5.58	GD	0.675	VR	P
7.0	4.5	4.0	60.21	-5.91	GD	0.798	R	P
11.0	5.5	3.5	65.19	-6.03	B	0.597	SR	T
6.0	5.0	3.5	61.03	-5.93	B	0.742	SR	T
10.0	6.0	4.5	75.00	-6.23	GT	0.698	R	P
5.7	3.6	2.5	43.83	-5.45	B	0.673	SR	P
5.5	4.4	2.0	48.33	-5.59	GD	0.549	R	P
6.0	3.5	2.6	43.60	-5.45	B	0.685	VR	T
11.0	8.5	5.0	98.62	-6.62	GD	0.644	R	P
6.0	5.0	3.5	61.03	-5.93	GD	0.742	R	P
5.5	4.0	2.5	47.17	-5.56	GD	0.657	SR	P
7.5	4.0	3.0	50.00	-5.64	GD	0.669	R	P
7.5	5.0	3.5	61.03	-5.93	B	0.689	VR	P
6.0	3.5	2.5	43.01	-5.43	GD	0.668	VR	P
8.0	5.5	3.5	65.19	-6.03	B	0.653	R	P
16.0	9.5	7.0	118.00	-6.88	GT	0.686	VR	P
9.5	7.0	4.5	83.22	-6.38	GD	0.673	R	P

Axial dimensions (cm)			Clast/sieve size[1] (mm)	Clast/sieve size[2] (ϕ)	Lithology[3]	Maximum Projection Sphericity[4]	Visual Roundness Class[5]	Clast a-axis Orientation[6]
a	b	c						
5.2	4.0	2.0	44.72	-5.48	B	0.577	VR	T
9.5	5.5	4.0	68.01	-6.09	B	0.674	R	P
6.0	5.0	3.5	61.03	-5.93	D	0.742	VR	T
6.0	4.5	1.5	47.43	-5.57	B	0.437	VR	T
7.0	3.5	1.5	38.08	-5.25	B	0.451	VR	T
5.0	4.0	2.8	48.83	-5.61	GD	0.732	VR	T
6.0	4.5	3.5	57.01	-5.83	GD	0.768	VR	T
6.0	3.0	2.5	39.05	-5.29	GD	0.703	SA	P
5.5	3.5	1.5	38.08	-5.26	B	0.489	SR	T
5.2	4.0	2.5	47.17	-5.56	GD	0.670	SR	T
7.0	5.5	3.0	62.65	-5.97	GD	0.616	SR	P
7.0	4.5	4.0	60.21	-5.91	GD	0.708	R	P
7.8	6.5	5.0	82.01	-6.36	GD	0.700	VR	T
Q30 (84.59 km)[7]								
12.0	9.0	7.5	117.15	-6.87	D	0.805	VR	
13.0	11.0	9.5	145.34	-7.18	GD	0.858	VR	
18.0	10.0	7.0	122.07	-6.93	B	0.648	R	
28.0	19.5	13.0	234.38	-7.87	D	0.676	R	
23.0	17.0	15.5	230.05	-7.85	B	0.850	VR	
14.0	12.0	7.5	141.51	-7.14	GD	0.694	VR	
17.0	12.0	10.0	156.20	-7.29	B	0.788	R	
14.0	11.0	8.0	136.01	-7.09	B	0.746	SR	
17.0	12.0	5.5	132.00	-7.04	B	0.529	VR	
23.0	15.0	11.5	189.01	-7.56	GD	0.726	VR	
22.0	16.0	12.0	200.00	-7.64	D	0.742	VR	
17.0	12.5	10.5	163.25	-7.35	B	0.804	VR	
16.0	11.5	8.5	143.00	-7.16	D	0.732	VR	
13.0	11.0	7.5	133.14	-7.06	GD	0.733	VR	
19.0	12.0	10.0	156.20	-7.29	GD	0.760	R	
17.0	13.0	10.0	164.01	-7.36	D	0.768	VR	
17.0	15.0	11.5	189.01	-7.56	GD	0.803	VR	
21.0	15.0	10.0	180.28	-7.49	GT	0.682	VR	
18.0	13.0	11.0	170.29	-7.41	GD	0.803	VR	
22.0	18.5	14.5	235.05	-7.88	GD	0.802	VR	
17.0	13.0	9.0	158.11	-7.30	GD	0.716	VR	
15.0	11.0	7.0	130.38	-7.03	B	0.667	SR	
28.0	19.0	15.0	242.07	-7.92	GD	0.751	R	
17.0	13.0	10.0	164.01	-7.36	B	0.768	R	
13.0	11.0	10.0	148.66	-7.22	GD	0.888	VR	
16.0	11.0	7.0	130.38	-7.03	B	0.653	VR	
15.0	12.0	10.0	156.20	-7.29	GD	0.822	VR	
17.0	14.0	9.0	166.43	-7.38	GD	0.698	VR	
15.0	11.0	7.0	130.38	-7.03	B	0.667	SA	
13.0	11.0	7.5	133.14	-7.06	D	0.733	VR	
19.0	14.0	8.0	161.25	-7.33	B	0.622	VR	
19.0	18.0	14.0	228.04	-7.83	GD	0.831	VR	
18.0	12.0	6.5	136.47	-7.09	B	0.580	R	
19.5	15.0	9.0	174.93	-7.45	GD	0.852	VR	
15.0	10.0	6.5	119.27	-6.90	B	0.658	VR	
16.5	11.0	9.0	142.13	-7.15	AG	0.764	R	
29.0	16.0	11.0	194.16	-7.60	GD	0.639	VR	
11.5	10.5	7.0	126.19	-6.98	GD	0.740	VR	
13.5	10.0	7.5	125.00	-6.97	GD	0.747	VR	
12.0	10.5	7.0	126.19	-6.98	B	0.730	R	
15.5	10.0	7.5	125.00	-6.97	GD	0.713	VR	

Axial dimensions (cm)			Clast/sieve size[1] (mm)	Clast/sieve size[2] (ϕ)	Lithology[3]	Maximum Projection Sphericity[4]	Visual Roundness Class[5]	Clast a-axis Orientation[6]
a	b	c						
11.5	9.5	5.0	107.35	-6.75	GD	0.612	VR	
15.5	9.0	6.0	108.17	-6.76	B	0.637	VR	
11.0	8.5	5.5	101.24	-6.66	GD	0.686	VR	
9.5	7.5	6.5	99.26	-6.63	GD	0.840	VR	
12.0	10.5	7.5	129.03	-7.01	D	0.764	SR	
20.5	9.0	6.5	111.02	-6.79	D	0.612	VR	
13.0	12.0	9.5	153.05	-7.26	B	0.833	R	
13.0	8.5	6.0	104.04	-6.70	D	0.688	VR	
12.0	9.5	7.0	118.00	-6.88	D	0.755	VR	
15.5	9.5	5.0	107.35	-6.75	D	0.554	VR	
12.0	7.5	5.0	90.14	-6.49	GD	0.652	VR	
15.0	10.5	6.0	120.93	-6.92	D	0.611	VR	
11.0	10.0	7.5	125.00	-6.97	B	0.800	SR	
18.5	13.0	9.5	161.01	-7.33	B	0.721	VR	
12.0	8.0	6.0	100.00	-6.64	GD	0.721	R	
18.0	13.0	10.0	164.01	-7.36	B	0.753	VR	
11.0	8.0	7.0	106.30	-6.73	B	0.823	VR	
27.0	15.0	13.0	198.49	-7.63	GD	0.747	VR	
20.0	16.0	15.0	219.32	-7.78	GD	0.889	VR	
Q21 (80.17 km)								
14.7	9.0	5.5	105.48	-6.72	D	0.611	VR	T
8.8	7.0	3.0	76.16	-6.25	D	0.527	R	P
7.2	6.5	4.0	76.32	-6.25	D	0.699	VR	T
7.6	5.5	3.0	62.65	-5.97	D	0.599	VR	T
7.2	6.0	2.0	63.25	-5.98	D	0.452	R	P
6.3	5.4	3.8	66.03	-6.05	D	0.752	SR	P
6.3	5.5	3.8	66.85	-6.06	B	0.747	R	N
5.5	4.2	2.0	46.52	-5.54	B	0.557	SA	P
5.6	3.8	3.0	48.41	-5.60	AG	0.751	R	T
9.5	8.0	3.6	87.73	-6.45	B	0.555	R	P
6.8	3.2	2.5	40.61	-5.34	B	0.680	SA	T
9.9	9.5	3.0	90.62	-6.64	B	0.457	VR	N
11.2	8.0	7.5	100.66	-6.78	D	0.858	R	P
9.8	7.5	6.0	96.05	-6.59	D	0.788	VR	P
7.0	4.6	3.4	57.20	-5.84	B	0.711	SR	P
5.5	4.0	3.2	51.22	-5.68	D	0.775	VR	O
7.6	4.8	4.4	65.12	-6.02	GD	0.810	VR	T
8.4	7.2	3.5	80.06	-6.32	B	0.587	R	T
10.6	8.4	5.0	97.75	-6.61	B	0.655	SR	P
6.3	4.5	3.7	58.26	-5.88	D	0.785	SR	T
6.0	5.5	3.0	62.65	-5.97	B	0.589	VR	T
11.7	8.6	6.4	107.20	-6.74	B	0.741	VR	T
7.0	7.0	4.3	82.15	-6.36	GT	0.723	VR	N
7.1	3.5	3.0	46.10	-5.53	AG	0.713	VR	P
15.0	11.5	11.0	159.14	-7.31	D	0.889	VR	P
15.0	8.0	4.5	91.79	-6.52	B	0.553	VR	T
8.6	5.0	3.5	61.03	-5.93	D	0.658	SR	P
5.7	5.5	1.5	57.01	-5.83	D	0.416	VR	T
10.3	9.5	4.4	104.69	-6.71	GT	0.583	VR	T
14.6	9.4	4.0	102.16	-6.67	D	0.489	VR	T
8.0	5.8	5.0	76.58	-6.26	D	0.814	VR	T
10.0	7.2	3.0	78.00	-6.29	B	0.500	R	T
9.7	8.0	3.5	87.32	-6.45	B	0.540	SR	T
10.0	7.0	4.5	83.22	-6.38	GD	0.661	VR	P
10.3	7.0	4.5	83.22	-6.38	B	0.655	VR	P

Axial dimensions (cm)			Clast/sieve size[1] (mm)	Clast/sieve size[2] (ϕ)	Lithology[3]	Maximum Projection Sphericity[4]	Visual Roundness Class[5]	Clast a-axis Orientation[6]
a	b	c						
9.5	6.5	3.0	71.59	-6.16	AG	0.526	VR	P
7.2	6.2	3.4	70.71	-6.14	AG	0.637	R	P
6.0	3.6	2.2	42.19	-5.40	B	0.607	VR	T
13.7	10.0	6.8	120.93	-6.92	B	0.606	VR	P
7.5	5.6	4.2	70.00	-6.13	GD	0.749	VR	P
6.3	5.5	3.3	64.14	-6.00	GD	0.680	VR	T
9.1	7.5	5.6	94.61	-6.57	B	0.790	R	T
6.7	4.7	2.3	52.33	-5.71	GN	0.552	SR	P
6.0	4.0	1.5	42.72	-5.42	D	0.454	SR	P
6.0	4.0	3.8	55.17	-5.79	GD	0.844	VR	T
6.8	5.5	4.7	72.35	-6.18	GT	0.839	VR	T
9.2	7.6	4.7	89.38	-6.48	B	0.681	R	T
7.7	4.8	3.2	57.69	-5.85	AG	0.652	VR	P
10.5	8.0	4.5	91.79	-6.52	D	0.622	VR	T
11.6	6.8	5.5	87.46	-6.45	B	0.727	VR	O
12.5	9.2	8.5	125.26	-6.97	AG	0.856	VR	O
5.2	4.5	3.8	58.90	-5.88	D	0.851	VR	T
9.0	6.0	4.2	73.24	-6.19	GD	0.689	VR	P
5.9	4.0	3.3	51.86	-5.70	AG	0.773	SA	P
18.5	9.5	9.0	130.66	-7.03	B	0.772	R	T
7.8	5.5	3.0	62.65	-5.97	GD	0.594	R	P
6.5	4.7	3.0	55.76	-5.80	B	0.665	VR	T
9.5	5.4	3.2	62.77	-5.97	D	0.584	R	T
9.5	9.0	6.0	108.17	-6.76	GT	0.750	VR	T
6.1	4.0	2.3	46.14	-5.53	GT	0.601	R	P
7.0	5.5	3.8	66.85	-6.06	B	0.721	SR	T
4.0	3.5	2.0	40.31	-5.33	D	0.659	VR	P
8.0	4.5	3.0	54.08	-5.76	B	0.630	SR	P
8.0	5.6	2.5	61.33	-5.94	D	0.519	VR	T
9.5	7.5	5.5	93.01	-6.54	B	0.752	R	T
7.5	6.5	3.0	71.59	-6.16	B	0.569	R	P
13.0	10.0	4.5	109.66	-6.78	B	0.536	R	P
6.0	3.6	2.5	45.49	-5.51	GD	0.650	R	P
4.0	2.8	2.1	35.00	-5.13	D	0.733	R	T
7.0	4.8	3.6	60.00	-5.91	D	0.728	VR	P
6.4	4.5	2.8	53.00	-5.73	B	0.648	VR	T
21.0	10.5	9.0	138.20	-7.11	B	0.716	VR	P
6.2	4.8	3.2	57.60	-5.85	D	0.701	SR	T
5.0	3.0	2.6	39.70	-5.31	GD	0.767	VR	P
7.2	5.5	2.1	58.87	-5.88	B	0.481	SR	T
13.0	8.0	4.2	90.35	-6.50	GD	0.554	R	P
9.8	6.0	2.5	65.00	-6.02	B	0.474	VR	T
7.8	6.5	4.0	76.32	-6.25	GD	0.681	VR	P
11.5	8.0	6.6	105.00	-6.71	D	0.795	VR	P
12.0	8.0	5.5	97.08	-6.60	D	0.680	VR	P
6.0	3.8	3.0	48.41	-5.60	D	0.734	VR	P
6.8	3.2	1.8	38.72	-5.20	B	0.530	VR	P
5.8	4.2	2.6	49.40	-5.63	GD	0.652	R	P
10.8	8.0	6.5	100.06	-6.69	D	0.788	VR	P
9.0	5.8	4.6	74.03	-6.21	B	0.740	SR	T
8.6	7.0	4.6	83.76	-6.39	D	0.706	R	P
9.8	8.5	2.6	88.89	-6.47	D	0.433	VR	T
5.0	4.2	2.5	48.88	-5.61	B	0.668	SR	T
15.0	13.5	9.0	162.25	-7.34	GD	0.737	VR	T
6.2	5.4	2.5	59.51	-5.89	D	0.572	R	P
5.5	3.5	2.5	43.01	-5.43	GT	0.687	R	P

Axial dimensions (cm)			Clast/sieve size[1] (mm)	Clast/sieve size[2] (ϕ)	Lithology[3]	Maximum Projection Sphericity[4]	Visual Roundness Class[5]	Clast a-axis Orientation[6]
a	b	c						
18.5	12.5	6.5	140.69	-7.14	B	0.597	VR	T
12.0	9.5	6.5	115.11	-6.85	GD	0.716	VR	T
12.5	8.5	4.5	79.06	-6.30	B	0.629	SA	P
10.5	8.5	5.5	101.24	-6.66	GD	0.697	VR	T
9.8	8.0	4.2	90.35	-6.50	GD	0.608	R	T
12.0	10.5	6.0	120.93	-6.92	B	0.659	VR	T
10.5	7.0	4.0	80.62	-6.33	D	0.602	VR	P
8.5	5.4	2.8	60.83	-5.93	B	0.555	R	T
7.2	5.0	3.0	58.31	-5.87	B	0.630	R	P
4.1	3.5	1.5	38.08	-5.25	D	0.539	VR	T
8.6	6.3	4.2	75.72	-6.24	B	0.688	VR	P
4.5	4.2	3.5	54.67	-5.77	GD	0.885	VR	P
6.1	4.2	3.1	52.20	-5.71	GT	0.721	VR	T
3.0	2.5	1.3	28.18	-4.82	GD	0.809	VR	T
6.3	5.5	1.7	57.57	-5.85	B	0.437	VR	P
5.2	3.6	2.6	44.41	-5.47	B	0.712	R	P
5.2	3.0	2.8	41.04	-5.36	B	0.706	R	T
3.7	3.5	3.0	46.10	-5.53	B	0.886	SR	T
3.9	3.6	2.0	41.18	-5.36	AG	0.658	VR	T
4.4	2.8	2.3	36.24	-5.18	B	0.754	SA	T
12.3	8.3	7.0	108.58	-6.76	D	0.783	VR	T
9.8	6.5	5.4	84.50	-6.40	GD	0.771	VR	P
6.6	4.8	4.0	62.48	-5.97	B	0.796	SR	P
4.6	2.5	2.2	33.30	-5.06	B	0.749	SA	T
3.2	2.5	2.0	32.02	-5.00	GT	0.794	VR	T
5.0	4.0	3.0	50.00	-5.64	AG	0.725	R	P
6.5	4.5	3.2	55.22	-5.79	GN	0.705	SR	T
6.6	4.5	2.0	49.24	-5.62	B	0.513	SR	T
5.1	4.4	1.7	47.17	-5.56	D	0.505	SR	T
Q23 (50.63 km)								
24.0	16.0	8.0	176.89	-7.46	GB	0.560	VR	T
16.0	13.0	7.0	147.65	-7.21	D	0.618	VR	T
14.0	8.0	5.0	94.34	-6.56	B	0.607	R	T
14.0	11.0	7.0	130.38	-7.03	B	0.683	SR	T
10.0	8.5	4.0	93.94	-6.55	GB	0.573	VR	T
12.0	9.0	5.0	102.96	-6.69	B	0.614	VR	P
17.0	16.0	13.0	205.16	-7.69	GT	0.853	VR	N
17.0	12.0	8.0	144.22	-7.17	GD	0.670	VR	P
10.0	7.0	4.5	83.22	-6.38	B	0.661	R	P
11.0	7.0	3.0	76.16	-6.25	B	0.489	VR	T
15.0	11.0	7.0	130.38	-7.03	B	0.667	R	P
8.0	6.0	5.5	81.39	-6.35	GD	0.857	VR	T
13.0	8.0	5.0	94.34	-6.56	GD	0.622	VR	T
20.0	14.0	7.0	156.52	-7.29	GT	0.559	SR	P
11.0	7.0	4.0	80.62	-6.33	D	0.592	VR	P
9.0	4.0	3.0	50.00	-5.64	GB	0.630	VR	P
27.0	21.0	11.0	237.07	-7.89	GD	0.598	VR	P
16.0	12.0	7.0	138.92	-7.12	GD	0.634	VR	P
13.0	7.0	4.5	83.22	-6.38	GB	0.605	VR	P
8.0	6.5	3.0	71.59	-6.16	B	0.557	R	T
11.0	8.0	6.0	100.00	-6.64	GD	0.742	VR	P
12.0	9.0	6.0	108.17	-6.76	GD	0.693	VR	T
10.0	6.5	4.5	79.06	-6.30	GD	0.678	VR	T
11.0	8.5	6.5	107.00	-6.74	GT	0.767	VR	P
16.0	9.5	5.5	109.77	-6.78	B	0.584	VR	P

Axial dimensions (cm)			Clast/sieve size[1] (mm)	Clast/sieve size[2] (ϕ)	Lithology[3]	Maximum Projection Sphericity[4]	Visual Roundness Class[5]	Clast a-axis Orientation[6]
a	b	c						
16.0	13.0	10.0	164.01	-7.36	GD	0.753	VR	P
12.5	7.5	6.0	96.06	-6.59	B	0.727	SR	P
13.0	10.0	9.0	134.54	-7.07	D	0.854	VR	T
11.0	11.0	8.5	139.01	-7.12	GD	0.842	VR	N
11.0	7.0	5.0	86.02	-6.43	B	0.687	VR	T
11.0	7.0	4.5	83.22	-6.38	GD	0.841	VR	P
9.0	6.0	3.0	65.44	-6.42	B	0.500	VR	T
25.0	19.0	7.0	302.48	-7.86	D	0.480	VR	T
9.0	8.5	5.0	98.82	-6.62	GD	0.689	R	T
11.0	9.0	6.0	108.17	-6.76	D	0.714	VR	T
19.0	13.0	12.0	176.02	-7.47	GD	0.835	VR	P
11.5	10.0	4.5	109.66	-6.78	GB	0.661	VR	T
10.5	6.0	5.5	81.39	-6.35	GD	0.783	VR	P
14.0	11.0	7.0	130.38	-7.03	GD	0.683	VR	P
11.0	9.0	7.0	114.02	-6.83	GD	0.791	VR	T
17.0	12.0	9.0	150.00	-7.23	GD	0.735	VR	T
12.5	10.0	5.5	114.13	-6.83	GB	0.623	R	T
70.0	30.0	30.0	424.26	-8.73	GD	0.754	VR	P
38.0	30.0	20.0	360.56	-8.49	GD	0.718	VR	P
13.3	11.0	6.5	127.77	-7.00	GB	0.661	VR	Q
12.0	10.0	5.0	111.80	-6.80	GD	0.693	VR	P
17.0	10.5	5.0	116.30	-6.86	B	0.519	VR	T
11.0	9.5	8.0	124.30	-6.96	GT	0.840	VR	P
8.0	6.5	2.5	69.64	-6.12	B	0.494	VR	T
24.0	18.0	8.0	196.98	-7.62	GD	0.529	VR	P
12.3	10.0	5.0	111.80	-6.80	GB	0.588	VR	P
10.4	10.2	5.0	113.60	-6.83	GB	0.618	R	N
8.0	7.0	5.0	86.02	-6.43	GB	0.764	VR	P
11.0	6.5	5.0	82.01	-6.36	GB	0.704	VR	T
9.0	7.0	4.5	83.22	-6.38	GB	0.685	VR	P
6.5	6.0	4.0	72.11	-6.17	GD	0.743	VR	T
43.0	28.0	19.0	338.38	-8.40	D	0.660	VR	T
30.0	25.0	16.0	295.82	-8.21	GD	0.699	VR	T
31.0	24.0	17.0	294.11	-8.20	GT	0.730	VR	P
24.0	15.0	13.0	195.49	-7.63	B	0.777	VR	P
17.0	12.5	9.0	154.03	-7.27	GD	0.725	VR	P
7.8	5.3	4.3	68.25	-6.09	GD	0.765	VR	P
4.1	3.5	2.3	41.88	-5.39	D	0.717	VR	T
3.2	2.7	2.3	35.47	-5.15	GD	0.849	VR	P
5.8	3.5	3.0	46.10	-5.53	GT	0.763	VR	T
5.5	4.0	3.5	53.15	-5.73	GD	0.823	VR	P
6.5	4.0	3.0	50.00	-5.64	GD	0.702	R	P
5.2	5.0	2.3	55.04	-5.78	B	0.588	SR	P
9.0	8.0	6.0	100.00	-6.64	B	0.794	R	P
6.0	5.7	3.8	68.51	-6.10	GD	0.750	SR	T
6.2	4.8	3.6	60.00	-5.91	GB	0.758	VR	P
6.7	5.0	1.8	53.14	-5.73	B	0.459	SA	P
4.4	2.5	1.8	30.81	-4.95	GB	0.685	SA	T
14.5	6.2	5.0	79.65	-6.32	B	0.653	VR	P
5.1	2.2	1.6	27.20	-4.77	B	0.611	SA	T
3.1	2.7	1.6	31.38	-4.97	GD	0.674	SR	T
6.0	5.5	3.0	62.65	-5.97	GD	0.649	SR	T
5.5	3.0	2.1	35.62	-5.19	GB	0.644	R	T
3.4	1.9	1.4	23.60	-4.56	GB	0.672	VR	T
4.8	3.9	2.5	46.32	-5.53	GT	0.694	R	P
5.2	3.3	1.7	37.12	-5.21	B	0.552	SR	T

Axial dimensions (cm)			Clast/sieve size[1] (mm)	Clast/sieve size[2] (ϕ)	Lithology[3]	Maximum Projection Sphericity[4]	Visual Roundness Class[5]	Clast a-axis Orientation[6]
a	b	c						
4.8	4.0	3.5	53.15	-5.73	GD	0.881	VR	T
4.2	4.0	1.5	42.72	-5.42	GT	0.512	SR	T
7.5	5.7	4.3	71.40	-6.16	B	0.756	R	T
8.3	6.0	4.5	75.00	-6.23	GD	0.741	VR	P
5.9	5.0	3.5	61.03	-5.93	GD	0.759	VR	T
4.7	3.8	2.5	43.83	-5.45	GD	0.718	VR	T
5.1	4.0	2.0	44.72	-5.48	B	0.581	R	T
6.7	5.0	4.0	64.03	-6.00	GT	0.782	VR	P
3.0	2.8	1.7	32.76	-5.03	GT	0.701	VR	T
5.5	3.2	2.4	40.00	-5.32	GD	0.689	VR	T
4.0	3.5	2.5	43.01	-5.43	B	0.764	VR	P
5.0	3.0	2.3	37.60	-5.24	GT	0.707	VR	P
7.4	5.0	4.8	69.31	-6.12	B	0.854	SA	T
5.4	2.9	2.0	35.23	-5.14	GN	0.634	R	T
2.7	2.0	1.5	25.00	-4.64	GT	0.747	SA	P
5.3	3.8	2.7	46.62	-5.54	GD	0.713	R	P
4.0	2.5	1.3	28.18	-4.82	B	0.553	SR	P
9.0	7.0	4.5	83.22	-6.38	GT	0.685	SR	P
11.0	7.0	5.0	86.02	-6.43	GD	0.687	SR	T
8.0	4.0	2.0	44.72	-5.48	G[illegible]	0.500	R	T
4.0	3.0	1.0	31.62	-4.98	GD	0.437	SR	P
5.0	3.5	2.0	40.31	-5.33	B	0.611	SA	P
5.0	3.0	1.5	33.54	-5.07	GD	0.531	SR	P
4.0	2.5	1.5	29.15	-4.87	GD	0.608	SR	P
5.0	4.0	2.5	47.17	-5.56	GT	0.670	SR	T
7.5	4.5	3.5	57.01	-5.83	GD	0.713	R	P
8.0	6.0	4.5	75.00	-6.23	D	0.750	SR	T
11.5	9.0	6.0	108.17	-6.76	GD	0.703	VR	T
9.0	7.5	5.5	93.01	-6.54	GD	0.765	VR	T
24.0	20.0	14.0	244.13	-7.93	GD	0.742	VR	T
9.0	7.0	5.0	86.02	-6.43	GD	0.735	R	P
7.0	6.0	3.5	69.46	-6.12	GT	0.663	R	P
8.0	7.0	5.0	86.02	-6.43	GT	0.764	R	T
14.0	12.5	11.0	166.51	-7.38	D	0.884	VR	T
16.0	13.0	8.0	152.64	-7.25	GD	0.675	VR	T
8.5	6.0	5.0	76.10	-6.26	GD	0.788	VR	P
6.2	4.0	1.8	43.86	-5.45	B	0.507	SR	P
8.6	6.5	6.0	88.46	-6.47	GB	0.884	VR	P
8.4	6.0	5.0	78.10	-6.29	GT	0.702	VR	T
8.0	6.0	3.0	67.08	-6.07	GB	0.572	VR	P
5.1	3.2	1.3	34.54	-5.11	B	0.470	SA	T
13.0	7.0	4.0	80.62	-6.33	B	0.560	VR	T
15.0	14.0	7.0	156.52	-7.20	GD	0.816	VR	T
9.5	7.8	4.0	87.66	-6.45	GB	0.600	VR	T
6.0	3.3	3.0	44.60	-5.48	B	0.769	VR	T
4.0	3.0	2.5	39.05	-5.29	GD	0.805	R	T
5.0	4.2	2.0	46.52	-5.54	GB	0.575	VR	P
17.5	14.0	10.5	175.00	-7.45	GB	0.766	VR	P
7.0	6.5	4.5	79.06	-6.30	D	0.763	VR	N
12.0	9.5	6.0	112.36	-6.81	B	0.681	VR	T
15.0	8.0	5.0	94.34	-6.56	GB	0.593	R	P
6.4	4.1	1.7	44.38	-5.47	B	0.479	VR	P
9.0	6.5	4.5	79.06	-6.30	GD	0.702	SR	P
4.4	3.4	2.2	40.50	-5.34	GB	0.686	VR	P
3.7	3.2	2.6	41.23	-5.37	GB	0.830	VR	T
5.4	4.2	3.2	52.80	-5.72	GT	0.767	R	T

Axial dimensions (cm)			Clast/sieve size[1] (mm)	Clast/sieve size[2] (ϕ)	Lithology[3]	Maximum Projection Sphericity[4]	Visual Roundness Class[5]	Clast a-axis Orientation[6]
a	b	c						
10.1	5.7	2.0	60.41	-5.92	GB	0.411	VR	P
4.2	4.0	2.8	48.83	-5.61	GD	0.776	VR	P
8.0	5.5	3.2	63.63	-5.99	GT	0.615	VR	P
6.8	4.9	3.3	59.08	-5.88	GB	0.689	VR	T
13.9	9.7	4.0	104.92	-6.71	B	0.491	R	P
9.5	7.5	5.0	90.14	-6.49	GD	0.705	R	P
5.3	5.3	2.8	59.94	-5.91	GD	0.654	VR	N
4.1	3.0	2.0	38.08	-5.17	GT	0.688	R	P
15.5	13.0	9.0	158.11	-7.30	GD	0.738	VR	P
4.6	3.5	3.0	48.10	-5.53	GD	0.824	VR	P
18.0	13.5	9.0	182.25	-7.34	D	0.693	VR	T
8.4	5.0	3.2	59.38	-5.89	GD	0.684	VR	P
5.3	3.4	3.2	48.69	-5.55	GT	0.828	VR	T
8.0	7.0	3.8	70.65	-6.32	GD	0.636	VR	T
12.0	6.8	3.8	77.90	-6.28	GT	0.561	VR	O
18.0	13.0	8.0	152.64	-7.25	GT	0.649	VR	P
15.0	13.5	8.0	156.92	-7.29	D	0.681	VR	N
13.8	10.5	8.5	135.00	-7.08	GD	0.793	VR	T
7.8	6.5	5.4	84.50	-6.40	GD	0.832	VR	P
9.0	7.2	5.5	90.60	-6.50	GD	0.776	R	T
7.5	6.0	4.0	72.11	-6.17	GB	0.708	VR	P
12.0	10.5	8.0	132.00	-7.04	GD	0.798	VR	T
14.0	11.0	10.0	148.66	-7.22	GD	0.666	VR	T
9.5	8.0	5.5	97.08	-6.60	D	0.736	VR	P
11.0	9.0	5.5	105.48	-6.72	GD	0.674	VR	T
19.0	13.0	9.5	161.01	-7.33	GD	0.715	VR	T
17.0	14.0	8.0	152.32	-7.25	GD	0.533	VR	T
27.0	20.0	11.0	228.25	-7.83	GD	0.607	VR	T
20.0	18.0	7.0	193.13	-7.59	D	0.514	VR	P
16.0	12.5	11.0	166.51	-7.38	GD	0.646	VR	P
19.0	14.0	12.0	184.39	-7.53	GD	0.615	VR	T
32.0	18.0	17.0	247.59	-7.95	GD	0.705	VR	P
20.0	18.5	10.0	210.30	-7.72	D	0.647	VR	T
7.2	6.5	3.5	73.62	-6.21	GT	0.640	VR	P
8.2	4.0	3.5	53.15	-5.73	B	0.720	VR	T
5.2	4.6	3.0	54.92	-5.78	D	0.722	VR	P
7.7	6.0	3.7	70.40	-6.14	GD	0.667	VR	P
8.8	8.0	4.5	91.79	-6.52	D	0.660	VR	N
9.4	7.0	5.5	89.02	-6.48	GD	0.772	VR	P
25.0	15.0	9.0	174.93	-7.45	GD	0.600	VR	T
10.7	9.5	6.2	113.44	-6.83	GD	0.723	VR	P
20.0	12.0	7.0	138.92	-7.12	GD	0.589	R	O
8.0	8.0	7.0	108.30	-6.73	GT	0.915	VR	N
10.0	5.0	2.5	55.90	-5.80	B	0.500	SR	T
11.5	8.0	6.0	100.00	-6.64	B	0.731	VR	T
20.0	18.0	11.5	213.60	-7.74	D	0.716	VR	T
9.8	6.5	4.0	76.32	-6.25	GT	0.631	R	T
10.4	8.0	3.4	88.93	-6.44	GD	0.518	R	P
8.0	7.0	3.5	78.26	-6.29	GB	0.603	VR	T
22.0	13.0	12.0	176.92	-7.47	D	0.708	VR	T
9.8	8.0	3.5	87.32	-6.45	D	0.539	R	T
15.0	11.0	8.0	136.01	-7.09	GD	0.729	VR	T
11.5	10.0	8.0	128.06	-7.00	GD	0.823	VR	T
16.0	11.3	8.2	139.62	-7.13	GB	0.719	VR	O
12.2	10.3	7.5	127.41	-6.99	GD	0.765	VR	T
8.0	6.4	2.5	68.71	-6.10	B	0.498	R	P

Axial dimensions (cm)			Clast/sieve size[1] (mm)	Clast/sieve size[2] (ϕ)	Lithology[3]	Maximum Projection Sphericity[4]	Visual Roundness Class[5]	Clast a-axis Orientation[6]
a	b	c						
8.4	6.0	5.0	78.10	-6.29	GD	0.792	VR	O
17.0	14.0	11.0	178.04	-7.48	GD	0.798	VR	T
12.5	12.3	6.5	139.12	-7.12	GT	0.650	VR	N
26.5	16.5	12.0	204.02	-7.67	GD	0.691	VR	T
16.0	10.0	8.0	128.08	-7.00	B	0.737	SR	T
14.0	11.5	5.0	126.40	-6.97	GD	0.537	VR	T
11.5	6.5	5.0	82.01	-6.36	D	0.694	VR	T
19.0	15.0	10.0	180.28	-7.49	GD	0.705	VR	T
18.0	11.0	8.0	136.01	-7.09	GB	0.686	R	P
9.0	7.5	5.0	90.14	-6.49	GD	0.718	VR	P
22.0	19.0	11.0	210.54	-7.78	GT	0.662	VR	T
10.0	8.7	5.0	100.34	-6.65	B	0.660	VR	T
12.0	9.5	4.0	103.08	-6.69	B	0.520	SR	P
10.0	8.0	5.0	78.10	-6.29	GB	0.747	VR	T
6.0	5.0	3.5	61.03	-5.93	D	0.742	VR	P
7.0	6.0	3.0	67.08	-6.07	GT	0.598	VR	T
8.0	5.0	4.0	64.03	-6.00	B	0.737	SR	P
10.0	8.0	4.5	91.79	-6.52	B	0.633	R	P
12.0	9.0	5.0	102.96	-6.69	GD	0.614	VR	P
12.0	9.0	6.0	108.17	-6.76	D	0.693	VR	T
16.0	12.0	7.0	138.92	-7.12	GD	0.634	VR	T
22.0	17.0	8.0	187.68	-7.55	GD	0.555	VR	T
7.5	4.5	4.0	60.21	-5.91	GD	0.780	VR	P
18.0	14.0	8.0	161.25	-7.33	GD	0.633	VR	P
8.5	6.0	4.5	75.00	-6.23	D	0.735	VR	T
10.0	6.0	5.0	78.10	-6.29	GT	0.747	R	T
11.0	9.0	6.0	108.17	-6.76	GD	0.714	VR	T
11.0	8.0	3.0	85.44	-6.42	B	0.468	R	T
11.5	9.5	6.0	112.36	-6.81	B	0.691	R	T
8.0	6.0	4.0	72.11	-6.17	GB	0.693	VR	T
14.0	11.0	8.0	136.01	-7.09	GD	0.746	VR	T
14.0	8.0	7.0	105.30	-6.73	B	0.750	R	P
10.5	7.5	4.0	85.00	-6.41	B	0.588	VR	P
12.0	10.0	6.5	119.27	-6.90	GD	0.705	VR	T
12.0	8.0	5.0	94.34	-6.56	B	0.630	VR	P
10.0	7.0	3.0	76.16	-6.25	B	0.505	VR	P
8.5	7.0	5.5	89.02	-6.48	B	0.798	SR	P
17.0	10.0	7.0	122.07	-6.93	GD	0.661	VR	P
16.0	10.0	6.0	116.62	-6.87	D	0.608	R	T
16.0	12.0	7.0	138.92	-7.12	GD	0.634	VR	T
11.0	8.0	6.0	100.00	-6.64	GD	0.742	VR	P
8.0	6.5	4.5	79.06	-6.30	GD	0.730	VR	T
6.0	4.0	3.0	50.00	-5.64	D	0.721	VR	P
22.0	17.0	9.0	192.35	-7.59	GD	0.601	R	T
18.0	10.0	9.0	134.54	-7.07	D	0.766	VR	P
11.0	7.5	4.0	85.00	-6.41	D	0.570	VR	P
8.0	7.4	4.0	84.12	-6.39	GD	0.647	VR	P
9.0	8.5	6.5	107.00	-6.74	D	0.820	VR	N
15.0	9.5	7.0	118.00	-6.88	GD	0.701	R	T
9.0	8.0	5.0	94.34	-6.56	GT	0.703	VR	T
9.3	8.0	3.5	87.32	-6.45	GB	0.548	VR	T
7.0	5.3	4.0	66.40	-6.05	B	0.756	R	T
18.0	11.0	8.0	136.01	-7.09	GD	0.686	VR	T
20.0	11.0	9.0	142.13	-7.15	GB	0.717	VR	T
10.0	7.0	6.5	95.52	-6.58	GT	0.845	R	T
14.0	11.0	9.0	142.13	-7.15	GD	0.807	VR	T

Axial dimensions (cm)			Clast/sieve size[1] (mm)	Clast/sieve size[2] (ϕ)	Lithology[3]	Maximum Projection Sphericity[4]	Visual Roundness Class[5]	Clast a-axis Orientation[6]
a	b	c						
9.5	7.5	4.0	85.00	-6.41	GT	0.606	VR	P
19.0	12.0	8.0	144.22	-7.17	GT	0.655	VR	P
30.0	11.0	11.0	155.56	-7.28	D	0.619	VR	P
9.5	8.5	5.5	101.24	-6.66	GD	0.721	VR	T
14.0	10.0	6.0	116.62	-6.87	GB	0.636	VR	T
18.0	13.0	7.0	147.65	-7.21	GB	0.594	R	P
17.5	11.0	7.5	133.14	-7.06	GD	0.684	VR	P
19.0	17.0	13.0	214.01	-7.74	GD	0.606	VR	O
12.0	10.5	8.0	132.00	-7.04	GD	0.709	VR	P
12.0	10.0	7.5	126.00	-6.97	GD	0.777	R	T
6.0	6.0	4.4	74.40	-6.22	GB	0.613	VR	N
11.5	8.5	6.5	107.00	-6.74	B	0.756	SR	T
12.0	10.0	10.0	141.42	-7.14	GD	0.941	VR	T
19.0	13.0	6.0	143.18	-7.16	GD	0.536	VR	P
12.0	12.0	7.5	141.51	-7.14	GD	0.731	VR	N
15.0	10.0	7.5	125.00	-6.97	GD	0.721	VR	P
20.0	14.0	13.0	191.05	-7.58	GD	0.845	VR	T
24.0	16.0	12.0	200.00	-7.64	GD	0.721	VR	P
9.0	6.0	5.0	78.10	-6.29	GD	0.774	VR	P
12.0	8.0	4.5	91.79	-6.52	GD	0.595	VR	T
8.0	6.5	4.5	79.06	-6.30	GT	0.730	VR	T
6.0	4.0	3.0	50.00	-5.64	GT	0.721	VR	P
19.0	14.0	8.0	161.25	-7.33	GD	0.622	VR	T
20.0	15.0	9.0	174.93	-7.45	D	0.646	VR	T
18.0	16.0	8.0	176.89	-7.48	B	0.606	VR	T
14.0	11.0	6.0	125.30	-6.97	GD	0.616	R	T
13.0	9.0	6.0	108.17	-6.76	D	0.675	VR	P
21.0	11.0	7.0	130.38	-7.03	GD	0.596	VR	T
19.0	11.0	7.0	130.38	-7.03	B	0.617	R	T
16.0	12.0	8.0	144.22	-7.17	GD	0.693	VR	P
14.0	12.0	4.0	126.40	-6.98	B	0.457	VR	T
9.0	7.0	5.0	68.02	-6.43	GD	0.735	SR	P
7.0	5.0	3.0	58.31	-5.87	B	0.639	R	T
9.0	7.5	4.0	85.00	-6.41	GD	0.610	VR	T
8.0	6.0	4.5	75.00	-6.23	GD	0.750	VR	P
7.0	5.0	3.5	61.03	-5.93	GT	0.705	VR	T
13.0	9.0	8.0	120.42	-6.91	GT	0.818	VR	T
24.0	17.0	10.0	197.23	-7.62	GD	0.626	VR	T
17.0	10.0	7.0	122.07	-6.93	GD	0.661	VR	P
17.0	11.0	7.0	130.38	-7.03	GD	0.640	R	T
9.0	7.0	5.0	68.02	-6.43	D	0.735	VR	P
15.0	11.0	8.0	125.30	-6.97	GD	0.602	VR	P
13.0	9.0	5.0	102.96	-6.69	B	0.598	SR	T
9.0	6.0	2.0	63.25	-5.98	B	0.420	VR	T
12.0	8.0	5.0	78.10	-6.29	GD	0.703	VR	P
QF (38.38 km)								
11.0	7.5	7.0	102.59	-6.69	GD	0.841	VR	T
10.5	5.5	3.0	62.65	-5.97	B	0.536	R	T
7.5	7.0	4.8	84.88	-6.41	GT	0.760	R	N
8.8	7.8	4.5	90.05	-6.49	GT	0.666	R	P
13.2	8.0	4.7	92.78	-6.54	GB	0.594	VR	P
10.0	8.8	5.8	105.39	-6.72	GD	0.726	VR	P
6.7	4.2	2.5	48.88	-5.61	GD	0.605	R	T
8.6	6.4	2.5	68.71	-6.10	B	0.484	VR	T
9.4	6.5	4.2	77.39	-6.27	B	0.661	SR	P

Axial dimensions (cm)			Clast/sieve size[1] (mm)	Clast/sieve size[2] (ϕ)	Lithology[3]	Maximum Projection Sphericity[4]	Visual Roundness Class[5]	Clast a-axis Orientation[6]
a	b	c						
7.0	5.5	2.0	58.52	-5.87	GB	0.670	VR	P
11.5	6.5	4.0	93.94	-6.55	B	0.547	R	T
11.0	7.0	6.0	92.20	-6.53	B	0.778	VR	P
7.8	6.0	3.5	69.46	-6.12	GB	0.640	VR	P
10.0	7.5	6.0	95.05	-6.59	GD	0.783	VR	P
7.5	5.0	3.5	61.03	-5.93	B	0.680	VR	T
16.5	10.0	10.0	141.42	-7.14	GD	0.846	VR	P
8.5	8.3	4.4	93.94	-6.55	GB	0.650	VR	T
9.5	8.0	5.7	82.76	-6.37	D	0.829	VR	P
10.2	6.5	4.5	79.08	-6.30	GT	0.673	VR	T
10.0	7.0	5.0	88.02	-6.43	GD	0.709	VR	P
9.8	8.0	6.0	100.00	-6.64	GT	0.771	SR	P
7.0	5.0	3.0	58.31	-5.87	B	0.638	SA	T
5.3	4.3	3.0	52.43	-5.71	GD	0.734	VR	P
5.5	4.0	3.0	50.00	-5.64	GD	0.742	VR	P
10.2	8.6	5.0	99.48	-6.64	GB	0.658	VR	P
6.7	3.5	2.2	41.34	-5.37	B	0.591	R	T
7.8	5.5	4.0	68.01	-6.09	GD	0.726	VR	T
5.6	4.5	4.0	60.21	-5.91	GD	0.859	VR	T
13.5	9.0	7.0	114.02	-6.83	GD	0.739	VR	T
10.2	5.5	3.0	62.65	-5.97	GB	0.543	VR	T
11.5	8.0	6.0	100.00	-6.64	GT	0.731	R	T
8.5	7.5	2.0	77.62	-6.28	B	0.397	VR	T
11.5	6.5	3.0	71.59	-6.16	B	0.494	R	P
9.5	6.0	3.5	69.46	-6.12	GD	0.599	R	T
11.0	6.5	5.0	82.01	-6.36	GB	0.704	R	P
7.5	9.0	4.0	72.11	-6.17	GB	0.708	SR	N
10.5	9.0	6.5	111.02	-6.79	D	0.765	VR	T
8.0	6.5	4.5	79.06	-6.30	GB	0.730	VR	T
13.0	11.0	6.0	125.30	-6.97	GT	0.631	SR	P
8.5	5.0	2.5	55.90	-5.80	B	0.528	VR	T
10.0	7.0	5.5	89.02	-6.48	GT	0.756	R	T
10.0	8.5	7.0	110.11	-6.78	GD	0.832	R	P
9.5	6.0	3.5	69.46	-6.12	B	0.599	R	T
10.0	8.0	4.5	91.79	-6.52	B	0.633	R	P
20.0	17.0	6.0	180.28	-7.49	B	0.473	SR	P
8.0	7.0	3.0	76.16	-6.25	GD	0.544	R	T
6.0	4.0	2.5	47.17	-5.56	B	0.639	VR	P
6.5	4.0	3.5	53.15	-5.73	GD	0.778	SR	P
11.5	10.0	6.5	119.27	-6.90	GD	0.716	VR	T
7.0	5.0	3.5	61.03	-5.93	B	0.705	VR	T
7.0	6.5	4.0	76.32	-6.25	GT	0.708	VR	T
9.0	4.0	3.0	50.00	-5.64	B	0.630	SR	P
10.5	5.0	4.0	64.03	-6.00	B	0.673	SR	T
8.0	6.0	4.5	75.00	-6.23	GD	0.750	VR	P
5.5	4.0	3.0	50.00	-5.64	GD	0.742	R	T
7.0	5.5	4.5	71.06	-6.15	GD	0.807	VR	T
14.0	8.0	6.0	100.00	-6.64	B	0.685	VR	P
9.0	6.0	4.5	75.00	-6.23	GT	0.721	R	P
11.5	10.0	7.0	122.07	-6.93	GD	0.752	VR	P
6.5	5.5	4.0	68.01	-6.09	GD	0.765	VR	T
Q34 (38.04 km)								
8.0	5.0	4.0	64.03	-6.00	GT	0.737	R	P
9.5	6.5	5.5	85.15	-6.41	D	0.788	R	P
6.0	4.0	3.0	50.00	-5.64	B	0.721	SR	P

Axial dimensions (cm)			Clast/sieve size[1] (mm)	Clast/sieve size[2] (ϕ)	Lithology[3]	Maximum Projection Sphericity[4]	Visual roundness Class[5]	Clast a-axis Orientation[6]
a	b	c						
6.0	3.5	3.0	46.10	-5.53	GT	0.764	R	T
5.0	4.5	2.5	51.48	-5.69	B	0.662	R	P
4.5	3.5	1.5	38.08	-5.25	GD	0.523	SR	P
14.5	12.0	3.5	126.00	-6.97	B	0.413	SR	P
5.0	3.5	2.0	40.31	-5.33	GB	0.611	R	P
5.0	4.5	2.0	49.24	-5.62	GD	0.562	R	P
5.0	4.0	3.5	53.15	-5.73	D	0.849	VR	P
5.0	4.0	3.0	50.00	-5.64	GT	0.766	SA	T
3.5	3.0	1.0	31.62	-4.98	B	0.457	SR	T
3.5	3.5	2.0	40.31	-5.33	B	0.689	SR	N
8.0	6.0	5.0	78.10	-6.29	GB	0.805	VR	P
6.0	4.5	2.0	49.24	-5.62	GY	0.529	SR	P
6.0	3.5	2.5	43.01	-5.43	GD	0.668	SR	P
5.5	4.0	3.5	53.15	-5.73	GT	0.893	R	N
3.5	3.0	2.0	36.06	-5.17	GT	0.725	SR	T
4.5	3.0	2.0	36.06	-5.17	D	0.667	R	P
6.0	3.0	2.5	39.05	-5.29	B	0.703	A	P
5.0	4.5	2.5	51.48	-5.69	GT	0.662	R	T
8.5	6.5	6.0	88.48	-6.47	GT	0.887	VR	T
10.0	6.5	2.5	69.64	-6.12	B	0.458	R	T
12.5	10.0	6.0	116.62	-6.87	GT	0.660	R	P
7.5	6.5	4.0	76.32	-6.25	GT	0.690	SR	T
5.5	4.5	2.5	51.48	-5.69	GT	0.632	SR	P
4.5	3.5	2.5	43.01	-5.43	B	0.735	SR	T
5.5	4.5	3.0	54.08	-5.76	GT	0.714	R	T
6.5	3.0	2.5	39.05	-5.29	GT	0.684	R	T
6.5	5.5	4.0	68.01	-6.09	D	0.765	VR	P
3.0	2.0	1.9	27.59	-4.79	B	0.844	SR	T
5.5	4.8	4.0	62.48	-5.97	GD	0.846	SR	T
5.5	2.2	2.2	31.11	-4.96	B	0.737	R	T
5.5	3.8	1.3	40.16	-5.33	GY	0.432	R	T
13.5	9.0	6.5	111.02	-6.79	B	0.703	SA	T
4.3	4.2	2.7	49.03	-5.64	GT	0.739	R	N
8.2	6.5	1.8	67.45	-6.08	GB	0.393	VR	T
8.0	4.5	4.5	63.64	-5.99	GD	0.825	R	P
14.0	5.6	3.5	66.04	-6.05	B	0.530	R	P
3.0	3.0	2.5	39.05	-5.29	D	0.886	VR	N
5.3	3.3	2.0	38.59	-5.27	B	0.612	VR	P
4.3	3.8	2.0	42.94	-5.42	B	0.626	SA	T
5.7	4.0	2.8	48.83	-5.61	GT	0.701	VR	T
8.5	6.0	3.0	67.08	-6.07	GT	0.561	VR	P
8.0	5.3	4.2	67.62	-6.08	GD	0.747	R	P
6.0	3.0	2.5	39.05	-5.29	GT	0.703	SR	O
4.5	3.0	1.8	34.99	-5.13	GD	0.621	SR	N
6.3	3.0	2.8	41.04	-5.36	B	0.748	R	T
10.0	6.0	5.0	78.10	-6.29	GT	0.747	VR	T
6.8	3.7	2.0	42.06	-5.39	B	0.542	VR	T
4.9	3.8	1.3	40.16	-5.33	B	0.449	R	P
8.2	5.8	2.3	62.39	-5.95	GD	0.481	A	T
5.3	3.8	1.8	42.05	-5.39	B	0.544	VR	P
11.2	9.0	2.5	93.41	-6.55	GB	0.398	SA	P
6.0	4.5	3.5	57.01	-5.83	GT	0.768	VR	P
7.2	4.7	3.0	55.76	-5.80	GD	0.643	R	T
5.6	3.5	3.5	49.50	-5.63	GD	0.855	R	P
7.0	5.2	4.7	70.09	-6.13	GT	0.847	VR	T
13.2	5.3	4.0	66.40	-6.05	B	0.612	SR	P

Axial dimensions (cm)			Clast/sieve size[1] (mm)	Clast/sieve size[2] (ϕ)	Lithology[3]	Maximum Projection Sphericity[4]	Visual Roundness Class[5]	Clast a-axis Orientation[6]
a	b	c						
5.5	4.5	2.5	51.48	-5.69	GT	0.632	SA	P
Q35 (35.14 km)								
9.5	7.5	5.0	90.14	-6.49	GD	0.705	VR	T
11.5	8.5	7.0	110.11	-6.78	GD	0.794	R	T
10.5	9.0	6.0	108.17	-6.76	GD	0.726	VR	T
10.3	8.2	7.2	109.12	-6.77	D	0.650	VR	T
13.5	12.5	9.0	154.03	-7.27	GT	0.783	VR	P
10.2	9.5	5.5	109.77	-6.78	D	0.679	R	P
16.0	11.5	9.0	148.03	-7.19	GD	0.781	VR	P
12.5	9.5	7.0	118.00	-6.88	D	0.744	R	P
11.0	8.5	7.0	110.11	-6.78	GB	0.808	VR	P
9.0	7.0	7.0	98.99	-6.63	GD	0.990	VR	P
12.5	10.0	7.0	122.07	-6.93	D	0.732	R	P
16.0	11.5	7.0	134.63	-7.07	GD	0.643	VR	P
14.0	6.0	6.0	84.85	-6.41	GY	0.754	SA	O
9.5	7.0	5.0	86.02	-6.43	GD	0.722	VR	T
10.7	9.1	6.5	111.83	-6.81	GD	0.757	VR	P
24.0	9.0	4.5	100.62	-6.65	GY	0.454	A	P
21.0	13.0	5.0	139.28	-7.12	GY	0.451	R	P
20.0	16.0	12.0	200.00	-7.64	GD	0.766	SR	P
22.0	18.0	10.0	205.91	-7.69	GD	0.632	VR	P
17.0	14.0	10.0	172.05	-7.43	GD	0.749	VR	T
15.5	11.0	9.5	145.34	-7.18	GD	0.800	VR	P
13.3	12.0	7.0	138.92	-7.12	GT	0.675	R	T
22.5	19.0	8.5	208.15	-7.70	GD	0.553	R	T
20.0	13.0	8.0	152.64	-7.25	D	0.627	VR	T
22.0	18.0	11.0	210.95	-7.72	GD	0.674	R	T
23.0	15.0	10.0	180.28	-7.49	GD	0.662	VR	T
11.5	11.5	4.3	122.78	-6.94	GD	0.519	VR	N
17.5	11.0	5.4	122.54	-6.94	B	0.533	SR	P
14.0	8.0	8.0	113.14	-6.82	GB	0.630	VR	P
16.0	10.0	6.5	119.27	-6.90	D	0.642	R	P
Q36 (37.48 km)								
14.0	10.0	8.0	128.06	-7.00	GB	0.770	VR	T
12.5	8.5	4.0	93.94	-6.55	GB	0.532	VR	P
16.0	14.0	7.0	155.52	-7.20	GT	0.603	VR	T
14.0	11.0	10.0	148.66	-7.22	GD	0.888	R	T
21.0	15.0	10.0	180.28	-7.49	GT	0.682	VR	P
16.0	11.0	9.0	142.13	-7.15	GD	0.772	R	T
15.0	11.0	6.0	125.30	-6.97	GD	0.602	R	P
11.0	8.0	7.0	105.30	-6.73	GT	0.823	VR	P
15.0	[illegible]	6.0	125.30	-6.97	D	0.602	R	T
19.0	[illegible]	10.0	172.05	-7.43	GD	0.722	R	T
9.0	[illegible]	7.5	109.66	-6.78	GT	0.921	VR	N
14.0	9.0	6.0	108.17	-6.76	GD	0.659	VR	P
16.0	11.0	10.0	148.66	-7.22	GD	0.828	VR	T
17.0	13.0	9.0	158.11	-7.30	GD	0.716	VR	P
20.0	13.0	9.0	158.11	-7.30	D	0.678	VR	T
18.0	9.0	8.0	120.42	-6.91	GD	0.734	VR	P
21.0	16.0	6.0	170.88	-7.42	GD	0.475	R	T
14.0	11.0	7.0	130.38	-7.03	D	0.683	VR	T
10.0	8.0	6.0	100.00	-6.64	GT	0.766	VR	T
13.0	11.0	9.0	142.13	-7.15	D	0.827	VR	T
20.0	14.0	8.0	161.25	-7.33	B	0.611	VR	P
15.0	11.0	10.0	148.66	-7.22	GD	0.846	VR	T

Axial dimensions (cm)			Clast/sieve size[1] (mm)	Clast/sieve size[2] (ϕ)	Lithology[3]	Maximum Projection Sphericity[4]	Visual Roundness Class[5]	Clast a-axis Orientation[6]
a	b	c						
14.5	9.0	9.0	108.17	-6.76	GD	0.651	R	T
13.0	7.0	4.5	83.22	-6.38	D	0.606	VR	P
14.0	8.0	5.0	78.10	-6.29	B	0.586	VR	T
12.0	9.0	6.0	108.17	-6.76	GD	0.685	R	T
13.0	10.0	6.0	116.62	-6.87	B	0.653	SR	P
14.0	11.0	9.0	142.13	-7.15	GT	0.807	R	P
13.0	8.0	8.0	113.14	-6.82	GD	0.851	R	T
14.0	10.0	7.0	122.07	-6.93	B	0.705	SR	T
10.0	8.0	5.0	94.34	-6.56	GD	0.679	SR	T
16.0	12.0	8.0	134.16	-7.07	GD	0.672	R	T
29.0	20.0	14.0	244.13	-7.93	D	0.697	VR	T
13.0	9.0	5.0	102.96	-6.69	GD	0.588	R	P
14.0	13.0	3.0	133.42	-7.06	B	0.387	VR	T
10.0	7.0	5.0	86.02	-6.43	GD	0.709	R	P
11.0	9.0	6.0	108.17	-6.76	B	0.714	SR	T
10.0	8.0	6.0	100.00	-6.64	GT	0.766	VR	T

[1] Clast/sieve size (s) in mm: $s = \sqrt{(b^2 + c^2)}$, where clast b-axis and c-axis dimensions are converted to mm.

[2] Clast/sieve size (z) in ϕ: $z = (-\log_{10}s)/(\log_{10}2)$.

[3] Lithology: AD, andesite; AG, argillite; B, metabasalt; D, diorite; GB, gabbro; GD, granodiorite; GN, gneiss; GT, granite; GY, greywacke.

[4] Sphericity: Values calculated using Maximum Projection Sphericity (Ψ_p, Sneed and Folk, 1958).

[5] Roundness: Data collected in the form of visual roundness classes (Powers, 1953). Calculations in the Table 5.5 are based on the geometric means (GM) of the visual roundness classes. VR, very rounded (GM = 0.84); R, rounded (GM = 0.59); SR, subrounded (GM = 0.41); SA, subangular (GM = 0.30); A, angular (GM = 0.21); VA, very angular (GM = 0.14).

[6] Orientation: Orientation of the clast a-axis with respect to the orientation of the maximum dip of its ab-plane. N, no obvious a-axis; O, a-axis oblique; P, a-axis parallel; T, a-axis transverse.

[7] No a-axis orientation data available for pit Q20.

APPENDIX 8

Fabric data[1] from gravel facies and structures within the Harricana glaciofluvial complex, Québec[2].

Q1/1-3RHS (Plane-bedded gravel)

0	80	5	28	315	40	345	64	350	37	50	37	20	24	80	52	85	32	25	45	18	52	344	14
30	40	350	65	355	80	5	38	55	15	65	48	340	52	45	20	345	18	55	42	325	45	295	25
220	7	10	78	325	47	315	51	305	13	50	15	53	38	15	42	325	35	335	28	5	62	65	28
38	50	30	25	25	17	355	65	55	13	65	56	45	15	70	50	35	22	95	18	100	65	320	45
358	42	345	68	155	7	340	52	20	25	330	20	0	27	355	18	350	15	348	48	352	42	305	65

Q1/1-3LHS (Plane-bedded gravel)

340	22	115	28	5	31	210	36	5	26	15	26	20	52	354	68	75	15	245	18	285	35	135	38
150	57	335	30	90	90	0	34	25	30	35	32	295	42	55	15	295	48	35	24	322	25	295	36
350	38	350	21	185	61	345	18	105	30	85	22	285	18	115	25	316	32	5	26	345	38	18	18
350	33	287	38	350	58	110	48	255	12	275	45	35	36	155	22	95	28	60	20	235	68	272	45
300	58	115	12	265	57	0	32	265	38	345	28	340	46	348	26	255	27	38	18	45	22	265	36

Q2B/3-1 (Imbricate, polymodal gravel with in-phase wave surfaces)

305	27	265	3	248	10	130	24	325	32	200	16	258	25	325	40	317	17	275	15	300	10	295	45
280	22	350	30	255	17	300	9	315	32	260	11	270	5	300	10	285	25	320	5	245	20	305	17
275	11	285	12	255	12	259	39	245	22	270	5	265	13	300	20	65	10	303	14	285	2	290	7
265	14	290	12	300	30	300	5	265	26	320	32	272	10	285	8	145	11	252	20	275	14	345	33
65	12	252	22	254	9	240	9	64	16	273	15	350	5	270	10	80	2	300	26	308	15	300	26

Q3/3-4LHS (Alternating oblique accretion avalanche bed macroform - east set of alternating sequence, 'flipped' clasts only)

270	10	5	60	130	45	90	54	320	25	318	14	100	35	305	65	305	24	295	32	130	42	50	38
350	30	290	20	5	17	10	30	320	3	305	31	285	34	100	18	335	38	270	18	295	44	308	26
105	30	100	10	10	48	23	40	315	15	285	50	320	22	335	45	298	35	50	34	275	32	80	26
53	27	158	78	130	30	330	30	310	35	295	45	290	24	290	32	345	75	110	18	305	22	355	34
215	5	90	40	340	51	20	65	300	71	325	18	315	58	325	60	285	32	245	32	335	58	65	15

Q3/3-4RHS (Alternating oblique accretion avalanche bed macroform - west set of alternating sequence, 'flipped' clasts only)

70	30	295	27	45	28	20	11	55	34	70	50	65	25	30	46	55	34	80	28	45	38	328	48
334	9	58	9	60	14	60	30	40	48	35	44	48	32	40	42	125	38	130	40	110	35	30	13
80	31	58	48	60	22	68	74	35	46	70	46	95	52	85	22	70	32	65	32	68	34	70	27
75	11	125	16	42	14	55	41	73	17	55	50	58	26	105	16	35	30	82	44	55	24	25	18
70	30	45	42	75	39	65	50	20	46	85	65	15	25	95	45	355	26	85	45	58	54	108	35

Q4/3-3 (Oblique accretion avalanche bed macroform - dipping to the east, full sample)

105	10	110	24	50	9	100	15	25	24	115	12	5	32	310	27	315	35	345	14	285	8	130	45
310	10	115	16	110	9	100	8	150	37	110	20	80	23	85	38	200	40	125	43	290	2	70	21
255	38	95	20	110	22	55	14	50	22	345	8	85	32	285	20	154	37	250	28	60	38	110	28
280	16	50	33	95	6	53	20	180	15	115	30	120	27	28	28	115	24	242	7	75	20	240	60
68	28	258	15	85	22	75	28	90	30	358	20	85	32	12	44	142	34	20	20	105	20	310	8

Q4/3-3 (Oblique accretion avalanche bed macroform - dipping to the east, 'parallel' clasts only)

105	10	68	28	110	24	115	16	95	20	50	33	50	9	110	9	110	22	95	6	85	22	100	15
100	8	55	14	53	20	75	28	25	24	50	22	90	30	115	12	110	20	115	30	80	23	85	32
120	27	85	32	85	38	28	28	115	24	142	34	154	37	125	43	20	20	60	38	75	20	105	20
130	45	70	21	110	28	150	37	5	32	12	44												

Q4/3-3 (Oblique accretion avalanche bed macroform - dipping to the east, 'flipped' clasts only)

210	10	255	26	280	16	256	15	180	15	345	8	358	20	310	27	285	20	315	35	200	49	345	14
250	28	232	7	285	8	290	2	240	60	310	8												

Q6/1-3 (Bimodal, massive, clast-supported gravel from large-scale, downflow-dipping, rhythmically-graded, tabular beds - 'flipped' clasts only)

75	52	330	70	90	48	55	84	165	65	195	58	25	58	135	35	354	45	260	55	25	48	15	38
30	67	42	27	100	18	90	80	230	25	20	35	345	44	125	42	35	76	115	70	330	50	40	56
50	54	108	54	130	26	255	23	65	44	85	70	55	74	150	45	65	55	100	49	90	24	52	48
90	67	170	58	335	17	45	27	25	80	245	57	170	36	45	18	115	52	55	36	100	60	155	65
55	77	130	70	80	60	185	43	90	37	352	30	68	56	320	38	325	36	352	35	130	74	95	48

Q8/1-1LHS (Pseudosynclinal macroform - east side)

130	57	65	64	90	48	190	78	135	35	100	32	170	35	115	35	295	26	60	30	235	32	95	54
110	58	65	58	70	22	100	57	95	40	90	67	95	54	135	58	165	32	82	18	56	65	125	55
125	42	70	50	150	56	230	26	100	60	100	77	104	38	108	55	70	64	8	25	28	35	20	40
105	64	150	66	195	43	75	35	110	68	125	12	102	55	150	28	92	42	65	70	210	28	255	25
135	36	70	68	63	32	190	68	100	44	120	54	48	45	45	36	100	40	35	45	15	32	55	45

QA/1-1 (Heterogeneous, unstratified gravel)

260	22	260	42	230	44	315	20	275	53	255	16	300	34	355	25	358	48	245	34	265	42	15	28
355	23	295	12	275	5	280	4	290	73	340	5	350	46	285	22	295	42	252	25	250	25	40	24
295	17	233	38	302	32	40	10	335	18	340	22	325	22	304	45	262	18	325	66	225	20	65	35
300	34	227	62	295	44	280	24	280	34	345	59	335	28	344	55	275	26	238	30	270	45	215	20
290	54	335	32	330	24	260	12	280	10	290	12	305	18	10	34	350	18	305	35	245	28	10	34

Q11/1-1 (Imbricate, polymodal, matrix-rich gravel with tabular geometry)

70	10	20	48	115	66	65	27	270	30	270	58	75	48	110	25	35	28	35	35	120	35	130	46
216	18	352	22	70	32	110	28	55	31	160	30	26	22	10	26	58	42	94	24	38	36	74	45
85	35	80	34	70	15	75	27	80	48	65	57	95	30	120	72	110	24	35	26	25	18	15	24
100	53	110	55	80	22	90	65	0	15	115	26	65	34	95	64	65	45	100	22	8	26	120	22
70	67	355	27	50	37	80	20	35	25	100	54	330	55	25	38	5	32	225	35	24	16	150	34

Q13/1-1aRHS (Large cross-bedded gravel or south-dipping avalanche beds of macroform - east side, full sample)

210	18	195	15	240	40	200	25	210	10	280	6	230	26	210	18	190	25	220	45	265	28	220	22
210	6	230	6	115	50	105	45	40	28	5	18	225	22	215	26	160	42	30	12	165	64	335	14
30	44	150	18	50	48	245	25	320	10	340	68	5	15	200	35	315	36	200	34	235	32	215	20
40	43	100	56	338	56	200	47	105	20	348	43	215	25	15	45	25	50	185	25	345	15	320	15
55	48	200	10	200	56	200	27	45	55	100	32	195	22	250	22	175	38	215	45	110	25	240	25

Q13/1-1aRHS (Large cross-bedded gravel or south-dipping avalanche beds of macroform - east side, 'parallel' clasts only)

210	18	200	25	195	22	160	42	215	45	215	20	210	6	200	10	210	18	175	38	165	64	240	25
195	15	240	40	245	25	230	28	215	26	220	45	235	32	280	6	230	8	200	27	225	22	250	22
200	34	265	28	150	18	200	56	210	10	215	25	190	25	185	25	220	22	260	35	200	47		

Q13/1-1aRHS (Large cross-bedded gravel or south-dipping avalanche beds of macroform - east side, 'flipped' clasts only)

30	44	5	18	15	45	345	15	100	56	100	32	40	43	40	26	340	68	315	36	335	14	105	20
105	45	55	48	320	10	348	43	25	50	320	15	115	50	110	25	50	48	45	55	5	15	30	12
338	56																						

Q13/1-1aLHS (Large cross-bedded gravel or south-dipping avalanche beds of macroform - west side, full sample)

45	44	350	14	70	8	230	37	140	28	220	56	20	12	175	15	195	8	145	25	165	50	35	12
350	5	355	6	0	36	30	43	350	9	357	41	335	42	15	32	185	28	25	10	195	40	175	32
40	5	180	16	185	16	40	67	200	56	5	26	190	26	205	16	35	12	315	28	165	45	20	6
0	43	223	59	85	17	355	23	335	33	310	44	170	30	165	22	325	36	195	28	185	35	195	34
205	17	302	30	40	57	350	31	25	9	35	60	200	25	210	38	170	26	10	10	25	15	15	34

Q13/1-1aLHS (Large cross-bedded gravel or south-dipping avalanche beds of macroform - west side, 'parallel' clasts only)

190	26	165	22	145	25	185	35	223	59	200	56	170	30	210	38	195	26	175	32	185	16	220	56
200	25	195	8	165	50	195	34	175	15	185	28	195	40	205	17	230	37	205	16	170	26	165	45
180	16	140	28																				

Q12/1-1sLHS (Large cross-bedded gravel or south-dipping avalanche beds of macroform - west side, 'flipped' clasts only)

45	44	355	6	30	43	335	33	35	60	326	38	35	12	350	5	302	30	40	67	26	9	20	12
26	10	20	6	40	5	70	8	355	23	357	41	335	42	315	26	15	34	0	43	0	38	350	31
5	26	15	32	10	10	65	17	350	14	40	57	350	9	310	44	35	12	26	15				

Q12/1-1bLHS (Large cross-bedded gravel or south-dipping avalanche beds of macroform - west side, full sample)

200	22	25	6	325	38	265	68	215	47	7	35	25	10	40	5	30	10	15	15	194	28	205	26
210	34	180	40	0	11	215	44	48	13	0	6	190	28	192	32	212	26	184	34	15	18	172	45
340	30	185	45	170	15	205	26	192	25	0	23	168	26	185	48	35	5	28	12	194	25	58	6
200	35	325	26	218	32	20	6	178	20	10	14	192	45	210	26	220	31	70	5	55	6	195	43
180	22	180	47	173	33	262	26	228	35	340	17	198	35	188	30	178	42	188	35	75	25	50	26

Q12/1-1bLHS (Large cross-bedded gravel or south-dipping avalanche beds of macroform - west side, 'parallel' clasts only)

200	22	185	45	265	68	192	25	192	45	188	30	168	35	195	48	210	34	180	47	215	44	198	35
212	26	194	28	200	35	170	15	205	28	228	35	192	32	220	31	194	26	180	22	218	32	262	28
190	28	185	48	178	42	205	28	190	40	173	33	215	47	188	25	210	28	184	34	172	45	178	30

Q12/1-1bLHS (Large cross-bedded gravel or south-dipping avalanche beds of macroform - west side, 'flipped' clasts only)

340	30	20	6	10	14	35	5	55	8	25	8	48	13	340	17	15	15	75	25	325	28	7	35
25	10	28	12	56	8	325	38	0	6	40	5	70	5	50	25	0	11	0	23	20	10	15	18

Q16/4-2 (Heterogeneous, unstratified gravel)

45	32	130	6	144	12	35	11	70	27	164	45	40	26	130	24	85	15	35	38	110	46	30	26
60	38	125	41	320	72	90	65	258	54	345	48	55	40	110	32	70	38	120	20	25	15	105	13
15	68	185	55	38	54	35	30	345	30	340	30	145	25	355	34	25	22	125	65	225	12	40	30
85	50	130	23	87	31	8	25	255	18	335	63	25	34	25	38	340	18	20	8	120	28	325	52
105	20	80	34	80	18	205	20	55	5	70	20	80	30	100	25	10	35	95	12	85	32	15	18

Q17/1-7RHS (Bimodal, massive, clast-supported gravel from large-scale, downflow-dipping, rhythmically-graded, tabular beds - 'flipped' clasts only)

315	32	210	5	20	45	345	58	90	35	245	12	85	38	345	16	155	12	355	15	30	34	295	38
230	20	280	38	330	12	235	32	45	28	50	25	280	16	325	38	330	25	305	35	45	58	145	18
45	55	250	36	325	52	350	34	55	55	325	18	10	44	350	22	135	30	115	30	350	15	30	28
230	52	285	22	345	34	5	18	335	30	55	45	75	60	35	42	175	54	340	25	75	48	10	35
280	48	315	24	355	28	280	48	135	15	25	22	250	34	355	26	280	24	325	25	285	48	330	25

Q18/1-1 (Heterogeneous, unstratified gravel)

10	48	0	30	30	82	282	40	283	12	185	24	170	16	335	42	55	34	155	48	10	23	25	57
355	23	340	33	120	34	35	46	103	36	5	38	322	52	177	59	0	10	60	26	85	32	355	37
175	34	10	54	48	12	60	35	20	16	232	24	170	30	335	14	28	22	232	36	346	38	312	15
135	10	320	24	348	25	355	25	25	55	170	42	275	28	88	45	332	38	314	68	290	48	305	27
285	34	95	16																				

Q18/1-4 (Heterogeneous, unstratified gravel)

220	15	200	40	5	40	90	50	312	68	255	28	285	25	290	16	160	8	230	54	290	30	310	5
40	35	170	54	280	15	225	32	350	14	100	22	50	20	35	10	325	50	55	55	230	3	80	10
10	20	120	44	285	28	340	18	270	28	95	25	30	45	320	25	255	45	20	48	100	30	325	10
350	24	160	6	40	34	75	25	325	34	290	30	70	45	255	23	310	43	80	60	355	40	220	30
310	22	240	28	240	18	325	55	270	55	320	40	325	18	330	54	338	22	345	28	340	53	55	14
155	8	340	14	325	64	285	52	335	24	35	28	30	24	300	18	5	16	305	25	255	32	350	25
290	34	285	28	10	36	40	64	50	21	320	34	20	62	320	18	340	62	5	40	80	48	0	40
340	70	15	50	325	46	285	34	280	45	300	55	330	40	10	10	140	15	190	16	60	20	330	58
0	18	350	54	320	66																		

Q21/1-5 (Imbricate gravel lag)

358	45	32	13	55	18	280	40	55	14	80	25	15	62	85	41	350	45	320	80	230	69	355	33
10	32	80	34	30	55	0	30	350	24	165	50	95	5	15	14	330	68	30	55	25	70	85	12
55	11	53	6	80	24	10	37	20	33	55	28	190	5	25	21	58	24	5	8	45	13	350	68
350	14	10	20	15	55																		

Q31/5-1LH6 (Oblique accretion avalanche bed macroform dipping to the south-southeast - full sample)

145	39	0	36	190	19	310	37	196	48	5	10	115	38	330	12	260	60	110	38	15	22	210	52
185	35	300	43	340	14	0	14	300	33	355	8	300	32	100	34	230	47	260	3	335	35	68	43
345	26	150	60	265	11	275	40	280	10	310	6	175	26	180	43	185	16	275	34	105	48	185	36
175	18	260	65	170	37	135	15	90	16	220	55	175	55	5	14	180	24	192	55	95	44	180	11
315	3	230	70	140	52	180	40	215	45	195	45	145	18	300	18	185	32	310	25	180	10	140	24

Q31/5-1LH6 (Oblique accretion avalanche bed macroform dipping to the south-southeast - 'parallel' clasts only)

145	39	170	37	90	18	200	32	180	43	110	38	210	52	230	70	185	35	140	52	215	43	175	26
230	47	192	55	85	43	175	18	135	15	220	55	175	55	185	18	105	48	185	38	150	20	180	40
185	45	145	18	180	24	95	44	180	11	190	19	198	48	115	38	100	34	185	32	180	10	140	24

Q31/5-1LH6 (Oblique accretion avalanche bed macroform dipping to the south-southeast - 'flipped' clasts only)

345	26	275	40	310	6	275	34	315	3	340	14	300	33	5	14	310	25	0	26	265	11	260	10
300	18	15	22	300	43	310	37	5	10	265	60	335	35	280	65	0	14	355	6	260	3	330	12

Q33/1-1 (Large cross-bedded gravel - full sample)

145	18	270	26	93	50	330	10	160	21	320	3	260	35	145	13	30	37	325	14	330	76	340	18
180	10	190	14	120	30	165	28	158	35	345	12	335	35	330	8	345	16	340	56	270	36	290	30
330	30	180	19	300	44	312	5	155	19	138	17	125	17	305	32	320	3	90	35	290	48	180	21
335	5	190	48	300	18	280	37	190	26	330	6	115	5	200	30	175	26	350	36	110	23	340	5
340	22	105	16	265	60	290	5	135	27	75	12	110	55	135	25	350	4	95	17	290	11		

Q33/1-1 (Large cross-bedded gravel - 'parallel' clasts only)

145	18	93	50	165	28	138	17	145	13	90	35	160	10	120	30	160	21	135	27	95	17	190	14
200	44	158	36	125	17	110	55	180	21	180	19	200	18	155	19	115	5	200	30	110	23	190	48
105	16	190	36	75	12	135	25																

Q33/1-1 (Large cross-bedded gravel - 'flipped' clasts only)

330	30	330	10	320	3	325	14	270	35	290	11	335	5	312	5	345	12	305	32	340	56	290	48
340	5	280	37	330	6	275	26	350	36	270	26	285	50	260	16	345	16	350	4	340	18	340	22
320	5	335	35	320	3	330	76	290	20	330	6	30	37										

Q33/1-2 (Inclined, plane-bedded gravel)

5	27	335	62	0	49	345	51	265	55	295	22	305	25	250	15	310	12	320	27	310	14	10	30
335	24	290	34	330	14	20	17	280	65	255	32	345	42	350	25	345	38	320	58	265	21	85	30
10	44	300	32	350	28	280	8	340	55	40	50	340	28	285	14	305	27	320	30	295	30	70	10
280	22	280	10	230	46	0	33	355	27	275	60	305	30	0	38	300	33	345	44	340	20	350	45
350	24	340	72	15	38	210	35	340	44	330	30	0	15	252	45	290	30	280	50	355	34	280	51
270	38	350	35	300	58	0	52	300	22	345	44	330	45	335	49	285	75	5	49	95	30	10	38
305	37	330	25	275	30	105	22	210	48	340	50	5	33	310	47	10	30	340	43	185	35	330	19
180	4	0	38	285	30	30	55	60	40	235	22	340	28	0	8	5	25	60	12	0	15	10	15
280	78	150	15	330	5	5	30	330	25	300	28	170	35	280	38	205	15	275	38	85	14	90	14
40	35	355	15	225	5	255	35	300	16	10	28	205	50	270	42	30	15	330	47	110	20	65	38
50	70	265	48	315	50	100	34	330	13	0	20	350	16	340	34	265	27	330	27	315	15	290	28
150	52	100	15	310	40	345	28	340	42	280	33	275	48	280	10	340	20	20	12	20	38	345	16
305	40	5	28	280	6	315	60	310	62	178	22	280	52	192	11	330	55	255	76	255	20	120	38
80	68	45	28	210	48	15	34																

Q33/3-1 (Heterogeneous, unstratified gravel)

335	35	15	18	10	38	130	38	300	8	15	52	95	34	5	42	340	15	0	18	280	27	320	51
300	64	0	30	280	68	335	30	165	12	350	34	305	68	350	28	320	21	345	64	345	38	10	52
285	42	330	16	325	40	350	44	320	20	255	44	330	18	215	45	330	27	340	50	75	30	350	43
355	32	50	32	265	30	245	8	110	15	345	32	245	15	280	22	0	52	300	50	300	15	15	46
325	24	255	50	315	52	30	55	310	34	310	5	140	16	345	32	340	37	295	55	210	44	305	12

Q25/1-1b (Bimodal, massive, clast-supported gravel from large-scale, downflow-dipping, rhythmically-graded, tabular beds - 'flipped' clasts only)

280	38	280	40	325	62	100	32	35	40	80	26	280	61	215	32	230	50	355	40	220	33	252	45
340	68	70	24	280	28	330	38	295	25	0	20	280	32	345	40	85	58	350	34	295	84	310	32
10	27	135	42	315	73	130	40	110	34	230	5												

Q25/1-1LHS (Imbricate, polymodal, matrix-rich coarse gravel with poorly defined convex-up bedding surfaces)

300	30	30	55	0	30	310	40	315	16	330	58	310	26	325	65	330	15	340	16	295	34	210	24
310	32	130	15	305	58	330	48	290	30	345	25	335	40	340	52	0	58	315	50	15	30	300	35
330	16	10	20	335	35	330	25	340	32	340	30	340	45	330	20	350	20	330	44	30	40	275	45
340	35	45	50	305	25	325	35	335	48	215	15	330	42	300	52	325	42	285	15	330	30	355	20
10	26	15	65	280	45	330	30	20	25	295	20	310	48	80	45	5	72	330	16	340	16	335	30

Q25/1-2 (Heterogeneous, unstratified gravel)

350	40	330	45	325	74	310	42	282	38	355	40	10	55	340	34	80	30	270	12	330	65	340	22
310	44	350	26	295	59	0	68	325	54	300	48	350	38	25	24	350	63	280	33	305	20	310	27
335	14	335	20	340	23	340	54	258	48	325	47	310	40	80	63	290	20	285	15	355	50	355	28
355	35	335	53	90	70	145	2	305	26	240	8	264	37	305	27	285	32	280	10	340	35	350	50
340	35	335	50	270	36	90	32	10	54	10	77	345	22	5	65	345	33	250	18	340	70	45	30
20	15	337	40	334	36	4	37	39	28	9	65	9	72	10	72	21	42	34	40	44	75	19	54
104	35	54	68	4	55	354	12	60	45	334	42	80	25	20	56	334	68	320	21	337	30	4	35
150	31	300	36	321	26	337	24	295	28	337	62	4	16	10	28	327	34	315	24	20	22	15	32
24	14	327	10	341	12	354	26	24	10	301	45	350	40	30	14	284	32	10	18	320	16	30	20
343	26	335	32																				

[1] Data format: azimuth dip of clast ab-plane (in degrees).

[2] Pit fabrics reported in Table 5.3 were calculated from the above data sets as:

- Q1 = Q1/1-3RHS + Q1/1-3LHS
- Q2B = Q2B/2-1
- Q3 = Q3/2-4LHS + Q3/2-4RHS
- Q4 = Q4/3-3 ('parallel' clasts)
- Q5 = Q5/1-2
- Q9 = Q9/1-1LHS
- QA = QA/1-1
- Q11 = Q11/1-1
- Q12 = Q12/1-1aRHS ('parallel' clasts) + Q12/1-1aLHS ('parallel' clasts) + Q12/1-1bLHS ('parallel' clasts)
- Q16 = Q16/4-2
- Q17 = Q17/1-7RHS
- Q18 = Q18/1-1 + Q18/1-4
- Q21 = Q21/1-5 + Q21/5-1LHS ('flipped' clasts)
- Q23 = Q23/1-2
- Q25 = Q25/1-1b
- Q26 = Q26/1-1LHS + Q26/1-2

APPENDIX 9

Paleoflow direction measurements from cross-bedded and cross-laminated sand within the Harricana glaciofluvial complex, Québec.

Pit number	Sedimentary structure	Measurements (in degrees)														
Q1	Cross bedding	275	275	245	265	265	270	260	245	250	305	233	242	258	232	250
		240	255	238	250	240	312	308	218	190	260	250	240	230	220	225
		225	225	220	225	220	285	263	272	282	265	265	270	215	275	230
		254	265	265	285	260	270	260	270	285	275	270	305	300	245	250
		272	264	265	300	285	261	260	260	260	230	250	263	260	255	255
		243	252	263	274	262										
Q2A	Cross bedding	170	180	175	180	175	180									
Q2B	Cross bedding	220	235	230	225	220	235	235	240	235	240					
	Cross lamination	200	210	205	200	200	200	210	190							
Q3	Cross bedding	190	188	180	170	188	140	185	200	170	215	200	150	195	175	185
		155	155	190	193	165	190	205	150	215	190	190	165	200	180	175
		215	215	230	210	220	215	215	205	210	205	230	230	233	225	230
		210	197	200	190	200	145	145	155	155	150	180	185	185	163	185
		165	180	185	205	190										
Q4	Cross bedding	185	195	175	190	190	175	190	200	180	185	195	190	190	190	200
Q5	Cross bedding	190	205	225	220	215										
Q8	Cross lamination	258	270	253	260	223										
Q11	Cross bedding	195	203	190	185	235	205	195	215	230	190	210	200	200	185	80
		145	185	153	180	185	198	145	174	192	180	135	180	188	200	150
		133	120	130	130											
Q12	Cross bedding	220	208	210	217	220	220	225	235	237	228					
Q16	Cross bedding	220	200	145	180	185	188	155	175	210	190	195	180	190	185	170
		155	140	130	180	140	170	185	170	190	174	185	185	185	185	175
		205	210	200	210	190	193	208	205	185	195	200	188	175	170	188
		198	195	190	210	207	200	227	212	194	220	230	214	223	218	217
	Cross lamination	308	308	317	320	311										
Q17	Cross bedding	148	170	175	172	210	190	205	172	218	225	130	145	180	195	150
		190	185	200	175	170										
	Cross lamination	135	145	180	110	145	135	140	140	155	155	165	155	145	165	135
		150	145	165	135	135	165	155	175	170	135	165	170	170	165	165
		150	135	150	145	180	155	150	180	140	150	170	180	140	162	145
		145	140	167	165	155	135	180	180	138	155	175	145	152	180	173
		165	188	180	190	188	185	195	195	185	190	173	188	188	178	188
		188	165	190	155	173	165	180	155	190	213	204	185	188	202	182
Q20	Cross lamination	200	195	180	185	195	195	190	172	195	215	210	210	190	205	215
		220	235	190	235	200	160	200	180	185	210	225	223	220	220	215
		200														
Q21	Cross bedding	225	210	205	205	210	170	220	188	200	180	180	180	155	180	185
		187	200	180	187	185	135	215	205	188	170	180	195	195	175	175
		190	180	220	195	210	240	255	250	255	245	255	245	255	245	235